Impurities and defects in, and isotope compositions of, gemstones

by

Mandy Yvonne Krebs

A thesis submitted in partial fulfillment of the requirements for the degree of

Doctor of Philosophy

Department of Earth and Atmospheric Sciences
University of Alberta

Abstract

Different laser ablation and mass spectrometry techniques and FTIR spectroscopy have been used to investigate elemental impurities, defects, and stable and radiogenic isotope compositions in natural diamond and ruby, with the aim of expanding previous research into diamond and ruby genesis, aiding exploration efforts and developing techniques to “fingerprint” a gemstone’s origin.

First I use FTIR and SIMS techniques to evaluate the basis for using microdiamonds as grade predictors for diamond deposits. Predictions of the macrodiamond grade of newly discovered kimberlites are commonly obtained using size frequency distributions of microdiamonds, based on the implicit assumption of a genetic relationship between all diamonds across the entire size range. Despite the success of this approach, such a genetic relationship between microdiamonds and macrodiamonds has not been placed on a sound scientific footing. In contrast to previous comparative studies on microdiamonds and macrodiamonds from single deposits, here all diamonds analyzed – from the Misery deposit, Northwest Territories, Canada - originate from the same microdiamond bulk sample (558 diamonds; ranging in size from 0.212 to 3.35 mm). The diamonds were analyzed for their carbon isotopic compositions and nitrogen aggregation and concentration characteristics, and based on this dataset statistical comparisons were conducted across the size range to assess cogenesis.

Overall, a general geochemical similarity of diamonds from across the different size fractions was established, reinforcing the use of size-frequency analysis to predict diamond grade in kimberlite diamond deposits.

A novel off-line laser sampling technique has been applied to analyzing high purity diamonds. Quantitative trace element data from high-purity gem diamonds from the Victor Mine, Ontario, as well as near-gem diamonds from peridotite and eclogite xenoliths from the Finsch and Newlands mines, South Africa, acquired using an "offline" laser ablation method show that we see the same spectrum of fluids in gem diamonds that was previously documented in fibrous diamonds, strengthening the link between the parental fluids of both gem and fibrous diamonds. Differences in trace element characteristics are evident between Victor diamonds containing silicate inclusions compared with Victor diamonds containing sulphide inclusions. The sulphide-bearing diamonds show lower levels of inter-element fractionation and more widely varying siderophile element concentrations - indicating that the silicate and sulphide-bearing diamonds likely formed by gradations of the same processes, via melt-rock reaction or from a subtly different fluid source.

Trace element characteristics of rubies from Greenland, Mozambique, Myanmar and Vietnam obtained using LA-ICPMS, TOF-LA-ICPMS and offline ablation followed by solution ICPMS show that, with the exception of a small number of elements that can substitute for Al^{3+} in the crystal structure (e.g. Ti, Fe), trace elements in ruby are present in mineral inclusions or along fractures. Thus, the absolute trace element abundances in rubies are primarily a function of impurity density. TOF-LA-ICPMS, applied to rubies for the first time, effectively maps trace element spatial variation in these gems and clearly demonstrates a mineral inclusion host in some rubies for elements such as Sr, Rb, U and Th.

Using the same offline laser ablation technique that was applied to the diamonds, followed by thermal ionization mass spectrometry (TIMS) we were able to measure radiogenic isotope compositions in ruby for the first time. Pb-Pb isochron ages for the two subpopulations in the Aappaluttoq suite (2558 ± 68 Ma for a low-V group and 3059 ± 380 Ma for the high-V group) are the first ever direct ages determined on a ruby suite, independent of associated minerals and - if reflecting ruby crystallisation or re-crystallisation - prove either their crystallisation or re-crystallisation and re-setting of the U-Pb system in the Neoarchean in SW Greenland.

We have demonstrated, using rubies from four different localities and two different deposit types, that Ni and Pb, in conjunction with established discriminator elements such as Ti and V show great potential for the use in geographical origin determination. A triangular plot of Ni-V-Pb makes it possible to distinguish between both the different localities and the different deposit types for all analysed rubies in this study. Measured $^{87}Sr/^{86}Sr$ and Pb isotope ratios show pronounced differences for rubies from different localities and deposit types, suggesting that radiogenic isotopes potentially offer a powerful means of provenance discrimination even for geologically similar deposits.

Preface

This thesis contains three separate manuscripts based on the findings of M.Y.K.'s Ph.D. research supervised by Prof. D. Graham Pearson.

A modified version of Chapter 2 has been published as: *Krebs, M.Y., Pearson, D.G., Stachel T., Stern R.A., Nowicki T., and Cairns, S. (2015): Using Microdiamonds in Kimberlite Diamond Grade Prediction: A Case Study of the Variability in Diamond Population Characteristics across the Size Range 0.2 - 3.4 mm in Misery kimberlite, Ekati Mine, NWT, Canada. Economic Geology 111, 503–525.* The samples were provided by Jon Carlson (Ekati), M.Y.K. conducted all of the analytical work, and wrote the paper. R.A. Stern assisted with SIMS analyses. T. Nowicki organized the samples and provided crucial input on the sample origin. D.G. Pearson and T. Stachel, supervised the research project and provided valuable discussions and manuscript edits. S. Cairns provided additional funding, crucial for the analytical work in this project.

A modified version of Chapter 3 will be submitted to Chemical Geology as*: Krebs, M.Y., Pearson, D.G., Stachel, T., Laiginhas, F.A.T.P., Woodland, S., Chinn, I., and Kong, J. Trace elements in Gem-Quality Diamonds – Origin and evolution of diamond-forming fluid inclusions.* M.Y.K. conducted the analytical work on the Victor diamond suite and wrote the paper. Laiginhas, F.A.T.P conducted the analytical work on the Finsch and Newlands diamonds. D.G. Pearson and T. Stachel supervised the project and provided valuable discussions and manuscript edits. S. Woodland assisted with the analytical work. I. Chinn and J. Kong provided the samples.

Chapter 4 constitutes a study on rubies. M.Y.K. performed most of the analytical work and wrote the manuscript. Sample preparation and most of the analytical work and wrote the paper. Y.B. conducted TOF-LA-ICPMS at TOFWERK AG, Thun, Switzerland. C. Sarkar assisted with analytical work at the University of Alberta. A.J. Fagan and G.E. Harlow provided ruby samples and contributed valuable information on the origin of the samples and geological framework. D.G. Pearson supervised the project and provided valuable discussions and manuscript edits. The manuscript has not yet been submitted.

Acknowledgements

First and foremost I would like to thank my dissertation advisors Dr. D. Graham Pearson and Dr. Thomas Stachel. Without their guidance and support this work would not have been possible. I would like to thank Graham for always being available for discussions and problem-solving despite his hugely busy schedule and large number of graduate students. I am also thankful for the many opportunities for attending conferences where I have had the opportunity to present my research and pursue constructive discussions with other researchers. Thank you Thomas Stachel, for always having an open door and for countless insightful and encouraging comments that greatly improved this work.

Many thanks also go to Long Li, Robert Luth, Emma Tomlinson and Sarah Gleeson for agreeing to be examiners during my Candidacy exam and/or my Thesis defense. Both experiences provided fruitful discussions that ultimately improved this work.

Several other individuals have provided useful advice or instruction throughout the course of this project. Dr. Sarah Woodland is thanked for proving training and assistance in clean room procedures, solution ICPMS measurement and, in conjunction with Dr. Yannick Busweiler, in offline laser ablation procedures. Dr. Chiranjeeb Sarkar provided assistance and training in Sr and Pb separation chemistry and isotope measurements using TIMS. Thanks to Dr. Richard Stern and Dr. Yan Luo for their help during SIMS and LA-ICP-MS analyses and Martin von Dollen and Anna Oh for their help with sample preparation. I also thank Mike McCubbing and his staff at the SRC for generously providing both the facilities and their expertise for sieving of the microdiamonds. Many thanks also to Qiao, Chiranjeeb and Pedro for always being available for questions, no matter how trivial, and discussions about trace element and isotope data.

Samples used in this study were generously supplied by several companies, research institutes and individuals. Jon Carlson (Ekati diamond mine) is thanked for providing a

comprehensive microdiamond bulk sample from the Misery mine in the Northwest Territories, Canada. De Beers Canada provided large high quality diamonds from the Victor mine in Ontario, Canada. Andrew Fagan and True North Gems provided several gem quality rubies from the Aapaluttoq deposit in SW Greenland and from the Namahaca deposit in the Montepuez district, Mozambique. George Harlow from the American Museum of Natural History is also thanked for providing gem quality rubies from several localities in Myanmar and from Luc Yen, Vietnam.

Through Graham Pearson, funding was received from the Canada Excellence Research Chairs Program. Additional funding was received from The Northwest Territories Geoscience Office (NTGO) for analyses in Chapter 2 and from the Society of Economic Geology (SEG) and the Geological Society of America (GSA) for analyses in Chapter 3.

Thanks also to all of my fellow grad students in EAS, especially Kate, Lauren, Matt, Nicole, Janina, Julia, Pedro and Yannick, making the U of A an excellent research (and more) environment with an excellent group of people.

And last but not least, I would like to thank my sister Alina for her continuous moral support that has played a huge part in helping me stay balanced during my PhD, and Vlad without whose unquestionable support, patience and understanding this past year I would not be where I am now.

Contents

4 New Approaches to Constraining Ruby Provenance using Sr - Pb Isotopes and Trace Elements 107

List of Figures

List of Tables

Chapter 1

Introduction

Throughout history gemstones have been highly prized and sought after, inspiring myths and superstitions. They have been esteemed as religious symbols, as talismans, as symbols of rank and status, and for their purported medicinal value. Today, although some myths and superstitions persist, gemstones such as diamond, and the gem corundum varieties sapphire and ruby are mostly popular as precious stones in jewellery. Furthermore, both diamond and corundum are extremely valuable for industrial usage. The extreme physical properties of diamond, i.e., its unique Mohs hardness (10), and very high density, refractive index, dispersion and thermal conductivity, make it suitable for use in cutting, grinding, drilling, and polishing procedures. Corundum, due to its high melting point of 2040 °C and hardness of 9 on Mohs scale, is used industrially as an abrasive, as ceramic additive in scratch-proof varnish, as additive to assist the slip-resistivity of materials and to fire-proof materials. For industrial purposes, synthetic diamond and corundum are usually used.

Gemstones have always been associated with specific countries and mining localities by virtue of their outstanding beauty and quality, for example, a ruby of an "intense, highly fluorescent red" was sometimes called "Burma-type," or "Burma-like," even when the ruby was not mined in Burma, and until the middle of the 20th century a diamond or gemstone was classified by "mine-type", that was strictly based on overall quality and appearance or color. In the 1940's and 1950,'s the Gemological Institute of America (GIA), the main provider of education services and diamond and colored gemstone grading reports, along with others in the gemology field, developed the system of quality analysis for diamonds, resulting in a new diamond classification scheme. Around the same time Dr. Eduard J. Gübelin, the father of the science of determining the origin of gemstones, proved that it was possible to identity a gemstone's geographical origin and sometimes even the exact mine it came from based on the gemstone's inclusions or microscopic features rather than using its overall appearance (Hughes, 1990). This led to increased interest in different mining sources, the science of gemstone geographical origin determination, and gemological laboratory country-of-origin reports which are used by every auction house today.

In addition, gemstones have become the object of intense research efforts, to understand the geochemical and mineralogical environment required for their formation by focusing on contributing agents such as temperature, redox reactions, chemistry of fluids and source of trace elements.

Diamond has been intensively studied over the last 40 years, fundamentally shaping our understanding of the mantle environment required for diamond precipitation, and thereby, aiding the development of new exploration models, while at the same time providing extraordinary information on our planet's interior, such as the deep carbon cycle or the migration of mantle fluids (Shirey et al., 2013, and references therein). Research on gem corundum, rubies and sapphires, has also increased significantly over the past two decades, mostly due to economic geologists realizing the importance of having precise knowledge of the mechanisms of formation and the origin of the mineralizing fluids in the prospecting and mining of gemstone deposits (e.g., Dissanayake and Rupasinghe, 1993; Mendis et al., 1993). Another aspect of gemstone research focuses on the development of a chemical 'fingerprint'. The predominant use of such a fingerprint lies in the geographical discrimination of gemstone sources, because the geographical origin has a large impact on a gemstone's value, but there are other applications such as the discrimination of synthetic from natural and treated from untreated gems.

In many cases this research focuses not on the gemstones themselves, especially in diamond research, but on mineral or fluid inclusions – unwanted blemishes in the gemstone trade – that were incorporated during growth and from a genetic standpoint represent some sort of sample of the growth medium.

In this study I focus on the expansion of previous research into diamond and ruby genesis, aiding exploration efforts and developing a gemstone's chemical 'fingerprint', by focusing on elemental impurities, defects, and stable and radiogenic isotope compositions in natural diamond and ruby. In Section 1.1 and 1.2 I summarize the current knowledge and methods of diamond and ruby research aspects relevant for the frame of this thesis.

1.1 Diamond

Diamond, mineralogically the cubic high-pressure phase of elemental carbon, is one of the three native carbon minerals on Earth (along with graphite and lonsdaleite) and can crystallize throughout the mantle below about 150 km and also occur metastably in the crust (Shirey et al., 2013; Stachel, 2014). Diamond is a rare mineral, occurring at the part-per-billion level, ranging from zero (non-diamondiferous kimberlites) up to about 2 ppm (i.e. 10 carats/ton for the most diamondiferous volcanic host rock) (e.g. Richardson et al, 1984; Haggerty, 1999), within kimberlite. As a trace mineral it is unevenly distributed and is a xenocrystic phase within kimberlites and other less common volcanic rocks (olivine lamproites and ultramafic lamprophyres), which bring it to the surface and host it. One exception to this are diamond occurrences in metamorphosed crustal rocks. Diamonds can also occur in secondary deposits that result from erosion of primary deposits and transport and re-sedimentation of diamonds in rivers and along oceanic coastlines.

1.1.1 Origin of diamond

The growth of diamonds is unrelated to their volcanic host rocks. Instead, mineral inclusion studies indicate that diamonds have grown predominantly within peridotite and eclogite in the lithosphere, and this is verified by the occurrence of diamondiferous xenoliths of these inferred host rocks (Stachel and Harris, 2008). Peridotite makes up the bulk of the upper mantle and includes lherzolite, harzburgite and extremely depleted dunite. Lherzolite, moderately depleted, is composed of olivine, orthopyroxene, clinopyroxene, and garnet. Harzburgite is formed when increasing depletion removes clinopyroxene from the assemblage. Even more extreme melt extraction (>50% melt removed) removes both pyroxenes from the residue, resulting in dunite, which is composed of >90% olivine. Eclogite, the high pressure equivalent of oceanic basalt, is composed of ≥90% clinopyroxene and garnet in roughly equal proportions.

Rare diamonds are derived from the sublithospheric mantle, called "superdeep". Their mineral inclusions reflect, like lithospheric diamonds, their host rocks with bulk mafic and ultramafic compositions, although the mineralogy differs according to phase changes with depth (Stachel et al., 2005; Kaminsky, 2012).

Diamond formation in the lithosphere is restricted to regions where lithospheric mantle reaches into the diamond stability field to establish a "diamond window", defined as the depth range between the graphite-diamond transition and the base of the lithosphere (Fig. 1). These regions are generally restricted to Archean cratons, remnants of old crustal domains that have survived destructive tectonic processes for billions of years, that retained deep reaching lithospheric mantle roots, thicker and colder than younger continental lithosphere. Typical continental lithosphere extends to depths of ~100 km, whereas cratonic "keels" can be as deep as 250 km (Boyd and Gurney, 1986). These lithospheric keels are rigid and largely stripped of heat-producing elements, resulting in cooler temperatures in comparison to convecting asthenospheric mantle at similar depth (e.g., Rudnick and Nyblade, 1999), and have a lower oxygen fugacity (eg., Pollack and Chapman, 1977; Foley, 2011), resulting in temperatures and pressures favorable for diamond formation, i.e. 900-1500°C and 50-60 kbar, respectively (Haggerty, 1986). A close association between diamondiferous kimberlite and Archean cratons, known as "Clifford's Rule", was first observed by Clifford (1966) and revised by Janse (1994), and forms the basic principle in diamond exploration.

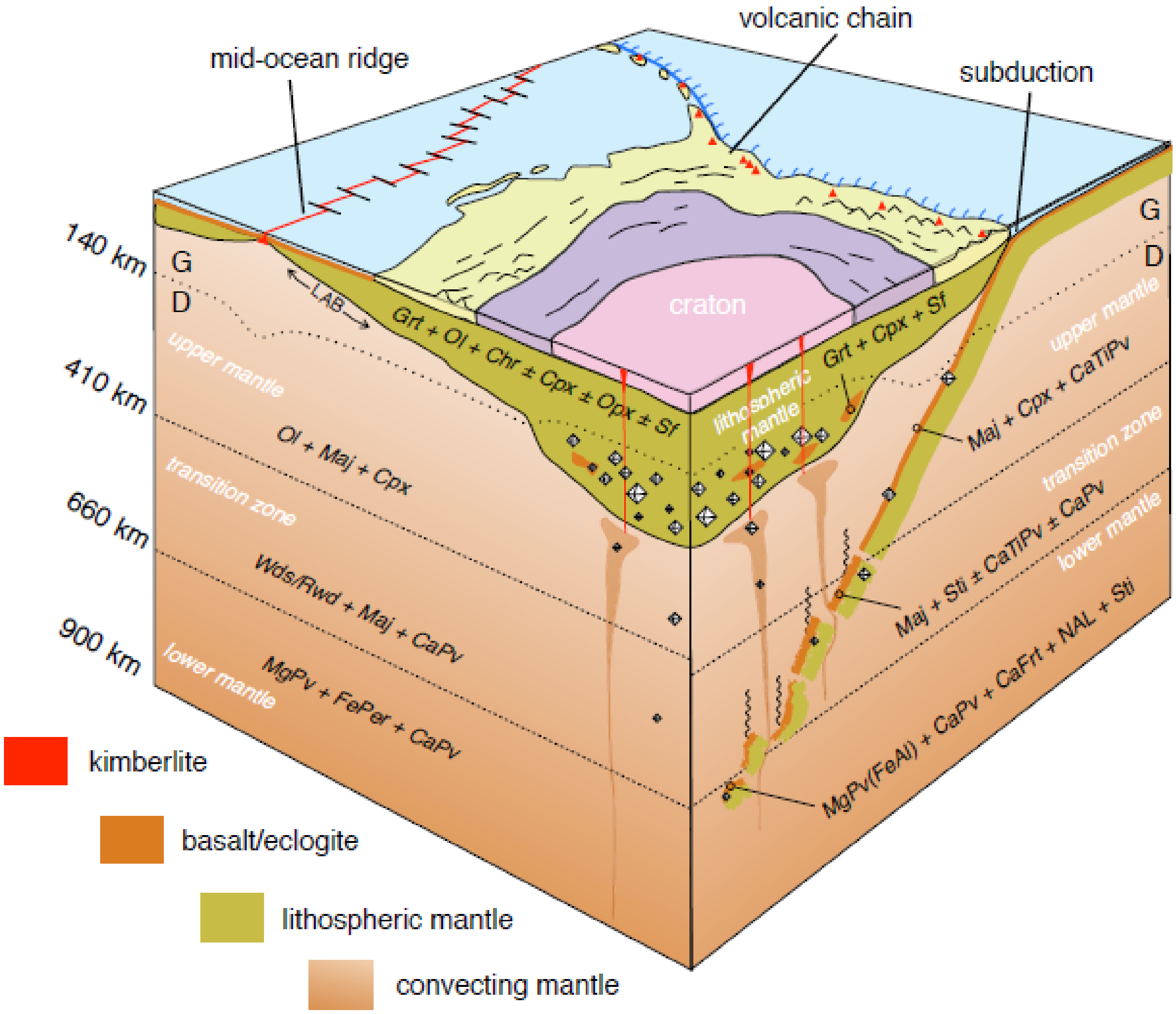

Figure 1.1: Block diagram taken from Figure 2 of Shirey et al., 2013, redrawn from an original by Tappert and Tappert (2011) with additions, showing the basic relationship between a continental craton, its lithospheric mantle keel and diamond stable regions in the keel, and the convecting mantle. Under the right f_{O2}, diamonds can form in the convecting mantle, the subducting slab, and the mantle keel. (Figure 2 from Shirey et al., 2013 redrawn from an original by Tappert and Tappert (2011) with additions). G=graphite, D=diamond, LAB=lithosphere/ asthenosphere boundary, Ol = olivine, Chr =chromite, Sf = sulfide, Cpx = clinopyroxene, Grt = garnet, Maj = majorite, Wds = wadsleyite, Rwd = ringwoodite, CaPv = calcium perovskite, MgPv(FeAl) = magnesium perovskite, FePer = ferropericlase, CaTiPv = calcium-titianium perovskite, Sti = stishovite, NAL = new aluminum phase, CaFrt = calcium ferrite, Mineral assemblages give the expected inclusions to be found in peridotitic or ultramafic (left) and eclogitic or basaltic (right) rock compositions.

1.1.2. Diamond exploration and deposit evaluation

Diamond exploration is a complex, long term process that can be broken down into six different stages. The first step is the identification of likely exploration targets, usually through a combination of different methods, such as geophysical techniques, geologic modeling, and indicator mineral analysis. Once targets are identified, they are tested using drilling, to determine whether or not the rock is kimberlite, and micro-diamond analysis of kimberlite intercepts using caustic fusion to test for the presence of diamonds and determine their size distribution. If the results of this early stage evaluation are favourable the target is tested for larger diamonds. To do this mini-bulk samples are taken and their macro-diamonds analysed (from the dense media separator (DMS), 1-100 tonnes). Subsequently, the grade and value will be tested via bulk sampling and analysis of diamonds from the DMS (>100 tonnes). This fourth stage determines grade and stone value and if successful sets testing for economic viability in motion. This stage involves feasibility studies, environmental studies and socio-economic studies. The final stage is the development of the mine, including licensing, permitting, design and construction.

Diamond exploration relies heavily on research on diamonds and their associated mineral inclusions obtained from existing deposits for the development of new exploration models.

1.1.3 Diamond morphology

Diamond occurs in four main forms: (i) monocrystalline diamond (octahedral and cuboid), including twins or aggregates of a few crystals, (ii) coated diamond, i.e., single crystalline diamond with fibrous overgrowth, (iii) fibrous cuboid diamond, and (iv) polycrystalline diamond aggregate (Stachel, 2014 and references therein). Monocrystalline diamonds, micro (<1 mm) and macro (>1 mm), grow via smooth dislocation and smooth hopper growth (producing concave crystal faces) and often display a complicated internal growth history with episodes of resorption and regrowth. The transition from smooth growth for single crystal diamonds to rough growth for fibrous and polycrystalline diamonds reflects increasing supersaturation and growth rate (Sunagawa, 1984). Coated diamonds, therefore, represent two distinct stages of diamond precipitation. Fibrous diamonds are produced by dendritic growth, which tends to incorporate many sub-micron sized inclusions of the growth medium. Polycrystalline diamonds are of varied origin, e.g. mantle-derived (framesite and boart) or of impact origin (yakutite and possibly carbonado).

Resorption of diamond, either in the transporting kimberlite or lamproite magma or during mantle residence, leads to secondary shapes by developing rounded dodecahedral faces at the expense of primary cubic and octahedral faces (Orlov, 1977; Harte et al., 1999).

1.1.4 Defects in diamond

Imperfections in the crystal lattice of diamond are the result of lattice irregularities, extrinsic substitutional impurities or interstitial impurities, introduced during or after diamond growth. They affect the material properties of diamond, such as color and electrical conductivity. Certain defects, e.g. platelets (nm to μm sized planar defects in the diamond lattice) and hydrogen defects, can be used to gain information of the growth environment and mantle residence history, and can also be used to distinguish natural from synthetic or enhanced diamonds.

1.1.4.1 Nitrogen

Nitrogen is the most common impurity in diamond, substituting for carbon in the diamond lattice, and variable amounts may be incorporated during diamond growth, likely depending on kinetic factors related to the speed of diamond growth (Boyd et al., 1994) and/or variations in the availability of N during diamond precipitation (Stachel and Harris, 2009).

Diamonds with measureable nitrogen, classified as Type I, are sub-divided based on their nitrogen aggregation state (relative abundance of Nitrogen (in at. ppm) in the moderately aggregated nitrogen A centre and the fully aggregated B centre expressed as %B =100 IaB / [IaA + IaB]), into Type Ib, when nitrogen is single substitutional, and Type Ia, when nitrogen has aggregated within the carbon lattice (Evans and Qi, 1982). For diamonds containing aggregated nitrogen there is a progression from pairs of nitrogen atoms (A-center, Type IaA) to groups of four atoms surrounding a vacancy (B-center, Type IaB). Most diamonds contain appreciable nitrogen in both the A- and B-centers (i.e., 10-90 %B) and are classified as Type IaAB (Evans et al., 1995). Diamonds with nitrogen contents below the limit of detection of

FTIR spectroscopy at about 5–10 at.ppm, are classified as Type II, and are subdivided further based on their boron content into boron-free (Type IIa) and boron-bearing samples (Type IIb).

The inter-relationships of nitrogen content, nitrogen aggregation state, mantle residence time, and mantle residence temperature can be used to constrain either the mantle residence time or the time-averaged residence temperature of a diamond from the content and aggregation of nitrogen (Taylor et al., 1990). Temperatures derived by this method usually compare reasonably well to those obtained by mineral inclusion based geothermobarometry (Leahy and Taylor, 1997).

1.1.5 Carbon isotopes

The carbon isotopic composition of diamond depends upon the carbon isotopic composition of its growth medium. This relationship makes it a useful geochemical fingerprint that can help determine the source of the carbon and give insight into the formation of diamond and possibly into its source rock. Carbon has two stable isotopes, ^{12}C and ^{13}C, their ^{13}C/^{12}C ratio (expressed as δ^{13}C) is measured relative to the international Vienna Pee Dee Belemnite (VPDB) standard and reported in parts per thousand (‰).

Globally, diamonds from peridotitic sources show a unimodal distribution in δ^{13}C around –5 ‰, with most values lying between –10 and –1‰ (e.g. Stachel et al., 2009). Diamonds of eclogitic paragenesis display a much wider range of values but also show a prominent mode at -5‰. The common mode at -5‰ is the generally accepted value for mantle derived carbon (Deines, 1980). The low δ^{13}C values within some eclogitic diamonds are suggested to derive from original organic matter recycled into the mantle via subduction zones (e.g., Navon, 1999).

1.1.6 Diamond Ages

Monocrystalline diamonds are commonly dated by radiometric dating of their silicate and sulfide inclusions, using the isotopic systems samarium-neodymium (Sm-Nd) and rhenium-osmium (Re-Os). A comprehensive review on inclusion-based dating of diamonds was presented by Pearson and Shirey (1999), with recent updates in Stachel and Harris (2008), Gurney et al. (2010) and Shirey et al. (2013). Peridotitic suite diamonds containing harzburgitic inclusions are thought to have formed dominantly in the Paleoarchean, those with lherzolitic inclusions in the Paleoproterozoic to Mesoproterozoic (Stachel, 2014). Eclogitic suite diamonds have been dated to between 2.9 and 0.99 Ga (e.g., Shirey et al., 2013).

Generally, most fibrous diamonds are thought to have formed within less than 5 Ma of the age of kimberlite eruption based on low nitrogen aggregation states and the similarity of their fluid inclusions to kimberlitic fluids (e.g., Gurney et al., 2010), with only a small percentage having formed tens to hundreds of million years before eruption of their host kimberlite during earlier diamond-forming events (Timmerman et al., 2018). The majority of known kimberlites, and thus fibrous diamonds are Phanerozoic; however, there are exceptions, e.g. the fibrous diamonds found in the Archean Wawa metaconglomerate in Canada (Smith et al., 2012).

1.1.7 Diamond formation

The widely accepted model of diamond formation in the mantle is regarded as a metasomatic process involving redox reactions associated with melt/fluid infiltration (Deines, 1980; Luth, 1993; Gurney et al., 2005). Diamond will crystallize when mobile carbon, as hydrocarbons, carbonate, or methane is precipitated from the fluid, either by the reduction of CO_2- or CO_3^{2-}-species or by the oxidation of methane (CH_4) species, depending on the relative redox states of the fluid and wall rock (Rosenhauer et al., 1977; Eggler and Baker, 1982, Taylor and Green, 1989). Based on comparisons of geothermobarometric data with hydrous (-carbonated) solidi, diamond formation in lherzolitic and eclogitic substrates is thought to occur in the presence of a melt, whereas harzburgitic diamonds are thought to form under sub-solidus conditions (Stachel and Luth, 2015). Under such conditions, the increased solidus temperature associated with reduced fluids is permissive of melt-absent diamond formation in lherzolite and eclogite as well.

Until recently, it was assumed that the oxygen fugacity (fO_2) of the lithospheric mantle is buffered by ferrous–ferric iron equilibria in the constituent rocks. However, in a recent study Luth and Stachel (2014) showed that the buffering capacity of depleted cratonic peridotite (the main diamond substrate) is so low that the fO_2 of lithospheric mantle is effectively fluid- rather than wall rock-buffered. This inability of cratonic peridotites to effectively buffer oxygen fugacities when infiltrated by CHO or carbonatitic fluids led Luth and Stachel (2014) to propose that diamond formation in cratonic peridotites occurs by an oxygen-conserving reaction in which minor coexisting CH_4 and CO_2 components in a water-rich fluid react to form diamond ($CO_2+CH_4=2C+2H_2O$) and not by rock-buffered redox reactions as previously thought. This reaction is driven by decreasing solubility in carbon species in cooling (isobaric or during ascent) water-maximum fluids (Stachel and Luth, 2015). Due to the absence of adequate thermodynamic data the redox buffering capacity of cratonic eclogites cannot be quantitatively evaluated at this time but their much higher Fe contents indicates that it hs to be significantly higher than for peridotites.

1.1.8 Diamond-forming Fluids

The metasomatic origin of diamond has been established by various methods, including trace element compositions of diamond inclusions (e.g., Stachel and Harris, 1997b; Tomlinson et al., 2009) and textural relationships within diamondiferous xenoliths (Taylor et al., 2000; Spetsius and Taylor, 2002) but also direct observation of diamond-forming fluids preserved as inclusions in diamonds, that are referred to as high density fluids (HDFs) in the literature (e.g. Navon et al., 1988). It is important to note that while the diamond-forming metasomatic agent is referred to as a fluid, in reality it may be a supercritical fluid, a melt or a miscible mixture of the two, as the pressure for diamond-bearing mantle (>150 km) is near the second critical end-point (disappearance of the solidus) in a lherzolite-H_2O-CO_2 system (Wyllie and Ryabchikov, 2000).

Due to the chemical inertness and robust nature of diamond, fluid inclusions in natural diamond are the best preserved samples of mantle fluids and, therefore, the best source of information on processes of diamond growth, the source and evolution of diamond-forming fluids, and on deep mantle metasomatism in general. Fibrous and cloudy diamonds are characterized by high abundances of high-density fluids (HDFs) ± daughter minerals trapped during diamond growth and, as such, have been the subject of extensive research during the last two decades. The fluid compositions are typically measured for major elements by electron microprobe (e.g., Navon et al., 1988; Izraeli et al., 2001, 2004; Tomlinson et al., 2006, Weiss et al. 2009, 2013, 2015; Klein-BenDavid et al., 2007, 2009), and for trace elements by INAA (Schrauder et al. 1996) and ICPMS, both by “online” (Tomlinson et al. 2005, 2009; Zedgenizov et al. 2007; Rege et al., 2010; Weiss et al. 2011, 2013, 2015) and "offline" (Klein-BenDavid et al., 2010, 2014) ablation techniques. These studies resulted in the identification of two wide compositional arrays in the major-element compositions of HDFs (Fig. 2); One array ranges from a silicic end-member to a low-Mg carbonatitic end-member, and a second array extends between a saline end-member and a high-Mg carbonatitic end-member. Trace elements measured in diamond HDFs from worldwide sources were found to display a limited range of fluid trace element patterns varying between two end-members: a flat, unfractionated pattern ("planed") and a highly fractionated ("ribbed") pattern (Fig. 1.3). As the observed trace element patterns show similarities to those of Group I and II kimberlites and carbonatites, a direct relationship between these melts and HDFs was suggested.

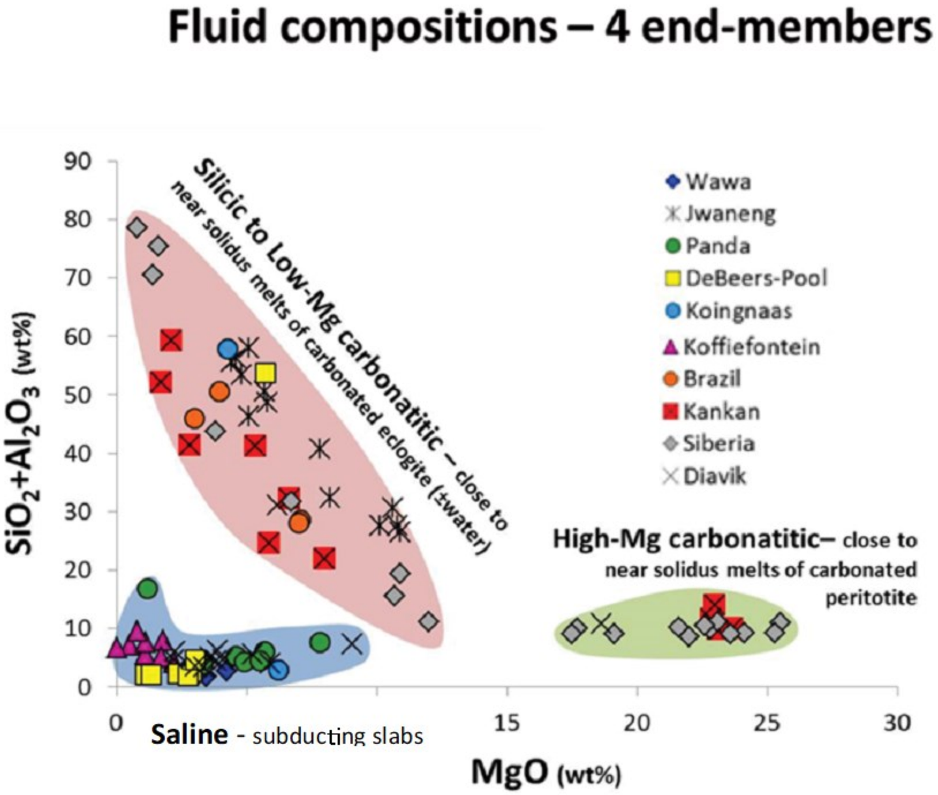

Figure 1.2: SiO_2+Al_2O_3 vs. MgO in HDFs (wt% on a water- and carbonate-free basis). Figure modified from Weiss et al. (2015). The high-Mg carbonatitic compositions are close to experimental near-solidus melts of carbonate-peridotite, while the low-Mg carbonatitic to silicic HDFs form an array close in composition to experimentally produced fluids/melts in the eclogite+carbonate ±water system (Weiss et al., 2009). Data points include HDF compositions from the published literature.

To further constrain the origin of diamond-forming fluids, radiogenic isotope characteristics have been measured by combustion (Akagi and Masuda, 1988) and more recently by "offline" laser ablation (Klein-BenDavid et al., 2010, 2014; Weiss et al., 2015). While major and trace elements may be modified by a variety of mantle processes and stable isotopes can be fractionated during the diamond forming process, radiogenic isotopes are unaffected by mineral fractionation and reflect more the time-integrated effects of radiogenic decay together with modification by mixing/metasomatism or interaction with isotopically distinct sources. Therefore, radiogenic isotope ratios can provide useful information on mantle processes as well as the time-integrated evolution of diamond forming fluids. Klein-BenDavid et al. (2010), for example, have shown that fluids in fibrous diamonds have Sr isotopic compositions too radiogenic and Nd isotopic compositions too unradiogenic to be related just to the kimberlite hosting the diamonds and Klein-BenDavid et al. (2014) proposed a multistage evolution of the diamond forming fluids that requires a contribution from an ancient source component, likely within the subcontinental lithosphere.

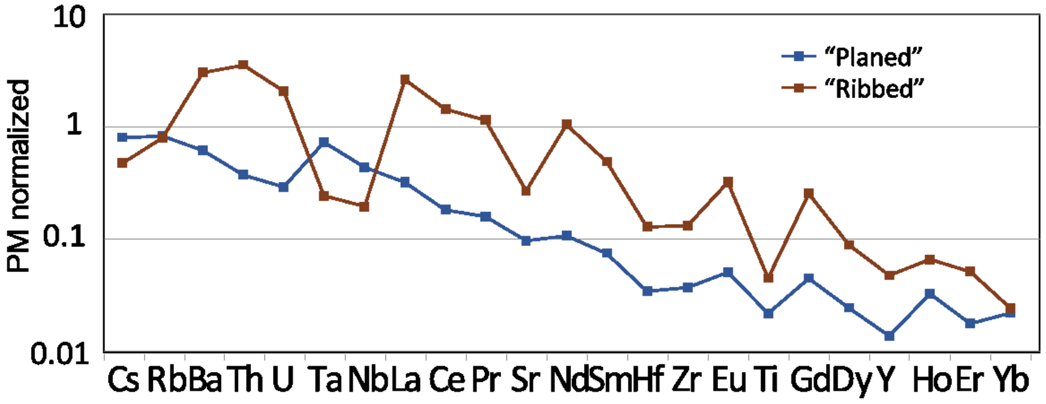

Figure 1.3: Primitive-mantle-normalized (McDonough and Sun, 1995) incompatible element pattern demonstrating the two common patterns of HDFs in fibrous diamonds, "planed" and "ribbed", obtained by LA-ICPMS. Using this analytical method, the uncertainties on the values of Yb and Lu are large and they can only be regarded as qualitative. Reproduced from Weiss et al. (2013).

Studies of fluid inclusions in diamond are still mainly carried out on fibrous diamonds, because of the extremely low concentrations of impurities that monocrystalline diamonds contain. However, trace element systematics on monocrystalline diamonds have been acquired both by "online" (Rege et al., 2010) and "offline" (McNeill et al., 2009, Melton et al., 2012) laser ablation. These studies found that trace element systematics seen in monocrystalline diamonds appear, broadly, to be similar to those seen in fluid-rich diamonds from a variety of locations, suggesting that their associated HDFs may share a chemical link. This is supported by Tomlinson et al. (2009), who, based on similar trace element signatures, argued that silicate inclusions trapped within fibrous diamonds and those trapped within octahedral monocrystalline diamonds have equilibrated with fluid of similar composition, and by Jablon and Navon (2016), who discovered rare fluid inclusions in monocrystalline diamonds that showed similar major element chemistry ranges to fluid-rich fibrous diamonds (Fig. 1.4).

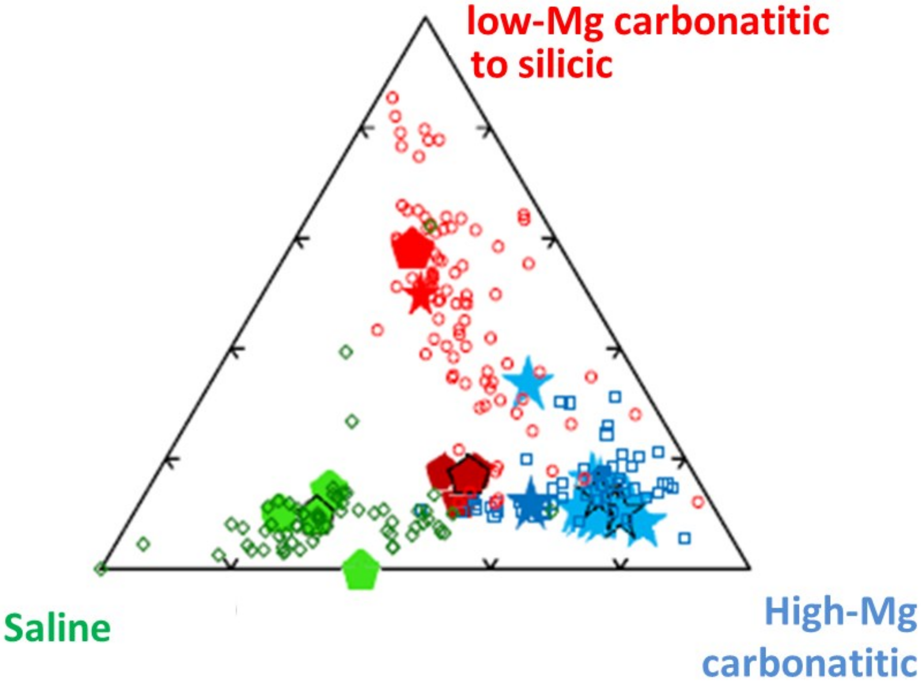

Figure 1.4: Major element composition of microinclusions in twinned and fibrous diamonds. Large symbols - microinclusions in twinned diamonds, Open symbols – HDFs in fibrous diamonds. Shades of blue – High-Mg carbonatitic compositions, green – Saline compositions, Shades of red – low-Mg carbonatitic to silicic compositions. Modified from Jablon and Navon, 2016.

Melton et al. (2012) on the other hand found that, with one exception, the trace element patterns of the analysed monocrystalline diamonds did not yield a faithful representation of the diamond growth medium, suggesting that the trace element content in monocrystalline diamond is not hosted in nano-inclusions of the diamond forming fluid, but instead likely reflect complex and variable mixtures of mineral inclusions.

1.2 Gem corundum

Ruby and sapphire, varieties of natural corundum (α-Al_2O_3) crystallized in the trigonal crystallographic system, count amongst the most precious gemstones. Their colour is dependent on so-called chromophores, the elements Cr, V, Fe, Ni, Ga, Ca and Mn that are common impurities in the corundum structure, giving the minerals their color (Schmetzer and Bank, 1980; 1981; Ferguson and Fielding 1971; 1972). The deep red colour of ruby is caused by the substitution of a small quantity of Cr^{3+} for Al^{3+}, the more Cr^{3+} the more intense the colour. The blue color of sapphire is given by Fe^{2+} -> Ti^{4+} intervalence charge transfer (Lee et al., 2006), the color yellow is caused by Fe^{3+}, green by V^{3+} or a combination of Fe^{2+} -> Ti^{4+} intervalence charge transfer and Fe^{3+}, orange by Cr^{3+} + Fe and purple by Cr^{3+} + Fe^{2+} -> Ti^{4+} charge transfer.

1.2.1 Geology of gem corundum deposits

Deposits of gem-quality corundum are well distributed all around the world and occur in various different geological settings, generated via several different petrogenetical processes. A recent comprehensive review is presented by Giuliani et al. (2014).

Corundum forms in mafic and siliceous geological environments, always associated with rocks depleted in silica and enriched in alumina, because in the presence of silica, Al will be preferentially incorporated into aluminosilicate minerals such as feldspars and micas (Garnier et al., 2004). Gem corundum is rare because it also requires the presence of Cr, Fe, and Ti to substitute for Al in the structure (Muhlmeister et al., 1998, Abduriyim and Kitawaki, 2006), and thermobarometric conditions favorable for its crystallization and stability (Kievlenko, 2003, Simonet et al., 2008).

Two major geological environments have been found to be favorable for the generation of gem-quality corundum; amphibolite- to medium pressure granulite-facies metamorphic belts and alkaline basaltic volcanism in continental rifting environments. The global distribution of corundum deposits is closely linked to collision, rift and subduction geodynamics, and three main periods of corundum formation are recognized worldwide (Giuliani et al., 2007, Graham et al., 2008, Stern et al., 2013): (1) The Pan-African orogeny (750 – 450 Ma), (2) The Cenozoic Himalayan orogeny (45 Ma – Quaternary) and (3) The Cenozoic alkali basalt extrusions (65 Ma – Quaternary).

Corundum deposits can be classified into primary, where the corundum is either hosted in the rock where it crystallized, or in the rock that carried it from the zone of crystallization in the crust or mantle to the Earth's surface, and secondary, where the corundum is of detrital origin, i.e. it formed in a different petrogenetic setting as where it is deposited (e.g., Simonet et al., 2008, Giuliani et al., 2014). Primary corundum deposits are either magmatic or metamorphic, with the metamorphic primary deposits further subdivided into metamorphic *sensu stricto* (s.s.) and metasomatic (Fig. 1.5).

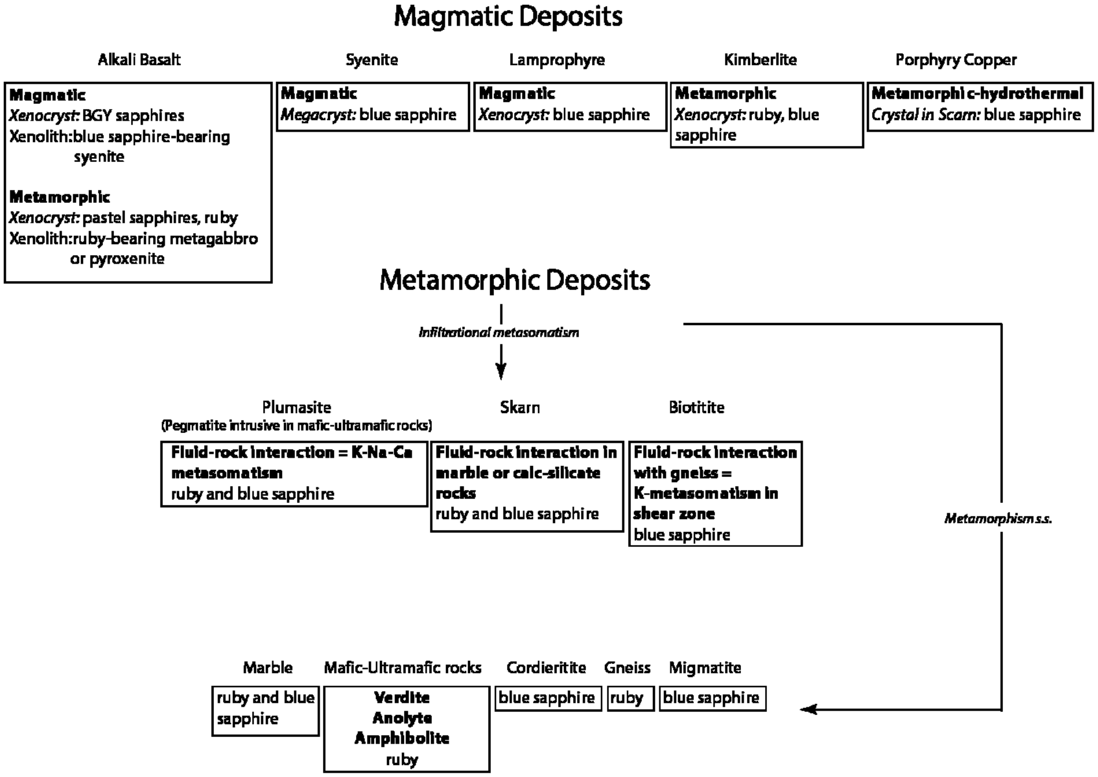

Figure 1.5: Classification of primary corundum deposits based on the lithology of the corundum-host rocks. For the magmatic deposits each type the origin of ruby and/or sapphire is defined as either magmatic *versus* metamorphic. After Giuliani et al. (2014).

Metamorphic deposits s.s. are those where corundum crystallized during metamorphism of alumina-rich rocks, such as gneisses, granulites, and meta-limestones. Corundum in metasomatic deposits forms via the introduction of fluids into tectonic structures or via contact metamorphism. Examples of metasomatic corundum bearing rock types are plumasites (i.e., desilicated pegmatite in mafic and ultramafic rocks) and skarns. Today genetic data on primary gem corundum deposits, i.e., gem corundum that is hosted by a mother rock, is still relatively sparse, hampering our ability to develop precise genetic models. A comprehensive review of our current knowledge is summarized in Giuliani et al. (2014).

1.2.1 Geographical origin determination

The commercial value of gem corundum depends on their size, colour and clarity. High quality rubies are worth more than diamonds. Historically, rubies are mined from Burma (recently renamed Myanmar), Thailand, Sri Lanka, India, Afghanistan, and Cambodia; Tanzania, Kenya, Madagascar, Vietnam, Nepal and Tajikistan are other more recent suppliers. In the late 1960s large ruby deposits have been found under the receding ice shelf of Greenland. Recent prospecting by True North Gems revealed that the so-called Aappaluttoq deposit is very likely the largest geologically defined ruby and pink sapphire deposit in the world at this time, with over 400 million carats of corundum within 65 m of the surface (Fagan and Groat, 2014). So far the most desired rubies are of the “pigeon's blood” variety extracted from the Mogok stone tract, in Myanmar. These rubies are known for their strong fluorescence, clarity and quality. However, because the mining of these rubies helps fund the Myanmaran military junta and thus their human rights abuses, the import of these ‘blood rubies’ and other gems in the US and EU has been banned for the past decade. Therefore, a vested interest exists in establishing accurate methods to identify the source localities of these gems.

The most important gemological-mineralogical criteria used for the characterization of gemstones are (i) Inclusion features (cavity fillings, growth features, solid inclusions), (ii) chemical fingerprinting (major, minor, trace elements), (iii) spectral fingerprinting (UV-Vis-NIR range), (iv) Optical properties (refractive indices, birefringence), (v) IR characteristics and (vi) Luminescence behavior. For origin determination trace element and oxygen isotope compositions have been found to be of particular interest and will be introduced below.

1.2.1.1 Trace Elements

Corundum contains several trace elements in low but measurable quantities, most commonly seen are Cr, Ti, Fe, V and Ga because they can substitute for Al^{3+} in the crystal structure. They are fractionated in differing fashions depending on the geological conditions during corundum formation resulting in varied abundances and ratios between individual corundum deposits. Several studies have shown that differences in the composition of trace elements exist between rubies and sapphires of different geological origin (e.g., Sutherland et al., 1998; Limtrakun et al., 2001; Saminpanya et al., 2003; Abduriyim and Kitawaki, 2006). Binary and ternary plots of the significant minor elements Cr, Ti, Fe, V and Ga, are used as discriminants.

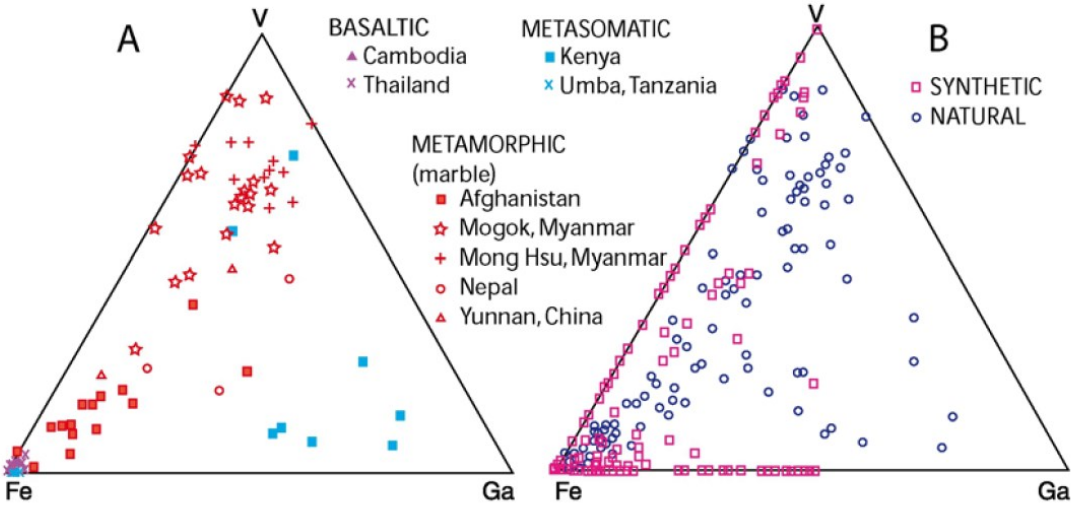

Figure 1.6: Chemical composition of natural and synthetic rubies. Gallium (Ga)–vanadium (V)–iron (Fe) diagrams (in wt.%) of (A) natural ruby from different geologic deposit types, and (B) natural versus synthetic ruby. From Giuliani et al. (2014), after Muhlmeister et al. (1998).

For example, using a Fe vs. Cr plot it could be established that rubies can broadly be divided into three different groups based on their different formational environments: a metamorphic (marble-hosted) group I (generally defined by low Fe), a metasomatic/metamorphic group II (fluid interactions with host rock) and a magmatic (basaltic) group III (Calligaro et al., 1999; Rankin et al., 2003; Muhlmeister et al., 1998; Giuliani et al., 2007, 2012; Harlow and Bender, 2013). The same approach can also be useful in distinguishing synthetic from natural gem corundum (Fig 1.6B). However, although somewhat distinctive ranges among the sources can be shown, the resolution is not yet sufficient to be useful for the kind of "determination of source" that is desired by gemological laboratories (Harlow and Bender, 2013). Trace element data from rubies from widely differing geographical locations yet similar geological settings may overlap and thus are often still indistinguishable from each other (Fig. 1.6A).

The rapid developments in laser ablation technology (quasi 'non-destructive') and improvements of ICPMS instrumentation (highly increased sensitivity) in recent years has made LA-ICPMS a suitable technique for the analyses of precious, and especially for polished precious, gemstones (e.g., Guillong and Günther, 2001). This has led to the measurement of other trace elements that are present in gem corundum only at very low abundances, such as Be, B, Na, Mg, Si, P, K, Sc, Ni, Cu, Zn, Rb, Sr, Zr, Nb, Mo, Sn, Cs, Ba, Ce, Ta, W, Pb, Th, and U (e.g., Guillong and Günther, 2001; Schwarz et al., 2008; Pornwilard et al., 2011; Keulen and Kalvig, 2013). Unfortunately, the concentrations are often still below the limit of detection (LOD) for most ICPMS instrumentation and when concentrations above the LOD are reported, they are generally not interpreted. It seems that at this point in time the use of trace elements in combination with gemological features is still not conclusive enough to act as a "fingerprint" to discriminate the different geographic origins of gem corundum, especially if the gems are of excellent quality and poor in inclusions.

1.2.1.2 Oxygen Isotopes

Oxygen isotope systematics ($\delta^{18}O$) in lattice oxygen of rubies and sapphires have recently been explored as a new tool to aid in identifying the locality of origin of gem corundum and to constrain a ruby's geological source (e.g., Zaw et al., 2006; Yui et al., 2006, 2008; Giuliani et al., 2005, 2007; Schwarz et al., 2008; Keulen and Kalvig, 2013). These studies established that $\delta^{18}O$ values of corundum are consistent for individual deposits, and the specific isotopic composition range of rubies and sapphires is a good indicator of its geological environment. Ranges for worldwide deposits are summarized in Fig. 1.7. The homogeneous oxygen isotopic composition of rubies for a single deposit reflects host-rock buffering in a definite reaction zone where rubies formed. This direct control on the final isotopic composition of corundum by the isotopic composition of the host rocks is also apparent in the overlap for some deposits of the same genetic type (Fig. 1.7). Therefore, while $\delta^{18}O$ values are potentially useful in aiding with the identification of different geographic origins, it is not possible to distinguish between geographic regions with a similar geological setting based on oxygen isotopic compositions alone.

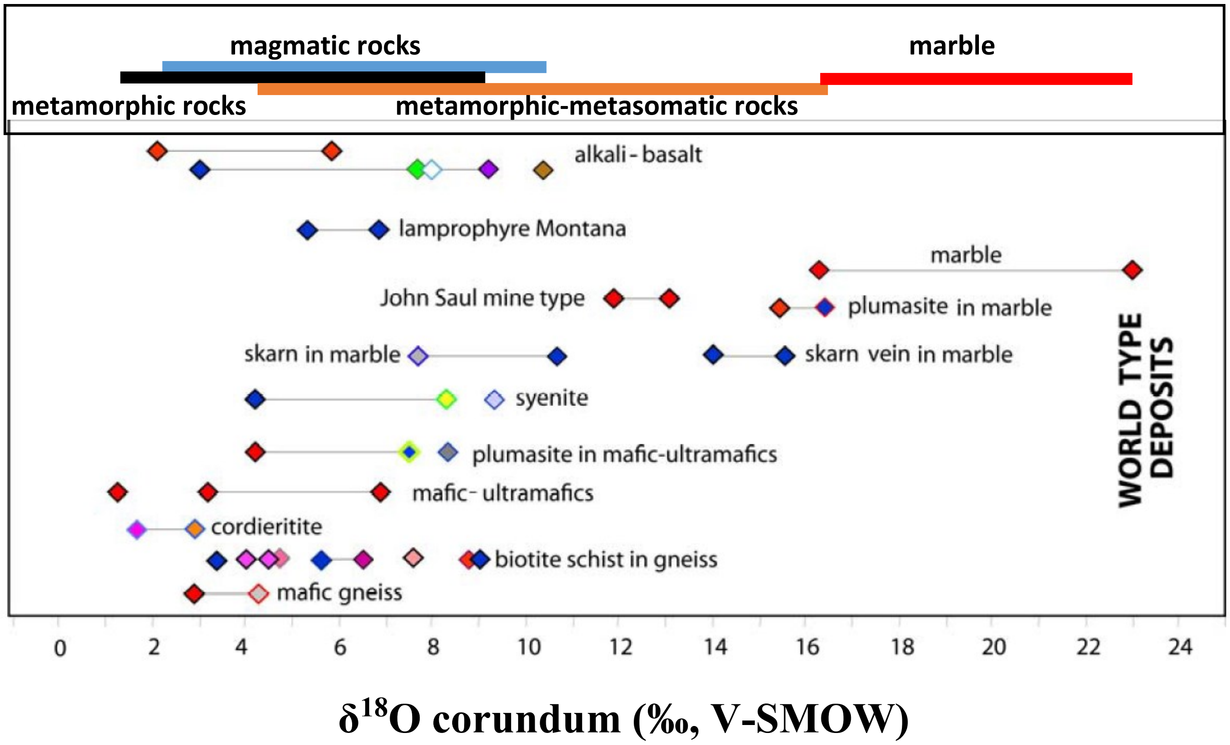

Figure 1.7: Oxygen isotopic ranges defined for corundum types of deposit worldwide (Giuliani et al., 2005, 2007, 2009, 2012; Yui et al., 2003, 2006, 2008). Color in diamonds represent color for ruby (in red) and colored sapphires (others). White diamonds represent colorless sapphires. Bars at the top are generalized ranges in oxygen isotopic composition from Vysotskiy et al. (2015). Modified from Giuliani et al. (2014).

1.3 Thesis layout

This PhD project addresses several gaps in our knowledge surrounding impurity and defect related studies of diamond and gem corundum (with respect to their genesis and application to gemstone exploration). These include (i) uncertainties in the genetic relationship among diamonds of different sizes and inherent implications for diamond exploration, and (ii) the relationship of fluids trapped by octahedrally-grown gem-quality diamond to those trapped by fibrous diamond, (iii) shortcomings in techniques for studying fluid inclusions in octahedrally-grown gem-quality diamond, and (iv) the trace element content in rubies, and (v) limitations of current methods for the determination of a gemstone's origin. The following chapters published in or to be submitted to peer-reviewed journals address at least one of these gaps:

Chapter 2 addresses the genetic relationship among diamonds of different sizes and its implication for the use of micro-diamond size frequency analysis, a widespread tool used in diamond exploration for grade evaluation of kimberlites. To assess cogenesis, micro- and macro-diamonds extracted from the same bulk sample from the Misery kimberlite, Canada, have been analyzed for their carbon isotopic compositions and nitrogen characteristics and, based on the acquired dataset, statistical comparisons were conducted across the size range.

- This chapter is published as Krebs, M.Y., Pearson, D.G., Stachel T., Stern R.A., Nowicki T., and Cairns, S. (2015): Using Microdiamonds in Kimberlite Diamond Grade Prediction: A Case Study of the Variability in Diamond Population Characteristics across the Size Range 0.2 - 3.4 mm in Misery kimberlite, Ekati Mine, NWT, Canada. Economic Geology 111, 503–525.

Chapter 3 describes trace element compositions of fluid inclusions in octahedrally-grown, gem quality diamonds from the Victor kimberlite, Canada, and near-gem quality diamonds from peridotite and eclogite xenoliths from the Finsch and Newlands mines, South Africa, to compare with gem and fibrous diamond fluids in the literature, in order to examine potential similarities and evaluate the likely origin of the fluids.

- A modified version of this chapter will be submitted to Chemical Geology as: Krebs, M.Y., Pearson, D.G., Stachel, T., Woodland, S., Chinn, I., and Kong, J. Trace elements in Gem-Quality Diamonds – Origin and evolution of diamond-forming fluid inclusions.

Chapter 4 reports trace element characteristics, obtained both by "online" and "offline" laser ablation, of rubies from four different localities (Aappaluttoq, SW Greenland; Namahaca, Mozambique; Namya and Mandaley, Myanmar; Luc Yen, Vietnam) with two each having similar geological characteristics (ruby hosted in ultramafic rocks and ruby hosted in marble).

Also reported are the first ever Sr and Pb isotope systematics and Pb-Pb crystallization ages for a smaller subset of said rubies, focussing on new and refined methods to overcome limitations of current methods for the determination of a gemstone's origin. Specifically, this chapter explores the potential of trace element data obtained by "online" LA-ICPMS using state of the art instruments, and Sr and Pb isotope systematics for the establishment of a reliable fingerprint for provenance discrimination and to improve our understanding of gemstone genesis.

- This chapter is intended to be split in two and to be submitted as: (1) Krebs, M.Y., Pearson, D.G., Sarkar, C. Fagan, A.J., and Harlow, G.: Constraining Ruby Provenance using Sr - Pb Isotopes and Trace Elements. And (2) Krebs, M.Y., Pearson, D.G., Sarkar, C. and Fagan, A.J. Dating Ruby Crystallisation using Pb - Pb Geochronology.

Chapter 2

Using Microdiamonds in Kimberlite Diamond Grade Prediction: A Case Study of the Variability in Diamond Population Characteristics Across the Size Range 0.2 to 3.4 mm in Misery Kimberlite, Ekati Mine, NWT, Canada

2.1 Introduction

In diamond exploration the evaluation of newly discovered kimberlites and lamproites consists of several stages (e.g., Rombouts, 1995, 1999). The first direct assessment of diamond content is usually recovery of microdiamonds from relatively small samples (~ 20 to 250 kg) in the form of drill core, grab samples or material from pitting and trenching. These rock samples then undergo caustic fusion, and subsequently all diamonds are recovered by visual sorting of the residues. First used by Deakin and Boxer (1989) on diamonds from the Argyle mine (Western Australia), an initial prediction of the macrodiamond grade (carats/tonne) can then be obtained using size frequency distributions. These size distributions can be expressed as a weight or number frequency distribution versus diamond diameter (sieve size) or weight (in carats). For microdiamond samples, sieve size is usually chosen as diamonds in a typical exploration sample are too small and numerous to make weighing of individual diamonds practical (Rombouts, 1995). On a log-log plot, the frequency of microdiamonds and the sieve class display a near-linear correlation. A shallow gradient combined with a high number of larger (heavier) diamonds indicates a higher economic potential than a curve with a steep gradient and/or low diamond count per unit size/weight (Boxer, 2004). There are two published methods of extrapolating these size distributions to estimate the grade of macrodiamonds; one is based on the lognormal model (Rombouts, 1997), the other on a Pareto tail model (see Rombouts, 1999 for details). While the size-frequency distributions and the coefficients defining their linear relationship for microdiamonds can be used to make an early assessment of the expected diamond content, it is believed that quantitative grade estimates of macrodiamonds on the basis of microdiamonds only are not achievable (Chapman and Boxer, 2004). If the results of a microdiamond analysis are favorable, i.e. indicating a recoverable macrodiamond (typically >1.8 mm) grade above 0.1 carats/tonne, the target will move on to the next stage of assessment.

Although microdiamond evaluation has led to misinterpretation of deposit grade in some cases (e.g., Pattison and Levinson, 1995), the approach generally works very well as an exploration tool and is currently in widespread use. The resulting size distributions are based solely on statistics and the success of the method implies a common origin of micro- and macrodiamonds. This implication of co-genesis has been addressed in several comparative studies investigating differences in diamond morphology, mineral inclusion chemistry, N characteristics and $\delta^{13}C$ compositions of micro- and macrodiamonds, however, it has not yet been conclusively established or disproved (e.g., McCandless et al., 1994; Haggerty, 1986; Pattison and Levinson, 1995; Kaminsky and Khachatryan, 2001; Sobolev et al., 2004; Johnson et al., 2012; Melton et al., 2013). McCandless et al. (1994) for example suggested a common origin whereas several other studies found evidence that microdiamonds may represent separate diamond populations produced partially or entirely by different diamond-forming processes or in distinct mantle sources (e.g., Haggerty, 1986; Pattison and Levinson, 1995; Kaminsky and Khachatryan, 2001; Sobolev et al., 2004; Johnson et al., 2012; Melton et al., 2013). The microdiamonds and macrodiamonds analyzed in these studies, however, originated from different samples and hence were not well suited to test the co-genesis hypothesis.

Microdiamonds are obtained from total dissolution of relatively small samples whereas macrodiamonds are recovered from much larger volumes of host rock (bulk samples), weighing several hundred to over 1000 tonnes. It has long been shown that a full diamond suite in any given primary deposit incorporates several overlapping diamond populations with diverse origins (e.g., Moore and Gurney, 1985, 1989; Deines et al., 1987; Otter and Gurney, 1989; McDade and Harris, 1999; Gurney et al., 2004). The exploration industry assumes efficient mixing of macrodiamonds within a kimberlite body, thus making bulk sample results a proxy for commercial diamond potential. If efficient mixing applies to macrodiamonds, then it must also apply to microdiamonds. However, in kimberlites which are re-worked under subaerial or subaqueous conditions, a disconnect between the two size fractions may exist. It is, therefore, difficult to determine to what extent diamonds from microdiamond samples are representative of macrodiamonds recovered from bulk sampling, unless great care is taken to ensure that the microdiamond samples are representative of the same material processed for macrodiamonds. This could very well account for differences between microdiamonds and macrodiamonds found in previous comparative studies.

Here we attempt a new evaluation of the microdiamond prediction method in which all diamonds analyzed originate from the same microdiamond samples. The term microdiamond usually refers to diamonds < 0.5 mm (e.g., Chapman and Boxer, 2004; Johnson et al., 2012) or < 1 mm (e.g. McCandless et al., 1994; Pattison and Levinson, 1995; Rombouts, 1999; Sobolev et al., 2004; Melton et al., 2013). For the purpose of this study the term microdiamond is applied to all samples due to the nature of their sampling, and comparisons of geochemical characteristics are carried out spanning a range of sieve classes. Diamonds were analyzed with regard to their carbon isotope characteristics ($\delta^{13}C$), nitrogen characteristics (concentration and aggregation state) and their hydrogen and platelet peak areas. Based on this data set a statistical comparison of these geochemical characteristics was conducted on diamonds of five different size fractions to assess their relationship and determine if an inferred common origin of diamonds of different sizes can be established. While co-genesis is ultimately difficult to prove, the fundamental question that can be addressed is the variability of the contribution of different diamond subpopulations across the size ranges examined given the geochemical criteria used. This at least provides a geochemical basis for relating different diamond size classes and hence may, or may not inspire confidence in using microdiamond size-frequency distributions as a predictive tool in mine evaluation.

2.1.1 Geological Background

The Archean Slave craton is located in the northwestern Canadian Shield, a large area of exposed Precambrian igneous and high-grade metamorphic rocks that forms the ancient geological core of the North American continent. The Slave is one of the better exposed cratons in the world, approximately 600 km (N–S) by 400 km (E–W) in areal extent. It is characterized by a large Mesoarchean basement complex, in its central and western parts, whose oldest and best-known components are the Eoarchean (~4.0 Ga) Acasta gneisses (e.g., Bowring et al., 1989b; Bowring and Williams, 1999), and a Neoarchean juvenile arc (Hackett River Arc; Kusky, 1989) in the east. The craton is surrounded by Paleoproterozoic rifted margins which predetermine it to be merely a small fragment from a much larger late Archean landmass, the supercraton Sclavia (e.g., Bleeker, 2003). The Slave is a classic setting for diamondiferous kimberlites, a stable Archean craton with a cool mantle root. Over three hundred kimberlite occurrences are known from the Slave craton spread across the Northwest Territories and Nunavut (Kjarsgaard and Levinson, 2002). The majority of kimberlites in the Slave Province occur in discrete fields or clusters (Fig. 2.1). They usually do not crop out at the surface and are identified using a combination of heavy mineral sampling, geophysical techniques and drilling. Kimberlites are particularly concentrated in the Lac de Gras area in the east-central Slave Province where U-Pb (e.g., Heaman et al., 2003; Lockhart et al., 2003) and Rb-Sr (e.g., Armstrong, 1988; Creaser et al., 2003) radiometric age determinations indicate that pipe emplacement occurred in the Late Cretaceous and Eocene. Middle Jurassic (e.g., Heaman et al., 1997) and Cambrian (e.g. Heaman et al., 1997, 2003) kimberlites have been discovered in the eastern Slave Province, late Ordovician (e.g., Heaman et al., 1997, 2003) kimberlites in the southwestern part, and Eocambrian kimberlites (e.g., Masun et al., 2004) in the northern Slave Craton. The regional distribution of Slave kimberlites was analyzed by Stubley (2004) who recognized that the major kimberlite fields are located within two corridors, a NNE trending western corridor, including the western Slave and Coronation Gulf fields, and a less well defined, NNW trending central corridor, encompassing the Southern Slave, Lac de Gras, and Jericho fields. Re-Os dating of sulfide inclusions from peridotitic diamonds from the Panda (Ekati) and A154 South (Diavik) kimberlites established that Central Slave peridotitic diamonds are Paleoarchean (3.5-3.3 Ga; Aulbach et al., 2009; Westerlund et al., 2006) in age.

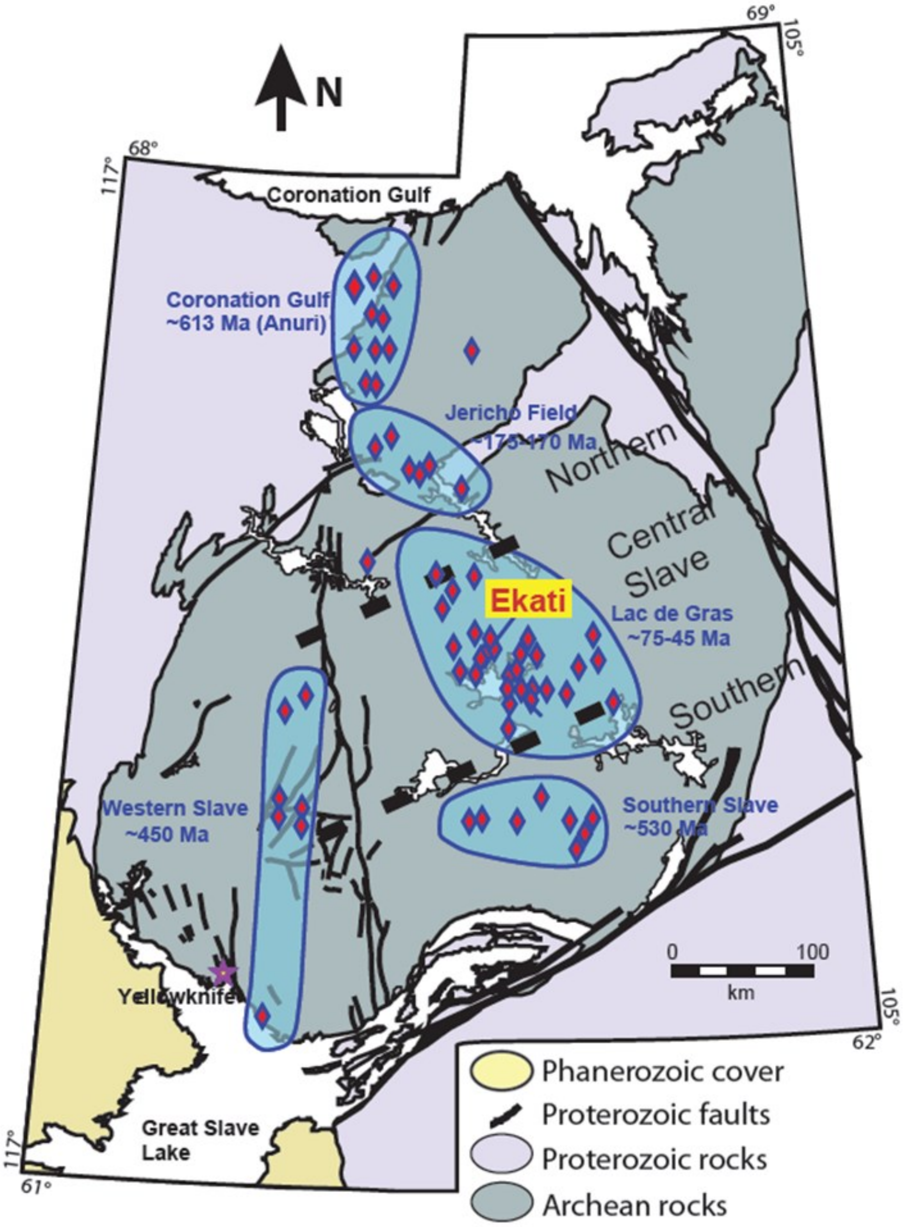

Figure 2.1: Location map of kimberlite occurrences (diamonds) and kimberlite fields (dark blue outlines) on the Archean Slave Craton (modified after Bleeker and Hall, 2007 and Johnson et al., 2012). Thick dashed lines show northeast-trending mantle domains in the craton (Grütter et al., 1999).

Misery, one of the highest grade primary diamond deposits in the world with an average grade of ~ 4 ct/tonne, is part of the Ekati property that is located in the central part of the Slave Province and occupies a claim block of approximately 1800 km^2 in the north-central and northeastern part of the Lac de Gras area (Fig. 2.1; Nowicki et al., 2004; Webb et al., 2012;

Heimersson and Carlson, 2013). The property encompasses the Ekati diamond mine and includes 150 kimberlites that form a significant proportion of the Lac de Gras kimberlite field. Misery is located 7 km northeast of the Diavik diamond mine and approximately 30 km from the Ekati plant complex. Unlike most kimberlites on the property that form discrete, single pipe intrusions, Misery is a complex of six main kimberlite bodies (Main, South, Southwest Extension, Southeast Complex, Northeast, and East) plus several additional small dykes and intrusives (East Extension, Northeast Extension, Mideast Dyke, and numerous other unnamed small kimberlitic intervals). Misery was mined from 2001 to 2005 by open cut methods and an expansion of the open pit was approved in 2011 with the first ore production expected in 2015. Exploration and mining focus on the Main Pipe and two peripheral bodies; the so-called Southwest Extension (SWE), a body of pyroclastic kimberlite that links the Misery Main pipe to the Misery South pipe, and the South Pipe (Fig. 2.2).

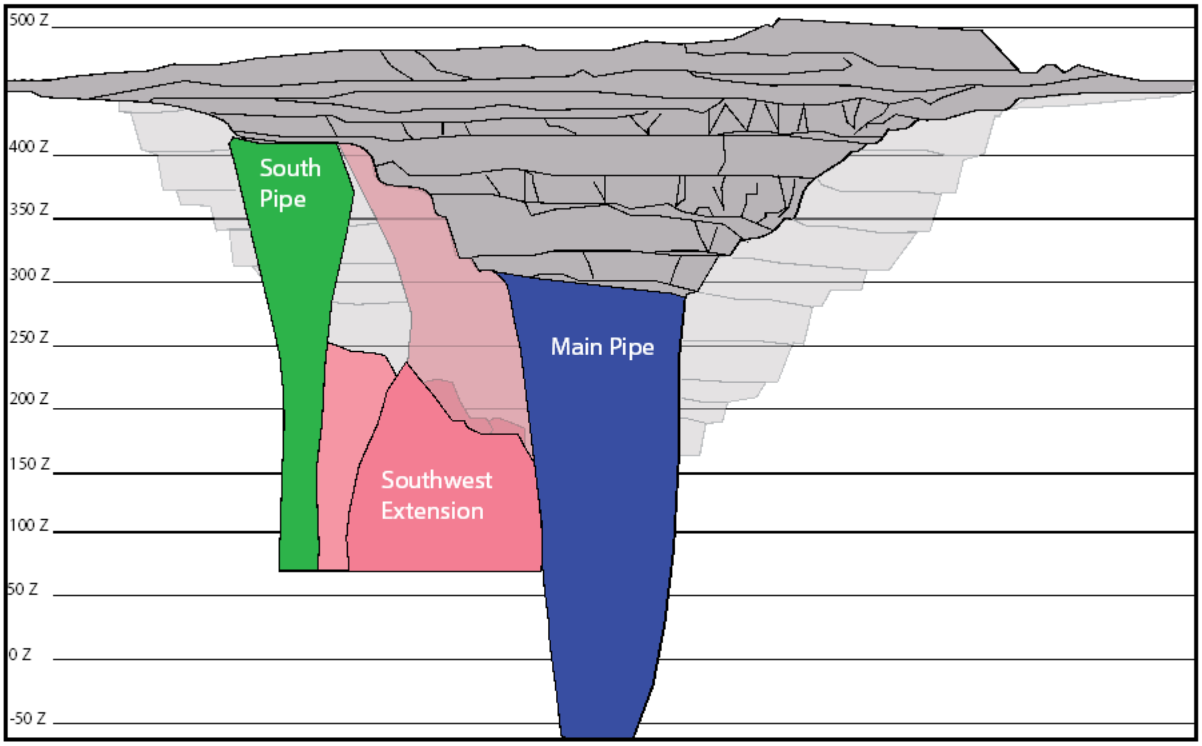

Figure 2.2: Isometric Cross-Section, Misery Pipe. (Red = Southwest Extension, blue = Main Pipe, green = South Pipe, dark grey = surface at end of 2012, silver grey = Final pit design, drill hole trace. Data used are as at end-December 2012. (Modified after Heimersson and Carlson, 2013). Samples originate from the southern part of the Main Pipe and from the Southwest Extension.

Three main rock types were recognized within Misery Main and the Southwest Extension, KIMB3, KIMB5 and KIMB6. KIMB3, composed of fine to medium grained, variably bedded, and dominantly olivine-rich (25-70%) re-sedimented volcaniclastic kimberlite (RVK), is the dominant rock type in the Misery Main pipe. KIMB5 is an RVK that closely resembles KIMB3 and may actually be an olivine-rich end-member of the same. KIMB6 is a well-bedded mud-rich RVK. KIMB5 and KIMB6 are the dominant rock types in the Misery Southwest Extension. In addition, material believed to be KIMB5 occurs in the boundary zone between the Main Pipe and Southwest Extension. Only one radiometric age has been produced for the Misery kimberlite complex - 67.8 Ma U-Pb perovskite (Sarkar et al., 2015a) - for the Misery East dyke, the oldest of the intrusive phases. The remaining bodies in the Misery complex have not been dated, but extensive geochronology of kimberlites of the Lac de Gras field has shown that kimberlites of economic significance appear to be exclusively Eocene (Armstrong, 1988; Creaser et al., 2003; Heaman et al., 2003; Lockhart et al., 2003; Sarkar et al., 2015a).

2.2 Samples

The Misery diamond suite analyzed in this study is derived from four microdiamond samples that were taken in 2011 to assess the economic potential of the Misery Southwest Extension. Each microdiamond sample is comprised of several 8 kg sub-samples taken from drill core intersecting two connected localities within the Misery kimberlite complex. Two samples are derived from the southern part of the Misery Main pipe, termed KIMB3-MS and KIMB5-MS; KIMB3 and KIMB5 referring to the rock type and the suffix MS denotes derivation from Misery Main South; The other two samples are derived from the Misery Southwest Extension and are termed KIMB5-SWE and KIMB6-SWE; again KIMB5 and KIMB6 refer to the rock type and the suffix SWE denotes derivation from Misery Southwest Extension. The respective weights of the rock samples were ~45 kg for KIMB3-MS, ~55 kg for KIMB5-MS, ~175 kg for KIMB5-SWE and ~185 kg for KIMB6-SWE.

The diamonds were extracted from their host rocks via caustic fusion carried out by Geoanalytical Laboratories Diamond Services (GLDS) of the Saskatchewan Research Council (SRC) in Canada. Individual samples were fused in kilns containing caustic soda and then poured through a stainless steel wire mesh with an aperture width of 106 µm; the collected material >106 µm was chemically treated to reduce the residue to a manageable size. The quality of the microdiamond recovery method is monitored by SRC using synthetic diamond spike grains added to the sample during the caustic fusion and chemical treatment processes and the results indicated minimal likelihood of diamond loss or cross-contamination during sample processing.

Recovered diamonds were screened into standard square mesh sieve sizes as per CIM (Canadian Institute of Mining, Metallurgy and Petroleum) guidelines for reporting of microdiamond data. In total 1627 diamonds were recovered, ranging in size from 0.106 mm to 3.35 mm across 12 sieve classes.

Figure 2.3 shows stone size distributions of the four microdiamond samples analyzed in this study. The microdiamond data indicate that KIMB3, KIMB5 and KIMB6 have different size distributions. KIMB3-MS shows a relatively high number of diamonds and has the shallowest slope when compared to the other three microdiamond samples. KIMB5-MS has the highest concentration of diamonds but has a steeper slope compared to KIMB3-MS.

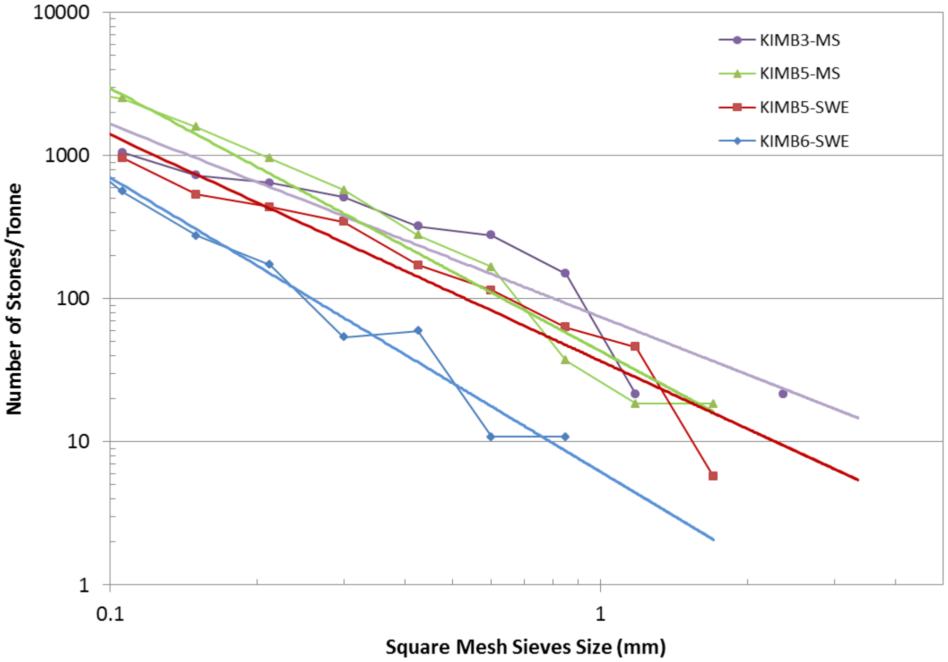

Figure 2.3: Stone size distribution for Misery kimberlite microdiamond samples. The straight lines are best-fit lines determined using the EXCEL power trendline function. R-squared values range from ~ 0.87-0.97.

The slope of KIMB5-SWE is less steep but the concentration of diamonds is lower than in KIMB5-MS. KIMB6-SWE has the lowest concentration of diamonds and the steepest slope of all four microdiamond samples. In summary, KIMB5 and KIMB6 have finer-grained diamond populations when compared to KIMB3, and, therefore, factoring in the number of diamonds per sample, microdiamond data suggests that the relative interest rating is KIMB3 > KIMB5 > KIMB6.

For a comparative study across size classes it would be ideal if all analyzed diamonds would be derived from a single large sample; however, due to the small size of microdiamond samples they only yield a limited number of diamonds. Therefore, to obtain a sample suite of the desired size, the combination of several microdiamond samples was necessary. Figure 2.4 shows the proportions of diamonds of the four microdiamond samples through the size classes. They stay reasonably constant, verifying that the cumulative nature of the sample origin does not compromise the comparison of the different diamond size populations, as no systematic bias exists.

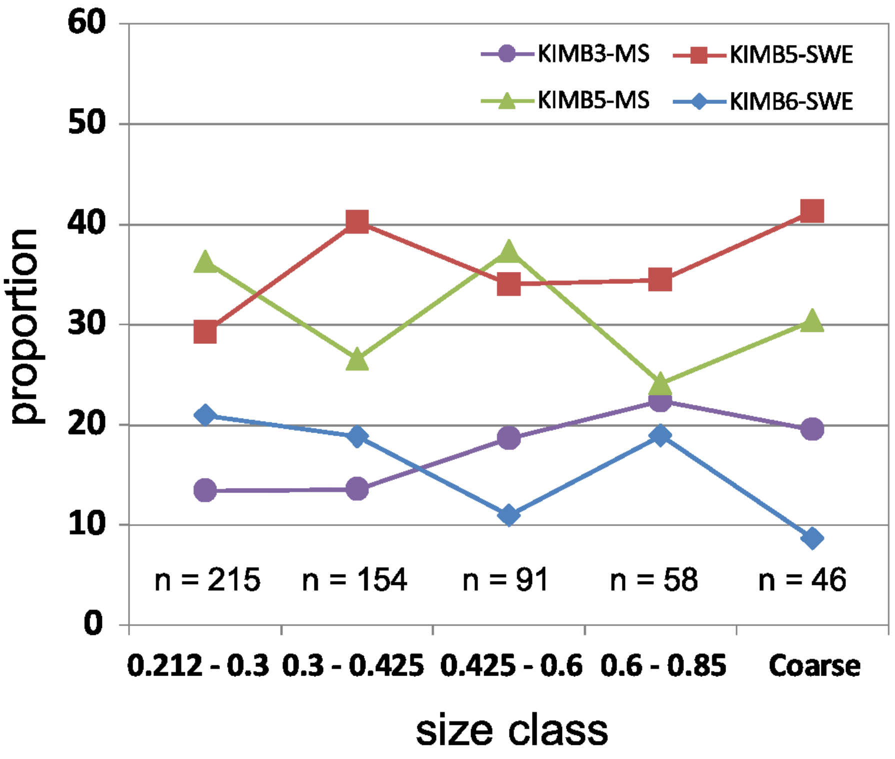

Figure 2.4: Proportions of the four microdiamond samples across five size classes.

For reasons of practicality, all diamonds < 0.212 mm were excluded from this study, as handling of such small stones for FTIR analysis is very difficult. This resulted in a sample suite consisting of 564 diamonds ranging in size from > 0.212 to 3.35 mm (Table 2.1). Six diamonds were lost during descriptions and FTIR measurements: Two diamonds of the 0.212 – 0.3 mm size class (one from KIMB3-MS, the other from KIMB5-SWE), two diamonds from the 0.425 – 0.6 mm fraction (one from KIMB5-MS, the other from KIMB6-SWE), one diamond > 0.85 mm from the KIMB5-SWE sample and one diamond > 1.18 mm from KIMB5-SWE sample. The Misery diamond suite is heavily biased towards very small stones, typical for microdiamond samples. To make the larger stone classes (very low sample numbers) statistically more significant all diamonds > 0.85 mm were combined into one size fraction which will henceforth be referred to as the coarse fraction.

Table 2.1: Number of diamonds according to sieve size in mm listed for each of the four microdiamond samples comprising the Misery diamond suite. Also listed is sample weight in kg. The coarse fraction contains all diamonds > 0.85 mm.

Locality	**Rock Type**	**Sample Weight (kg)**	**Numbers of Diamonds According to Sieve Size Fraction (mm)**									**Total Diamonds**
			0.212 - 0.3	**0.3 - 0.425**	**0.425 - 0.6**	**0.6 - 0.85**	**0.85 - 1.18**	**1.18 - 1.7**	**1.7 - 2.36**	**2.36 - 3.35**	***Coarse***	
Misery Main S	**KIMB3-MS**	46.72	29	21	17	13	7	1	0	1	*9*	**89**
Misery Main S	**KIMB5-MS**	54.16	78	41	34	14	9	3	1	1	*14*	**181**
Misery SWExt	**KIMB5-SWE**	174.56	63	62	31	20	10	8	1	0	*19*	**195**
Misery SWExt	**KIMB6-SWE**	185.06	45	29	10	11	2	2	0	0	*4*	**99**
All		460.5	215	154	91	58	28	14	2	2	*46*	**564**

2.2.1 Physical characterization

All diamonds were examined with regard to their morphology, color and grade of resorption. Diamond morphologies are described following the scheme outlined in Stachel (2014).

Diamond has two primary growth forms, octahedra and cuboids (cubes with minor dodecahedral resorption and re-entrant cubes with concave {001} faces). They may also form cubo-octahedra (combinations of the two), aggregates and twins, the most common twins being triangular macles (spinel law twins). Resorption of diamond during mantle residence and/or kimberlite ascent leads to the development of secondary shapes. Primary cuboid and octahedral faces are resorbed and consequently form rounded dodecahedral faces. This results in a distinct tetrahexahedral shape for cuboids and "rounded dodecahedra" (or "dodecahedroids") for octahedral diamond. Irregular diamonds form a tertiary morphology class that contains fragmented diamonds without discernible primary or secondary morphological features. Fragmented diamonds showing residual primary or secondary features were assigned to the above categories.

A high number of Misery diamonds display secondary or tertiary shapes; dodecahedral morphologies dominate (40%) followed by irregular shapes (32%). Less common are octahedra (23%). Cuboid, twinned, and aggregated morphologies are rare and, combined, amount to 5% of the Misery diamond suite. In total 60% of the diamond suite is made up of diamond fragments, a circumstance that is reflected within all size fractions. Sample KIMB5-MS has the highest proportion of fragments (72%) while KIMB3-MS, KIMB5-SWE and KIMB6-SWE have 49%, 54% and 63% fragments, respectively. This high proportion of fragmented diamonds has to be considered when doing comparative geochemical studies across size classes, as these fragments are originally larger micro- to macro-sized diamonds broken into small fragments and may therefore reflect a different diamond population.

The 558 examined diamonds display a range of colors, including colorless, brown, yellow, grey, and pink, but are predominantly either colorless (75%) or brown (18%). This overall color distribution is also seen within the individual samples with diamonds from KIMB3-MS having the highest proportion of brown stones (23%). Any apparent differences in color distribution between diamonds of different sizes very likely relate to difficulties in assessing the true body color of very small diamonds, as in part they are approaching the thickness of a thin section; therefore, the color distribution will not be evaluated further.

Of the entire sample suite 50% show a high degree of resorption (only minor residual faces), 28% of all diamonds show some resorption (50% residual faces visible), and 22% of the diamonds show little to no resorption (residual faces dominate). Diamonds derived from sample

KIMB3-MS contain a particularly high proportion of highly resorbed diamonds (64%), whilst diamonds derived from KIMB6-SWE contain a particularly high proportion of diamonds with no or very little resorption (30%); KIMB5-MS and KIMB5-SWE contain proportions reflecting the general characteristics of the whole diamond suite. Between different diamond size fractions no systematic differences in shape, color or degree of resorption could be determined. About 80% of all fragments show at least some degree of resorption, indicating that the breakage is natural, i.e. that it occurred in the mantle before kimberlite deposition.

Gurney et al. (2004) reported >50% dodecahedral morphologies and >50% brown color for physical characteristics of Misery diamonds from an exploration diamond parcel that was characterized as part of a purely descriptive diamond study of exploration diamond parcels from 13 kimberlites on the Ekati Diamond Mine property. In addition, they also found the full range of common diamond shapes, colors and degrees of resorption (no resorption to >45% resorption). Although the number of dodecahedral morphologies and brown colored stones reported by Gurney et al. (2004) is higher than those reported in this study this is likely due to the size of the examined diamonds. As mentioned above it is difficult to assess the true body color of very small diamonds which is likely the reason for the lower percentage of brown stones reported in this study. In addition the percentage of fragments is higher in microdiamond samples which likely accounts for the lower percentage of diamonds with dodecahedral morphologies in this study.

2.3 Analytical methods

2.3.1 Nitrogen - FTIR

Nitrogen abundance (at. ppm) and aggregation state (relative abundance of the moderately aggregated nitrogen A center and the fully aggregated B center expressed as %B =100 B / [A + B]) determinations were carried out in the De Beers Laboratory for Diamond Research at the University of Alberta, Canada, using a Thermo Nicolet Nexus 470 FT-IR Spectrometer coupled with a Continuum infrared microscope with motorized stage. The spectra (650 to 4000 cm^{-1}) were collected for 200 scans in transmittance mode with a spectral resolution of 4 cm^{-1} and an aperture of 100 µm. Methods and procedures were the same as described in Banas et al. (2007). To identify intra-diamond variation in nitrogen contents and aggregation state, 2-3 spots were analyzed when possible. Detection limits generally range from 5 - 15 at. ppm, depending on the quality of the diamond, analytical precision (i.e. uncertainty) is about 5–10% of the total measured nitrogen concentration.

When present, the intensities of the platelet peak, generally located between 1358 cm^{-1} and 1372 cm^{-1}, and the hydrogen related peak at 3107 cm^{-1} were quantified using the peak area function of the OMNIC software supplied by Thermo Nicolet, after local background fitting to eliminate diamond and nitrogen related absorbance.

2.3.2 Carbon isotope measurements

The carbon isotope ratios (reported in per mil $\delta^{13}C_{VPDB}$) of the Misery diamonds were determined by multicollector secondary ion mass spectrometry (MC-SIMS) at the Canadian Centre for Isotopic Microanalysis (CCIM) at the University of Alberta, using a Cameca IMS 1280 ion microprobe following the method described in Stern et al. (2014) and summarized here.

For this purpose the 260 diamonds from all size fractions of the 558 diamonds analyzed using FTIR were randomly selected (RAND function in Excel). The diamonds were placed close together on double sided thermal tape according to size and then embedded in epoxy. In total 16 epoxy mounts (25 mm diameter) were made and then ground and polished using conventional rotary lapping equipment. Grinding utilized a 30 µm electroplated diamond pad to expose partial diamond sections, followed by grinding with a 15 µm and then polishing with a <6 µm diamond pad. Exposed sections through the diamonds are randomly oriented. The finished mounts were coated with 5 nm Au and the internal growth structures of the diamonds imaged using cathodoluminescence (CL) employing a Zeiss EVO MA 15 scanning electron microscope at CCIM equipped with both GatanChromaCL and Robinson wide spectrum CL detectors. After CL imaging the epoxy mounts were cut into small blocks. Multiple blocks were pressed into three indium assemblies surrounding centrally positioned reference materials, cleaned with ultra-pure ethanol and coated with 25 nm Au to ensure conductivity for analysis. The reference materials used include fragments of CCIM S0270 natural diamond ($\delta^{13}C$ = -8.84 ‰; Stern et al., 2014).

The primary ions used were 20 keV $^{133}Cs^+$ with on-target currents of 3–4 nA, sputtering a 15 x 20 μm region of the diamond. No electron charge compensation was needed or utilized for these diamonds. Negative C^- ions were extracted through 10 kV, then focused and deflected through 110 μm and 5 mm wide entrance and field aperture slits, respectively. No energy truncation was applied. Both nuclides were analyzed simultaneously with Faraday cups (L'2, FC2) at mass resolutions of 1950 and 2900, respectively, to eliminate isobaric interferences (e.g., $^{12}C^1H^-$). Count rates for $^{12}C^-$ and $^{13}C^-$ were typically $2x10^9$ and $2x10^7$ counts/s, respectively. Baseline count rates were measured at the start of the analytical session for each mount. Each analysis comprised automated secondary ion tuning followed by 75 s continuous peak counting. The S0270 reference diamond was analyzed once for every four unknowns to correct for instrumental mass fractionation (IMF) and for error analysis. The standard deviations of IMF corrected $\delta^{13}C$ data for S0270 diamond were 0.06 – 0.08‰. The uncertainties propagated to the individual unknowns include the internal counting statistics, spot-to-spot excess errors, and inter-session calibration errors, and range from 0.13‰ – 0.22 ‰ (2σ) per spot. The external uncertainty in the calibration value of S0270 reference material (±0.12 ‰; Stern et al., 2014) has not been propagated, but can be added as required for comparison with literature data.

2.3.3 Statistical methods

The quantitative statistical comparison of diamond data of different size fractions and rock samples was done using statistical hypothesis testing. A two-sample Kolmogorov-Smirnov test (Smirnov, 1939) was performed on all distributions. For diamond data distributions with $n > 40$, quantitative statistical comparisons were also done using the unequal variance t-test, also known as the Welch's t-test (Welch, 1938). For both tests the null hypothesis (H_0) is that the two populations being tested derive from populations with identical distributions; the t-test examines the significance of the difference in the means from the two distributions, the Kolmogorov-Smirnov test examines the significance of differences in the cumulative distributions.

A significance level $\alpha=0.05$ was chosen for all tests. If the calculated p-value - the probability that you would obtain evidence against H_0 which is at least as strong as that actually observed, if H_0 were true - is less than or equal to α, the null hypothesis is rejected, i.e. the two compared data sets differ significantly. If the calculated p-value exceeds α, we accept the null hypothesis, i.e. equality of the two compared data sets cannot be rejected. Kolmogorov-Smirnov tests were carried out using the on-line calculator developed by Kirkman (1996); t-tests were performed using EXCEL. The results of both tests agree well with each other. In addition each data set was tested for normality of the distribution using the Kolmogorov-Smirnov goodness-of-fit test (Kolmogorov, 1933; Smirnov, 1948).

It is important to keep in mind that statistically significant differences between diamond populations in this study only imply that the null hypothesis "the two samples derive from populations with identical distributions" was rejected; it does not mean that the detected difference is important, which is what "significant" usually means. In other words, when a test results in a significant difference, this only implies that the difference is not exactly zero. Finding that two samples differ significantly has no bearing on how large or important a difference is, i.e. it does not necessarily mean that the compared diamond data sets originate from drastically different diamond populations.

2.4 Results

2.4.1 Carbon isotopic compositions

The carbon isotopic composition of diamond depends upon the carbon isotopic composition and fluid speciation of its growth medium. This relationship makes it a useful geochemical fingerprint that can help determine the source of the carbon and give insight into the formation of diamond and possibly into its source rock.

Carbon isotopic characteristics have been determined for 260 diamonds with a total of 640 spots analyzed. For CL imaging the diamonds were not oriented on specific crystallographic directions. As a result, and because sections through the crystal centres were only achieved in rare cases, CL images can be difficult to interpret. Multiple spots (2 to 6) were measured per diamond depending on diamond size, internal growth layers and presence of internal resorption faces.

The isotopic variation between distinct growth zones in individual diamonds is less than 0.5‰ in 141 of the 260 samples (54%), only 10 diamonds (4%) show internal variations greater than 3‰. Isotopic variation between growth zones across the individual size classes varies little. Four percent of the coarse stones have internal variations greater than 3‰; values for the size ranges > 0.6 – 0.85 mm, > 0.425 – 0.6 mm, > 0.3 – 0.425 mm and > 0.212 – 0.3 mm are 0%, 6%, 3% and 6%, respectively. Within the small range of internal δ^{13}C variations, no systematic trends of increasing or decreasing δ^{13}C values, which would indicate isotope fractionation during diamond precipitation, are observed across growth zones. Diamonds displaying large intra-diamond variations either show evidence of a resorption event at the interface between distinct growth zones or have complex CL patterns that are difficult to interpret (Fig. 2.5). Variations in the complexity of CL patterns across the examined size fractions were not observed.

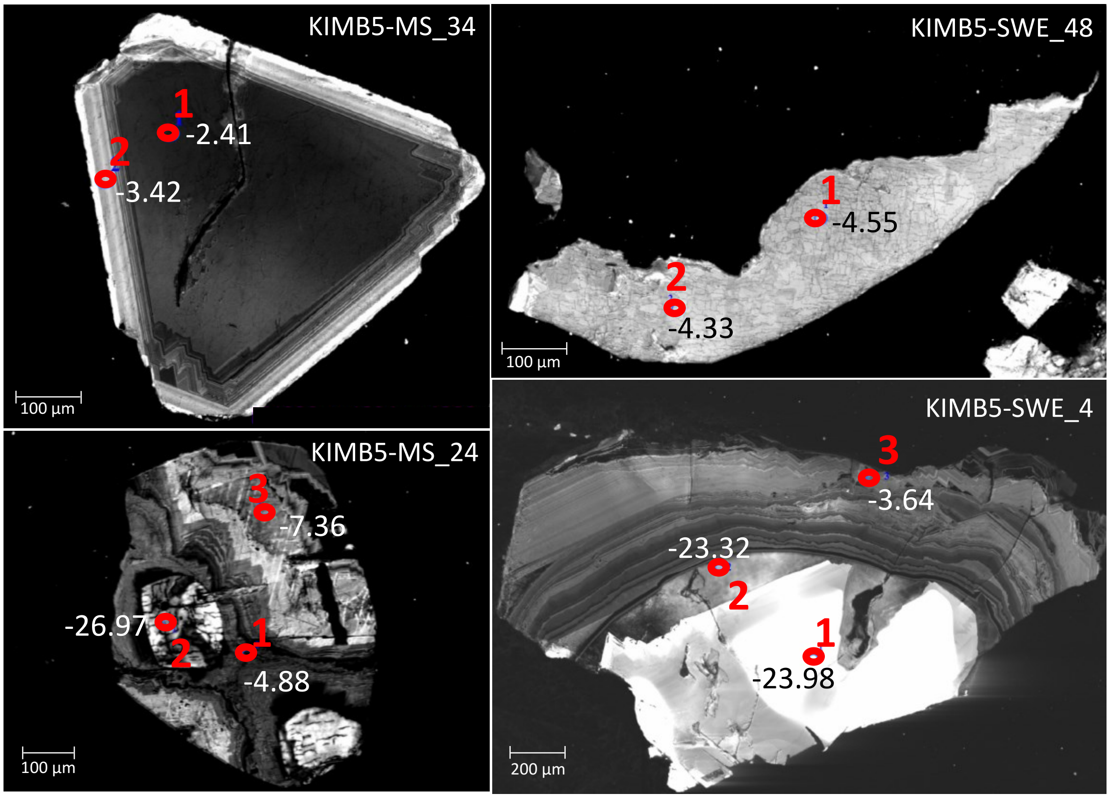

Figure 2.5: Examples of CL internal growth structures. The concentric growth bands exhibited by diamond KIMB5-MS_34 represent octahedral growth. Diamond KIMB5-SWE_48 shows homogenous CL. Diamonds KIMB5-MS_24 and KIMB5-SWE_4 are examples that show more complex internal growth structures. KIMB5-MS_24 seems to be a single diamond that formed from several small diamond "nuclei" joined together by later overgrowths. KIMB5-SWE_4 exhibits obvious evidence of resorption between at least two different growth stages. Red circles mark SIMS spots (spot size is approximately 15 µm), δ^{13}C values are in ‰.

The Misery diamond suite ranges in carbon isotopic composition from −35.4‰ to +1.9‰. While this range encompasses >90% of the known range in natural diamonds, the majority of data (>95%) falls into a narrow range between -8‰ to -2‰ with a symmetrical distribution and a median of −4.4‰ (Fig. 2.6); this is isotopically slightly heavier than the typical global mantle mode (Table A1).

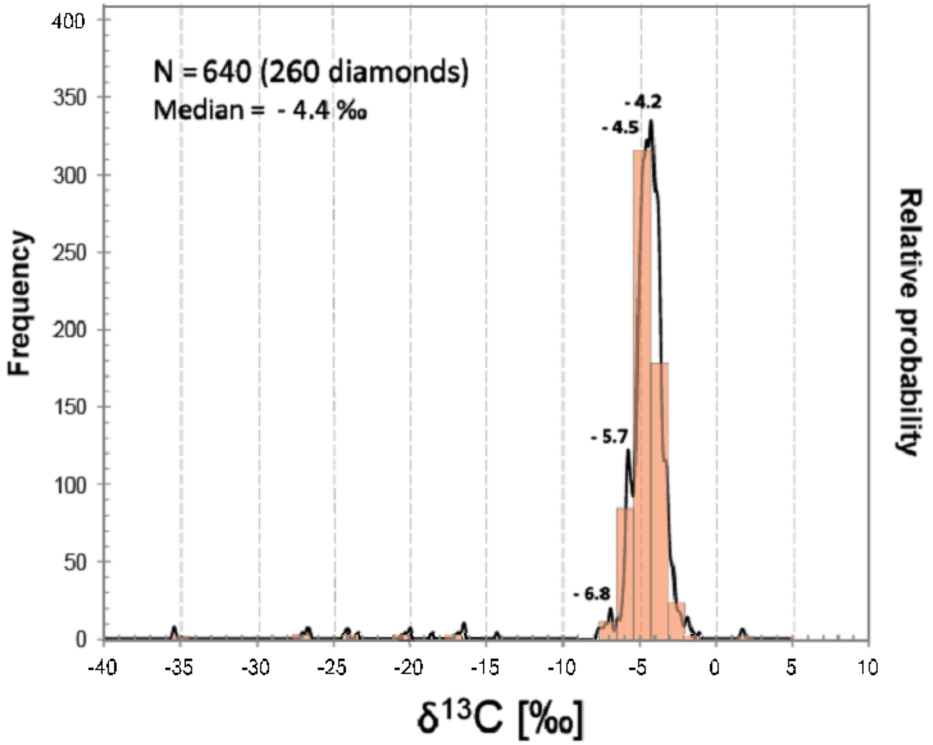

Figure 2.6: Histogram and probability density curve (calculated using Isoplot 4; Ludwig, 1999) for the $\delta^{13}C$ distribution of the Misery diamond suite.

A probability density curve (calculated using Isoplot 4; Ludwig, 1999) of the acquired data shows a prominent mode at -4.2‰ with a broad shoulder at -4.5‰. Additional modes at -5.7‰ and -6.8‰, as well as a few strongly ^{13}C-depleted modes are clearly visible (Fig. 2.6). Median values of the individual size fractions and of the individual bulk-rock samples are similar, ranging between -4.2‰ and −4.6‰ (Table 2.2, Fig. 2.7). The Unmix ages function in Isoplot was used to calculate, using Gaussian mixture modelling, the various $\delta^{13}C$ modes for the whole Misery diamond suite, the individual size fractions, and the individual microdiamond samples. This function utilizes the algorithm of Sambridge and Compston (1994) for multi component mixtures that uses iterative calculation to determine if a given dataset is composed of more than one population. By introducing the number of suspected populations the algorithm calculates the weighted $\delta^{13}C$ modes, their uncertainties (± 2 sigma) and their relative proportions (Table 2.2).

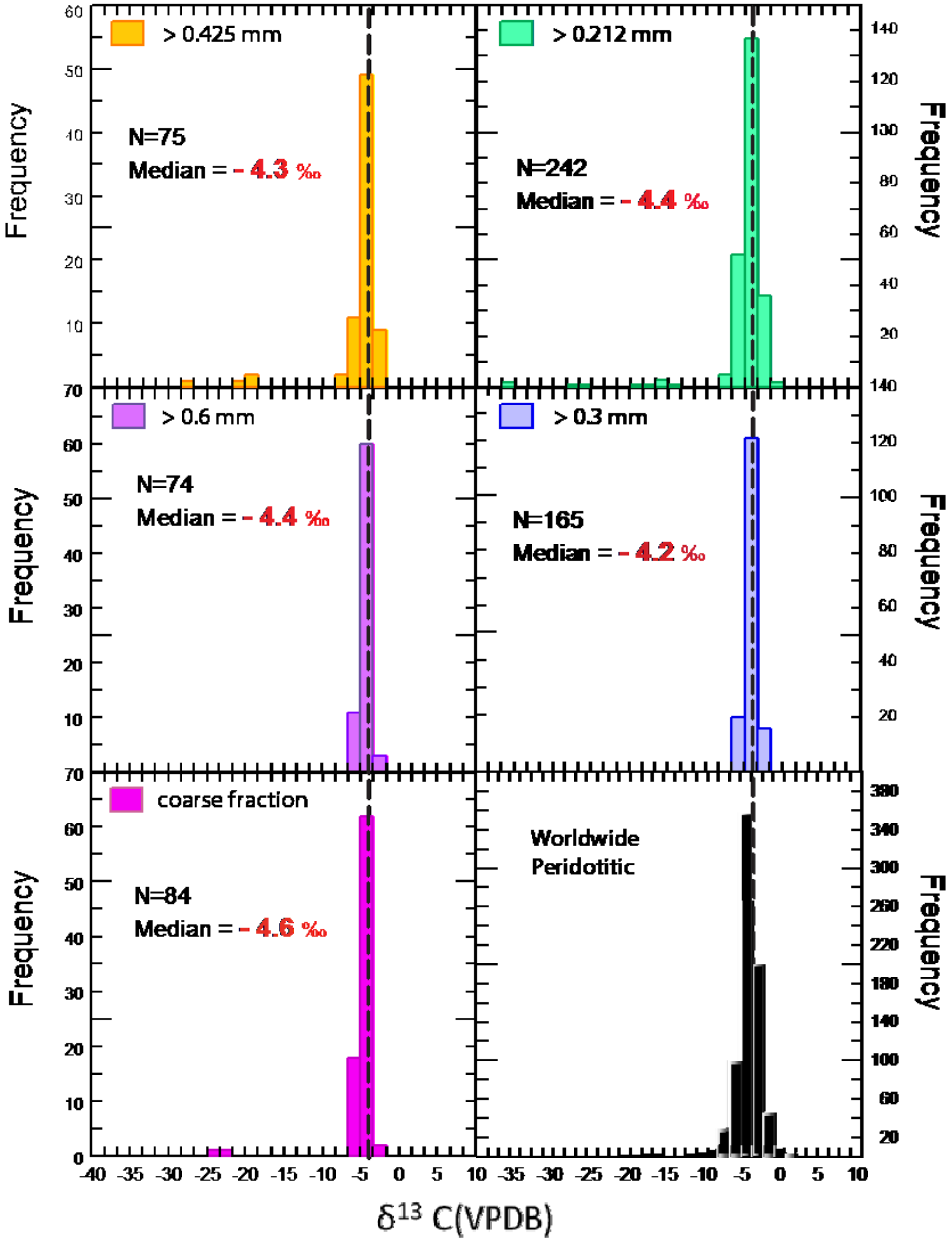

Figure 2.7: Histograms of the carbon isotopic composition of the different size fractions and the peridotitic diamond suite worldwide (Stachel, 2014). The dashed line defines the primary main mode in each sample set.

2.4.2 Nitrogen abundance and aggregation states

In total 558 Misery diamonds were analyzed by FTIR, where possible using two and sometimes even three spots per diamond (Table A1). Fifty-eight diamonds were heavily included or coated with semi-opaque diamond and no quantifiable spectra could be obtained. The acquired data show a very large spread in both nitrogen concentration and aggregation state (Fig. 2.8). This spread is visible not only for the whole set but also within the individual size classes and within the different rock samples (Table 2.2).

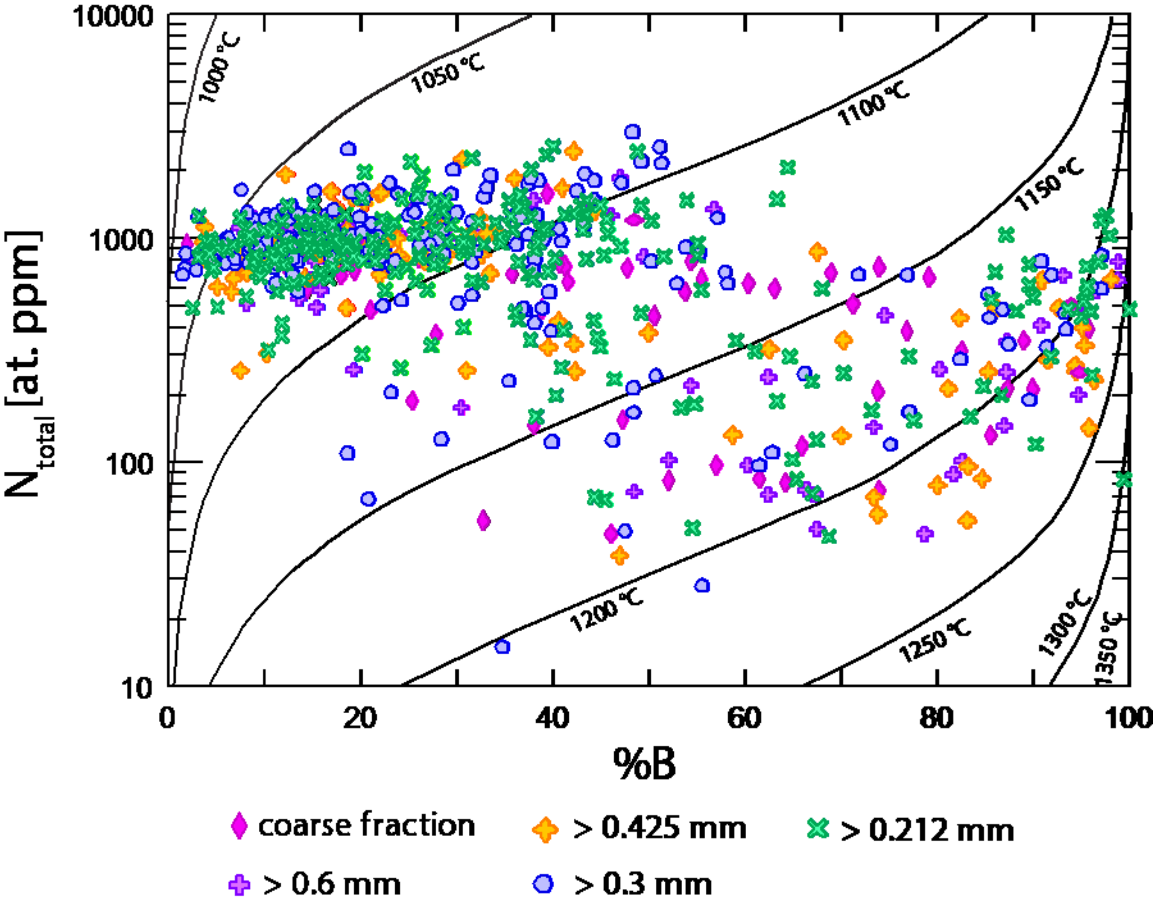

Figure 2.8: Total nitrogen content versus %B component for Misery diamonds. Isotherms are shown for a 3 Ga mantle residence period and were calculated after Taylor et al. (1990) and Leahy and Taylor (1997).

Nitrogen contents range from below the limit of detection (Type II, $N_{total} < 10$ at. ppm, 4% of all analyzed diamonds) to 2990 at. ppm, with a median at 850 at. ppm. For the complete Misery diamond suite, aggregation states range from 0% to 100%B with a median at 30%B.

Table 2.2: Summary of median values and value ranges for measured geochemical characteristics for the Misery diamond suite and the individual micro-diamond samples and the individual size fractions within the sub-samples. Also listed are calculated 'shallow'/'deep' ratio based on T_N and calculated $\delta^{13}C$ modes.

Sieve class	**N^1**	**N^2**	**Total N (at. ppm) - Mdn**	**Total N (at. ppm) - range**	**%B – range**	**N^1**	**N^2**	**3,107 cm^{-1} peak area (cm^{-2}) – Mdn**	**3,107 cm^{-1} peak area (cm^{-2}) – range**	**N^1**	**N^2**	**B' peak area (cm^{-2}) – Mdn**	**B' peak area (cm^{-2}) – range**
Coarse	35	52	596	81–1,582	2–96	34	51	18	2–238	27	39	48	3–348
>0.6 mm	52	66	789	0–1,871	3–99	49	60	21	1–406	40	51	26	1–368
>0.425 mm	82	104	839	0–2,442	4–98	78	96	29	0.04–426	59	74	36	0.7–383
>0.3 mm	134	215	914	0–2,987	0–97	137	205	25	1–879	123	185	46	1–662
>0.212 mm	175	253	868	0–2,567	0–100	170	236	24	1–561	159	217	37	0.4–769
All (>0.212–3.35 mm)	478	690	846	0–2,987	0–100	468	648	25	0.04–879	408	566	38	0.4–769
KIMB3-MS													
Coarse	7	14	173	48–946	2–90	7	14	10	2–40	4	4	78	25–149
>0.6 mm	13	13	1042	143–1,292	7–87	11	11	41	2.8–111	10	10	40	25–149
>0.425 mm	17	20	828	70–1,360	4–93	14	16	24	3–118	11	13	44	3–214
>0.3 mm	19	19	921	243–2,557	2–92	17	17	35	4.2–153	11	11	46	3.2–436
>0.212 mm	20	21	959	0–2,283	4–98	18	18	78	4.3–263	14	14	57	23–512
All (>0.212–3.35 mm)	76	87	891	0–2,557	2–98	67	76	35	2–263	50	54	44	2–512
KIMB5-MS													
Coarse	7	7	875	596–1,582	4–63	7	7	37	5.5–168	5	5	11	7–76
>0.6 mm	13	13	994	102–1,871	7–94	13	13	47	2.3–406	12	12	21	3–219
>0.425 mm	30	31	872	0–2,442	4–92	29	29	35	1.6–426	21	21	46	3.2–302
>0.3 mm	39	67	1,008	97–2,987	4–93	39	67	34	2–879	39	67	58	2–662
>0.212 mm	64	102	897	0–2,283	4–98	64	97	34	1–525	56	83	32	0.4–579
All (>0.212–3.35 mm)	153	220	934	0–2,987	4–98	152	213	35	1–879	133	188	43	0.4–662
KIMB5-SWE													
Coarse	18	28	587	81–1,002	12–96	18	28	16	2–238	16	26	37	3–347
>0.6 mm	17	27	683	0–1,482	3–99	16	24	17	3–386	13	22	45	1–368
>0.425 mm	28	44	812	0–2,259	4–98	28	44	28	0.04–180	22	35	36	1–383
>0.3 mm	55	95	847	0–2,499	0–97	56	90	21	1–307	52	79	46	1–429
>0.212 mm	54	83	814	0–2,567	0–100	51	79	16	2–561	52	78	36	2–292
All (>0.212–3.35 mm)	172	277	791	0–2,987	0–100	169	295	20	0.04–561	155	240	37	0.7–429

KIMB6-SWE													
Coarse	3	3	509	477–642	21–71	2	2	17	9.3–24	2	2	65	57–72
>0.6 mm	9	13	220	72–1,101	10–87	9	12	16	1–77	5	7	12	1–89
>0.425 mm	7	9	134	0–965	12–40	7	7	33	15.5–39	5	5	3	1.3–31
>0.3 mm	21	34	782	0–1,692	2–97	23	31	27	1–204	21	28	16	2–334
>0.212 mm	38	47	711	0–1,517	3–99	37	42	10	1–324	37	42	37	2–769
All (>0.212–3.35 mm)	78	106	708	0–2,987	0–100	78	94	17	1–323	70	84	29	1–769

Table 2.2 *(Cont.)*

Sieve class	**N^2 (<$T_{1,125°C}$)**	**N2 (>$T_{1,125°C}$)**	**Shallow/ deep ratio**	**N^1**	**N^2**	**δ^{13}C (‰) – Mdn**	**N^1**	**N^2**	**δ^{13}C (‰) – 1st mode^3**	**±2σ**	**Fraction**	**δ^{13}C (‰) – 2nd mode^3**	**±2σ**	**Fraction**
Coarse	24	14	1.7	25	84	–4.6	25	82	–4.7	0.046	0.41	–3.9	0.042	0.36
>0.6 mm	39	21	1.9	25	72	–4.4	25	72	–4.7	0.072	0.53	–3.8	0.093	0.39
>0.425 mm	69	21	3.3	34	77	–4.3	32	73	–4.7	0.041	0.45	–3.8	0.049	0.35
>0.3 mm	166	22	7.5	69	165	–4.2	69	162	–4.2	0.028	0.46	–3.5	0.037	0.29
>0.212 mm	185	28	6.6	107	242	–4.4	103	232	–4.7	0.027	0.33	–3.9	0.034	0.33
All (>0.212–3.35 mm)	483	106	4.6	260	640	–4.4	255	620	–3.9	0.016	0.38	–4.7	0.016	0.37
KIMB3-MS														
Coarse	4	8	0.5	6	20	–4.6	6	20	–4.5	0.049	0.71	–5.4	0.078	0.29
>0.6 mm	11	2	5.5	2	6	–4.2	2	6	–4.6	0.11	0.67	–3.3	0.16	0.33
>0.425 mm	13	3	4.3	4	10	–4	4	10	–4.7	0.1	0.4	–3.9	0.1	0.4
>0.3 mm	16	2	8.0	11	27	–4.4	11	26	–4.4	0.067	0.39	–5.2	0.071	0.31
>0.212 mm	16	2	8.0	17	37	–4.5	17	36	–4	0.063	0.33	–5.7	0.063	0.28
All (>0.212–3.35 mm)	60	17	3.5	40	100	–4.5	40	98	–4.7	0.044	0.43	–3.8	0.041	0.36
KIMB5-MS														
Coarse	6	0	100.0	6	20	–4.5	6	20	–4.5	0.071	0.4	–5.5	0.076	0.35
>0.6 mm	10	1	10.0	10	27	–4.2	10	27	–3.9	0.054	0.52	–4.8	0.056	0.48
>0.425 mm	21	6	3.5	11	24	–4.5	10	20	–4.8	0.067	0.45	–3.6	0.067	0.45
>0.3 mm	60	5	12.0	15	35	–4.3	15	35	–4.5	0.067	0.33	–5.2	0.071	0.23
>0.212 mm	80	8	10.0	40	92	–4.3	40	92	–3.9	0.041	0.39	–4.7	0.056	0.33
All (>0.212–3.35 mm)	177	20	8.9	82	198	–4.3	81	194	–4.7	0.025	0.41	–4	0.028	0.39
KIMB5-SWE														
Coarse	12	6	2.0	11	39	–4.6	11	37	–4.8	0.049	0.46	–4.1	0.062	0.3
>0.6 mm	14	11	1.3	10	28	–4.7	10	28	–4.7	0.57	0.05	–4	0.076	0.25
>0.425 mm	29	12	2.4	16	37	–4.3	16	37	–4	0.41	0.054	–4.8	0.06	0.32

>0.3 mm	67	14	4.8	28	65	–4	28	63	–3.9	0.037	0.59	–5	0.067	0.22
>0.212 mm	54	13	4.2	28	62	–4.6	25	55	–4.6	0.034	0.64	–3	0.053	0.27
All (>0.212–3.35 mm)	176	56	3.1	93	231	–4.4	90	220	–3.9	0.025	0.42	–4.8	0.02	0.35
<u>KIMB6-SWE</u>														
Coarse	2	0	100.0	2	5	–4.4	2	5	–4.7	0.1	0.8	–3.8	0.2	0.2
>0.6 mm	4	6	0.7	4	11	–4.3	4	11	–4.3	0.071	0.73	–3.4	0.12	0.27
>0.425 mm	6	0	100.0	3	6	–4.5	3	6	–4.7	0.1	0.67	–3.9	0.15	0.33
>0.3 mm	23	1	23.0	15	38	–4.2	15	38	–4.7	0.053	0.39	–3.5	0.083	0.28
>0.212 mm	35	5	7.0	24	51	–4.1	23	49	–3.8	0.062	0.39	–5.8	0.067	0.18
All (>0.212–3.35 mm)	70	12	5.8	48	111	–4.2	47	109	–4	0.043	0.41	–4.7	0.042	0.37

mdn = median

[1] Total number of diamonds included in analysis

[2] Total number of spots measured on diamonds per sieve class (for N content: type II included)

[3] Calculated using unmix ages function in Isoplot; 1st mode is the most frequently occuring mode, and 2nd mode the second most frequent

A slight decrease in median nitrogen abundance (Fig. 2.9, Table 2.2) with increasing diamond size is discernible. Variations in nitrogen abundance are also observed among diamonds originating from the different geological domains. Diamonds originating from the two rock samples from the Misery Southwest Extension, KIMB5-SWE and KIMB6-SWE, have median values that are ~ 100 at. ppm lower than median values of diamonds from the two samples from the Southern part of the Misery Main Pipe, KIMB3-MS and KIMB5-MS. The lower nitrogen abundances of diamonds from the Misery Southwest Extension are also seen in the individual size fractions of the different rock samples (Table 2.2). Aggregation states show the same trends and similar values between the individual size classes and rock samples.

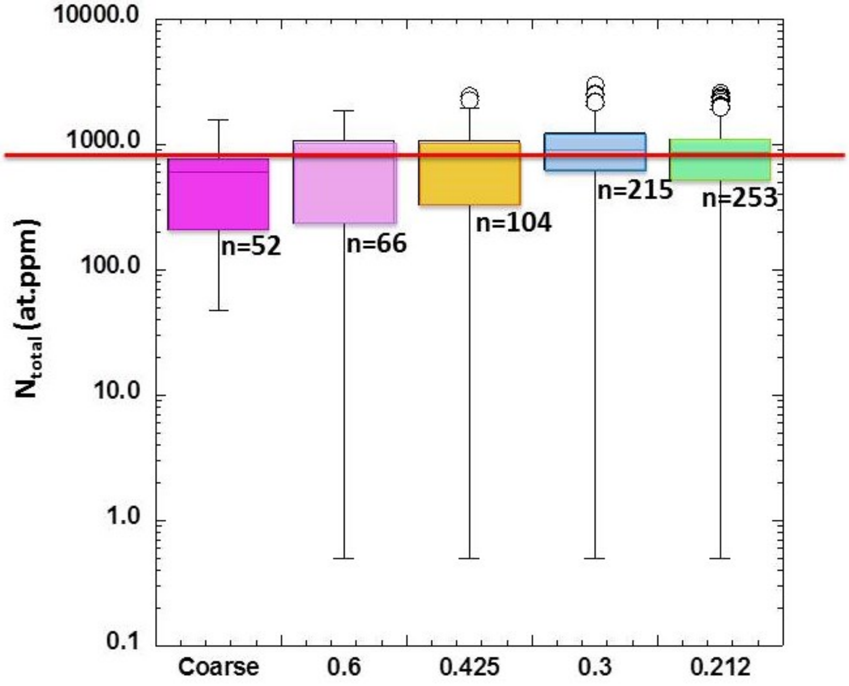

Figure 2.9: Box and whisker plot graphically displaying the spread in nitrogen content (ends of black lines), first and third quartiles ("interquartile," top and bottom of boxes), and medians (line through the middle of the boxes) of the different size fractions. The red line is the median of the whole Misery sample suite. n = number of samples represented by each box and whisker.

2.4.3 Platelet and Hydrogen peaks

Platelets - nm to µm sized planar defects in the diamond lattice - are an assemblage of interstitial carbon atoms that cause an absorption peak (B'), usually between 1358 to 1372 cm^{-1} (Sobolev et al., 1968; Mendelssohn and Milledge, 1995; Woods, 1986). The shift of the peak is dependent on the size of the platelets, with larger platelets found at lower wave numbers (Mendelssohn and Milledge, 1995). Hydrogen impurities in diamond result in IR absorption at various wave numbers (e.g., Goss et al., 2002; Fritsch et al., 2007). A hydrogen center with a vibrational mode at 3107 cm^{-1} occurs in almost all Type Ia natural diamonds worldwide, although sometimes in very small amounts, and is most readily observed (Fritsch et al., 2007). The 3107 cm^{-1} absorption peak is assigned to a C–H stretching vibrational mode and is now believed to represent a VN_3H center (three N surrounding a vacancy decorated by a single H; Goss et al., 2014). Platelet peak intensities (B') and intensities of the hydrogen-related peak at 3107 cm^{-1} are measured as peak area (cm^{-2}).

In total 408 samples (85%) have platelet peaks with peak areas ranging from 0.4 cm^{-2} to 770 cm^{-2} but the data distribution is strongly skewed to lower values (median = 40 cm^{-2}) with >85% of the data ranging from 0.4 cm^{-2} to 150 cm^{-2} (Tables A2.1 and 2.2). It appears that fewer larger stones show platelet peaks compared to the smaller diamonds; in the larger size fractions ~ 75% of the diamonds have platelet peaks compared to >90% in the smaller fractions. Bulk-rock Sample KIMB3-MS contained the lowest proportion of diamonds showing a platelet peak; KIMB5-MS, KIMB5-SWE and KIMB6-SWE diamonds show a platelet peaks in ~ 90% of the diamonds. A comparison of peak area median values shows that diamonds originating from sample KIMB6-SWE have the lowest median peak area, followed by diamonds from sample KIMB5-SWE, the diamonds from the two rock samples from Misery Main Pipe, KIMB3-MS and KIMB5-MS, showing higher I(B') median values (Table 2.2).

Hydrogen peak intensities (3107 cm^{-1} center) in Misery diamonds range between 0.04 cm^{-2} to 880 cm^{-2} but the majority (~88%) of diamonds fall between 1 cm^{-2} to 100 cm^{-2} (Table A1). Except for the coarse fraction where all but one diamond show a peak at 3107 cm^{-1}, the peak at 3107 cm^{-1} occurs in similar proportions (~90%) among the different size fractions. Rock sample KIMB3-MS contained the lowest proportion of diamonds with the 3107 cm^{-1} peak and KIMB5-MS the highest proportion. Out of the 24 Type II diamonds 13 have peaks at 3107 cm^{-1} with integrated strengths between 0.04 cm^{-2} to 21 cm^{-2} (median ~5 cm^{-2}). A comparison of median values shows that diamonds originating from the Main Pipe are more "H-rich" than diamonds originating from the Southwest Extension (Table 2.2).

2.5 Discussion

2.5.1 Carbon isotopic compositions

The observation that isotopic variation among distinct growth zones of Misery diamonds is low in most cases suggests growth from a fairly uniform mantle-related reservoir (c.f., Deines et al., 1984, 1989). Distinct internal variations in $\delta^{13}C$ across growth zones for some samples, with evidence for intermittent stages of resorption visible in CL images, suggest that multiple pulses of fluid/melt were involved in their growth. The negligible internal C isotopic variation observed for most Misery diamonds permits the use of the $\delta^{13}C$ values as a potential indicator for a distinct origin of different diamond size fractions. Similarities in isotopic composition and range across the different size fractions can be taken as a broad indication that they may be derived from the same population.

Previous studies on diamonds from deposits in the Lac the Gras kimberlite field (Ekati, DO-27, Diavik; Davies et al., 1999, 2004a; Cartigny et al., 2009; Donnelly et al., 2007; Melton et al., 2013) show that $\delta^{13}C$ values of Central Slave diamonds range from −21.1‰ to +1.6‰ with a median value of −4.9‰ for all analyses. This median value agrees well with the main global diamond mode of -5‰ (Cartigny et al., 2014). In comparison, the prominent mode at -4.2‰ with a broad shoulder at -4.5‰ (Fig. 2.6) for the Misery diamond suite studied here is more positive. Similarly, on average more positive $\delta^{13}C$ values have also been reported by Melton et al. (2013) for microdiamonds from Panda (Ekati) where gem-quality and cloudy microdiamonds have median values of -4.4‰ and -4.2‰, respectively.

Greater than 95% of the Misery diamonds fall into a narrow range between -8‰ to -2‰. Only 10 (3.8%) of the 260 analyzed Misery diamonds have $\delta^{13}C$ values below -10‰ (Table A1). An assignment of source paragenesis in the absence of mineral inclusion data should be performed with some caution, but the observed narrow range in $\delta^{13}C$ strongly suggests that the Misery diamond suite studied derives mainly from a peridotitic source. The negligible number of Type II diamonds makes a significant contribution of lower mantle sources unlikely. A previous study on mineral inclusions in Misery diamonds by Chinn et al. (1998) also showed that diamonds at Misery derive largely from peridotitic sources.

Only 1.3% of diamonds with peridotitic inclusions analyzed from worldwide sources have $\delta^{13}C$ values below -10‰ (Stachel et al., 2009). At the same time, not all eclogitic diamonds display $\delta^{13}C$ values below -10‰. Worldwide 75% of eclogitic diamonds that have been analyzed have carbon isotopic values between 0 and -10‰ (McCandless and Gurney, 1995), with the Premier (Cullinan) Mine representing the most prominent example of a predominantly eclogitic diamond production showing a narrow carbon isotopic distribution, dispersing about a mode of -4.7‰ (Deines et al., 1989). Therefore, it seems safe to assume that the presence of 3.8% diamonds in the Misery suite with $\delta^{13}C$ values below -10‰ likely reflects an eclogitic component that may include samples falling into the normal peridotitic range. This inference is supported by Chinn et al. (1998) who reported the presence of some eclogitic diamonds at Misery (ratio e:p of 1:3.5), identified via their mineral inclusions, with $\delta^{13}C$ values of -5, -17 and -25‰. The 10 diamonds in our suite showing $\delta^{13}C$ values below -10‰ are either fragments or whole stones >0.425 mm in size; this apparent restriction to "coarser" samples is in agreement with the suggestion that eclogitic diamonds may, on average, be larger than peridotitic diamonds (Gurney, 1989).

2.5.2 Nitrogen concentration and aggregation states

Previous studies have reported highly variable nitrogen concentrations and aggregation states in diamonds from the Central Slave Craton (Chinn et al., 1998; Davies et al., 1999, 2004a; Stachel et al., 2003; Tappert et al., 2005b; Donnelly et al., 2007; Melton et al., 2013), with concentrations ranging from <10 at. ppm (Type II) to over 1000 at. ppm and nitrogen aggregation ranging from pure Type IaA to pure Type IaB. Nitrogen concentrations for Misery diamonds overlap with the published data but show a much higher proportion of diamonds with nitrogen concentrations > 1000 at. ppm (32%) compared to all other studied Lac De Gras samples (5%). An exception are microdiamonds (< 1 mm) from Panda that also have a very high proportion of diamonds with nitrogen concentrations > 1000 at. ppm (24%; Melton et al., 2013). These authors consider this to be primarily due to the inclusion of clouded and coated samples into the Panda microdiamond data set, which were not present in other studies.

Looking at the individual size classes shows that only 4% of the coarse diamonds from Misery have nitrogen concentrations > 1000 at. ppm while all finer size fractions have proportions of diamonds with nitrogen concentrations > 1000 at. ppm from 30 – 39%. Misery diamonds show intermediate nitrogen aggregation states with a median of 30 %B, a higher value than found in most other Lac De Gras samples (Melton et al., 2013), with the exception of Panda diamonds (median = 23%B). This difference is considered to be principally due to lower nitrogen concentrations in diamonds from the other Lac De Gras localities, as evidenced by nitrogen based mantle residence temperatures (see below) that are similar to those calculated for Panda (Melton et al., 2013) and Misery (Chinn et al., 1998; this study).

2.5.3 Nitrogen Thermometry

Nitrogen concentration and aggregation data can be used to constrain mantle residence histories if the period of mantle residence of a population of diamonds is known (Taylor et al., 1990; Leahy and Taylor, 1997). Re-Os dating of sulfide inclusions from peridotitic diamonds from the Panda (Ekati) and A154 South (Diavik) kimberlites established that Central Slave peridotitic diamonds are Paleoarchean (3.5-3.3 Ga; Aulbach et al., 2009; Westerlund et al., 2006) in age. Assuming that the Misery diamonds from the present study are principally peridotitic and share a single age of formation, similar to Panda and A154 South peridotitic diamonds (i.e., that they resided in the mantle for ~ 3 Ga), time-averaged mantle residence temperatures (T_N) were calculated. Temperatures derived using nitrogen thermometry were found to compare reasonably well to those obtained by mineral inclusion-based geothermobarometry (Leahy and Taylor, 1997); associated uncertainties are assumed to be comparable to conventional silicate thermometry (± 50°C, Taylor et al., 1990).

A small percentage of the diamonds (15%) were excluded from temperature estimates since they yielded only poor quality or no IR spectra. For 175 diamonds multiple analyses were completed per diamond to detect possible internal variations in aggregation state and nitrogen content; apparent time-averaged temperature differences of 25-70°C were detected within individual diamonds, but for the majority of samples (84%) internal temperature differences are less than 25°C and are viewed as within the uncertainty of the method. Misery diamonds span a range of time-averaged mantle residence temperatures, from ~ 1030 to 1320°C (Table A1; Fig. 2.8). The majority of the analyzed diamonds cluster between about 1050°C to 1125°C with <50 %B and nitrogen concentrations between about 600 at. ppm to 1100 at. ppm. A second, smaller population represents higher temperatures between about 1175°C to 1225°C, associated with 40 %B to 100 %B and more variable nitrogen concentrations ranging from about 50 at. ppm to 1000 at. ppm. A histogram of T_N (Fig. 2.10) clearly illustrates the two distinct subpopulations, one ≤ 1125 °C and a second ≥ 1175 °C. A similar bimodal mantle residence temperature distribution was reported by Melton et al. (2013) for diamonds from the Panda kimberlite, also on the Ekati mine property.

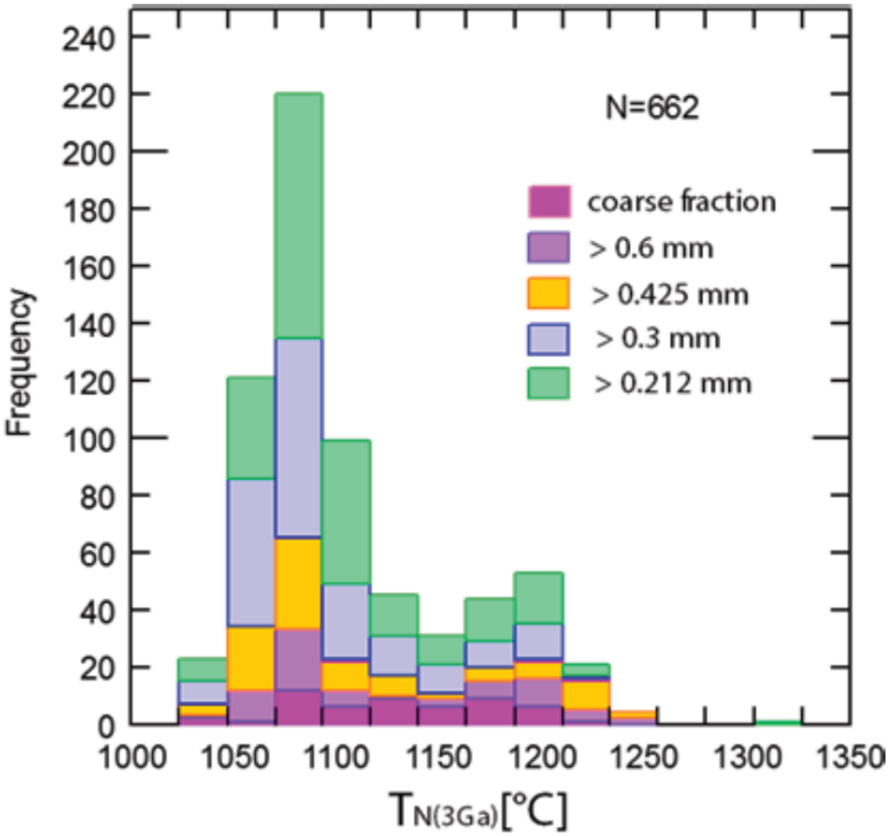

Figure 2.10: Histogram showing calculated time-averaged mantle residence temperatures. Misery diamonds show a range in temperature from ~1030 to 1320°C. The majority of diamonds fall within the mantle residence temperature range of 1030-1125°C; at temperatures > 1175°C a second subpopulation in TN is visible, and the temperature interval between ~ 1125 °C and 1175 °C is marked a notable decrease in sample density. N represents the number of analyses.

At Panda, one distinct diamond subpopulation has mantle residence temperatures below 1130°C and a second group ≥1160 °C. Projected on a central Slave geotherm (Grütter, 2009), these temperatures correspond to diamonds coming from depths less than about 155 km and greater than about 165 km, respectively. For Misery, the two temperature groups correspond to diamonds coming from depths less than about 160 km and greater than about 170 km. Melton et al. (2013) proposed that the bimodal temperature/depth distribution most likely reflects diamonds deriving from both the (ultra-depleted) upper and the (less depleted) lower layer of the Central Slave subcratonic lithospheric mantle (Griffin et al., 1999). A paucity of Cr-pyrope garnet xenocrysts is observed in a ~10 km thick region at the transition between these two layers, associated with a distinct spike in Mg-chromite abundance in some Lac de Gras kimberlites (Griffin et al., 1999). Based on the inference that high Mg-chromite/garnet ratios in the deep lithospheric mantle are indicative of poor diamond grades (Malkovets et al., 2007), this observation suggests that conditions may have been unfavorable for diamond formation in that particular depth interval.

The bimodal distribution in mantle residence temperatures is visible in all size fractions. The relative proportion of 'shallow' (<160 km) to 'deep' (>170 km) diamonds, however, decreases with sieve size (Table 2.2). The total sample set has a ratio of 'shallow' to 'deep' diamonds of ~ 5:1, but a systematically increasing ratio of "shallow" to "deep" diamonds as the size fraction decreases, e.g., at ~2:1 shallow:deep in the 0.6–0.85 mm sized diamonds to ~7:1 in the 0.212–0.3 mm fraction (Table 2.2). A possible explanation for this increasing proportion of shallow-derived diamonds with decreasing size is a lower survival rate of smaller diamonds during ascent from greater depths. The relative levels of diamond resorption features contradict this notion in that the high temperature ("deeper") subpopulation shows a notably higher proportion of diamonds with little to no resorption (34%) compared to the low temperature diamond population (20%). This suggests that a significant number of the high temperature diamonds were retained in their host xenoliths/xenocrysts during upward transport whilst "unprotected" high temperature diamonds were destroyed. The increasing proportion of shallow-derived diamonds likely relates to a different sampling efficiency for small and large diamonds at different depth, also possibly relating to primary abundance ratios at different depth. Complete destruction of unprotected deep diamonds may also account for the overall high shallow:deep ratio. This decrease of the 'shallow' to 'deep' ratio with decreasing sieve size is only to some extent visible in the subpopulations of the individual rock samples simply because samples populations are very small (Table 2.2).

2.5.4 Platelets

The large number of diamonds from a single locality analyzed via FTIR spectroscopy in this study provides an excellent opportunity to further constrain the origin of platelets in diamonds, which may, in turn, be a function of the degree of strain accommodated in the lithospheric mantle in the Lac de Gras region. Woods (1986) found that during the aggregation of nitrogen from A to B centers vacancies are created and showed a linear correlation between the platelet peak area and the strength of the B center absorption at 1282 cm^{-1}, i.e. the B-center concentration. Diamonds following this linear correlation are considered to be "regular" with an assumed smooth progression of nitrogen aggregation; diamonds that fall below the correlation line are "irregular", i.e. they show weaker platelet related absorption than predicted for their observed N_B concentration. This so-called platelet degradation is most likely a result of transient heating (Evans et al., 1995) or strain (Woods, 1986). Howell et al. (2012b) recently found that for cuboid diamonds platelet formation may have been stunted by intrinsic defects (disc-like fractures). Consequently, only non-cuboid diamonds that are not fully aggregated and do not adhere to the linear relationship between N_B and I(B') can be termed "irregular". Therefore, the identification of diamonds where cuboid growth potentially accounts for a significant proportion of a diamond's volume is crucial.

The Misery microdiamonds examined in this study include a significant number of fragments and highly resorbed crystals (see Section 2.2.1). This makes it difficult to detect cuboid or mixed habit growth diamonds based on morphological criteria. CL images, which could be used to detect mixed habit growth (e.g., though center-cross patterns) were only recorded for the sub-sample of 260 diamonds polished for SIMS analysis. Identification of cuboid-growth related diamonds was therefore achieved through evaluation of the 3107 cm^{-1} peak data. Cuboid-growth sectors in diamond are commonly hydrogen rich (e.g., Rondeau et al., 2004); following Fritsch and Scarratt (1993) diamonds are defined as "H-rich" when the absorbance at 3107 cm^{-1} exceeds the intrinsic diamond absorbance at 2450 cm^{-1}. Fig. 2.11 shows the relationship between platelet peak intensity and nitrogen in B centers (N_B). For platelet degradation calculations only diamonds with N_B concentrations > 50 at. ppm (allowing for robust spectral deconvolution), aggregation states between 2-98 %B (excluding pure Type IaA and IaB diamonds), and hydrogen related absorbance at 3107 cm^{-1} not exceeding diamond-related absorbance at 2450 cm^{-1} were used (35% of the sample suite). Across all size fractions, the majority of the Misery diamonds fall below the platelet correlation line of Woods (1986), i.e. they are "irregular".

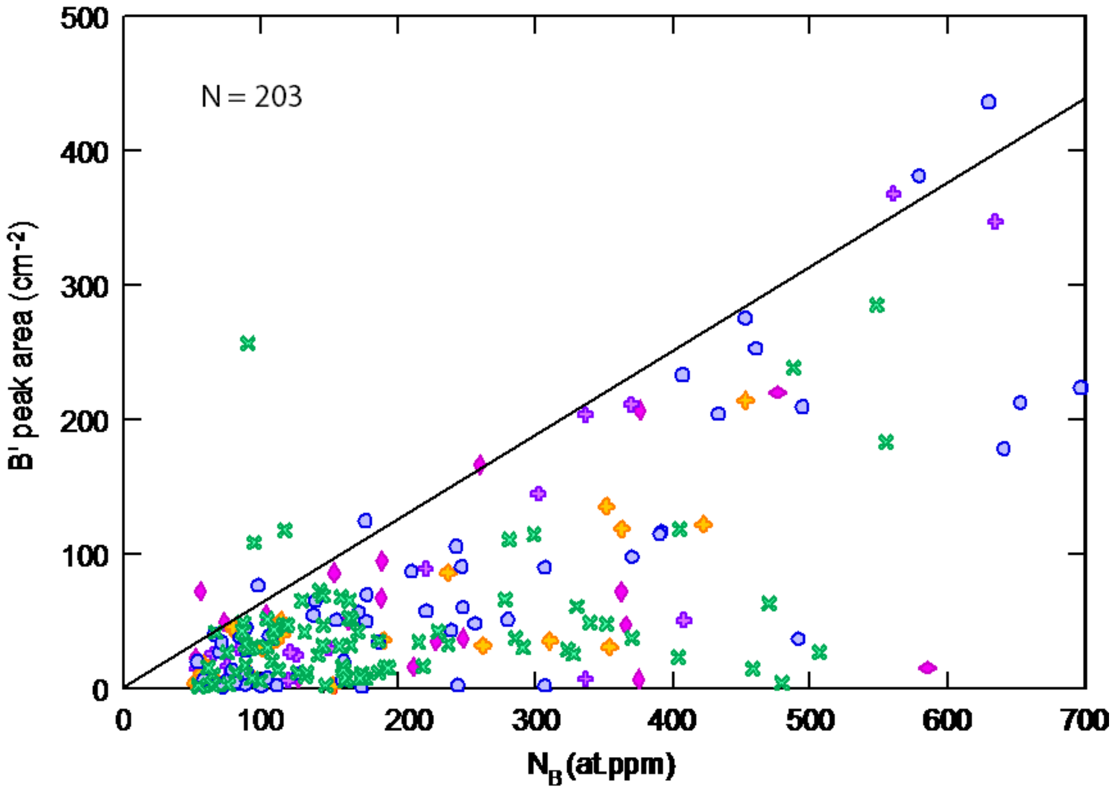

Figure 2.11: The relationship between platelet peak intensity and nitrogen in B centres (N_B). The solid line represents the linear relationship (slope of 0.61) from Woods (1986) between peak intensity and N_B for regular diamonds. "Irregular" diamonds plot below the regular trend line.

Fig. 2.12 shows the degree of platelet degradation versus the time-averaged mantle residence temperature. Evans et al. (1995) proposed that platelet degradation was due to transient heating which should result in a correlation between degree of "irregularity" and time-averaged mantle residence temperatures. No such relationship is visible here, which indicates that platelet degradation is not primarily dependent on temperature, in support of Woods (1986) suggestion that platelet degradation principally results from strain. To the contrary, the proportion of degraded samples increases with decreasing temperature. Only 4% of the plotted low-T ("shallow") diamonds are 'regular' versus a much higher proportion (26%) in the high-T ("deep") subpopulation. This suggests more common strain in diamonds from the shallow layer in the Central Slave lithospheric mantle. The overall high degree of platelet degradation coincides with a high number of brown stones found in the Misery diamond suite, which also is indicative of overall high degrees of plastic deformation (e.g., Fisher, 2009).

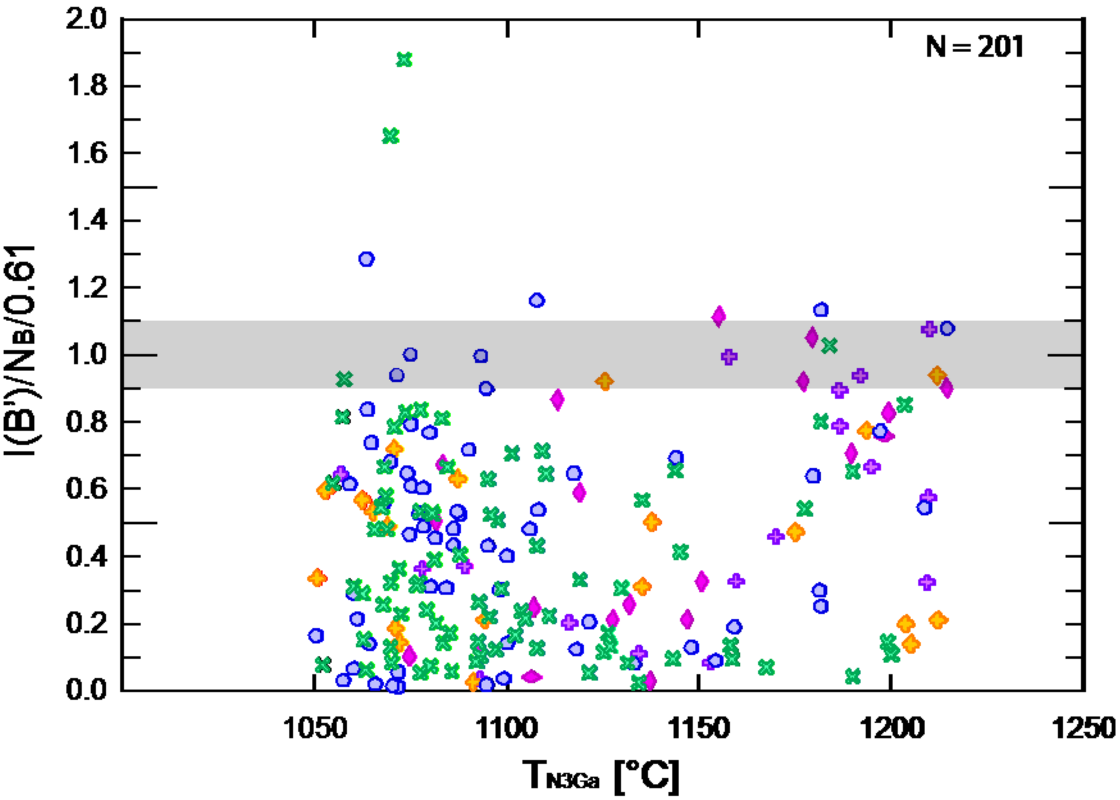

Figure 2.12: Degree of platelet degradation versus mantle residence temperature. The grey band represents regular diamonds, the area below represents increasing levels of platelet degradation. There is no relationship between the degree of platelet degradation and residence temperature, suggesting that platelet degradation principally results from strain (Woods, 1986).

2.5.5 Hydrogen peak

A correlative relationship between the area of the hydrogen-related peak at 3107 cm^{-1} and nitrogen characteristics has been observed in synthetic diamond (Kiflawi et al., 1996) and in natural diamond from Argyle (Lakoubovskii and Adriaenssens, 2002). Recent theoretical models have established a link between the 3107 cm^{-1} absorption with nitrogen, at least indirectly. De Weerdt and Collins (2006) and Goss et al. (2011) related the 3107 cm^{-1} center to nitrogen aggregates using experiments and theoretical calculations. A recent study by Goss et al. (2014) suggested, based upon the most recent experimental data, a VN_3H defect to be responsible for the 3107 cm^{-1} absorption center: a N_3 center (three nitrogen around a vacancy, VN_3) traps a mobile H atom. This model implies that the 3107 cm^{-1} center is not a direct measure of the hydrogen content in diamond, as formation of N_3 centers is the precondition of its existence.

Table 2.3: Comparison of median 3,107 cm^{-1} center values for Type II, IaA, IaAB, and IaB diamonds[1].

	N [%]		3107 cm^{-1} median [cm^{-2}]	
	Melton (2013)	**Misery**	**Melton (2013)**	**Misery**
all	80	94	1.79	24
Type II	68	54	1.02	4.7
Type IaA	64	97	1.42	15.7
Type IaAB	85	95	2.16	27.1
Type IaB	91	95	7.3	32.4

[1] Melton (2013) and this study; both show a trend of increasing IR-active hydrogen at 3,107 cm^{-1} with increasing aggregation

Melton (2013) explored a potential relationship between the area of the hydrogen-related peak at 3107 cm^{-1} and nitrogen characteristics using a database of 696 natural diamond samples from Brazil, Botswana, South Africa and Canada of varying paragenesis.

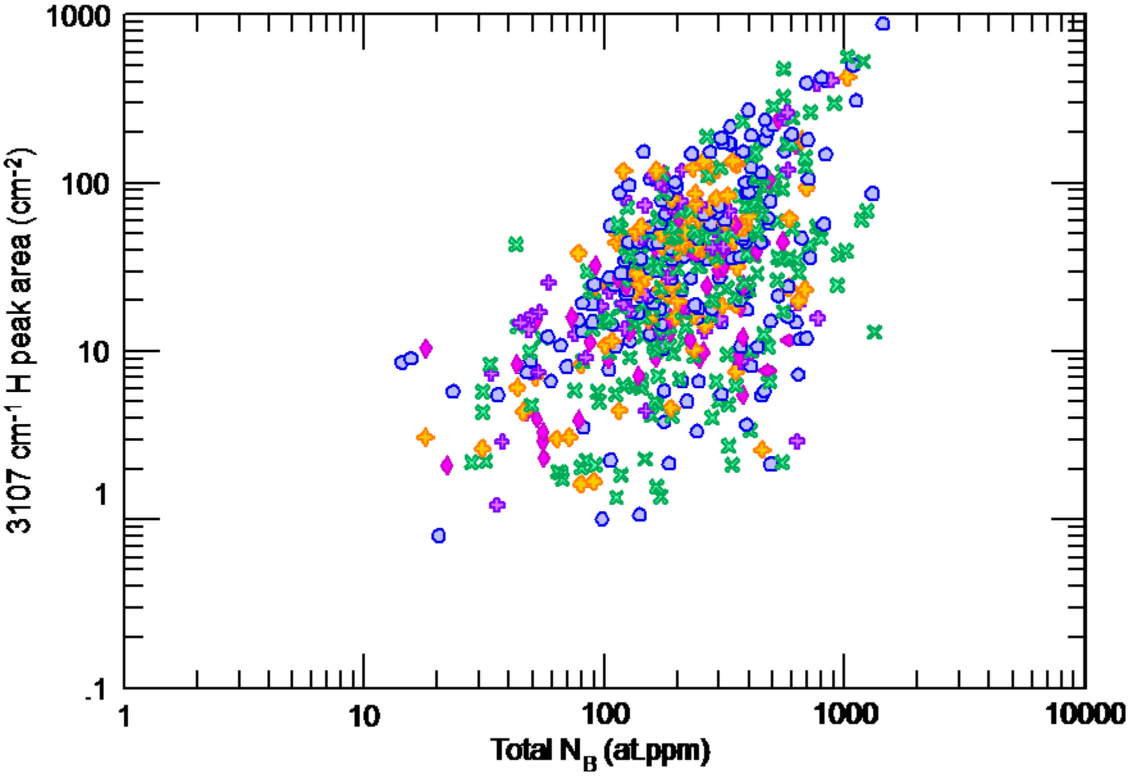

Figure 2.13: Plot of peak area of hydrogen related peak at 3107 cm^{-1} versus N_B concentration showing the distribution of samples based on size fraction. Type II and Type IaA diamonds are excluded.

He found increasing median values for the peak area of the 3107 cm^{-1} center with increasing concentration of nitrogen in the form of B-centers, consistent with the N_3VH model. This trend of positively correlated median/maximum area of the 3107 cm^{-1} center and N_B can also be observed for Misery diamonds (Table 2.3 and Fig. 2.13). In addition, it is apparent that Misery diamonds are uncommonly "H-rich". While the sample suite of Melton (2013) has a median 3107 cm^{-1} peak area of ~2 cm^{-2}, the median of the Misery diamond suite is an order of magnitude larger (24 cm^{-2}). There is no discernible relationship between the 3107 cm^{-1} peak area and diamond size.

2.5.6 Variability of diamond characteristics across different eruptive facies of the Misery kimberlite complex

The diamond suite studied here was derived from four microdiamond samples taken from two connected localities within the Misery kimberlite complex. The diamonds originating from the different rock samples have been compared with each other with regard to the analyzed geochemical characteristics and the statistical significance of potential differences between sample sets was tested. Physical characteristics vary little between diamonds of the different microdiamond samples. Sample KIMB5-MS has the highest proportion of fragments (72%) while KIMB3-MS, KIMB5-SWE and KIMB6-SWE have 49%, 54% and 63% fragments, respectively. The observation of KIMB5-MS and KIMB6-SWE having higher proportions of fragmented diamonds reflects the higher proportions of smaller diamonds in these samples.

Diamonds from the four different microdiamond bulk samples show differences in their nitrogen abundance. The two samples originating from the Misery Southwest Extension have median values that are about 100 at. ppm lower than the median values of the two samples from the Southern part of the Misery Main Pipe (Table 2.2). These observed differences between the Misery Southwest Extension samples and the Main pipe samples were determined to be statistically significant (Table 2.4).

Comparison of the T_N distributions and testing for possible statistically significant differences show that the 'shallow'/'deep' ratio for the smaller size fractions may be slightly

Table 2.4: Quantitative Statistical Comparison

N_{total} (incl. Type II)

	whole stones	coarse	> 0.6 mm	> 0.425 mm	> 0.3 mm	> 0.212 mm	KIMB3-MS	KIMB5-MS	KIMB5-SWE	KIMB6-SWE
fragments	0.441 (0.412)									
coarse		*0.715 (0.999)*								
> 0.6 mm		**0.001 (0.037)**	*0.07* ***(0.03)***							
> 0.425 mm		**0 (0.002)**	0.591 (0.3)	*0.64 (0.534)*						
> 0.3 mm		**0 (0)**	**0.008 (0.019)**	0.061 **(0.02)**	*0.16 (0.592)*					
> 0.212 mm		**0 (0)**	0.105 **(0.037)**	0.385 (0.348)	0.154 (0.054)	*0.32 (0.366)*				
KIMB3-MS							*0.128* ***(0.043)***			
KIMB5-MS							0.152 (0.084)	*0.472 (0.159)*		
KIMB5-SWE							0.143 (0.309)	**0 (0)**	*0.82 (0.788)*	
KIMB6-SWE							**0.025 (0.01)**	**0 (0)**	0.338 **(0.034)**	*0.985 (0.94)*

$T_{N(3Ga)}$

	whole stones	coarse	> 0.6 mm	> 0.425 mm	> 0.3 mm	> 0.212 mm	KIMB3-MS	KIMB5-MS	KIMB5-SWE	KIMB6-SWE
fragments	0.064 (0.054)									
coarse		*0.583*								
> 0.6 mm		0.05 (0.438)	***0.04***							
> 0.425 mm		**0 (0.019)**	0.908 (0.179)	*0.07*						
> 0.3 mm		**0 (0)**	**0.004 (0.021)**	0.229 **(0.01)**	*0.94 (0.656)*					
> 0.212 mm		**0 (0)**	**0.016 (0.007)**	0.37 (0.364)	**0.013 (0.036)**	*0.161 (0.567)*				
KIMB3-MS							*0.214*			
KIMB5-MS							0.147 (0.115)	*0.907 (0.54)*		
KIMB5-SWE							0.154 (0.176)	**0 (0)**	*0.168* ***(0.039)***	
KIMB6-SWE							0.434 (0.679)	0.09 (0.3)	**0.047** (0.055)	*0.152*

I(B')[1]

	whole stones	coarse	> 0.6 mm	> 0.425 mm	> 0.3 mm	> 0.212 mm	KIMB3-MS	KIMB5-MS	KIMB5-SWE	KIMB6-SWE
fragments	0.327 (0.602)									
coarse		*0.284*								
> 0.6 mm		0.084	*0.28*							
> 0.425 mm		0.359	0.233	***0.03***						
> 0.3 mm		0.724	0.127	0.829	*0.25*					
> 0.212 mm		0.478	0.233	0.855	0.475	*0.128*				
KIMB3-MS							*0.587*			

	whole stones	coarse	> 0.6 mm	> 0.425 mm	> 0.3 mm	> 0.212 mm	KIMB3-MS	KIMB5-MS	KIMB5-SWE	KIMB6-SWE
KIMB5-MS							**0.012**	*0.814*		
KIMB5-SWE							**0.011**	0.59	*0.236*	
KIMB6-SWE							**0.007**	0.167	0.339	*0.094*

3107 cm^{-1} centre[2]

	whole stones	coarse	> 0.6 mm	> 0.425 mm	> 0.3 mm	> 0.212 mm	KIMB3-MS	KIMB5-MS	KIMB5-SWE	KIMB6-SWE
fragments	0.429 (0.118)									
coarse		*0.272*								
> 0.6 mm		0.335	***0.00***							
> 0.425 mm		**0.044**	0.109	*0.43*						
> 0.3 mm		0.229	0.975	0.113	*0.34*					
> 0.212 mm		0.107	0.38	**0.031**	0.15	*0.454*				
KIMB3-MS							*0.211*			
KIMB5-MS							0.637	*0.439*		
KIMB5-SWE							**0.008**	**0**	*0.865*	
KIMB6-SWE							**0.002**	**0.008**	0.077	*0.753*

δ^{13}C[3]

	whole stones	coarse	> 0.6 mm	> 0.425 mm	> 0.3 mm	> 0.212 mm	KIMB3-MS	KIMB5-MS	KIMB5-SWE	KIMB6-SWE
fragments	**0 (0)**									
coarse		*0.077*								
> 0.6 mm		0.534	***0.03***							
> 0.425 mm		0.282	0.29	*0.52*						
> 0.3 mm		**0.025**	**0.035**	0.621	***0.01***					
> 0.212 mm		0.055	0.089	0.987	0.134	***0***				
KIMB3-MS							***0.012***			
KIMB5-MS							0.819	***0***		
KIMB5-SWE							0.322	0.86	***0.044***	
KIMB6-SWE							0.282	0.634	0.374	***0.024***

Subpopulations

Population	N	distribution type	Population	N	distribution type	Population	N	distribution type
N$_{total}$ (incl. Type II)			**I(B')**			**δ^{13}C**		
fragments	440	non-normal	fragments	310	non-normal	fragments	366	non-normal
whole stones	250	non-normal	whole stones	179	non-normal	whole stones	255	non-normal
coarse	52	normal	coarse	35	normal	coarse	84	non-normal

> 0.6	66	non-normal	> 0.6	44	log-normal	> 0.6	74	normal
> 0.425	104	non-normal	> 0.425	64	non-normal	> 0.425	75	non-normal
> 0.3	215	non-normal	> 0.3	152	non-normal	> 0.3	165	non-normal
> 0.212	253	non-normal	> 0.212	194	non-normal	> 0.212	242	non-normal
KIMB3-MS	87	non-normal	KIMB3-MS	51	non-normal	KIMB3-MS	98	non-normal
KIMB5-MS	220	non-normal	KIMB5-MS	159	non-normal	KIMB5-MS	194	non-normal
KIMB5-SWE	277	non-normal	KIMB5-SWE	203	non-normal	KIMB5-SWE	220	non-normal
KIMB6-SWE	106	non-normal	KIMB6-SWE	76	non-normal	KIMB6-SWE	109	non-normal
coarse frag	30	normal	coarse frag	18	normal	coarse frag	51	normal
coarse w.s.	22	normal	coarse w.s.	17	normal	coarse w.s.	31	normal
> 0.6 frag	43	non-normal	> 0.6 frag	26	log-normal	> 0.6 frag	36	non-normal
> 0.6 w.s.	23	normal	> 0.6 w.s.	18	normal	> 0.6 w.s.	36	normal
> 0.425 frag	67	non-normal	> 0.425 frag	45	non-normal	> 0.425 frag	36	non-normal
> 0.425 w.s.	37	normal	> 0.425 w.s.	19	log-normal	> 0.425 w.s.	37	normal
> 0.3 frag	148	non-normal	> 0.3 frag	108	non-normal	> 0.3 frag	117	non-normal
> 0.3 w.s.	67	normal	> 0.3 w.s.	44	non-normal	> 0.3 w.s.	45	non-normal
> 0.212 frag	152	non-normal	> 0.212 frag	113	non-normal	> 0.212 frag	126	normal
> 0.212 w.s.	101	non-normal	> 0.212 w.s.	81	non-normal	> 0.212 w.s.	106	normal
KIMB3-MS frag	48	non-normal	KIMB3-MS frag	27	log-normal	KIMB3-MS frag	58	normal
KIMB3-MS w.s.	39	normal	KIMB3-MS w.s.	24	normal	KIMB3-MS w.s.	40	non-normal
KIMB5-MS frag	163	non-normal	KIMB5-MS frag	116	non-normal	KIMB5-MS frag	128	normal
KIMB5-MS w.s.	57	normal	KIMB5-MS w.s.	43	non-normal	KIMB5-MS w.s.	66	non-normal
KIMB5-SWE frag	156	non-normal	KIMB5-SWE frag	114	log-normal	KIMB5-SWE frag	131	non-normal
KIMB5-SWE w.s.	121	non-normal	KIMB5-SWE w.s.	89	non-normal	KIMB5-SWE w.s.	89	log-normal
KIMB6-SWE frag	73	normal	KIMB6-SWE frag	53	log-normal	KIMB6-SWE frag	67	non-normal
KIMB6-SWE w.s.	33	normal	KIMB6-SWE w.s.	23	log-normal	KIMB6-SWE w.s.	42	normal

$T_{N(3Ga)}$			3107 cm^{-1} centre		
fragments	423	non-normal	fragments	375	non-normal
whole stones	238	non-normal	whole stones	195	non-normal
coarse	52	normal + log-normal	coarse	51	log-normal
> 0.6	65	non-normal	> 0.6	61	log-normal
> 0.425	100	non-normal	> 0.425	95	non-normal
> 0.3	205	non-normal	> 0.3	205	log-normal
> 0.212	239	non-normal	> 0.212	236	log-normal
KIMB3-MS	86	non-normal	KIMB3-MS	65	non-normal
KIMB5-MS	214	non-normal	KIMB5-MS	185	non-normal
KIMB5-SWE	267	non-normal	KIMB5-SWE	231	non-normal
KIMB6-SWE	95	non-normal	KIMB6-SWE	89	non-normal
coarse frag	30	non-normal	coarse frag	26	normal
coarse w.s.	22	non-normal	coarse w.s.	21	normal
> 0.6 frag	42	non-normal	> 0.6 frag	34	log-normal

> 0.6 w.s.	23	non-normal	> 0.6 w.s.	19	normal
> 0.425 frag	65	non-normal	> 0.425 frag	56	non-normal
> 0.425 w.s.	35	non-normal	> 0.425 w.s.	29	non-normal
> 0.3 frag	142	non-normal	> 0.3 frag	126	non-normal
> 0.3 w.s.	63	non-normal	> 0.3 w.s.	47	non-normal
> 0.212 frag	144	non-normal	> 0.212 frag	133	non-normal
> 0.212 w.s.	95	non-normal	> 0.212 w.s.	79	log-normal
KIMB3-MS frag	48	non-normal	KIMB3-MS frag	38	log-normal
KIMB3-MS w.s.	38	non-normal	KIMB3-MS w.s.	27	normal
KIMB5-MS frag	157	non-normal	KIMB5-MS frag	142	non-normal
KIMB5-MS w.s.	57	non-normal	KIMB5-MS w.s.	43	log-normal
KIMB5-SWE frag	152	non-normal	KIMB5-SWE frag	132	non-normal
KIMB5-SWE w.s.	115	non-normal	KIMB5-SWE w.s.	99	non-normal
KIMB6-SWE frag	66	non-normal	KIMB6-SWE frag	63	log-normal
KIMB6-SWE w.s.	28	non-normal	KIMB6-SWE w.s.	26	normal

Notes: Summary of p-values calculated using the online two-sample K-S test developed by Kirkman (1996), with p-values in parentheses calculated via two-sample
F-test for variances followed by a two-tailed Welch's t-test using EXCEL (Office 2013); bold font = p-value < α; italic font = fragments vs. whole stones

[1] All values >150 cm^{-2} excluded

[2] All values >100 cm^{-2} excluded

[3] All values >0‰ and <–10‰ excluded

lower for sample KIMB5-SWE than for the other samples (Table 2.2; 2.4). The number of the high and low temperature diamonds in the different size fractions of the four samples is so small that a quantitative statistical comparison of the diamonds is not possible.

A comparison of median hydrogen-related peak area values indicates that diamonds from the southern part of the Misery Main Pipe are even more enriched in IR-active hydrogen than diamonds from the Misery Southwest Extension (Table 2.2). Testing for statistical significance showed that diamonds of different size from the same rock sample are statistically indistinct from each other with regard to their hydrogen-related peak intensity distributions, whilst diamonds recovered from different samples are statistically distinct (Table 2.4), emphasizing the observed difference in median values.

2.5.7 A comparison of fragments versus whole stones

The Misery diamond suite has a significant proportion of originally macro-sized diamonds that subsequently broke into fragments (>50%). The presence of abundant fragments in all sieve classes that are derived from diamonds of greater but unknown size has to be considered during comparative geochemical studies. Therefore, we performed statistical tests to determine whether a significant difference exists between whole stones and fragments (Table 2.4). The presence of a high proportion of fragments in microdiamond sample sets is not unusual (e.g., McCandless, 1989) and their presence may blur geochemical distinctions between different size fractions.

Testing the nitrogen concentration distributions showed that whole stones and fragments within the individual size fractions and microdiamond samples are statistically indistinct from each other; the null hypothesis, stating that the tested samples derive from populations with identical distributions, was upheld in all cases as the p-value was more than the significance level threshold ($\alpha=0.05$). Tests comparing the time-averaged mantle residence temperature (T_N) and the 3107 cm^{-1} IR peak intensity distributions also indicated that, with one exception (0.6–0.85 mm fraction), fragments and whole stones within the individual size fractions and microdiamond samples are statistically indistinct from each other. Similarly, the distributions of the platelet peak intensity are indistinguishable for fragments and whole stones in all size fractions with the exception of the 0.425–0.6 mm fraction. Notwithstanding these two exceptions, the quantitative statistical comparison of nitrogen concentration, T_N, 3107 cm^{-1} peak intensity, and platelet peak intensity strongly suggest that fragments and whole stones are geochemically indistinct.

K-S tests comparing the $\delta^{13}C$ distributions of fragments and whole stones for the four individual microdiamond samples all indicate that they are statistically distinct. Comparisons of $\delta^{13}C$ distributions of fragments and whole stones within the individual size fractions show that fragments and whole stones are statistically distinct from each other within the 0.6–0.85 mm, 0.3–0.425 mm and 0.212–0.3 mm fractions, and statistically indistinct within the coarse and the 0.425–0.6 mm fraction. A comparison of median $\delta^{13}C$ values calculated for fragments and for whole stones shows that for the 0.6–0.85 mm, 0.3–0.425 mm and 0.212–0.3 mm fractions whole stones have slightly higher $\delta^{13}C$ values (by 0.3‰, 0.2‰ and 0.6‰, respectively; Table 2.5). Slightly higher median $\delta^{13}C$ values for whole diamonds relative to fragments are also visible for all four microdiamond samples.

While the $\delta^{13}C$ results contrast with the results obtained for other geochemical parameters, this likely only reflects the very high precision of the carbon isotopic measurements and their high spatial resolution. In most isotopic studies of diamonds samples are treated as being similar if their C isotopic compositions agree within better than 1 ‰ (e.g., the typical binning interval in histograms showing $\delta^{13}C$ distributions is 1 ‰). So while the statistical tests reveal that there is a greater than 95% probability that the median C isotope composition may be different, the actual differences are so small (0.2-0.6‰) that they are geologically likely not meaningful; for example, from the observed small shifts one cannot confidently conclude that diamond fragments and whole stones have crystallized from different fluids or in different substrates.

Table 2.5: Median $\delta^{13}C$ Values for the Individual Size Fractions of the Misery Diamond Suite, split into Fragments and Whole Stones

	N (sp/dia)	All - $\delta^{13}C$ [‰] - median	N (sp/dia)	Frag - $\delta^{13}C$ [‰] - median	N (sp/dia)	Wh. St. - $\delta^{13}C$ [‰] - median
Coarse	84/25	-4.6	53/16	-4.7	31/10	-4.5
> 0.6 mm	74/26	-4.4	36/13	-4.5	38/13	-4.2
> 0.425 mm	75/33	-4.3	39/16	-4.5	36/17	-4.2
> 0.3 mm	165/69	-4.2	120/50	-4.3	45/19	-4.1
> 0.212 mm	242/107	-4.4	136/61	-4.7	106/45	-4.1
all	640/260	-4.4	384/156	-4.5	256/104	-4.1

Abbreviations: dia = diamond, frag = fragmented diamond, sp = spot, Wh. st. = whole stone

2.5.8 Relationship between the different size fractions

A comparison of the physical characteristics between diamonds of different size fractions yields no obvious systematic differences (Table 2.6). Although the larger fractions have a higher percentage of brown stones this is likely only a reflection of difficulties in assessing the true body color of very small crystals. The 0.425–0.6 mm sieve class has a lower percentage of dodecahedra compared to the other fractions but also a higher percentage of stones exhibiting “irregular” shapes; in total all size classes have similar high proportions of secondary/ternary shapes. All size fractions have a high proportion of resorbed diamonds.

As previously noted, the Misery diamond suite contains a significant number of fragments (60% of all analyzed samples). The proportion of fragments is highest in the two smallest size fractions but even the larger size fractions have a significant number of diamond fragments.

Table 2.6: Relative proportions of physical characteristics of the different size fractions of the Misery diamond suite

	All	coarse	> 0.6 mm	> 0.425 mm	> 0.3 mm	> 0.21 mm
			Shape			
dodecahedra	*40%*	41%	40%	29%	48%	38%
octahedra	*23%*	34%	26%	29%	17%	22%
irregular	*32%*	25%	29%	40%	27%	35%
other	*5%*	3%	5%	2%	8%	5%
			Degree of resorption			
no to little resorption	*22%*	25%	24%	32%	17%	20%
resorbed	*28%*	20%	21%	26%	27%	33%
strongly resorbed	*50%*	55%	55%	42%	56%	47%
			Color			
colorless	*75%*	57%	60%	74%	77%	81%
brown	*18%*	32%	29%	20%	14%	13%
yellow	*3%*	0%	3%	3%	5%	2%
other	*4%*	11%	7%	3%	4%	4%

A lower median nitrogen concentration for diamonds of the coarse fraction was observed (see 4.2, Table 2.2). The statistical significance of this difference was determined using the two-sample K–S test as well as an unequal variance t-test (Table 2.4). The results indicate that diamonds < 0.85 mm are derived from one population while the coarse diamonds are statistically distinct, i.e. they may represent a different population. The lower nitrogen abundance of the larger diamonds is also seen within the individual diamond sub-populations of the microdiamond samples.

All five size fractions display a similar bimodal distribution in T_N, a larger low temperature group ($T_N < 1125°C$) and a smaller high temperature group ($T_N < 1125°C$) (Table 2.2). The T_N distributions of all size fractions were tested using the two-sample K-S test to determine if they differ statistically or if the individual sample populations have identical distributions in T_N. The results reported in Table 2.4 show that the smaller diamonds are statistically distinct from the larger stones, noticeably reflecting the observed increase of the 'shallow'/'deep' ratio with decreasing sieve size (Table 2.2).

The Misery diamond suite as a whole has proven to be very "H-rich", which is reflected in the individual size fractions. Statistical analyses have indicated that diamonds of different size fractions are distinct in some cases with regard to their hydrogen-related peak intensities;

however no correlation between diamond size and hydrogen-related peak intensity is apparent (Table 2.4).

A platelet peak is observed in ~75% of diamonds > 0.425 mm, of the smaller stones a higher percentage shows a platelet peak (> 90%). Although the median platelet peak intensities of the individual size fractions fall into a relatively wide range from 26 cm^{-2} to 48 cm^{-2} (Table 2.2), testing for statistical significance has shown that diamonds of the different size fractions are statistically indistinct from each other with regard to their platelet peak intensity distributions (Table 2.4).

With respect to carbon isotopic compositions, median values of the individual size fractions are similar ranging between -4.2‰ and −4.6‰ (Table 2.2). Statistical tests indicate that the 0.3–0.425 mm fraction is distinct from the coarse fraction and the 0.6–0.85 mm fraction. In comparison to all other size fractions, showing two similar main modes in $\delta^{13}C$ about -4.7‰ and -3.9‰, the 0.3–0.425 mm fraction is shifted by about 0.5‰ to higher $\delta^{13}C$ values (modes at -4.2‰ and -3.5‰; Table 2.2).

There is little variation in the number of samples showing internal isotopic variation greater than 3‰ across the individual size classes. The relative proportion of internally isotopically homogeneous (defined as internal variations of less than 0.5‰) samples increases with decreasing diamond size: 40%, 42%, 52%, 57% and 60% are internally homogenous for the size fractions coarse, 0.6–0.85 mm, 0.425–0.6 mm, 0.3–0.425 mm and 0.212–0.3 mm, respectively.

2.6 Summary and Conclusions

Misery diamonds in the size range 0.2-3.4 mm show overall high nitrogen contents (median=850 at. ppm), a bimodal distribution in time-averaged mantle residence temperatures (two distinct subpopulations in T_N; ≤ 1125 °C and ≥ 1175 °C), a high degree of platelet degradation, $\delta^{13}C$ values that are slightly higher (median = -4.4‰) than the global median (-5.2 ‰; based on data from Stachel, 2014) and are uncommonly “H-rich” (median 3107 cm^{-1} peak area = 24 cm^{-2}).

The high nitrogen contents of the Misery diamond suite do not match the distributions of peridotitic diamonds from worldwide sources (median=82 at. ppm, Stachel, 2014) but are known to be typical for Slave Craton diamonds (Stachel et al., 2009). The two distinct subpopulations in time-averaged mantle residence temperatures correspond to diamonds coming from depths less than about 160 km and greater than about 170 km, respectively, indicating derivation from the depleted upper and less-depleted lower portions of the subcratonic lithospheric mantle below the Central Slave (Griffin et al., 1999, 2004; Melton et al., 2013). The high degree of platelet degradation corresponds to the high number of brown stones at Misery, and indicates that the diamonds were strongly deformed during their mantle residence.

Statistical comparisons between whole crystals and diamond fragments at Misery indicate that, with the exception of $\delta^{13}C$ compositions, fragments and whole stones are statistically indistinct from each other. Median $\delta^{13}C$ values for diamond fragments are lower than for whole stones. For three size fractions (0.6–0.85 mm, 0.3–0.425 mm and 0.212–0.3 mm) these differences were found to be statistically significant but amounted to less than 1‰ – a difference that is insignificant in terms of diamond paragenesis. Strongly ^{13}C depleted carbon isotopic signatures of some diamond fragments are visible within all four microdiamond samples studied and indicate the presence of an eclogitic diamond component.

Statistical comparisons of geochemical diamond characteristics for the four studied microdiamond samples reveal minor differences and many similarities. Differences include median nitrogen contents in diamonds from the two samples from Misery Southwest Extension that are more than 100 at. ppm lower compared to the two samples from the southern part of the Misery Main Pipe. In addition, diamonds from the southern part of the Misery Main Pipe are more "H-rich" than diamonds from the Misery Southwest Extension. The decrease in the relative proportion of 'shallow' to 'deep' diamonds with increasing sieve size is a consistent feature of three of the four microdiamond samples (exception is KIMB5-SWE).

Comparing geochemical characteristics across the different size fractions reveals a slight decrease in median nitrogen abundance - the diamonds of sieve classes < 0.85 mm show median values between ~ 790 and 920 at. ppm while coarser diamonds have a median of ~ 600 at. ppm - and a decrease of the relative proportion of 'shallow' to 'deep' diamonds with sieve size. The lower nitrogen concentration of the coarse diamonds was found to be statistically significant (K-S test). This difference may reflect gradual nitrogen depletion in a fluid that grew both large and small diamonds. Statistical tests showed that no significant variation in $\delta^{13}C$ exist across the studied size classes.

Overall, we can conclude that each size fraction of diamonds derives from a very similar "population" of diamonds with respect to chemical characteristics; this observation includes the presence of a small percentage of strongly ^{13}C depleted diamond (eclogitic or websteritic suite) in most size fractions. Our data supports a similar origin for the majority of the microdiamonds studied, regardless of rock type or size fraction. This suggests that observed differences in stone size distributions (Fig. 2.3) are most likely introduced by volcanic processes operating on populations of diamonds that are probably of the same origin and very likely started out with the same size distribution. For the Misery bulk samples taken during the exploration phase of kimberlite evaluation, the here reported general geochemical similarity of diamonds from across the different size fractions examined reinforces the use of size-frequency analysis to predict diamond grade in kimberlite diamond deposits. Further detailed studies such as this are required to more extensively evaluate this approach.

Chapter 3

The origin and evolution of diamond-forming fluids in gem diamonds

3.1 Introduction

Diamond crystallizes from a fluid/melt phase - relics of which may become trapped and, thus preserved in the form of inclusions (Navon et al., 1988). To understand the origin of diamonds it is essential to constrain the nature of these so-called high-density fluid (HDF) inclusions. Fibrous and cloudy diamonds trap a high density of HDFs and, therefore, have been extensively studied using major and trace element compositions, resulting in the identification of four major compositional types of HDFs (saline, silicic, and high-Mg and low-Mg carbonatitic) that lie on two wide compositional arrays. One array ranges from a silicic end-member to a low-Mg carbonatitic end-member, and a second array extends between a saline end-member and a high-Mg carbonatitic end-member (e.g., Navon et al., 1988; Izraeli et al., 2001, 2004; Tomlinson et al., 2006; Klein-BenDavid et al., 2007, 2009, 2014; Weiss et al., 2009; 2015).

Trace elements measured in diamond HDFs from worldwide sources have been classified into two general end-member normalized trace element patterns: a flat, unfractionated class of patterns ("planed") and a highly fractionated ("ribbed") class of patterns (e.g., Tomlinson et al., 2009; Weiss et al., 2009, 2011; Klein-BenDavid et al., 2010; Smith et al., 2012). The "planed" patterns can be related to small degree asthenospherically derived melts whereas the "ribbed" patterns are proposed to represent increased interaction with the sub-continental lithospheric mantle (Weiss et al., 2013).

Fibrous diamonds can represent a significant fraction of mine production, as either cuboids or coated stones. Most fluid-rich fibrous and cloudy diamonds are thought to have formed within less than 5 Ma of the age of kimberlite eruption based on low nitrogen aggregation states and the similarity of their fluid inclusions to kimberlitic fluids (e.g., Gurney et al., 2010). A recent study by Timmerman et al. (2017) has reported minimum U-Th/He ages that suggest that some fibrous diamonds formed tens to hundreds of million years before eruption of their host kimberlite during earlier diamond-forming events. As the majority of known kimberlites are Phanerozoic, this means that the study of diamond-forming fluids in fibrous diamonds may be largely limited to the Phanerozoic record, with the exception of the Archean Wawa diamonds studied by Smith et al. (2012). In contrast, common gem diamonds (here defined as clear smooth-surfaced monocrystalline diamond) of peridotitic or eclogitic association are generally ancient (3.6 – 0.99 Ga; Pearson and Shirey, 1999; Gurney et al., 2010). Peridotitic suite diamonds containing harzburgitic inclusions are thought to have formed dominantly in the Paleoarchean and those with lherzolitic inclusions in the Paleoproterozoic to Mesoproterozoic (Gurney et al., 2010; Stachel, 2014) whereas the crystallization of eclogitic suite diamonds has been documented between 2.9 and 0.99 Ga (e.g., Shirey et al., 2013). In addition to differences in habit and growth rates between fibrous and gem diamonds (e.g., Sunagawa, 1984), the discrepancy in formation ages between the two diamond types has created doubts as to the significance of fibrous diamond-forming fluids for the growth of gem-quality diamonds. To address this issue it is clearly important to seek out and characterise any trace amounts of growth fluids that may be trapped in gem diamonds.

Jablon and Navon (2016) recently discovered rare fluid inclusions in gem diamonds that showed similar major element chemistry ranges to fluid-rich fibrous diamonds, suggesting that many diamonds may share a common spectrum of parental fluids. Further evidence of this link might be gained by trace element measurements in gem diamonds, which can be used to constrain whether the fluids from which gem diamonds grow stem from the same sources and undergo the same processes leading to diamond growth. Constraining the nature of the diamond-forming fluid or melt for high purity gem-quality diamonds, however, is hampered by the sparsity of available high quality trace element data, mainly due to the extremely low concentrations of impurities that these diamonds contain. The development of a new technique by McNeill et al. (2009) and Klein-BenDavid et al. (2010) - in-situ, closed-cell laser ablation –

that allows the accumulation of higher volumes of analyte, greatly increasing the chance of producing quantitative data by improving the signal to noise ratio many times over ‘on-line’ laser ablation, has resulted in two studies reporting quantitative data on gem diamond (McNeill et al., 2009, Melton et al., 2012). Trace element systematics on gem diamonds have also been reported by Rege et al. (2010) who analysed > 400 monocrystalline diamonds from deposits worldwide, using LA-ICPMS techniques described in Rege et al. (2005). The authors found very strong similarities between all analysed diamonds regardless of locality and paragenesis. As Rege et al. (2010) did not clearly demonstrate that their measurements met rigorous criteria for being above defined limits of quantitation (LOQ), these data will not be considered in any of the comparisons made here.

Here we present a dataset of trace element data from high-purity gem diamonds from the Victor Mine, Ontario, as well as near-gem diamonds from peridotite and eclogite xenoliths from the Finsch and Newlands mines, South Africa, to evaluate the likely origin of the fluids and their similarities to those that form fibrous diamonds.

3.2 Samples

In this study we analysed diamonds from three different locations (Table 1). The majority of samples originate from the Victor Mine, Ontario, Canada, and are ultra-pure gem-quality P-type diamonds in the form of polished plates. The Victor plates range between 0.23 and 0.55 carats and their paragenesis was constrained from the solid macro-inclusions that they contain. Eight peridotitic garnet inclusion-bearing and eight sulphide inclusion-bearing diamonds were selected for analysis. Victor diamonds containing silicate inclusions were previously characterized by Fourier transform infra-red (FTIR) spectroscopy and found to be Type Ia with N contents ranging from 13 ppm to 955 ppm. Based on the nitrogen content and aggregation state data, an average mantle residence temperature of ~ 1140 ± 19 °C was obtained for a mantle residence time of 0.54 Ga (Stachel et al, 2017).

In addition to the Victor samples, gem diamond samples of lower clarity originating from different diamondiferous xenoliths from the Finsch and Newlands kimberlites, South Africa, have been analyzed. Four diamonds come from Newlands eclogite xenoliths.

Table 3.1: Provenance, host lithology, formation age and inclusion paragenesis of the fluids in the analyzed diamonds and those used for comparisons. *References for formation ages: Victor (Aulbach et al. (2018), Cullinan E-type (Richardson, 1986, Burgess et al. 1989, Phillips et al. 1989) Cullinan P-type (Richardson et al., 1993), Udachnaya, P-type ~ 3.1 - 3.5 Ga; Pearson et al., 1999), Finsch (Richardson et al., 1984) and Newlands (Menzies et al., 2003).

Name	Provenance	host lithology	Age	Inclusion
V3-01	Victor, Superior Craton, Canada	P-type	~ 718 Ma	Garnet
V3-03	Victor, Superior Craton, Canada	P-type	~ 718 Ma	Garnet
V3-05	Victor, Superior Craton, Canada	P-type	~ 718 Ma	Garnet
V3-11	Victor, Superior Craton, Canada	P-type	~ 718 Ma	Garnet
A578-01	Victor, Superior Craton, Canada	P-type	~ 718 Ma	Garnet
A578-02	Victor, Superior Craton, Canada	P-type	~ 718 Ma	Garnet
A578-03	Victor, Superior Craton, Canada	P-type	~ 718 Ma	Garnet
A578-04	Victor, Superior Craton, Canada	P-type	~ 718 Ma	Garnet
V2-01	Victor, Superior Craton, Canada	P-type	~ 718 Ma	Sulphide
V2-02	Victor, Superior Craton, Canada	P-type	~ 718 Ma	Sulphide
V2-03	Victor, Superior Craton, Canada	P-type	~ 718 Ma	Sulphide
V2-04	Victor, Superior Craton, Canada	P-type	~ 718 Ma	Sulphide
V2-06	Victor, Superior Craton, Canada	P-type	~ 718 Ma	Sulphide
V2-07	Victor, Superior Craton, Canada	P-type	~ 718 Ma	Sulphide
V2-09	Victor, Superior Craton, Canada	P-type	~ 718 Ma	Sulphide
V2-10	Victor, Superior Craton, Canada	P-type	~ 718 Ma	Sulphide
New 01	Newlands, Kaapvaal craton, South Africa	E-type	~2.9 Ga	unknown
New 02	Newlands, Kaapvaal craton, South Africa	E-type	~2.9 Ga	unknown
New 03	Newlands, Kaapvaal craton, South Africa	E-type	~2.9 Ga	unknown
New 04	Newlands, Kaapvaal craton, South Africa	E-type	~2.9 Ga	unknown
f866 1	Finsch, Kaapvaal craton, South Africa	P-type (h)	~3.2 Ga	unknown
f866 2	Finsch, Kaapvaal craton, South Africa	P-type (h)	~3.2 Ga	unknown
jjg 1	Finsch, Kaapvaal craton, South Africa	P-type (h)	~3.2 Ga	unknown
jjg 2	Finsch, Kaapvaal craton, South Africa	P-type (h)	~3.2 Ga	unknown

Table 3.1 continued

Published Gem diamonds used for comparison					
1581-Mir	Mir, Siberian craton, Siberia	E-type	~ 2.1 Ga	Sulphide	McNeill et al. (2009)
1812P-Udachnaya	Udachnaya, Siberian craton, Siberia	P-Type	~ 3.1 - 3.5 Ga	Sulphide	McNeill et al. (2009)
AP25	Cullinan, Kaapvaal craton, South Africa	E-type	~2 Ga, ~ 1.2 Ga	Silicate	McNeill et al. (2009)
AP26	Cullinan, Kaapvaal craton, South Africa	E-type	~2 Ga, ~ 1.2 Ga	Silicate	McNeill et al. (2009)
AP28	Cullinan, Kaapvaal craton, South Africa	P-type (h)	~2 Ga	Silicate	McNeill et al. (2009)
AP30	Cullinan, Kaapvaal craton, South Africa	P-type (l)	~2 Ga	Silicate	McNeill et al. (2009)
AP31	Cullinan, Kaapvaal craton, South Africa	E-type	~2 Ga, ~ 1.2 Ga	Silicate	McNeill et al. (2009)
AP34	Cullinan, Kaapvaal craton, South Africa	E-type	~2 Ga, ~ 1.2 Ga	Silicate	McNeill et al. (2009)
AP35	Cullinan, Kaapvaal craton, South Africa	E-type	~2 Ga, ~ 1.2 Ga	Silicate	McNeill et al. (2009)
AP36	Cullinan, Kaapvaal craton, South Africa	E-type	~2 Ga, ~ 1.2 Ga	Silicate	McNeill et al. (2009)
AP37	Cullinan, Kaapvaal craton, South Africa	E-type	~2 Ga, ~ 1.2 Ga	Silicate	McNeill et al. (2009)
AP38	Cullinan, Kaapvaal craton, South Africa	E-type	~2 Ga, ~ 1.2 Ga	Silicate	McNeill et al. (2009)
G103	Akwatia, West African Craton, Ghana	P-type (h)		Silicate	Melton et al. (2012)

These diamonds were selected on the basis of their known paragenesis. N aggregation and concentration data have been published on one of these diamonds, yielding a temperature of ~1100 °C at a residence time of 1 Ga that is consistent with the cpx-gt temperature from diamondiferous Roberts Victor xenolith RV124 (1097 °C – Taylor et al., 1995). The formation age of the Newlands diamonds is unknown, however whole rock Re-Os dating of diamond bearing eclogites from the Newlands kimberlite indicates that eclogitic diamonds are likely of Archean and Proterozoic age (Menzies et al., 2003). Four diamonds analysed in this study originate from two different Finsch harzburgite xenoliths (F866, JJG1 and JJG4). N aggregation and concentration data of one diamond from the F866 xenolith yield a temperature of ~ 1125 °C (at a mantle residence time of 1 Ga) that agrees with previous data from Taylor et al. (1995). Finsch P-type diamonds formed in the Archean (3.3-3.2 Ga, Richardson et al., 1984).

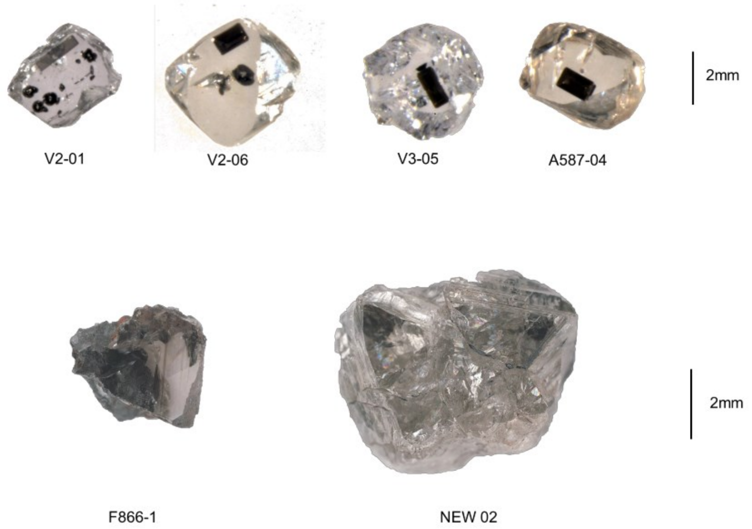

Figure 3.1: Selected diamonds analysed in this study, showing laser ablated areas. V2-01 and V2-06 are sulphide-bearing diamonds from Victor (Canada) and V3-05 and A587-04 are silicate bearing diamonds from Victor. F866-1 is a diamond from a Finsch harzburgite xenolith; NEW 02 is a diamond from a Newlands eclogite xenolith. The Victor diamonds demonstrate clearly the size of the offline ablation pit, which is blackened due to graphitisation.

3.2.1 Geology of diamond sample sources

3.2.1.1 Victor, Canada

De Beers' Victor Mine - the first diamond mine on the Superior Craton - is part of the Jurassic Attawapiskat kimberlite field, Ontario, Canada (Kong et al., 1999). It is a low-grade mine at 0.23 carat per tonne, but its diamond value is among the highest in the world (about US$440/ct).

The Victor Mine exploits a diamond resource that is principally (~85%) derived from lherzolitic mantle substrates (Stachel et al., submitted). Based on garnet inclusion trace element characteristics and geothermobarometric results, Victor diamonds formed under subsolidus conditions in a narrow (<10 km thick) layer at about 180 km depth (Stachel et al., 2017). Re-Os dating of peridotitic sulphide inclusions in Victor diamonds yielded a robust model-3 isochron age of 718 ±49 Ma (Aulbach et al., 2018). The young diamond age and lherzolitic association make Victor unique among diamond mines worldwide.

3.2.1.2 Newlands, South Africa

The Newlands kimberlite cluster, located approximately 60 km NW of Kimberley, South Africa, in the Northern Cape Province, is Cretaceous in age (114±1.6 Ma) and classifies as a Group-2 kimberlite (Smith, 1983; Smith et al., 1985). Newlands consists of a series of five small pipes or "blows" located along a dyke. The mine, owned and operated by Dwyka Diamonds Limited since 2005, has produced a wide variety of mantle xenoliths, including diamond-bearing sub-calcic harzburgites and eclogites (Gurney and Menzies, 1998). Re-Os isotope analyses of diamond-bearing garnet macrocrysts indicate three main events in the lithospheric mantle beneath Newlands: 3.1–3.4 Ga, 2.7–2.8 Ga and 1.8–2.1 Ga (Menzies et al., 2003).

3.2.1.3 Finsch, South Africa

The Finsch kimberlite pipe is located approximately 150 km west of Kimberley, South Africa, and was discovered in 1960 (Field et al., 2008). Diamond production commenced in 1965 (Viljoen and Lawless, 1988). Finsch is a Group-2 kimberlite (Smith, 1983), with an Rb–Sr pipe emplacement age of 118±2.8 Ma (Smith et al., 1985). The pipe was emplaced through a thick sequence of Proterozoic sedimentary rocks comprising dolomites, banded iron formation and shales (Clement, 1982). Inclusions in Finsch diamonds are predominantly peridotitic (harzburgitic; Harris and Gurney, 1979; Tsai et al., 1979) with a Sm–Nd model age of 3.3±0.1 Ga (Richardson et al., 1984). Eclogitic inclusions were found to be significantly younger (1580±50 Ma, Richardson et al., 1990; Sm–Nd model ages from 1443±166 to 1657±77 Ma, Smith et al., 1991).

3.3 Analytical methods

All laboratory and analytical work on the Victor diamond suite was carried out in the Arctic Resources Laboratory at the Department of Earth and Atmospheric Sciences, University of Alberta. The laboratory and analytical work on the Newlands and Finsch diamond suites was performed in the Arthur Holmes Isotope Geology Laboratory at the Department of Earth Science, University of Durham, using the same analytical procedures adopted in Alberta (summarised in McNeill et al., 2009).

3.3.1 Offline laser ablation

Diamond ablations were performed using an “off-line” laser ablation sampling technique developed by McNeill et al. (2009) and Klein-BenDavid et al. (2010) that utilizes a closed-system laser ablation cell in which a diamond is ablated and the products trapped, allowing the accumulation of much higher volumes of analyte compared to “online” methods. The custom-designed, sealed PFA ablation cell is capped with a pre-cleaned fused silica laser window that is blank tested in every analysis batch. Comparison of the method to on-line laser methods has been documented by Klein-BenDavid et al. (2014). The closed nature of the cell and laser decomposition of the sample mean that detection limits can be improved simply by increasing the ablation time, providing increased analyte signal at constant “blank”. The solution-based nature of the trace element analyses allows for calibration against matrix-matched standards. All these factors facilitate the production of quantitative data for the very low abundances of elemental impurities in gem diamonds.

3.3.1.1 Sample preparation

All diamonds were leached in 16 N Seastar triple distilled UPA-grade HNO_3 and 29 N UPA-grade HF on a hotplate at 100 °C for 24 hrs and then rinsed in 18.2 MΩ MQ H_2O before being leached in Teflon distilled 6N HCl for another 24 hrs at 100 °C, followed by a final rinse in MQ H_2O. All samples were dried and weighed on a Mettler Toledo™ UMT2 Micro Balance prior to placing them in the ablation cell. The diamond is held under its own weight, presenting a flat surface orthogonal to the laser beam. Once the diamond is in place the ablation cell is capped with the laser window.

3.3.1.2 Ablation and sample collection

Ablations of the Victor diamond suite were performed using a RESOlution M-50HR (Resonetics) 193 nm ArF Excimer (CompexPro 102, Coherent) laser ablation system. The system is equipped with a custom-designed cell holder mounted onto a high-precision stage (step resolution 0.02 μm), allowing the placement of up to 9 closed ablation cells. All ablations were performed using a raster pattern with the following ablation conditions: Energy density (fluence) 4–7 J/cm^2; repetition rate 100 Hz; spot size 90 μm. Ablation times varied from 3–8 h. The analysed area of each diamond was optically free of solid inclusions or other impurities visible at the 10 micron scale.

Following ablation, the window was removed, 3 ml of 6 N HCl UPA was added to the ablation cell and an acid-cleaned PFA Teflon cap was inserted to cover the cell. The sealed cell was then placed in an ultrasonic bath for 40 min. Subsequently the liquid was then transferred from the ablation cell to a 7 ml Teflon beaker and dried on a hotplate at 100 °C. The dried ablation product was taken up in 1 ml 3% HNO_3 for 48 hrs at 120°C, with 500 ppt Ir and In added as internal standards, for trace element analysis.

Between two to four total procedural blanks (TPBs) were determined for each batch of samples processed, using the same ablation cells and reagents as used for the samples, to determine the average size of the blank contribution. The only step omitted was the step of ablating a solid. Including an ablation step would require a solid that is essentially devoid of all trace elements or have trace element concentrations below the LOD of our method (McNeill, 2011).

Diamonds were rinsed in MQ H_2O and dried before being re-weighed. The weight loss (0.01–0.98 mg) resulting from the ablation was then calculated. Detailed descriptions of the sample ablation and collection procedures are given in McNeill et al. (2009) and Klein-BenDavid et al. (2010). Ablation and sample collection procedures for the Newlands and Finsch diamond analyses can be found in McNeill et al. (2009).

3.3.2 Trace element analysis

The dilute HNO_3 solutions resulting from the ablation of the Victor diamonds, and their associated TPB solutions were analyzed for trace element concentrations on a Thermo Scientific Element XR2 magnetic sector ICPMS equipped with a JET interface, running at an RF power of 1320 W. Plasma cooling gas, auxiliary gas and nebulizer gas flow rates were 16 l min^{-1}, 0.82 l min^{-1} and 1.067 l min^{-1}, respectively. To increase plasma robustness and ICP sensitivity, N_2 was added into the central channel of plasma. An APEX-Q high-efficiency sample introduction system (Elemental Scientific Inc.) fitted with an ACM (**A**ctively **C**ooled **M**embrane) membrane desolvator was used for sample introduction.

At the start of each analytical session the mass spectrometer was tuned to optimize sensitivity for ^{7}Li, ^{115}In and ^{238}U using an Element standard tune solution. The oxide production rate was checked using 1 ppb solutions of Ce and U. Sensitivity is optimized to give low oxide generation whilst maintaining high overall sensitivity and CeO/Ce UO/U is maintained at <0.4 and 0.6%, respectively.

In total 32 elements were analysed in either low (LR) or medium mass resolution (MR: $M/\Delta M \sim 4500$). The isotopes measured were: ^{52}Cr (MR), ^{55}Mn (MR), ^{56}Fe (MR), ^{59}Co (MR), ^{60}Ni (MR), ^{63}Cu (MR), ^{64}Zn (MR), ^{69}Ga (LR), ^{85}Rb (LR), ^{88}Sr (LR), ^{89}Y (LR), ^{90}Zr (MR), ^{93}Nb (LR), ^{98}Mo (LR), ^{133}Cs (LR), ^{137}Ba (LR), ^{139}La (LR), ^{140}Ce (LR), ^{141}Pr (LR), ^{143}Nd (LR), ^{147}Sm (LR), ^{151}Eu (LR), ^{157}Gd (LR), ^{161}Dy (LR), ^{165}Ho (LR), ^{167}Er (LR), ^{173}Yb (LR), ^{175}Lu (LR), ^{178}Hf (LR), ^{208}Pb (LR), ^{232}Th (LR) and ^{238}U (LR). Each analysis ran for 90-105 s with a 200 s wash (3% UpA HNO_3) run in between every sample. Solution concentrations were measured against a 5-point calibration line derived from dilutions of a synthetic rock multi-element standard solution, MES-0314-01. The standard was diluted 50,000, 100,000, 250,000 and 500,000 times yielding concentrations in the range of 1 ppt to 35 ppb for different elements and different dilutions, thus providing an appropriate matrix-match for the samples so calibration lines did not require extrapolation into the region of sample analyte concentrations. All concentrations were corrected for instrument drift and all sample concentrations were normalized to the weight loss of the diamond. Weighted regression calibrations lines were used and the stated uncertainties on concentrations include fully propagated errors for the calibration line and sample weighing.

3.3.3 Limits of Quantification (LOQ)

Due to the extremely low concentrations of impurities in gem-quality diamonds it is important to have a robust knowledge of analytical blanks, to allow accurate estimates of the limits of quantification. In this study we use the limit of quantification (LOQ) as originally defined by Currie (1968): LOQ = 7σ (with σ = the standard deviation of the TPB). Further details are given in McNeill et al. (2009) and Klein-BenDavid et al. (2010).

A total of 13 total procedural blanks (TPBs) for the Victor diamond ablations were performed. The repeatability of blanks yielded consistently low values so that our LOQs for the elements Y, Nb, Cs, La, Pr, Nd, Sm, Eu, Gd, Tb, Dy, Ho, Er, Yb, Lu, Th, and U are less than 1 pg, for the elements Co, Rb, Ce and Hf less than 5 pg, for the elements Mn, Sr, Zr, Mo and Ba less than 40 pg, and for the elements Cr, Fe, Ni, Cu and Zn less than 1.2 ng.

We use LOQ as an important data quality filter, as opposed to the limit of detection – defined as ‘the true net signal level that may be expected a priori to lead to detection’ (Currie, 1968). Limit of detection is often used as a data cut off filter by authors using direct laser ablation approaches to diamond analysis (e.g., Rege et al., 2005, Tomlinson et al., 2005, Zedgenizov et al., 2007). The LOD cut off only provides confidence that a signal has been detected, yet the best-case uncertainty on concentrations at or just above LOD are ± 92% at the 95% confidence level compared to ± 40% for LOQ using the 7 σ cut off (Taylor, 1987). As such, in presenting the data we have calculated two different median values for all analysed elements for the Victor diamonds, one for all acquired data > LOD (3 σ) and one for all data > LOQ (7σ). As can be seen in the primitive mantle normalized multi-element pattern in Fig. 3.2, the pattern does not change significantly, however, the concentrations of the very low abundance elements change to significantly higher values when only values > LOQ are included. Because of the exceptionally low concentrations of some trace elements in Victor diamonds we discuss and show some data that are > LOD but < LOQ but in doing so, we emphasise that such data is merely "indicative" and not fully quantitative. The reported median values, 25% quartiles and 75% quartiles for the Victor data encompass all acquired data, including data ≤ LOD. Data with values of 0 and outliers whose values are either greater than UQ + 1.5 * IQD or less than LQ - 1.5 * IQD (with UQ = upper quartile, LQ = lower quartile, IQD = Inter quartile distance) were winsorized (Tukey, 1962) to minimize the influence of outliers. The values of high outlier data points were converted to the value of the highest data point not considered an outlier; all points with a value of 0 were converted to the LOD. As the distribution of data can be heavily influenced by outliers, setting all outliers to a specified percentile of the data, results in estimators that are more robust to outliers.

The accuracy of the off-line ablation method has been verified by Klein-BenDavid et al. (2014) by comparison to data produced by a high concentration fibrous diamond. The reader is referred to that publication for details of accuracy.

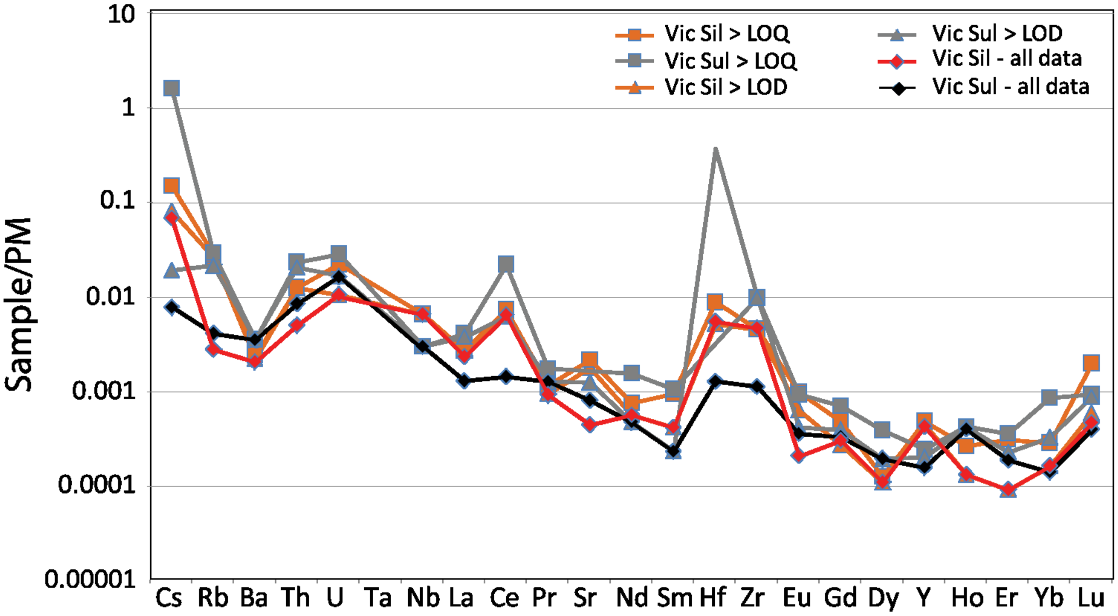

Figure 3.2: Median primitive mantle-normalised (McDonough and Sun, 1995) incompatible-element patterns of diamonds from Victor (Canada; sulphide and silicate paragenesis) for all acquired data, for data > LOD and for data > LOQ.

3.4 Results

3.4.1 Victor

Trace element concentrations of the Victor diamond suite are very low, with all samples being highly depleted relative to chondrite and primitive mantle abundances (Table 2, Fig. 3.3, 3.4). The Victor diamonds consistently have the lowest trace element contents of any gem diamond samples so far analysed. Elemental abundances of REE along with Nb, Th, and U range from 10s of ppt to 10s of ppb and large ion lithophile elements (LILE) such as Cs, Rb and Ba range from 100s of ppt to 100s of ppb. Transition metals such as Cr, Mn and Fe range from ppb levels up to 100s of ppm (Figure B1).

In the following description of the data it is important to keep in mind that absolute trace element abundances in gem diamonds, as with fibrous diamonds, are primarily a function of the impurity density. In the text below we discuss whether the trace element signature that we measure is likely to be from fluid or solid inclusion impurities.

Chondrite-normalized trace element patterns show a wide range in relative enrichment of LREE compared to HREE, with La_N/Yb_N ratios of 2 – 37 (Fig. 3.3).

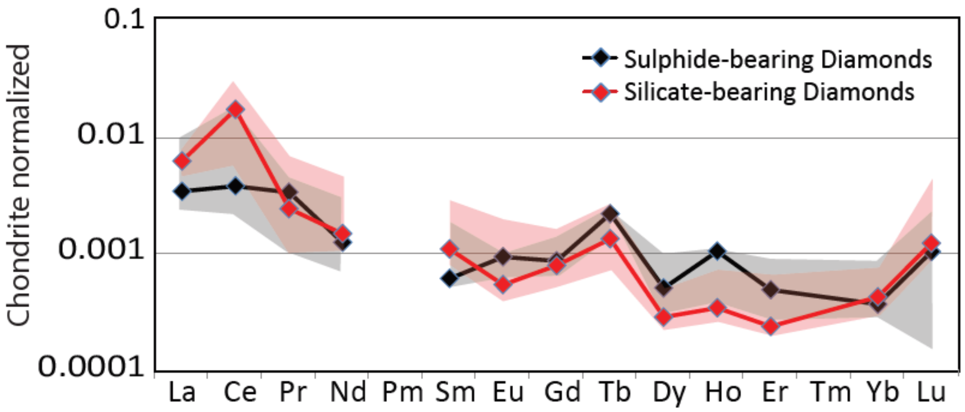

Figure 3.3: Chondrite-normalized (McDonough and Sun, 1995) median and range of trace element concentrations in Victor diamonds. Sulphide (black) and silicate (red) paragenesis analyzed in this study are defined by observed inclusion type. The range includes all data above the 25% and below the 75% quartile. Where no data points are present the lines are extrapolated, except for Pm as it does not occur naturally.

Distinct differences are evident between the normalised REE patterns of diamonds containing silicate inclusions (median La_N/Yb_N ~ 17) and diamonds containing sulphide inclusions (median $La_N/Yb_N \sim 9$). In general, the fluids from the sulphide-bearing diamonds are less REE-enriched than the silicate-bearing diamonds, but the ranges overlap significantly. When multi-element patterns are considered, the sulphide-bearing diamonds are more planar, i.e. they show a smaller degree of inter-element fractionation (Fig. 3.4).

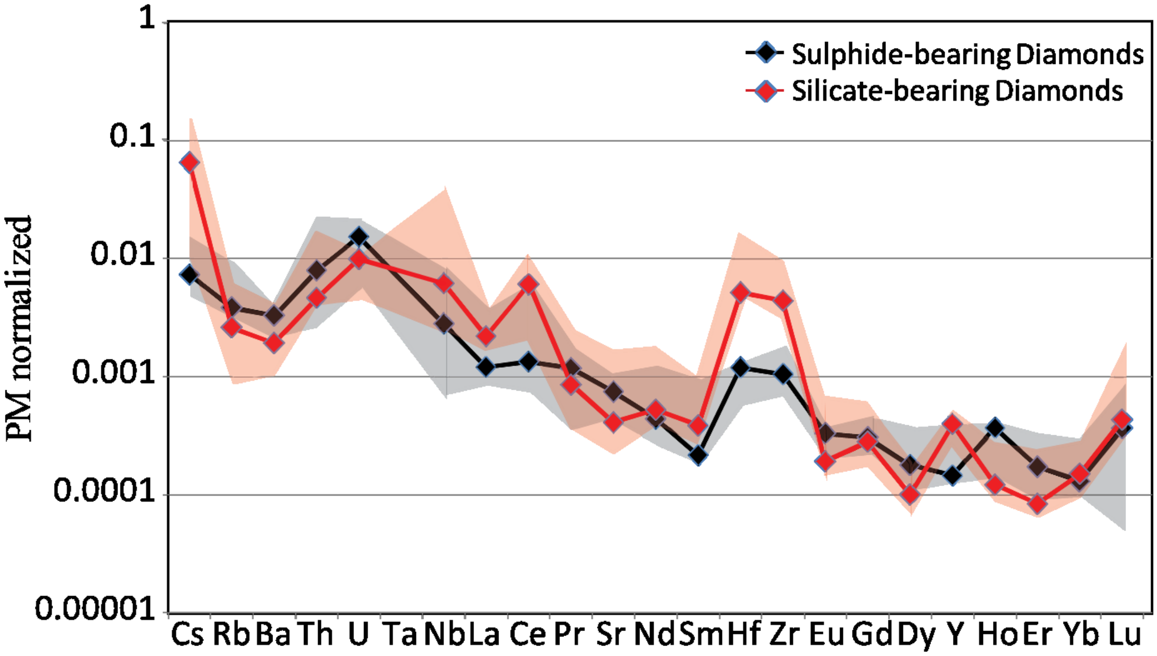

Figure 3.4: Primitive mantle-normalized (McDonough and Sun, 1995) median and range of trace element concentrations in the Victor diamonds (sulphide – black; silicate – red - paragenesis) analyzed in this study. The range includes all data above the 25% and below the 75% quartile. Where no data points are present the lines are extrapolated.

This observation can be quantified with reference to elemental ratios that use the most robust of the data analysed. For instance, Ba_N/Nb_N (Silicate median 0.17; Sulphide median 1.2) and Sm_N/Hf_N (Silicate median 0.07; Sulphide median 0.18) are significantly more fractionated in the silicate-bearing diamonds at Victor (Fig. 3.5). Statistical comparison using the equal variance t-test (Fisher, 1925; performed using Excel), indicates that there is a greater than 95% probability that the sulphide-bearing and silicate-bearing diamonds are drawn from different populations with regard to their La_N/Yb_N, Ba_N/Nb_N and Sm_N/Hf_N ratios, i.e., they may represent different populations. However, it is important to note that this result is qualitative only, because the distributions are only quantifiable if sample sizes exceed $n > 40$.

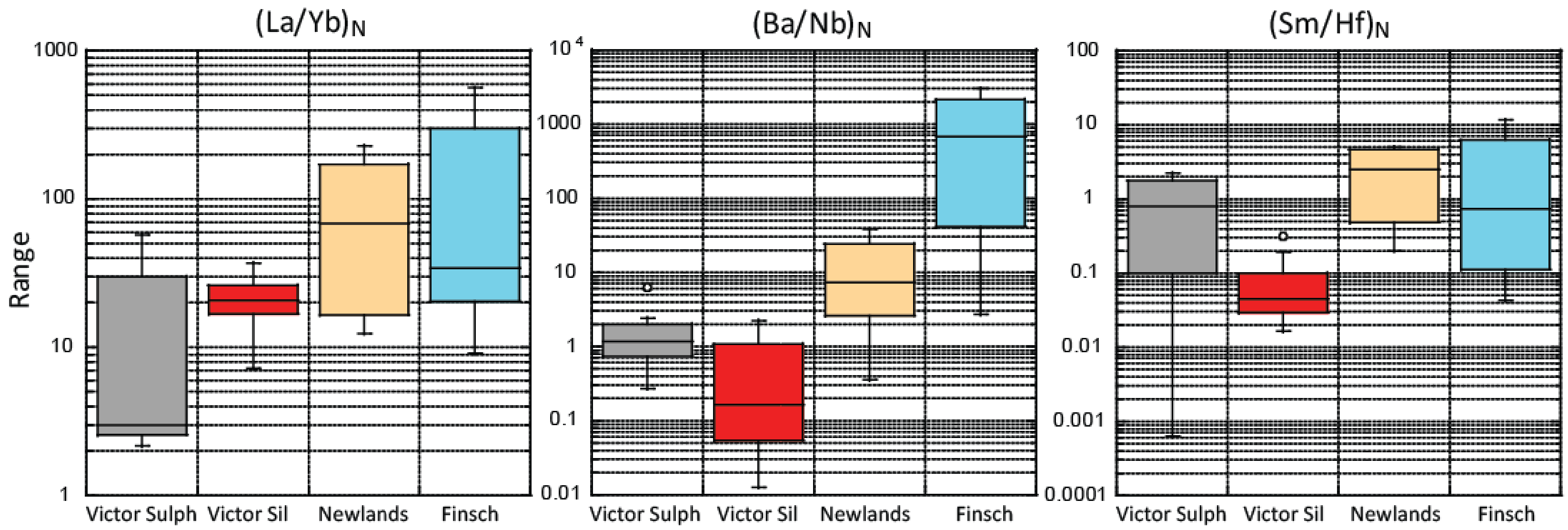

Figure 3.5: Box and whisker plots of primitive mantle-normalised La/Yb, Ba/Nb and Sm/Hf ratios for gem quality diamonds from Victor (sulphide and silicate paragenesis) and S. Africa (Newlands and Finsch). The Sm_N/Hf_N ratios for the Victor diamonds include all acquired data, all other ratios include all data > LOD. Individual data points are outliers whose value is either: greater than UQ + 1.5 * IQD or less than LQ – 1.5 * IQD.

As a suite, the Victor silicate-bearing diamonds are characterized by a slight negative Sr anomaly and positive Cs, Ce, Y and Zr-Hf anomalies. The Victor sulphide-bearing diamonds show positive Zr-Hf anomalies. Two of the sulphide bearing diamonds, V2-01 and V2-07, show highly fractionated multi-element patterns that are characterised by positive Ce and Cs anomalies (Fig. 3.6). Interestingly, both these diamonds have a distinct appearance to the other sulphide-bearing Victor diamonds in that they have a high density of small sulphide inclusions scattered right through them. This suggests that for these two diamonds, sub-micron solid sulphide inclusions were probably analysed along with the fluid inclusions. The differences in trace element characteristics between V2-01 and the other Victor diamonds are so large (most elements >> 2 standard deviations), that the diamond has been excluded from subsequent plots.

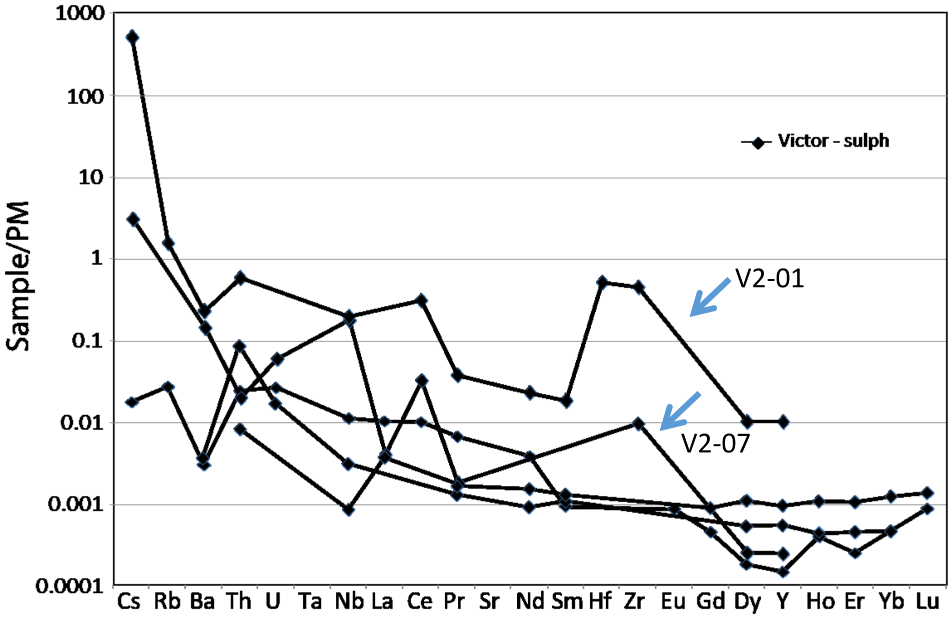

Figure 3.6: Primitive mantle-normalized (McDonough and Sun, 1995) trace element concentrations in the sulphide bearing Victor diamonds analyzed in this study. Data in this plot is > LOQ.

Unsurprisingly, concentrations of transition metals such as Ni, Fe and Co vary more widely for the diamonds containing sulphide inclusions than the silicate containing diamonds (Fig. 3.7), extending to higher concentrations of Cu, Fe, Ni, Zn and Co for the former, especially in V2-01, V2-07 and V2-09, perhaps reflecting the ablation of sub-micron invisible sulphides.

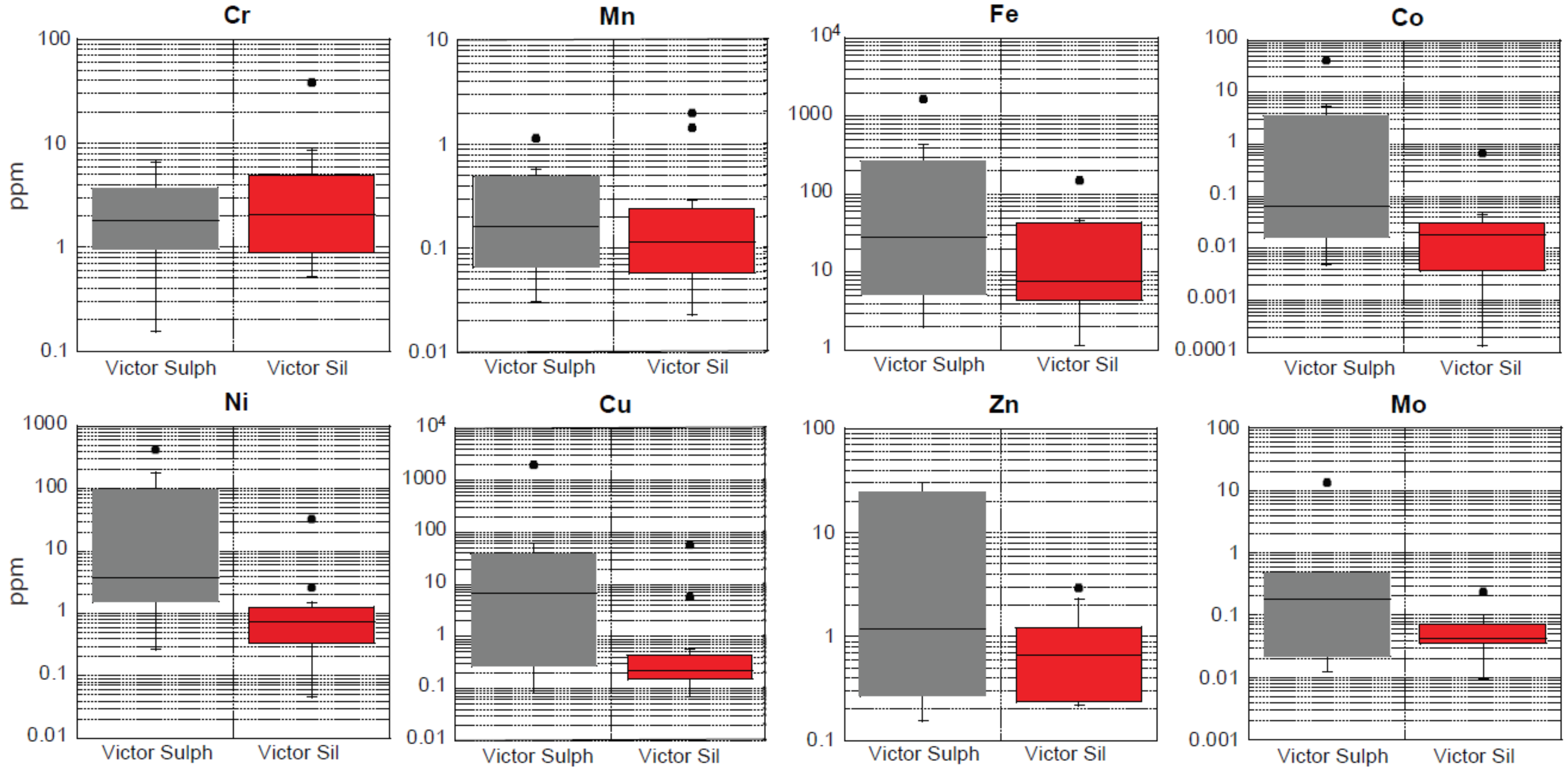

Figure 3.7: Box and whisker plots of siderophile element concentrations in the Victor diamonds (sulphide and silicate paragenesis) analyzed in this study. The plots include all acquired data. Individual data points are outliers whose value is either: greater than UQ + 1.5 * IQD or less than LQ – 1.5 * IQD.

Table 3.2: Trace element abundances (ppb) determined for fluids in the Victor, Newlands and Finsch diamonds. Quantification is achieved via normalization to the weight loss of the diamond crystals during ablation. Limits of detection and quantification in ppt are based on a large representative blank set (n = 13). (Note: ≤LOD: value below 3*σ of the blank value; n/a: no value reported/analyzed; red values: value above LOD but below LOQ (7*σ of the blank value). The concentration of the samples in ppb is normalized to the wt loss during ablation; LOD and LOQ: values in pg/g.)

Provenance	**Victor**									
Sample	V3-01	V3-03	V3-05	V3-11	A578-01	A578-02	A578-03	A578-04	A578-03-2	V3-03-2
Inclusion Paragenesis	silicate	silicate	silicate	silicate	silicate	silicate	silicate	silicate	silicate	silicate
Cs	0.24	16	2.8	0.13	1.8	3.1	1.4	0.17	0.34	≤ LOD
Rb	≤ LOD	≤ LOD	17	≤ LOD	15	≤ LOD	1.8	≤ LOD	≤ LOD	≤ LOD
Ba	13	15	162	24	33	1.0	6.3	≤ LOD	42	0.91
Th	0.37	≤ LOD	2.6	≤ LOD	4.6	1.2	0.34	0.66	≤ LOD	≤ LOD
U	0.52	0.20	1.1	0.09	1.1	0.01	0.32	0.33	0.20	0.10
Nb	1.2	1.4	27	1.1	49	1.9	20	1.7	27	7.3
La	0.61	1.1	6.8	1.8	6.4	1.0	1.6	1.7	≤ LOD	≤ LOD
Ce	1.9	10	24	12	22	6.1	11	3.6	55	≤ LOD
Pr	≤ LOD	0.08	1.1	0.28	1.5	0.15	0.22	0.23	0.95	0.12
Sr	≤ LOD	≤ LOD	26	≤ LOD	40.47	≤ LOD	≤ LOD	≤ LOD	≤ LOD	≤ LOD
Nd	0.09	0.03	4.2	0.67	5.4	0.45	0.65	0.89	3.2	0.83
Pb	5578	9.0	41	6.8	4.0	2.5	4.1	5.1	≤ LOD	≤ LOD
Sm	0.05	0.03	0.82	0.13	0.54	0.09	0.13	0.18	0.68	0.26
Hf	1.4	1.4	13	0.5	1.2	1.0	4.4	3.3	≤ LOD	5.6
Zr	41	44	523	34	26	46	67	28	131	236
Eu	0.12	≤ LOD	0.17	0.03	0.09	≤ LOD	≤ LOD	≤ LOD	0.15	0.03
Ti	n/a	n/a	n/a	n/a	n/a	n/a	n/a	n/a	n/a	n/a
Gd	0.12	0.16	0.61	0.10	0.34	0.10	0.08	0.08	0.50	0.21
Tb	0.29	0.22	0.11	0.03	0.07	≤ LOD	≤ LOD	≤ LOD	0.05	0.06
Dy	0.01	0.03	0.38	0.06	0.17	0.05	0.07	0.08	0.28	0.09
Y	579	0.99	7.6	1.0	2.0	2.5	2.0	1.6	1.7	1.2

Ho	0.01	0.01	0.06	0.01	0.04	0.01	0.02	0.02	0.09	0.04
Er	0.04	0.03	0.29	0.02	0.13	0.03	0.03	0.05	0.20	0.08
Yb	0.06	0.03	0.25	0.03	0.16	0.03	0.07	0.07	0.28	0.08
Lu	0.02	0.03	0.09	0.02	0.05	≤ LOD	0.01	0.02	0.13	0.16
Mn	23	55	2004	51	1449	115	184	59	290	138
Fe	4828	3403	46907	1164	151768	28103	46475	4094	39115	7598
Ni	850	469	630	78	32180	212	739	46	2643	966
Cr	522	1378	38194	609	3393	1040	729	2095	8601	3359
Co	2.5	3.6	31	≤ LOD	688	19	21	0.14	44	17
Cu	59311	117	561	188	5864	288	227	222	117	72
Zn	1210	237	1109	≤ LOD	2288	218	326	218	2914	≤ LOD
Mo	42	9.6	42	≤ LOD	68	100	53	35	237	≤ LOD

Provenance	Victor									**Newlands**
Sample	V3-11-2	V2-01	V2-02	V2-03	V2-04	V2-06	V2-07	V2-09	V2-10	33 New 01
Inclusion Paragenesis	silicate	sulphide	sulphide	sulphide	sulphide	sulphide	sulphide	sulphide	sulphide	unknown
Cs	207	10389	≤ LOD	≤ LOD	≤ LOD	0.22	63	0.37	≤ LOD	2.7
Rb	≤ LOD	892	≤ LOD	≤ LOD	≤ LOD	≤ LOD	7.7	16	≤ LOD	67
Ba	7.24	1452	8.7	25	22	22	916	20	9.1	1923
Th	≤ LOD	45	0.63	0.28	6.0	≤ LOD	1.5	2.0	≤ LOD	115
U	0.08	15	0.11	≤ LOD	0.31	0.32	1.2	0.54	≤ LOD	72
Nb	4.1	124	0.54	0.40	1.9	3.2	113	7.5	0.37	39
La	≤ LOD	42	2.3	≤ LOD	0.61	0.79	2.5	6.8	≤ LOD	215
Ce	≤ LOD	496	2.5	≤ LOD	2.3	≤ LOD	52	17	≤ LOD	411
Pr	0.02	9.1	0.40	0.10	0.30	0.04	0.43	1.7	0.09	46
Sr	≤ LOD	309	≤ LOD	≤ LOD	23	≤ LOD	34	18	≤ LOD	3976
Nd	0.53	27	1.8	0.6	1.0	0.17	0.47	4.9	0.17	203
Pb	73	≤ LOD	5.3	6.0	32	≤ LOD	98	16	6.3	250
Sm	0.16	7.1	0.51	0.07	0.40	0.08	0.09	0.38	0.07	32

Hf	≤ LOD	139	≤ LOD	≤ LOD	≤ LOD	≤ LOD	98	≤ LOD	≤ LOD	29
Zr	≤ LOD	4518	≤ LOD	≤ LOD	≤ LOD	≤ LOD	97	≤ LOD	≤ LOD	1469
Eu	0.02	≤ LOD	0.05	≤ LOD	≤ LOD	≤ LOD	≤ LOD	0.13	0.06	5.3
Ti	n/a	n/a	n/a	n/a	n/a	n/a	n/a	n/a	n/a	16152
Gd	≤ LOD	11.5	0.47	0.13	0.17	≤ LOD	0.23	0.25	0.07	25
Tb	0.04	≤ LOD	0.09	≤ LOD	0.08	0.21	≤ LOD	0.08	0.08	3.9
Dy	0.07	6.5	0.71	0.06	0.33	0.09	0.16	0.12	0.05	≤ LOD
Y	0.00	42	3.9	0.47	2.2	0.60	0.99	0.64	≤ LOD	≤ LOD
Ho	0.02	0.98	0.16	≤ LOD	0.06	≤ LOD	0.03	0.06	0.06	n/a
Er	0.04	1.3	0.45	0.05	0.18	≤ LOD	0.02	0.11	0.08	11
Yb	0.08	1.4	0.52	≤ LOD	0.19	≤ LOD	≤ LOD	0.08	0.06	12
Lu	0.12	≤ LOD	0.09	≤ LOD	0.00	≤ LOD	≤ LOD	0.06	0.05	2.0
Mn	99	1147	76	90	401	31	569	233	56	n/a
Fe	6505	1690212	3524	6768	17542	39024	93421	433552	2020	n/a
Ni	1541	180864	398	3878	2765	3662	12790	426400	271	n/a
Cr	6479	6541	1451	709	4743	156	2104	2707	1210	n/a
Co	15	41900	8.6	76	49	24	1740	5322	4.8	n/a
Cu	235	1988525	129	7002	416	15258	6874	61333	90	n/a
Zn	1015	27081	513	≤ LOD	1856	160	29899	21160	≤ LOD	n/a
Mo	20	13326	22	≤ LOD	202	≤ LOD	166	461	≤ LOD	n/a

Provenance		**Newlands**				**Finsch**			
Sample	34 New 02	35 new 02	30 new 03	31 f866 1	32 f866 2	33 jjg 1	34 jjg 2	LOD (3*σ)	LOQ (7*σ)
Inclusion Paragenesis	unknown	unknown	unknown	unknown	unknown	unknown	unknown	ppt	ppt
Cs	1173	42	38	11	3.8	12	22	0.07	0.17
Rb	41810	2471	3501	278	43	795	850	1.4	3.3
Ba	538237	7466	26982	1575785	1802131	13484	31112	4.5	10
Th	25611	787	78	17	87	33	119	0.15	0.35

U	999	60	25	2.2	2.7	4.4	6.2	0.09	0.20
Nb	5366	2111	71	52	137	17	1146	0.04	0.10
La	183361	3282	119	62	160	32	2298	0.30	0.71
Ce	276883	5703	179	≤ LOD	295	39	3846	1.0	2.4
Pr	22734	557	18	12	32	3.6	349	0.05	0.12
Sr	940576	1729	4873	71274	81246	1909	40150	10	24
Nd	71286	524	435	19	156	35	211	0.18	0.41
Pb	31760	366	643	491	106	198	353	3.1	7.1
Sm	4172	225	11	11	22	3.1	81	0.04	0.10
Hf	692	32	38	6.1	84	49	4.9	0.56	1.3
Zr	30904	1394	1448	248	3430	1198	165	14	33
Eu	784	51	3.1	≤ LOD	≤ LOD	5.2	15	0.03	0.06
Ti	267348	20006	21552	4182	8775	13478	13282	n/a	n/a
Gd	1587	106	5.3	9.1	16	2.1	20	0.06	0.14
Tb	133	9.5	0.92	0.64	1.6	0.48	1.6	0.02	0.05
Dy	≤ LOD	33	4.4	3.3	6.8	2.9	6.6	0.03	0.06
Y	≤ LOD	168	28	48	70	19	39	0.14	0.32
Ho	n/a	n/a	n/a	n/a	n/a	n/a	n/a	0.01	0.02
Er	429	12	2.4	1.1	1.7	0.78	1.0	0.02	0.04
Yb	542	19	3.9	1.4	2.9	2.3	2.8	0.03	0.06
Lu	94	2.9	0.62	0.34	0.66	0.34	0.43	0.01	0.03
Mn	n/a	n/a	n/a	n/a	n/a	n/a	n/a	10	23
Fe	n/a	n/a	n/a	n/a	n/a	n/a	n/a	490	1144
Ni	n/a	n/a	n/a	n/a	n/a	n/a	n/a	30	69
Cr	n/a	n/a	n/a	n/a	n/a	n/a	n/a	36	84
Co	n/a	n/a	n/a	n/a	n/a	n/a	n/a	1.1	2.5
Cu	n/a	n/a	n/a	n/a	n/a	n/a	n/a	28	65
Zn	n/a	n/a	n/a	n/a	n/a	n/a	n/a	308	718
Mo	n/a	n/a	n/a	n/a	n/a	n/a	n/a	16	38

3.4.1 Newlands and Finsch

Trace element concentrations of both the Newlands and the Finsch diamond suites are much higher than those of all Victor diamonds, in some cases up to three orders of magnitude greater, correlating broadly with their lower clarity. Elemental abundances of REE along with Nb, Th, and U range from 100s of ppt to 100s of ppm for the Newlands diamonds and from 100s of ppt to 10s of ppm for the Finsch diamonds, overlapping the range of concentrations shown by fibrous diamonds. LILE such as Rb, Sr and Ba range from single digit ppb levels to 100s of ppm for both Newlands and Finsch. Two Finsch diamonds have Ba concentrations of >1000 ppm (Table 3.2). The chondrite-normalized trace element patterns for both the Newlands and Finsch suites show strong enrichment of LREE compared to HREE, with La_N/Yb_N ratios for the Newlands diamonds ranging from 12 – 230 (median La_N/Yb_N 68) and for the Finsch diamonds from 9 – 561 (median La_N/Yb_N 34) (Fig. 3.5, 3.8).

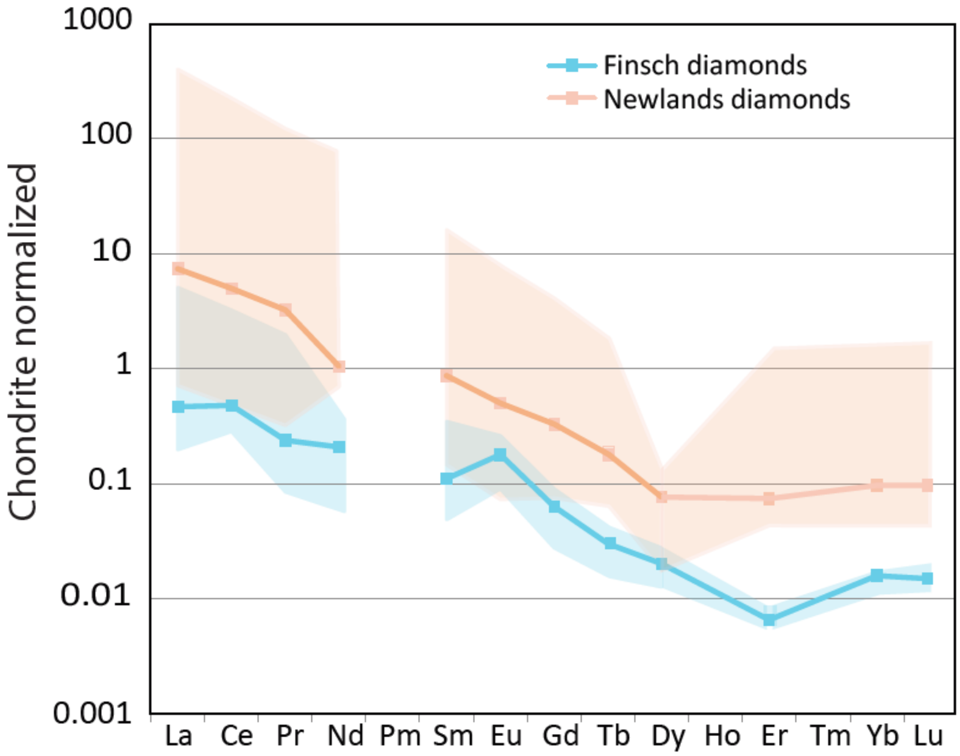

Figure 3.8: Chondrite-normalized (McDonough and Sun, 1995) median and range of trace element concentrations in Newlands (orange) and Finsch (blue) diamonds separated from mantle xenoliths, The range includes all data above the 25% and below the 75% quartile. Where no data points are present the lines are extrapolated, except for Pm as it does not occur naturally.

Both suites show higher and more variable inter-element fractionation than the Victor diamonds with Ba_N/Nb_N from 0.4 - 38 for Newlands and from 3 - 3011 for Finsch and Sm_N/Hf_N from 0.2 – 5 for Newlands and from 0.04 – 12 for Finsch. The Newlands diamonds are characterized by negative Nb, Ti and Zr-Hf anomalies (Fig. 3.9). As a suite the Finsch diamonds display a negative Ti anomaly and positive Sr and Ba anomalies, with the Ba anomaly being significantly larger in the two Finsch diamonds originating from the F866 harzburgite xenolith (Fig. B2). Two of the diamonds, JJG1 and F8662, also show positive Zr-Hf anomalies, one sample (JJG4) shows a negative Zr-Hf anomaly and one a positive Eu anomaly (JJG1). The two Finsch diamond samples originating from the more depleted harzburgitic xenoliths (JJG) are, in addition, characterized by a negative Nb anomaly. Overall, the E-type Newlands and P-type Finsch diamonds show very similar trace element characteristics, but differ in Ba, Sr and Zr-Hf, with the Newlands diamonds displaying no or negative anomalies in Ba and Sr and negative Zr-Hf anomalies whereas the Finsch diamonds have positive Ba, Sr and, with one exception, Zr-Hf anomalies.

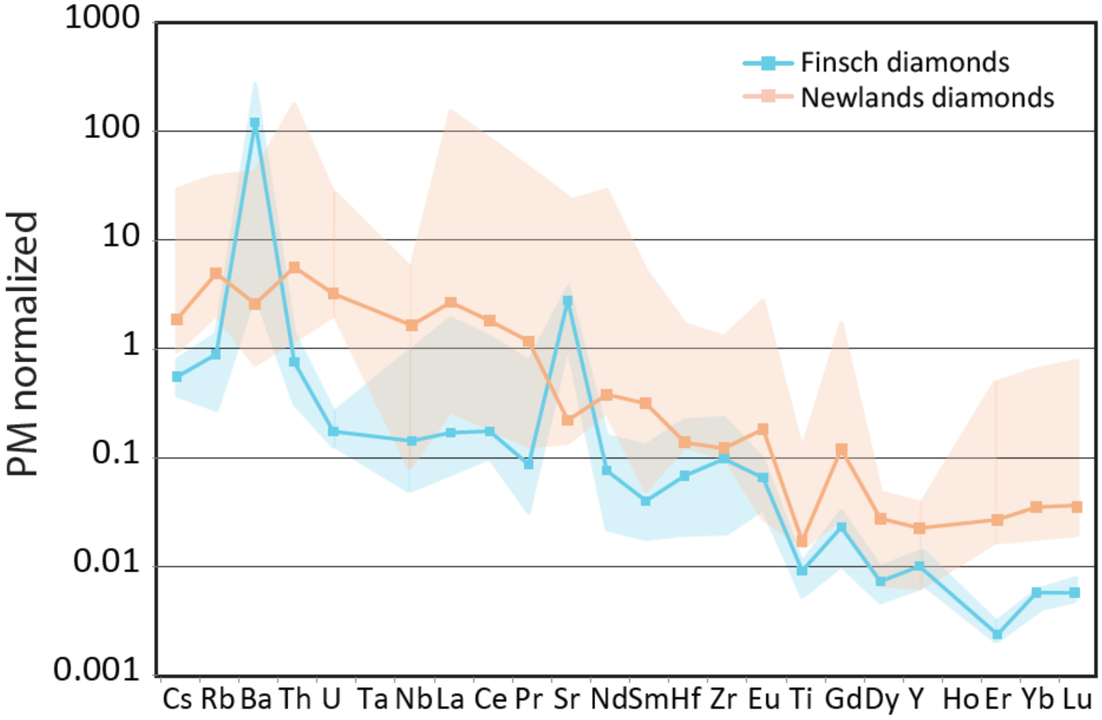

Figure 3.9: Primitive mantle-normalized (McDonough and Sun, 1995) median and range of trace element concentrations in Newlands and Finsch diamonds separated from mantle xenoliths.

3.5 Discussion

3.5.1 Origin of the trace element signatures

While it has long been established that fibrous diamonds grow from carbon-bearing HDFs that can be found in micro inclusions in most fibrous diamonds (e.g., Klein-BenDavid et al., 2004; Shiryaev et al., 2005), the mechanism of formation for gem diamond remains more ambiguous. A genetic relationship between fibrous and gem diamonds has recently been affirmed through the finding that the same major element composition of fluids found in fibrous, fluid-rich diamonds also exist as rare micro inclusions in gem diamonds (Jablon and Navon, 2016). The vast majority of the compositional arrays in major element space defined by HDFs in fibrous diamonds are found within the rare fluids trapped in gem diamonds. This finding strengthens the connection between the parental fluids of both.

Indications of this similarity between fluids in fibrous and gem diamonds can be seen in rare analyses of trace elements in gem diamonds that are above limits of detection. For instance, Melton et al. (2012) found a very similar trace element pattern to low-Mg carbonatitic HDFs in fibrous diamonds, at far more dilute concentrations, in a gem diamond from Akwatia, Ghana. However, with the exception of that diamond, the trace element patterns of the other gem diamonds analysed in that study did not yield a faithful representation of the diamond growth medium, leading the authors to suggest that trace elements in gem diamonds are largely not hosted in nano-inclusions of the diamond forming fluid/melt, but instead reflect complex and variable mixtures of minute mineral inclusions.

The REE_N patterns of the Victor, Finsch and Newlands diamonds are quite smooth, linear and characterized by shallow negative $LREE_N$-$HREE_N$ slopes (Fig. 3.10), similar to those commonly found in fibrous diamonds, albeit at much lower concentrations (e.g., Zedgenizov et al., 2009; Weiss et al., 2009, 2011, 2013, 2015; Tomlinson et al., 2009; McNeill et al., 2009; Klein-BenDavid et al., 2010, 2014). This similarity clearly indicates that sub-micron fluid/melt inclusions ≤25 nm (Melton et al., 2012) are dominating the chemical signature of some gem diamonds, where their trace element systematics are similar in composition to those observed in fibrous diamonds.

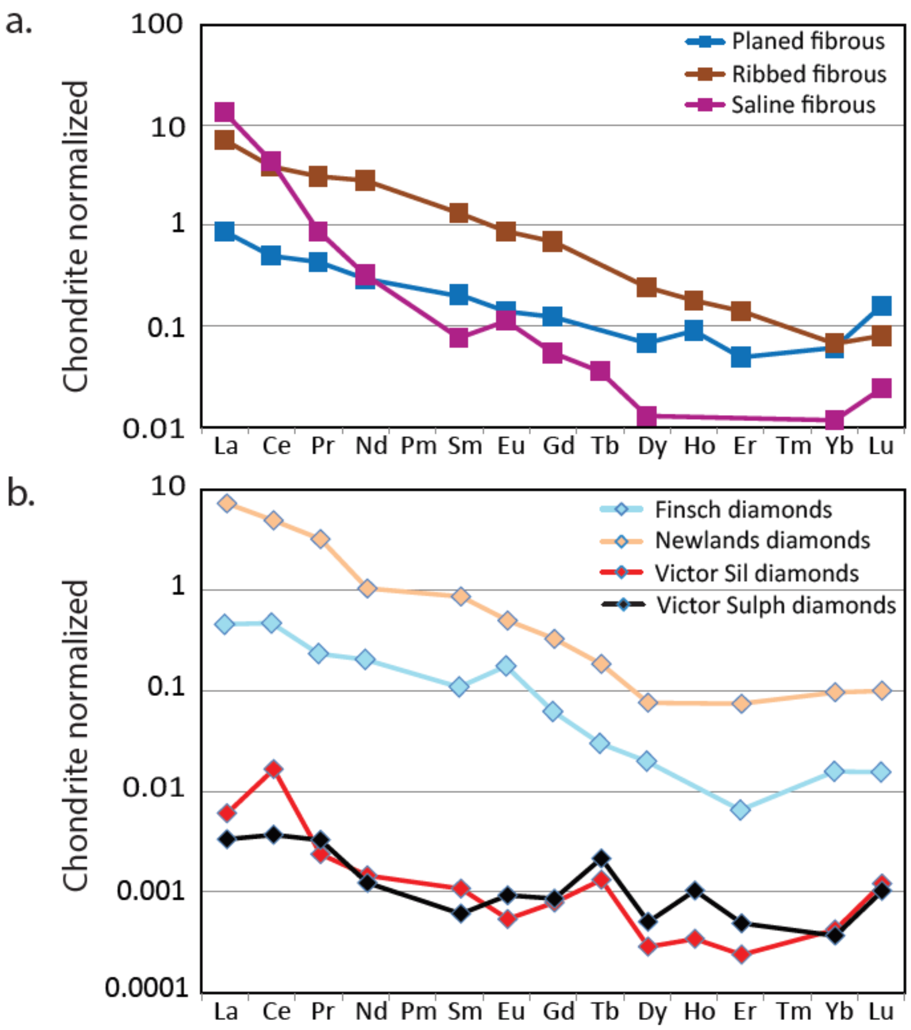

Figure 3.10: a. Chondrite-normalized (McDonough and Sun, 1995) REE concentrations for the two “end-member” patterns - ‘planed’ and ‘ribbed’ - of carbonatitic HDFs in fibrous diamonds (Weiss et al., 2013) and median REE concentrations for fibrous diamonds bearing saline HDFs from Ekati, Canada (Weiss et al., 2015). b. Median chondrite-normalized (McDonough and Sun, 1995) REE concentrations for the Victor (sulphide and silicate paragenesis), Newlands and Finsch diamonds analyzed in this study.

Some of the trace element patterns observed in the gem diamond studied here can be directly linked to specific fluid compositions found in fibrous diamonds. The diamonds extracted from the Finsch harzburgite xenoliths show striking positive Ba and Sr anomalies, similar to those found in saline HDFs in fibrous diamonds (Fig. 3.11; Smith et al., 2012; Weiss et al., 2015), a clear indication that the diamonds contain inclusions that are comparable in composition to saline fluids, as will be explored below.

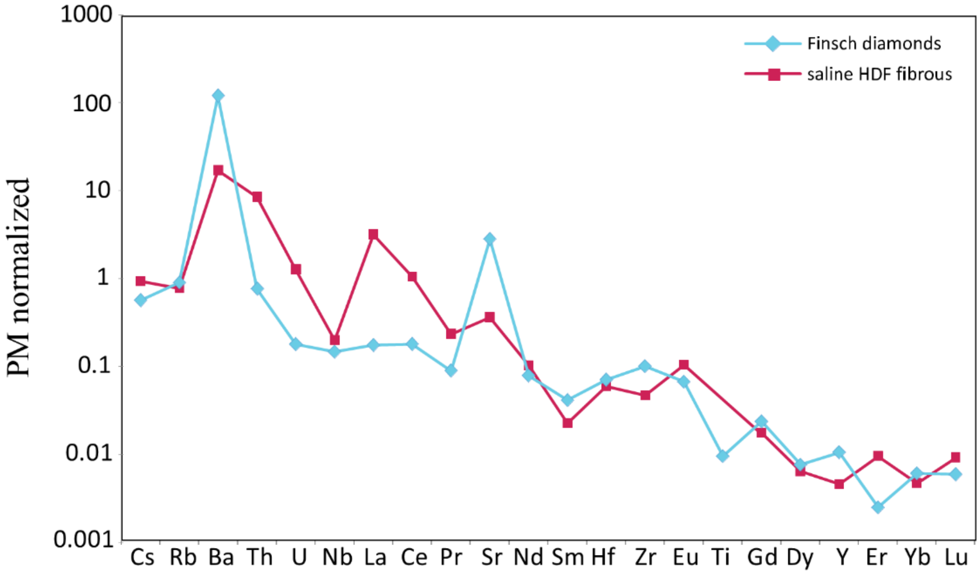

Figure 3.11: Primitive mantle-normalized (McDonough and Sun, 1995) median multi-element concentrations for diamonds from Finsch (this study) and fibrous diamonds containing saline HDFs, as established by major element analyses (Smith et al., 2012; Weiss et al., 2015).

3.5.2 Trace elements in high-purity gem diamonds from the Victor Mine

The Victor diamond trace element systematics broadly align with the two petrogenetic groups indicated by inclusion compositions, i.e., sulphide and silicate types. Silicate inclusion-bearing diamonds have generally more fractionated REE_N patterns and show greater inter-element fractionations for some element ratios (e.g., Ba_N/Nb_N, Sm_N/Hf_N). The most significant differences are positive Cs, Ce and Y anomalies and a negative Sr anomaly displayed by the silicate bearing diamonds, that are absent in the multi-element patterns of the sulphide diamonds. Stachel et al. (2017) have shown that the Victor diamonds formed under sub-solidus conditions at depths where melts stall and freeze, potentially delivering diamond forming fluids, a strong indication that subsolidus fluids (H_2O–CO_2–CH_4 system) are the principal diamond forming agent at Victor.

As Weiss et al. (2013) have shown, diamond forming fluids very swiftly fractionate during percolation through the lithosphere, suggesting that diamonds that trapped HDFs with flat, unfractionated trace element patterns formed very soon after the metasomatic fluid entered the lithosphere. Given that both the sulphide inclusion-bearing and the silicate inclusion-bearing Victor diamond suites have relatively flat trace element patterns this may have been the case at Victor, with the sulphide-inclusion bearing diamonds forming prior to the more fractionated silicate-inclusion bearing diamonds. Thus, the fluid forming the silicate-bearing diamonds interacted more with the wall rocks resulting in more fractionated trace element characteristics. The negative Sr anomaly may stem from interaction with, and sequestration of Sr within clinopyroxene. The enrichment of U and Th relative to Nb, the positive Zr-Hf anomaly and higher Hf relative to Zr, may indicate percolation of the diamond-forming fluid through parts of the lithosphere containing amphibole and mica, which both have a high partition coefficient for Nb. The Ce anomaly may indicate the presence of a crustal component in the diamond forming lithosphere, as it was shown experimentally that Ce anomalies cannot form by igneous processes (Schreiber et al., 1980). Alternately, the Ce anomaly may have formed by a change in oxidation state of Ce due to a change in oxygen fugacity of the diamond-forming fluid. Minerals that fractionate Rb from Cs are mainly clays and mica, which suggests that the enrichment of Cs relative to Rb seen in the silicate-bearing Victor diamonds could be evidence of a crustal component in the diamond-forming lithosphere. However, Cs can also be fractionated from Rb by H_2O vapour-solid partitioning (Volfinger, 1976). Alternately, the fluids forming the sulphide bearing and silicate bearing diamonds may have had subtly different sources.

3.5.3 Comparison with other gem diamonds

The results for the high-quality gem diamonds from Victor agree with the findings of McNeill et al. (2009) who analysed gem quality diamonds from the Cullinan Mine (previously known as Premier), South Africa, along with gem quality diamonds from Siberia (Mir and Udachnaya). The Cullinan diamonds contain silicate inclusions, the Siberian diamonds are sulphide bearing. McNeill et al. (2009) also reported very low levels of REE_N and enrichment of $LREE_N$ compared to $HREE_N$ for all analysed gem diamonds. The multi-element patterns for Cullinan diamonds compare well with the Victor diamonds in terms of overall abundances – there are some differences between the two suites, namely negative Nb, Sr and Zr anomalies in the Cullinan diamonds (Fig. 3.12). In some the enrichment in LILE over Nb is slightly more pronounced (Fig. A4). In addition, the REE_N patterns are slightly more fractionated than for the Victor diamonds. Overall, however, Cullinan diamonds analysed so far are characterized by relatively unfractionated trace element patterns, with no significant anomalies and a moderate decrease in concentrations from the most incompatible elements toward the more compatible elements, similar to the gem diamonds from Victor. These differences may relate to differences in the nature and extent of fluid-rock interaction during percolation of diamond-forming fluids through the lithosphere.

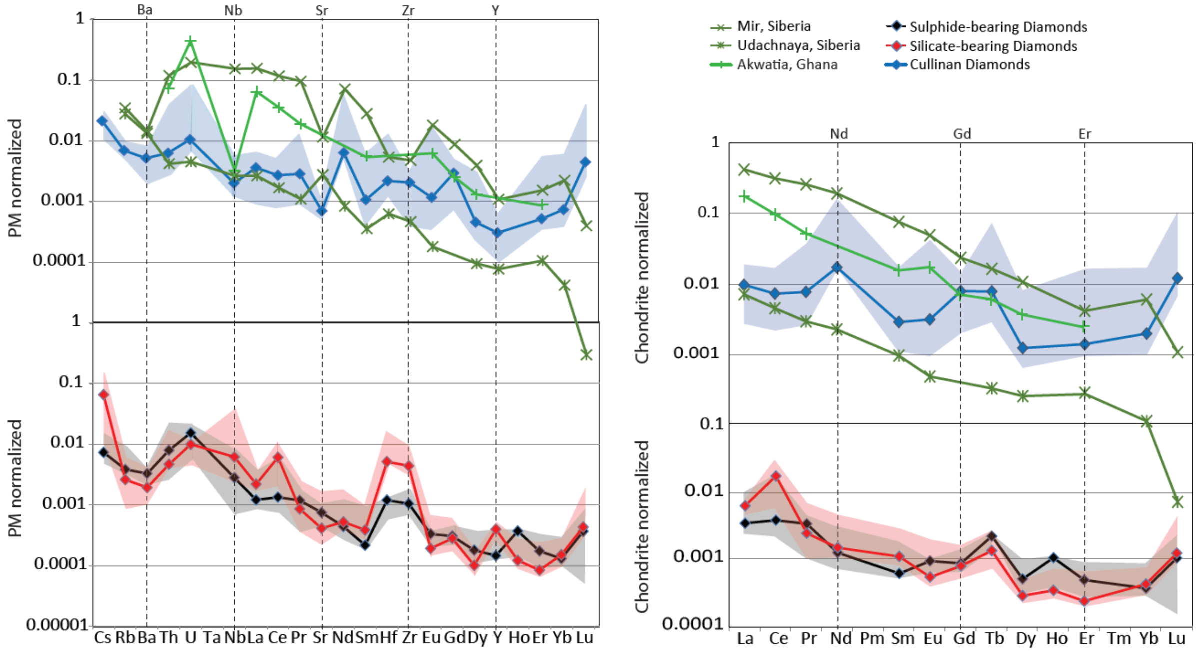

Figure 3.12: Primitive mantle-normalised multi-element and chondrite-normalized REE patterns for the range and medians of gem diamonds from Victor, Canada (sulphide and silicate paragenesis: this study). Also plotted are the range and median primitive mantle-normalised multi-element and chondrite-normalized REE patterns of diamonds from Cullinan mine, S. Africa (McNeill et al., 2009) and primitive mantle-normalised multi-element and chondrite-normalized REE patterns for gem-quality diamonds from Siberia (Mir and Udachnaya, McNeill et al. 2009) and from Akwatia, Ghana (Melton et al., 2012). Ranges include all data above the 25% and below the 75% quartile. Where no data points are present the lines are extrapolated.

The few Siberian diamonds for which high quality trace element data exist have much more fractionated chondrite-normalized REE patterns compared to the diamonds from Victor and Cullinan (Fig. 3.12). The multi-element pattern of the Mir diamond is characterized by negative Sr, Hf-Zr, and Y anomalies, similar to the Cullinan diamonds, whereas the other Siberian sample from Udachnaya (3812) shows a much flatter multi-element pattern with elevated Ba, and positive Sr and Zr-Hf anomalies. As noted above, only one diamond from the Akwatia, Ghana, suite analysed by Melton et al. (2012) was found to match the trace element pattern of fibrous diamonds and was classified as being similar to the trace element patterns observed in fibrous diamonds with low-Mg carbonatitic melt inclusions. That diamond displays a smooth REE_N pattern with enrichment of $LREE_N$ compared to $HREE_N$ (Fig. 3.12) and pronounced enrichment of LILE over Nb.

On the basis of the few gem diamonds analysed so far differences emerge for different geographical regions. We will explore the possible significance of this below.

3.5.4 Comparison with fibrous, fluid-rich diamonds

To compare the Victor data more broadly with both the Newlands and Finsch diamonds and typical trace element patterns for fluid-rich diamonds, we normalized all these data first to primitive mantle and then to a Yb_N value of 1, so as to reduce the large variations in abundance that are solely due to fluid inclusion density (Fig. 3.13).

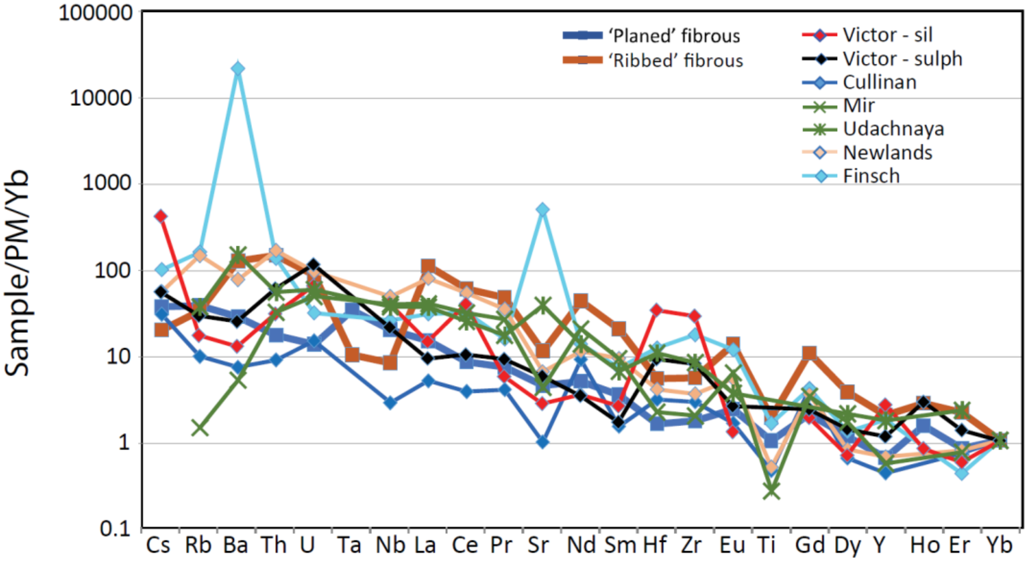

Figure 3.13: Double-normalised trace element patterns for gem quality diamonds from Victor (Canada; sulphide and silicate paragenesis), S. Africa (Cullinan, Newlands & Finsch) and Siberia (Mir and Udachnaya) (this study and McNeill et al., 2009), for two "end-member" patterns, 'planed' and 'ribbed' that characterize the HDFs in fibrous diamond (Weiss et al., 2013). Data are normalised to Primitive Upper Mantle and to a Yb value of 1x PUM to equalise variations in abundance levels caused largely by differences in fluid inclusion abundance. Where no data points are present the lines are extrapolated.

This allows a focus on the variation in slopes of trace element patterns and on inter-element fractionations. The resulting double-normalised multi-element patterns reveal many similarities between the trace element characteristics of the gem diamonds (this study) and of fibrous, fluid-rich diamonds.

The Victor diamond patterns most closely resemble the so-called “planed” pattern of Weiss et al. (2013). The Cullinan diamond suite more closely resembles the other end-member trace-element pattern commonly found in fibrous diamonds referred to as ‘ribbed’, but at lower concentrations and a shallower slope. The Newlands diamond suite also resembles the ‘ribbed’ pattern as does the diamond from Mir, although the Mir diamond lacks the negative Nb anomaly and is depleted in Rb and Ba. The patterns for the Finsch diamond suite fall somewhat in between both end-members (Fig. 3.14), similar to the pattern for the diamond from Udachnaya with some deviations that will be discussed below. The trace element systematics seen in gem diamonds appear, broadly, to be similar to those seen in fluid-rich diamonds from a variety of locations and, thus also correspond to different types of HDFs. The Victor gem diamond suite has trace element characteristics that correspond to those reported in fibrous diamonds from various locations by Klein-BenDavid et al. (2014) for high Mg-carbonatitic and the less fractionated patterns of silicic to low-Mg carbonatitic fluids (Fig. 3.15). The silicate-bearing Victor diamonds also display the negative Sr anomaly observed in high Mg-carbonatitic fluids.

The Newlands gem diamonds have La_N/Nb_N and Ba_N/Nb_N in the range for both high Mg-carbonatitic and silicic to low-Mg carbonatitic fluids reported by Klein-BenDavid et al. (2014), however, the Th_N/Nb_N ratios are much higher, indicating that the Newlands diamonds likely formed from a silicic to low-Mg carbonatitic fluid, with the elevated Th perhaps indicating a higher H_2O component in the fluid as Th is an element thought to be mobile in hydrous fluids in the mantle (e.g., Elliot et al., 1997). This is supported by the observation of Weiss et al. (2015) who found that silicic fluid compositions were related exclusively to eclogitic inclusions of omphacitic clinopyroxene.

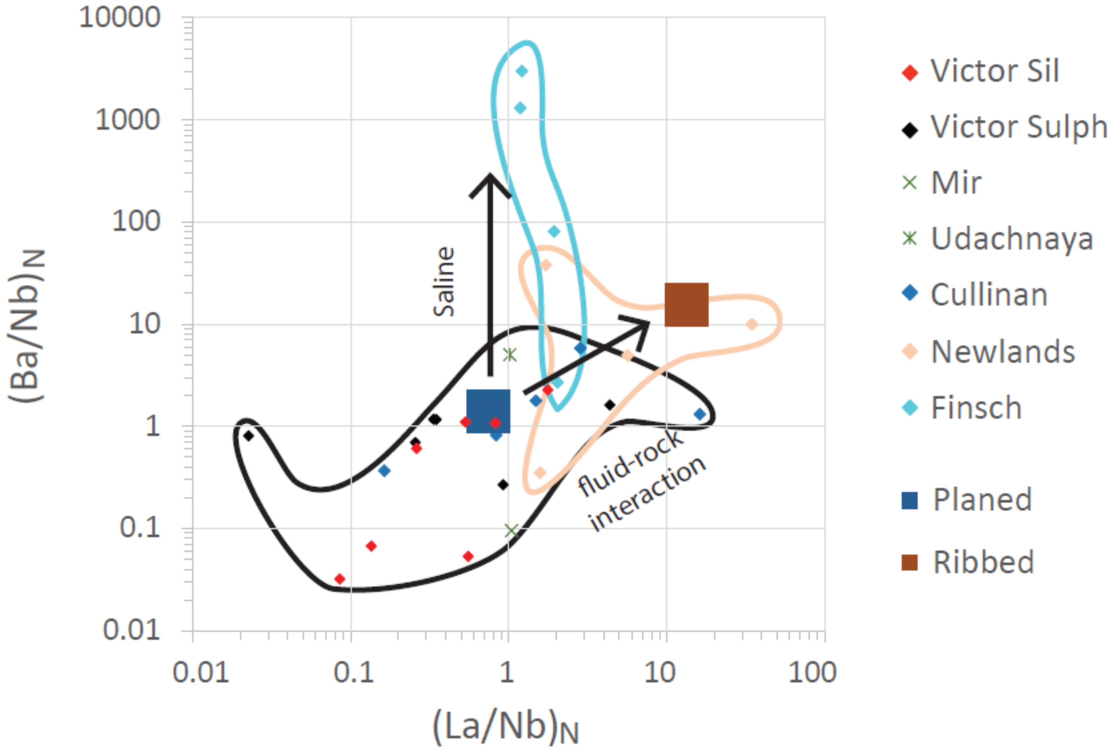

Figure 3.14: Primitive mantle-normalised Ba/Nb vs La/Nb ratio for gem quality diamonds from Victor (Canada), S. Africa (Cullinan, Newlands and Finsch) and Siberia (Mir and Udachnaya) (this study and McNeill et al., 2009), and for the two endmember patterns - 'planed' and 'ribbed'- of HDFs in fibrous diamond (Weiss et al., 2013). The black outlined field is for ultra-pure gem quality diamonds corresponding to the 'planed' HDF's in fibrous diamonds, the blue field encircles the Finsch diamonds and the orange field the Newlands diamond suite.

The Cullinan diamonds have trace element characteristics comparable to the Newlands diamonds indicating a likely formation from a silicic to low-Mg carbonatitic fluid, consistent with their predominantly eclogitic paragenesis (Fig. 3.15). The elevated Nb and low Ba contents in the diamond from Mir results in normalized trace element ratios that are a poor match to ratios reported for high Mg-carbonatitic, silicic to low-Mg carbonatitic or saline fluids in fibrous diamonds. Considering the similarity of the double-normalised trace element pattern of this diamond to that of 'ribbed'- HDFs in fibrous diamond (Fig. 3.13) and the eclogitic host lithology, however, it is likely the diamond formed from a silicic to low-Mg carbonatitic fluid.

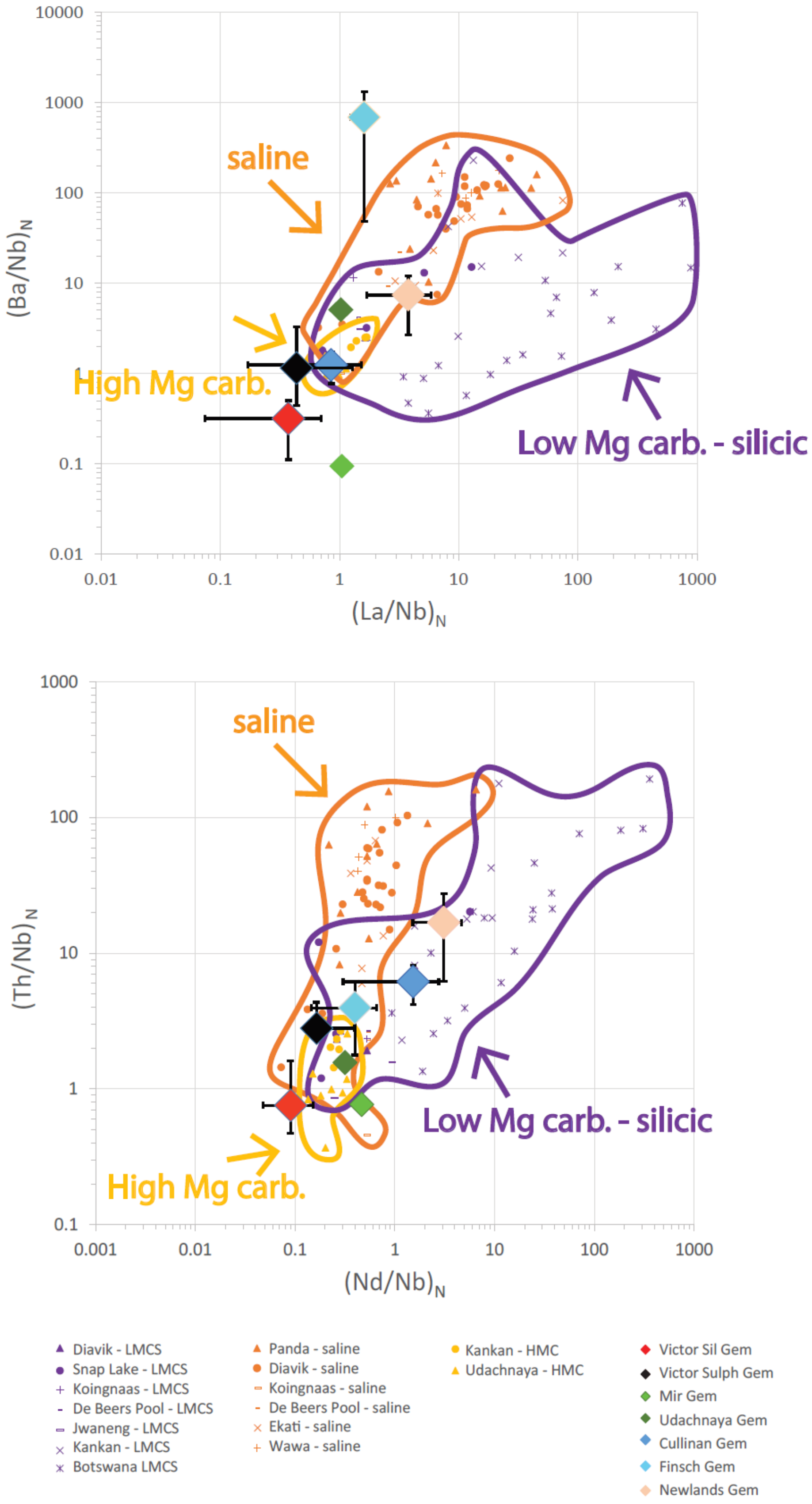

10000
1000
100
10
0.1
0.01
(Ba/Nb)$_N$
0.01
0.1
1
10
100
1000
(La/Nb)$_N$
saline
High Mg carb.
Low Mg carb. - silicic
1000
100
10
1
0.1
(Th/Nb)$_N$
0.001
0.01
0.1
1
10
100
1000
(Nd/Nb)$_N$
saline
High Mg carb.
Low Mg carb. - silicic
Diavik - LMCS
Snap Lake - LMCS
Koingnaas - LMCS
De Beers Pool - LMCS
Jwaneng - LMCS
Kankan - LMCS
Botswana LMCS
Panda - saline
Diavik - saline
Koingnaas - saline
De Beers Pool - saline
Ekati - saline
Wawa - saline
Kankan - HMC
Udachnaya - HMC
Victor Sil Gem
Victor Sulph Gem
Mir Gem
Udachnaya Gem
Cullinan Gem
Finsch Gem
Newlands Gem

Figure 3.15: Primitive mantle-normalised diamond fluid trace element ratios in fibrous diamonds: (a) Ba/Nb vs the La/Nb ratio and (b) Th/Nb vs Nd/Nb (after Klein-BenDavid et al., 2014). Data from Klein-BenDavid et al., 2010, 2014; Weiss et al., 2013, 2015 and Smith et al., 2012. Also plotted are median ratios for gem quality diamonds from Victor (Canada), and S. Africa (Cullinan, Newlands and Finsch), and ratios for gem quality diamonds from Siberia (Mir and Udachnaya) (this study and McNeill et al., 2009). The orange field is for saline HDFs, the yellow field for high Mg carbonatitic HDFs and the purple field for Low Mg carbonatitic – silicic HDFs. Legend: LMCS – Low Mg carbonatitic – silicic, HMC - high Mg carbonatitic.

The trace element characteristics of the Finsch diamond suite bears marked similarities to those reported for saline HDFs (Klein-BenDavid et al., 2014, Smith et al., 2012; Weiss et al., 2015) (Fig. 3.16). The PM normalized trace element patterns display prominent positive Sr anomalies and the chondrite normalized REE pattern of one diamond (JJG1) shows a positive Eu anomaly. Another key feature is the very high Ba contents, resulting in elevated Ba_N/Nb_N ratios (Fig. 3.14; Fig. 3.15). The strong similarity between the trace element systematics of Finsch monocrystalline diamonds and saline fluids from Wawa, Ekati and Diavik diamonds in particular (Fig. 3.15) is very strong support for the close link between the parental fluids of gem and fluid-rich fibrous diamonds, showing that highly saline fluids are widespread as diamond-forming fluids (Weiss et al., 2015). The high Ba/Nb, positive Sr and positive Eu anomalies have been linked to a subduction origin by Weiss et al. (2015). In the case of the Finsch diamond fluids, it is noteworthy that these signatures occur in diamonds from a Group II kimberlite characterised by strong whole rock Ba enrichments and very low εNd values (Fraser et al., 1985). The enriched isotopic characteristics of the Finsch kimberlite may have resulted from ancient enrichment of the lithospheric mantle source region before diamond formation billions of years ago (Richardson et al., 1984). Similarly, the elemental characteristics of the Finsch harzburgitic diamonds may also reflect this ancient, subduction-related enrichment event.

The single diamond from Udachnaya reported by McNeill et al. (2009) also shows some of the same elemental systematics as those identified as having saline fluids compositions, i.e. elevated positive Sr and Ba anomalies (Fig. 3.14, Fig. 3.15). The chondrite normalized REE pattern of this diamond, however, does not show a Eu anomaly. These trace element signatures do not agree with most patterns found for HDFs in fibrous diamonds from Udachnaya that have predominantly high-Mg carbonatitic fluid compositions with negative Sr anomalies relative to PM and moderate negative Zr-Hf (Zedgenizov et al., 2007; Klein-BenDavid et al., 2009; 2014).

So far, no fibrous diamonds with HDFs of saline composition have been reported from Udachnaya. However, one fibrous diamond analysed by Klein-BenDavid et al. (2009) had microinclusions that carried K–Ba–Sr-rich fluids dominated by K_2O and carbonate with exceptionally high BaO and SrO concentrations. This geochemical signature appears to be reflected in the Udachnaya gem diamond 3812 (Fig. 3.12).

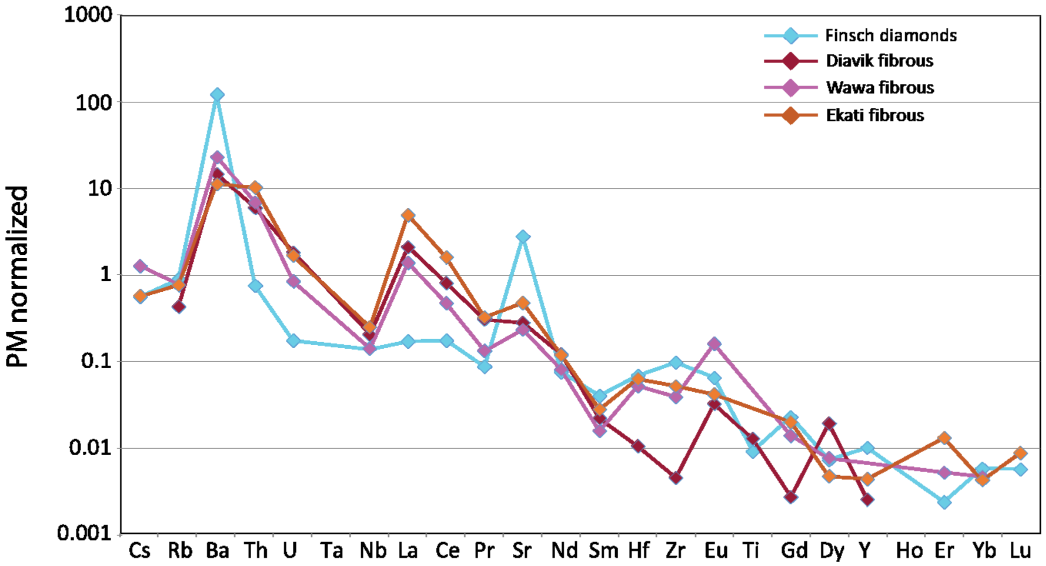

Figure 3.16: Primitive mantle-normalised multi-element patterns for gem diamonds from Finsch (S.Africa, this study) and fibrous diamonds bearing saline HDFs from Canada (Diavik, Wawa and Ekati: Klein-BenDavid et al., 2014; Smith et al., 2012; Weiss et al., 2015).

In summary, the trace element characteristics of diamond-forming fluids in the E-type Cullinan and Newlands diamond suites and the E-type Mir diamond indicate diamond formation from a silicic to low-Mg carbonatitic fluid, consistent with the formation of such fluids in eclogitic rocks, possibly by fractional percolation of low fraction asthenospheric melts through an ancient, enriched SCLM (Weiss et al., 2009). The trace element characteristics of the Victor diamonds, together with the strong connection established between high-Mg carbonatitic HDFs and a carbonated peridotite source, are either lithospheric or asthenospheric in origin (Weiss et al., 2009, 2011; Klein-BenDavid et al., 2014) and indicate that the Victor diamonds may have formed from a high Mg-carbonatitic fluid. The Finsch diamonds very likely trapped saline HDFs, suggesting their formation from fluids derived from recycled crustal sources. Such sources could generate the Nd-Sr isotopic characteristics recorded in Finsch harzburgitic diamonds.

3.5.5 Implications for the isotopic evolution of diamond-metasomatised mantle

As diamond-forming fluids have been invoked as metasomatic agents in the lithospheric mantle (Weiss et al., 2015; Klein-BenDavid and Pearson, 2009; Gibson et al., 2008), it is useful to explore the possible time-integrated radiogenic isotopic growth trajectories for the Victor and Finsch diamond fluids measured. In particular, the Nd-Sr isotope systematics of some subcalcic garnets included in diamond – especially those from Finsch gem diamonds – have unusually low ε_{Nd} and $^{87}Sr/^{86}Sr$ values (Richardson et al., 1984) that require complex multi-stage origins. The parent-daughter element ratio systematics of gem diamond fluids might illuminate other possibilities for generating these unusual isotopic signatures.

Several studies have documented striking similarities in chemical and Nd isotope compositions between subcalcic garnet xenocrysts and garnet inclusions in diamonds (e.g., Richardson et al., 1984; Pearson et al., 1995b; Jacob et al., 1998; Klein-BenDavid and Pearson, 2009; Shu and Brey, 2015). The REE composition of subcalcic garnet is generally sinusoidal in a chondrite (CI) normalized REE pattern indicating obvious links between garnet xenocrysts and inclusions in diamonds (e.g., Shimizu and Sobolev, 1995; Stachel et al., 2004a). Isotopic work on subcalcic garnets from peridotite xenoliths, kimberlites and diamond inclusions has shown extremely heterogeneous Sr and Nd isotopic variations (Richardson et al., 1984; Nixon, 1987; Pearson et al., 1995b; Richardson and Harris, 1997; Jacob et al., 1998; Klein-BenDavid and Pearson, 2009; Shu and Brey, 2015). ε_{Nd} values span a range of over 60 epsilon units (Pearson et al., 2003 and references therein) and the Sr isotopic composition can be extremely radiogenic (Richardson et al., 1984). The extreme Sr isotopic enrichments are commonly unsupported by their measured Rb contents, i.e. they have low Rb/Sr combined with much too high $^{87}Sr/^{86}Sr$ to be explained by in-situ decay of ^{87}Rb, indicating crystallization from an enriched precursor and/or metasomatism by fractionated radiogenic fluids.

Based on strong similarities of trace element characteristics of diamond forming fluids sampled from fibrous diamonds to those of subcalcic garnets (i.e. steep REE patterns, negative Ti and Sr anomalies and very low Sm/Nd ratios) and recent isotope studies (Klein-BenDavid et al., 2010; 2014) that have shown extreme Sr and Nd isotopic compositions of diamond forming fluids that are closely concordant with subcalcic garnets, Klein-BenDavid and Pearson (2009) suggested that diamond forming fluids may be intimately involved in the evolution of subcalcic garnets in the lithospheric mantle. They appear to either act as a metasomatic agent, or alternately be integral to triggering or enhancing garnet growth in a Cr-rich protolith.

The low trace element concentrations in the diamonds analysed in this study precluded the measurement of radiogenic isotope compositions, however, the Sm/Nd and Rb/Sr ratios are similar to those found in diamond forming fluid sampled by fibrous diamonds and subcalcic garnets (Fig. 3.17A).

Garnet/fluid partition coefficients suitable for the formation of garnet from a diamond forming fluid are not available. When attempted using partition coefficients for garnet/silico-carbonate melts (Girnis et al., 2013) these D values do not generate the strongly sub-chondritic Sm/Nd ratios and sinusoidal REE_N patterns observed in subcalcic garnets, especially those associated with diamonds. Garnets forming from our fluid using partition coefficients for basaltic melts (e.g., McKenzie and O'Nions, 1991), yield slightly sinusoidal REE_N patterns but not the strongly sub-chondritic Sm/Nd ratios and hence the resulting garnets have much higher Sm/Nd ratios but show little variation in Rb/Sr. As such, we abandoned the use of partition coefficients, and use instead simply the parent-daughter ratios of the fluids themselves, noting that their low Sm/Nd is similar to those of the most enriched of the sub-calcic garnet inclusions in diamond (Fig. 3.17A) and noting the observation from Klein-BenDavid et al. (2010) that fluids from fibrous diamonds span a similar parent-daughter elemental and measured isotopic range as the subcalcic garnets – an indication that the diamond-forming fluid composition is more closely imprinted on subcalcic garnets than the available partition coefficient data would imply.

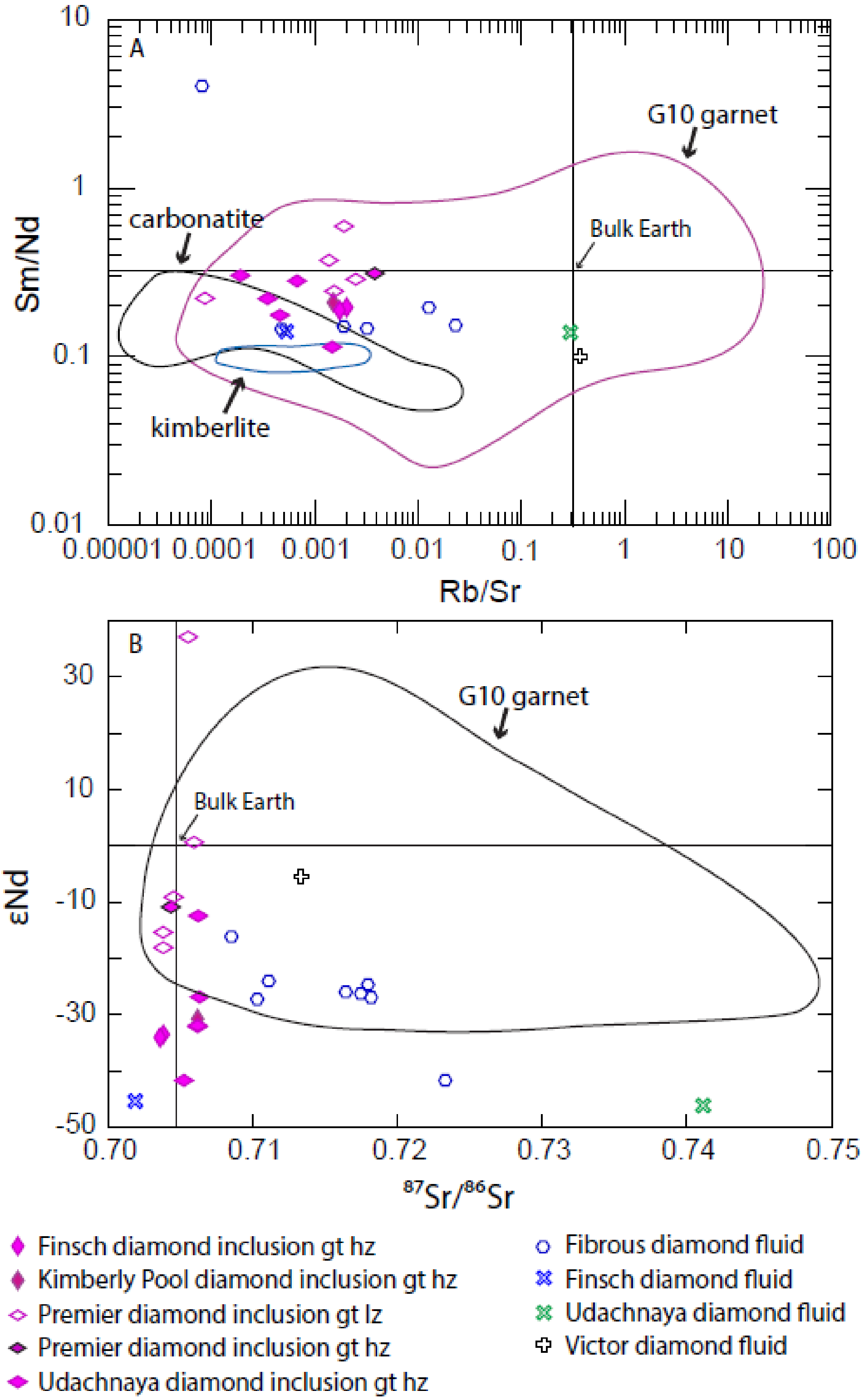

Figure 3.17: A. Sm/Nd versus Rb/Sr ratio in diamond-forming fluid and diamond inclusion G10 garnets. The Kimberly pool and Finsch concentrate and diamond inclusion data is from Richardson et al. (1984). Fibrous diamond fluid data is from Klein-BenDavid et al. (2010), (2014). Udachnaya diamond inclusion data is from

Stachel and Harris (1997). Premier diamond inclusion data is from Richardson et al. (1993). The G10 garnet field is constructed using data from Stachel and Harris (1997), Stachel et al. (1999), (2004), Davies et al. (2004), Logvinova et al. (2005); Klein-BenDavid and Pearson (2009). The carbonatite field is constructed using data from Bizimis et al. (2003), the kimberlite field using data from Tappe et al. (2013). B. ε_{Nd} vs. $^{87}Sr/^{86}Sr$ in in diamond-forming fluid and diamond inclusion G10 garnets. Inclusion data as in A (measured present day values). Gem diamond-forming fluid (Finsch, Udachnaya and Victor) are modelled values based on the elemental daughter-parent ratios and an assumed initial isotope ratio. The G10 garnet field is constructed using data from Richardson et al. (1984) and Klein-BenDavid and Pearson (2009).

Using the age of the diamonds (~3.2 Ga for Finsch, Richardson et al., 1984 and 718 Ma for Victor, Aulbach et al., 2018) and the elemental parent-daughter ratios, i.e. Sm/Nd and Rb/Sr, of their fluids allows forward modelling of the present day ε_{Nd} and $^{87}Sr/^{86}Sr$ isotopic compositions. As the low concentrations of some of the trace element data in gem diamonds can produce some noise in the trace element pattern, we chose the most enriched sample displaying the smoothest chondrite REE pattern to do this. Isotopic modelling for the Finsch (F866 2) fluids from a diamond within a low-Ca garnet bearing harzburgite, yields a highly negative ε_{Nd} of - 45.4 and an unradiogenic $^{87}Sr/^{86}Sr$ ratio of 0.7019. These systematics are strikingly similar to the unusual isotopic compositions of garnet inclusions in diamonds from Finsch (Richardson et al., 1984). The Victor sample (A578-01) has a much less extreme ε_{Nd} of -5.54 and a much more radiogenic $^{87}Sr/^{86}Sr$ ratio of 0.7133, more consistent with the higher but still negative ε_{Nd} values observed in lherzolitic garnets (Fig. 3.18B).

The similarities in the Sm/Nd and Rb/Sr trace element systematics and forward-modelled isotopic compositions of the best measurements of the gem-diamond fluids measured here and those measured in fluid-rich non-gem diamonds confirms the links already made between these fluid types (Jablon and Navon, 2016). The range in forward modeled isotopic compositions produced from the gem-diamond forming fluids, and their similarity with subcalcic garnet diamond inclusions, also strengthens the inferences already made from fluid-rich fibrous diamonds by Klein-BenDavid et al. (2010), that diamond-forming fluids are effective metasomatic agents in the lowermost lithospheric mantle. Moreover, some of these fluids provide a simple single-stage evolution for the generation of some of the highly unusual low ε_{Nd} and low $^{87}Sr/^{86}Sr$ systematics measured in garnets within diamonds.

3.5.6 Prospects for diamond provenance

The gem diamonds discussed here come from different host lithologies and have distinct formation ages, opening up the possibility of examining differences and similarities among diamond-forming fluids in petrologically distinct environments. Comparison of the trace element systematics between the relatively small numbers of E- and P-type gem diamonds discussed here shows that the fluids in E-type diamonds are generally more fractionated, resembling the "ribbed" trace element pattern of fibrous HDFs. In addition, several E-type diamonds display a negative Zr anomaly and most of the E-type diamonds have a positive Eu anomaly. In contrast, many of the P-type diamonds have a negative or no Eu anomaly (Fig. B2-B4, 3.12). However, these trace element signatures are not consistent for all the diamonds and, considering the very small sample pool, we do not yet have enough data for a statistically valid comparison.

As shown above the Victor diamonds display some consistent differences in trace element systematics based on their inclusion paragenesis (silicate versus sulphide). However, comparisons of trace element characteristics based on inclusion paragenesis (silicate and sulphide) across the present data set of fluids in gem diamonds does not reveal any systematic differences. This indicates that the Victor diamonds may have formed from related fluids whose subtle differences in degree of trace element fractionation may be related to differences in the degree of melting of the source and extent of fluid-rock interaction or even a subtly different source altogether.

Comparison of gem diamond trace element characteristics with regard to their formation age reveals that most diamonds of Proterozoic age, including Victor lherzolitic diamonds (718 Ma, Aulbach et al., 2018) and Cullinan (E-type ~2 – ~1.2 Ga, e.g. Richardson, 1986; Burgess et al., 1989; Phillips et al., 1989; P-type ~ 2 Ga, Richardson et al.,1993), show much flatter REE_N patterns with median La_N/Yb_N ~ 18 and La_N/Yb_N ~ 1.3 respectively, than the Archean diamonds from Siberia (Udachnaya, P-type (sulphide) ~ 3.1 - 3.5 Ga; Pearson et al., 1999) and P-type (garnet) ~ 2 Ga; Richardson and Harris, 1997), Finsch (3.3-3.2 Ga, Richardson et al., 1984) and Newlands (likely Archean and Proterozoic, Menzies et al., 2003) with La_N/Yb_N ~ 63, median La_N/Yb_N ~ 34 and median La_N/Yb_N ~ 68, respectively.

Overall, there are some differences in trace element signatures among diamonds of different paragenesis and among diamonds with different formation ages that may prove to be useful for diamond provenancing once a larger database of diamond-forming fluids in gem quality diamonds exists.

3.6 Conclusions

The concentrations of a wide range of elements, including Ba, Nb, U, Y and REEs, for all analyzed gem diamonds from the Victor diamond mine are very low, significantly lower than values reported for fibrous stones (e.g., Schrauder et al., 1996; Rege et al., 2005; Zedgenizov et al., 2007; Weiss et al., 2009, 2011; Klein-BenDavid et al., 2010) but consistent with "closed-cell" ablation data previously reported for other gem diamonds from other mines (McNeill et al., 2009; Melton et al., 2012). Trace element concentrations for the Newlands and Finsch diamonds derived from mantle xenoliths are much higher, in some cases up to three orders of magnitude, correlating broadly with their lower clarity.

Distinct differences are evident in the REE_N patterns of Victor diamonds containing silicate inclusions (median La_N/Yb_N ~ 17) compared with diamonds containing sulphide inclusions that have much less fractionated patterns (median La_N/Yb_N ~ 9). In addition, the sulphide bearing diamonds have more widely varying Ni, Fe and Co concentrations. These differences are neither striking nor consistent across all key trace element ratios, therefore, it seems likely that the fluids in the Victor diamonds have broadly the same origin, and the silicate and sulphide-bearing diamonds formed by gradations of the same processes or from a source that was only subtly different.

The available high quality data for trace elements in gem diamonds analysed and discussed in this study show many similarities to those reported for fluids from fibrous, fluid-rich diamonds. The quantitative nature of the data produced in this study and that of McNeill et al. (2009) establishes clearly that "planed" and "ribbed" trace element patterns characterise the parental fluids of both gem and fibrous diamonds. These fluids likely are small-degree hydrous melts of carbonated peridotite and from our data, appear to invade both peridotitic and eclogitic diamond substrates. The trace element data and similarities in Sm/Nd and Rb/Sr trace element systematics and forward-modelled isotopic compositions of gem-diamond fluids measured here and those measured in fluid-rich non-gem diamonds further strengthen the link between the parental fluids to both gem and fibrous diamonds established on a major element basis by Jablon and Navon (2016). Our data also document the first direct link between some gem diamonds, sampled from a Finsch harzburgite xenolith, and highly saline fluids that have been proposed to originate from subducted slabs (Weiss et al., 2015). Overall, we see the same spectrum of fluids in gem diamonds that was previously documented in fibrous diamonds, consistent with similar compositions of diamond-forming fluids (in terms of major and trace elements) over billions of years (Smith et al., 2012).

The striking similarity in the range and nature of trace element and forward modeled radiogenic isotope signatures (i.e., ε_{Nd} and $^{87}Sr/^{86}Sr$ ratio) for the gem-diamond forming fluids to subcalcic garnet inclusions, strengthens the inferences that they may be intimately involved in the evolution of subcalcic garnets in the lithospheric mantle.

Differences in trace element characteristics between fluids in diamonds of different host lithologies and among fluids in diamonds of different formation ages indicate that HDFs trapped in gem diamond may be a useful tool in the determination of a diamond's provenance once a larger database of diamond-forming fluids in gem quality diamond exists.

Chapter 4

New Approaches to Constraining Ruby Provenance using Sr - Pb Isotopes and Trace Elements

4.1 Introduction

Rubies are amongst the most valuable gemstones. The commercial value of a ruby depends on its size, its color and its clarity. The geographical origin of rubies has also become a critical factor in their desirability, for ethical reasons. Hence, trying to resolve the geographic provenance of rubies has developed into one of the main tasks for gem-testing laboratories, driving technological approaches to establishing accurate methods of identifying the provenance of rubies.

Rubies – a gem form of corundum – can be found in very different geological contexts and, although the realization of the importance of the geology of gemstone deposits for prospecting and mining has led to a significant improvement in our knowledge of the formation of those deposits, details of the mechanisms of formation, and the origin of the mineralizing fluids remain insufficient for the development of precise genetic models (e.g., Giuliani et al., 2014).

Techniques that have been applied to determining gem corundum provenance include the optical observation of inclusions and gemological features by optical microscopy, spectroscopic analysis using Raman and Fourier Transform Infrared (FTIR) spectroscopy, chemical analysis by energy-dispersive X-ray fluorescence (EDXRF), laser ablation inductively coupled plasma mass spectrometry (LA-ICPMS), laser-induced breakdown spectroscopy (LIBS), and stable isotope analysis using oxygen isotopes (e.g., Anderson and

Jobbins, 1990; Muhlmeister et al., 1998; Giuliani et al., 1998; Kochelek et al., 2015; Giuliani et al., 2005). Link (2015) dated zircon inclusions in high-quality faceted sapphires using the U-Pb system by LA-ICPMS, because the age determination of zircon inclusions may provide a valuable tool to support geographical origin determination, although the inclusion ages do not necessarily date the formation of the sapphire. So far no direct radiometric age has been obtained for ruby itself. All these approaches have shown promising results and have proven useful in distinguishing rubies and sapphires from different geological settings but they are not yet able to reliably distinguish between gems from different geographic regions with a similar geological setting. So far no unique fingerprint exists and a more powerful tool is needed. Here we try to develop a combined trace element and radiogenic isotope approach to ruby analysis with the aim of; 1) better understanding the timing of ruby formation and 2) developing more powerful discriminants to determine the point of origin of rubies.

Trace element analysis can potentially provide an elemental fingerprint of rubies and improve our understanding of the source characteristics of ruby-forming fluids and crystallization environments. However, because most elements in ruby are present at ultra-trace levels, fully quantitative data remain sparse, despite the rapid developments in laser ablation technology and improvements in ICPMS instrumentation. So far no radiogenic isotope systematics have been measured for ruby due to difficulties in dissolving corundum to perform the necessary chromatographic purification of the elements to be analysed. Radiogenic isotope tracers such as ^{87}Sr/^{86}Sr, ^{143}Nd/^{144}Nd and the radiogenic isotope ratios of Pb are an attractive approach to geographic provenancing because they remain largely unaffected by processes that can disturb elemental ratios, such as crystal growth from melts. Here we present new trace element characteristics for rubies, including high resolution elemental mapping of some crystals to allow a better understanding of where elements are located/hosted within rubies. In addition, we present the first ever Sr and Pb isotope analyses for rubies from four different localities (three for the isotope systematics) with two each having similar geological characteristics. Lastly, we present the first radiometric age estimate for ruby formation from a suite of samples from SW Greenland.

Our results show great potential for both online LA-ICPMS and Sr and Pb isotope systematics in the establishment of a reliable fingerprint for provenance discrimination understanding the petrogenesis of gemstones.

4.2 Samples

Samples analysed in this study originate from four different geographic locations and represent two different geologic deposit types. The rubies range in color from light pink to deep red, representing both “true” gemological ruby as well as pink sapphires that do not fit a rigorous definition - for simplicity we will refer to all samples as ruby. The sample selection is not meant to be in anyway comprehensive, but was selected to provide a reconnaissance study to assess the potential for the new approaches that we explore.

The geologic deposit type “metamorphic deposits in amphibolite and gabbro” (e.g., Giuliani et al., 2014) is represented by rubies from the Aappaluttoq ruby deposit, SW Greenland and by rubies from the Namahaca ruby deposit, Montepuez District, Mozambique. The Aappaluttoq rubies were taken from a bulk sample of ore composed of three main rock types, sapphirine-gedrite, leucogabbro and phlogopitite. The Namahaca rubies were sampled from an alluvial deposit. In total 17 samples from Aappaluttoq and 27 samples from Namahaca were analysed for trace elements using LA-ICPMS. A subset of nine samples from each deposit was chosen for radiogenic isotope analysis.

Marble-hosted rubies analysed in this study were selected from the mineral collection at the American Museum of Natural History (AMNH). This geological deposit type is represented by rubies from Myanmar and from North Vietnam.

Figure 4.1: A political map showing northern Myanmar and the localities producing rubies. Regions of origin for rubies analysed in this study are circled in red (from Harlow and Bender, 2013 after Kane and Kammerling, 1992).

The Myanmar region is represented by 16 samples from four different localities: Five from Sagyin and six from the Mogok Stone Tract, including four from Wet Loo that consist of ruby coating painite crystals, in the Mandalay Region, and four from Namya, located in the Kachin state approximately 300 km north of Mogok (Fig. 4.1).

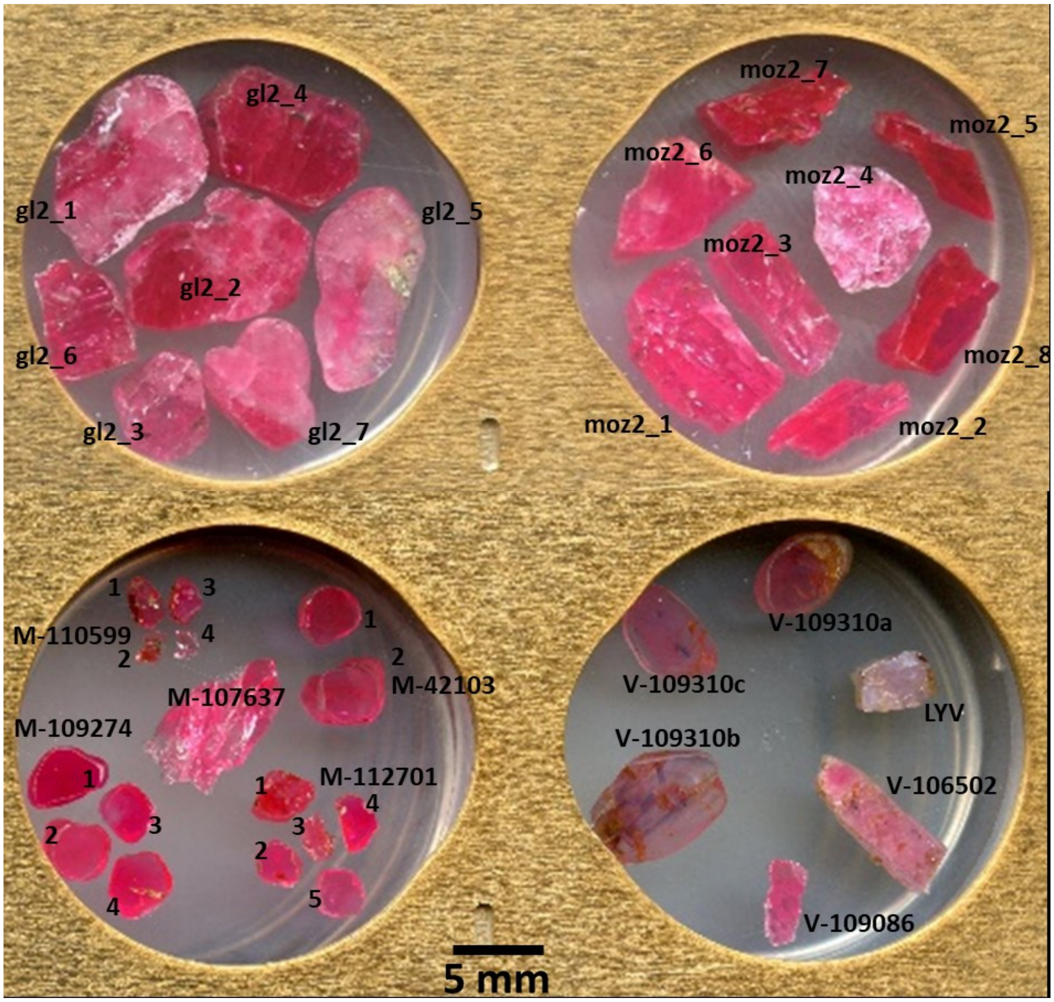

Figure 4.2: 1-inch resin sample mounts for LA-ICPMS analysis showing for rubies from Aappaluttoq, Greenland (gl), Namahaca, Mozambique (moz), Myanmar (M-xxx) and Luc Yen, Vietnam (V-xxx). A range of colour and clarity is shown by these rubies and pink sapphires.

A subset, consisting of four rubies from Namya, one from Sagyin and one from the Mogok Stone Tract, were analysed for radiogenic isotopes. The second marble-hosted ruby deposit covered in this study is the Luc Yen district in Northern Vietnam. Six alluvial rubies were analysed for trace elements using LA-ICPMS, no isotopic analyses were carried out for these samples.

4.2.1 Geology of ruby sample sources

4.2.1.1 Aappaluttoq, SW Greenland

The Aappaluttoq ruby deposit is located within the Mesoarchean (2.86 Ga, Polat et al. 2010) Fiskenæsset Anorthosite Complex (FAC), a layered cumulate igneous complex that occurs in the lower zone of the Bjørnesund structural block (e.g., Herd et al., 1969; Windley and Smith, 1974). Prograde granulite facies metamorphism occurred at around 2.82 Ga in the area (Friend and Nutman, 2001) and was followed by retrograde amphibolite facies metamorphism at circa 2.66 Ga (Pidgeon and Kalsbeek, 1978). The geology of the Aappaluttoq deposit is confined to the lower part of the stratigraphy of the FAC, namely the Lower Gabbro, Ultramafic, Lower Leucogabbro, and Middle Gabbro sequences, and no anorthosite or chromite bodies have been observed within the deposit. The corundum mineralization is connected with a specific stratigraphic horizon in the complex, lying between layers of regionally metamorphosed ultramafic rock (peridotite), characterised by low silica and Al-rich leucocratic gabbro (Reggin and Chow, 2011, Fagan, 2012). The boundary between these two units is a metasomatized reaction zone consisting mainly of a sapphirine-gedrite rock and phlogopitite. The phlogopitite is the host for the majority of the ruby held within Aappaluttoq, but the metasomatised leucogabbro also contains some gem corundum, mainly in the form of pink sapphire. The rubies and pink sapphires are usually associated with sapphirine, phlogopite, ±plagioclase, ±gedrite, ±cordierite, ±spinel and ±pargasite (Appel and Ghisler, 2014). Inclusions that are commonly found in rubies from Aappaluttoq are rutile, talc, mica, sillimanite, plagioclase, pargasite, zircon and apatite (Smith et al., 2016).

A U-Pb age of 2646 ± 43.3 Ma obtained for monazites along grain boundaries in the highly metasomatized, metamorphic ruby host rocks suggests that the rubies formed during the retrograde amphibolite facies metamorphism dated to circa 2.66 Ga by Pidgeon and Kalsbeek (1978) (Fagan and Groat, ongoing research). In addition, the ruby crystals have retrogressive rims of plagioclase around them, evidence that the rubies interacted with fluids causing the primary ruby phase to be destabilized. These reactions are thought to have occurred late during the retrogressive phase and show the crystals were interacting with metasomatic fluids at this time. Mica crystals surrounding the rubies yield a ^{40}Ar/^{39}Ar age of 1941 ± 4.5 Ma indicating that the ruby must have been formed prior to closure of the K-Ar system at this time. The

Aappaluttoq rubies are very likely amongst the oldest coloured stone deposits in the world and a direct age on these gems would be a valuable piece of information.

4.2.1.2 Namahaca, Montepuez District, Mozambique

The alluvial Namahaca ruby deposit, discovered in May 2009, is located approximately 30 km from Montepuez. The deposit is hosted in the Pan-African Montepuez complex, comprised of Neoproterozoic orthogneisses, ranging from granitic to amphibolitic in composition, and paragneisses, mainly formed by quartzite, meta-arkose, marble, quartz-feldspar gneiss, and biotite gneiss (Boyd et al., 2010). It is part of the Cabo Delgado Nappe Complex, a dominantly Neoproterozoic domain grouping the Xixano, Lalamo, Montepuez, M'Sawize and Muaquia complexes, and interpreted as an allochthonous domain transported northwestwards (e.g., Engvik and Bingen, 2017). No quantitative pressure temperature or metamorphic age data are available from the Montepuez complex, but based on the mineral parageneses present (hornblende–plagioclase–quartz ±garnet) it appears that the rocks are characterized by amphibolite-facies metamorphism and also contain lenses of granulite-facies rocks (Boyd et al., 2010). Ueda et al. (2012) reported U-Pb titanite ages for different rock types of the complex: A migmatitic gneiss yielded a U-Pb age of 565±15 Ma and impure marble 484±18 Ma. So far, rubies have only been found in amphibolite but none in the marble.

Ruby deposits in the Montepuez District are both primary and alluvial (Pardieu et al., 2013). The alluvial sedimentary sequence ranges in thickness from 0.5 m to over 10 m with grain size varying from 10 cm cobbles through to fine quartz sand. The bulk of the unit is minor muddy matrix material and quartz grains in the 5–10 mm size range, no significant quantities of lithic fragments or clay fractions have been noted. Grains tend to be equi-dimensional with significant rounding along the grain edges. The primary deposit appears to be a highly metamorphosed or metasomatized rock that has been completely altered from its primary nature, the resulting clay appears to be a complex Cr-rich smectite-group clay, with at least 5% of the layer made up of corundum, altered amphibole, and yellowish mica (Pardieu et al., 2009). Inclusions reported in rubies from the Montepuez district are most commonly rutile, amphibole, mica and chalcopyrite (Pardieu et al., 2013). At the time of writing, no detailed geological work has been published on the Namahaca deposit.

4.2.1.3 Mogok and Namya, Myanmar

The Myanmar ruby deposits occur in the Mogok Metamorphic Belt (MMB), that forms part of the Shan Highlands, an elevated region along the east side of Myanmar (Bender, 1983; Barley et al., 2003; Searle et al., 2007; Mitchell et al., 2004, 2007). The 1,000 km long belt extends from southern Myanmar through Yebokson, Kyaukse, Mandalay, to Mogok and then bends westward to the eastern Himalayas. It is characterised by high temperature ductile Oligocene stretching and post-Miocene brittle dextral faults such as the Shan scarp fault zone and the Sagaing fault (Bertrand and Rangin, 2003). The MMB has experienced multiple tectonic magmatic and metamorphic, uplift and exhumation processes, most likely accompanied by metamorphic core complex formation from as early as the Jurassic, extending to recent times, i.e. metamorphism of these rocks was a multi-step process related to the closure of the Tethyan Ocean (e.g., Harlow and Bender, 2013, Khin et al., 2015). Kyaw Thu (2007) defined four ages for the emplacement of magmatic rocks based on radiometric dates of zircon by the U–Pb method: (1) 129 ±8.2 Ma (Early Cretaceous) for augite-biotite granite; (2) 32 ±1 Ma (Early Oligocene) for leucogranite; (3) 25 Ma (late Oligocene) for foliated syenite; and (4) 16 ±5 Ma (Middle Miocene) for painite-bearing skarn formed at the contact leucogranite–marble.

The Mogok area consists of a series of undifferentiated high-grade metamorphic rocks that are associated with alkaline rocks (mostly sodic nepheline–syenite and syenite–pegmatite) and leucogranites, accompanied by a mafic–ultramafic suite of peridotite, minor gabbro, and norite (e.g., Kyaw Thu, 2007, Themelis, 2008). The dominant unit is banded gneiss, with biotite, garnet, sillimanite and oligoclase, interspersed with quartzite and bands and lenses of marble. The marbles mainly contain calcite. Primary ruby in Myanmar occurs mainly in the calcitic marble, associated phases include pyrite, pyrrhotite, sodalite, balliranoite, clinohumite, and montmorillonite (Harlow and Bender, 2013). Common inclusions in Mogok rubies include rutile, colorless calcite and dolomite, apatite, zircon, feldspar, pyrrhotite, titanite, magnetite, micas, spinel, and possibly tourmaline and diopside (Hughes, 1997).

Age dating of minerals associated with ruby yields an U-Pb age of 31–32 Ma for a zircon inclusion in a Mogok ruby (Khin et al., 2008) and ^{40}Ar–^{39}Ar ages of 18.7 ± 0.2 to 17.1 ± 0.2 Ma for phlogopite associated with metamorphic ruby (Garnier et al., 2006). These results indicate that more than one ruby forming event took place.

4.2.1.4 Luc Yen, Yen Bai Province, Vietnam

The marble-hosted ruby deposits from northern Vietnam are located in the Red River shear zone, the major Cenozoic discontinuity in East Asia in the Day Nui Con Voi range, composed of high-grade metamorphic rocks with sillimanite-biotite-garnet gneisses, mica schists with local successions of marbles and amphibolites, which extend to the southeast from the Ailao Shan in Yunnan (China) (Leloup et al., 2001, Van Long et al., 2004). The range was affected by extensional tectonics and coeval magmatism, active during the Cenozoic Indo-Asian collision from Afghanistan to Vietnam, in the ruby-bearing metamorphic belts, between the Oligocene and the Pliocene. Deformation occurred under amphibolite facies conditions (Jolivet et al., 1999; Leloup et al., 2001; Barley et al., 2003). In Luc Yen (Vietnam) amphibolite bodies alternate with calcitic and dolomitic marbles. The primary deposits occur in weakly deformed, moderate-to-high temperature recrystallised marble units from the Lo Gam tectonic zone, located on the eastern side of the Red River shear zone (Leloup et al., 2001).

Ruby crystals occur disseminated within marbles and associated with phlogopite, dravite, margarite, spinel, rutile, edenite, pyrite, pargasite and graphite, and in some occurrences in veinlets associated with calcite, dravite, phlogopite, margarite, and pyrite, and in fissures associated with orthoclase, phlogopite, margarite, graphite and pyrite (Van Long et al., 2004). Secondary ruby occurrences can be found in karst topography and in alluvial fans in the Luc Yen valleys formed by gravels.

In-situ U–Pb dating of a syngenetic zircon included in a ruby from Luc Yen yielded a ^{206}U–^{238}Pb age of 38.1±0.5 Ma, indicating that ruby formed when ductile deformation was active under peak metamorphic conditions in the Red River shear zone (Garnier et al., 2005).

4.2.2 Metamorphic deposits in amphibolite and gabbro

Both Aappaluttoq in SW Greenland (e.g., Fagan et al., 2011) and Namahaca at Montepuez in Mozambique (e.g., Pardieu et al., 2013) are deposits where corundum is found in amphibolite originating from the metamorphism of gabbroic and dunitic rocks. Often ruby from this type of deposit is not of gem quality and crystals are used for cabochons and ornamental uses. However, three recently discovered deposits are highly economic for their quality and quantity, including Aappaluttoq, the Montepuez area and Winza in Tanzania (Peretti et al., 2008, Schwarz et al., 2008).

These deposits are characterised by several common features: (1) The corundum-bearing amphibolite is associated with mafic and ultramafic complexes metamorphosed to granulite facies, (2) The common mineral assemblage is composed of corundum, anorthite, gedrite and margarite while others minerals such as sapphirine, garnet, spinel, kornerupine, phlogopite and zoisite may be present, and (3) The initial basic composition of the protolith includes gabbro, but also troctolite (e.g., Nicollet, 1986; Forestier and Lasnier, 1969; Tenthorey et al., 1996; Rohtert and Ritchie, 2006; Dirlam et al., 1992; summarized in Guiliani et al., 2014). Trace element characteristics reported for metamorphic deposits in amphibolite and gabbro are generally moderate contents of Cr and Fe, very low to low amounts of Ti and V, and low to moderate amounts of Ga (e.g., Giuliani et al., 2014). The worldwide range in oxygen isotopic composition of ruby hosted in mafic and ultramafic rocks is 0.25 to 6.8‰ (n = 21).

The formation of gem corundum in metabasite deposits is thought to result from the dehydration of plagioclase-rich rocks (anorthosites, troctolites, norites) under granulite facies conditions (e.g., Herd et al., 1969; Tenthorey et al., 1996, Fagan and Groat, 2014). During regional metamorphism, fluid interactions between ultramafic rocks and plagioclase-rich rocks create a metasomatic reaction zone encompassing part of the ultramafic rock, the plagioclase-rich rock and the contact zone between the two units. Within this zone, silica is leached from the plagioclase-rich rock and the chromophoric elements are removed from the ultramafic rock. Upon regional cooling, the reaction zone forms significant volumes of corundum-rich ore. The concentration of Al in the reaction zone is high, and the availability of Cr from the adjacent ultramafic rock allows the substitution of Cr^{3+} for Al^{3+} in the corundum, producing the pink to red coloration.

4.2.3 Metamorphic deposits associated with marble

Marble-hosted ruby and pink sapphire deposits are of two types: (1) in marble where the corundum crystallized as a result of retrograde isochemical reactions mainly in a closed system and (2) in impure marble containing gneiss and silicate layers where ruby crystallized at the peak of prograde metamorphism (Guiliani et al., 2014). Both the deposits in Myanmar, Mogkok and Namya, and Luc Yen, Vietnam, from which the samples in our study originate are of the first type.

These deposits share many common geological, structural and mineralogical features: (1) They are hosted by metamorphosed platform carbonate assemblages associated generally with intercalations of garnet-biotite-sillimanite- or biotite-kyanite-bearing schist or gneiss, that commonly contain alternations of quartzite and amphibolite, (2) these metamorphosed sedimentary rocks, are generally intruded by dikes of granite and/or pegmatite, but the ruby mineralization is not directly linked with granitoid bodies, (3) the mineralization is generally stratiform and occasionally disseminated within a particular level in the marble, (4) a 'ruby zone' (0.5 to 10 m thick) is formed by a succession of benches of cme- to m-scale marble, where ruby is located in veinlets, gashveins, lenses or disseminations in the carbonate gangue, and (5) ruby-bearing marble is composed of calcite and dolomite and contains corundum, spinel, diopside, phlogopite, garnet, chlorite, margarite, tremolite, pargasite, edenite and forsterite. Other minerals include graphite, anorthite, anhydrite, aspidolite, titanite, fuchsite, scapolite, zoisite, K-feldspar, epidote, pyrite, and pyrrhotite (e.g., Iyer, 1953, Harding and Scarratt, 1986, Kissin, 1994; summarized in Garnier et al., 2008 and Guiliani et al., 2014).

Trace element characteristics reported for this type of marble-hosted deposit include moderate contents of Cr, low Fe, low to moderate amounts of Ti, elevated V and low Ga (e.g., Muhlmeister et al., 1998). The worldwide range in oxygen isotopic composition of ruby hosted in marble is 16.3 to 23‰ (n = 41) (Guiliani et al., 2005).

Several hypotheses on the genesis of these ruby deposits have been advanced and are summarized in Guiliani et al. (2014). The model currently favoured has been proposed by Garnier et al. (2008) for the formation of the Indo-Asian ruby deposits, including those in the Luc Yen area, and suggests that gem ruby formed at P ~3 kbar and 620<T<670 °C, during thermal reduction of evaporitic sulfates by organic matter, at high temperature-medium pressure metamorphism of platform carbonates. The carbonates were enriched in Al- and Cr-bearing detrital minerals, such as clay minerals that were deposited on the platform with the carbonates, and in organic matter. The metamorphic fluid system was rich in CO_2 released from devolatilisation of carbonates, and in F, Cl and B, released by molten salts (NaCl, KCl, $CaSO_4$). These mobilized (over short distances) in situ Al and transition metal elements contained in the marble, most likely in the form of mica, formed by the metamorphism of clay minerals, organic matter, and spinel minerals, leading to crystallization of ruby.

Micro-Raman spectrometry of inclusions in Mogok rubies revealed the presence of quenched molten salt and sulfate inclusions coexisting with other mineral inclusions such as fluorite, calcite, dolomite, apatite, boehmite, magnetite, graphite, and rutile. Their presence corroborates the model of formation for marble-hosted ruby based on the thermal reduction of sulfates of evaporitic origin (Giuliani et al., 2012).

4.3 Analytical methods

4.3.1 Laser ablation-inductively coupled plasma-mass spectrometry (LA-ICPMS) analysis

For LA-ICPMS analysis samples were mounted on 1-inch epoxy grain mounts and polished with diamond to obtain a flat surface. Analyses were carried out at the Arctic Resources Geochemistry Laboratory at the Department of Earth and Atmospheric Sciences, University of Alberta. The laser ablation system used was a RESOlution M-50 (Resonetics) 193 nm ArF Excimer (CompexPro 102, Coherent) coupled to a sector-field Thermo Finnigan Element XR mass spectrometer. Samples and standards were ablated using a laser spot size of 285 μm, a repetition rate of 20 Hz and a fluence, measured at the sample surface, of ~ 6.6 J/cm^2. These parameters resulted in clean, circular ablation pits with precise geometry, indicating low levels of inter-element fractionation (Fig. 4.3). Most analyses consisted of 60 s background acquisition followed by a 60 s sample data acquisition, some of the earlier measurements consisted of 35 s background acquisition followed by 43 s or 56 s sample data acquisition. The mass spectrometer was operated in low mass resolution mode (m/Δm=ca. 300). Data were acquired for ^{25}Mg, ^{29}Si, ^{39}K, ^{43}Ca, ^{49}Ti, ^{51}V, ^{52}Cr, ^{55}Mn, ^{57}Fe, ^{60}Ni, ^{64}Zn, ^{65}Cu, ^{71}Ga, ^{85}Rb, ^{88}Sr, ^{89}Y, ^{90}Zr, ^{93}Nb, ^{98}Mo, ^{120}Sn, ^{137}Ba, ^{139}La, ^{140}Ce, ^{141}Pr, ^{146}Nd, ^{165}Ho, ^{172}Yb, ^{178}Hf, ^{181}Ta, ^{184}W, ^{208}Pb, ^{232}Th, and ^{238}U with a dwell time of 10 ms for Mg, Si, K, Ca, Ti, V, Cr, Fe, Zn, Ga, Sb and W, a dwell time of 20 ms for Mn, Ni, Cu, Y, Zr, Nb, Ba, La, Ce, Pr, Nd, Ho, Yb, Hf, Ta, Th and U, and a dwell time of 30 ms for Rb, Sr, Mo, Sn and Pb. Some measurements made early in the research program had a dwell time of 10 ms for all measured elements, or 10 ms for all but Rb, Sr, Y, and the REEs with a dwell time of 20 ms. NIST SRM 612 multi-element standard glass was used as a primary standard and ^{27}Al as an internal standard using the stoichiometric Al content of Al_2O_3.

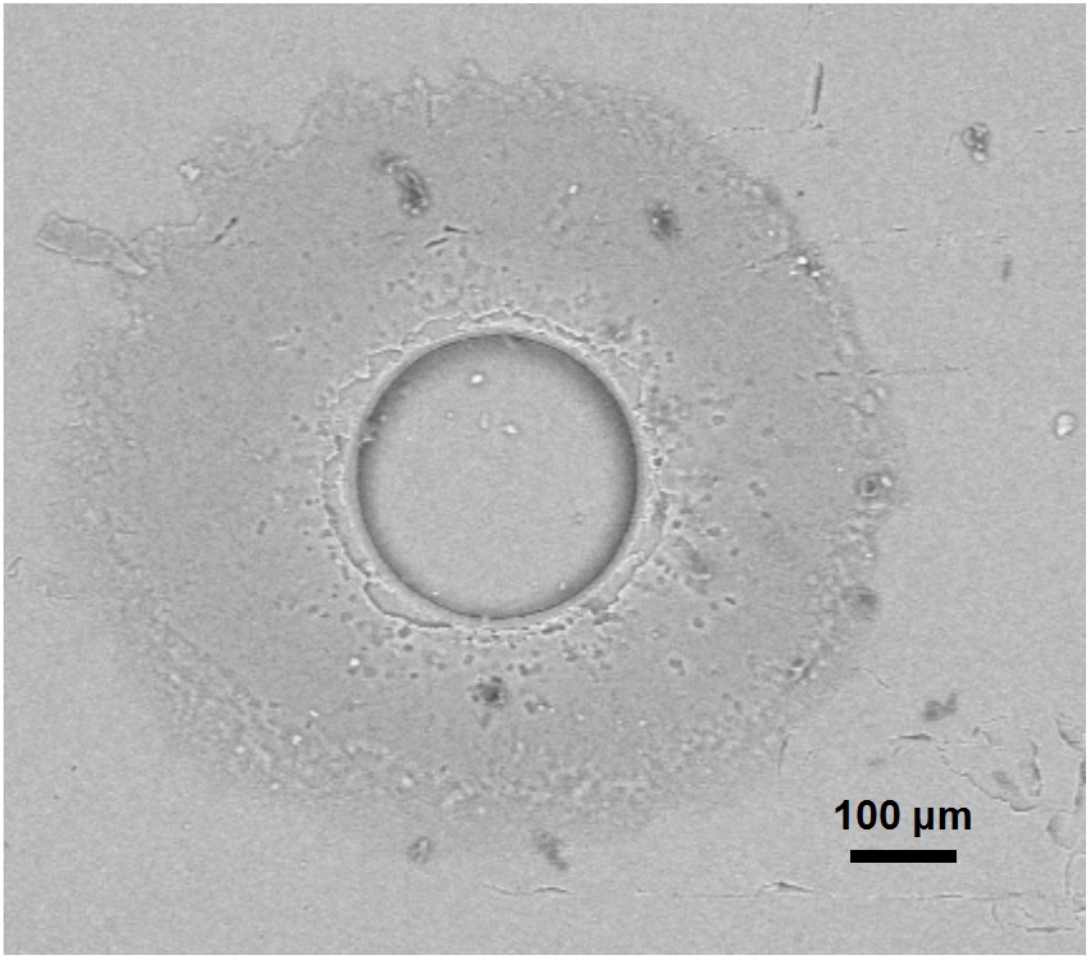

Figure 4.3: Laser ablation pit in natural ruby resulting from ablations with a spot size of 285 µm, a repetition rate of 20 Hz and a fluence of ~ 6.6 J/cm^2. The clean, flat-bottomed circular pit is conducive to minimising inter-element fractionation during laser ablation.

NIST SRM 614 and NIST SRM 616 glasses were used as secondary standards to monitor accuracy, instrumental drift and matrix effects (Table C1). For each sample at least two points were targeted and measured to ensure accuracy and reproducibility of results. Standards were analysed after every 5-8 samples analyses.

Data reduction and processing was conducted using the Iolite software (Paton et al., 2011). The time-resolved display and segment-picking for data integration in Iolite permits the identification of signal spikes from inclusions which could thus be avoided during data reduction.

Limits of Detection (LOD = 3 σ_{blank}; Currie, 1968) were calculated in Iolite using an equation developed by Pettke et al. (2012), based on Poisson statistics, for very low count rates. The LOD defines only the limit of the inherent detection capability in any chemical measurement procedure (e.g., Currie, 1968, 1999; Olivieri et al., 2006), for data to be referred to as truly quantitative it must exceed the limit of quantification (LOQ: the minimum quantifiable accurate value). In this study we use the LOQ as originally defined by Currie (1968), LOQ = 10 σ (with σ = the standard deviation of the background), as data quality filter.

4.3.2 Laser ablation and inductively coupled plasma–Time-of-Flight mass spectrometry

For two rubies from the Aappaluttoq, multi-element variation images were recorded for two areas each by laser ablation inductively coupled plasma time-of-flight mass spectrometry (TOF-LA-ICPMS). Measurements were carried out using an icpTOF time-of-flight mass spectrometer (TOFWERK AG, Thun, Switzerland) coupled to an Analyte G2 193 nm excimer laser ablation system (Teledyne CETAC Technologies, Omaha, USA), equipped with a HelEx II dual-volume ablation cell and an Aerosol Rapid Introduction System (ARIS) for fast washout of the sample aerosol, at TOFWERK AG, Thun, Switzerland. The transport gas used was helium with an overall flow rate of 0.6 L/min and argon was added to the sample gas inside the ARIS device prior to introduction into the inductively coupled plasma (ICP), also made up of argon (flow rate of 15 L/min).

Optimization of the system was achieved by ablating a line on the NIST SRM 612 glass using a laser fluence of 3 J/cm^2, 40 µm spot size, 20 Hz repetition rate, and a scan speed of 5 µm/s. Sensitivity, resolution, and peak shape were then tuned observing the masses ^{23}Na, ^{59}Co, ^{115}In, ^{232}Th, and ^{238}U. The count rate for ^{238}U was ~40,000 cps at a resolution of ~3000 (m/Δm at FWHM) and the ^{232}Th/^{238}U ratio was tuned to be close to unity. A notch filter was applied throughout all measurements in order to attenuate the Ar peak at 40 m/q.

Ablation parameters used for mapping were a laser fluence of 3 J/cm^2, a spot size of 20 μm and a repetition rate of 10 Hz, the latter based on the signal duration resulting from one laser shot on the sample (~100 ms). Spot-resolved imaging was performed implying that each laser shot results in one pixel in the image - for this, the laser was programmed to raster across the sample area along an array of side-by-side spots. The icpTOF records full mass spectra (from ^{23}Na to ^{238}U) at a rate of 33 kHz (Borovinskaya et al., 2013). Thus, multiple measurements can be obtained across the signal of a single laser shot. The spot-resolved, multi-elemental imaging approach for LA-ICP-TOF-MS has previously been described in detail elsewhere (Burger et al., 2017; Bussweiler et al., 2017). The calibration reference material NIST SRM 612 was measured in the same way as the ruby images, including gas blanks, immediately before and after each image.

Quantification of the intensity images was carried out using in-house software (Tofware) for TOF baseline subtraction and peak integration (Hendriks et al., 2017; Burger et al., 2017). The TOF baseline was characterized using a smooth function based on a running average of the background signal. Isotope channels of interest were integrated and exported as .csv files. Subsequently, the images were quantified against the reference material using the Iolite software (Paton et al., 2011). This included subtraction of the gas blank, and selection of appropriate integration intervals for reference material and sample. The "Trace_Elements_IS" data reduction scheme was used with ^{27}Al as the internal standard, assuming a constant content of 52.9 wt% Al. The quantified images were reconstructed in Iolite using the "Images from Selections" function.

4.3.3 Offline laser ablation

To collect sufficient analyte for isotope analysis the ruby samples were ablated using an "offline" laser ablation sampling technique originally developed by McNeill et al. (2009) and Klein-BenDavid et al. (2010) for the ablation of diamond. The technique utilizes a closed-system, custom-designed PFA laser ablation cell in which a sample is ablated and the products trapped, allowing the accumulation of higher volumes of analyte need for isotope analysis. Further details are given in McNeill et al. (2009) and Klein-BenDavid et al. (2010).

4.3.2.1 Sample preparation

For "offline" ablations the rubies were extracted from the 1-inch grain mounts and leached in 16 N Seastar UPA-grade HNO_3 on a hotplate at 100 °C for 24 hrs and then rinsed in 18.2 MΩ MQ H_2O before being leached in 6N HCl for another 24 hrs again at 100 °C followed by another rinse in MQ H_2O. Subsequently all samples were dried and weighed on a Mettler Toledo™ UMT2 Micro Balance and mounted within the ablation cell. In cases where the sample geometry did not allow for the ruby to present its flat surface to the laser beam the sample was fixed in place with pre-cut parafilm squares that had been pre-leached in MQ H_2O for at least 5 days.

4.3.2.2 Ablation and sample collection

Ablation and sample collection of the rubies was performed following methods and procedures outlined in Chapter 3, Section 3.3.1. Ablation times varied from 4–7 h.

For most samples the dried ablation products were taken up in 200 µL of 3N HNO_3 and placed on the hot plate for at least 24 h to homogenize. After cooling a ~20% aliquot by volume was transferred into a pre-leached 7 mL Teflon beaker for trace element analysis and the remaining sample was processed for isotopic analysis.

4.3.2.2 Separation chemistry

The Sr separation procedure is based on the method described by Charlier et al. (2006), using Sr-spec resin but with modifications for ng to sub-ng samples as outlined by Harlou et al. (2009). For most samples Pb was eluted following Sr in the same column. However, semi-transparent, sticky jam-like residues in the Pb fraction are insoluble in HCl or HNO_3 acid. This made loading of the samples on the filament difficult and led to low intensities of Pb for TIMS analysis, resulting in relatively large analytical errors. Such jam-like residues have previously been reported by Deniel and Pin (2001) and Li et al. (2015) and are presumably organic components released from the Sr Spec resin as a result of using HCl $\geq$ 6 M. Even after extensive pre-treatment of the Sr Spec resin using high volumes of 7 M HNO_3 and 6 M HCl the residues persisted and we switched to two separate columns for the separation of Pb and Sr. Here, the Pb fraction was separated using BioRad AG1-X8 anion exchange resin (100-200 µm mesh) in

50 µl Teflon columns. The columns were washed with 0.2M HNO_3 and 18Ω MQ and primed with 0.5M HBr before samples were loaded in 0.5M HBr. After washing with 0.5M HBr, the Pb was eluted in 0.5M HNO_3 and dried down. The collected 0.5M HBr wash was then dried down and Sr separated using the Sr-spec resin.

A drop of 0.1 N H_3PO_4 was added to each sample before drying down, because it does not evaporate at dry-down temperatures leaving a brown residue, thus enabling easy sample location.

4.3.2.3 Limits of Quantification (LOQ)

The calculation of Limits of Quantification (LOQ) for trace element analysis was carried out following the same procedures detailed in Chapter 3, Section 3.3.3. A total of 36 total procedural blanks (TPBs) were performed for the ruby ablations, resulting in the following LOQs: the elements Cs, Pr, Sm, Eu, Gd, Tb, Dy, Ho, Er, Yb, Lu, and U are less than 1 pg, the elements Rb, Y, Nb, La, Nd and Th less than 5 pg, Co, Ce, Hf, and Pb less than 20 pg, the elements Sr and Ba less than 70 pg, Mn, Cu, Zr and Mo less than 350 pg and the elements Cr, Fe, Ni, and Zn less than 10.4 ng. In cases where the sample had to be fixed in place with pre-cut parafilm squares, the TPBs for the elements Cr, Mn, Co, Ni, Cu, Nb, Mo and Pb are consistently higher resulting in elevated LOQs (Table C2).

The Total procedural blanks (TPB) for the isotopic analysis are 55.6 ± 10 pg (n = 32) on average for Sr, the contribution from the Sr spec resin is ~ 0.13 pg. Pb blanks averaged 2.75 ± 2.15 pg (n = 17) and 5.72 ± 2.87 (n = 14) for samples fixed with parafilm, plus ~ 0.48 pg from the Sr spec resin.

The average signal intensity of ^{84}Sr, ^{86}Sr and ^{88}Sr of the TPBs (n=6) is 43-times lower than the average signal intensity of ^{84}Sr, ^{86}Sr and ^{88}Sr of the analysed ruby samples (n = 34) and 48-times lower for ^{87}Sr. The isotopic composition of the laboratory blank could not be determined accurately, and due to the low total analyte sizes of the TPBs the contributions are deemed insignificant hence no corrections to the reported data were made.

4.3.3 Isotope analysis

4.3.3.1 Filament loading

Sr and Pb samples were loaded onto outgassed zone refined single Re filaments in a clean Class 10 laminar airflow unit. Samples were loaded with 4 µl of a purified TaF_5 activator to enhance Sr ionisation. The loads were slowly evaporated on the filament at 1.2 A. To ensure sample evaporation from a small (2 mm) area in the centre of the filament, a thin coat of parafilm was applied on either side of the filament before loading the sample. Subsequently the current was slowly increased to 1.6 A to burn-off the parafilm and to 1.8 - 2 A to burn of the H_3PO_4. Finally the filament current was increased (2.1–2.2 A) to glow for a couple of seconds before bringing it down to zero very gradually.

Pb samples were loaded with a mixture of 3.5 µL of silicic acid activator and 0.5 µL 0.1N H_3PO_4. The loading procedure for Pb samples is the same as for Sr, with the exception of the final increase of the current to make the filament glow. The Pb and Sr loading blanks using the same materials as for samples (a combination of filament and activator impurities) are between 0.15 and 0.40 pg (Sarkar et al., 2015b).

4.3.3.2 $^{87}Sr/^{86}Sr$ ratio analysis

Sr isotope analyses were performed on a Thermo Scientific Triton Plus TIMS, equipped with nine movable Faraday cups. There are 10 amplifiers, consisting of six 10^{11} Ω and four 10^{12} Ω amplifiers, installed in the instrument. Any amplifier can be connected to any of the Faraday cups using a relay matrix, the collection scheme used in this study for static Sr isotope analyses is described in Fig. 4.4. The largest ion beam (^{88}Sr) was placed on a Faraday cup attached to a 10^{11} Ω amplifier. At the start of an analytical session a gain calibration was performed and all intensities reported in this paper are gain corrected intensities. A longer baseline is required to accurately and precisely determine the uncertainties of the 10^{12} Ω amplifiers. A baseline of 20 min duration (1195 cycles with 30 s pre-baseline wait time) was determined before analysis, during filament heating, with the line of sight (LOS) valve closed. An additional baseline of 20 min duration was acquired after the sample run, during the warm-up of the next filament. The average of both baselines were used to correct the data offline.

Cup	**H4**	**H3**	**H2**	**H1**	**C**	**L1**	**L2**	**L3**	**L4**
Mass		^{88}Sr	^{87}Sr	^{86}Sr	^{85}Rb	^{84}Sr			
Amp		10^{11}	10^{12}	10^{12}	10^{11}	10^{12}			

Figure 4.4: Collection scheme used for static analysis of Sr isotopes by TRITON Plus TIMS.

Filaments were slowly warmed to a current of 2300 mA in 20 min after which the LOS valve was opened. The ion beam was then focused and the filament was further heated very slowly (@ 30 mA/min) until the signal at ^{88}Sr reached 4-5 mV, the intensity needed for tuning. The filament is then further heated to around 1450 -1500 °C and Sr fractionation was continuously monitored by repeatedly measuring ^{88}Sr/^{86}Sr ratio until it is ~ 8.32 - 8.35. The signal is tuned again followed by peak centering and faraday cup overlapping which were performed just before the start of the analysis. All isotopic data were collected in static mode for 10 blocks of 20 cycles with 8.39 s integration time. The magnet settling time ('idle time') in the analysis method was set to 5 s, because of longer settling time required for the 10^{12} Ω amplifiers.

The raw data were exported and later corrected for the baseline in an offline procedure where the average of the two long baselines before and after the sample analysis was used and an internal mass fractionation correction was applied to the baseline subtracted and interference corrected ^{87}Sr/^{86}Sr data using the exponential law and ^{88}Sr/^{86}Sr = 8.375209. Rubidium interference on the ^{87}Sr mass was corrected by monitoring ^{85}Rb in cup C. The Rb signal measured was generally sub mV level, resulting in a correction of <50 ppm. To avoid overcorrecting the ^{87}Sr intensity non-Rb corrected data was used when the measured ^{85}Rb was negative.

Multiple loads (n=17) of NBS987 of between 5 and 10 ng size gave an average value of 0.710260±79 (2SD; n=17), which compares well with long-term data published in other laboratories (Thirlwall, 1991), with data for similar sized loads and with values measured in the Arctic Resources laboratory for similar sized standards.

Three loads of dissolved BHVO-2 of 6ng size gave an average value of 0.70356 ±7 (2SD; n=3), slightly more radiogenic than the reported average value of 0.70348 ± 7 (GeoREM Database).

4.3.3.3 Pb isotope analysis

Pb was analyzed on a Triton Plus TIMS using a single SEM in peak-hopping mode using the method described in detail in Sarkar et al. (2015b). Yield, dark noise and plateau voltage calibration were measured at the start of the day on a ^{208}Pb signal and the same yield value (usually between 90 and 95%) was achieved throughout the measurement session. After optimizing the signal intensity, data were acquired in dynamic mode via a 4-peak mass scan with the following integration times: ^{208}Pb — 2.097 s, ^{206}Pb — 4.194 s, ^{207}Pb — 4.194 s and ^{204}Pb — 4.194 s. Data was acquired over 3 to 4 temperature increments between 1240 and 1480 °C while one block of 30 mass scans was taken at each temperature stage. Total measurement time, including the filament heating, was ~2.30 h for each analysis.

The average ^{206}Pb/^{204}Pb and ^{207}Pb/^{204}Pb values for NBS981 were 16.950±0.015 and 15.456±0.013 respectively based on 21 analyses which are within uncertainty of the values published for double spike analyses of the reference material by Todt et al. (1996) of ^{206}Pb/^{204}Pb = 16.937 ± 0.0022 and ^{207}Pb/^{204}Pb = 15.492 ± 0.0025.

4.4 Results

4.4.1 Trace Element analysis

4.4.1.1 LA-ICPMS

With the selected LA-ICPMS operating conditions the limits of quantification for 32 elements are summarized in Table 4.1. The trace element results for medians or mean values from spot analyses on polished grains are listed in Table C3. The most abundant trace elements are Cr, Fe, Ti, Ca, Mg, and Ga for all analysed sample suites. Trace elements also consistently above the limits of quantification are V, Zn, Nb, Ni, and Pb for all samples and Si, K, Zr, La, Ce, Pr, Th and U for the sample suites hosted in metasomatised ultramafic rocks. Other elements that are above the limits of quantification include Cu, Sr, Ba, Nd and W for some of the rubies hosted in metasomatised ultramafic rocks. Sn and Zr are above LOQ for rubies from the marble-hosted deposits.

Table 4.1: Limits of Quantification (> LOQ @ 10σ bg) obtained for 32 elements using the following ablation parameters: spot size = 285 μm, repetition rate = 20 Hz, fluence ~ 6.6 J/cm^2.

Element	LOQ [ppb]	Element	LOQ [ppb]	Element	LOQ [ppb]
Mg	437	**Zn**	117	**Pr**	0.6
Si	17509	**Ga**	29	**Nd**	3
K	423	**Rb**	23	**Ho**	0.3
Ca	41994	**Sr**	13	**Yb**	1.4
Ti	292	**Y**	3	**Hf**	2.5
V	19	**Zr**	6.7	**Ta**	1.6
Mn	23	**Nb**	1.6	**W**	2.2
Cr	338	**Sn**	12	**Pb**	8.5
Fe	3554	**Ba**	9	**Th**	0.6
Ni	133	**La**	0.9	**U**	0.3
Cu	93	**Ce**	0.7		

Among the rubies hosted in ultramafic rocks, the Namahaca and Aappaluttoq rubies have very similar trace element characteristics, however, the Aappaluttoq rubies have greater variance and higher median concentrations for several of the analysed elements, including the HFSE Ti, Nb, Th, U and Ce (Fig. 4.5).

The trace element characteristics are consistent with those previously reported for metamorphic deposits in amphibolite and gabbro, i.e. moderate contents of Cr (MOZ ~ 0.1 – 0.8 wt% Cr; GL ~ 0.01–0.3 wt.% Cr) and Fe (MOZ ~ 0.09 – 0.1 wt% Fe; GL ~ 0.07–0.2 wt.% Fe), very low to low amounts of Ti (MOZ ~ 24 – 78 ppm Ti; GL ~ 66–151 ppm Ti) and V (MOZ up to ~8 ppm V; GL up to ~ 35 ppm V), and low Ga (up to ~ 37 ppm Ga for MOZ and GL) (e.g., Giuliani et al., 2014). The Cr/Fe ratios for the Namahaca and Aappaluttoq samples vary between 0.1 and 2. A third of the Aappaluttoq rubies analysed have much higher V concentrations than the the rest (V > 14 ppm (median ~ 23 ppm, n = 6) versus V < 8 ppm (median ~ 6 ppm, n=12) (Table C3, Fig. 4.6), indicating that two different populations may be present in our sample set. The rubies with higher V concentration are also characterised by higher Ga/Mg ratios (Fig. 4.6B).

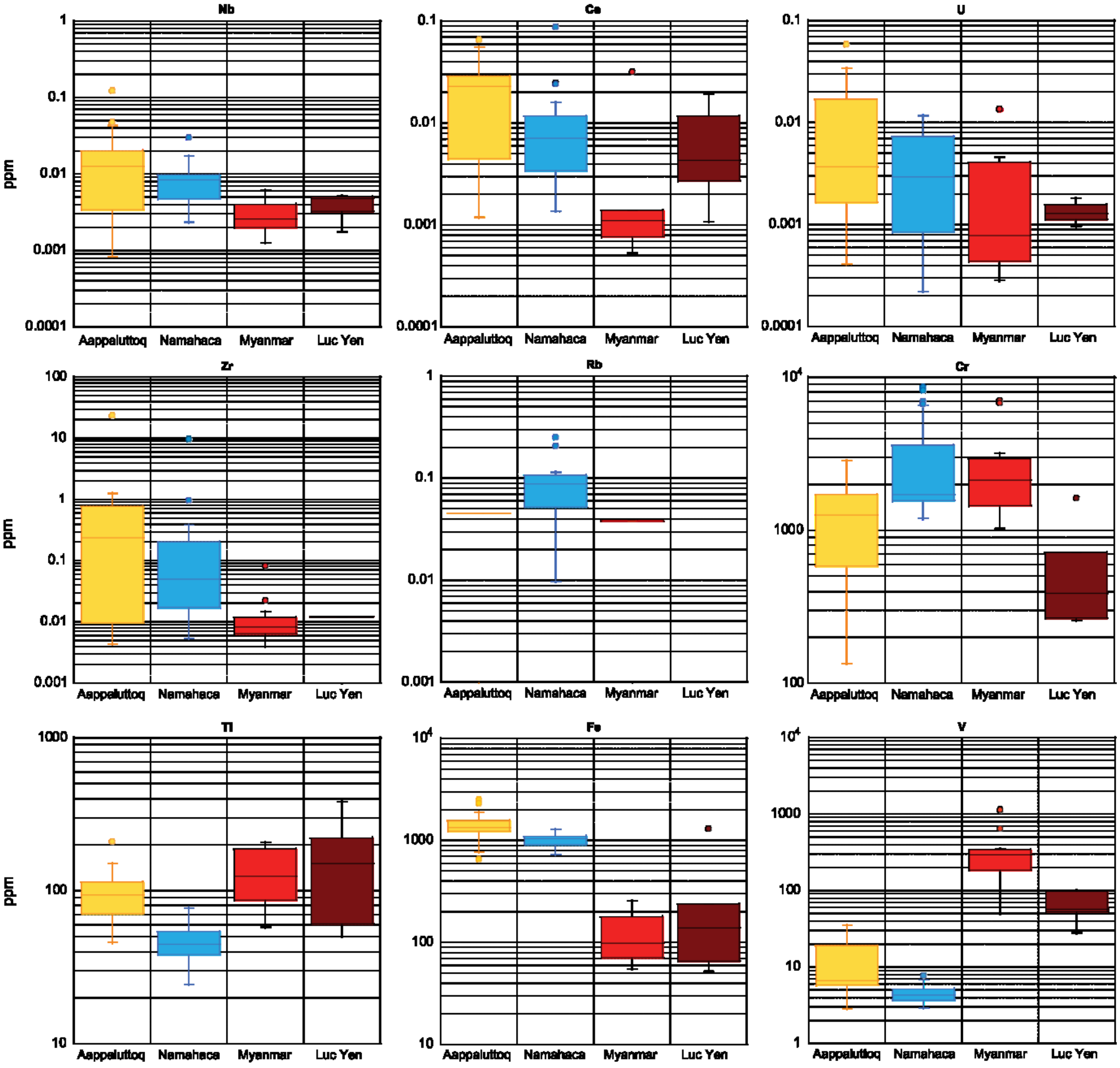

Figure 4.5: Box and whisker plots of selected trace element concentrations in rubies from Aappaluttoq (yellow), Namahaca (blue), Myanmar (red) and Luc Yen (dark red) analysed by "online" LA-ICPMS. Individual data points are outliers whose value is either: greater than UQ + 1.5 * IQD or less than LQ – 1.5 * IQD.

The ruby suites analysed from Myanmar and Luc Yen both display trace element characteristics consistent with those reported for marble-hosted deposits, i.e. moderate contents of Cr (M ~ 0.1 – 0.7 wt% Cr; LY ~ 0.02–0.17 wt.% Cr), low Fe (M ~ 57 – 255 ppm Fe; LY ~ 51–1332 ppm Fe), low to moderate amounts of Ti (M ~ 59 – 224 ppm Ti; LY ~ 50–385 ppm Ti) and elevated V (M ~50 - 123 ppm V; LY ~27 - 98 ppm V), and low Ga (up to ~ 174 ppm Ga for M and LY) (e.g., Muhlmeister et al., 1998).

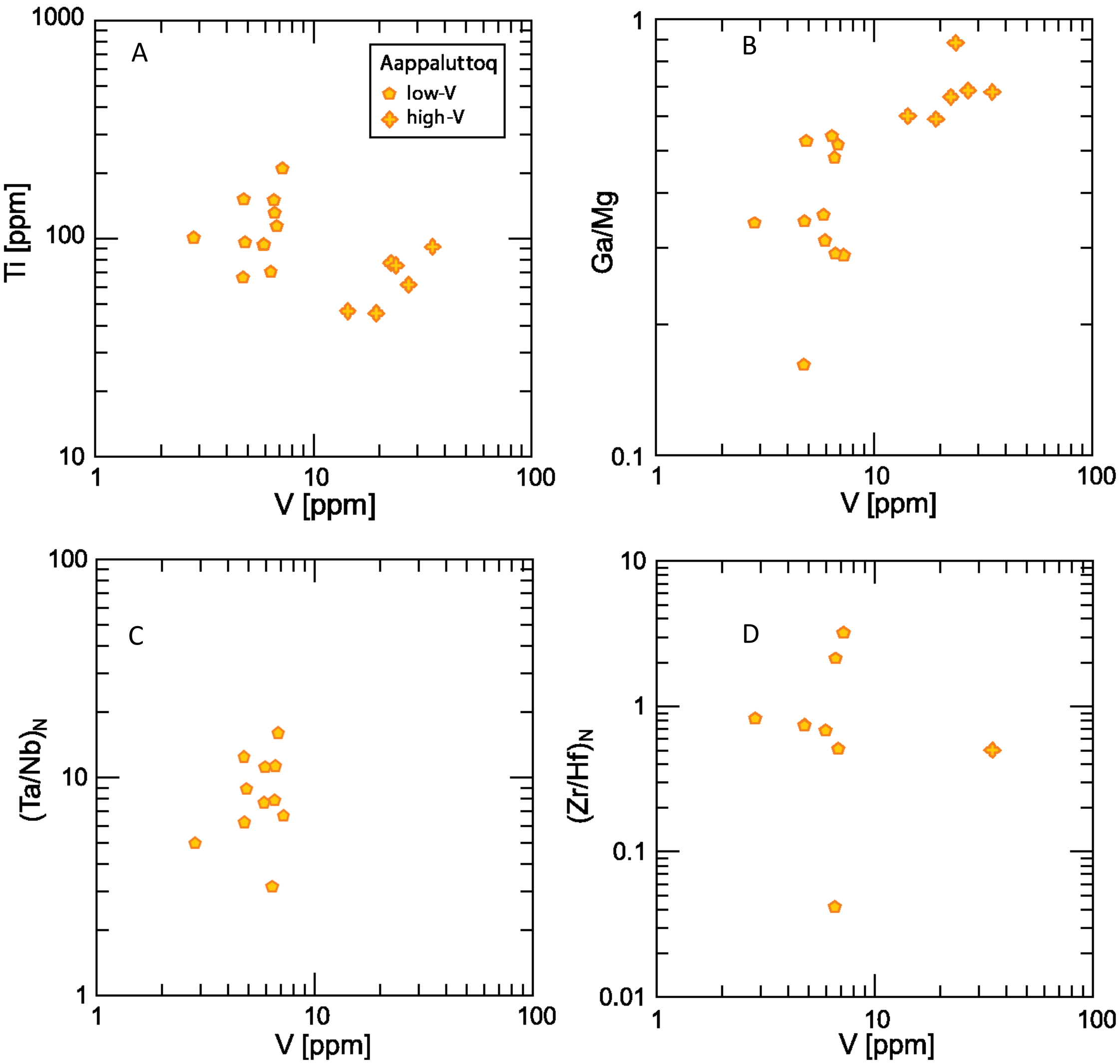

Figure 4.6: Median trace element composition of rubies ablated using the "online" LA-ICPMS method, from Aappaluttoq, Greenland. Aappaluttoq rubies fall into two groups based on their V content – a low-V (pentagon) and a high-V group (cross). (A) Ti versus V showing lower Ti concentrations for the high-V group. (B) Ga/Mg versus V showing higher Ga/Mg ratios for the high-V group. (C) $(Ta/Nb)_N$ versus V showing that for all high-V rubies Ta and/or Nb are below LOQ. (D) $(Zr/Hf)_N$ versus V showing that with one exception Zr and/or Hf are below LOQ. $(Ta/Nb)_N$ and $(Zr/Hf)_N$ are normalized to primitive mantle (McDonough and Sun, 1995).

The Cr/Fe ratio in the rubies from marble-hosted deposits is significantly higher than for the Namahaca and Aappaluttoq samples (Myanmar Cr/Fe ~ 6 – 60; Luc Yen Cr/Fe ~ 3 – 12), with the exception of ruby LYV from Luc Yen, Vietnam that has a Cr/Fe ratio of ~ 0.2.

A clear correlation between the number of quantifiable trace elements and ruby clarity is apparent. The rubies and sapphires of the Myanmar sample suite are the most clear and have the lowest trace element abundances (Fig. 4.1, Table A4.3). The samples from Luc Yen have visible inclusions and/or fractures that correlate with the higher number of trace elements detected. The number of quantifiable trace elements is higher in the Namahaca and Aappaluttoq sample suites, very likely due to their geologic origin, as they have formed in ultramafic rocks that have higher and more variable trace element contents when compared to carbonates. Nevertheless, within these sample suites trace element abundances and the number of quantifiable elements vary corresponding with clarity, i.e. inclusion and fracture density.

When normalized to primitive mantle values (Fig. 4.7) all rubies show trace element patterns that have high levels of inter-element fractionation, with little overall slope, but all are systematically depleted relative to PM. Patterns for median concentrations for both localities show remarkable similarity, with enrichment of HFSE over LREE and Nb, negative Sr and Zr-Hf anomalies and positive Pb and Ti anomalies. Th/U are < 1, Hf/Zr and Ta/Nb are >1.

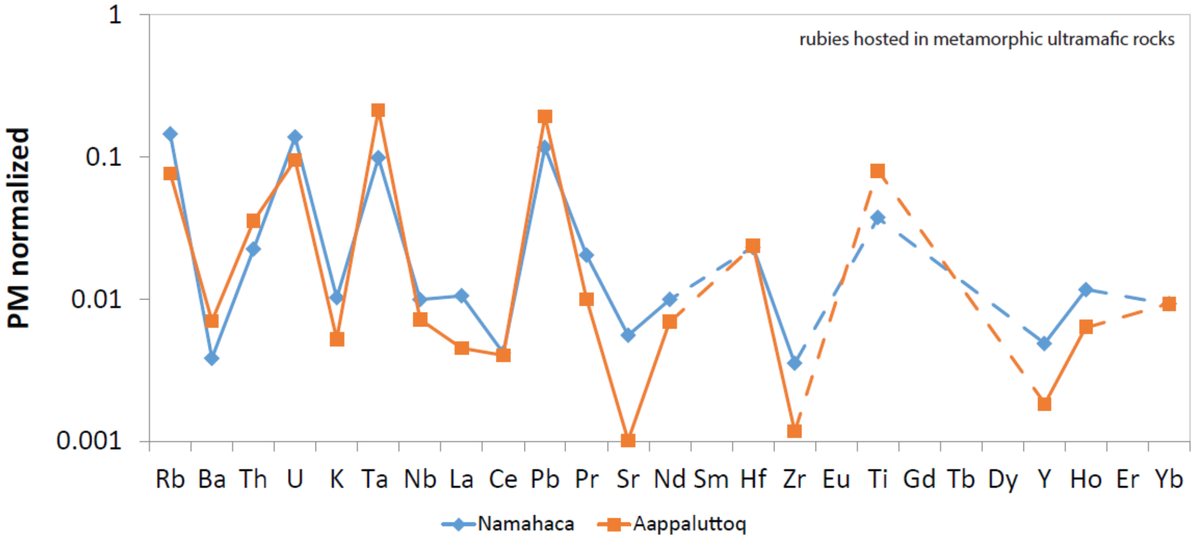

Figure 4.7: Primitive mantle-normalized (McDonough and Sun, 1995) median trace element concentrations in rubies from Aappaluttoq, Greenland and Namahaca, Mozambique analysed by LA-ICPMS in this study.

Most HREE are below the LOQ whereas most LREE are above the LOQ. The trace element characteristics of the low-V and high-V group of the Aappaluttoq suite show many similarities, however, some differences are apparent: The high-V group has lower Ti, Nb-Ta and Zr-Hf than the high-V group (Fig. 4.6A, C, D).

As most trace elements in the marble-hosted suites are below LOQ, to primitive mantle normalized multi-element patterns are incomplete and it is difficult to determine trends (Fig. 4.8). However, all patterns have low levels of trace elements relative to PM, and where present, Th and U are enriched over LREE and Nb. In general Th content is lower than U and more often <LOQ than U, with PM-normalised Th/U < 1. In addition, Hf/Zr and Ta/Nb are consistently >1. Two samples from Luc Yen show negative Sr anomalies. Pb and Ti are present in measureable quantities in almost all samples and multi-element patterns show positive anomalies for both elements.

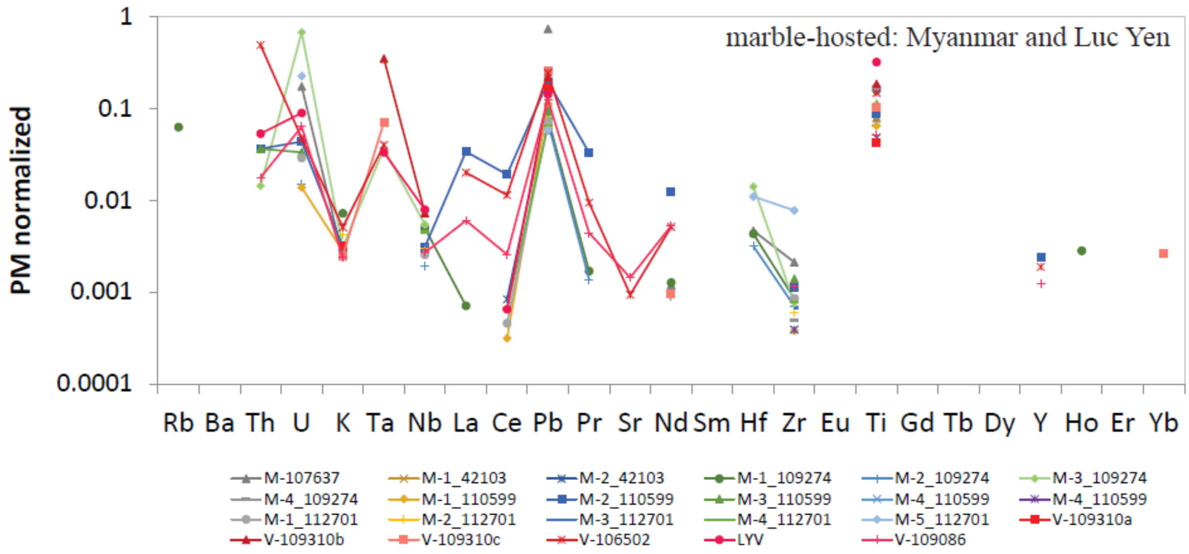

Figure 4.8: Primitive mantle-normalized (McDonough and Sun, 1995) trace element concentrations in rubies from Myanmar and Luc Yen, Vietnam analysed by LA-ICPMS in this study.

4.4.1.2 Laser Ablation and Inductively Coupled Plasma–Time-of-Flight Mass Spectrometry

To gain a clearer insight into the possible variations in spatial location of trace elements in ruby, a few selected samples were analysed, in a reconnaissance study, by TOF-LA-ICPMS. Intensity maps of the elements Na, Mg, Al, K, Ca, Ti, V, Cr, Mn, Fe, Ni, Ga, Rb, Sr, Sn, Ba, La, Pb, Th and U were acquired for all four areas on the analysed rubies gl3_3 and gl3_4. In addition, V was mapped for ruby gl3_4, Cu for gl3_4 and gl3_3-1, Zr for ruby gl3_3, Cs for ruby gl3_3-1 and gl3_4-1, and Ce for ruby gl3_4-1 and gl3_3-2. All intensity maps are shown in Fig. A4.1 while a selection are presented in Fig. 4.9.

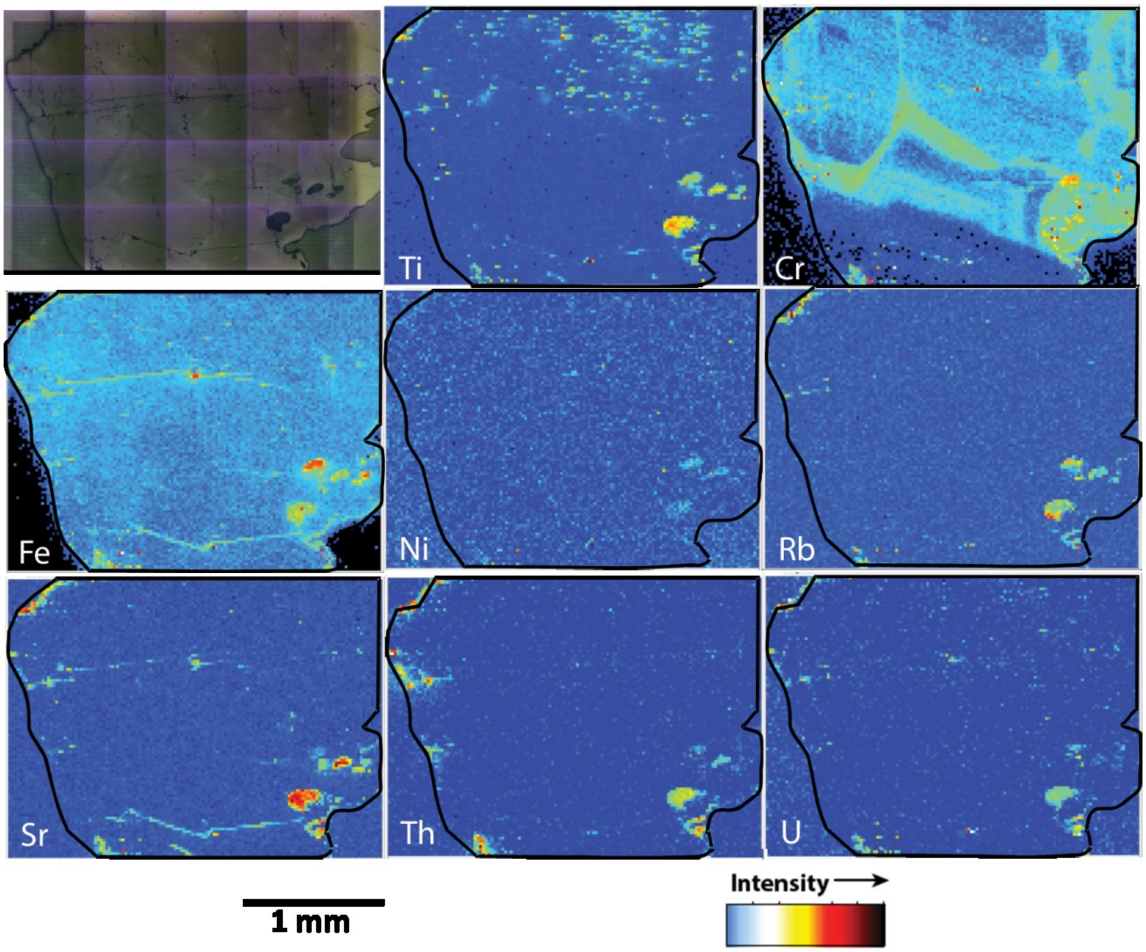

Figure 4.9: Optical image (reflected light) of ruby gl3_3-2 (upper left) and corresponding multi-elemental intensity images for select elements analysed by TOF-LA-ICPMS. The total analysis time was ~12 minutes. The signal intensity increases from blue over yellow and red to black. The black line encircles the ruby grain.

The most abundant elements - Cr and Fe (aside from Al) - show clearly zoned distribution patterns in the rubies (Fig. 4.9). While a zoned distribution is evident for Cr, there are local "hot-spots" of concentration that indicate the concentration of these elements within inclusions. These "hot-spots" are also enriched in other elements that show much more localized distributions such as Ti, Ni, Rb, Sr, Th, and U. These elements show very low intensities in the rubies themselves, with many close to instrumental detection limits, which are relatively high because of the very short integration times used for mapping. The intensity images are qualitative, showing relative differences in signal intensity for a chosen element. Thus the concentrations of the different elements cannot be compared relative to each other, making identification of the inclusions and quantification of the elemental concentrations impossible. However, as can be seen in Fig. 4.9 and Fig. A4.1, while the signal intensity of elements such as Rb, Sr, Zr, Th, U, Pb and LREE vary somewhat between the intensity "hot spots" they are generally high. Selected elements were then imaged on a more quantitative basis, principally Ti, Cr, Fe and Ga. Where this was performed, the concentrations were in good agreement with the LA-ICPMS results (Fig. 4.1, Fig. 4.10).

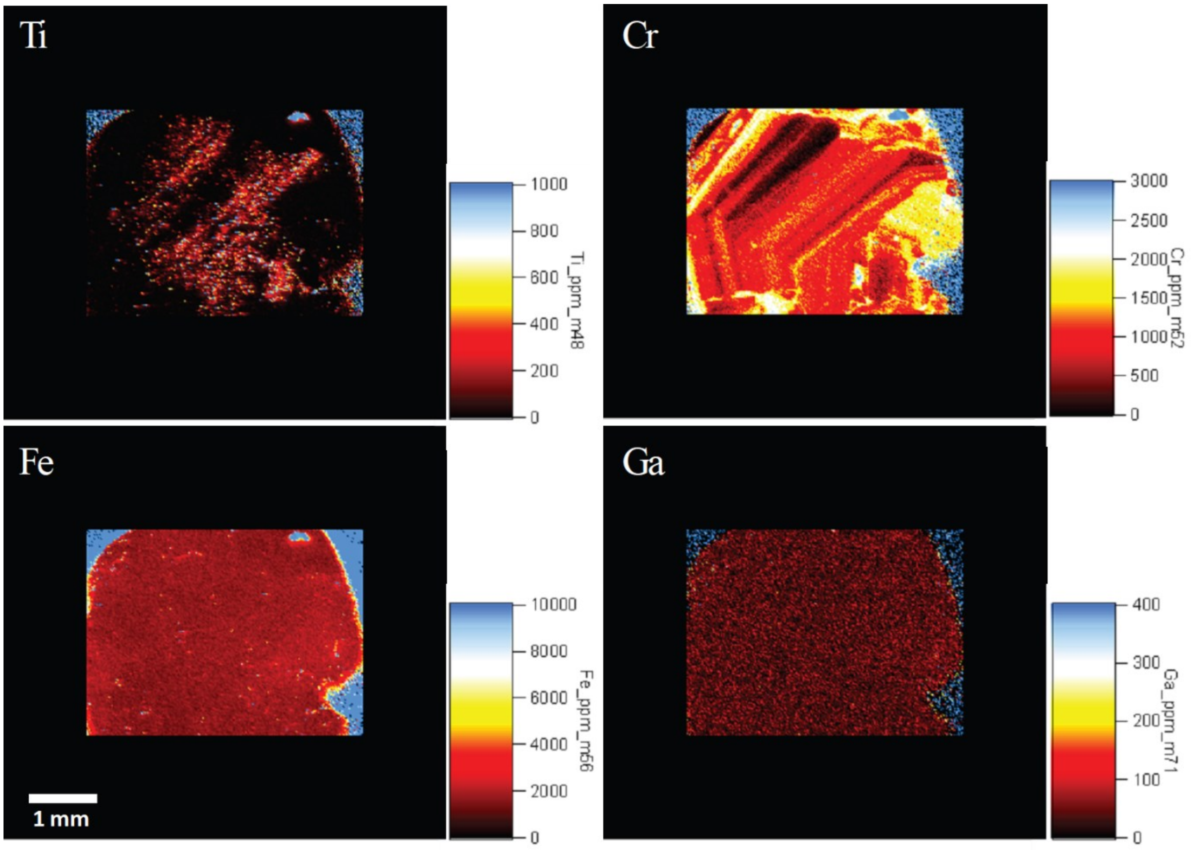

Figure 4.10: Quantitative images of Ti, Cr, Fe and Ga in ruby gl3_3-1 measured by TOF-LA-ICPMS. The total analysis time was ~26 minutes. Concentrations (ppm) increase from black over red, yellow and white to blue.

The systematic zoning in Cr can be seen much more clearly in the concentration map (Fig. 4.10). In the case of the Aappaluttoq rubies, the zonation shown in Cr concentration is matched by that visible to the eye, as expected because Cr is the chromophore element in ruby. The Ti intensity seems to correlate antithetically with the zonation in Cr, with higher Ti in "low-Cr zones", seen most clearly in quantitative images of Cr and Ti acquired for gl3_3-1 (Fig. 4.10). This is not a universal characteristic in ruby but has been observed previously (e.g., Harlow and Bender, 2013) and is thought to be due to variations in the abundances of these elements in the metasomatic fluid during ruby crystallisation. In addition, the higher Ti in "low-Cr zones" is matched by higher U (Fig. 4.9).

4.4.1.3 Solution ICPMS

For 26 rubies a fraction of the "offline" ablated material was analysed for trace elements using solution ICPMS. This comprised 10 samples from Aappaluttoq (six low-V and 4 high-V samples), nine from Namahaca and seven from Myanmar. For five Aappaluttoq and two Namahaca rubies, multiple "offline" ablations were performed to examine homogeneity and to look for isotopic variations within single crystals. The elemental abundances of all analysed samples for REE along with Nb, Th, and U range from 100s of ppt to 100s of ppb. Large ion lithophile elements (LILE) such as Cs, Rb and Ba range from 10s of ppb up to 100s of ppm in some cases. Transition metals such as Cr, Mn and Fe range from 100s of ppb up to 1000s of ppm (Table 4.2, Fig. 4.11). Ti, V and Ga could not be reliably determined using solution ICPMS due to spectral interferences. The Cr and Fe concentrations, however, are consistent with LA-ICPMS data, with Cr ranging from ~ 0.02 – 0.3 wt% and Fe from ~ 0.08–0.7 wt% for Aappaluttoq and Cr ranging from ~ 0.08 – 0.7 wt% and Fe from ~ 0.03–0.3 wt% for Namahaca. For the rubies from Myanmar Cr and Fe concentrations range from ~ 0.07 – 0.4 wt% and from ~ 36 ppm – 970 ppm, respectively. The Cr/Fe ratios for the Namahaca and Aappaluttoq samples vary between ~ 0.05 – 8.8, with the Namahaca samples falling towards the higher end of the range. Consistent with the results of the LA-ICPMS data the marble-hosted Myanmar rubies have higher Cr/Fe ratios ranging from ~ 1.3 – 52.

Table 4.2: Trace element abundances (ppm) determined using offline LA followed by solution ICPMS for Aappaluttoq, Namahaca and Myanmar rubies. Quantification is achieved via normalization to the weight loss of the ruby crystals during ablation. Limits of quantification in ppt are provided also, based on a large representative blank set (n = 36).

Provenance			**Namahaca, Mozambique**											**Aappaluttoq, Greenland**			
Sample	**mass analysed**	**R**	**moz1_1**	**moz1_2**	**moz1_4**	**moz1_4-2**	**moz1_7**	**moz2_1**	**moz2_2**	**moz2_2-2**	**moz2_3**	**moz2_6-2**	**moz2_8-2**	**gl1_1**	**gl1_3**	**gl1_4-2**	***gl1_6***
Rb	**85**	**LR**	1.27	< LOQ	0.069	< LOQ	< LOQ	2.8	0.62	0.26	0.34	0.62	10	1.20	0.43	0.16	1.97
Sr	**88**	**LR**	< LOQ	0.64	< LOQ	< LOQ	< LOQ	38	4.3	11	1.31	4.4	12	66	< LOQ	1.30	0.99
Y	**89**	**LR**	< LOQ	0.0063	0.30	0.17	< LOQ	0.052	0.048	0.045	0.022	0.045	0.028	0.0078	< LOQ	0.016	0.88
Nb	**93**	**LR**	0.18	0.014	0.031	0.077	0.024	0.40	0.17	0.045	0.099	0.099	0.12	0.024	0.012	0.020	0.12
Mo	**98**	**LR**	< LOQ	< LOQ	n/a	< LOQ	< LOQ	< LOQ	< LOQ	< LOQ	0.53	< LOQ	< LOQ	< LOQ	n/a	< LOQ	n/a
Cs	**133**	**LR**	0.022	0.026	0.0032	< LOQ	< LOQ	0.016	0.021	0.019	0.0059	0.042	0.090	0.023	0.0097	0.014	1.25
Ba	**138**	**LR**	< LOQ	0.22	0.37	0.38	0.28	112	5.4	0.97	6.2	2.8	340	17	3.3	1.01	20
La	**139**	**LR**	< LOQ	0.057	0.17	0.12	0.013	0.77	0.40	0.19	0.22	0.35	0.042	0.090	0.071	0.091	3.7
Ce	**140**	**LR**	< LOQ	0.090	< LOQ	< LOQ	< LOQ	1.50	1.30	0.37	0.46	0.92	< LOQ	0.45	1.33	0.62	10
Pr	**141**	**LR**	< LOQ	0.0061	0.065	0.042	< LOQ	0.16	0.11	0.053	0.050	0.12	0.012	0.015	0.010	0.034	1.21
Nd	**143**	**LR**	< LOQ	0.021	0.30	0.17	< LOQ	0.58	0.48	0.25	0.18	0.46	0.049	0.041	< LOQ	0.13	4.9
Sm	**147**	**LR**	< LOQ	0.0029	0.074	0.038	< LOQ	0.095	0.090	0.051	0.028	0.087	0.0097	0.0047	< LOQ	0.020	1.03
Eu	**151**	**LR**	< LOQ	0.0075	0.021	0.012	< LOQ	0.14	0.12	0.091	0.022	0.16	0.0058	0.012	0.0005	0.0078	0.49
Gd	**157**	**LR**	< LOQ	0.0029	0.059	0.038	< LOQ	0.052	0.054	0.033	0.017	0.045	0.0082	0.0038	< LOQ	0.012	0.78
Tb	**159**	**LR**	< LOQ	< LOQ	0.0029	0.0063	< LOQ	0.0067	0.0071	0.0041	0.0017	0.0058	0.00075	0.00051	< LOQ	0.00092	0.083
Dy	**163**	**LR**	< LOQ	0.0018	0.069	0.035	< LOQ	0.024	0.032	0.018	0.0067	0.027	0.0069	0.0017	< LOQ	0.0057	0.33
Ho	**165**	**LR**	< LOQ	0.00039	0.014	0.0073	< LOQ	0.0030	0.0040	0.0027	0.0011	0.0035	0.0012	0.00054	< LOQ	0.00092	0.041
Er	**167**	**LR**	< LOQ	< LOQ	0.047	0.023	< LOQ	0.0091	0.010	0.0060	0.0028	0.0092	0.0044	0.001	< LOQ	0.0022	0.077
Yb	**173**	**LR**	< LOQ	< LOQ	0.049	0.023	< LOQ	< LOQ	0.0066	0.0037	< LOQ	0.0048	0.0058	0.0020	< LOQ	0.0018	0.039
Lu	**175**	**LR**	< LOQ	< LOQ	0.0078	0.0034	< LOQ	< LOQ	< LOQ	< LOQ	< LOQ	< LOQ	0.0009	0.00058	< LOQ	< LOQ	0.0056
Hf	**178**	**LR**	< LOQ	< LOQ	< LOQ	1.43	0.040	< LOQ	0.17	< LOQ	< LOQ	< LOQ	0.053	0.048	< LOQ	< LOQ	0.046
Pb	**208**	**LR**	< LOQ	< LOQ	< LOQ	0.85	< LOQ	< LOQ	0.87	0.13	0.59	< LOQ	< LOQ	0.54	0.51	1.65	1.10
Th	**232**	**LR**	< LOQ	0.011	0.18	0.12	< LOQ	0.41	0.064	0.036	0.038	0.078	0.016	0.11	< LOQ	0.020	1.80
U	**238**	**LR**	0.12	0.0023	< LOQ	< LOQ	0.0064	0.019	0.020	0.0058	0.0074	0.0095	0.0057	0.055	< LOQ	0.033	0.57

Cr	**52**	**MR**	7307	1272	n/a	7415	21114	1626	4506	2953	783	1254	6115	484	n/a	1232	n/a
Mn	**55**	**MR**	< LOQ	7.3	n/a	30	5.0	11	< LOQ	2.5	7.5	4.2	3.0	6.7	n/a	5.4	n/a
Fe	**56**	**MR**	< LOQ	1031	n/a	3331	2399	< LOQ	< LOQ	692	292	1058	3482	1018	n/a	789	n/a
Co	**59**	**MR**	< LOQ	0.23	n/a	0.98	9.3	2.3	< LOQ	0.32	1.23	0.71	3.7	< LOQ	n/a	0.25	n/a
Ni	**60**	**MR**	< LOQ	< LOQ	< LOQ	< LOQ	< LOQ	< LOQ	< LOQ	5.7	< LOQ	9.7	275	5.7	< LOQ	12	68
Cu	**63**	**MR**	5.6	0.62	n/a	5.9	264	14	< LOQ	1.91	27	3.5	143	< LOQ	n/a	1.01	n/a
Zn	**64**	**MR**	< LOQ	< LOQ	n/a	16	16	< LOQ	< LOQ	< LOQ	< LOQ	< LOQ	24	2.5	n/a	< LOQ	n/a
Zr	**90**	**MR**	< LOQ	< LOQ	< LOQ	64	1.72	< LOQ	7.8	< LOQ	0.83	< LOQ	1.23	1.14	< LOQ	< LOQ	2.4

Provenance			**Aappaluttoq, Greenland**												**Kachin State, Namya**			
Sample	**mass analysed**	**R**	***gl1_6-2***	***gl1_7-2***	***gl1_7-3***	**gl2_2**	***gl2_3***	**gl2_5**	**gl2_5-2**	**gl2_5-3**	***gl2-6***	***gl2_6-2***	**gl2_7**	**gl2_7-3**	**M-1-109274**	**M-2-109274**	**M-3-109274**	**M-4-109274**
Rb	**85**	**LR**	0.12	0.29	0.13	0.71	8.6	6.6	9.7	9.0	2.5	1.38	3.7	3.6	0.022	0.034	< LOQ	1.04
Sr	**88**	**LR**	< LOQ	0.76	1.67	12	6.1	7.2	42	8.8	8.0	5.4	121	87	< LOQ	< LOQ	< LOQ	0.26
Y	**89**	**LR**	< LOQ	0.10	4.2	< LOQ	1.82	0.24	0.58	0.16	3.2	0.48	0.59	0.17	0.0061	< LOQ	< LOQ	0.17
Nb	**93**	**LR**	< LOQ	0.026	0.15	0.25	0.70	0.10	1.04	0.24	< LOQ	< LOQ	0.012	0.040	0.044	0.011	0.016	2.8
Mo	**98**	**LR**	< LOQ	< LOQ	n/a	1.84	2.0	< LOQ	9.1	0.15	< LOQ	< LOQ	0.99	0.17	< LOQ	< LOQ	< LOQ	< LOQ
Cs	**133**	**LR**	0.042	0.024	0.039	0.044	0.88	0.14	0.20	0.21	0.72	0.72	0.097	0.069	< LOQ	< LOQ	< LOQ	0.049
Ba	**138**	**LR**	1.33	2.3	0.76	20	19	26	65	33	12	2.7	27	37	0.42	0.23	0.097	2.3
La	**139**	**LR**	0.088	0.31	0.57	0.061	0.066	0.053	0.29	0.085	4.3	0.18	1.03	0.47	< LOQ	< LOQ	< LOQ	0.15
Ce	**140**	**LR**	< LOQ	6.3	2.4	0.13	0.38	0.18	0.97	0.33	4.6	0.46	1.14	0.66	0.037	0.022	< LOQ	1.23
Pr	**141**	**LR**	0.030	0.052	0.35	0.0040	0.065	0.030	0.14	0.048	0.42	0.032	0.068	0.052	0.0021	0.0012	< LOQ	0.047
Nd	**143**	**LR**	0.12	0.028	1.93	0.0089	0.43	0.16	0.75	0.24	1.74	0.14	0.20	0.19	0.0065	0.0047	< LOQ	0.17
Sm	**147**	**LR**	0.023	0.011	0.79	< LOQ	0.22	0.047	0.20	0.056	0.50	0.051	0.030	0.038	0.0016	0.0007	< LOQ	0.046
Eu	**151**	**LR**	0.0091	0.010	0.85	0.0037	0.12	0.012	0.046	0.014	0.33	0.086	0.066	0.045	< LOQ	< LOQ	< LOQ	0.012
Gd	**157**	**LR**	0.016	0.019	0.94	< LOQ	0.30	0.058	0.22	0.057	0.69	0.069	0.030	0.041	0.0020	< LOQ	< LOQ	0.039
Tb	**159**	**LR**	0.0017	0.0033	0.16	< LOQ	0.052	0.0083	0.023	0.0068	0.11	0.012	0.0054	0.0060	0.0004	< LOQ	< LOQ	0.0093
Dy	**163**	**LR**	< LOQ	0.023	0.98	< LOQ	0.33	0.045	0.14	0.035	0.61	0.083	0.051	0.035	0.0016	0.0045	< LOQ	0.074
Ho	**165**	**LR**	< LOQ	0.0038	0.18	< LOQ	0.072	0.0094	0.023	0.0063	0.11	0.019	0.017	0.0069	0.0002	< LOQ	< LOQ	0.014
Er	**167**	**LR**	< LOQ	0.0096	0.49	< LOQ	0.23	0.024	0.058	0.016	0.27	0.065	0.088	0.019	< LOQ	< LOQ	< LOQ	0.044

Yb	**173**	**LR**	< LOQ	0.0052	0.39	< LOQ	0.19	0.020	0.048	0.012	0.21	0.10	0.22	0.026	0.0015	< LOQ	< LOQ	0.079
Lu	**175**	**LR**	< LOQ	0.0010	0.056	< LOQ	0.036	0.0028	0.010	0.0030	0.028	0.018	0.059	0.0048	< LOQ	< LOQ	< LOQ	0.0049
Hf	**178**	**LR**	< LOQ	< LOQ	0.050	< LOQ	2.7	0.038	0.17	0.039	< LOQ	0.98	15	0.15	0.027	0.034	0.017	1.92
Pb	**208**	**LR**	< LOQ	0.067	0.24	0.19	0.65	0.38	1.4	0.50	0.41	0.70	2.9	1.42	0.080	< LOQ	< LOQ	4.6
Th	**232**	**LR**	0.25	0.017	0.052	0.053	0.27	< LOQ	0.024	0.0059	0.24	0.067	1.62	0.23	< LOQ	< LOQ	< LOQ	1.78
U	**238**	**LR**	0.018	0.0060	0.038	0.012	0.11	0.015	0.093	0.017	0.11	0.40	18	0.17	< LOQ	< LOQ	< LOQ	16
Cr	**52**	**MR**	194	566	n/a	3380	415	< LOQ	1722	233	1080	1462	309	1805	3885	1260	1889	2080
Mn	**55**	**MR**	< LOQ	3.3	n/a	56	104	15	50	12	153	23	17	30	0.35	0.18	< LOQ	3.7
Fe	**56**	**MR**	n/a	803	n/a	3723	7011	< LOQ	3804	880	n/a	5123	2062	1288	115	46	36	971
Co	**59**	**MR**	0.29	0.29	n/a	1.86	3.4	0.18	5.7	0.29	1.50	2.1	7.3	0.32	0.15	0.027	< LOQ	0.67
Ni	**60**	**MR**	< LOQ	12	29	< LOQ	75	< LOQ	< LOQ	9.8	23	< LOQ	< LOQ	8.7	1.51	1.17	< LOQ	16
Cu	**63**	**MR**	n/a	1.02	n/a	5.2	< LOQ	0.73	16	< LOQ	n/a	< LOQ	< LOQ	< LOQ	1.13	0.63	0.65	6.8
Zn	**64**	**MR**	n/a	< LOQ	n/a	21	24	< LOQ	32	1.99	n/a	< LOQ	8.1	2.9	439	< LOQ	< LOQ	40
Zr	**90**	**MR**	< LOQ	< LOQ	1.13	< LOQ	123	1.00	4.4	0.63	< LOQ	32	485	5.0	0.66	0.83	< LOQ	47

Provenance			**Mandalay Region, Mogok**		**Mandalay Region, Sagyin**	
Sample	**mass analysed**	**R**	**M-1-42103**	**M-2-42103**	**M-112701-1**	**LOQ (7*σ)**
Rb	**85**	**LR**	< LOQ	0.032	2.9	3.4
Sr	**88**	**LR**	< LOQ	0.20	31	67
Y	**89**	**LR**	< LOQ	< LOQ	0.055	2.5
Nb	**93**	**LR**	0.140	0.0077	0.096	3.6
Mo	**98**	**LR**	< LOQ	< LOQ	< LOQ	134
Cs	**133**	**LR**	< LOQ	< LOQ	0.14	0.28
Ba	**138**	**LR**	4.0	0.19	7.9	64
La	**139**	**LR**	< LOQ	< LOQ	0.057	2.9
Ce	**140**	**LR**	< LOQ	0.015	0.14	19
Pr	**141**	**LR**	< LOQ	0.0010	0.017	0.77
Nd	**143**	**LR**	< LOQ	0.0046	0.054	2.8
Sm	**147**	**LR**	< LOQ	0.00056	0.013	0.49

Eu	**151**	**LR**	< LOQ	< LOQ	0.0023	0.11
Gd	**157**	**LR**	< LOQ	0.001	0.012	0.64
Tb	**159**	**LR**	< LOQ	< LOQ	0.0018	0.083
Dy	**163**	**LR**	< LOQ	0.00092	0.013	0.54
Ho	**165**	**LR**	< LOQ	0.00020	0.0021	0.087
Er	**167**	**LR**	< LOQ	< LOQ	< LOQ	0.30
Yb	**173**	**LR**	< LOQ	0.00052	0.0092	0.40
Lu	**175**	**LR**	< LOQ	< LOQ	< LOQ	0.20
Hf	**178**	**LR**	0.48	0.019	0.11	8.3
Pb	**208**	**LR**	< LOQ	0.34	< LOQ	15
Th	**232**	**LR**	< LOQ	< LOQ	0.55	1.87
U	**238**	**LR**	< LOQ	< LOQ	< LOQ	0.63
Cr	**52**	**MR**	730	683	1223	7861
Mn	**55**	**MR**	< LOQ	0.27	2.3	347
Fe	**56**	**MR**	< LOQ	64	124	104014
Co	**59**	**MR**	< LOQ	0.043	< LOQ	14
Ni	**60**	**MR**	< LOQ	1.58	< LOQ	1619
Cu	**63**	**MR**	< LOQ	0.93	1.26	195
Zn	**64**	**MR**	< LOQ	27	5.3	2165
Zr	**90**	**MR**	< LOQ	0.25	1.99	313

Notes: <LOQ: value below blank value
n/a: no value analyzed
kursiv gl = high-V group samples
R = mass resolution mode
LR = low mass resolution mode
MR = medium mass resolution mode

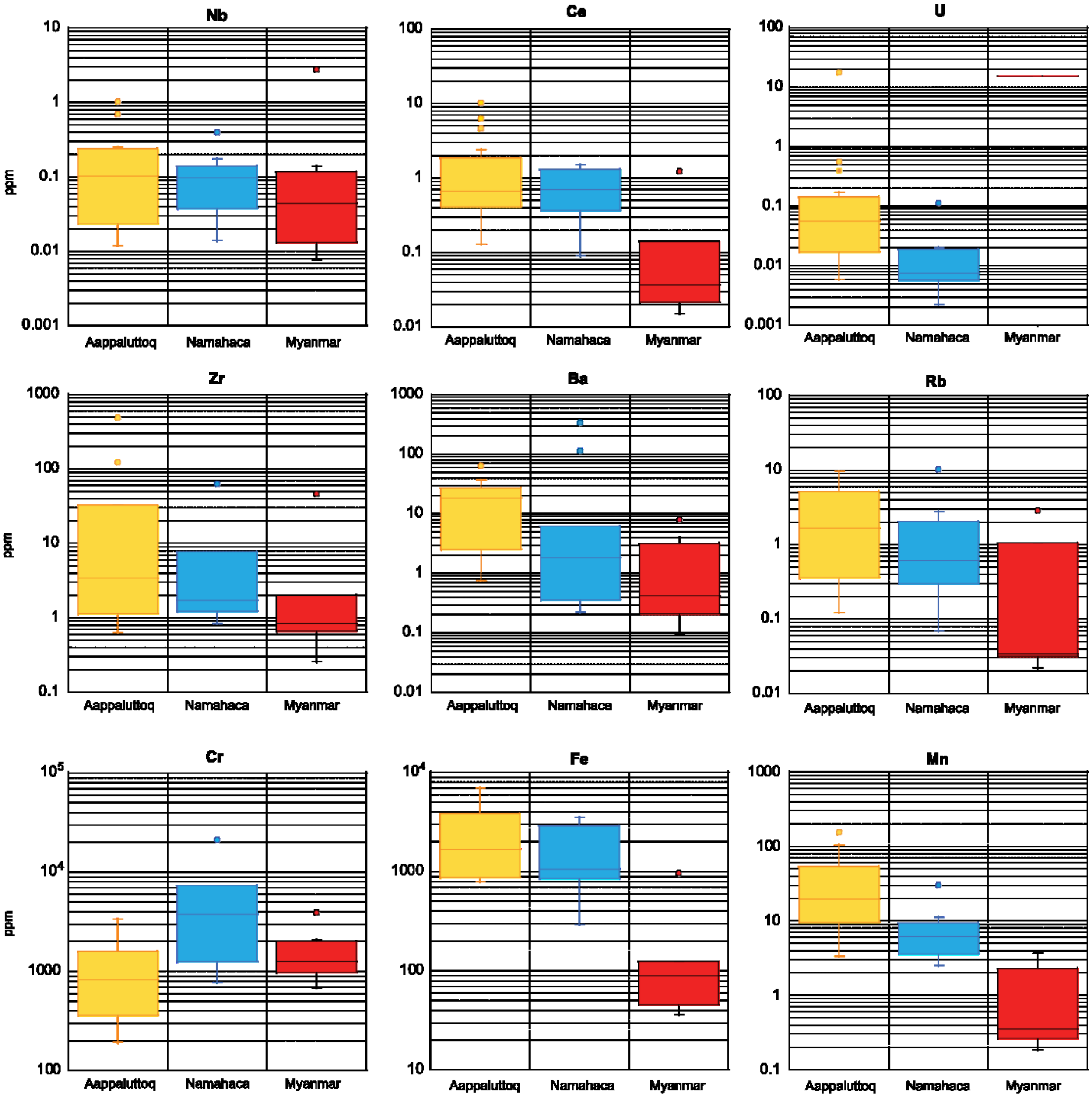

Figure 4.11: Box and whisker plots of selected trace element concentrations in rubies from Aappaluttoq (yellow), Namahaca (blue) and Myanmar (red) analysed by "offline" ablation plus solution ICPMS. Individual data points are outliers whose value is either: greater than UQ + 1.5 * IQD or less than LQ – 1.5 * IQD.

When normalized to primitive mantle values most Aappaluttoq samples show enrichment of LILE and HFSE over LREE and Nb, a positive Pb anomaly and LREE enrichment relative to HREE (Ce/Yb$_N$ ~ 1.3 – 319), with the exception of sample gl2_3 (Ce/Yb$_N$ ~ 0.5).

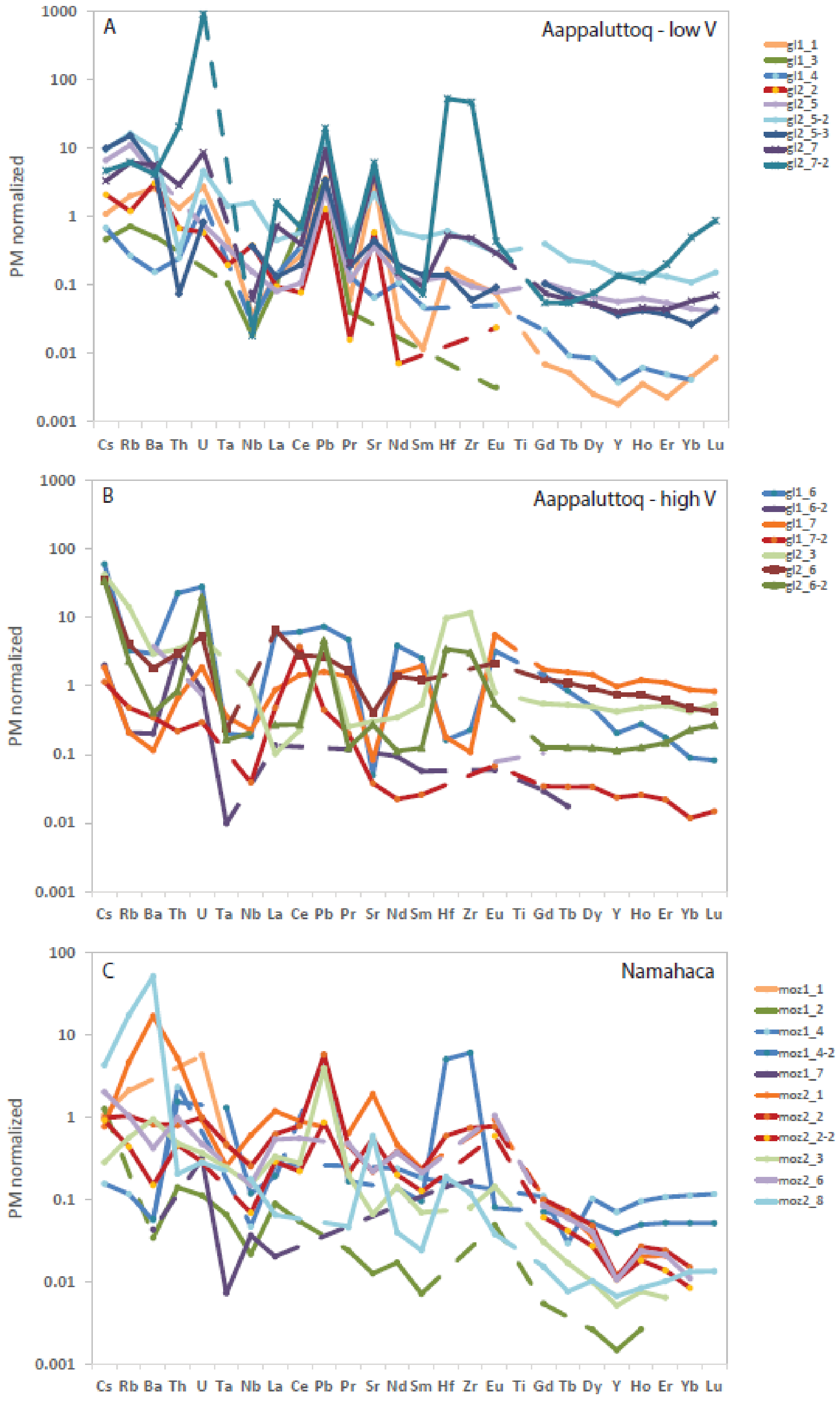

Figure 4.12: A. Primitive mantle-normalized (McDonough and Sun, 1995) trace element concentrations in low-V rubies from Aappaluttoq, Greenland analysed by offline ablation followed by solution ICPMS in this study. B. Primitive mantle-normalized (McDonough and Sun, 1995) trace element concentrations in high-V rubies from

Aappaluttoq, Greenland analysed by offline ablation followed by solution ICPMS in this study. C. Primitive mantle-normalized (McDonough and Sun, 1995) trace element concentrations in rubies from Namahaca, Mozambique analysed by offline ablation followed by solution ICPMS in this study. All data plotted is > LOQ.

Sr anomalies are mostly positive, however, and both Zr and Hf are enriched in several of the analyses, but with variable Zr/Hf ratios that range from <1 to >1. Th/U ratios are mostly < 1 (Fig. 4.12A,B). Several samples show positive Eu and/or Ce anomalies (Fig. 4.13H). Some of the analyses show extreme enrichment in Cs.

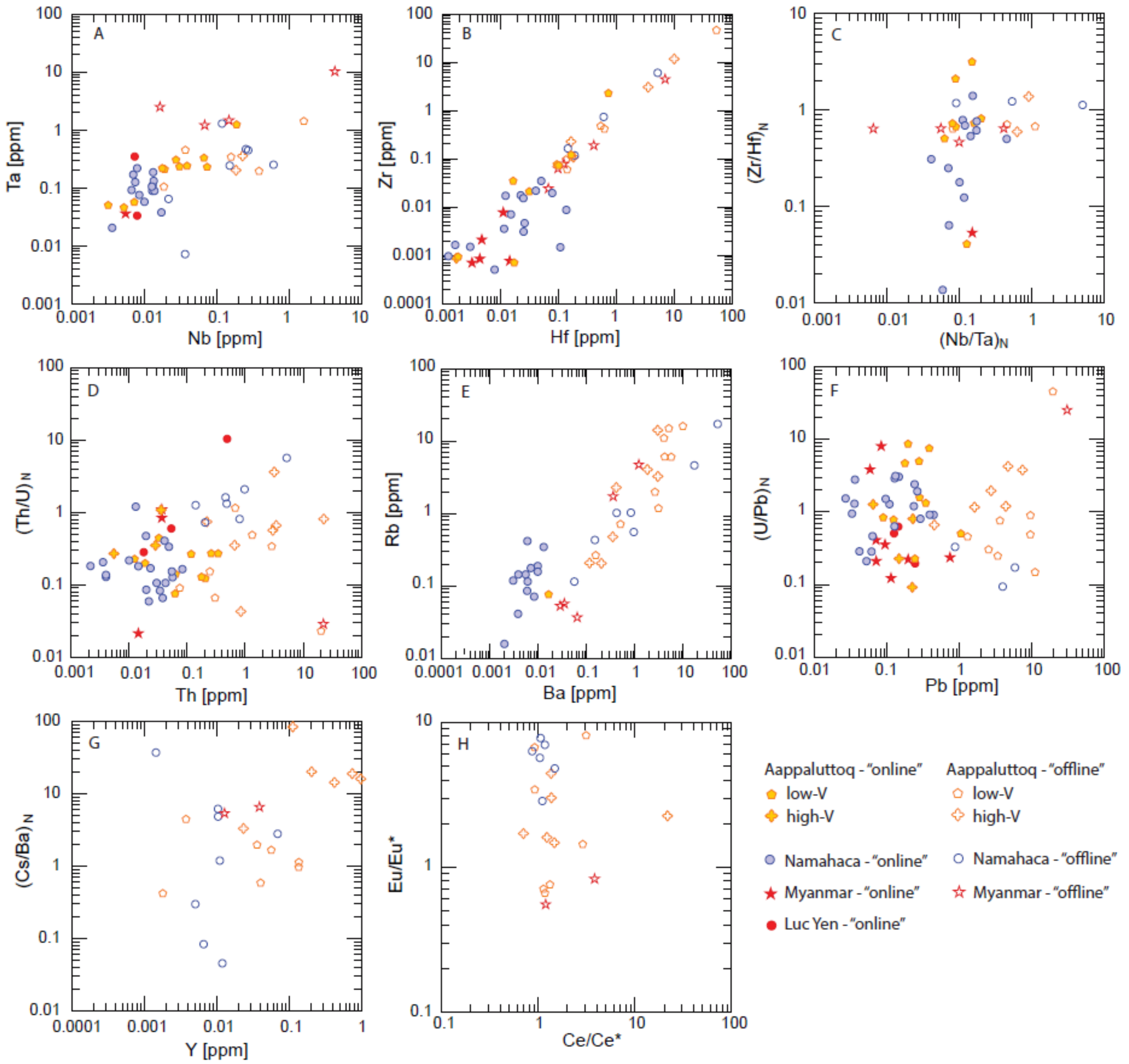

Figure 4.13: Primitive mantle-normalized (McDonough and Sun, 1995) trace element composition in "offline" (open symbols) and "online" ablated rubies (closed symbols) from Aappaluttoq, Namahaca, Myanmar and Luc Yen. Points represent individual analyses for "offline" ablated samples and median compositions for "online"

ablated samples. Aappaluttoq (yellow) and Namahaca (blue) are hosted in metasomatised metamorphic ultramafic rocks, Myanmar (red) and Luc Yen (red) are hosted in marble. (A) Ta versus Nb (B) Zr versus Hf (C) $(Zr/Hf)_N$ versus $(Nb/Ta)_N$ (D) $(Th/U)_N$ versus Th (E) Rb versus Ba (F) $(U/Pb)_N$ versus Pb (G) $(Cs/Ba)_N$ versus Y (H) Eu/Eu* versus Ce/Ce*. Anomalies calculated using $Eu/Eu^* = 2^*Eu_{CN}/(Sm+Gd)_{CN}$ and $Ce/Ce^* = Ce_{CN}/((La_{CN})^{0.667}{}^*(Nd_{CN})^{0.333})$ where CN represents normalization of Ce, La, Nd, Eu, Sm and Gd to average chondrites using the data of McDonough and Sun (1995).

The low-V and high-V group rubies at Aappaluttoq show some slight differences, including higher Cs, Y and HREE and slightly lower Sr for the high-V group rubies (Fig. 4.13G) as well as U/Pb ratios > 1 for the high-V group and < 1 for the low-V group (Fig. 4.13F).

The Namahaca rubies show mostly similar patterns, with some exceptions: whereas only a few Aappaluttoq samples display negative Y anomalies, they are present in all Namahaca rubies and several Namahaca samples have negative instead of positive Pb anomalies. In addition, Th/U ratios of the Namahaca samples are mostly > 1 (Fig. 4.12B).

No samples from Luc Yen were analysed using “offline” ablation followed by solution ICPMS. For all analysed rubies from Myanmar primitive mantle normalized trace element patterns of solution ICPMS data are very similar and are characterized by positive Pb and Zr-Hf anomalies (Fig. 4.14). Sr is mostly below the LOQ and where present displays either a positive or negative anomaly. HFSE are generally enriched over LREE and Nb. LREE are enriched over HREE ($Ce/Yb_N \sim 4 - 8$), but the slopes are flatter when compared to both the Aappaluttoq and Namahaca suites. Hf/Zr and Ta/Nb ratios are >1.

More than one “offline” ablation was performed on several rubies to investigate the reproducibility of data. In most instances when this was performed, the trace element patterns of the different offline ablations of the same ruby are similar while the concentrations varied (Fig. 4.15); however, in some cases the trace element patterns of the replicates are quite different. In the case of ruby gl2_6, for instance, one ablation is characterized by positive Sr and Zr-Hf anomalies and U-shaped REEs, while a second ablation on the same sample yields a trace element pattern characterized by enrichment of LREE relative to HREE, Zr and Hf below the LOQ and a negative Sr anomaly.

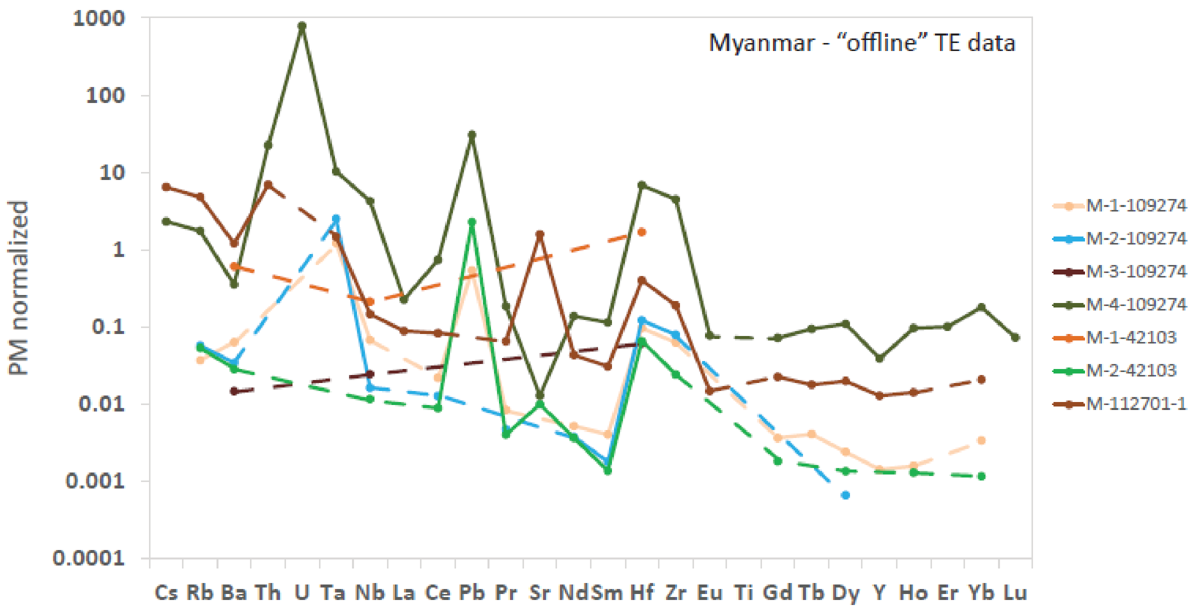

Figure 4.14: Primitive mantle-normalized (McDonough and Sun, 1995) trace element concentrations in rubies from Myanmar analysed by offline ablation followed by solution ICPMS in this study.

4.4.1.4 LA-ICPMS versus solution ICPMS

Results of trace element determinations of the elements Cr, Fe, V, Ti, and Ga that substitute for Al^{3+} in the ruby crystal structure obtained by LA-ICPMS and by solution ICPMS data agree very well. However, primitive mantle normalized trace element patterns of the solution ICPMS data and the LA-ICPMS data show some notable differences for several elements that are concentrated within inclusions as indicated by TOF-ICPMS intensity maps. While all trace element patterns have high levels of inter-element fractionation, with little overall slope, the solution ICPMS data has more data above the LOQ, most notably HREE and Cs, due to the greater sample to blank ratio of this method, and concentrations are on average 10-100 times higher than those obtained by LA-ICPMS (Tables A4.2 and 4.2, Fig. 4.13 and 4.15). $(Th/U)_N$ are mostly <1 for all samples analysed by LA-ICPMS and for the Aappaluttoq and Myanmar samples analysed by solution ICPMS (Fig. 4.13D). $(Th/U)_N$ ratios for the Namahaca rubies analysed by solution ICPMS, however, are mostly >1. Positive correlations between Nb and Ta and Zr and Hf are somewhat visible in the LA-ICPMS whereas they are very strong in the solution ICPMS data (Fig. 4.13A, B).

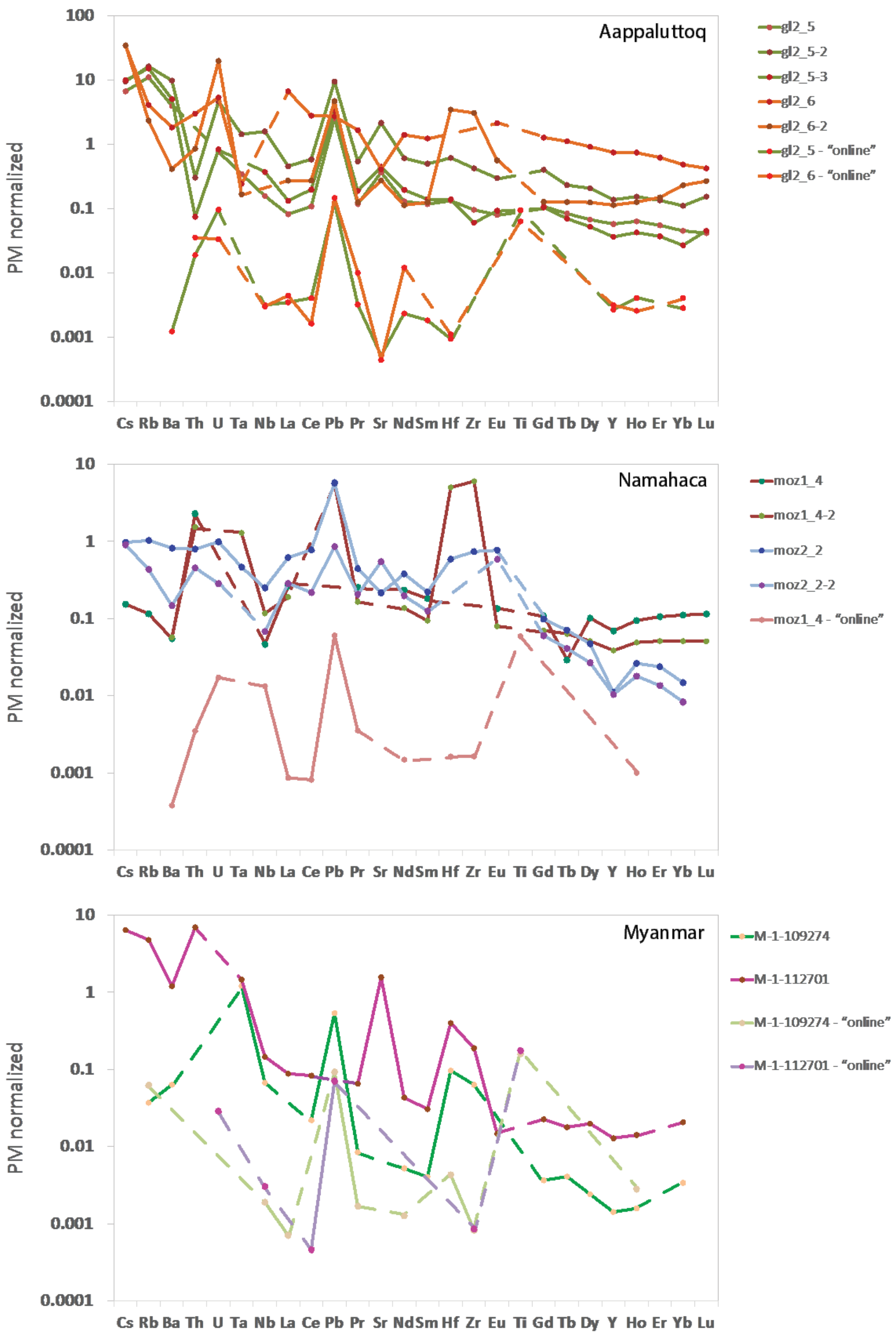

Figure 4.15: Primitive mantle-normalized (McDonough and Sun, 1995) trace element concentrations in "offline" ablated rubies from Aappaluttoq (upper panel), Namahaca (middle panel) and Myanmar (lower panel) along with primitive mantle-normalized (McDonough and Sun, 1995) medians of trace element concentrations in rubies from Aappaluttoq, Namahaca and Myanmar obtained by "online" LA-ICPMS.

In addition, $(Nb/Ta)_N$ ratios for Aappaluttoq and Namahaca are higher for the latter (Fig. 13C). The lower Nb-Ta and Zr-Hf of the high-V group compared to the low-V group in the "online" data is not mirrored in the "offline" data, however the two groups show other differences in trace element characteristics, i.e. higher Cs, Y and HREE for the high-V group (Fig. 13G). A strong positive correlation between Rb and Ba is apparent in the solution ICPMS data while in the LA-ICPMS data Rb and Ba are not obviously correlated for Namahaca, and below the LOQ for the rubies from the other deposits (for Aappaluttoq only Rb is below LOQ) (Fig. 13E).

4.4.2 Sr isotopic composition

Rubies from different locations and deposit types span a very wide range of Sr isotopic compositions (Table 4.3). The Aappaluttoq suite (16 analyses – five duplicate, one triplicate) spans the widest isotopic range, between $^{87}Sr/^{86}Sr = 0.7114 \pm 22$ and $^{87}Sr/^{86}Sr = 3.82595 \pm 41$. The range in $^{87}Sr/^{86}Sr$ isotope ratios is much wider for the high-V group ($^{87}Sr/^{86}Sr = 0.7247 \pm 23$ and $^{87}Sr/^{86}Sr = 3.82595 \pm 41$, median $^{87}Sr/^{86}Sr \sim 0.8077$) than for the low-V group ($^{87}Sr/^{86}Sr = 0.7114 \pm 22$ and $^{87}Sr/^{86}Sr = 0.9337 \pm 29$, median $^{87}Sr/^{86}Sr \sim 0.7749$) but both span a much wider range than any other deposit analysed in this study.

The $^{87}Sr/^{86}Sr$ ratios of the Namahaca suite (12 analyses – three duplicate) range between 0.70754 ± 57 and 0.7291 ± 26. The range in Sr isotopic compositions for the rubies from Myanmar is the narrowest (0.70821 ± 66 to 0.7122 ± 15), even though the analyses cover three different deposits. The four rubies from Namya, Kashin State, range between $^{87}Sr/^{86}Sr = 0.7095 \pm 15$ and $^{87}Sr/^{86}Sr = 0.7122 \pm 15$. Only one ruby each was analysed from the Mogok Stone Tract and from Sagyin in the Mandalay Region, and these rubies have less radiogenic Sr isotopic compositions of $^{87}Sr/^{86}Sr = 0.7087 \pm 45$ and $^{87}Sr/^{86}Sr = 0.70821 \pm 66$, compared with all the other data.

The $^{87}Sr/^{86}Sr$ ratios of the duplicate ablations are different, indicating variable levels of Sr isotopic homogeneity that is likely controlled by inclusions (e.g., $^{87}Sr/^{86}Sr = 0.77556 \pm 31$ and 0.77487 ± 67 for ruby gl1_4 vs $^{87}Sr/^{86}Sr = 0.80766 \pm 55$ and 0.7714 ± 12 for ruby gl2_6).

Table 4.3: Rb-Sr and Pb isotope systematics of rubies.

Provenance	**Sample**	**Age**	**Rb ppm**	**Sr ppm**	**Load size (pg)**	**^{87}Sr/^{86}Sr**	**2 SD**	**^{87}Sr/^{86}Sr$_i$**	**Pb ppm**	**Load size (pg)**	**^{206}Pb/^{204}Pb**	**2 SE**	**^{207}Pb/^{204}Pb**	**2 SE**	**μ**
Aappaluttoq, Greenland	**gl1_1***	~2.6 Ga	1.20	66	66044	0.7114	0.0023	0.7094	0.54	541	34.26	0.01	19.10	0.01	8
	gl1_4	~2.6 Ga	0.16	1.30	1616	0.7756	0.0003	0.7622	1.65	2051	35.65	0.09	18.57	0.06	2
	gl1_4-2		n/a	n/a		0.7749	0.0007								
	gl1_6-2	~2.6 Ga	0.12	*0.35*		0.7575	0.0014	0.7194							
	gl1_7	~2.6 Ga	n/a	n/a		0.7247	0.0023		n/a		17.63	0.18	15.29	0.14	
	gl1_7-2		0.29	0.76	941	0.8684	0.0014	0.8269	0.07	83	18.78	0.09	15.59	0.05	6
	gl2_2	~2.6 Ga	0.71	12	20083	0.7824	0.0015	0.7757							
	gl2_3	~2.6 Ga	8.6	6.07	7553	3.8260	0.0004	3.6725	0.65	404	15.92	0.04	14.90	0.03	9
	gl2_3-2		n/a	n/a		1.7315	0.0015		n/a		15.89	0.10	14.96	0.09	
	gl2_5	~2.6 Ga	6.6	7.2	10687	0.9337	0.0029	0.8337							
	gl2_5-3*		9.1	8.8	9337	0.9179	0.0010	0.8064	0.50	531	31.29	0.03	18.02	0.02	3
	gl2_6	~2.6 Ga	2.5	8.0	3129	0.8077	0.0006	0.7744							
	gl2_6-2		1.38	5.4	1862	0.7714	0.0012	0.7436							
	gl2_7	~2.6 Ga	3.7	121	150767	0.7436	0.0005	0.7403	2.9	3605	56.29	0.26	22.36	0.08	640
	gl2_7-2		n/a	n/a	?	0.7526	0.0005		n/a	?	230.97	0.34	52.33	0.06	
	gl2_7-3*		3.6	87.1	42172	0.7710	0.0006	0.7664	1.42	1375	38.23	0.06	20.04	0.01	10
Mozambique, Namahaca	**moz1_1**	600 Ma	1.27	< LOD		0.7092	0.0014								
	moz1_2	600 Ma	< LOD	0.64	512	0.7101	0.0014								
	moz1_4	600 Ma	< LOD	*0.20*	156	0.7121	0.0018								
	moz2_1	600 Ma	2.8	38	8598	0.7130	0.0004	0.7111							
	moz2_2	600 Ma	0.62	4.3	1413	0.7089	0.0030	0.7053							
	moz2_2-2		0.26	11	13527	0.7075	0.0006	0.7069	0.13	81	18.01	0.10	15.33	0.08	3
	moz2_3	600 Ma	0.34	1.31	2037	0.7113	0.0008	0.7050							
	moz2_6	600 Ma	n/a	n/a		0.7148	0.0009		n/a		17.86	0.11	15.40	0.08	
	moz2_6-2		0.62	4.4	2716	0.7108	0.0007	0.7073	*0.004*	13	18.59	0.20	15.41	0.16	*158*
	moz2_7	600 Ma	n/a	n/a		0.7291	0.0026		n/a		18.57	0.08	15.60	0.06	

	moz2_8	600 Ma	n/a	n/a		0.7164	0.0005								
	moz2_8-2		10	12	14644	0.7112	0.0009	0.6893	*0.01*	17	19.00	0.75	15.49	0.10	*56*
Myanmar, Mogok Stone Tract, Mandalay Region	**M-2-42103***	17 Ma, 32 Ma	0.03	0.20	170	0.7088	0.0046	0.70864, 0.70854	0.34	2229	18.02	0.02	15.56	0.02	
Myanmar, Namya, Kashin State	**M-1-109274***	17 Ma, 32 Ma	0.02	*0.09*	?	0.7122	0.0015	0.71202, 0.71187	0.08	49	18.94	0.02	15.66	0.03	
	M-2-109274*	17 Ma, 32 Ma	0.03	*0.02*	?	0.7095	0.0015	0.70857, 0.70774	< LOD		18.05	0.01	15.58	0.01	
	M-3-109274*	17 Ma, 32 Ma	*0.01*	< LOD	?	0.71035	0.0043		< LOD		18.49	0.08	15.60	0.05	
	M-4-109274*	17 Ma, 32 Ma	1.04	0.26	126	0.71040	0.0022	0.70756, 0.70506	4.57	292	19.59	0.01	15.71	0.01	226
Myanmar, Sagyin, Mandalay Region	**M-112701-1***	17 Ma, 32 Ma	2.87	31.34	21060	0.70821	0.0007	0.70814, 0.70809	< LOD		19.75	0.05	15.72	0.03	

Notes:

kursiv gl: high-V group

Rb, Sr and Pb concentrations normalized to ruby weight loss

kursiv values: LOD < x < LOQ

< LOD = below detection limit (3σ bg)

n/a: no value analyzed

* samples processed with separate columns

The initial ^{87}Sr/^{86}Sr$_i$ were calculated based on estimated crystallization ages

Age references: Aappaluttoq, Greenland - Fagan and Groat, ongoing; Namahaca, Mozambique - Boyd et al., 2010; Myanmar - Garnier et al. (2006), Khin Zaw et al. (2008)

This mirrors the trend already observed in the trace elements and, from the intensity maps of Rb and Sr is explicable by both being hosted within inclusions. If these inclusions have variable Rb and hence variable Sr then radiogenic ingrowth creates Sr heterogeneity.

4.4.3 Pb isotopic composition

The high organic content of the Pb isotope chemistry fraction lead to relatively poor ionisation and consequently high internal measurement errors compared to standard loads of the same size (discussed in Section 4.3.2.2). For those samples where Pb and Sr were separated using discrete columns the error on the Pb analyses was decreased by up to a factor of 10 (Table 4.3).

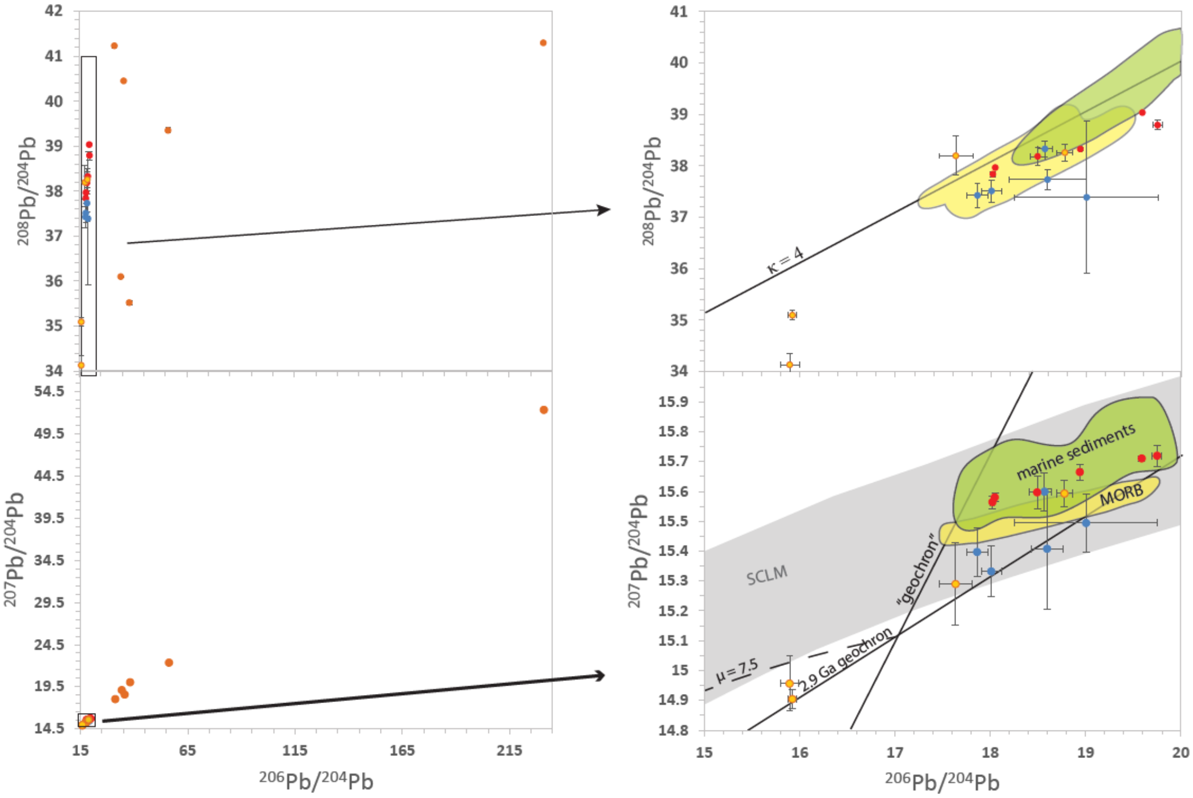

Figure 4.16: Pb isotope composition of rubies from Aappaluttoq (low-V: orange; high-V: yellow with orange rim), Namahaca (blue) and Myanmar (red). Shown for comparison are modern MORB and marine sediments (fields are after Hofmann, 2003). The SCLM field is taken from Klein-BenDavid et al. (2014). Two geochrons are indicated – that labelled "Geochron" is the present day geochron after 4.56 Ga of Earth evolution. A geochron at 2.9 Ga is also plotted. The line labelled with κ = 4.0 represents a closed system that has evolved since 4.55 Ga for a μ value of 8.4 (as an estimate for Bulk Earth).

The relative variations in Pb isotopic compositions in the rubies mirror the variation observed in Sr. The Aappaluttoq suite (10 analyses – two duplicate, one triplicate) span the widest Pb isotopic range, with ^{207}Pb/^{204}Pb varying enormously (^{207}Pb/^{204}Pb = 14.90 ± 3 to ^{207}Pb/^{204}Pb = 52.33 ± 6; Fig. 4.16). The high-V group rubies analysed for Pb isotope compositions show much more radiogenic ratios (^{207}Pb/^{204}Pb = 18.02 ± 1 to ^{207}Pb/^{204}Pb = 52.33 ± 6) than the two high-V group rubies analysed (^{207}Pb/^{204}Pb = 14.90 ± 3 to ^{207}Pb/^{204}Pb = 15.59 ± 5). This is opposite to the trend seen in Sr, i.e. there exists an inverse correlation between Sr and Pb isotope ratios for the high-V group at Aappaluttoq (Fig. 4.17).

The Pb isotopic compositions of the Namahaca suite (5 analyses – one duplicate) is much narrower than the Greenland suite, due, in main to the much younger age of these rubies, with ^{207}Pb/^{204}Pb ranging between ^{207}Pb/^{204}Pb = 15.33 ± 8 and ^{207}Pb/^{204}Pb = 15.60 ± 6. The Pb isotopic compositions of the Myanmar suite range between ^{207}Pb/^{204}Pb = 15.56 ± 2 and ^{207}Pb/^{204}Pb = 15.72 ± 3 for ^{207}Pb/^{204}Pb, the narrowest range of all suites analysed in this study. Within the Mayanmar suite, the four rubies analysed from Namya, Kachin State, define a very restricted range in Pb isotope compositions, between ^{207}Pb/^{204}Pb = 15.58 ± 1 and ^{207}Pb/^{204}Pb = 15.71 ± 1, the ruby from the Mogok Stone Tract marking the lower end of the range, the ruby from Sagyin the upper end.

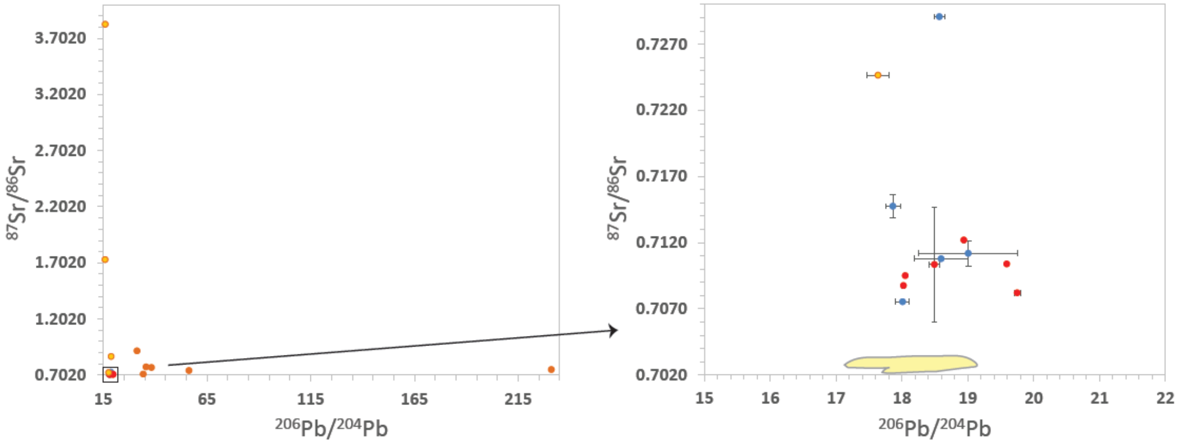

Figure 4.17: ^{87}Sr/^{86}Sr vs. ^{206}Pb/^{204}Pb ratios of rubies from Aappaluttoq (low-V: orange; high-V: yellow with orange rim), Namahaca (blue) and Myanmar (red). Shown for comparison is modern MORB (field after Hofmann, 2003).

The range in $^{206}Pb/^{204}Pb$ is larger, between $^{206}Pb/^{204}Pb = 18.02 \pm 2$ and $^{206}Pb/^{204}Pb = 19.75 \pm 5$, but similar to $^{207}Pb/^{204}Pb$ the ruby from the Mogok Stone Tract marks the lower end of the range and the ruby from Sagyin the upper end. No correlations between Sr and Pb isotopic compositions are apparent for the Namahaca and Myanmar suites (Fig. 4.17).

Generally, there is good agreement between the Pb isotopic compositions of the duplicate ablations, most of them are within error of each other. One exception is sample gl2_7, were the three different ablations give $^{207}Pb/^{204}Pb$ of $^{207}Pb/^{204}Pb = 22.36 \pm 8$, $^{207}Pb/^{204}Pb = 52.33 \pm 6$, and $^{207}Pb/^{204}Pb = 20.04 \pm 1$. The extreme variability of these ratios indicates that the Pb isotope ratios in the Aappaluttoq rubies are dominated by inclusions containing very variable U, Th and Pb, as documented in the TOF-LA-ICPMS mapping (Fig. 4.9, A4.1).

4.5 Discussion

4.5.1 Origin of the trace element signatures

Trace elements in a ruby or sapphire are either incorporated into the crystal structure as a substitute for Al^{3+} (e.g. Cr, Fe, V, Ti, and Ga), or are present in mineral inclusions (e.g., Zr in zircon) and along fractures. This is very well demonstrated by the multi-elemental intensity images acquired for two of the Aappaluttoq rubies (Fig. 4.9). Intensity images of gl3_3-1 show a clear even or zoned distribution of Cr, Fe, Ga and Ti in the ruby, reflecting their substitution for Al^{3+} in the crystal lattice, with the variations in these elements presumably reflecting variations in the original fluid composition or metamaorphic reactants, at any given time during ruby growth. In contrast, Rb, Sr, Zr, Pb, Th and U are clearly concentrated within inclusions as well as along fractures. Thus, with the exception of Cr, Fe, V, Ti, and Ga, the absolute trace element abundances in rubies are primarily a function of impurity density. This fact makes the comparison of trace element data obtained by LA-ICPMS and those obtained from "offline" ablation followed by solution ICPMS difficult as each approach is measuring distinctly different sampling volumes of a randomly impure substrate. For instance, the observation that trace element concentrations obtained by LA-ICPMS are on average 10-100 times lower than those obtained by solution ICPMS (Tables A4.2 and 4.2, Fig. 4.13 and 4.15) is in part due to the fact that a much smaller area of the ruby is ablated by LA-ICPMS making it much easier to select areas free of visible inclusions and fractures, while this is not always possible to do during “offline” ablation. Depending on the clarity of the samples, fractures may be hard to avoid and larger solid inclusions may not be visible on the surface. In addition, the data processing of LA-ICPMS data in Iolite allows the detection and exclusion of spikes in elemental abundances caused by the ablation of inclusions whereas these are homogenised once the ablation product is in solution in the “offline” approach. Hence while the “offline” solution data are more accurate measurements of what was sampled, because they are calibrated against matrix-matched solution standards, the measurements reflect trace elements hosted within inclusions and cracks more so than direct ruby trace element content. The clear implication of these considerations is that the trace element data reported here, more so in the case of the “offline” data, represents not just the ruby but the inclusion assemblage. However, this does not make the data less valuable, because the geologic environment in which a ruby forms influences the inclusion assemblage and density and thus the abundance of trace elements present. As such, both types of data – “offline” solution and direct “online” laser ablation – are used together here as they may reflect, in their different ways, the type of geologic deposit in which a stone originated and the nature of its source rock.

4.5.2 Trace Elements characteristics

As discussed above, trace elements in a ruby are either incorporated into the crystal structure as a substitute for Al^{3+} or are present as mineral inclusions or as constituents in fractures. Therefore, the geologic environment that the ruby crystallises in influences the range of trace elements present in significant quantities and their abundances may reflect the type of geologic deposit in which a stone originated. Here we explore some of those possible links.

Compositions of the trace elements Cr, Fe, V, Ti, and Ga that substitute for Al^{3+} for all rubies analysed in this study are consistent with those previously reported for their respective deposit types, i.e. moderate contents of Cr and Fe, low Ga and very low to low amounts of Ti and V in the rubies from metamorphic deposits in amphibolite and gabbro (e.g., Giuliani et al., 2014), and moderate contents of Cr, low Fe and Ga, low to moderate amounts of Ti and elevated V in the rubies hosted in marble (e.g., Muhlmeister et al., 1998).

Trace element patterns of the LA-ICPMS data normalized to primitive mantle for all four analysed locations are broadly similar, showing enrichment of HFSE with much lower

REE, Sr and Th concentrations. In addition, all four locations show high Ta/Nb and Hf/Zr ratios and low Th/U ratios. These trace element ratios are characteristic of rutile (e.g., Klemme et al., 2005; Meyer et al., 2011), the most common inclusion in rubies from Aappaluttoq (Smith et al., 2016) and also commonly found in rubies from Namahaca, Mozambique (Pardieu et al., 2013), Myanmar (e.g., Harlow and Bender, 2013) and Luc Yen, Vietnam (Van Long et al., 2004). This is consistent with the correlated distribution of Ti and U seen in the multi-elemental intensity images of the mapped Aappaluttoq rubies (Fig. 4.9). Rutile in ruby is present in the form of clouds of minute rutile particles (i.e. 'silk') and/or fine needles and arrowhead-shaped platelets, formed through exsolution, therefore the trace element patterns observed in the LA-ICPMS data likely reflect finely dispersed rutile. This is also consistent with the distribution patterns of element maps of Ti acquired by TOF-ICPMS that shows zones of higher Ti forming distinct zones or clouds within the ruby (Fig. A4.1, 4.9).

The more varied trace element characteristics observed in primitive mantle normalized trace element patterns of the solution ICPMS data can also be correlated with likely inclusion content. The enrichment in Rb and Ba and positive Sr anomalies observed in several of the Aappaluttoq, Namahaca and Myanmar rubies are characteristic for phlogopite and other mica (e.g., Ionov et al., 1997; Sweeney et al., 1995; Latourrette et al., 1995; Foley et al., 1996), also a very common inclusion in all analysed rubies. The Cs enrichment seen in some of the Aappaluttoq samples likely reflects the presence of talc, another common inclusion found in those rubies. Extreme enrichment in Zr-Hf, U and Th, HREE enrichment over LREE and positive Ce anomalies that are observed in some of the patterns may indicate that zircon was sampled in the ablation. Positive Eu anomalies are only present in rubies from metamorphic deposits in amphibolite and gabbro, Aappaluttoq and Namahaca, and very likely reflect the presence of plagioclase. The $(Th/U)_N$ ratios >1 characterising in the solution ICPMS data of several Namahaca rubies very likely reflects the presence of amphibole, one of the most common inclusions found in the Namahaca rubies (Pardieu et al., 2013). The different V contents of rubies at Aappaluttoq result in two different populations ("high-V" with $V > 14$ ppm and "low-V" with $V < 8$ ppm) likely represents different ruby forming environments. The Aappaluttoq rubies are known to form in a variety of different host rocks (Fagan, 2012). Those analysed in this study were taken from a bulk sample of ore composed of three main rock types, sapphirine-gedrite, leucogabbro and phlogopitite, suggesting that the two groups differentiated on the basis of their V contents may be derived from different host rocks. Other differences in the two groups are also evident. The higher Ti, Nb-Ta and Zr-Hf contents in the "online" data of the high-V group suggest that more rutile was included in these rubies. In addition, the higher Cs, Y and HREE as well as $(U/Pb)_N$ ratios > 1, indicate that the high-V group may have more inclusions of apatite and talc whereas the low-V group may have more mica inclusions. If this is indeed the case the low-V group may be derived from the phlogopitite, the host for the majority of the ruby held within Aappaluttoq, and the high-V from the leucogabbro. However, to be certain more detailed studies need to be carried out out beyond this initial study.

Overall, the trace element characteristics of the rubies measured in this study are consistent with those of their main inclusion types, indicating that the majority of the trace elements are present in finely dispersed inclusions. In instances where multiple "offline" ablations per ruby were performed, varying concentrations thus would reflect different densities of inclusions and, in cases where the trace element patterns of the replicates are quite different, indicate that a major inclusion of a specific composition was ablated, dominating the overall trace element systematics.

4.5.3 U-Pb isotope systematics

The very wide range in Pb isotopes for the Aappaluttoq suite (Table 4.3) with $^{206}Pb/^{204}Pb$ ratios ranging from 15.89 to 231 and $^{207}Pb/^{204}Pb$ ratios from 14.90 to 52.33 are striking characteristics of the Aappaluttoq rubies. These highly radiogenic Pb isotope ratios, particularly the very high $^{207}Pb/2^{04}Pb$ ratios, could only have been generated early in Earth's history, with high U/Pb at Archean times, because of the very low abundance of the relatively short-lived ^{235}U in the Phanerozoic Earth. One sample, gl2_3, has very low Pb isotope compositions ($^{206}Pb/^{204}Pb$ = 15.92 and $^{207}Pb/^{204}Pb$ = 14.90 and $^{206}Pb/^{204}Pb$= 15.89 and $^{207}Pb/^{204}Pb$ = 14.96 for two different ablations) plotting well to the left of the present day "geochron" – this sample must have retained long-term low U-Pb, similar to the compositions observed in ancient lower crust (e.g., Rudnick and Goldstein, 1990; Murphy et al., 2002), presumably not trapping significant amounts of high U-Pb inclusions such as rutile. The possible age implications for Aappaluttoq ruby genesis will be explored below (Section 4.5.4).

The relatively restricted range in Pb isotopes for rubies from Myanmar (Table 4.3, Fig. 4.16) is consistent with derivation of the Pb isotopic composition of these stones from a precursor rock or rocks whose Pb isotope compositions were similar to modern sediments, with ^{207}Pb/^{204}Pb ratios, at a given ^{206}Pb/^{204}Pb ratio all higher than the modern MORB range. The measurement uncertainties on the Namahaca samples are too high to make their ^{207}Pb/^{204}Pb ratios reliable. The uncertainties on the ^{206}Pb/^{204}Pb ratios are less and indicate that they span a similar range to the Myanmar samples. Neither of these localities, where ruby formation was relatively recent (Phanerozoic), show the extreme Pb isotope compositions observed at Aappaluttoq.

4.5.4 Age Constraints using Pb-Pb isotope systematics

The extremely radiogenic Pb isotope compositions of some of the Aappaluttoq rubies, especially their high ^{207}Pb/^{204}Pb ratios, belie an ancient age. There are no systematic U-Pb isochron relations, indicating recent U disturbance or very mobile U, or U loss during the sample chemistry process. There are no recent (Phanerozoic and younger) geological events in the Fiskenæsset Anorthosite Complex that could have generated the required U-loss. Recent weathering of U, during exposure of the Aappaluttoq rocks, could have fractionated U from Pb although we view ruby as being more robust than silicate minerals such as feldspar to U loss. U loss could have been generated by the acid leaching process used to clean the rubies, post-mining or pre-laser ablation. Instead of using U-Pb systematics, the linear correlation of ^{207}Pb/^{204}Pb vs ^{206}Pb/^{204}Pb can be used to constrain the time elapsed since ruby crystallization, assuming that the rubies formed at the same time, from a relatively homogenous parent and that U-Pb was lowered recently. Given these assumptions, the age of the major U-Pb fractionation event that created the slope of the Pb-Pb isotope array can be determined from the transcendental equation:

$$\frac{\left(\frac{^{207}Pb}{^{204}Pb}\right)_p - \left(\frac{^{207}Pb}{^{204}Pb}\right)_I}{\left(\frac{^{206}Pb}{^{204}Pb}\right)_p - \left(\frac{^{206}Pb}{^{204}Pb}\right)_I} = \frac{1}{137.88}\frac{e^{\lambda_{235}t}-1}{e^{\lambda_{238}t}-1} \qquad (1)$$

where *p* designates present day $^{207}Pb/^{206}Pb$ ratios, the *I* designates initial $^{207}Pb/^{206}Pb$ ratios, and λ_{235} and λ_{238} are the decay constants for ^{235}U and ^{238}U, respectively. Regression of the wide-ranging Aappaluttoq Pb isotopic compositions yields a Pb-Pb isochron age of 2581 ± 53 Ma (Fig. 4.18a), with a large MSWD of 355. The high MSWD is an indication that although this age may reflect ruby formation, the Pb isotopic system was not fully homogenised at the time of ruby formation. Further constraints can be drawn from this Pb-Pb isochron array. Taylor et al. (1980) have argued that the basement gneisses from the Fiskenæsset region formed at circa 2.9 Ga from mantle-derived sources. The trend of the Pb-Pb isochron in Fig. 4.16 indicates that the source of the Pb that formed the Aappaluttoq rubies was derived from a source that had experienced evolution with a considerably higher $^{238}U/^{204}Pb$ (μ) value prior to ruby formation.

Trace element analysis of the Aappaluttoq rubies group them into two populations based on their V content, a high-V group and a low-V group, possibly representing different host rocks, which will likely have different initial Pb isotope systematics. This provides a basis for regressing the Pb-Pb isotope systematics of the two groups separately. The low-V group yields a Pb-Pb isochron age of 2558 ± 68 Ma (MSWD = 525) (Fig. 4.18b), which is within uncertainty of the age derived from all Aappaluttoq rubies. The high-V rubies yield an older age of 3059 ± 380 Ma (Fig. 4.18c), that has a large uncertainty but agrees well with the 2.9 Ga isochron age of Taylor et al. (1980) for the Fiskenæsset gneisses, indicating the possible presence of two different age populations at Aappaluttoq. This finding requires further investigation to try to improve the Pb-Pb isotope systematics.

Some of the rubies were ablated multiple times and these allow a look at whether there is sufficient spread in isotopic compositions to extract age information from a single crystal. Pb-Pb isochrons for two of the three samples that were ablated multiple times (rubies gl1_7 and gl2_7), belonging to the high-V and low-V group, respectively, yield Pb-Pb isochrons of 3243 ± 1300 Ma (Fig. 19a) and of 2544 ± 440 Ma (Fig. 19b).

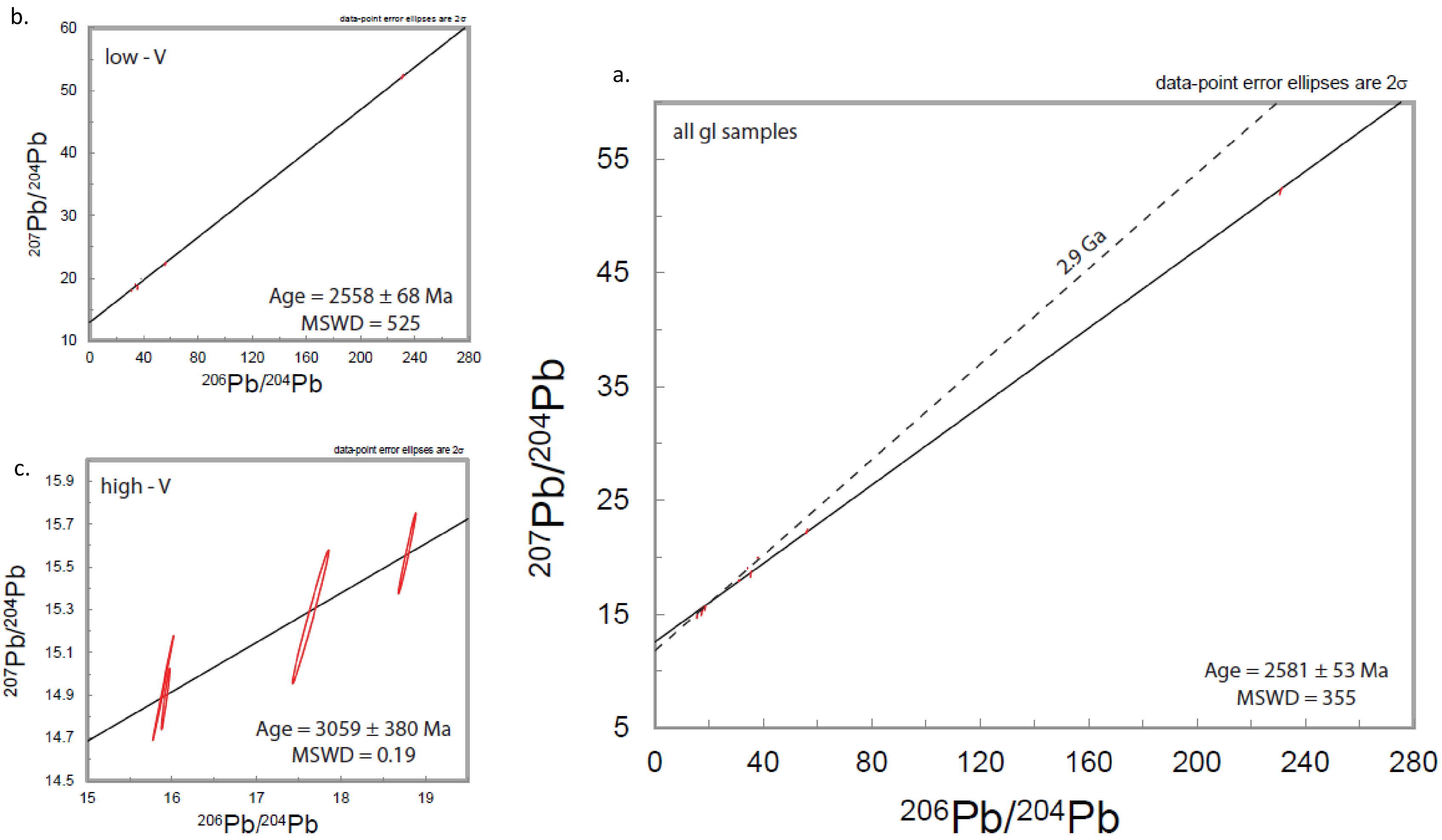

Figure 4.18: Pb–Pb isochron plots for rubies from Aappaluttoq, Greenland. (a) for all samples, (b) for all samples with V < 7 ppm, and (c) all samples with V > 23 ppm. Greenland. MSWD is a mean square of weighted deviates. Errors are 2 SE. Ages are calculated using Isoplot Ex v. 4 (Ludwig, 2003). The 2.9 Ga Pb–Pb isochron is for Nuk basement gneisses Fiskanaesset from Taylor et al., 1980.

The third ruby with multiple ablations (gl2_3) yields an inverse isochron, probably due to its very low Pb isotopic composition, which would be dominated by common Pb. The errors of these single grain ages are very large, but broadly reflect the two different ages found for the high-V and low-V groups at Aappaluttoq. If the Pb-Pb isochrons defined by the Aappaluttoq rubies are interpreted to represent ages of ruby formation, or at least the time of corundum "up-grading" to gem ruby, the ages appears to be consistent with the regional geology. The Fiskenæsset anorthosite Complex in SW Greenland that hosts the Aappaluttoq ruby deposit formed at 2.97-2.95 Ga (Polat et al., 2010). Granulite facies metamorphism occurred in the area at 2.82 Ga (Friend and Nutman, 2001) and was followed by retrograde amphibolite facies metamorphism at 2.66 ± 0.02 Ga (Pidgeon and Kalsbeek, 1978). The ruby host rocks are highly metasomatized metamorphic rocks and, based on an age of 2646 ± 43.3 Ma obtained for monazites along grain boundaries within these rocks, are believed to have formed, as gem rubies, in this retrogressive event (Fagan and Groat, un-published). Mica crystals surrounding the rubies yield a ^{40}Ar-^{39}Ar cooling age of 1941 ± 4.5 Ma (A. Fagan, personal communication) consistent with ruby formation prior to the Ar-Ar system closing. These constraints seem to support the Pb-Pb isochron ages as reflecting the timing of gem- ruby or "re-crystallization" at Aappaluttoq, however, more detailed analyses are necessary to constrain the exact history.

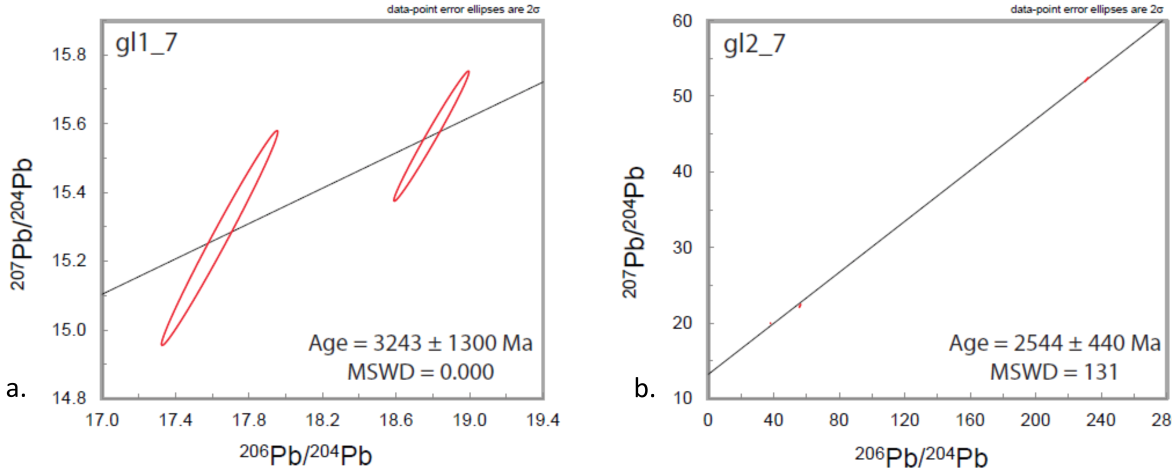

Figure 4.19: Pb–Pb isochron plots for (a) high-V ruby gl1_7 and (b) low-V ruby gl2_7 based on multiple ablations. MSWD is a mean square of weighted deviates. Errors are 2 SE. Ages are calculated using Isoplot Ex v. 4 (Ludwig, 2003). Uncertainties plotted are 95% errors.

Unfortunately, no Pb-Pb isochron age could be calculated for the Namahaca suite. This may be due to the low precision of the Pb isotope measurements or to high inherent variability in the Namahaca geological system that formed this ruby suite.

The Pb isotope measurements for the Myanmar rubies were much more precise. Despite the fact that the spread in $^{207}Pb/^{204}Pb$ ratios is very low, presumably due to the young age of the ruby suite, a linear spread is apparent and allowed the calculation of a $^{207}Pb/^{206}Pb$ isochron for the four samples from Namya, Kachin State (Fig. 4.20).

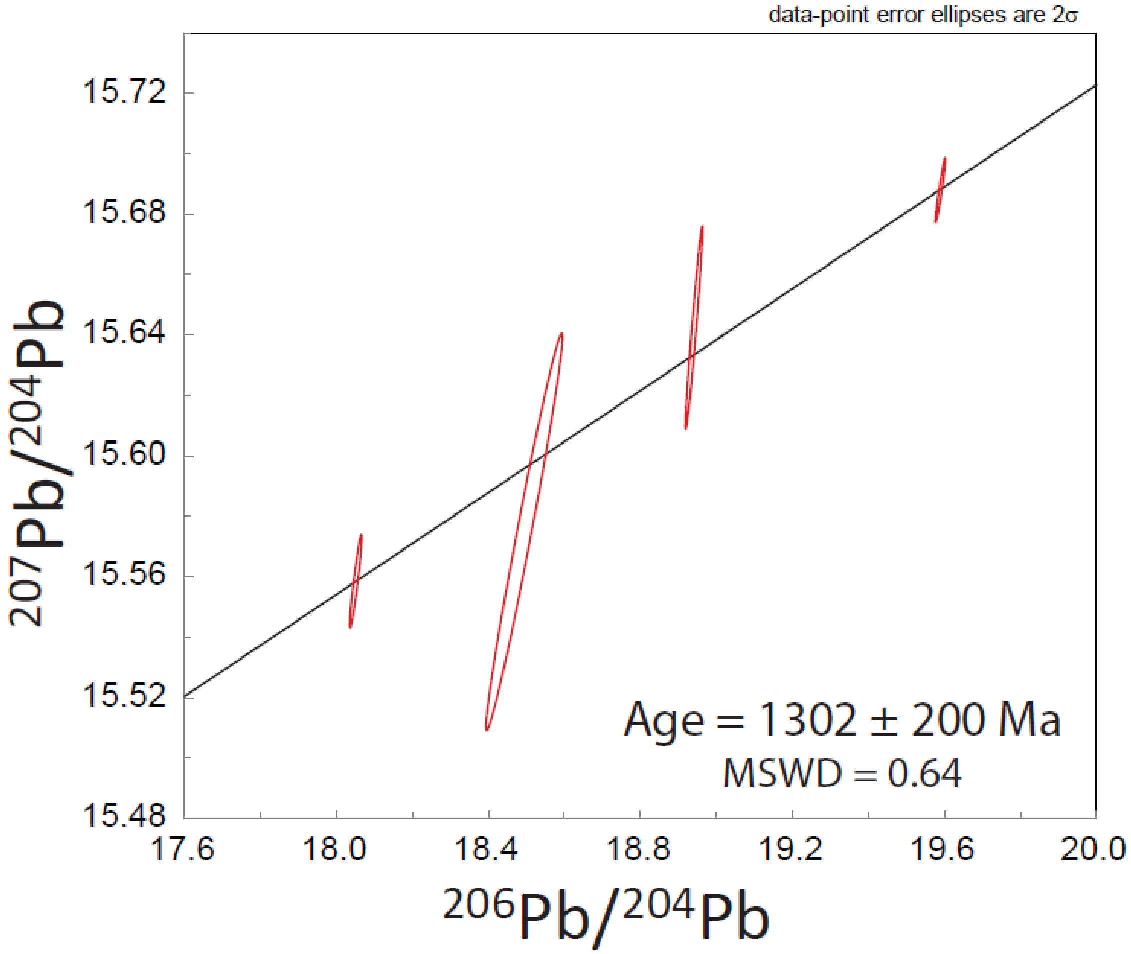

Figure 4.20: Pb–Pb isochron plot for rubies from Namya, Kachin State, Myanmar. MSWD is a mean square of weighted deviates. Errors are 2 SE. Ages are calculated using Isoplot Ex v. 4 (Ludwig, 2003). The relatively low MSWD is a function of the large uncertainties and does not indicate the likelihood of the correlation being an isochron.

However, contrary to the isochron obtained for the Aappaluttoq ruby suite, the slope of the line for Namya is unusually old (1302 ± 200 Ma; MSWD = 0.64) and unlikely to be useful in defining an apparent age for the rubies. Minerals associated with and included within ruby have been dated to ~17 – 19 Ma (Garnier et al., 2006) and 31–32 Ma (Khin Zaw et al., 2008), respectively, suggesting very young crystallisation ages and the marble host rocks are believed to be Ordovician to Permian (Mitchell et al., 2007). Most likely, the Pb-Pb correlation defined by these samples represents mixing between at least two Pb sources during the formation of these rubies.

4.5.3 Rb-Sr and Pb-Pb Isotope systematics – source evolution

The growth equations for $^{208}Pb/^{204}Pb$ and $^{206}Pb/^{204}Pb$ can be combined to form the following equation:

$$\frac{\Delta\left(\frac{^{208}Pb}{^{204}Pb}\right)}{\Delta\left(\frac{^{206}Pb}{^{204}Pb}\right)} = \frac{\kappa(e^{\lambda_{232}t}-1)}{(e^{\lambda_{238}t}-1)} \qquad (2)$$

where $\Delta(^{208}Pb/^{204}Pb)$ and $\Delta(^{206}Pb/^{204}Pb)$ represent the in-grown radiogenic Pb since formation (the present day minus the initial Pb ratios), κ is the $^{232}Th/^{238}U$ ratio, and λ_{232} and λ_{238} are the decay constants for ^{232}Th and ^{238}U, respectively. Provided κ is constant in a series of cogenetic rocks or minerals (i.e., that at t=0 they all had identical Pb isotope ratios), the slope of an array on a plot of $^{208}Pb/^{204}Pb$ and $^{206}Pb/^{204}Pb$ will depend only on t and κ, and κ can be calculated to give an insight into the parental material. As can be seen in Fig. 4.21a,b and c the Aappaluttoq rubies show a lot of scatter in a $^{208}Pb/^{204}Pb$ and $^{206}Pb/^{204}Pb$ plot resulting in large uncertainties and MSWDs for the derived slopes. This variability is further evidence that the Pb isotope ratios in the Aappaluttoq rubies are dominated by inclusions containing very variable U, Th and Pb, as documented in the TOF-LA-ICPMS mapping (Fig. 4.9). The calculated κ values, therefore, are unlikely to be meaningful and or will have large uncertainties; however, the very low κ values of 0.29 ± 0.4 and 0.22 ± 0.27 of the whole Aappaluttoq suite and the low-V group, respectively, broadly correlate with the low Th/U of rutile. This agrees with the likely presence of rutile indicated by the TOF-ICPMS mapping.

The rubies from Namya, Kachin State, Myanmar show much less scatter in a $^{208}Pb/^{204}Pb$ and $^{206}Pb/^{204}Pb$ plot, forming a linear array (Fig. 4.22). The calculated κ value of 2.2 ± 1.8 is higher than would be expected for carbonates or rutile, as both concentrate U and

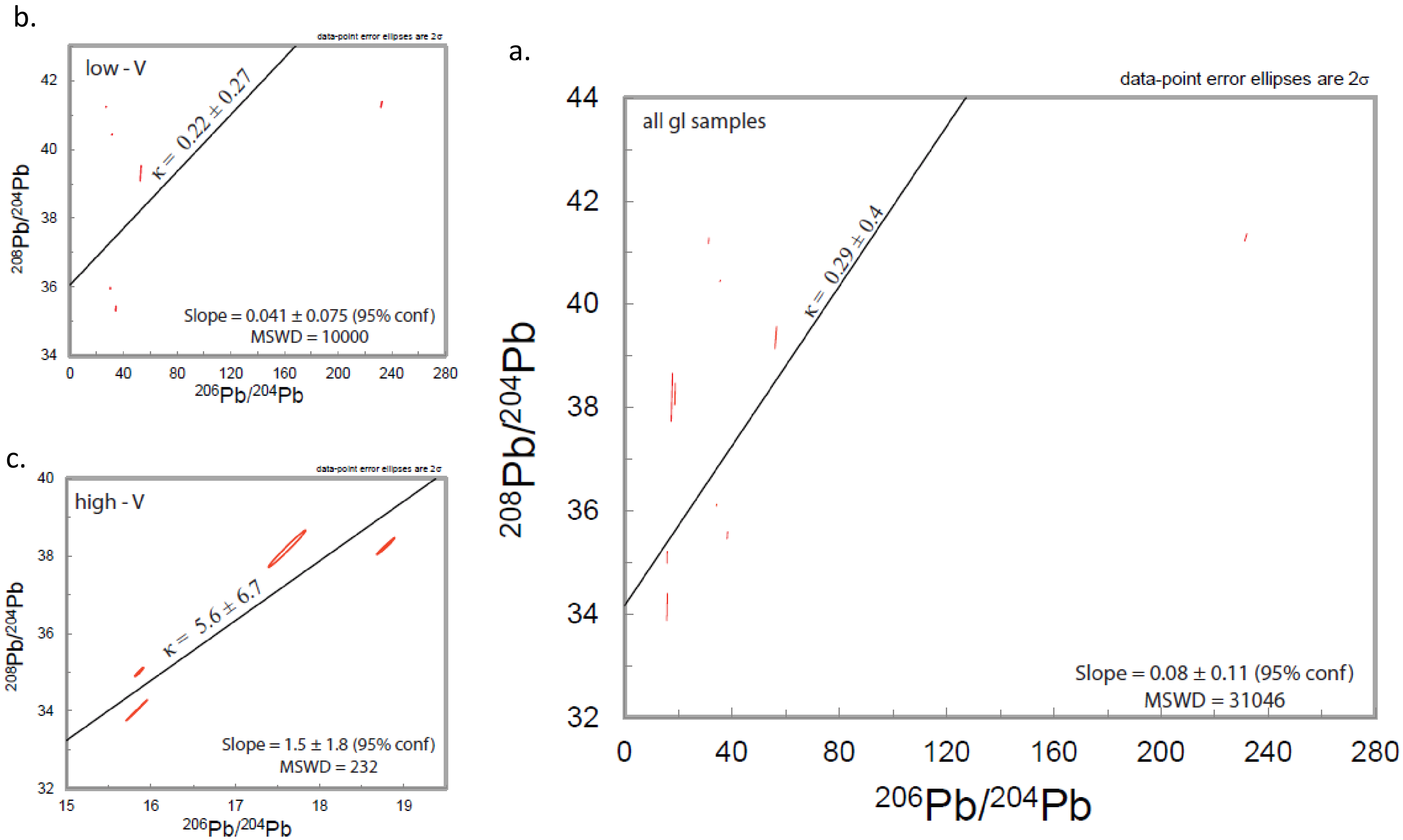

Figure 4.21: ^{208}Pb–^{206}Pb isochron plots for rubies from Aappaluttoq, Greenland. (a) for all samples, (b) for all samples with V < 7 ppm, and (c) all samples with V > 23 ppm. Greenland. MSWD is a mean square of weighted deviates. Errors are 2 SE. Slopes are calculated using Isoplot Ex v. 4 (Ludwig, 2003).

exclude Th. In carbonate rocks the ratio of ^{232}Th/^{238}U approximates to zero, however, the marble host rocks may have interacted with Th-rich crustal fluids carrying radiogenic ^{208}Pb during metamorphism, resulting in higher apparent time-integrated ratios of ^{232}Th/^{238}U and ^{208}Pb/^{204}Pb in the rubies, which may be related both to the Th and/or crustal Pb inflow and to the U outflow. Hence, as both carbonates and rutile generally have extremely low Th, it is likely that most ^{208}Pb measured can be attributed to "common" (i.e. initial) Pb.

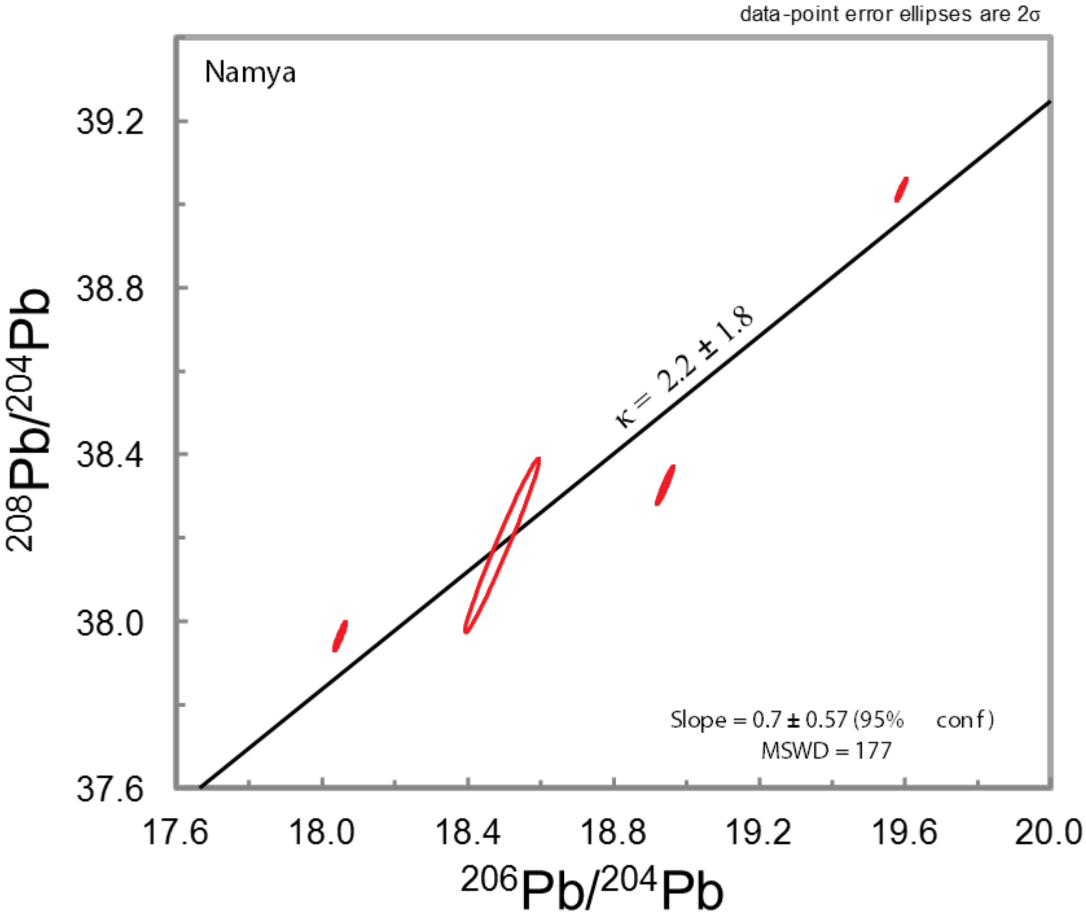

Figure 4.22: ^{208}Pb–^{206}Pb isochron plots for rubies from Namya, Myanmar. MSWD is a mean square of weighted deviates. Errors are 2 SE. Slopes are calculated using Isoplot Ex v. 4 (Ludwig, 2003).

The very wide range in Sr isotopic ratios of the Aappaluttoq suite (0.7114 ± 22 to 3.8260 ± 4) reflects the very old age of the rubies, compared to both the Namahaca and Myanmar suites. With time the difference in ^{87}Sr/^{86}Sr ratios, due to differing Rb/Sr ratios in the different rubies (i.e. their impurities) since their formation, is more pronounced, as more radiogenic ^{87}Sr is accumulated. The range of Sr isotopic compositions for the Namahaca suite is much narrower (0.70754 ± 57 to 0.7291 ± 26) and overall less radiogenic, consistent with their considerably younger age, but it is important to note that these rubies still span a very wide range in Sr isotopic compositions. Hence, some of the radiogenic Sr may either be generated by the incorporation of mica and amphibole inclusions or inheritance of radiogenic Sr from the parental rocks. The Myanmar ruby suite spans the narrowest range of Sr isotope compositions (0.70821 ± 66 to 0.7122 ± 15), and is also the youngest ruby suite studied here. Nonetheless, the Sr isotopic composition of the most radiogenic samples overlap those of the Namahaca suite.

A scattered but positive correlation between $^{87}Sr/^{86}Sr$ ratios and $^{87}Rb/^{86}Sr$ ratios is apparent in the Aappaluttoq suite and also observed for the Namahaca and Myanmar suites (Fig. 4.23). The correlation for the Aappaluttoq suite is considerably steeper than a 2.6 Ga reference isochron expected from the Pb-Pb results, with a slope that would yield an "age" of at least 8 Ga. This result clearly indicates the likelihood of either geological or experimental Rb-loss, in keeping with the inferred U loss deduced from the coherent Pb-Pb relations but incoherent U-Pb relations.

Initial $^{87}Sr/^{86}Sr$ ratios of rubies (Table 4.3), calculated using estimated crystallization ages, are variable, ranging from $^{87}Sr/^{86}Sr_{2.6Ga}$ = 0.70944 to $^{87}Sr/^{86}Sr_{2.6Ga}$ = 3.672537 for Aappaluttoq (both for the low-V and high-V groups), from $^{87}Sr/^{86}Sr_{600}$ = 0.68930 to$^{87}Sr/^{86}Sr_{600}$ = 0.71111 for the Namahaca suites, and, depending on which estimate of crystallisation age is used for the Myanmar rubies, from $^{87}Sr/^{86}Sr_{17}$ = 0.70756 to$^{87}Sr/^{86}Sr_{17}$ = 0.71202 and from $^{87}Sr/^{86}Sr_{32}$ = 0.70506 to $^{87}Sr/^{86}Sr_{32}$ = 0.71187. This variability reflects several possible influences. The first is that that the unfeasibly low initial Sr isotope ratios of some Myanmar rubies probably reflect inaccuracy in the measured Rb/Sr ratio in rubies where both Rb and Sr are at very low concentrations. Simple Rb-gain would explain the over-correction to very low values. The latter is difficult to envision for ruby unless there is a second phase of ruby growth, making a single stage age correction invalid. The highly varied, radiogenic initial ratios of the Aappaluttoq suite are an indication of recent Rb (and probably U) loss, as indicated from the isochron systematics. This may be of experimental origin, either via the leaching process that was used to clean the rubies or due to volatile Rb loss during the "off-line" ablation.

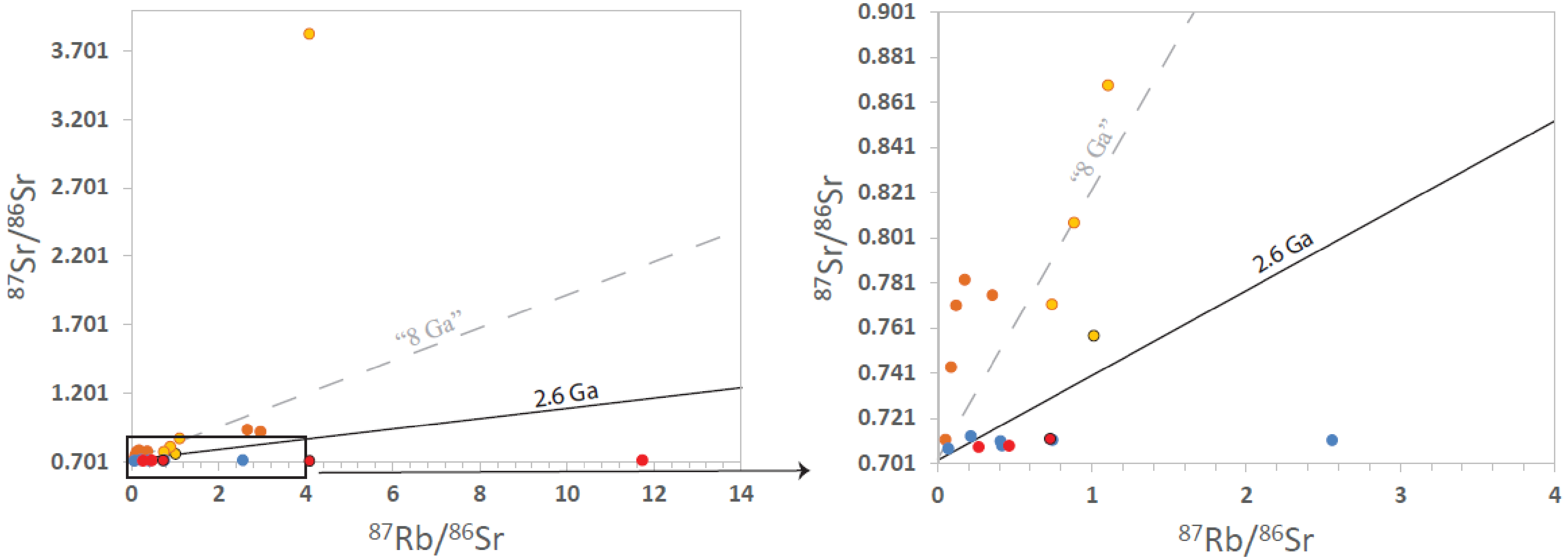

Figure 4.23: ^{87}Sr/^{86}Sr ratio vs ^{87}Rb/^{86}Sr ratio for rubies from Aappaluttoq (low-V: orange; high-V: yellow with orange rim), Namahaca (blue) and Myanmar (red). Uncertainties are smaller than the symbols. Symbols with black rim represent ^{87}Rb/^{86}Sr ratios calculated with either Rb or Sr concentrations < LOQ. 2.6 Ga and "8 Ga" reference isochrons are plotted calculated with an initial ^{87}Sr/^{86}Sr$_i$ for Fiskenæsset of 0.7016 ± 0.0003 (Moorbath and Pankhurst, 1976).

Further, given the relative coherence of the Pb-Pb isotope array (Fig. 4.18), it seems unlikely that such a well-defined correlation would result from a system which would have had such extreme isotopic variability. Although it is possible that the complex Rb-Sr systematics of the Aappaluttoq rubies could have been affected by metamorphic overprinting and metasomatic alteration of the Fiskenæsset igneous complex documented at ~ 1775-1676 Ma by Reggin and Horan (2015), significant impact of this event would have no doubt disturbed the much more coherent ~2.6 Ga Pb-Pb isochron correlation. The host of the majority of ruby at Aappaluttoq is phlogopitite, a metasomatic product comprising around 90% phlogopite, 5% biotite, and 5% corundum - likely this rock is the main source of any inherited radiogenic Sr in the Aappaluttoq suite.

Similar to the Aappaluttoq suite, the initial Sr isotope ratios of the Namahaca rubies likely do not represent the actual isotopic composition at the time of formation, but the variability in the source of the radiogenic Sr, especially for the sample with the nonsensical $^{87}Sr/^{86}Sr_{600} = 0.6893$. In addition, the Namahaca deposit is alluvial indicating that the rubies may derive from different primary deposits that formed at different times. Similar to Aappaluttoq, the source of most of the radiogenic Sr are most likely the associated minerals, such as mica and amphibole. Overall the initial Sr isotope ratios are relatively unradiogenic, consisted with limited input of crustal Sr during gem formation.

The initial Sr isotope ratios of the Myanmar rubies are relatively similar, with the exception of rubies M-1-109274 and M-4-109274 - which is to be expected considering their high clarity – reflecting roughly the composition of seawater at ~ 32 Ma and 17 Ma (Burke et al., 1982). The range in measured $^{87}Sr/^{86}Sr$ ratios (0.70821 ± 66 to 0.7122 ± 15), extends higher than that of present day seawater, but is similar to the measured $^{87}Sr/^{86}Sr$ ratios reported for ruby-bearing calcite and dolomite marbles (0.7085–0.710 and 0.7090–0.7102, respectively) of the southwestern Pamirs, where the geological setting is similar to that in Myanmar (Dufour et al., 2007). Possible sources of radiogenic ^{87}Sr for this type of deposit could be fluids inflowing from nearby schists or igneous rocks or detrital minerals that were contained in the carbonate rocks in the form of disseminated grains or thin beds. Unfortunately, due to the lack of Sr isotopic data for rocks associated with the ruby deposits in Myanmar, the source cannot be determined at this time. However, if the marble-hosted ruby deposits in Myanmar formed as suggested by Garnier et al. (2008), no externally derived fluids are interpreted to have circulated through the marble, and the source of the radiogenic Sr must have been detrital minerals deposited coevally with the carbonate rocks on the platform.

4.5.5 Using Trace Element and Radiogenic Isotope Geochemistry to constrain the Geographical Origin of Rubies

4.5.5.1 Trace elements

Due to the more variable trace element concentrations of the "offline" laser ablation approach, caused by the reduced control over the clarity of the ablated area (due to the larger size), they will be excluded from the following comparisons to determine ruby provenance.

Quantitative data for the most commonly observed elements in ruby and sapphire, Fe, Cr, Ti, V and Ga, have been used by many authors (e.g., Abduriyim and Kitawaki, 2006; Muhlmeister et al., 1998; Sutherland et al., 1998) in attempts to determine ruby provenance. A commonly used diagram is a logarithmic plot of wt% values Cr_2O_3/Ga_2O_3 vs. Fe_2O_3/TiO_2 (e.g., Saminpanya et al., 2003; Abduriyim and Kitawaki, 2006; Sutherland and Abduriyim, 2009). Fig. 4.24 shows a plot of Cr/Ga vs. Fe/Ti for the ruby suites analysed in this study. Published datasets used for comparisons are exclusively LA-ICPMS data, excluding EMPA data sets, because it has been shown that using data derived from both methods can produce systematic differences among elements in the same sample (Harlow and Bender, 2013; Kan-Nyunt et al., 2013). The better detection limits of LA-ICPMS result in a greater number of samples having quantitative data. The data obtained in this study for the two marble-hosted suites, Myanmar and Luc Yen, have compositions that can be distinguished from those of the rubies derived from metamorphic deposits in amphibolite and gabbro, i.e., the Namahaca and Aappaluttoq deposits. The two different groups at Aappaluttoq, low-V and high-V, show no systematic differences. Our data overlap with published compositions for marble-hosted rubies. The Luc Yen samples have lower Cr/Ga ratios than the samples from Myanmar but some overlap exists. The Namahaca and Aappaluttoq suites have similar compositions to rubies from a variety of metamorphic ultramafic deposits as well as basalt-hosted deposits. This overlap illustrates that Cr/Ga vs. Fe/Ti systematics are not well suited to distinguish between these deposit types. One exception is the clearly distinct population of data from an unusual suite of basalt-hosted rubies from the New England Gem field, Australia displaying relatively high Fe/Ti and low Cr/Ga ratios that are indicative of igneous origin (e.g., Saminpaya et al., 2003). This deposit is thought to have experienced magmatic–metasomatic inputs in its genesis (Sutherland et al., 2017).

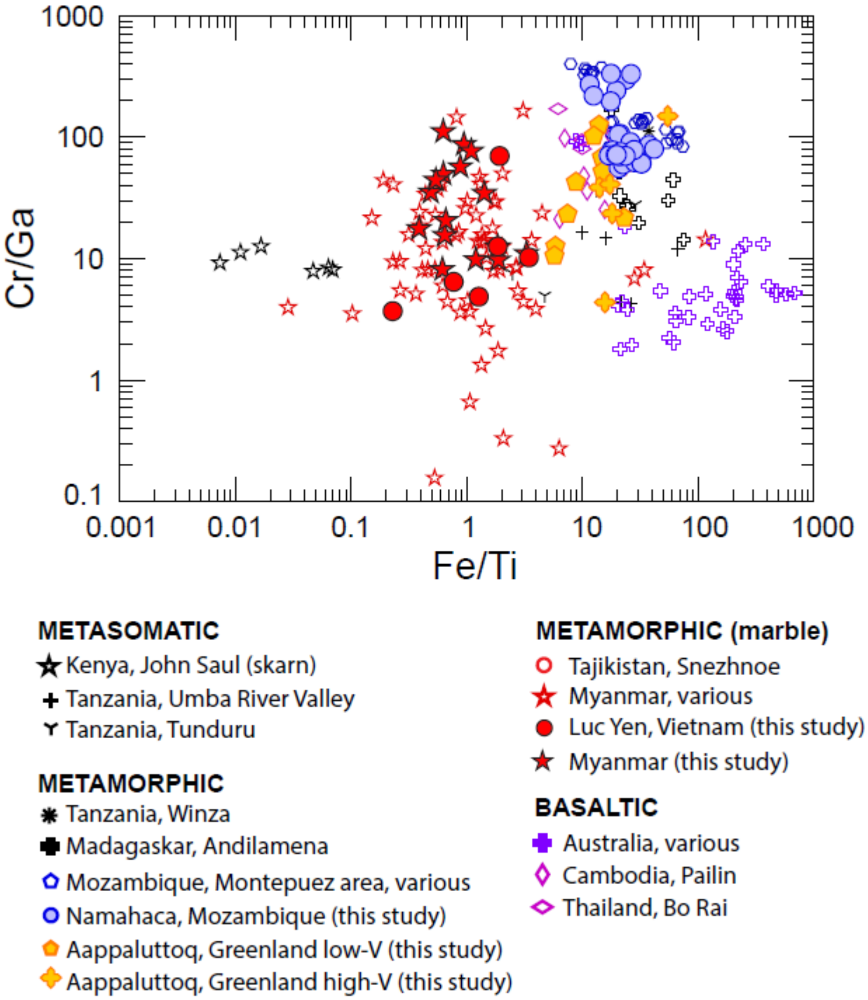

Figure 4.24: Plot of Cr/Ga (ppm) against Fe/Ti (ppm) in rubies from Aappaluttoq, Greenland, Namahaca, Mozambique, Myanmar and Luc Yen, Vietnam. All data plotted are LA-ICPMS values. Additional data from Cartier (2009), Harlow and Bender (2013), Pardieu et al. (2013), Pornwilard et al. (2011), Schwarz et al. (2008), Sorokina et al. (2015), Sutherland et al. (2009), Sutherland et al. (2015), Sutherland et al. (2017), Khin-Zaw et al. (2014).

Another diagram frequently used in efforts to determine ruby provenance is the ternary diagram depicting Fe-V-Ga concentrations (Fig. 4.25), which has been shown to discriminate rubies from basalt-hosted, metasomatic, and marble-hosted hosts (e.g., Muhlmeister et al., 1998; Giuliani et al., 2007; Harlow and Bender, 2013). As is clear from Fig. 4.25a, this approach is useful for distinguishing between the high-Fe rubies (metasomatic and basalt-hosted, Groups II and III, respectively), that all plot at the Fe-apex, and the low-Fe marble-hosted rubies. The plot shows that the Luc Yen suite analysed is this study has lower V than the rubies analysed from Myanmar, but that there is still significant overlap with published data for other marble-hosted ruby deposits.

The Namahaca and Aappaluttoq suites show significant overlap with each other in terms of their Fe-Ga-V systematics and with other rubies of similar deposit type as well as basalt-hosted rubies. Smith et al. (2016) modified the triangular plot to Fe/20-V*3-Ga*3 to provide more resolution in the Fe-apex area of the plot (Fig 4.25b). This approach allows the distinction of the basalt-hosted rubies from most rubies of metasomatic and metamorphic origin, but there is still significant overlap for the various localities. The low-V Aappaluttoq rubies still overlap with the rubies from Namahaca while the high-V rubies, as expected plot at higher V.

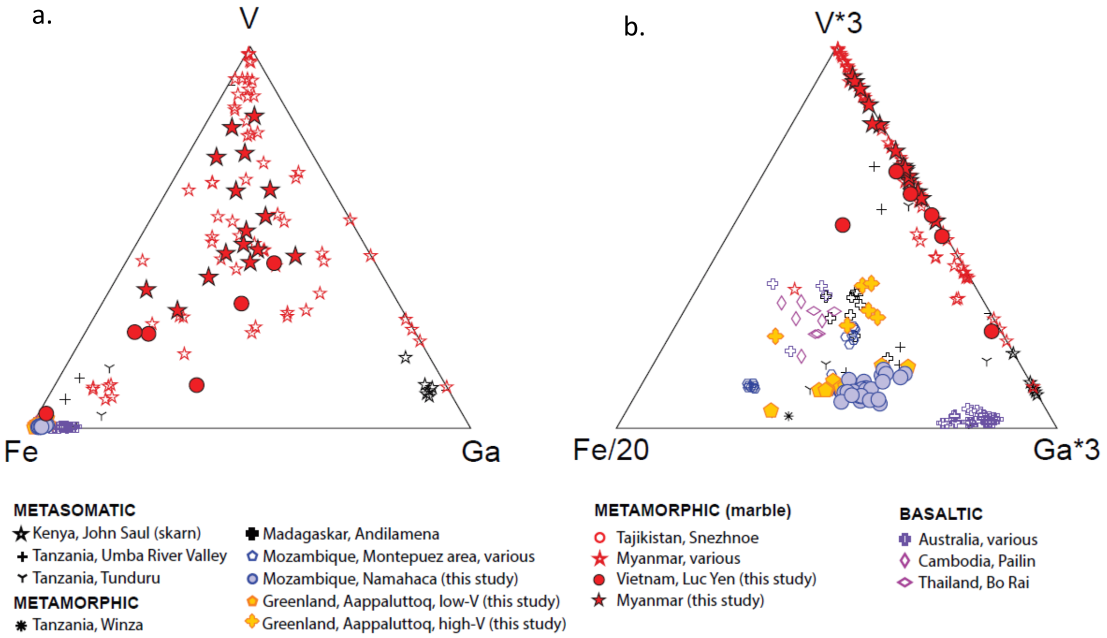

Figure 4.25: a. Triangular plot showing the ratio of the contents of Fe, V and Ga in the rubies from Aappaluttoq, Greenland, Namahaca, Mozambique, Myanmar and Luc Yen, Vietnam analysed in this study (after Muhlmeister et al., 1998) b. Triangular plot showing the ratio of the contents of Fe/20, V*3 and Ga*3 in the rubies from Aappaluttoq, Greenland, Namahaca, Mozambique, Myanmar and Luc Yen, Vietnam analysed in this study (after Smith et al., 2016, modified after Muhlmeister et al. 1998). All data plotted are LA-ICPMS values.

Combinations of the most abundant trace elements in ruby and sapphire: Fe, Cr, Ti, V and Ga, are useful in distinguishing rubies of different geological deposit types, however, this approach is not very effective in distinguishing between different localities of the same deposit type.

The broader spectrum of quantitative trace element data we were able to obtain using the ablation and measurement parameters detailed in Section 4.3.1 now makes it possible to evaluate the use of additional elements as provenance discriminators that have not been measured before. The rubies hosted in metasomatised ultramafic metamorphic rocks (Namahaca and Aappaluttoq) show a much broader spectrum of trace elements that are above limits of quantitation than the marble-hosted rubies (Myanmar and Luc Yen). The main reason for this is very likely the higher clarity of the marble-hosted rubies analysed in this study, the potential of using such low abundance elements is fairly limited, at least with the current sensitivity of the LA-ICPMS method, because the main goal of developing a geochemical fingerprint is the determination of provenance for high-quality gemstones. However, the elements Mg, Ca, Ni, Zn, and Pb are consistently above the LOQ for all rubies analysed in this study, regardless of geologic origin or clarity. Mg, Ca and Zn have proven to be ineffective as discriminators of geographic locality, at least for the deposit types and localities analysed in this study as contents between the analysed suites show significant overlap. Ni and Pb, however, show significant promise (Fig. 4.26). Both these elements show some variation between the two ruby suites of ultramafic-metamorphic origin (Namahaca and Aappaluttoq), with Ni more variable than Pb.

Surprisingly, Ni contents in the analysed marble-hosted suites overlap but Pb contents, in contrast, are clearly higher in Luc Yen samples. Hence, while Ni vs. Pb binary diagrams show good separation for the geographic localities of the samples analysed in this study, the two different geologic settings overlap.

Using binary plots of established discriminator elements such as Ti and V vs the new-found discriminators Pb and Ni can further resolve the geochemical fingerprint of the rubies and sapphires analysed. Plotting Ti vs. Pb and Ti vs. Ni still produces some overlap of the marble-hosted sample suites with those hosted in metasomatised ultramafic rocks, especially the Aappaluttoq samples, as they have higher Ti abundances than the Namahaca rubies (Fig. 4.27).

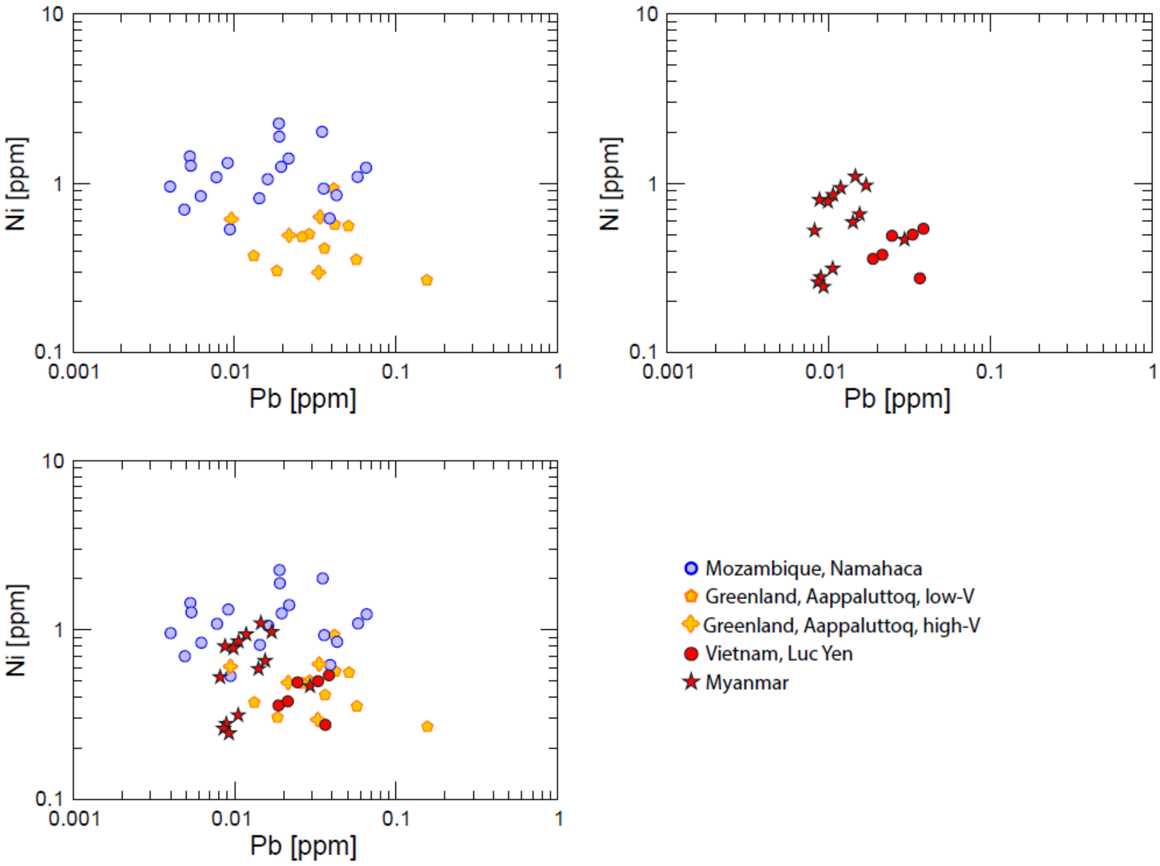

Figure 4.26: Binary plots of Ni (ppm) vs Pb (ppm) abundances in rubies from Aappaluttoq, Greenland (ultramafic-metamorphic origin), Namahaca, Mozambique (ultramafic-metamorphic origin), Myanmar (marble-hosted) and Luc Yen, Vietnam (marble-hosted) analysed in this study.

However, the geographic locations within the two different deposit types can still be resolved by plotting Ti vs Pb for the marble-hosted rubies, and by plotting Ti vs. Ni for the rubies hosted in metasomatised ultramafic rocks – this elemental combination is actually the best discriminator for these two deposits as both the Ni and Ti contents vary between them.

A binary plot of V vs. Pb is particularly useful in distinguishing between the two different localities of marble-hosted rubies as contents of both elements vary between them. This plot also shows some discriminatory power for the rubies hosted in metamorphic ultramafic rocks, although for those discrimination using V vs. Ni works better. Due to the relatively wide gap between V abundances in the marble-hosted rubies and the other ruby suites, these binary plots show distinct fields for all four different localities, showing great promise for geographical fingerprinting (Fig. 4.28).

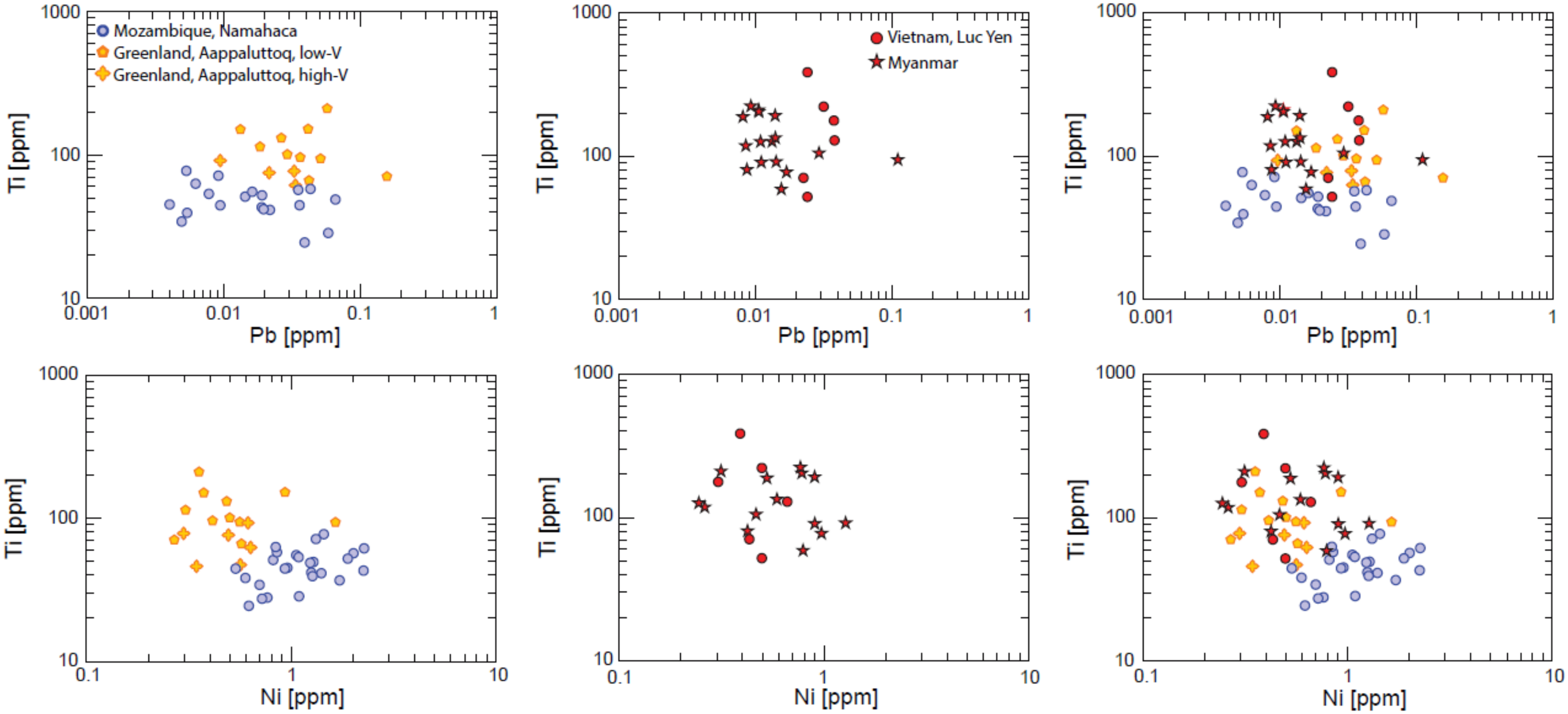

Figure 4.27: Binary plots of Ti (ppm) vs Pb (ppm) and of Ti (ppm) vs Ni (ppm) abundances for rubies from Aappaluttoq, Greenland, Namahaca, Mozambique, Myanmar and Luc Yen, Vietnam analysed in this study.

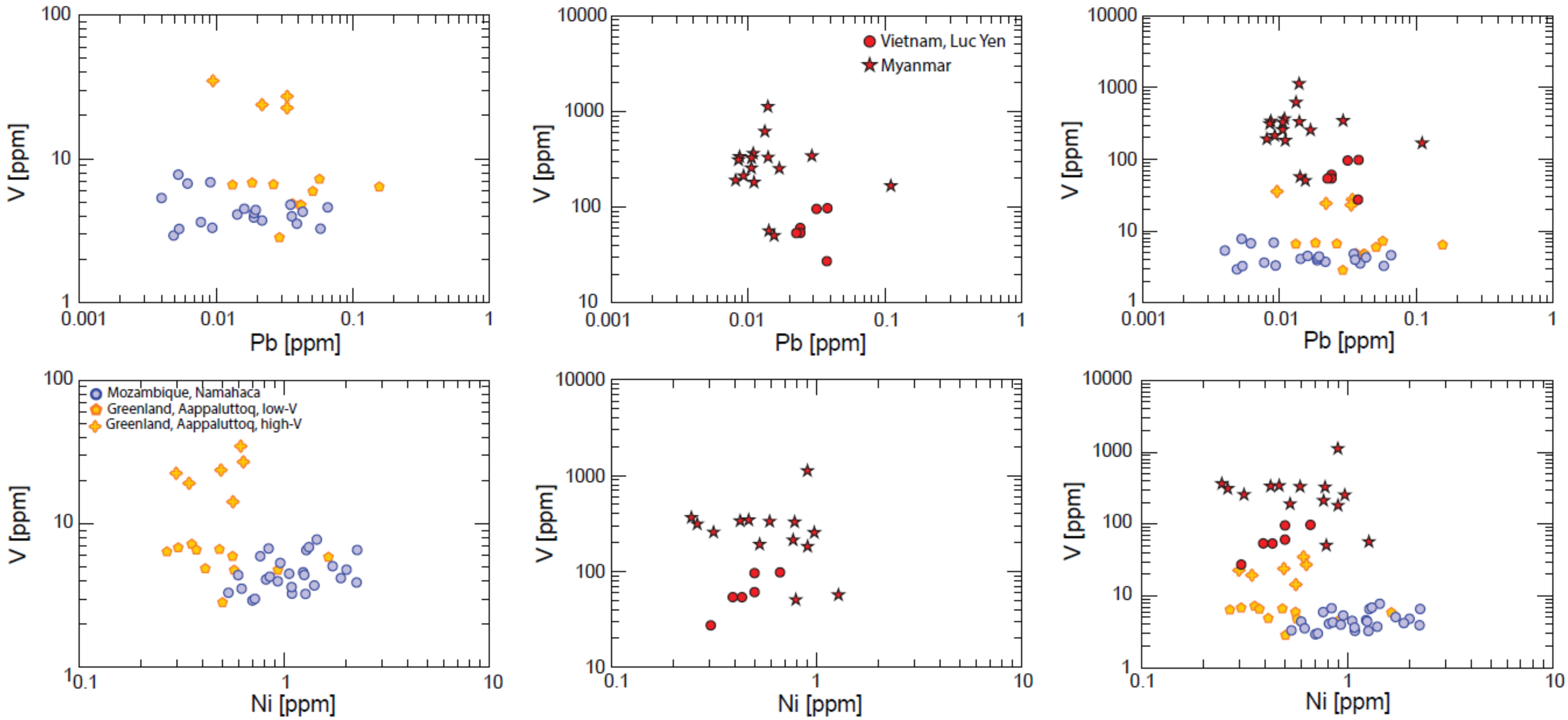

Figure 4.28: Binary plots of V (ppm) vs Pb (ppm) and of V (ppm) vs Ni (ppm) abundances for rubies from Aappaluttoq, Greenland, Namahaca, Mozambique, Myanmar and Luc Yen, Vietnam analysed in this study. All data LA-ICPMS.

Combining the two binary plots V vs Pb and V vs Ni to form a ternary Pb-V-Ni plot (Fig. 4.29) results in a ternary plot that, despite some small overlap, shows very good discriminatory power, allowing distinguishing between both different localities and different deposit types for all analysed rubies in this study.

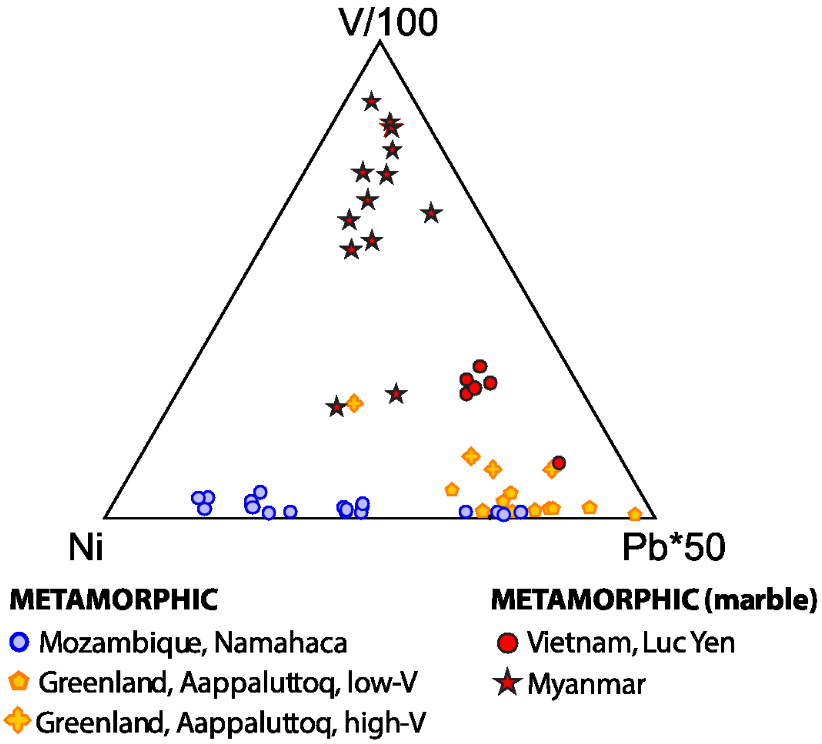

Figure 4.29: Triangular plot showing the ratio of the contents of Ni, V/100 and Pb*50 in the rubies from Aappaluttoq, Greenland, Namahaca, Mozambique, Myanmar and Luc Yen, Vietnam analysed in this study. All data plotted are LA-ICPMS values.

4.5.5.2 Radiogenic Isotopes

The Sr and Pb isotope compositions reported in this study are the first ever radiogenic isotope determinations obtained for ruby. These measurements allow us to examine the potential of using isotopic tracers to constrain geographical origin of rubies.

The two ruby suites of similar deposit type (metamorphic deposits in amphibolite and gabbro), Namahaca and Aappaluttoq, analysed in this study have clearly distinct Pb and Sr isotopic compositions due in large part to the great difference in the age of the rubies. A boxplot of measured $^{87}Sr/^{86}Sr$ ratios clearly shows that these ruby suites are distinct from each other

(Fig. 4.30a). The Namahaca rubies show a much narrower range compared to the very wide range and more radiogenic values for the Aappaluttoq rubies. In addition, although the two subpopulations at Aappaluttoq (high-V and low-V) show significant overlap, the data suggest that the high-V group has much more radiogenic Sr compositions than the low-V group. A similar trend is apparent in the Pb isotope compositions for both suites. As shown in Section 4.3, on a $^{207}Pb/^{204}Pb$ vs $^{206}Pb/^{204}Pb$ plot the Namahaca rubies define a much narrower range, to the right of the present day geochron at modest $^{207}Pb/^{204}Pb$ ratios compared to the Aappaluttoq rubies (Fig. 4.16).

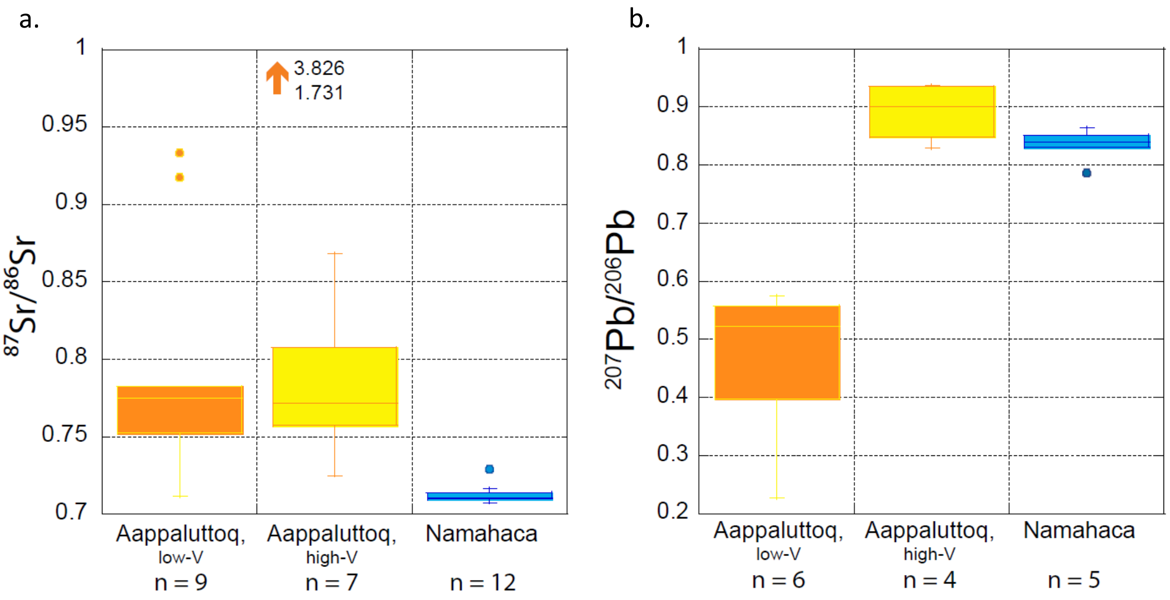

Figure 4.30: a. Boxplot displaying $^{87}Sr/^{86}Sr$ isotopic compositions of rubies from the Aappaluttoq (low-V and high-V) and Namahaca deposits measured in this study. b. Boxplot displaying $^{207}Pb/^{206}Pb$ isotopic compositions of rubies from the Aappaluttoq (low-V and high-V) and Namahaca deposits measured in this study Individual data points are outliers whose value is either: greater than UQ + 1.5 * IQD or less than LQ – 1.5 * IQD.

In addition, the two analysed rubies of the high-V group at Aappaluttoq have very unradiogenic Pb isotope compositions compared to the low-V group. This is even more clearly seen on a boxplot of measured $^{207}Pb/^{206}Pb$ ratios (Fig. 4.30b). The range in $^{207}Pb/^{206}Pb$ ratios of the high-V group overlaps with the Namahaca rubies whereas the low-V group Aappaluttoq rubies plot at much lower $^{207}Pb/^{206}Pb$ ratios. These results illustrate clearly that the rubies from the different localities from metamorphic deposits in amphibolite and gabbro are distinct from each other; however, obvious differences are also apparent between rubies of the same deposit type. In addition, it is clear that the very distinct differences in isotopic compositions are largely due to the vast difference in formation age for the Aappaluttoq and Namahaca deposits. Hence, analyses of rubies for Sr and Pb isotopes from additional localities are needed to verify the results.

As shown and discussed in Sections 4.4.2 and 4.5.3 the range in Sr isotopes of marble-hosted rubies is much narrower than those of the analysed suites of ruby from metamorphic deposits in amphibolite and gabbro. On a $^{207}Pb/^{204}Pb$ vs $^{206}Pb/^{204}Pb$ plot marble-hosted ruby plotted in a similarly narrow range to the Namahaca ruby suite but at higher $^{207}Pb/^{204}Pb$ ratios, with the Namya rubies falling on an array between the rubies from the Mandalay region (Fig. 4.16). However, the rubies from marble-hosted deposits are easily distinguished from those from metamorphic deposits in amphibolite and gabbro as shown in Section 5.5.5.1. A boxplot comparing the $^{87}Sr/^{86}Sr$ ratio obtained for the different localities in Myanmar, shows that the four rubies analysed from Namya have more radiogenic Sr isotope compositions than either of the analysed rubies from the Mandalay region (Fig. 4.31a). Similarly, a boxplot of $^{207}Pb/^{206}Pb$ ratios has the Namya rubies forming a narrow range in between the rubies from the Mandalay region (Fig. 4.31b).

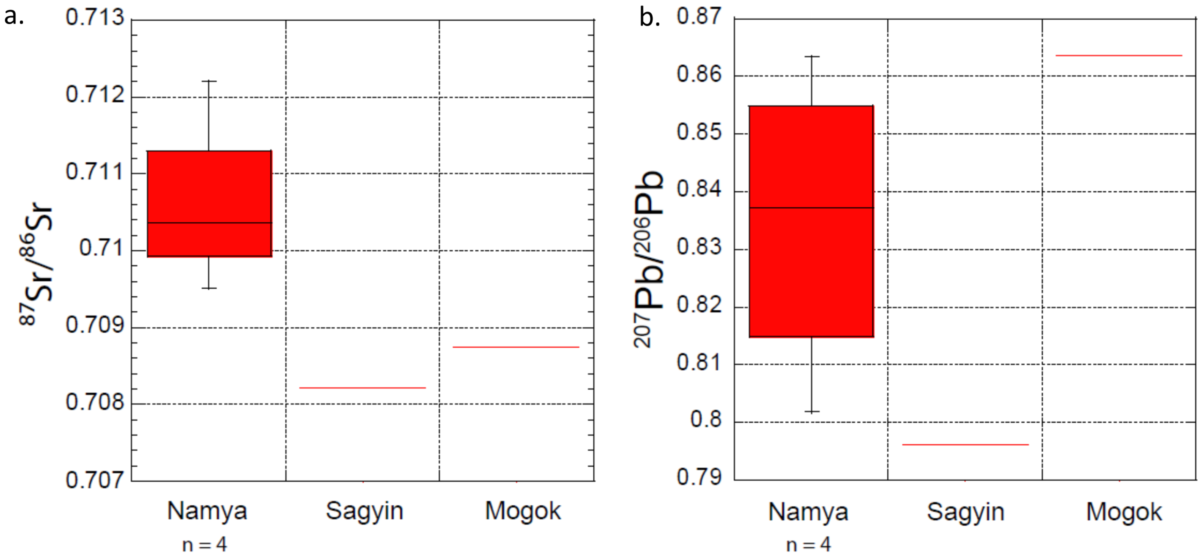

Figure 4.31: a. Boxplot displaying $^{87}Sr/^{86}Sr$ isotopic compositions of rubies from the Namya, Sagyin and Mogok areas in Myanmar measured in this study. b. Boxplot displaying $^{207}Pb/^{206}Pb$ isotopic compositions of rubies from the Namya, Sagyin and Mogok areas in Myanmar measured in this study.

Clearly the number of analyses is not sufficient to draw any firm conclusions, but the results are promising and indicate that both Sr and Pb isotopic compositions could potentially distinguish between rubies from the different localities in Myanmar, which is not possible using trace elements as shown in Section 5.5.5.1. This result requires further investigation with larger numbers of samples.

5.6 Summary and Conclusions

The use of a 193 nm laser coupled with a highly sensitive sector-field ICP mass spectrometer, and optimizing ablation parameters, allowed us to expand the very narrow range of elements that has been quantifiable in rubies to date by LA-ICPMS. Our approach yields upwards of 30 elements above LOQ in some rubies, including LREE such as La and Ce. Using an "offline" ablation followed by solution ICPMS allowed the detection and quantification of elements with even lower concentrations, such as HREE and also permits the sampling of sufficient corundum – a material normally indigestible by solution methods – to allow, for the first time, the analysis of Sr and Pb isotopic compositions in ruby. We also apply, for the first time, TOF-LA-ICPMS to map, at a 20 micron spatial scale, the trace element distribution in rubies.

With the exception of a small number of elements that can substitute for Al^{3+} in the crystal structure (e.g., Cr, Fe, V, Ti, and Ga), trace elements in ruby are likely present as mineral inclusions or as constituents in fractures, and this is confirmed by multi-elemental intensity images of rubies from the Aappaluttoq deposit, Greenland. The ubiquitous background of Ti and U in Aappaluttoq rubies seen in these multi-elemental maps, together with the broadly similar primitive mantle normalized trace element characteristics of the "online" ablation data for all four analysed locations (enrichment of HFSE over LREE, high Ta/Nb and Hf/Zr ratios and low Th/U ratios), indicates the presence of micron to sub-micron rutile inclusions that significantly influence the trace element systematics of these rubies. In addition, there is a clear correlation between the number of quantifiable trace elements and ruby clarity for the sample suites analysed by LA-ICPMS in this study. Thus, the absolute trace element abundances in rubies are primarily a function of impurity density. The larger sampling volumes of the "offline" ablation approach resulted in more varied trace element characteristics in primitive mantle normalized trace element patterns that correspond to the presence of mica, amphibole, zircon, apatite, talc and plagioclase – all minerals found as inclusions in the analysed rubies. Trace element analysis of the Aappaluttoq rubies revealed the presence of two different populations, their most notable difference being their V content. These two groups, high-V and low-V, may be derived from different host rocks.

Using a novel offline laser ablation technique followed by column chromatography and thermal ionization mass spectrometry (TIMS) we were able to precisely measure radiogenic isotope compositions in ruby for the first time.

Both the Aappaluttoq and Myanmar suites show linear trends in their Pb isotopic compositions on a ^{206}Pb/^{204}Pb vs ^{207}Pb/^{204}Pb plot. For Myanmar rubies a secondary Pb-Pb isochron age of 1302 ± 200 Ma (MSWD = 0.65) is much too old to be real, considering that their formation has been dated to ~17 – 19 Ma (Garnier et al., 2006) and 31–32 Ma (Khin Zaw et al., 2008) and this correlation most probably reflects a mixing relationship between the components that combined to form the ruby. The Aappaluttoq rubies, however, yield an isochron age of 2581 ± 53 Ma that relates well to the regional geology and their supposed formation during retrograde amphibolite facies metamorphism at about 2660 ± 20 Ma (Pidgeon and Kalsbeek, 1978). Plotting isochrones for the two subpopulations in the Aappaluttoq suite yields a Pb-Pb isochron age of 2558 ± 68 Ma for the low-V group, which is within uncertainty of the age derived from all Aappaluttoq rubies, and an older age of 3059 ± 380 Ma for the high-V group. The older age of the high-V group agrees well with the 2.9 Ga isochron age of Taylor et al. (1980) for the Fiskenæsset gneisses, indicating that the high-V group rubies may have formed earlier than the low-V group or that the low-V group may represent re-crystallisation of the high-V group rubies. These results, if reflecting ruby crystallisation or re-crystallisation, are the first ever direct ages determined on a ruby suite, independent of associated minerals and it proves either their crystallisation or re-crystallisation and re-setting of the U-Pb system in the Neoarchean.

Sr isotope compositions of the Aappaluttoq rubies span a very wide range (^{87}Sr/^{86}Sr = 0.7114 ± 22 to ^{87}Sr/^{86}Sr = 3.82595 ± 41), compared to both the Namahaca (^{87}Sr/^{86}Sr = 0.70754 ± 57 to ^{87}Sr/^{86}Sr = 0.7291 ± 26) and Myanmar (^{87}Sr/^{86}Sr = 0.70821 ± 66 to ^{87}Sr/^{86}Sr = 0.7122

± 15) suites, reflecting the very old age of the rubies (Archean) and consistent with a similarly wide range in Pb isotope compositions for (^{206}Pb/^{204}Pb = 15.89 to 56.30 and ^{207}Pb/^{204}Pb = 14.88 to 22.32). The two subpopulations at Aappaluttoq (high-V and low-V), however, show different Sr and Pb isotopic compositions. The high-V group has much more radiogenic Sr compositions than the low-V group, but much more unradiogenic Pb isotopic compositions. The Pb isotopic compositions of the Namahaca and Myanmar suites fall in much narrower ranges than the Aappaluttoq low-V suite (Namahaca: ^{206}Pb/^{204}Pb = 17.86 to 19.00 and ^{207}Pb/^{204}Pb = 15.31 to 15.57; Myanmar: ^{206}Pb/^{204}Pb =18.02 to19.75 and ^{207}Pb/^{204}Pb =15.55 to 15.68). It seems that both Rb and U were lost during either weathering or more likely, the acid leaching procedure used to clean the rubies. Hence initial isotopic ratios, corrected to the time of ruby formation are likely suspect, with the uncertainty increasing in proportion to ruby age.

The broader spectrum of quantitative trace element data we were able to obtain using the LA-ICPMS approach detailed in Section 4.3.1 now makes it possible to use more elements as potential provenance discriminators. Trace element concentrations are generally very low and only sporadically quantifiable, especially in rubies with high clarity, and, therefore, have only limited potential for geochemical fingerprinting of high-quality gemstones, at least with the current sensitivity of the LA-ICPMS method. However, a new suite of elements accessible by LA-ICPMS that are consistently above the LOQ for all rubies analysed in this study offer new discriminators with high potential. The use of binary plots of established discriminator elements such as Ti and V vs the newly found discriminators Pb and Ni are able to distinguish between the different localities of ruby suites from similar deposit type in the limited dataset analysed here. While the number of analysed samples is not high enough for statistical validation, the approach shows great promise in furthering the development of a geochemical fingerprint for ruby provenancing. A triangular plot of Ni-V/100-Pb*50 makes it possible to distinguish between both the different localities and the different deposit types for all analysed rubies in this study.

Measured ^{87}Sr/^{86}Sr and Pb isotope ratios clearly show two distinct populations for the two different localities of rubies hosted in metamorphic deposits in amphibolite and gabbro, most obviously related to their distinct ages. Combined Sr-Pb isotope systematics also discriminate successfully the two distinct populations at Aappaluttoq identified by differences in trace element characteristics (high- and low-V groups). The marble-hosted rubies likewise show differences in their $^{87}Sr/^{86}Sr$ and Pb isotope ratios. These results suggest that radiogenic isotopes potentially offer a powerful means of provenance discrimination even for geologically similar deposits. However, given the limited number of samples analysed, the analysis of a larger number of rubies from a wider variety of localities and geological deposit types is essential to test the validity and applicability for geographical origin determination.

Chapter 5

Conclusions and suggestions for future work

This thesis has contributed to the scientific knowledge on diamond and gem corundum formation, exploration and geographical origin determination.

The study of microdiamonds and macrodiamonds, originating from the same microdiamond samples, focusing on the genetic relationship among diamonds of different size, and its implication for the use of microdiamonds in diamond exploration established a general geochemical similarity of diamonds across different size fractions. As a whole, the Misery diamond suite shows high nitrogen contents (median=850 at. ppm), a bimodal distribution in time-averaged mantle residence temperatures (two distinct subpopulations in T_N; $\leq$ 1125 °C and $\geq$ 1175 °C), a high degree of platelet degradation, and $\delta^{13}C$ compositions that are isotopically slightly heavier (median=-4.4‰) than the global median. Geochemical differences indicated by statistical comparisons of the various size classes are very small in the context of the global diamond database and are viewed as petrogenetically insignificant. This reinforces the use of size-frequency analysis to predict diamond grade in kimberlite diamond deposits. Further detailed studies such as this on microdiamond samples from other locations and preferably of larger samples sizes with more diamonds, are required to evaluate this approach more extensively.

The study of fluids in high-purity gem diamonds from the Victor Mine, Ontario, as well as near-gem diamonds from peridotite and eclogite xenoliths from the Finsch and Newlands mines, South Africa strengthens the link between the parental fluids for gem and fibrous diamonds, suggesting that the fluids from which gem diamonds grow stem from the same sources as those previously documented in fibrous diamonds and undergo the same processes leading to diamond growth. This conclusion agrees with the results derived from major element analyses (Jablon and Navon, 2016). The similarity of forward modeled isotopic compositions produced from the gem-diamond forming fluids to those of subcalcic garnet diamond inclusions, also strengthens the inferences already made from fluid-rich fibrous diamonds by Klein-BenDavid et al. (2010), that diamond-forming fluids are effective metasomatic agents in the lowermost lithospheric mantle. In addition, some of these fluids provide a simple single-stage evolution for the generation of the highly unusual low ε_{Nd} and low $^{87}Sr/^{86}Sr$ systematics measured in garnets within diamonds. Moreover, differences in trace element characteristics between fluids in diamonds of different host lithologies and among fluids in diamonds of different formation ages indicate that HDFs trapped in gem diamond may be a useful tool in the determination of a diamond's provenance.

At present, the database for quantitative trace element characteristics in fluid-poor, gem diamonds is still very small. While the results indicate that distinguishable differences may exist between diamonds from different parageneses, it is necessary to analyse many more samples to effectively evaluate the trace element systematics of different diamond parageneses, i.e. peridotitic, eclogitic, lherzolitic, websteritic and ultradeep. In addition, diamond fingerprinting is only possible if distinguishable differences in trace element signatures can be found between diamonds from different mines. To do this a database sufficiently large to allow for statistical approaches is needed.

None of the partition coefficients currently available are able to produce sinusoidal REE_N patterns typical in subcalcic garnets from the Finsch diamond fluid, even though the forward modelling of the isotopes from the trace elemental fluid composition produces consistent results. This emphazises the need for studies to determine partition coeffecients of elements between diamond-forming fluid and garnet (and other minerals) in equilibrium at lithospheric mantle conditions.

This study produced the most extensive analysed trace element list acquired so far on rubies as well as the first trace element mapping. Rubies from several different localities and two different deposit types produced new insights into the nature of the trace element content of corundum. It was shown that, with the exception of a small number of elements that can substitute for Al^{3+} in the crystal structure, trace elements in ruby are present as mineral inclusions or as constituents in fractures and thus, that the absolute trace element abundances in rubies are primarily a function of inclusion/fracture density. Some spatial zonation in the nature of these impurities occurs, that mimics chemical zonation from lattice substitution, due to the small nature of the inclusions. This study also constitutes the first report of measured radiogenic isotope compositions in ruby (Sr and Pb) and the first ever direct dating of ruby formation or re-crystallization, from the Aappaluttoq Mine in SW Greenland, highlighting a new application of radiogenic isotope systems to the dating of coloured gems. Moreover, the production of the highest quality trace element data thus far obtained on rubies, allowed the identification of new provenance discriminators (Ni and Pb) with high potential to distinguish between rubies of different localities even from similar deposit types, something not possible to date using trace elements alone. In addition, measured $^{87}Sr/^{86}Sr$ and Pb isotope ratios show distinct differences for rubies from different localities and deposit types, suggesting that radiogenic isotopes potentially offer a powerful means of provenance discrimination even for geologically similar deposits.

While this study has shown that Ni and Pb have high potential as provenance discriminators to distinguish between rubies of different localities and similar deposit types the analysis of rubies from additional localities with the same geological setting is essential to provide a robust test of the discriminatory power of these systematics. In addition, rubies from different deposit types, such as migmatite or skarn-related deposits, may not be characterised by differences in Ni-Pb-V systematics but instead may yield different discriminatory element combinations that could be used to distinguish between stones from different geographic regions that have a similar geological setting. Therefore, the analysis of rubies from several different localities of similar deposit types is crucial to fully develop a trace element fingerprint for ruby provenance determination using LA-ICPMS. Similarly, to conclusively establish the potential of Sr and Pb isotopes for provenance discrimination even for geologically similar deposits, additional analyses of rubies for Sr and Pb isotopes from a variety of localities and deposit types is essential. A larger database of trace element and radiogenic isotope characteristics of rubies from different localities and geological settings will allow statistical processing of the data, such as logistic regression, to test if source discrimination of samples from unknown locations may be possible.

In addition to the analysis of rubies, the expansion of the applied methods, i.e. LA-ICPMS, TOF-LA-ICPMS and “offline” ablation followed by solution ICPMS, to include other colored stones, such as blue sapphires, emeralds, alexandrite or tsavorites may prove the approach to be more widely applicable. Ultimately, the proposed research may lead to the development of a unique, definitive, minimally-destructive fingerprinting technique for colored gemstones. One major drawback of both the LA-ICPMS and offline laser ablation methods is the fact that they are “destructive” techniques. However, the investigation of possible correlations between location or deposit specific trace element and radiogenic isotope characteristics, once established, and physical, optical and chemical features that can be detected by truly non-destructive techniques such as EDXRF, Raman or FTIR spectroscopy, could make this possible. In cases of doubt, additional trace element or radiogenic isotope analyses could be carried out.

References

Abduriyim, A., and Kitawaki, H. (2006): Applications of laser ablation-inductively coupled plasma-mass spectrometry (LA-ICP-MS) to gemology. Gems and Gemology 42, 98–118.

Akagi, T., and Masuda, A., (1988): Isotopic and elemental evidence for a relationship between kimberlite and Zaire cubic diamonds. Nature 336, 665-667.

Anderson, B. W., and Jobbins, E. A. (1990). Gem Testing. Butterworths, London.

Appel, P.W., Ghisler, M., (2014): Ruby- and sapphirine-bearing mineral occurrences in the Fiskenaesset, Nuuk and Maniitsoq Regions, West Greenland. Danmarks og Grønlands Geologiske Undersøgelse, Rapport 2014/72, 71 pp.

Armstrong, R.L., (1988): Mesozoic and early Cenozoic magmatic evolution of the Canadian Cordillera, in Clark, S.P., Burchfiel, B.C., and Suppe, J., eds., Processes in Continental Lithospheric Deformation. Special Paper-Geological Society of America 218, 55–91.

Aulbach, S., Griffin, W.L., Pearson, N.J., O'Reilly, S.Y., Kivi, K., and Doyle, B.J., (2004): Mantle formation and evolution, Slave Craton: constraints from HSE abundances and Re-Os isotope systematics of sulfide inclusions in mantle xenocrysts: Chemical Geology 208, 61-88.

Aulbach, A., Creaser. R.A., Stachel, T., Heaman, L.M., Chinn, I., Kong, J., (2018): Sulphide inclusions in diamond from Victor (Superior craton): Intra-mantle cycling of Os and volatiles (C,N,S) during plate reorganisation. Submitted to Earth and Planetary Science Letters

Banas, A., Stachel, T., Muehlenbachs, K., and McCandless, T.E., (2007): Diamonds from the Buffalo Head Hills, Alberta: formation in a non-conventional setting: Lithos 93 (1–2), 199–213.

Barley, M.E., Pickard, A.L., Khin Zaw, Rak. P., and Doyle, M.G. (2003). Jurassic to Miocene magmatism and metamorphism in the Mogok metamorphic belt and the India-Eurasia collision in Myanmar. Tectonics 22, 1019.

Barrett, J.P., and Goldsmith, L., (1976): When is n sufficiently large?: The American Statistician 30, 67–70.

Bender, F., (1983): Geology of Burma. Borntraeger, Berlin, p 293.

Bertrand, G. and Rangin, C. (2003). Tectonics of the western margin of the Shan plateau (central Myanmar): Implication for the India-Indochina oblique convergence since the Oligocene. Journal of Asian Earth Sciences 21, 1139–1157.

Bizimis, M., Salters, V.J.M., and Dawson, J.B., (2003): The brevity of carbonatite sources in the mantle: evidence from Hf isotopes. Contrib. Mineral. Petrol. 145, 281-300.

Bleeker, W., (2003): The late Archean record: puzzle in ca. 35 pieces: Lithos 71, 99–134.

Borovinskaya, O., Hattendorf, B., Tanner, M., Gschwind, S. and Günther, D., (2013). A prototype of a new inductively coupled plasma time-of-flight mass spectrometer providing temporally resolved, multi-element detection of short signals generated by single particles and droplets. Journal of Analytical Atomic Spectrometry 28(2), 226-233.

Bowring, S.A., Williams, I.S., and Compston, W., (1989b): 3.96 Ga gneisses from the Slave province, Northwest Territories, Canada: Geology 17, 971–975.

Bowring, S.A., and Williams, I.S., (1999): Priscoan (4.00-4.03 Ga) orthogneisses from northwestern Canada: Contributions to Mineralogy and Petrology 134, 3-16.

Boxer, G.L., (2004): Diamond Size Distributions: Rough Diamond Review 7, 21-24.

Boyd, F.R. and Gurney, J.J. (1986): Diamonds and the African lithosphere. Science 232, 472–477.

Boyd, S.R., Kiflawi, I. and Woods, G.S., (1994a): The Relationship between infrared-absorption and the A defect concentration in diamond. Philosophical Magazine B-Physics of Condensed Matter Statistical Mechanics Electronic Optical and Magnetic Properties 69, 1149-1153.

Boyd, S.R., Kiflawi, I., and Woods, G.S., (1995): Infrared-absorption by the B-nitrogen aggregate in diamond: Philosophical Magazine Part B 72, 351–361.

Boyd, R., Nordgulen, Ø., Thomas, R.J., Bingen, B., Bjerkgård, T., Grenne, T., Henderson, I., Melezhik, V.A., Often, M., Sandstad, J.S., Solli, A., Tveten, E., Viola, G., Key, R.M., Smith, R.A., Gonzalez, E., Hollick, L.J., Jacobs, J., Jamal, D., Motuza, G., Bauer, W., Daudi, E., Feitio, P., Manhica, V., Moniz, A., Rosse, D., (2010). The geology and geochemistry of the east african orogen in northeastern Mozambique. South African Journal of Geology 113, 87-129.

Bulanova, G.P., Wiggers de Vries, D., Pearson, D.G., Beard, A., Mikhail, S., Smelov, A.P., and Davies, G.R. (2014): Carbon recycling and polygenetic origin of eclogitic diamonds recorded by a single crystal from the Mir pipe (Yakutia). Chemical Geology 381, 40–55.

Burger, M., Schwarz, G., Gundlach-Graham, A., Käser, D., Hattendorf, B. and Günther, D., (2017). Capabilities of laser ablation inductively coupled plasma time-of-flight mass spectrometry. Journal of analytical atomic spectrometry, DOI 10.1039/C7JA00236J.

Burgess, R., Turner, G., Laurenzi, M., and Harris, J. W., (1989): ^{40}Ar/^{39}Ar laser probe dating of individual clinopyroxene inclusions in Premier eclogitic diamonds. Earth and Planetary Science Letters 94, 22–28.

Burke, W.H., Denison, R.E., Hetherington, E.A., Koepnick, R.B., Nelson, H.F. and Otto, J.B. (1982). Variation of seawater ^{87}Sr/^{86}Sr throughout Phanerozoic time. Geology 10, 516-519.

Bussweiler, Y., Borovinskaya, O., and Tanner, M., (2017). Laser Ablation and Inductively Coupled Plasma–Time-of-Flight Mass Spectrometry—A Powerful Combination for High-Speed Multi-elemental Imaging on the Micrometer Scale. Spectroscopy, 32(5), 14-20.

Calligaro, T., Poirot, J.-P., and Querre, G., (1999): Trace element fingerprinting of jewellery rubies by external beam PIXE. Nuclear Instruments and Methods in Physics Research B 150, 628 – 634.

Cartier, L.E. (2009). Ruby and sapphire from Marosely, Madagascar. The Journal of Gemmology 31 (5–8), 171 – 179.

Cartigny, P., Farquhar, J., Thomassot, E., Harris, J.W., Wing, B., Masterson, A., McKeegan, K., and Stachel, T., (2009): A mantle origin for Paleoarchean peridotitic diamonds from the Panda kimberlite, Slave Craton: evidence from 13C-, 15N- and 33,34S-stable isotope systematics: Lithos 112, 852–864.

Cartigny, P., Palot, M., Thomassot, E., and Harris, J.W., (2014): Diamond formation: A stable isotope perspective: Annual Review of the Earth and Planetary Sciences 42, 699-732.

Chapman, J.G., and Boxer, G.L., (2004): Size distribution analyses for estimating diamond grade and value: Lithos 76, 368–375.

Charlier, B.L.A., Ginibre, C., Morgan, D., Nowell, G.M., Pearson, D.G., Davidson, J.P., and Ottley, C.J., (2006). Methods for the microsampling and high-precision analysis of strontium and rubidium isotopes at single crystal scale for petrological and geochronological applications. Chem. Geol. 232, 114–133.

Chinn, I.L., Gurney, J.J., and Kyser, K.T., (1998): Diamond and mineral inclusions from NWT, Canada: 7th International Kimberlite Conference, Cape Town. Addendum, not paginated.

Clement, C.R., (1982): A comparative geological study of some major kimberlite pipes in the Northern Cape and Orange Free State. Unpublished Ph.D. thesis, University of Cape Town, Cape Town, 431 pp.

Clifford, T.N., (1966): Tectono-metallogenic units and metallogenic provinces of Africa. Earth and Planetary Science Letters, 1(6), 421-434.

Creaser, R.A., Grütter, H., Carlson, J.A., and Crawford, B., (2003): Macrocrystal phlogopite Rb–Sr dates for the Ekati property kimberlites, Slave Province, Canada: evidence for multiple intrusive episodes in the Palaeocene and Eocene: Proceedings of the 8th International Kimberlite Conference, Victoria, B.C., 61.

Creighton, S., Stachel, T., McLean, H., Muehlenbachs, K., Simonetti, A., Eichenberg, D., and Luth, R., (2008): Diamondiferous peridotitic microxenoliths from the Diavik Diamond Mine, NT: Contributions to Mineralogy and Petrology 155, 541–554.

Currie, L.A., (1968). Limits for qualitative detection and quantitative determination. Anal. Chem. 40, 586.

Currie, L.A. (1999). Detection and quantification limits: origins and historical overview. Anal. Chim. Acta 391 127–34.

Davies, R.M., Griffin, W.L., Pearson, N.J., Andrew, A.S., Doyle, B.J., and O'Reilly, S.Y., (1999): Diamonds from the deep; Pipe DO-27, Slave Craton, Canada: Proceedings of the 7th International Kimberlite Conference 1, 148–155.

Davies, R.M., Griffin, W.L., O'Reilly, S.Y., and Doyle, B.J., (2004): Mineral inclusions and geochemical characteristics of microdiamonds from the DO-27, A154, A21, A418, DO18, DD17 and Ranch Lake kimberlites at Lac de Gras, Slave Craton, Canada: Lithos 77, 39–55.

De Weerdt, F., and Collins, A.T., (2006): Optical study of the annealing behaviour of the 3107 cm−1 defect in natural diamonds: Diamond and Related Materials 15, 593-596.

Deakin, A.S., and Boxer, G.L., (1989): Argyle AK1 diamond size distribution: the use of fine diamonds to predict the occurrence of commercial sized diamonds, in Ross, J., Jaques, A.L., Ferguson, J., Green, D.H., O'Reilly, S.Y., Danchin, R.V., and Janse, A.J.A., eds., Kimberlites and Related Rocks, Geological Society of Australia, Special Publication, vol. 14. Blackwell, Carlton, 1117–1122.

Deines, P., (1980): The carbon isotopic composition of diamonds: relationship to diamond shape, color, occurrence and vapor composition. Geochimica et Cosmochimica Acta 44, 943–961.

Deines, P., Gurney, J.J., and Harris, J.W., (1984): Associated chemical and carbon isotopic composition variations in diamonds from Finch and Premier kimberlite, South Africa: Geochimica et Cosmochimica Acta 48, 325-342.

Deines, P., Harris, J.W., and Gurney, J.J., (1987): Carbon isotopic composition, nitrogen content and inclusion composition of diamonds from Roberts Victor kimberlite, South

Africa: evidence for ^{13}C depletion in the mantle: Geochimica et Cosmochimica Acta 51, 1227–1243.

Deines, P., Harris, J.W., Spear, P.M., and Gurney, J.J., (1989): Nitrogen and 13C content of Finch and Premier diamonds and their implications: Geochimica et Cosmochimica Acta 53, 1367-1378.

Deniel, C. and Pin, C. (2001). Single-stage method for the simultaneous isolation of lead and strontium from silicate samples for isotopic measurements. Anal. Chim Acta 426, 95 -104.

Dirlam, D.M., Misiorowski, E.B., Tozer, R., Stark, K.B. and Bassett, A.M. (1992). Gem wealth of Tanzania. Gems & Gemology 28, 80–102.

Dissanayake, C., Rupasinghe, M.S., (1993): A prospector's guide map to the gem deposits of Sri Lanka. Gems and Gemology 29, 173–191.

Donnelly, C.L., Stachel, T., Creighton, S., Muehlenbachs, K., and Whiteford, S., (2007): Diamonds and their mineral inclusions from the A154 South pipe, Diavik Diamond Mine, Northwest Territories, Canada: Lithos 98, 160–176.

Dufour, M.S., Kol'tsov, A.B., Zolotarev, A.A. and Kuznetsov, A.B. (2007). Corundum-Bearing Metasomatic Rocks in the Central Pamirs. Petrology 15(2), 151–167.

Eggler, D.H., and Baker, D.R., (1982): Reduced volatiles in the system C–O–H: implications for mantle melting, fluid formation and diamond genesis. In: Akimoto, S., Manghnani, M.H. (Eds.), High pressure research in geophysics. Center for Academic Publications, Tokyo, 237–250.

Elliot, T., Plank, T., Zindler, A., White, W., and Bourdon, B., (1997): Element transport from slab to volcanic front at the Mariana arc. Journal of Geophysical Research 102, 14,991-15,019.

Engvik, A. K., and Bingen, B., (2017): Granulite-facies metamorphism of the Palaeoproterozoic – early Palaeozoic gneiss domains of NE Mozambique, East African Orogen. Geological Magazine 154 (3), 491-515.

Evans, T., and Qi, Z., (1982): The kinetics of the aggregation of nitrogen atoms in diamond. Proceedings of the Royal Society of London Series A-Mathematical and Physical Sciences, 381(1780), 159-178.

Evans, T., Kiflawi, I., Luyten, W., Vantendeloo, G., and Woods, G.S., (1995): Conversion of platelets into dislocation loops and voidite formation in Type IAB diamonds. Proceedings of the Royal Society of London Series A -Mathematical and Physical Sciences, 449(1936), 295-313.

Fagan, A.J., Groves, I.D. & Carman, C. (2011): A field report into geological exploration on the True North Gems Inc. Fiskenaesset Project. Internal True North Gems Report, Vancouver, Canada.

Fagan, A.J. (2012). Geological Exploration at Tasit marluk and other gemstone deposits, SW Greenland: A field summary report. Internal True North Gems Report, Vancouver, Canada.

Fagan, A.J. and Groat, L.A. (2014). The geology of the Aappaluttoq ruby and pink sapphire deposit, SW Greenland. Geological Society of America Abstracts with Programs, 46(6), Vancouver, British Columbia, Canada, 19–22 October, 417.

Faure, G. (1986). Principles of Isotope Geology. 2nd edition, John Wiley and Sons, New York, 589 pp.

Ferguson, J., and Fielding, P. E., (1971): The origin of the colours of yellow, green and blue sapphire. Chemical Physics Letter 10, 262-265.

Ferguson, J., and Fielding, P. E., (1972): The origins of the colours of natural yellow, blue, and green sapphire. Australian Journal of Chemistry 25, 1371-1385.

Field, M., Stiefenhofer, J., Robey, J., and Kurszlaukis, S., (2008): Kimberlite-hosted diamond deposits of southern Africa: A review. Ore Geology Reviews 34, 33-75.

Fisher, D., Sibley, S.J., and Kelly, C.J., (2009): Brown colour in natural diamond and interaction between the brown related and other colour-inducing defects: Journal of Physics-Condensed Matter 21, 364213.

Fisher, R.A. (1925). Statistical Methods for Research Workers. Oliver and Boyd (Edinburgh).

Foley, S.F., (2011): A Reappraisal of Redox Melting in the Earth's Mantle as a Function of Tectonic Setting and Time. Journal of Petrology, 52(7-8), 1363-1391.

Foley, S.F., Prelević, D., Rehfeldt, T., and Jacob, D. (2013). Minor and trace elements in olivine as probes into early igneous and mantle melting processes. Earth Planet Sci Lett 363, 181–191.

Forestier, F. and Lasnier, B. (1969). Découverte de niveaux d’amphibolites à pargasite, anorthite, corindon et saphirine dans les schistes cristallins du Haut-Allier. Contrib. Mineral. Petrol. 23, 194–235.

Fraser, K.J., Hawkesworth, C.J., Erlank, A.J., Mitchell, R.H., and Scott-Smith, B.H., (1985): Sr, Nd and Pb isotope and minor element geochemistry of lamproites and kimberlites. Earth and Planetary Science Letters 76, 57-70.

Fraser. K.J., and Hawkesworth, C.J., (1992): The petrogenesis of group 2 ultrapotassic kimberlites from Finsch Mine. South Africa. Lithos 28, 327-345.

Friend, C.R.L., and Nutman, A.P. (2001): U–Pb zircon study of tectonically bounded blocks of 2940–2840 Ma crust with different metamorphic histories, Paamiut region, South-West Greenland: implications for the tectonic assembly of the North Atlantic craton. Precambrian Research 105, 143–164.

Fritsch, E., and Scarratt, K., (1993): Gemmological properties of type Ia diamonds with an unusually high hydrogen content: Journal of Gemmology 23, 451–460.

Fritsch, E., Hainschwang, T., Massi, L. and Rondeau, B., (2007): Hydrogen-related optical centers in natural diamond: An update: New Diamond and Frontier Carbon Technology 17, 63-89.

Garnier, V., Giuliani, G., Ohnenstetter, D., and Schwarz, D., (2004): Saphirs et rubis. Classification des gisements de corindon. Le Règne Minéral 55, 4–47.

Garnier, V., Ohnenstetter, D., Giuliani, G.,Maluski, H., Deloule, E., Phan Trong, T., Pham Van, L., and Hoang Quang, V. (2005). Age and significance of ruby-bearing marbles from the Red River shear zone, northern Vietnam. The Canadian Mineralogist 43, 1315–1329.

Garnier. V., Maluski, H., Giuliani, G., Ohnenstetter, D., and Schwarz, D. (2006). Ar-Ar and U-Pb ages of marble-hosted ruby deposits from central and southeast Asia. Canadian Journal of Earth Sciences 43, 509–532.

Garnier, V., Giuliani, G., Ohnenstetter, D., Fallick, A.E. Dubessy, J., Banks, D., Vinh, H.Q., Lhomme, T., Maluski, H., Pêcher, A., Bakhsh, K.A., Long, P.V., Trinh, P.T., and Schwarz, D. (2008). Marble-hosted ruby deposits from Central and Southeast Asia: Towards a new genetic model. Ore Geology Review 34, 169–191.

Gibson, S.A., Malarkey, J., and Day, J.A. (2008): Melt Depletion and Enrichment beneath the Western Kaapvaal Craton: Evidence from Finsch Peridotite Xenoliths. Journal of Petrology 49(10), 1817–1852.

Girnis, A., Bulatov, V.K., Brey, G.P., Gerdes, A., and Höfer, E.H., (2013): Trace element partitioning between mantle minerals and silicate–carbonate melts at 6–12 GPa and applications to mantle metasomatism and kimberlite genesis. Lithos 160–161, 183-200.

Giuliani, G., France-Lanord, C., Coget, P., Schwarz, D., Cheilletz, A., Branquet, Y., Giard, D., Pavel, A., Martin-Izard, A., and Piat, D.H., (1998): Oxygen isotope systematics of emerald—Relevance for its origin and geological significance. Mineralium Deposita 33, 513–519.

Giuliani, G., Fallick, A.E., Garnier, V., France-Lanord, C., Ohnenstetter, D., and Schwarz, D. (2005): Oxygen isotope composition as a tracer for the origins of rubies and sapphires. Geology 33, 249–252.

Giuliani, G., Ohnenstetter, D., Garnier, V., Fallick, A.E., Rakotondrazafy, M. and Schwarz, D. (2007). The geology and genesis of gem corundum deposits In L.A. Groat, Ed., Geology of Gem Deposits, Mineralogical Association of Canada Short Course 37, p. 23–78. Mineralogical Association of Canada, Quebec, Canada.

Giuliani, G., Fallick, A.E, Ohnenstetter, D., and Pegere, G. (2009): Oxygen isotopes of sapphire from the French Massif Central: implications for the origin of gem corundum in basaltic fields. Mineral. Deposita 44, 221–231.

Giuliani, G., Dubessy, J., Lhomme, T.H. and Ohnenstetter, D. (2012). Raman microspectrometry applied to the identification of inclusions in ruby from marble deposits in central and south-east Asia. GeoRaman 10, Nancy (June 11–13), University of Lorraine, France.

Giuliani, G., Ohnenstetter, D., Fallick, A.E., Groat, L., and Fagan, A.J. (2014). The geology and genesis of gem corundum deposits. In: Geology of Gem Deposits. 2nd Ed. MAC Short Course 44, 113-134.

Goss, J.P., Jones, R., Heggie, M.I., Ewels, C.P., Briddon, P.R. and Öberg, S., (2002): Theory of hydrogen in diamond: Physical Review B - Condensed Matter and Materials Physics 65, 115207-1-115207-13.

Goss, J.P., Ewels, C.P., Briddon, P.R., and Fritsch, E., (2011): Bistable N_2–H complexes: The first proposed structure of a H-related colour-causing defect in diamond: Diamond and Related Materials 20, 896–901.

Goss, J.P., Briddon, P.R., Hill, V., Jones, R., and Rayson, M.J., (2014): Identification of the structure of the 3107 cm^{-1} H-related defect in diamond: Journal of Physics: Condensed Matter 26, 145801-7.

Graham, I. T., Sutherland, L., Khin Zaw, Nechaev, V., and Khanchuk, A., (2008): Advances in our understanding of the gem corundum deposits of the West Pacific continental margins intraplate basaltic fields. Ore Geol. Rev. 34, 200–215.

Graham, I.T., Khin Zaw, and Cook, N.J., (2008): The genesis of gem deposits. Special Issue Ore Geology Reviews, Elsevier B.V., Amsterdam, Netherlands.

Griffin, W.L., Doyle, B.J., Ryan, C.G., Pearson, N.J., Suzanne, Y.O., Davies, R., Kivi, K., Van Achterbergh, E., and Natapov, L.M., (1999): Layered mantle lithosphere in the Lac de Gras area, Slave Craton: composition, structure and origin: Journal of Petrology 40, 705–727.

Griffin, W.L., O'Reilly, S.Y., Doyle, B.J., Pearson, N.J., Coopersmith, H., Kivi, K., Malkovets, V., and Pokhilenko, N., (2004): Lithosphere mapping beneath the north American plate: Lithos 77, 873-922.

Grütter, H.S., Apter, D.B., and Kong, J., (1999): Crust–mantle coupling: Evidence from mantle-derived xenocrystic garnets, in Gurney, J.J., Gurney, J.L., Pascoe, M.D., Richardson, S.H., eds., Proceedings of 7th International Kimberlite Conference 2 (P.H. Nixon Volume): Red Roof Design, Cape Town, South Africa, 307-313.

Grütter, H.S., (2009): Pyroxene xenocryst geotherms: Techniques and application: Lithos 112, 1167–1178.

Gulliong, M., and Günther, D. (2001): Quasi 'nondestructive' laser ablation–inductively coupled plasma–mass spectrometry fingerprinting of sapphire. Spectrochim. Acta B 56, 1219–1231.

Gurney, J.J., (1989): Diamonds, in Ross, J., ed., Kimberlites and Related Rocks, v. 1. Geological Society of Australia, Special Publication, v. 14. Blackwell Scientific Publications, Perth, 935–965.

Gurney, J.J., and Menzies, A.H., (1998): The Newlands kimberlite pipes and dyke complex. Small Mines Field Excursion guide. 7th International Kimberlite Conference. Cape Town, South Africa, 23-30.

Gurney, J.J., Hildebrand, P.R., Carlson, J.A., Fedortchouk, Y., and Dyck, D.R., (2004): The morphological characteristics of diamonds from the Ekati Property, Northwest Territories, Canada: Lithos 77, 21–38.

Gurney, J.J., Helmstaedt, H.H., Le Roex, A.P., Nowicki, T.E., Richardson, S.H., and Westerlund, K.J., (2005). Diamonds: crustal distribution and formation processes in time and space and an integrated deposit model. In: J.W. Hedenquist, J.F.H. Thompson, R.J. Goldfarb and J.P. Richards (Editors), Economic Geology 100th Anniversary Volume. Society of Economic Geologists, 143-177.

Gurney, J.J., Helmstaedt, H.H., Richardson, S.H. and Shirey, S.B., (2010): Diamonds through time. Economic Geology, 105(3): 689-712.

Haggerty, S.E., (1986): Diamond genesis in a multiply-constrained model. Nature, 320(6057), 34-38.

Haggerty, S.E., (1999): A diamond trilogy: Superplumes, supercontinents, and supernovae. Science, 285(5429), 851-860.

Harding, R.R. and Scarratt, K. (1986). A description of ruby from Nepal. J. Gemmol. 20, 3–10.

Harlou, R., Pearson, D.G., Nowell, G.M., Ottley, C.J. and Davidson, J.P. (2009). Combined Sr isotope and trace element analysis of melt inclusions at sub-ng levels using micro-milling, TIMS and ICPMS. Chem. Geol. 260**,** 254–68.

Harlow, G.E. and Bender, W. (2013). A study of ruby (corundum) compositions from the Mogok Belt: searching for chemical fringerprints. Am Mineral 98,1120–1132.

Harris, J.W., and Gurney, J.J., (1979): Inclusions in diamond. - In: J.E. FIELD (Editor), The properties of diamond. Academic Press, London, 555-591.

Harte, B., Fitzsimons, I.C.W., Harris, J.W. and Otter, M.L. (1999): Carbon isotope ratios and nitrogen abundances in relation to cathodoluminescence characteristics for some diamonds from the Kaapvaal Province, S-Africa. Mineral. Mag. 63, 829–856.

Heaman, L.M., Kjarsgaard, B.A., Creaser, R.A., Cookenboo, H.O., and Kretschmar, U., (1997): Multiple episodes of kimberlite magmatism in the Slave Province, North America: Lithoprobe Workshop Report 56, 14–17.

Heaman, L.M., Kjarsgaard, B., and Creaser, R.A., (2003): The timing of kimberlite magmatism in North America: Implications for global kimberlite genesis and diamond exploration: Lithos 71, 153-184.

Heimersson, M., and Carlson, J.A., (2013): Ekati Diamond Mine Northwest Territories, Canada NI 43-101 Technical Report: Dominion Diamond Corporation. Pdf available at http://ddcorp.ca/operations; last opened: July 1, 2014.

Hendriks, L., Gundlach-Graham, A., Hattendorf, B. and Günther, D., (2017). Characterization of a new ICP-TOFMS instrument with continuous and discrete introduction of solutions. Journal of Analytical Atomic Spectrometry 32(3), 548-561.

Herd, R., Windley, B.F. & Ghisler, M. (1969). The mode of occurrence and petrogenesis of the sapphirine-bearing and associated rocks in West Greenland. Gronlands Geol. Undersogelse, Report 24, 44.

Hofmann, A.W. (2003): Sampling mantle heterogeneity through oceanic basalts: Isotopes and trace elements. In: Carlson, R.W., Holland, H.D., and Turekian, K.K. (eds.) Treatise on Geochemistry: *The Mantle and Core,* pp. 61-101. Oxford: Elsevier-Pergamon.

Howell, D., O'Neill, C.J., Grant, K.J., Griffin, W.L., O'Reilly, S.Y., Pearson, N.J., Stern, R.A., and Stachel, T., (2012b): Platelet development in cuboid diamonds: Insights from micro-FTIR mapping: Contributions to Mineralogy and Petrology 164, 1011-1025.

Huang, H., Fryer, B. J., Polat, A., and Pan, Y. (2014). Amphibole, plagioclase and clinopyroxene geochemistry of the Archean Fiskenæsset Complex at Majorqap qâva, southwestern Greenland: Implications for Archean petrogenetic and geodynamic processes. Precambrian Research 247, 64-91.

Hughes, R. W. (1990): A Question of Origin. Gemological Digest 3 (1), 16–32.

Hughes, R.W. (1997). Burma (Myanmar) 300-343. In Ruby & Sapphire. RWH Publishing, Boulder, CO. pp. 511.

Iakoubovskii, K., and Adriaenssens, G.J., (2002): Optical characterization of natural Argyle diamonds: Diamond and Related Materials 11, 125-131.

Ionov, D.A., Griffin, W.L., and Oreilly, S.Y., (1997). Volatile-bearing minerals and lithophile trace elements in the upper mantle. Chemical Geology 141, 153-184.

Iyer, L.A.N. (1953). The geology of gem-stones of the Mogok Stone Tract, Burma. Geological map of the Mogok Stone Tract. Mem. Geol. Survey India 82.

Izraeli, E.S., Harris, J.W., and Navon, O., (2001): Brine inclusions in diamonds: a new upper mantle fluid: Earth and Planetary Science Letters 187, 323-332.

Izraeli, E.S., Harris, J.W., and Navon, O. (2004): Fluid and mineral inclusions in cloudy diamonds from Koffiefontein, South Africa: Geochimica et Cosmochimica Acta 68, 2561-2575.

Jablon, B.M. and Navon, O., (2016): Most diamonds were created equal. Earth and Planetary Science Letters 443, 41-47.

Jacob, D.E., Jagoutz, E., and Sobolev, N.V. (1998): Neodymium and strontium isotopic measurements on single subcalcic garnet grains from Yakutian kimberlites. Neues Jahrbuch Fur Mineralogie-Abhandlungen 172 (2–3), 357–379.

Janse, A.J.A., (1994): Is Clifford's Rule still valid? Affirmative examples from around the World. Diamonds: Characterization, Genesis and Exploration, 2. CPRM, Araxa, Brazil, 215-235 pp.

Johnson, C.N., Stachel, T., Muehlenbachs, K., Stern, R.A., Armstrong, J.P., and EIMF, (2012): The micro-/macro-diamond relationship: a case study from the Artemisia kimberlite (Northern Slave Craton, Canada): Lithos 148, 86–97.

Jolivet, L., Maluski, H., Beyssac, O., Goffé, B., Lepvrier, Cl., Phan Truong, T., and Nguyen Van, V., (1999). Oligocene–Miocene Bu Khang extensional gneiss dome in Vietnam: geodynamic implications. Geology 27, 67–70.

Kaminsky, F.V., and Khachatryan, G.K., (2001): Characteristics of nitrogen and other impurities in diamond, as revealed by infrared absorption data: The Canadian Mineralogist 39, 1733-1748.

Kaminsky, F., (2012): Mineralogy of the lower mantle: A review of 'super-deep' mineral inclusions in diamond. Earth-Science Reviews, 110(1-4), 127-147.

Kan-Nyunt, H.P.; Karampelas, S.; Link, K.; Thu, K.; Kiefert, L. and Hardy, P (2013). Blue sapphires from the Baw Mar Mine in Mogok. Gems Gemol. 49, 223–232.

Kane, R.E., and Kammerling, R.C., (1992). Status of ruby and sapphire mining in the Mogok Stone Tract. Gems and Gemology 28, 152–174.

Keulen, N., and Kalvig, P., (2013). Fingerprinting of corundum (ruby) from Fiskenæsset, West Greenland. Geological Survey of Denmark and Greenland Bulletin 28, 53–56.

Khin, Z., Sutherland, F.L., Graham, I.T., and McGee, B. (2008). Dating zircon inclusions in gem corundums from placer deposits, as a guide to their origin. 33rd International Geological Congress (IGC), 5–14 August, 2008, Oslo, Norway.

Khin, Z., Sutherland, L., Yui, T.F., Meffre, S., and Thu, K. (2015). Vanadium-rich ruby and sapphire within Mogok Gemfield, Myanmar: Implications for gem color and genesis. *Miner. Depos.* 50, 25-39.

Kissin, A.J. (1994). Ruby and sapphire from the Southern Ural Mountains, Russia. Gems & Gemology 30, 243–252.

Kievlenko, E.Y., (2003): Geology of Gems. Ocean Pictures Ltd, Littleton, CO, USA.

Kiflawi, I., Bruley, J., Luyten, W., and Van Tendeloo, G., (1998): “Natural” and “man-made” platelets in type-Ia diamonds: Philosophical Magazine Part B 78, 299–314.

Kirkman, T.W., (1996): Statistics to Use. http://www.physics.csbsju.edu/stats/ (03 June 2014)

Kjarsgaard, B.A., and Levinson, A.A., (2002): Diamonds in Canada: Gems and Gemology 38, 208-238.

Klein-BenDavid, O., Izraeli, E.S., Hauri, E., Navon, O., (2007): Fluid inclusions in diamonds from the Diavik mine, Canada and the evolution of diamond-forming fluids. Geochimica et Cosmochimica Acta 71, 723–744.

Klein-BenDavid, O., and Pearson, D.G., (2009): Origins of subcalcic garnets and their relation to diamond forming fluids – case studies from Ekati (NWT-Canada) and Murowa (Zimbabwe). Geochimica et Cosmochimica Acta 73(3), 837–855.

Klein-BenDavid, O., Pearson, D.G., Nowell, G.M., Ottley, C., McNeill, J.C.R., Cartigny, P. (2010): Mixed fluid sources involved in diamond growth constrained by Sr–Nd–Pb–C–N isotopes and trace elements. Earth Planet. Sci. Lett. 289, 123–133.

Klein-BenDavid, O., Pearson, D.G., Nowell, G.M., Ottley, C., McNeill, J.C.R., Logvinova, A., Sobolev, N. V., (2014): The sources and time-integrated evolution of diamond-forming fluids – Trace elements and isotopic evidence. Geochim. Cosmochim. Acta 125, 146–169.

Kolmogorov, A. N., (1933): Sulla determinazione empirica di una legge di distribuzione: Giornale dell'Istituto Italiano degli Attuari 4, 83-91.

Kochelek, K.A., McMillan,N.J., McManus, K.E., and Daniel, D.L. (2015): Provenance determination of sapphires and rubies using laser-induced breakdown spectroscopy and multivariate analysis. American Mineralogist 100, 1921–1931.

Kong, J.M., Boucher, D.R., and Scott Smith, B.H., (1999): Exploration and geology of the Attawapiskat kimberlites, James Bay Lowland, Northern Ontario, Canada. Proceedings of the 7th International Kimberlite Conference 1, Red Roof Design, Cape Town, South Africa, 452–467.

Kusky, T.M., (1989): Accretion of the Archean Slave Province: Geology 17, 63–67.

Kyaw Thu (2007): The igneous rocks of the Mogok Stone Tract: Their distribution, petrography, petrochemistry, sequence, geochronology and economic geology. Ph.D. thesis, Yangon University, Yangon, Myanmar, 139 pp.

Labrosse, S., and Jaupart, C., (2007): Thermal Evolution of the Earth: Secular Changes and Fluctuations of Plate Characteristics, Earth Planet. Sci. Lett. 260, 465-481.

Latourrette, T., Hervig, R.L., and Holloway, J.R., (1995): Trace-Element Partitioning between Amphibole, Phlogopite, and Basanite Melt. Earth and Planetary Science Letters 135, 13-30.

Leahy, K., and Taylor, W.R., (1997): The influence of the glennie domain deep structure on the diamonds in Saskatchewan kimberlites. Geologiya i Geofizika (2), 451-460.

Lee, J-H., Seo, J-K., and Park, J-W., (2006): Characterization of natural corundum (rubies and sapphires) and beryllium diffused corundum. ECS Meeting Abstracts, no. 58, 209th ECS Meeting.

Leloup, P.H., Arnaud, N., Lacassin, R., Kienast, J.R., Harrison, T.M., Phan Trong, T., Replumaz, A., and Tapponnier, P., (2001). New constraints on the structure, thermochronology, and timing of the Ailao Shan-Red River shear zone, SE Asia. Journal of Geophysical Research 106, 6683–6732.

Li, CF, Chu, ZY, Guo, JH, Li, YL, Yanga, YH and L, XH (2015). A rapid single column separation scheme for high-precision Sr–Nd–Pb isotopic analysis in geological samples using thermal ionization mass spectrometry. Anal. Methods 7, 4793.

Limtrakun P., Zaw K., Ryan C. G., and Mernagh T. P., (2001): Formation of the Denchai gem sapphires, northern Thailand: evidence from mineral chemistry and fluid/melt inclusion characteristics. Mineralogical Magazine 65, 725-735.

Link (2015). Age Determination of Zircon Inclusions in Faceted Sapphires. J. Gemmol. 34(8), 692–700.

Lockhart, G.D., Grütter, H.S., and Carlson, J.A., (2003): Temporal and geomagnetic relationships of Ekati economic kimberlites: Proceedings of the 8th International Kimberlite Conference, p. 6.

Logvinova, A.M., Taylor, L.A., Floss, C., and Sobolev, N.V., (2005): Geochemistry of multiple diamond inclusions of harzburgitic garnets as examined in situ. International Geology Review 47, 1223-1233

Ludwig, K.R., (1999): User's Manual for Isoplot/Ex, Version 2.10, A Geochronological Toolkit for Microsoft Excel. Berkeley Geochronology Center Special Publication, no. 1a.

Ludwig, K.R., (2003): User's Manual for Isoplot/Ex 3.00: A Geochronological Toolkit for Microsoft Excel, Berkeley Geochronological Center Special, Publication 4.

Luth, R.W., (1993): Diamonds, eclogites, and the oxidation state of the Earth's mantle. Science 261, 66-68.

Luth, R.W., and Stachel, T., (2014): The buffering capacity of lithospheric mantle: implications for diamond formation. Contributions to Mineralogy and Petrology 168, 1083.

Malkovets, V.G., Griffin, W.l., O'Reilly, S.Y., and Wood, B.J., (2007): Diamond, subcalcic garnet, and mantle metasomatism: kimberlite sampling patterns define the link: Geology 35, 339–342.

Masun, K.M., Doyle, B.J., Ball, S. and Walker, S., (2004): The geology and mineralogy of the Anuri kimberlite, Nunavut, Canada: Lithos 76, 75–97.

McCandless, T.E., (1989): Microdiamonds from the Sloan 1 and 2 kimberlites, Colorado, USA: 28th International Geological Congress, Extended Abstracts, Workshop on Diamonds, 44-46.

McCandless, T.E., Waldman, M.A., and Gurney, J.J., (1994): Macrodiamonds and microdiamonds from Murfreesboro lamproites, Arkansas: morphology, mineral inclusions, and carbon isotope geochemistry, in Meyer, H.O.A., and Leonardos, O.H., Eds., Proceedings of the Fifth International Kimberlite Conference 2, 78–97.

McCandless, T.E., and Gurney, J.J., (1995): Microdiamonds from kimberlites and lamproites: observations and ideas concerning their origin: Extended Abstracts 6th Kimberlite Conference, Siberian Branch, Russian Academy od Sciences, Novosibirsk, Siberia, 368-370.

McDade, P., and Harris, J.W., (1999): Syngenetic inclusion bearing diamonds from Letseng-la-Terai, Lesotho, in Gurney, J.J., Gurney, J.L., Pascoe, M.D., Richardson, S.H., eds., Proceedings of 7th International Kimberlite Conference, v. 2 (P.H. Nixon Volume). Red Roof Design, Cape Town, 557–565.

McKenzie, D., and O'Nions, R.K., (1991). Partial melt distributions from inversion of rare Earth element concentrations. Journal of Petrology 32, 1021-1091.

McNeill, J., Pearson, D.G., Klein-Bendavid, O., Nowell, G.M., Ottley, C.J., and Chinn, I., (2009): Quantitative analysis of trace element concentrations in some gem-quality diamonds. J. Phys. Condens. Matter 21, 364207.

McNeill, J.C.R., (2011): New techniques for trace element and radiogenic isotope measurment of 990 diamonds: their application to diamond petrogenesis and source tracing. Durham theses, Durham University. Available at Durham E-Theses Online: http://etheses.dur.ac.uk/713/

Melton, G.L., McNeill, J., Stachel, T., Pearson, D.G. and Harris, J.W., (2012): Trace elements in gem diamond from Akwatia, Ghana and DeBeers Pool, South Africa. Chemical Geology 314-317.

Melton, G.L., Stachel, T., Stern, R.A., Carlson, J., and Harris, J.W., (2013): Infrared spectral and carbon isotopic characteristics of micro- and macro-diamonds from the Panda kimberlite (Central Slave Craton, Canada): Lithos 177, 110-119.

Melton, G.L., (2013): Elemental impurities, defects and carbon isotopes in mantle diamond: Unpublished Ph.D. thesis, Edmonton, Canada, The University of Alberta, p. 168.

Mendelssohn, M.J., and Milledge, H.J., (1995): Geologically significant information from routine analysis of the mid-infrared spectra of diamonds: International Geology Review 37, 95–110.

Mendis, D., Rupasinghe, M.S., Dissanayake, C.B., (1993): Application of structural geology in the exploration for residual gem deposits of Sri Lanka. Bulletin of the Geological Society of Finland 65, 31–40.

Menzies, A.H., Milledge, H.J., and Gurney, J.J., (1998): Fourier transform infrared (FTIR) spectroscopy of Newlands diamonds. In Seventh Int. Kimberlite Conf. (Cape Town), Extended Abstr., 576-578.

Menzies, A.H., Carlson, R.W., Shirey, S.B., and Gurney, J.J., (2003): Re–Os systematics of diamond-bearing eclogites from the Newlands kimberlite. Lithos 71, 323–336.

Menzies, A., Westerlund, K., Grütter, H., Gurney, J., Carlson, J., Fung, A., and Nowicki, T., (2004): Peridotitic mantle xenoliths from kimberlites on the Ekati Diamond Mine property, N.W.T., Canada: major element compositions and implications for the lithosphere beneath the Central Slave Craton: Lithos 77, 395–412.

Mitchell, A.H.G., Ausa, C.A., Deiparine, L., Hlaing, T., Htay, N. and Khine, A. (2004). The Modi Taung–Nankwe gold district, Slate belt, central Myanmar: mesothermal veins in aMesozoic orogen. JAsian Earth Sci 23, 321–341.

Mitchell, A.H.G., Htay, M.T., Htun, K.M., Win, M.N., Oo, T. and Hlaing, T. (2007). Rock relationships in the Mogok metamorphic belt, Takon to Mandalay, central Myanmar. J Asian Earth Sci 29, 891–910.

Moorbath, S., and Pankhurst, R. J., (1976): Further rubidium–strontium age and isotope evidence for the nature of the late Archaean plutonic event in West Greenland. Nature 262, 124–126.

Moore, R.O., and Gurney, J.J., (1985): Pyroxene solid solution in garnets included in diamond: Nature 318, 553–555.

Moore, R.O., and Gurney, J.J., (1989): Mineral inclusions in diamond from the Monastery kimberlite, South Africa, in Ross, J. ed., Kimberlites and Related Rocks, v. 2. Geological Society of Australia, Special Publication, v. 14. Blackwell Scientific Publications, Perth, 1029–1041.

Muhlmeister, S., Fritsch, E., Shigley, J.E., Devouard, B., and Laurs, B.M. (1998): Separating natural and synthetic rubies on the basis of trace element chemistry. Gems & Gemology 34, 80–101.

Murphy, D.T., Kamber, B.S., and Collerson, K.D. (2002). A Refined Solution to the First Terrestrial Pb-isotope Paradox. Journal of Petrology 44(1), 39-53.

Navon, O., Hutcheon, I., Rossman, G., and Wasserburg, G., (1988): Mantle-derived fluids in diamond micro-inclusions. Nature 335, 784–789.

Navon, O., (1999): Diamond formation in the Earth's mantle. In: Gurney, J.J., Gurney, J.L., Pascoe, M.D., Richardson, S.H. (Eds.), Proceedings of the 7th International Kimberlite Conference, vol. 2. Red Roof Design, Cape Town, 584–604.

Nicollet, C. (1986): Saphirine et staurotide riche en magnésium et chrome dans les amphibolites et anorthosites à corindon du Vohibory Sud, Madagascar. Bull. Minéral. 109, 599–612.

Nixon, P-H., (1987): Mantle Xenoliths. John Wiley and sons, Chichester, p. 844.

Nowicki, T., Crawford, B., Dyck, D., Carlson, J., McElroy, R., Oshust, P., and Helmstaedt, H., (2004): The geology of kimberlite pipes of the Ekati property, Northwest Territories, Canada: Lithos 76, 1–27.

Olivieri, A.C., Faber, N.M., Ferré, J., Boqué, R., Kalivas, J.H. and Mark, H. (2006). Uncertainty estimation and figures of merit for multivariate calibration. Pure Appl. Chem. 78 633–61.

Orlov, Y.L., (1977): The Mineralogy of the Diamond. John Wiley & Sons, Inc., Toronto.

Otter, M.L., and Gurney, J.J., (1989): Mineral inclusions in diamonds from the Sloan diatremes, Colorado-Wyoming State Line kimberlite district, North America, in, Ross, J., ed., Kimberlites and Related Rocks, v. 2. Geological Society of Australia, Special Publication, v. 14. Blackwell Scientific Publications, Perth, 1042–1053.

Paton, C., Hellstrom, J., Paul, B., Woodhead, J. and Hergt, J. (2011). Iolite: freeware for the visualisation and processing of mass spectrometric data. J Anal At Spectrom 26, 2508–2518.

Pattison, D.R.M., and Levinson, A.A., (1995): Are euhedral microdiamonds formed during ascent and decompression of kimberlite magma? Implications of use of microdiamonds in diamond grade estimation: Applied Geochemistry 10, 725–738.

Pardieu, V., Jacquat, S., Bryl, L.P. and Senoble, J.B (2009): Rubies from northern Mozambique. InColor 12, 32–36.

Pardieu, V., Sangsawong, S., Muyal, J., Chauviré, B., Massi, L., and Sturman, N. (2013). Rubies from the Montepuez area (Mozambique). GIA Report, Bangok laboratory, https://www.gia.edu/doc/GIA_Ruby_Montepuez_Mozambique.pdf

Pearson, D.G., Carlson, R.W., Shirey, S.B., Boyd, F.R., and Nixon, P.H., (1995a): Stabilization of archean lithospheric mantle—a Re–Os isotope study of peridotite xenoliths from the Kaapvaal craton. Earth Planet. Sci. Lett. 134 (3–4), 341–357.

Pearson, D.G., Shirey, S.B., Carlson, R.W., Boyd, F.R., Pokhilenko, N.P., and Shimizu, N. (1995b): Re–Os, Sm–Nd, and Rb–Sr isotope evidence for thick archean lithospheric mantle beneath the Siberian Craton modified by multistage metasomatism. Geochim. Cosmochim. Acta 59 (5), 959–977.

Pearson, D.G., Shirey, S.B., Harris, J.W., and Carlson, R.W., (1998): Sulphide inclusions in diamonds from the Koffiefontein kimberlite, S Africa: constraints on diamond ages and mantle Re-Os systematics. Earth Planet Sci Lett 160, 311-326.

Pearson, D.G., Shirey, S.B., Bulanova, G.P., Carlson, R.W., and Milledge, J., (1999): Dating and paragenetic distinction of diamonds using the Re-Os isotope system: Application to some Siberian diamonds. In Gurney, J.J., Gurney, J.L., Pascoe, M.D., and Richardson, S.H., eds., Proceedings of the 7th International Kimberlite Conference, Vol. 2, P.H. Nixon Volume: Cape Town, 637–643.

Pearson, D.G., and Shirey, S.B., (1999): Isotopic dating of diamonds. SEG Reviews in Econ. Geol. 9, 143–171.

Pearson D.G., Canil D.C., and Shirey, S.B., (2003): Mantle samples included in volcanic rocks: xenoliths and diamonds. In *Treatise on Geochemistry*, vol. 2, Elsevier, 171–275.

Peretti, A., Peretti, F., Kanpraphai, A., Bieri, W., Hametner, C. & Günther, D. (2008). Winza rubies identified. Contrib. Gemol. **7**, 1–97.

Pettke, T., Oberli, F., Audetat, A., Guillong, M., Simon, A., Hanley, J., and Klemm, L.M. (2012). Recent developments in element concentration and isotope ratio analysis of individual fluid inclusions by laser ablation single and multiple collector ICP–MS. Ore Geology Reviews 44, 10-38.

Phillips, D., Onstott, T. C., and Harris, J. W., (1989): 40Ar/39Ar laser-probe dating of diamond inclusions from the Premier kimberlite. Nature 340, 460–462.

Pidgeon, R.T., Kalsbeek, F., (1978). Dating of igneous and metamorphic events in the Fiskenæsset region of southern West Greenland. Can. J. Earth Sci. 15, 2021–2025.

Polat, A., Frei, R., Scherstén, A. and Appel, P.W.U., (2010). New age (ca. 2970 Ma), mantle source composition and geodynamic constraints on the Archean Fiskenæsset anorthosite complex, SW Greenland. Chemical Geology **277**(1–2), 1–20.

Pollack, H.N. and Chapman, D.S., (1977): On the regional variation of heat flow, geotherms, and lithospheric thickness. Tectonophysics 38, 279-296.

Pornwilard, M.M.; Hansawek, R.; Shiowatana, J., and Siripinyanond, A. (2011). Geographical origin of gem corundum using elemental fingerprinting analysis by laser ablation inductively coupled plasma mass spectrometry. Int. J. Mass Spectr. 306, 57–62.

Rankin, A.H., Greenwood, J., and Hargreaves, D., (2003): Chemical fingerprinting of some East African gem rubies by Laser Ablation ICP-MS. The Journal of Gemmology 28, 473–482.

Rege, S., Jackson, S., Griffin, W.L., Davies, R.M., Pearson, N.J., and O'Reilly, S.Y., (2005): Quantitative trace-element analysis of diamond by laser ablation inductively coupled plasma mass spectrometry: Journal of Analytical Atomic Spectrometry 20, 601-611.

Rege, S., Griffin, W.L., Pearson, N.J., Araujo, D., Zedgenizov, D., and O'Reilly, S.Y., (2010): Trace-element patterns of fibrous and monocrystalline diamonds: Insights into mantle fluids: Lithos 118, 313-337.

Reggin, L. and Chow, J., (2011). Pre-Feasibility Report on the Aappaluttoq Ruby Project, Greenland. True North Gems, Vancouver, British Columbia, Canada, 164 pp., www. truenorthgems.com/wp-content/uploads/2015/05/True_
orth_Gems_2011_PFS_Report_2.pdf.

Reggin, L. and Horan, M. (2015). An Updated Pre-Feasibility Report on the Aappaluttoq Ruby Project, Greenland— National Instrument 43-101 Technical Report. True North Gems, Vancouver, British Columbia, Canada, 170 pp., www.truenorthgems.com/wp-content/uploads/2015/05/ Aappaluttoq-PFS-report-2015.pdf.

Richardson, S.H., Gurney, J.J., Erlank, A.J. and Harris, J.W., (1984): Origin of diamonds in old enriched mantle. Nature, 310(5974), 198-202.

Richardson, S.H., (1986): Latter-day origin of diamonds of eclogitic paragenesis. Nature 322, 623–626.

Richardson, S.H., Erlank, A.J., Harris, J.W., and Hart, S.R., (1990): Eclogitic diamonds from of Proterozoic age from Cretaceous kimberlites. Nature 346, 54–56.

Richardson, S.H., Harris, J.W., and Gurney, J J., (1993): Three generations of diamonds from old continental mantle. Nature 366, 256–258.

Richardson, S.H., and Harris, J.W., (1997): Antiquity of peridotitic diamonds from the Siberian craton. Earth and Planetary Science Letters 151 (3–4), 271-277.

Rohtert, W. and Ritchie, M. (2006). Three parageneses of ruby and pink sapphire discovered at Fiskenæsset, Greenland. Gems & Gemology 42, 149–150.

Rombouts, L., (1995): Sampling and statistical evaluation of diamond deposits: Journal of Geochemical Exploration 53, 351-367.

Rombouts, L., (1997): Distribution size and value of diamonds in kimberlites and lambproites: Russian Geology and Geophysics 38, 599–611.

Rombouts, L., (1999): Extreme Value Analysis of Diamond Sizes and Values, in Gurney, J.J., Gurney, J.L., Pascoe, M.D., Richardson, S.H., eds., Proceedings of 7th International Kimberlite Conference, v. 2 (P.H. Nixon Volume). Red Roof Design, Cape Town, 721–727.

Rondeau, B., Fritsch, E., Guiraud, M., Chalain, J.P., and Notari, F., (2004): Three historical 'asteriated' hydrogen-rich diamonds: Growth history and sector-dependent impurity incorporation: Diamond and Related Materials 13, 1658-1673.

Rosenhauer, M., Woermann, E., Knecht, B., and Ulmer, C.G., (1977): The stability of graphite and diamond as a function of the oxygen fugacity in themantle. 2nd International Kimberlite Conference, Santa Fe, p. 297.

Rudnick, R. L., and Goldstein, S.L. (1990). The Pb isotopic compositions of lower crustal xenoliths and the evolution of lower crustal Pb. Earth and Planetary Science Letters 98, 192-207.

Rudnick, R.L. and Nyblade, A.A. (1999): The thickness and heat production of Archean lithosphere: constraints from xenolith thermobarometry and surface heat flow. In Mantle Petrology: Field Observations and High Pressure Experimentation: A tribute to Francis R. (Joe) Boyd (Y. Fei, C.M. Bertka & B.O. Mysen, eds.), The Geochemical Society, Houston, 3–12.

Saminpanya, S., Manning, D.A.C., Droop, G.T.R., and Henderson, C.M.B. (2003). Trace elements in Thai gem corundums. Journal of Gemmology 28, 399–415.

Sarkar, C., Heaman, L.M., and Pearson, D.G., (2015a): Duration and periodicity of kimberlite volcanic activity in the Lac de Gras kimberlite field, Canada and some recommendations for kimberlite geochronology: Lithos 218–219, 155–166.

Sarkar, C., Pearson, D.G., Heaman, L.M. and Woodland, S.J. (2015b): Precise Pb isotope ratio determination of picogram-size samples: A comparison between multiple Faraday collectors equipped with 10^{12} Ω amplifiers and multiple ion counters. Chemical Geology 395, 27–40.

Sambridge, M. S., and Compston, W., (1994): Mixture modelling of multi-component data sets with application to ion-probe zircon ages: Earth and Planetary Science Letters 128, 373-390.

Satterthwaite, F. E., (1946): An approximate distribution of estimates of variance components: Biometrics Bulletin 2, 110–114.

Schaeffer, A.J., and Lebedev, S., (2014): Imaging the North American continent using waveform inversion of global and USArray data. Earth and Planetary Science Letters 402, 26-41.

Schmetzer, K., and Bank, H., (1980): Explanations of the absorption spectra of natural and synthetic Fe- and Ti-containing corundums. Neues Jahrbuch für Mineralogie - Abhandlungen 139, 216-225.

Schmetzer, K., and Bank, H., (1981): The color of natural corundum. Neues Jahrbuch für Mineralogie - Monatshefte 2, 59-68.

Schrauder, M., Koeberl, C., and Navon, O., (1996): Trace element analyses of fluidbearing diamonds from Jwaneng, Botswana: Geochimica et Cosmochimica Acta 60, 4711-4724.

Schreiber, H.D., Lauer, H.V. and Thitinant, T., (1980): The redox state of Ce in basaltic magmas: An experimental study of iron-cerium interaction in silicate melts. Geochim. Cosmochim. Acta 44, 1599-1612.

Schwarz, D., Pardieu, V., Saul, J.M., Schmetzer, K., Laurs, B., Giuliani, G., Klemm, L., Malsy, A.K., Erel, E., Hauzenberger. C., Du Toit, G., Fallick, A.E., Ohnenstetter, D., (2008). Rubies and sapphires from Winza, central Tanzania. Gems & Gemology 44(4), 322–347.

Searle, M.P., Noble, S.R., Cottle, J.M., Waters, D.J., Mitchell, A.H.G., Hlaing, T., and Horstwood, M.S.A. (2007). Tectonic evolution of the Mogok metamorphic belt, Burma (Myanmar) constrained by U-Th-Pb dating of metamorphic and magmatic rocks. Tectonics 26, TC 3014.

Shimizu, N., and Sobolev, N.V., (1995): Young peridotitic diamonds from the Mir kimberlite pipe. Nature 375, 394–397.

Shiryaev, A.A., Izraeli, E.S., Hauri, E.H., Zakharchenko, O.D., and Navon, O., (2005): Chemical, optical and isotopic investigation of fibrous diamonds from Brazil. Russ. Geol. Geophys.46, 1185–1201.

Shirey, S.B., Cartigny, P., Frost, D.J., Keshav, S., Nestola, F., Nimis, P., Pearson, D.G., Sobolev, N.V., Walter, M.J., (2013): Diamonds and the geology of mantle carbon. Reviews in Mineralogy and Geochemistry 75(1), 355–421.

Shu, Q., and Brey, G.P., (2015): Ancient mantle metasomatism recorded in subcalcic garnet xenocrysts: Temporal links between mantle metasomatism, diamond growth and crustal tectonomagmatism. Earth and Planetary Science Letters 418, 27-39.

Simonet, C., Fritsch, E., and Lasnier, B., (2008): A classification of gem corundum deposits aimed towards gem exploration. Ore Geology Reviews 34, 127-133.

Smirnov, N. V., (1948): Table for estimating the goodness of fit of empirical distributions: Annals of Mathematical Statistics 19, 279-281.

Smirnov, N. V., (1939): Estimates of Deviation between Empirical Distribution Functions in Two Independent Samples: Bulletin Moscow University 2, 3-16.

Smit, K. V., Stachel, T., Creaser, R. A., Ickert, R. B., DuFrane, S. A., Stern, R. A., and Seller, M., (2014): Origin of eclogite and pyroxenite xenoliths from the Victor kimberlite, Canada, and implications for Superior craton formation. Geochimica et Cosmochimica Acta 25, 308-337.

Smit, K.V., Shirey, S.B. and Wang, W., (2016): Type Ib diamond formation and preservation in the West African lithospheric mantle: Re–Os age constraints from sulphide inclusions in Zimmi diamonds. Precambrian Research 286, 152-166.

Smith, C.B., (1983): Pb, Sr, and Nd isotopic evidence for sources of African kimberlite. Nature 304, 51–54.

Smith, C.B., Gurney, J. J., Skinner, E. M. W., Clement, C. R. & Ebrahim, N., (1985): Geochemical character of southern African kimberlites: a new approach based on isotopic constraints. Transactions of the Geological Society of South Africa 88, 267-280.

Smith, C.B., Gurney, J.J., Harris, J.W., Otter, M.L., Kirkley, M.B., and Jagoutz, E., (1991): Neodymium and strontium isotope systematics of eclogite and websterite paragenesis inclusions from single diamonds, Finsch and Kimberley Pool, RSA. Geochimica et Cosmochimica Acta 55, 2579–2590.

Smith, C.P., Fagan, A.J. and Clark, B., (2016): Ruby and Pink Sapphire from Aappaluttoq, Greenland. The Journal of Gemmology 35(4), 294-306.

Smith, E.M., Kopylova M. G., Nowell G. M., Pearson D. G., and Ryder J., (2012): Archean mantle fluids preserved in fibrous diamonds from Wawa, Superior craton. Geology 40, 1071 - 1046.

Sobolev, E.V., Lenskaya, S.V., and Lisoivan, V.I., (1968): Lamellar formations in the structure of natural diamonds: Journal of Structural Chemistry 9, 917–920.

Sobolev, N.V., Logvinova, A.M., Zedgenizov, D.A., Seryotkin, Y.V., Yefimova, E.S., Floss, C., and Taylor, L.A., (2004): Mineral inclusions in microdiamonds and macrodiamonds from kimberlites of Yakuta: a comparative study: Lithos 77, 225–242.

Sorokina, E.S., Litvinenko, A.K., Hofmeister, W., Häger, T., Jacob, D.E. and Nasriddinov, Z.Z. (2015): Rubies and Sapphires from Snezhnoe, Tajikistan. Gems & Gemology 51(2), 160–175.

Spetsius, Z.V., and Taylor, L.A., (2002): Partial Melting in Mantle Eclogite Xenoliths: Connections with Diamond Paragenesis. International Geology Review 44(11), 973-987.

Stacey, J.S. and Kramers, J.D. (1975). Approximation of Terrestrial Lead Isotope Evolution by a 2-Stage Model. Earth and Planetary Science Letters 26(2), 207-221.

Stachel, T., and Harris, J.W., (1997a): Syngenetic inclusions in diamond from the Birim field (Ghana)—a deep peridotitic profile with a history of depletion and re-enrichment. Contributions to Mineralogy and Petrology 127, 336–352.

Stachel, T., and Harris, J.W., (1997b): Diamond precipitation and mantle metasomatism − evidence from the trace element chemistry of silicate inclusions in diamonds from Akwatia, Ghana. Contributions to Mineralogy and Petrology 129(2-3), 143-154.

Stachel, T., Harris, J.W., and Brey, G.P., (1999): REE patterns of peridotitic and eclogitic inclusions in diamonds from Mwadui (Tanzania). In: Gurney, J.J., Gurney, J.L., Pascoe, M.D., Richardson, S.H. (Eds.), The P.H. Nixon Volume, Proceedings of the VIIth International Kimberlite Conference. Red Roof Design, Cape Town, 829–835.

Stachel, T., Harris, J.W., Tappert, R., and Brey, G.P., (2003): Peridotitic diamonds from the Slave and the Kaapvaal cratons — similarities and differences based on a preliminary data set: Lithos 71, 489–503.

Stachel, T., Viljoen, K.S., McDade, P., abd Harris, J.W. (2004): Diamondiferous lithospheric roots along the western margin of the Kalahari Craton—the peridotitic inclusion suite in diamonds from Orapa and Jwaneng. Contrib. Mineral. Petrol. 147(1), 32–47.

Stachel, T., Brey, G., and Harris, J.W., (2005): Inlcusions in sublithospheric diamonds: glimpses of deep earth. Elements 1, 73-78.

Stachel, T. and Harris, J.W., (2008): The origin of cratonic diamonds - Constraints from mineral inclusions. Ore Geology Reviews 34(1-2), 5-32.

Stachel, T., and Harris, J.W., (2009): Formation of diamond in the Earth's mantle. J Phys Condens Mat 2, 364206.

Stachel, T., Harris, J.W., and Muehlenbachs, K., (2009): Sources of carbon in inclusion bearing diamonds. Lithos 112 (S2), 625–637.

Stachel, T., (2014): Diamond. In: Groat L.A. (Ed.), Geology of Gem Deposits. Second Edition. Mineralogical Association of Canada Short Course 44, Tucson AZ, 1-28.

Stachel, T., and Luth, R.W., (2015): Diamond formation — Where, when and how? Lithos 220–223, 200–220.

Stachel, T., Banas, A., Aulbach, S., Smit, K.V., Wescott, P., Chinn, I., Fisher, D. and Kong, J., (2017): The Victor Diamond Mine (Superior Craton, Canada) – A new paradigm for exploration in unconventional settings. Extended abstracts of the 11th IKC, 11IKC-4453.

Stern, R.A, Palot, M., Howell, D., Stachel, T., Pearson, D.G., Cartigny, P., and Oh, A., (2014): Methods and reference materials for SIMS diamond C- and N-isotope analysis. Canadian Centre for Isotopic Microanalysis, Research Report 14-01: University of Alberta, Education and Research Archive. http://hdl.handle.net/10402/era.38738

Stern, R.J., Tsujimori, T., Harlow, G., and Groat, L., (2013): Plate tectonic gemstones. Geology 41(7), 723-726.

Stubley, M., (2004): Spatial distribution of kimberlite in the Slave craton: a geometrical approach: Lithos 77, 683–693.

Sunagawa, I., (1984): Morphology of natural and synthetic diamond crystals. In Materials science of the Earth's interior, (I. Sunagawa, ed.), Terra Scientific, Tokyo, 303–330.

Sutherland, F.L., Hoskin, P.W.O., Fanning, C.M., Coenraads, R.R. (1998). Models of corundum origin from alkali basalt terrains: a reappraisal. Contributions to Mineralogy and Petrology 133, 356–372.

Sutherland, F.L., and Abduriyim, A. (2009). Geographic typing of gem corundum: A test case from Australia. Journal of Gemmology 31, 203–210.

Sutherland, F.L., Khin, Z., Meffre, S., Giuliani,. G., Fallick, A.E., Graham, I.T. and Webb, G.B. (2009). Gem-corundum megacrysts from east Australian basalt fields: trace elements, oxygen isotopes and origins. Australian Journal of Earth Sciences 56, 1003–1022.

Sutherland, F.L., Khin, Z., Meffre, S., Yui, TZ, and Kyaw Thu (2015). Advances in Trace Element "Fingerprinting" of Gem Corundum, Ruby and Sapphire, Mogok Area, Myanmar. Minerals *5*, 61-79.

Sutherland, F.L., Graham, I.T., Harris, S.J., Coldhamc, T., Powell, W. Belousova, E.A. and Martin, L. (2017). Unusual ruby–sapphire transition in alluvial megacrysts, Cenozoic basaltic gem field, New England, New South Wales, Australia. Lithos 278–281, 347–360.

Sweeney, R. J., Prozesky, V., and Przybylowicz, W., (1995). Selected trace and minor element partitioning between peridotite minerals and carbonatite melts at 18-46 kb pressure. Geochim. Cosmochim. Acta 59, 3671-3683.

Tappe, S., Pearson, D.G., Kjarsgaard, B.A., Nowell, G., and Dowall, D., (2013): Mantle transition zone input to kimberlite magmatism near a subduction zone: Origin of anomalous Nd–Hf isotope systematics at Lac de Gras, Canada. Earth Planet. Sci. Lett. 371-372, 235–251.

Tappert, R., Stachel, T., Harris, J.W., Shimizu, N., and Brey, G.P., (2005): Mineral inclusions in diamonds from the Panda kimberlite, Slave Province, Canada: European Journal of Mineralogy 17, 423–440.

Tappert, R., and Tappert, M.C., (2011): Diamonds in Nature: A Guide to Rough Diamonds. Springer Verlag, Berlin

Taylor, L.A., Keller, R.A., Snyder, G.A., Wang, W., Carlson, W.D., Hauri, E.H., McCandless, T., Kim, K.-R., Sobolev, N.V., and Bezborodov, S.M., (2000): Diamonds and their mineral inclusions, and what they tell us: A detailed "pull-apart" of a diamondiferous eclogite. International Geology Review, 42(11), 959-983.

Taylor, J.K., (1987): Quality assurance of chemical measurements. Lweis Publishers, Chealsea, MI.

Taylor, P.N., Moorbath, S., Goodwin, R., and Petrykowski, A. C., (1980): Crustal contamination as an indicator of the extent of early Archaean continental crust: Pb isotopic evidence from the late Archaean gneisses of West Greenland. Geochim. Cosmochim. Acta 44, 1437–53.

Taylor, W.R., and Green, D.H., (1989): The role of reduced C–O–H fluids in mantle partial melting. In: Ross, J., et al. (Eds.), Kimberlites and Related Rocks: Their Composition, Occurrence, Origin and Emplacement. GSA Spec Publ No 14. Blackwell, Carlton, 592–602.

Taylor, W.R., Jaques, A.L., and Ridd, M., (1990): Nitrogen-defect aggregation characteristics of some Australasian diamonds: time-temperature constraints on the source regions of pipe and alluvial diamonds. American Mineralogist 75(11-12), 1290-1310.

Taylor, W.R., and Milledge, H.J., (1995): Nitrogen aggregation character, thermal history, and stable isotope composition of some xenolith-derived diamonds from Roberts Victor and Finsch. Extended abstracts of the 6th IKC, 620-622.

Tenthorey, E.A., Ryan, J.G. and Snow, E.A. (1996): Petrogenesis of sapphirine-bearing metatroctolites from the Buck Creek ultramafic body, southern Appalachians. J. Metam. Geol. 14, 103–114.

Themelis, T. (2008) Gems and Mines of Mogok, 356 p. A&T Publishing, Los Angeles.

Thirlwall, M.F., (1991): Long-term reproducibility of multicollector Sr and Nd isotope ratio analysis. Chemical Geology 94, 84–104.

Timmerman, S., Yeow, H., Honda, M., Howell, D., Jaques, A.L., Krebs, M., Woodland, S., Pearson, D.G.,Avila, J.N., and Ireland, T.R., (2018): U-Th/He dating of fluid-rich 'fibrous' diamonds - a history of Phanerozoic diamond growth. *submitted to chemical geology*

Todt, W., Cliff, R.A., Hanser, A., and Hofmann, A.W., (1996): Evaluation of a ^{202}Pb–^{205}Pb double spike for high-precision lead isotope analysis. in: Earth Processes: Reading the Isotopic Code, edited by: Basu, A. and Hart, S. R., Am. Geophys. Union Geophysical Monograph 95, 429–437.

Tomlinson, E., De Schrijver, I., De Corte, K., Jones, A.P., Moens, L., and Vanhaecke, F., (2005): Trace element compositions of submicroscopic inclusions in coated diamond: A tool for understanding diamond petrogenesis: Geochimica et Cosmochimica Acta 69, 4719-4732.

Tomlinson, E.L., Jones, A.P., and Harris, J.W., (2006): Co-existing fluid and silicate inclusions in mantle diamond: Earth and Planetary Science Letters 250, 581-595.

Tomlinson, E.L., Müller, W., and Eimf, (2009): A snapshot of mantle metasomatism: Trace element analysis of coexisting fluid (LA-ICP-MS) and silicate (SIMS) inclusions in fibrous diamonds. Earth and Planetary Science Letters 279, 362-372.

Tsai, H.M., Meyer, H. O. A., Moreau, J., and Milledge, H. J., (1979): Mineral inclusions in diamond: Premier, Jagersfontein and Finsch kimberlites, South Africa, and Williamson Mine, Tanzania. In: Meyer, H. O. A. & Boyd, F. R. (eds) Proceedings of the 2nd Kimberlite Conference. Geophysical Monograph, American Geophysical Union 1, 16-26.

Tukey, J.W., (1962): The Future of Data Analysis. Annals of Mathematical Statistics. 33(1), 1–67, p. 18.

Ueda, K., Jacobs, J., Thomas, R.J., Kosler, J., Horstwood, M.S.A., Wartho, J.-A., Jourdan, F., Emmel, B., and Matola, R., (2012): Postcollisional high-grade metamorphism, orogenic collapse, and differential cooling of the East African Orogen of Northeast Mozambique. Journal of Geology 120, 507–30.

Van Long, P., Quang Vinh, H., Garnier, V., Giuliani, G., Ohnenstetter, D., Lhomme, T., Schwarz, D., Fallick, A.E., Dubessy, J. and Trong Trinh, P. (2004). Gem corundum deposits in Vietnam. Journal of Gemmology 29, 129-142.

Van Rythoven, A.D., and Schulze, D.J., (2009): In-situ analysis of diamonds and their inclusions from the Diavik Mine, Northwest Territories, Canada: mapping diamond growth: Lithos 112 (Supplement 2), 870–879.

Viljoen, K.S., and Lawless, P.J., (1988): Finsch Mine—the largest diamond producer in South Africa. Geo bulletin—Quarterly News Bulletin of the Geological Society of South Africa 31, 48–49.

Volfinger, M., (1976): Effet de la température sur les distributions de Na, Rb et Cs entre la sanidine, la muscovite, la phlogopite et une solution hydrothermale sous une pression de 1 kbar. Geochimica et Cosmochimica Acta 40, 267-282.

Vysotskiy, S.V., Nechaev, V.P., Kissin, A.Yu., Yakovenko, V.V., Ignat'ev, A.V., Velivetskaya, T.A., Sutherland, F.L., and Agoshkov, A.I., (2015): Oxygen isotopic composition as an indicator of ruby and sapphire origin: A review of Russian occurrences. Ore Geology Reviews 68, 164–170.

Webb K., Hetman, C., Nowicki, T., Harrison, S., Carlson, J., Parsons, S., and Paul, J., (2012): An updated geological model of the Misery kimberlite complex, EKATI mine, Northwest Territories, Canada: Poster at the 10th International Kimberlite Conference, Bangalore, India.

Weiss, Y., Griffin, W.L., Harris, J.W., and Navon, O., (2008b): Diamond-forming fluids and kimberlites: the trace element perspective. In 9th International Kimberlite Conference, 9IKCA-00108.

Weiss, Y., Kessel, R., Griffin, W.L., Kiflawi, I., Klein-BenDavid, O., Bell, D.R., Harris, J.W., Navon, O., (2009): A new model for the evolution of diamond-forming fluids: Evidence from microinclusion-bearing diamonds from Kankan, Guinea. Lithos 112, 660–674.

Weiss, Y., Griffin, W.L., Bell, D.R., and Navon, O., (2011): High-Mg carbonatitic melts in diamonds, kimberlites and the subcontinental lithosphere. Earth and Planetary Science Letters 309(3–4), 337–347.

Weiss, Y., Griffin, W.L., Navon, O., (2013): Diamond-forming fluids in fibrous diamonds: The trace-element perspective. Earth and Planetary Science Letters 376, 110-125.

Weiss, Y., Kiflawi, I., Davies, N., and Navon, O., (2014): High-density fluids and the growth of monocrystalline diamonds. Geochim. Cosmochim. Acta 141, 145–159.

Weiss, Y., McNeill, J., Pearson, D.G., Nowell, G.M., Ottley, C.J., (2015): Highly saline fluids from a subducting slab as the source for fluid-rich diamonds. Nature 524, 339–342.

Welch, B.L., (1938): The significance of the difference between two means when the population variances are unequal: Biometrika 29, 350–62.

Welch, B.L., (1947): The generalisation of students problem when several different population variances are involved: Biometrika 34, 23–35.

Westerlund, K.J., Shirey, S.B., Richardson, S.H., Carlson, R.W., Gurney, J.J., and Harris, J.W., (2006): A subduction wedge origin for Paleoarchean peridotitic diamonds and harzburgites from the Panda kimberlite, Slave craton: Evidence from Re-Os isotope systematics: Contributions to Mineralogy and Petrology 152, 275–294.

White, W.S., (1972): Keweenawan flood basalts and continental rifting. Geol Assoc Am Abstr Programs 4,732–734,

Windley, B.F. and Smith, J.V. (1974). The Fiskenaesset complex. Bull. Gronlands Geol. Undersogelse 108, 54.

Woods, G.S., (1986): Platelets and the infrared absorption of Type Ia diamonds: Proceedings of the Royal Society of London. A. Mathematical and Physical Sciences 407, 219–238.

Wyllie, P.J., and Ryabchikov, I.D., (2000). Volatile components, magmas, and critical fluids in upwelling mantle. Journal of Petrology 41(7), 1195-1206.

Yui, T. F., Khin Zaw, and Limtrakun, P., (2003): Oxygen isotope composition of the Denchai sapphire, Thailand: a clue to its enigmatic origin. Lithos 67, 153-161.

Yui, T. F., Wu, C. M., Limtrakum P., Sricharn W., and Boonsoog A., (2006): Oxygen isotope studies on placer sapphire and ruby in the Chantaburi-Trat alkali basaltic gemfield, Thailand. Lithos 86, 197-211.

Yui, T. F., Khin Zaw, and Wu, C.-M., (2008): A preliminary stable isotope study on Mogok ruby, Myanmar. Ore Geol. Rev. 34, 182–199.

Zaw K., Sutherland F. L., Dellapasqua F., Ryan C. G., Yui T.-F., Mernagh T. P., and Duncan D., (2006): Contrasts in gem corundum characteristics, eastern Australian basaltic fields: trace elements, fluid/melt inclusions and oxygen isotopes. Mineralogical Magazine 70, 669-687.

Zedgenizov, D.A., Rege, S., Griffin, W.L., Kagi, H. and Shatsky, V.S., (2007): Compositional variations of micro-inclusions in fluidbearing diamonds from Udachnaya kimberlite pipe as revealed by LA-ICP-MS. Chem. Geol. 240(1–2), 151–162.

Zedgenizov, D.A., Ragozin, A.L., Shatsky, V.S., Araujo, D., Griffin, W.L., and Kagi, H., (2009): Mg and Fe-rich carbonate-silicate high-density fluids in cuboid diamonds from the Internationalnaya kimberlite pipe (Yakutia). Lithos 112, 638-647.

Appendix A

Physical and chemical characteristics of Misery microdiamonds

Table A1: Physical and chemical characteristics of Misery microdiamonds.

sieve size [mm]	Sample	N_A [ppm]	N_B [ppm]	$N_A + N_B$ [ppm]	B %	H peak area	B' position [cm^{-1}]	B' peak area	type	shape	degree of resorption	color	T [Nitrogen, 3Ga], after Leahy and Taylor (1997)	ΔT	depth * [km]	$\delta^{13}C$ (VPDB)	2σ (‰)
2.36	KIMB3MainS_88_1									ir	high	brown				-4.74	0.16
2.36	KIMB3MainS_88_2															-4.46	0.15
2.36	KIMB3MainS_88_3															-4.72	0.14
2.36	KIMB3MainS_88_4															-4.87	0.15
2.36	KIMB3MainS_88_5															-4.69	0.15
2.36	KIMB5MainS_176_1									ir	high	brown				-5.44	0.14
2.36	KIMB5MainS_176_2															-5.37	0.15
2.36	KIMB5MainS_176_3															-4.80	0.14
2.36	KIMB5MainS_176_4															-5.62	0.15
1.7	KIMB5MainS_177_1									ir	high	colorless				-5.56	0.14
1.7	KIMB5MainS_177_2															-4.83	0.15
1.7	KIMB5MainS_177_3															-5.57	0.14
1.7	KIMB5MainS_177_4															-5.67	0.16
1.7	KIMB5MainS_177_5															-5.21	0.15
1.7	KIMB5SwExt_1_1	89.4	296.5	385.9	76.8	30.42	1362.2	196.549	IaAB	do	high	brown	1165.0		169.5	-4.68	0.15
1.7	KIMB5SwExt_1_2															-4.87	0.15
1.7	KIMB5SwExt_1_3															-4.96	0.15
1.7	KIMB5SwExt_1_4															-4.93	0.16
1.7	KIMB5SwExt_1_5															-4.60	0.15
1.18	KIMB3MainS_1_1	360.5	428.7	789.2	54.3	39.388	1373	3.203	IaAB	do	high	colorless	1121.9		163.2	-3.89	0.23
1.18	KIMB3MainS_1_2	293.8	365.9	659.7	55.5	18.058	1372.7	47.215	IaAB				1127.3	5.4	164.0	-3.71	0.22
1.18	KIMB3MainS_1_3															-4.03	0.22
1.18	KIMB5MainS_179_1									do	high	colorless				-3.32	0.22
1.18	KIMB5MainS_179_2															-4.25	0.22

1.18	KIMB5MainS_179_3															-4.24	0.22
1.18	KIMB5SwExt_2_1	798	204	1002.0	20.4	62.666	1378	4.893	IaAB	ir	some	pinkish	1080.6		157.2	-3.70	0.23
1.18	KIMB5SwExt_2_2	720.3	176.6	896.9	19.7	111.469	1379	3.353	IaAB				1082.2	1.6	157.5	-2.80	0.22
1.18	KIMB5SwExt_2_3															-3.64	0.22
1.18	KIMB5SwExt_3_1	55	259.2	314.2	82.5	9.897	1362.1	166.513	IaAB	oc	some	colorless	1179.3		171.6		
1.18	KIMB5SwExt_3_2	54.4	153.2	207.6	73.8	15.113	1361.4	86.274	IaAB				1177	2.6	171.2		
1.18	KIMB5SwExt_4_1	194.1	550.6	744.7	73.9	44.783	1370.3	347.825	IaAB	do (frag)	high	grey	1144.5		166.5	-3.64	0.22
1.18	KIMB5SwExt_4_2	642	91.1	733.1	12.4	32.207	1374.7	21.282	IaAB				1074	70.1	156.3	-23.98	0.23
1.18	KIMB5SwExt_4_3															-23.32	0.22
1.18	KIMB5SwExt_5_1	223.1	227.2	450.3	50.5	11.717	1369.5	35.622	IaAB	oc	low	colorless	1131.7		164.7		
1.18	KIMB5SwExt_5_2	445.9	247.5	693.4	35.7	8.955	1370.1	37.614	IaAB				1106.9	24.8	161.1		
1.18	KIMB5SwExt_6_1	17.1	376.2	393.3	95.7	12.097	1366.2	207.247	IaB	ir	low	colorless	1214.3		176.7	-4.79	0.22
1.18	KIMB5SwExt_6_2															-4.80	0.21
1.18	KIMB5SwExt_6_3															-5.12	0.22
1.18	KIMB5SwExt_7_1	249.5	378.7	628.2	60.3	24.571			IaAB	oc (frag)	low	colorless	1133.3		164.9		
1.18	KIMB5SwExt_7_2	266.6	309.6	576.2	53.7	41.466			IaAB				1128.9	4.4	164.3		
1.18	KIMB5SwExt_8_1	27.4	187.8	215.2	87.3	15.586	1363.4	94.862	IaAB	do (frag)	high	brown	1199.1		174.5	-5.80	0.23
1.18	KIMB5SwExt_8_2															-5.38	0.22
1.18	KIMB5SwExt_8_3															-5.07	0.21
1.18	KIMB5SwExt_9_1	140.4	47.5	187.9	25.3	4.354	1359.5	9.002	IaAB	oc	high	colorless	1126.2		163.9	-4.08	0.23
1.18	KIMB5SwExt_9_2	81.8	73.1	154.9	47.2	15.826	1360.9	49.671	IaAB				1155	28.7	168.0	-4.28	0.21
1.18	KIMB5SwExt_9_3															-3.61	0.21
1.18	KIMB6SwExt_1_1	146.9	362.3	509.2	71.2	9.271	1374.3	72.153	IaAB	do	high	colorless	1150.5		167.4	-5.46	0.21
1.18	KIMB6SwExt_1_2															-3.81	0.22
1.18	KIMB6SwExt_1_3															-4.53	0.22
1.18	KIMB6SwExt_2	375.2	266.7	641.9	41.5	24.289	1374	57.425	IaAB	ir	high	colorless	1114.6		162.2		
0.85	KIMB3MainS_3_1	38.3	310.7	349.0	89.0	31.321	1365.8	149.034	IaAB	ir	some	colorless	1190.8		173.3	-5.48	0.16
0.85	KIMB3MainS_3_2															-5.29	0.15
0.85	KIMB3MainS_3_3															-5.38	0.16
0.85	KIMB3MainS_4_1	562.3	122.8	685.1	17.9	24.466			IaAB	oc	some	brown	1085.6		158.0	-4.49	0.12
0.85	KIMB3MainS_4_2	578.8	138.2	717.0	19.3	7.124			IaAB				1086.6	1.0	158.1	-4.02	0.15

0.85	KIMB3MainS_5_1	40.3	77.9	118.2	65.9	3.906			IaAB	do (frag)	high	brown	1182		171.9	-3.57	0.13
0.85	KIMB3MainS_5_2	41.7	55.3	97.0	57.0	2.897	1362.9	72.439	IaAB						0.0	-3.77	0.14
0.85	KIMB3MainS_5_3	19.5	55.3	74.8	73.9	3.316			IaAB					26.9	0.0	-4.56	0.14
0.85	KIMB3MainS_6_1	37	18	55.0	32.7	10.377			IaAB	ir	high	brown	1165.7		169.6		
0.85	KIMB3MainS_6_2	32.7	52.1	84.8	61.4	3.978			IaAB						0.0		
0.85	KIMB3MainS_6_3	25.8	22	47.8	46.0	2.1			IaAB					19.5	0.0		
0.85	KIMB3MainS_7	926.9	19	945.9	2.0	24.895			IaA	oc	some	colorless	1027.1		149.4		
0.85	KIMB3MainS_8_1	19.2	113.1	132.3	85.5	27.277	1361.4	57.763	IaAB	do	high	brown	1208.1		175.8	-4.75	0.12
0.85	KIMB3MainS_8_2	21.5	191.7	213.2	89.9	34.607	1365.8	83.055	IaAB				1206.4	1.7	175.5	-4.55	0.13
0.85	KIMB3MainS_8_3															-5.04	0.13
0.85	KIMB3MainS_8_4															-3.97	0.12
0.85	KIMB5MainS_1	669.8	162.2	832.0	19.5	41.86	1372.9	72.502	IaAB	do (frag)	high	colorless	1083.6		157.7		
0.85	KIMB5MainS_2	220.6	375	595.6	63.0	5.526	1374.9	7.036	IaAB	do	high	colorless	1137		165.5		
0.85	KIMB5MainS_3_1	959.2	622.6	1581.8	39.4	168.022	1376.2	47.642	IaAB	oc	low	colorless	1091.4		158.8	-3.77	0.15
0.85	KIMB5MainS_3_2															-3.73	0.15
0.85	KIMB5MainS_3_3															-3.62	0.15
0.85	KIMB5MainS_4	748.3	127	875.3	14.5	13.01	1377.2	8.026	IaAB	oc	low	colorless	1074.4		156.3		
0.85	KIMB5MainS_5_1									do (frag)	high	colorless				-4.32	0.15
0.85	KIMB5MainS_5_2															-4.14	0.16
0.85	KIMB5MainS_6	787.7	30.5	818.2	3.7	31.303	1372.5	10.681	IaA	ir	high	colorless	1043.6		151.8		
0.85	KIMB5MainS_7	868.3	77	945.3	8.1	36.91			IaA	ir	some	brown	1058		154.0		
0.85	KIMB5MainS_8_1	794.6	193.7	988.3	19.6	40.473			IaAB	ir	some	colorless	1079.8		157.1	-4.58	0.15
0.85	KIMB5MainS_8_2															-4.48	0.15
0.85	KIMB5MainS_8_3															-3.95	0.15
0.85	KIMB5SwExt_10_1	385.4	350.8	736.2	47.7	56.273	1374.7	23.182	IaAB	oc (frag)	low	colorless	1117.2		162.6	-4.41	0.16
0.85	KIMB5SwExt_10_2															-4.64	0.15
0.85	KIMB5SwExt_10_3															-4.18	0.15
0.85	KIMB5SwExt_10_4															-5.12	0.15
0.85	KIMB5SwExt_11_1	91.2	55.9	147.1	38.0	2.324	1359.3	7.248	IaAB	oc (frag)	low	brown	1146.7		166.9	-3.97	0.15
0.85	KIMB5SwExt_11_2	39.7	43	82.7	52.0	8.38	1357.8	6.49	IaAB	oc (frag)	low	brown	1175.8	29.0	171.1	-4.84	0.16
0.85	KIMB5SwExt_11_3															-4.68	0.14

0.85	KIMB5SwExt_11_4															-3.88	0.15
0.85	KIMB5SwExt_11_5															-4.26	0.14
0.85	KIMB5SwExt_11_6															-4.93	0.14
0.85	KIMB5SwExt_12	708.3	163.1	871.4	18.7	9.196	1372.3	50.25	IaAB	oc	low	colorless	1081.4		157.3		
0.85	KIMB5SwExt_13_1	443.3	311.3	754.6	41.3	31.743	1374.9	27.609	IaAB	do (frag)	high	colorless	1110		161.6	-4.63	0.13
0.85	KIMB5SwExt_13_2															-5.46	0.12
0.85	KIMB5SwExt_13_3															-3.89	0.12
0.85	KIMB5SwExt_14	457.5	314.4	771.9	40.7	40.538	1376.8	13.307	IaAB	oc	some	colorless	1109.4		161.4		
0.85	KIMB5SwExt_15_1	600.5	210.9	811.4	26.0	18.735	1376.9	15.961	IaAB	do (frag)	some	pinkish	1092.6		159.0	-4.01	0.14
0.85	KIMB5SwExt_15_2	510.4	86.4	596.8	14.5	11.291	1370.2	35.496	IaAB				1083	9.6	157.6	-4.15	0.13
0.85	KIMB5SwExt_15_3															-4.76	0.13
0.85	KIMB5SwExt_16_1	218.8	484.3	703.1	68.9	104.494	1373.2	140.056	IaAB	do (frag)	high	colorless	1139.8		165.8	-3.91	0.13
0.85	KIMB5SwExt_16_2	139.5	529	668.5	79.1	238.031	1374.9	106.916	IaAB				1154.5	14.6	168.0	-4.89	0.14
0.85	KIMB5SwExt_16_3															-3.61	0.12
0.85	KIMB5SwExt_17	29.1	52.2	81.3	64.2	15.373	1359.8	22.523	IaAB	oc	high	brown	1189.4		173.1		
0.85	KIMB5SwExt_18_1	294.6	187.1	481.7	38.8	13.145	1363.3	67.346	IaAB	oc	high	brown	1118.7		162.8		
0.85	KIMB5SwExt_18_2	269.2	103.7	372.9	27.8	9.011	1363	54.941	IaAB				1112.9	5.8	161.9		
0.85	KIMB6SwExt_3_1	377	100	477.0	21.0				IaAB	ir	low	grey	1098.4		159.8	-4.40	0.15
0.85	KIMB6SwExt_3_2															-4.41	0.15
0.6	KIMB3MainS_10	792.3	250.1	1042.4	24.0	73.454	1372.4	99.899	IaAB	do	high	brown	1084		157.8		
0.6	KIMB3MainS_11	932.1	126.6	1058.7	12.0	20.936	1373.3	43.883	IaAB	do (frag)	high	colorless	1065.2		155.0		
0.6	KIMB3MainS_12	1181.7	109.9	1291.6	8.5	24.502	1377.1	30.094	IaA	macle	high	brown	1052.6		153.2		
0.6	KIMB3MainS_13	961.9	159.1	1121.0	14.2	110.926			IaAB	do (frag)	high	brown	1068.3		155.4		
0.6	KIMB3MainS_14	831.9	65.2	897.1	7.3	2.812	1369.7	25.648	IaA	oc (frag)	low	colorless	1056.8		153.8		
0.6	KIMB3MainS_15	494.6	93	587.6	15.8				IaAB	do (frag)	high	brown	1085.7		158.0		
0.6	KIMB3MainS_16	18.8	125.7	144.5	87.0	17.622	1360.1	24.78	IaAB	do (frag)	high	brown	1209.2		175.9		
0.6	KIMB3MainS_17_1	753.2	283	1036.2	27.3	41.352	1363	1.746	IaAB	do	high	colorless	1089		158.4	-4.28	0.22
0.6	KIMB3MainS_17_2															-3.73	0.22
0.6	KIMB3MainS_17_3															-2.93	0.22
0.6	KIMB3MainS_18	873	168.6	1041.6	16.2	99.203	1376	7.597	IaAB	do	high	colorless	1073.4		156.2		
0.6	KIMB3MainS_19	38.2	105.2	143.4	73.4	22.497	1365.5	39.767	IaAB	oc	some	colorless	1186		172.5		

0.6	KIMB3MainS_20	724.4	336.8	1061.2	31.7		1370.2	7.281	IaAB	ir	some	colorless	1092.9	159.0		
0.6	KIMB3MainS_21	855.9	148.0	1003.9	14.7	73.454	1374.4	21.001	IaAB	do (frag)	high	colorless	1071.8	155.9		
0.6	KIMB3MainS_9_1	967.8	121.1	1088.9	11.1	81.14			IaAB	do	high	colorless	1062.8	154.6	-4.15	0.23
0.6	KIMB3MainS_9_2														-4.91	0.22
0.6	KIMB3MainS_9_3														-5.04	0.22
0.6	KIMB5MainS_10_1	978.4	330.7	1309.1	25.3	68.24	1361.6	2.756	IaAB	do (frag)	high	colorless	1080.9	157.3	-5.07	0.16
0.6	KIMB5MainS_10_2														-4.70	0.14
0.6	KIMB5MainS_10_3														-4.92	0.14
0.6	KIMB5MainS_11_1	1032.6	82.9	1115.5	7.4	44.833	1376.8	12.389	IaA	do	high	colorless	1053	153.2	-4.02	0.22
0.6	KIMB5MainS_11_2														-4.18	0.22
0.6	KIMB5MainS_11_3														-4.10	0.23
0.6	KIMB5MainS_12_1	858.8	88.5	947.3	9.3	2.303			IaA	do (frag)	high	colorless	1061.6	154.5	-4.54	0.22
0.6	KIMB5MainS_12_2														-3.25	0.21
0.6	KIMB5MainS_12_3														-4.70	0.22
0.6	KIMB5MainS_13	89.8	149.3	239.1	62.4	4.417	1361.5	29.739	IaAB	do (frag)	high	brown	1159.6	168.7		
0.6	KIMB5MainS_14	749.6	583.3	1332.9	43.8	118.831	1373.4	125.53	IaAB	ir	high	colorless	1099.5	160.0		
0.6	KIMB5MainS_15	208.2	49.9	258.1	19.3	7.384	1372.1	21.89	IaAB	ir	low	colorless	1110.4	161.6		
0.6	KIMB5MainS_16	49	53.3	102.3	52.1	7.488	1362.9	14.892	IaAB	ir	some	yellow/brown	1170	170.3		
0.6	KIMB5MainS_17_1	704.7	289.3	994.0	29.1	52.156	1377.2	8.862	IaAB	ir	low	colorless	1091.6	158.8	-5.12	0.22
0.6	KIMB5MainS_17_2														-4.42	0.22
0.6	KIMB5MainS_18_1	466.4	41.5	507.9	8.2	51.224	1374.6	7.625	IaA	oc	some	colorless	1072.2	156.0	-5.04	0.22
0.6	KIMB5MainS_18_2														-4.18	0.23
0.6	KIMB5MainS_18_3														-3.95	0.21
0.6	KIMB5MainS_19_1									oc	high	colorless			-5.58	0.22
0.6	KIMB5MainS_19_2														-4.24	0.22
0.6	KIMB5MainS_19_3														-3.16	0.22
0.6	KIMB5MainS_20_1	27.6	457.7	485.3	94.3	44.17	1363.4	219.458	IaB	ir	low	colorless	1201	174.7	-4.39	0.22
0.6	KIMB5MainS_20_2														-4.43	0.23
0.6	KIMB5MainS_21_1	914.9	211.1	1126.0	18.7	118.555	1375.4	20.758	IaAB	ir	high	brown	1075.7	156.5	-4.65	0.22
0.6	KIMB5MainS_21_2														-4.17	0.22
0.6	KIMB5MainS_22_1	991.7	879.6	1871.3	47.0	405.858	1379.9	49.575	IaAB	oc	some	colorless	1094.7	159.3	-4.19	0.22

0.6	KIMB5MainS_22_2															-4.98	0.22
0.6	KIMB5MainS_22_3															-3.81	0.22
0.6	KIMB5MainS_23_1	864.3	142.1	1006.4	14.1	46.765	1374.7	32.154	IaAB	oc	low	colorless	1070.6		155.8	-3.80	0.14
0.6	KIMB5MainS_23_2															-3.79	0.16
0.6	KIMB5MainS_23_3															-3.41	0.14
0.6	KIMB5SwExt_19_1	16.3	33.9	50.2	67.5	7.339	1359.4	6.517	IaAB	oc (frag)	high	brown	1206.2		175.5		
0.6	KIMB5SwExt_19_2	10.2	37.6	47.8	78.7	2.886	1360.8	1.945	IaAB				1223.1	16.9	178.0		
0.6	KIMB5SwExt_20_1	416	75.6	491.6	15.4	12.561	1375	17.079	IaAB	oc	low	colorless	1089.0		158.5	-4.67	0.21
0.6	KIMB5SwExt_20_2	770.9	184.6	955.5	19.3	27.275	1375.5	50.368	IaAB				1080.2	8.8	157.2	-3.98	0.22
0.6	KIMB5SwExt_20_3															-4.73	0.22
0.6	KIMB5SwExt_21	0	0	0.0					Type II	do (frag)	high	brown					
0.6	KIMB5SwExt_22	559.6	97.2	656.8	14.8	18.367			IaAB	do (frag)	high	brown	1081.4		157.3		
0.6	KIMB5SwExt_23_1	671.8	121.2	793.0	15.3	13.509	1372.6	26.938	IaAB	ir	high	colorless	1078.0		156.9	-3.83	0.23
0.6	KIMB5SwExt_23_2	416.8	408.1	824.9	49.5	9.67	1372.2	50.579	IaAB				1116.2	38.2	162.4	-4.11	0.21
0.6	KIMB5SwExt_23_3															-4.56	0.22
0.6	KIMB5SwExt_24_1	6.9	642.4	649.3	98.9	19.088	1363.7	320.369	IaB	ir	some	colorless	1240.4		180.5	-5.72	0.23
0.6	KIMB5SwExt_24_2	8.7	775.7	784.4	98.9	15.607	1363.4	329.465	IaB				1234	6.5	179.5	-4.97	0.22
0.6	KIMB5SwExt_24_3															-5.77	0.22
0.6	KIMB5SwExt_26_1	989.9	148	1137.9	13.0	21.612	1363	1.359	IaAB	ir	high	yellow	1065.8		155.1	-3.58	0.15
0.6	KIMB5SwExt_26_2	807.0	314.1	1121.1	28.0	41.492	1362.7	2.924	IaAB				1087.6	21.8	158.2	-4.56	0.14
0.6	KIMB5SwExt_26_3															-4.95	0.16
0.6	KIMB5SwExt_27	970.0	140.6	1110.6	12.7	24.805			IaAB	ir	some	grey	1065.6		155.0		
0.6	KIMB5SwExt_28_1	37.4	369.7	407.1	90.8	8.621	1362.6	211.369	IaB	do (frag)	high	brown	1192		173.4	-4.77	0.15
0.6	KIMB5SwExt_28_2	44	302.2	346.2	87.3	15.431	1361.5	145.06	IaAB				1186.6	5.3	172.7	-4.74	0.16
0.6	KIMB5SwExt_28_3															-4.64	0.15
0.6	KIMB5SwExt_29	10.6	188.8	199.4	94.7	71.197	1362.1	81.241	IaB	do (frag)	high	brown	1227		178.6		
0.6	KIMB5SwExt_31_1	582.5	765.1	1347.6	56.8	385.886	1376.7	99.061	IaAB	ir	low	colorless	1111.6		161.7	-4.10	0.22
0.6	KIMB5SwExt_31_2															-4.52	0.21
0.6	KIMB5SwExt_31_3															-3.90	0.22
0.6	KIMB5SwExt_32	687.2	261.2	948.4	27.5	13.074			IaAB	ir	some	colorless	1091		158.7		
0.6	KIMB5SwExt_33_1	909.8	177.7	1087.5	16.3	96.38	1377.6	7.529	IaAB	oc	low	colorless	1072.7		156.1	-4.55	0.14

0.6	KIMB5SwExt_33_2															-4.76	0.15
0.6	KIMB5SwExt_33_3															-4.77	0.15
0.6	KIMB5SwExt_33_4															-4.50	0.15
0.6	KIMB5SwExt_34	775.8	22.5	798.3	2.8	7.029			IaA	oc	low	colorless	1038		151.0		
0.6	KIMB5SwExt_35_1	919.6	562.5	1482.1	38.0	240.43	1377.9	25.367	IaAB	oc	high	colorless	1091.5		158.8		
0.6	KIMB5SwExt_35_2	679.6	580.4	1260.0	46.1	261.849	1376.8	39.242	IaAB				1103	11.5	160.5		
0.6	KIMB5SwExt_36_1	38.5	58.4	96.9	60.3	25.509	1361.1	21.436	IaAB	do	high	brown	1180.4		171.7		
0.6	KIMB5SwExt_36_2	23.6	48.4	72.0	67.2	13.401	1361.7	24.681	IaAB				1196.2	15.8	174.0		
0.6	KIMB5SwExt_37_1	20.2	561	581.2	96.5		1362.2	368.195	IaB	do (frag)	some	brown	1210.0		176.1	-5.88	0.15
0.6	KIMB5SwExt_37_2	47.2	635.3	682.5	93.1	2.919	1363.9	347.197	IaB				1186.4	23.6	172.6	-5.76	0.14
0.6	KIMB5SwExt_37_3															-5.63	0.15
0.6	KIMB5SwExt_38_1	114.9	336.8	451.7	74.6		1361.7	204.121	IaAB	do	high	colorless	1157.8		168.5	-4.45	0.22
0.6	KIMB5SwExt_38_2															-5.08	0.21
0.6	KIMB5SwExt_38_3															-4.23	0.22
0.6	KIMB6SwExt_10	463.3	72.9	536.2	13.6	13.5			IaA	oc (frag)	low	colorless	1083.8		157.7		
0.6	KIMB6SwExt_11	929.3	171.9	1101.2	15.6	12.864			IaA	do	high	coated	1071.2		155.9		
0.6	KIMB6SwExt_12	778.4	81.4	859.8	9.5	36.717			IaA	ir	some	colorless	1064.1		154.8		
0.6	KIMB6SwExt_14_1	16.1	71.8	87.9	81.7				IaAB	ir	low	brown	1192.3		173.5	-4.25	0.21
0.6	KIMB6SwExt_14_2	38	35.8	73.8	48.5	1.217			IaAB				1175.1		171.0	-3.44	0.22
0.6	KIMB6SwExt_14_3															-4.37	0.23
0.6	KIMB6SwExt_5_2	51.1	208.3	259.4	80.3	77.078	1365.8	69.438	IaAB	ir	some	brown	1180.5		171.8		
0.6	KIMB6SwExt_5_3	32.2	219.9	252.1	87.2	18.041	1367.5	89.373	IaAB				1194.8	14.3	173.8		
0.6	KIMB6SwExt_6_1	26.9	44.7	71.6	62.4	14.709			IaAB	oc (frag)	low	colorless	1191		173.3	-4.37	0.15
0.6	KIMB6SwExt_6_2	25.2	49.8	75.0	66.4	16.279	1360.5	1.337					1194.1	4.1	173.7	-4.45	0.14
0.6	KIMB6SwExt_6_3															-4.36	0.15
0.6	KIMB6SwExt_7_1	800.7	105.1	905.8	11.6	26.729	1372.5	12.498	IaAB	oc	some	colorless	1068		155.4	-3.36	0.22
0.6	KIMB6SwExt_7_2															-4.31	0.22
0.6	KIMB6SwExt_7_3															-3.42	0.21
0.6	KIMB6SwExt_8	17.6	83.8	101.4	82.6	9.168	1364.8	29.441	IaAB	do	high	colorless	1209.6		176.0		
0.6	KIMB6SwExt_9_1	100.5	119.7	220.2	54.4	19.074	1372.4	6.155	IaAB	ir	low	colorless	1153		167.8	-4.03	0.23
0.6	KIMB6SwExt_9_2	122.2	53.7	175.9	30.5	16.972	1371.5	3.619					1134.2	19.1	165.0	-4.21	0.23

0.425	KIMB3MainS_22	18.6	51.4	70.0	73.4	6.982	1361.1	4.36	IaAB	do (frag)	high	brown	1204.9		175.3		
0.425	KIMB3MainS_23	576.7	31	607.7	5.1	10.645			IaA	do (frag)	high	colorless	1057.1		153.8		
0.425	KIMB3MainS_24_1	77.8	362.7	440.5	82.3		1361.7	119.038	IaAB	oc (frag)	some	brown	1170.3		170.3		
0.425	KIMB3MainS_24_2	67.9	422.1	490.0	86.1		1361.5	122.003	IaAB				1175.0	4.7	171.0		
0.425	KIMB3MainS_25_1	707.4	183.9	891.3	20.6	21.741	1373.9	17.698	IaAB	oc	high	colorless	1083.6		157.7	-2.16	0.22
0.425	KIMB3MainS_25_2															-3.89	0.22
0.425	KIMB3MainS_25_3															-4.50	0.22
0.425	KIMB3MainS_26_1	599.7	246.4	846.1	29.1	61.084	1373.6	68.563	IaAB	ir	low	colorless	1095.3		159.4	-5.01	0.21
0.425	KIMB3MainS_26_2															-4.46	0.21
0.425	KIMB3MainS_27	994	119.8	1113.8	10.8	117.521			IaAB	do	high	colorless	1061.5		154.4		
0.425	KIMB3MainS_28	36	452.8	488.8	92.6	2.602	1357.9	214.322	IaB	oc (frag)	low	colorless	1193.5		173.6		
0.425	KIMB3MainS_29	569.7	94	663.7	14.2				IaAB	do	high	colorless	1080.0		157.1		
0.425	KIMB3MainS_30	1235.2	292.3	1527.5	19.1	81.081	1363.6	3.268	IaAB	ir	some	colorless	1069		155.6		
0.425	KIMB3MainS_31_1	704.1	363.9	1068.0	34.1	54.506	1372.4	26.111	IaAB	do (frag)	high	colorless	1095.2		159.4		
0.425	KIMB3MainS_31_2	702.0	347.4	1049.4	33.1	44.829			IaAB				1094.6	0.0	159.3		
0.425	KIMB3MainS_32	146.6	107.5	254.1	42.3	11.531	1374.5	33.006	IaAB	do (frag)	high	colorless	1137.7		165.5		
0.425	KIMB3MainS_33_1	1123.8	236.4	1360.2	17.4	16.344			IaAB	ir	some	colorless	1069.4		155.6	-4.04	0.15
0.425	KIMB3MainS_33_2															-3.97	0.15
0.425	KIMB3MainS_34_1	104.4	245.6	350.0	70.2	40.939	1362.1	64.59	IaAB	do (frag)	high	brown	1158.7		168.6		
0.425	KIMB3MainS_34_2	120.3	200.3	320.6	62.5	44.055	1361.7	44.314	IaAB				1152.2	6.5	167.7		
0.425	KIMB3MainS_35	928.4	35.1	963.5	3.6	22.42			IaA	do (frag)	high	colorless	1039.6		151.3		
0.425	KIMB3MainS_36_1	668.2	140.8	809.0	17.4	24.98			IaAB	do (frag)	high	brown	1081.1		157.3	-4.84	0.14
0.425	KIMB3MainS_36_2															-2.76	0.13
0.425	KIMB3MainS_36_3															-3.69	0.14
0.425	KIMB3MainS_37	959.4	114.9	1074.3	10.7	4.434	1372.5	39.9	IaAB	do (frag)	high	colorless	1062.2		154.5		
0.425	KIMB3MainS_38	781.0	114.6	895.6	12.8		1369.8	50.4	IaAB	do (frag)	high	colorless	1070.7		155.8		
0.425	KIMB5MainS_24_1	283.3	588.3	871.6	67.5				IaAB	do	high	colorless	1133.0		164.9	-26.97	0.22
0.425	KIMB5MainS_24_2															-4.88	0.22
0.425	KIMB5MainS_24_3															-7.36	0.22
0.425	KIMB5MainS_25	1237.8	347.2	1585.0	21.9	130.598	1377	60.927	IaAB	ir	high	colorless	1072.4		156.0		
0.425	KIMB5MainS_26	177.1	79.6	256.7	31.0	1.62	1361.5	44.758	IaAB	ir	low	brown	1125.5		163.8		

0.425	KIMB5MainS_27	0	0	0.0					Type II	ir	low	brown				
0.425	KIMB5MainS_28_1	9.3	45.8	55.1	83.1	4.366			IaAB	oc	low	brown	1227.2	178.6	-5.40	0.21
0.425	KIMB5MainS_28_2														-4.73	0.22
0.425	KIMB5MainS_29_1	15.3	43.2	58.5	73.8	6.058			IaAB	ir	some	colorless	1210.3	176.1	-19.89	0.21
0.425	KIMB5MainS_29_2														-19.99	0.22
0.425	KIMB5MainS_29_3														-20.28	0.22
0.425	KIMB5MainS_30_1										low	coated			-3.57	0.22
0.425	KIMB5MainS_30_2														-3.20	0.23
0.425	KIMB5MainS_31	644.7	57.8	702.5	8.2	19.461	1373.8	18.794	IaA	ir	low	colorless	1065.1	155.0		
0.425	KIMB5MainS_32	24.2	261.7	285.9	91.5	14.269	1359.6	31.918	IaB	ir	some	brown	1203.7	175.1		
0.425	KIMB5MainS_33	879.6	201.0	1080.6	18.6	38.851			IaAB	ir	low	colorless	1076.4	156.6		
0.425	KIMB5MainS_34_1									oc	low	colorless			-2.41	0.22
0.425	KIMB5MainS_34_2														-3.42	0.21
0.425	KIMB5MainS_35	855.7	351.7	1207.4	29.1	7.566	1372.9	135.481	IaAB	ir	low	brown	1087.1	158.2		
0.425	KIMB5MainS_36_1	697.4	52.1	749.5	7.0	30.412	1371.8	10.636	IaA	oc	high	colorless	1060	154.2	-3.64	0.22
0.425	KIMB5MainS_36_2														-4.28	0.22
0.425	KIMB5MainS_37_1	1019.3	191.2	1210.5	15.8	80.509	1374.9	26.387	IaAB	oc	high	colorless	1069.4	155.6	-4.65	0.22
0.425	KIMB5MainS_37_2														-4.82	0.22
0.425	KIMB5MainS_38_1	908	57.2	965.2	5.9	11.118	1373.4	11.728	IaA	do	high	colorless	1050.5	152.8	-3.82	0.21
0.425	KIMB5MainS_38_2														-4.31	0.22
0.425	KIMB5MainS_39_2	20.3	17.9	38.2	46.9	3.074			IaAB	ir	low	brown	1191	173.2		
0.425	KIMB5MainS_40_1	799.4	292.7	1092.1	26.8	35.08	1373.4	106.696	IaAB	ir	some	colorless	1086.8	158.1	-4.08	0.14
0.425	KIMB5MainS_40_2														-4.34	0.14
0.425	KIMB5MainS_41	1026.4	163.9	1190.3	13.8	118.376	1376	53.82	IaAB	oc	low	colorless	1066.2	155.1		
0.425	KIMB5MainS_42	853.7	259.3	1113.0	23.3	135.022	1373.7	89.589	IaAB	oc	low	colorless	1082.1	157.4		
0.425	KIMB5MainS_43	1693.2	236.2	1929.4	12.2	10.219	1375.3	86.182	IaAB	ir	high	colorless	1052.7	153.2		
0.425	KIMB5MainS_44	39.5	92	131.5	70.0	24.451	1359.8	8.49	IaAB	ir	high	brown	1184	172.2		
0.425	KIMB5MainS_45	770.5	101.1	871.6	11.6	10.81	1369.3	30.254	IaAB	ir	high	colorless	1068.8	155.5		
0.425	KIMB5MainS_46	1082.7	42.9	1125.6	3.8	24.876			IaA	do	high	colorless	1037	150.9		
0.425	KIMB5MainS_47	1144.6	294.1	1438.7	20.4	119.126	1378	29.168	IaAB	oc	low	colorless	1072.6	156.1		
0.425	KIMB5MainS_48	578	211.4	789.4	26.8	44.116			IaAB	ir	high	colorless	1094.2	159.2		

0.425	KIMB5MainS_49_1	1413.4	1028.4	2441.8	42.1	426.094	1379.8	50.841	IaAB	ir	low	colorless	1084.1		157.7	-3.97	0.12
0.425	KIMB5MainS_49_2															-3.92	0.13
0.425	KIMB5MainS_50	195.5	142.6	338.1	42.2	54.754	1370.4	45.706	IaAB	ir	low	colorless	1130.6		164.5		
0.425	KIMB5MainS_51	732.7	582.9	1315.6	44.3	23.885	1370.9	301.656	IaAB	ir	low	colorless	1100.4		160.1		
0.425	KIMB5MainS_52_1	463	232.1	695.1	33.4	121.729	1372.8	61.393	IaAB	ir	some	colorless	1104.5		160.7	-7.64	0.14
0.425	KIMB5MainS_52_2															-5.61	0.14
0.425	KIMB5MainS_53	253.4	172.4	425.8	40.5	50.124			IaAB	ir	some	brown	1123.3		163.4		
0.425	KIMB5MainS_54	864.1	238.2	1102.3	21.6	86.164			IaAB	ir	some	brown	1080.1		157.2		
0.425	KIMB5MainS_55	37.3	217.0	254.3	85.3	51.312	1363.3	159.011	IaAB	oc	some	colorless	1190.3		173.2		
0.425	KIMB5MainS_56	835.7	399.8	1235.5	32.4	62.439	1363.4	3.224	IaAB	ir	some	yellow	1090.1		158.6		
0.425	KIMB5SwExt_39	13	71.3	84.3	84.6	3.093			IaAB	ir	low	colorless	1218.5		177.3		
0.425	KIMB5SwExt_40	987.5	685.7	1673.2	41.0	23.152	1375.2	147.075	IaAB	oc	some	colorless	1092		158.8		
0.425	KIMB5SwExt_41_1	397.9	90.1	488.0	18.5	1.683	1373.4	11.654	IaAB	oc	low	yellow	1094.2		159.2	-4.30	0.13
0.425	KIMB5SwExt_41_2															-3.82	0.13
0.425	KIMB5SwExt_42	19.4	379	398.4	95.1	54.317	1363.3	239.767	IaB	oc	low	colorless	1210.7		176.2		
0.425	KIMB5SwExt_43_1	716	325.9	1041.9	31.3	83.996	1375	38.817	IaAB	oc (frag)	some	colorless	1093		159.0		
0.425	KIMB5SwExt_43_2	655	341.4	996.4	34.3	133.952	1376.7	13.155	IaAB				1097.0	4.2	159.6		
0.425	KIMB5SwExt_44_1	760.2	239.0	999.2	23.9	75.256	1375.8	17.854	IaAB	do (frag)	high	colorless	1085.3		157.9	-4.64	0.23
0.425	KIMB5SwExt_44_2															-4.77	0.12
0.425	KIMB5SwExt_44_3															-5.17	0.14
0.425	KIMB5SwExt_44_4															-4.72	0.15
0.425	KIMB5SwExt_45_1	1567	692.3	2259.3	30.6	93.127	1375.6	190.295	IaAB	ir	some	colorless	1075		156.4	-2.55	0.16
0.425	KIMB5SwExt_45_2	1182.7	663.9	1846.6	36.0	179.932	1376.2	148.828	IaAB				1084.6	9.9	157.8	-2.41	0.15
0.425	KIMB5SwExt_46_1	617.3	197.1	814.4	24.2	16.003			IaAB	oc	some	colorless	1090.4		158.6	-4.19	0.13
0.425	KIMB5SwExt_46_2	638.4	202.1	840.5	24.0	19.817			IaAB				1089	0.9	158.5	-3.81	0.13
0.425	KIMB5SwExt_47_1															-6.48	0.13
0.425	KIMB5SwExt_47_2	189.6	189	378.6	49.9	4.598	1363.1	35.909	IaAB	do (frag)	high	brown	1135		165.2	-4.77	0.13
0.425	KIMB5SwExt_47_3															-4.26	0.13
0.425	KIMB5SwExt_48_1	674.1	354.8	1028.9	34.5	31.536	1373.2	69.615	IaAB	ir	some	colorless	1096.5		159.5	-4.55	0.15
0.425	KIMB5SwExt_48_2															-4.33	0.16
0.425	KIMB5SwExt_49_1	764.8	74.8	839.6	8.9	26.553	1374.2	14.195	IaA	ir	some	colorless	1063.1		154.7	-4.06	0.13

0.425	KIMB5SwExt_49_2	714.2	77.4	791.6	9.8	20.233	1372.5	10.728	IaA				1066.7	3.6	155.2	-3.90	0.14
0.425	KIMB5SwExt_50_1	788.5	147.1	935.6	15.7	27.439			IaAB	do (frag)	some	brown	1075		156.4	-3.50	0.15
0.425	KIMB5SwExt_50_2	695.7	190.4	886.1	21.5	24.729			IaAB				1085	9.9	157.9	-4.23	0.13
0.425	KIMB5SwExt_51_1	883.4	355.3	1238.7	28.7	128.695	1376.1	5.14	IaAB	oc (frag)	high	colorless	1086.1		158.0	-3.46	0.15
0.425	KIMB5SwExt_51_2															-3.65	0.13
0.425	KIMB5SwExt_52_1	8.6	224.8	233.4	96.3	64.366	1362.9	75.865	IaB	ir	low	colorless	1234		179.5	-4.67	0.14
0.425	KIMB5SwExt_52_2	40.2	172.6	212.8	81.1	42.045	1361.7	62.81	IaAB				1187.0		172.7	-4.31	0.14
0.425	KIMB5SwExt_52_3	54.6	77.6	132.2	58.7	38.344	1363.4	36.651	IaAB				1171	62.8	170.3	-3.84	0.14
0.425	KIMB5SwExt_53_1	237.3	19.3	256.6	7.5	6.69	1368.9	5.292	IaA	oc	low	colorless	1086		157.9	-5.16	0.15
0.425	KIMB5SwExt_53_2	275.3	31.1	306.4	10.2	2.645	1375.9	22.01	IaAB				1089	3.4	158.4	-5.62	0.15
0.425	KIMB5SwExt_55_1	0	0	0.0		0.0358			Type II	ir	high	colorless				-3.20	0.14
0.425	KIMB5SwExt_55_2															-2.53	0.14
0.425	KIMB5SwExt_56_1	729.9	214.2	944.1	22.7	42.686	1363.8	2.721	IaAB	do (frag)	high	yellow	1085.1		157.9		
0.425	KIMB5SwExt_56_2	868.6	39.8	908.4	4.4	27.947	1363.1	1.57	IaA				1045.0		152.0		
0.425	KIMB5SwExt_56_3	964.5	87.5	1052.0	8.3	30.369	1363.2	1.856	IaA				1056.5	40.1	153.7		
0.425	KIMB5SwExt_57_1	15.8	317.5	333.3	95.3	58.035	1363.5	193.592	IaB	oc	low	colorless	1216		177.0		
0.425	KIMB5SwExt_57_2	14.4	240.7	255.1	94.4	42.303	1363.7	159.638	IaB				1218.7	2.3	177.3		
0.425	KIMB5SwExt_58	12.2	642.8	655.0	98.1	19.945	1363.3	328.308	IaB	ir	low	colorless	1224		178.1		
0.425	KIMB5SwExt_60_1	906.9	90.4	997.3	9.1	32.717			IaA	ir	some	colorless	1059.8		154.2		
0.425	KIMB5SwExt_60_2	618.4	45.1	663.5	6.8	27.177	1370.3	0.685	IaA				1061.8	2.1	154.5		
0.425	KIMB5SwExt_61_1	58.8	588.8	647.6	90.9	61.329	1365.4	382.881	IaB	oc	low	colorless	1180.1		171.7	-6.03	0.13
0.425	KIMB5SwExt_61_2															-5.83	0.14
0.425	KIMB5SwExt_61_3															-5.75	0.14
0.425	KIMB5SwExt_62_1	1245.8	353.8	1599.6	22.1	18.934	1368.5	31.046	IaAB	macle	low	colorless	1072		156.0	-3.03	0.14
0.425	KIMB5SwExt_62_2	1231.1	310.3	1541.4	20.1	18.548	1375	35.591	IaAB				1071	1.8	155.8	-3.70	0.14
0.425	KIMB5SwExt_63	778.9	29.7	808.6	3.7	7.417	1376.6	10.139	IaA	do	high	colorless	1043.5		151.8		
0.425	KIMB5SwExt_64_1	16.1	79.6	95.7	83.2	8.381	1361.5	45.622	IaAB	do (frag)	high	colorless	1212		176.4	-4.95	0.12
0.425	KIMB5SwExt_64_2	15.8	63.3	79.1	80.0	3.015	1361.3	8.149	IaAB				1212	0.5	176.3	-4.43	0.16
0.425	KIMB5SwExt_65	538.1	37.9	576.0	6.6	20.511			IaA	ir	high	brown	1064.2		154.8		
0.425	KIMB5SwExt_66	1346.9	273.5	1620.4	16.9	110.131			IaAB	oc	some	colorless	1065		154.9		
0.425	KIMB5SwExt_67_1	801.4	67.2	868.6	7.7	37.593	1372.8	7.491	IaA	oc	low	colorless	1059.0		154.1		

0.425	KIMB5SwExt_67_2	890.9	113	1003.9	11.3	50.164	1375.6	5.737	IaAB				1065	5.9	154.9		
0.425	KIMB5SwExt_69_1	5.9	136.1	142.0	95.8	28.887	1362.7	99.435	IaB	ir	low	colorless	1244.0		181.0	-5.07	0.12
0.425	KIMB5SwExt_69_2	15.4	255.4	270.8	94.3	40.415	1363.4	165.68	IaB				1217	27.2	177.0	-4.92	0.14
0.425	KIMB6SwExt_15_1	0.0	0.0	0.0		4.773			Type II	do	high	brown				-4.87	0.21
0.425	KIMB6SwExt_15_2															-4.91	0.21
0.425	KIMB6SwExt_16	197	128.6	325.6	39.5				IaAB	do	high	brown	1128.8		164.2		
0.425	KIMB6SwExt_17_1	0.0	0.0	0.0					Type II	agg		colorless				-4.58	0.13
0.425	KIMB6SwExt_17_2															-4.37	0.13
0.425	KIMB6SwExt_18	566.7	272.5	839.2	32.5	71.424	1378	1.285	IaAB	do (frag)	high	colorless	1099.1		159.9		
0.425	KIMB6SwExt_19	674.5	170.4	844.9	20.2	23.375			IaAB	do	high	colorless	1084.2		157.7		
0.425	KIMB6SwExt_20_1	834.9	111.9	946.8	11.8	44.241	1374	29.259	IaAB	oc	low	colorless	1067.4		155.3	-3.74	0.14
0.425	KIMB6SwExt_20_2															-4.15	0.12
0.425	KIMB6SwExt_21	720.0	134.6	854.6	15.8	22.511	1373.3	31.361	IaAB	oc	some	colorless	1077.1		156.7		
0.425	KIMB6SwExt_23	539.9	152.2	692.1	22.0	15.494	1375.7	2.504	IaAB	do (frag)	high	colorless	1091.2		158.8		
0.425	KIMB6SwExt_24	830.8	133.9	964.7	13.9	50.683	1375.8	3.007	IaAB	do	high	colorless	1071.1		155.8		
0.3	KIMB3MainS_39	601.8	89	690.8	12.9	14.855	1371.8	28.663	IaAB	macle	low	colorless	1077		156.7		
0.3	KIMB3MainS_40	938	836	1774.0	47.1	147.972	1377.2	55.684	IaAB	oc	some	colorless	1096.1		159.5		
0.3	KIMB3MainS_41_1	679.9	268.8	948.7	28.3	34.977	1364	91.317	IaAB	do	high	colorless	1091.8		158.9	-5.03	0.22
0.3	KIMB3MainS_41_2															-5.22	0.22
0.3	KIMB3MainS_41_3															-4.01	0.21
0.3	KIMB3MainS_41_4															-4.30	0.21
0.3	KIMB3MainS_42_1	120	123.3	243.3	50.7	21.815			IaAB	oc (frag)	high	colorless	1147.1		166.9	-24.11	0.22
0.3	KIMB3MainS_42_2															-4.30	0.21
0.3	KIMB3MainS_42_3															-3.60	0.21
0.3	KIMB3MainS_43_1	1251	1306.3	2557.3	51.1	86.124	1377.2	7.572	IaAB	do (frag)	high	colorless	1091		158.8	-4.49	0.22
0.3	KIMB3MainS_43_2															-4.62	0.21
0.3	KIMB3MainS_44_1	725.4	12.5	737.9	1.7				IaA	do	high	colorless	1028.7		149.7	-4.18	0.21
0.3	KIMB3MainS_44_2															-4.54	0.22
0.3	KIMB3MainS_44_3															-4.34	0.21
0.3	KIMB3MainS_45	1526.3	126.3	1652.6	7.6	29.397			IaA	do	high	colorless	1044.8		152.0		
0.3	KIMB3MainS_46	872.9	48.4	921.3	5.3	33.894			IaA	ir	low	yellow	1049		152.6		

0.3	KIMB3MainS_47	51.1	238.5	289.6	82.4	18.74	1358.9	43.617	IaAB	do (frag)	high	colorless	1181.2		171.9		
0.3	KIMB3MainS_48	422.2	491.3	913.5	53.8	15.102	1367.7	37.423	IaAB	agg	some	colorless	1117.9		162.7		
0.3	KIMB3MainS_49	956.4	376.3	1332.7	28.2	46.36	1372	79.471	IaAB	ir	low	colorless	1083.9		157.7		
0.3	KIMB3MainS_50_1	817.3	226.9	1044.2	21.7	49.88			IaAB	oc	some	colorless	1082		157.4	-3.97	0.21
0.3	KIMB3MainS_50_2															-3.84	0.21
0.3	KIMB3MainS_51	904.8	255.9	1160.7	22.0		1373.4	48.677	IaAB	ir	some	brown	1080		157.1		
0.3	KIMB3MainS_52	761.2	115.2	876.4	13.1	87.327	1375.2	3.169	IaAB	do	high	colorless	1071.8		156.0		
0.3	KIMB3MainS_53_1	55.9	630.2	686.1	91.9	14.837	1365.3	436.277	IaB	do (frag)	high	colorless	1181.7		171.9	-4.97	0.21
0.3	KIMB3MainS_53_2															-5.04	0.22
0.3	KIMB3MainS_53_3															-5.33	0.23
0.3	KIMB3MainS_54_1	708.6	64.9	773.5	8.4	84.269			IaA	oc (frag)	some	colorless	1063.5		154.7	-4.43	0.22
0.3	KIMB3MainS_54_2															-4.24	0.22
0.3	KIMB3MainS_55_1									do (frag)	high	brown				-3.74	0.21
0.3	KIMB3MainS_55_2															-4.97	0.21
0.3	KIMB3MainS_56_1	681.6	10.6	692.2	1.5	4.212			IaA	do	high	brown	1027.9		149.6	-3.95	0.22
0.3	KIMB3MainS_56_2															-3.48	0.21
0.3	KIMB3MainS_57_1									do (frag)	high	colorless				-3.13	0.21
0.3	KIMB3MainS_57_2															-5.64	0.22
0.3	KIMB3MainS_58_1	1087.4	145.6	1233.0	11.8	153.403			IaAB	do	high	colorless	1062		154.5	-5.03	0.21
0.3	KIMB3MainS_58_2															-4.53	0.23
0.3	KIMB3MainS_59	713.1	278.2	991.3	28.1	56.995	1374.8	46.174	IaAB	do (frag)	high	colorless	1090.5		158.7		
0.3	KIMB5MainS_57_1	26.1	366.7	392.8	93.4	36.153	1361.3	154.409	IaB	do (frag)	high	brown	1202.2		174.9	-5.14	0.22
0.3	KIMB5MainS_57_2	28.4	300.5	328.9	91.4	27.524	1361.5	111.326	IaB				1199	2.8	174.5	-5.03	0.22
0.3	KIMB5MainS_58_1	806.9	107.3	914.2	11.7	14.386	1376.8	36.793	IaAB	do (frag)	high	colorless	1068.0		155.4	-4.41	0.22
0.3	KIMB5MainS_58_2															-2.87	0.22
0.3	KIMB5MainS_59	19.8	170.9	190.7	89.6	17.791	1362.1	57.004	IaAB	ir	some	colorless	1208.6		175.8		
0.3	KIMB5MainS_60_1	768.5	277.2	1045.7	26.5	56.362	1377.7	111.728	IaAB	do (frag)	high	colorless	1087.4		158.2		
0.3	KIMB5MainS_60_2	777.1	104.5	881.6	11.9	27.247	1377.8	22.064	IaAB				1069	18.4	155.6		
0.3	KIMB5MainS_62_1	741.4	158.2	899.6	17.6	43.611	1377.3	327.268	IaAB	ir	high	colorless	1078.9		157.0		
0.3	KIMB5MainS_62_2	653.1	448.7	1101.8	40.7	44.296	1376.9	661.839	IaAB				1101.1	22.1	160.2		
0.3	KIMB5MainS_63_1	951.2	317.5	1268.7	25.0	60.682	1377	40.348	IaAB	ir	high	colorless	1081.3		157.3		

0.3	KIMB5MainS_63_2	1220.4	179.3	1399.7	12.8	65.374	1378.1	24.376	IaAB				1061	20.5	154.4		
0.3	KIMB5MainS_64_1	783.9	460.5	1244.4	37.0	5.773	1369.2	253.243	IaAB	do	high	colorless	1094.6		159.3		
0.3	KIMB5MainS_64_2	807.6	452.7	1260.3	35.9	5.451	1369.4	275.537	IaAB				1093.3	1.4	159.1		
0.3	KIMB5MainS_65_1	672.1	174.3	846.4	20.6	37.733	1377.3	7.71	IaAB	ir	high	colorless	1085		157.8	-4.50	0.22
0.3	KIMB5MainS_65_2	599.8	167.6	767.4	21.8	44.072	1377	11.292	IaAB				1088.7	3.9	158.4	-4.31	0.22
0.3	KIMB5MainS_65_3															-3.73	0.21
0.3	KIMB5MainS_66_1	994.1	385.8	1379.9	28.0	100.883	1376.9	98.772	IaAB	do	high	colorless	1083		157.5		
0.3	KIMB5MainS_66_2	901.7	370.1	1271.8	29.1	10.718	1376.5	98.256	IaAB				1085.9	3.1	158.0		
0.3	KIMB5MainS_67_1	1275	641.2	1916.2	33.5	7.261	1375.6	178.478	IaAB	do (frag)	high	colorless	1081.2		157.3	-4.07	0.22
0.3	KIMB5MainS_67_2															-4.00	0.22
0.3	KIMB5MainS_67_3															-4.28	0.22
0.3	KIMB5MainS_68_1	906.2	40.4	946.6	4.3	12.859	1377.6	2.8	IaA	do (frag)	high	colorless	1043		151.8	-4.11	0.22
0.3	KIMB5MainS_68_2	952.2	62.2	1014.4	6.1	7.888	1377	6.27	IaA				1050.2	6.7	152.8	-4.66	0.22
0.3	KIMB5MainS_69_1	794	72.8	866.8	8.4	24.678	1377.7	4.697	IaA	do (frag)	high	brown	1061.0		154.4		
0.3	KIMB5MainS_69_2	844.4	124.9	969.3	12.9	22.949	1378	4.913	IaAB				1069.1	8.1	155.6		
0.3	KIMB5MainS_70_1	788.2	40.7	828.9	4.9	21.911	1376.9	12.027	IaA	ir	some	brown	1049.5		152.7	-2.96	0.22
0.3	KIMB5MainS_70_2															-3.11	0.21
0.3	KIMB5MainS_71	579.3	220.3	799.6	27.6	5.015	1376	58.114	IaAB	do (frag)	high	colorless	1095		159.3		
0.3	KIMB5MainS_72_1									ir	high	yellow				-3.41	0.22
0.3	KIMB5MainS_72_2															-3.34	0.21
0.3	KIMB5MainS_73_1	869.3	176.6	1045.9	16.9	3.805	1373.8	50.342	IaAB	oc (frag)	some	colorless	1074.5		156.3	-4.36	0.22
0.3	KIMB5MainS_73_2	821	89.1	910.1	9.8	3.442	1373.8	45.564	IaA				1063.6		154.8	-4.12	0.22
0.3	KIMB5MainS_73_3	824.9	121	945.9	12.8	34.53	1377.2	11.452	IaAB				1069	10.8	155.6	-3.67	0.22
0.3	KIMB5MainS_74_1	995.3	247.3	1242.6	19.9	37.109	1376.9	62.351	IaAB	ir	low	colorless	1075		156.4		
0.3	KIMB5MainS_74_2	819	378.7	1197.7	31.6	23.686	1377	127.398	IaAB				1090.0	14.9	158.6		
0.3	KIMB5MainS_75_1	297	407.8	704.8	57.9	190.894	1376.7	136.791	IaAB	oc (frag)	some	colorless	1128.1		164.1	-5.50	0.22
0.3	KIMB5MainS_75_2															-4.94	0.22
0.3	KIMB5MainS_76_1	782.3	485.4	1267.7	38.3	57.674	1376.7	102.238	IaAB	ir	some	colorless	1095.5		159.4		
0.3	KIMB5MainS_76_2	974	94.9	1068.9	8.9	54.958	1378.2	19.522	IaA				1057.7	37.7	153.9		
0.3	KIMB5MainS_77	782.5	84.6	867.1	9.8	2.542	1373.1	38.148	IaA	ir	some	colorless	1064.6		154.9		
0.3	KIMB5MainS_78_1	968.6	191.2	1159.8	16.5	34.985	1378	59.406	IaAB	ir	low	colorless	1072		155.9		

0.3	KIMB5MainS_78_2	1067.5	183.2	1250.7	14.6	87.017	1376.8	48.952	IaAB				1066.7	4.8	155.2		
0.3	KIMB5MainS_79_1	982.9	396.9	1379.8	28.8	269.619	1375.6	66.68	IaAB	do (frag)	high	colorless	1083.7		157.7	-5.71	0.21
0.3	KIMB5MainS_79_2	777.9	311.3	1089.2	28.6	173.684	1376.6	91.206	IaAB				1089	5.2	158.4	-4.95	0.21
0.3	KIMB5MainS_79_3															-4.23	0.22
0.3	KIMB5MainS_80	803.9	73.8	877.7	8.4	33.556	1375.9	184.787	IaA	do (frag)	high	colorless	1060.8		154.3		
0.3	KIMB5MainS_81	751.4	75.5	826.9	9.1	17.193	1378.1	6.492	IaA	do (frag)	high	colorless	1064		154.8		
0.3	KIMB5MainS_82_1	973.5	385.9	1359.4	28.4	44.488	1375.4	173.638	IaAB	ir	some	colorless	1083.6		157.7	-4.47	0.22
0.3	KIMB5MainS_82_2	1111	696.9	1807.9	38.5	11.897	1375.1	223.966	IaAB				1087.6		158.2	-4.54	0.21
0.3	KIMB5MainS_82_3	1094.5	653.1	1747.6	37.4	11.771	1375.3	212.878	IaAB				1087	4.0	158.2	-4.45	0.22
0.3	KIMB5MainS_83_1	1103.1	843	1946.1	43.3	400.598	1376.7	181.331	IaAB	ir	some	colorless	1090.4		158.7		
0.3	KIMB5MainS_83_2	1009.2	801.3	1810.5	44.3	424.834	1376.8	157.256	IaAB				1093		159.0		
0.3	KIMB5MainS_83_3	1544.2	1442.7	2986.9	48.3	878.6	1378.6	119.8	IaAB				1085.2	7.7	157.9		
0.3	KIMB5MainS_84_1	544.5	65.7	610.2	10.8	10.843	1376.7	40.171	IaAB	do (frag)	high	colorless	1074.9		156.4		
0.3	KIMB5MainS_84_2	792.6	41.7	834.3	5.0	12.218	1378.6	2.496	IaA				1049.8	25.1	152.7		
0.3	KIMB5MainS_85_1	828.6	126.5	955.1	13.2	96.914	1377.6	18.425	IaAB	ir	some	colorless	1070		155.7		
0.3	KIMB5MainS_85_2	690.7	258.6	949.3	27.2	64.405	1376.5	22.145	IaAB				1090.5	20.4	158.7		
0.3	KIMB5MainS_86_1	299.6	177.0	476.6	37.1	5.81	1376.5	69.909	IaAB	do (frag)	high	colorless	1117.3		162.6	-5.18	0.22
0.3	KIMB5MainS_86_2	359.9	154.8	514.7	30.1	12.614	1376.7	50.912	IaAB				1108	9.3	161.2	-3.36	0.22
0.3	KIMB5MainS_87_1	685.1	241.9	927.0	26.1	3.333	1376.9	105.951	IaAB	ir	some	colorless	1090		158.6	-3.55	0.22
0.3	KIMB5MainS_87_2	700.2	185.5	885.7	20.9	2.147	1376.4	34.822	IaAB				1084.2	5.5	157.8	-3.33	0.23
0.3	KIMB5MainS_88_1	1176.4	159.5	1335.9	11.9	19.36	1376.7	6.512	IaAB	oc (frag)	low	colorless	1060		154.2	-4.71	0.22
0.3	KIMB5MainS_88_2															-4.55	0.22
0.3	KIMB5MainS_89_1	1121.4	1085.8	2207.2	49.2	499.551	1377.4	188.589	IaAB	do	high	colorless	1092.9		159.0		
0.3	KIMB5MainS_89_2	939.2	694.7	1633.9	42.5	390.9	1376.0	176.3	IaAB				1093.7	0.7	159.1		
0.3	KIMB5MainS_90_2	37.5	59.8	97.3	61.5	6.636	1376.5	9.23	IaB	ir	high	colorless	1181.6		171.9		
0.3	KIMB5MainS_91	1068	153.9	1221.9	12.6	31.139	1374.9	57.346	IaAB	do (frag)	high	colorless	1063.4		154.7		
0.3	KIMB5MainS_92_1	530.3	706.2	1236.5	57.1	105.808	1376.8	253.094	IaAB	ir	some	colorless	1113.9		162.1		
0.3	KIMB5MainS_92_2	691.3	199.4	890.7	22.4	94.884	1376	35.467	IaAB				1086	27.9	158.0		
0.3	KIMB5MainS_93	599.1	340.2	939.3	36.2	35.582	1376.9	93.363	IaAB	ir	some	colorless	1100.4		160.1		
0.3	KIMB5MainS_94_1	849	78.9	927.9	8.5	15.587	1377	13.932	IaA	do (frag)	high	colorless	1060		154.2		
0.3	KIMB5MainS_94_2	881.3	126.3	1007.6	12.5	44.326	1376.7	16.683	IaAB				1067.5	7.7	155.3		

0.3	KIMB5MainS_95_1	1115.4	465.2	1580.6	29.4	236.157	1377.5	110.286	IaAB	do	high	colorless	1081.4		157.3		
0.3	KIMB5MainS_95_2	1027.5	502.2	1529.7	32.8	221.712	1377.3	68.538	IaAB				1085.7	4.3	158.0		
0.3	KIMB5MainS_96_1	892.1	187.4	1079.5	17.4	75.734	1377.6	11.63	IaAB	do (frag)	high	colorless	1074.5		156.3	-4.07	0.21
0.3	KIMB5MainS_96_2															-4.88	0.22
0.3	KIMB5MainS_97_1	41.3	69.7	111.0	62.8	8.07	1376.8	27.211	IaAB	do (frag)	high	colorless	1179.6		171.6		
0.3	KIMB5MainS_97_2	83.7	163.9	247.6	66.2	22.397	1376.6	66.731	IaAB				1163	16.8	169.2		
0.3	KIMB5SwExt_100_1	644.5	182.9	827.4	22.1	86.285	1373	12.261	IaAB	do	high	colorless	1087.3		158.2		
0.3	KIMB5SwExt_100_2	847.5	154.7	1002.2	15.4	105.668	1374.9	13.73	IaAB				1073.0	14.3	156.1		
0.3	KIMB5SwExt_101_1	854.1	139.2	993.3	14.0	44.376	1378.3	4.489	IaAB	do	some	colorless	1070.7		155.8	-3.92	0.13
0.3	KIMB5SwExt_101_2															-4.40	0.14
0.3	KIMB5SwExt_101_3															-3.56	0.15
0.3	KIMB5SwExt_102_1	623.9	585.7	1209.6	48.4	11.588	1375.8	15.556	IaAB	ir	some	yellow	1106.2		161.0	-4.01	0.13
0.3	KIMB5SwExt_102_2															-3.99	0.13
0.3	KIMB5SwExt_103_1	30.8	476.2	507.0	93.9	7.694	1362.4	220.584	IaB	ir	high	brown	1198		174.3		
0.3	KIMB5SwExt_103_2	13.2	239.7	252.9	94.8	37.348	1363.7	84.699	IaB				1221.2		177.7		
0.3	KIMB5SwExt_103_3	31.6	433.2	464.8	93.2	10.674	1362.6	204.331	IaB				1197.1	24.1	174.2		
0.3	KIMB5SwExt_104_1	501.6	78	579.6	13.5	15.244			IaAB	oc	low	colorless	1081.7		157.4	-3.89	0.12
0.3	KIMB5SwExt_104_2	752.1	56.1	808.2	6.9	15.5			IaA				1058.0	23.7	153.9	-3.55	0.14
0.3	KIMB5SwExt_105	54.3	14.3	68.6	20.8	8.586	1361.6	2.204	IaAB	do	high	colorless	1144.7		166.6		
0.3	KIMB5SwExt_106_1	638.6	280.8	919.4	30.5	69.26	1363	2.353	IaAB	do	high	colorless	1095		159.3		
0.3	KIMB5SwExt_106_2	559.1	171.2	730.3	23.4	57.106	1376.8	12.85	IaAB				1091.9	3.0	158.9		
0.3	KIMB5SwExt_107	30.1	90.6	120.7	75.1	25.038	1376.8	11.779	IaAB	do (frag)	high	brown	1193		173.5		
0.3	KIMB5SwExt_108_1	974.2	335.3	1309.5	25.6	169.128	1377	68.453	IaAB	oc (frag)	low	colorless	1081		157.3	-4.84	0.23
0.3	KIMB5SwExt_108_2	834.1	196.4	1030.5	19.1	100.829	1376	51.89	IaAB				1078.1	3.2	156.9	-5.20	0.22
0.3	KIMB5SwExt_108_3															-5.23	0.22
0.3	KIMB5SwExt_110_1	704.8	71.6	776.4	9.2	15.217	1363.4	0.959	IaA	do	high	brown	1065.7		155.1		
0.3	KIMB5SwExt_110_2	770.4	37	807.4	4.6	14.325	1373.9	3.095	IaA				1048	17.2	152.6		
0.3	KIMB5SwExt_111_1	17.2	579.2	596.4	97.1	16.141	1363.5	381.53	IaB	do (frag)	high	colorless	1214.6		176.7	-4.58	0.14
0.3	KIMB5SwExt_111_2	23.9	581.6	605.5	96.1	24.337	1363.6	311.848	IaB				1205	9.2	175.4	-4.83	0.13
0.3	KIMB5SwExt_112_1	780	211.2	991.2	21.3	22.956	1372.4	27.973	IaAB	do (frag)	high	colorless	1082.1		157.5	-3.75	0.14
0.3	KIMB5SwExt_112_2															-4.84	0.14

0.3	KIMB5SwExt_112_3															-4.02	0.12
0.3	KIMB5SwExt_113	605.6	243.2	848.8	28.7	15.839	1365.2	2.804	IaAB	ir	some	white/milky	1094.7		159.3		
0.3	KIMB5SwExt_114	606.7	389.2	995.9	39.1	87.655	1374.3	71.153	IaAB	ir	some	colorless	1101.8		160.3		
0.3	KIMB5SwExt_115	9.8	5.2	15.0	34.7	10.34			IaAB	oc	low	colorless	1201.9		174.9		
0.3	KIMB5SwExt_116_1	967.5	117.2	1084.7	10.8	28.996	1376.5	4.461	IaAB	oc (frag)	low	colorless	1062.2		154.5		
0.3	KIMB5SwExt_116_2	826	78.1	904.1	8.6	36.693	1377.4	25.02	IaA				1060.8	1.4	154.3		
0.3	KIMB5SwExt_117_1	400.1	127.9	528.0	24.2	11.504	1369.9	11.164	IaAB	oc	some	brown	1100		160.1	-3.05	0.24
0.3	KIMB5SwExt_117_2	348.7	228.4	577.1	39.6	27.047	1372.5	26.104	IaAB				1115.2	14.8	162.3	-3.51	0.22
0.3	KIMB5SwExt_118_1	1435	602.1	2037.1	29.6	193.995	1376.3	163.646	IaAB	ir	some	colorless	1075.8		156.5	-2.75	0.24
0.3	KIMB5SwExt_118_2	1161.9	702.3	1864.2	37.7	180.192	1377	155.011	IaAB				1086.0	10.3	158.0	-3.27	0.21
0.3	KIMB5SwExt_119	393.9	397	790.9	50.2	22.617	1374.4	17.786	IaAB	oc	low	yellow	1117.9		162.7		
0.3	KIMB5SwExt_120_1	1304.3	306.3	1610.6	19.0	185.154	1379	6.461	IaAB	oc	high	colorless	1068.1		155.4	-4.28	0.22
0.3	KIMB5SwExt_120_2	1203.7	377.9	1581.6	23.9	153.67	1379.1	6	IaAB				1075.0	6.9	156.4	-3.97	0.23
0.3	KIMB5SwExt_120_3															-3.06	0.22
0.3	KIMB5SwExt_121_1	1098.3	407.6	1505.9	27.1	123.263	1375.7	92.498	IaAB	oc (frag)	high	colorless	1079.8		157.1	-5.49	0.23
0.3	KIMB5SwExt_121_2	851.4	213.9	1065.3	20.1	36.556	1372.8	78.997	IaAB				1078.8	1.0	157.0	-4.47	0.22
0.3	KIMB5SwExt_121_3															-3.72	0.22
0.3	KIMB5SwExt_122_1	1081.5	139.9	1221.4	11.5	21.173	1374.7	64.291	IaAB	ir	low	colorless	1061.0		154.4	-4.81	0.21
0.3	KIMB5SwExt_122_2	985.9	164.5	1150.4	14.3	29.859	1374.1	51.213	IaAB				1068.0	6.9	155.4	-4.88	0.22
0.3	KIMB5SwExt_123_1	590.7	279.8	870.5	32.1	17.885	1373.6	51.404	IaAB	do (frag)	some	colorless	1098		159.7	-3.93	0.21
0.3	KIMB5SwExt_123_2															-3.83	0.23
0.3	KIMB5SwExt_124_1	1007.4	99.7	1107.1	9.0	15.167	1377.8	1.97	IaA	ir	some	milky	1057.3		153.8		
0.3	KIMB5SwExt_124_2	1140.2	129.3	1269.5	10.2	17.137			IaAB				1057.3	0.0	153.8		
0.3	KIMB5SwExt_125_1	576.3	399.4	975.7	40.9	88.219	1371.8	234.312	IaAB	oc (frag)	some	colorless	1104.1		160.6	-3.66	0.22
0.3	KIMB5SwExt_125_2	643.3	489.3	1132.6	43.2	77.874	1371.9	223.301	IaAB				1103	1.3	160.5	-3.93	0.22
0.3	KIMB5SwExt_125_3															-2.32	0.22
0.3	KIMB5SwExt_126_1	534.4	246.8	781.2	31.6	6.626	1372.1	60.5	IaAB	do (frag)	high	colorless	1099.8		160.0		
0.3	KIMB5SwExt_126_2	683	105.9	788.9	13.4	2.249	1372.6	39.474	IaAB				1075	25.1	156.4		
0.3	KIMB5SwExt_127	451	275.2	726.2	37.9	153.392	1378.5	9.798	IaAB	oc	low	colorless	1108.1		161.2		
0.3	KIMB5SwExt_128_1	1108.3	230.8	1339.1	17.2	148.729	1379	5.123	IaAB	ir	some	colorless	1069.5		155.6		
0.3	KIMB5SwExt_128_2	2030.8	468.5	2499.3	18.7	181.564			IaAB				1058.0	11.5	153.9		

0.3	KIMB5SwExt_129_1	786.7	138.1	924.8	14.9	16.953	1376.3	54.71	IaAB	ir	some	colorless	1073.9		156.3	-4.38	0.22
0.3	KIMB5SwExt_129_2	818	109.9	927.9	11.8	24.745	1375.7	45.959	IaAB				1068	6.0	155.4	-4.95	0.23
0.3	KIMB5SwExt_130_1									agg	low	colorless				-6.78	0.22
0.3	KIMB5SwExt_130_2															-6.81	0.22
0.3	KIMB5SwExt_131_1	63.5	417.8	481.3	86.8	101.792	1365.3	217.839	IaAB	do	high	brown	1177		171.2		
0.3	KIMB5SwExt_131_2	74.2	49.3	123.5	39.9	8.782	1363.5	9.516	IaAB				1153.1	23.8	167.8		
0.3	KIMB5SwExt_70	73.1	717.4	790.5	90.8	35.874	1364.8	429.2	IaB	oc	low	colorless	1174		170.9		
0.3	KIMB5SwExt_71_1	921.9	246	1167.9	21.1	18.041	1373	90.868	IaAB	oc	some	colorless	1078.1		156.9	-3.78	0.21
0.3	KIMB5SwExt_71_2															-3.16	0.22
0.3	KIMB5SwExt_72	232.6	153.7	386.3	39.8	54.198	1362	65.474	IaAB	do (frag)	high	brown	1125		163.7		
0.3	KIMB5SwExt_73_1	820.7	26.4	847.1	3.1				IaA	do	high	colorless	1038.9		151.2	-4.25	0.22
0.3	KIMB5SwExt_73_2	818.3	57.0	875.3	6.5	1.396			IaA				1054.8	15.9	153.5	-4.40	0.21
0.3	KIMB5SwExt_74	758.3	48.1	806.4	6.0	2.187	1370.5	23.438	IaA	ir	some	colorless	1054.5		153.4		
0.3	KIMB5SwExt_75_1	1209.7	299.1	1508.8	19.8	72.768	1376.9	8.171	IaAB	ir	low	colorless	1070.7		155.8	-3.97	0.23
0.3	KIMB5SwExt_75_2	1377.2	246.1	1623.3	15.2	46.603	1378.1	43.006	IaAB				1062	8.8	154.5	-4.13	0.21
0.3	KIMB5SwExt_75_3															-4.10	0.22
0.3	KIMB5SwExt_76_1	381.7	176	557.7	31.6	10.392	1364.9	124.818	IaAB	do	high	colorless	1107.7		161.2		
0.3	KIMB5SwExt_76_2	263.1	366.8	629.9	58.2	20.076	1363.9	112.878	IaAB				1131.2	23.5	164.6		
0.3	KIMB5SwExt_77_1	1126.7	391.6	1518.3	25.8	17.566	1373.2	117.002	IaAB	macle	low	colorless	1078.2		156.9	-3.86	0.22
0.3	KIMB5SwExt_77_2															-3.78	0.21
0.3	KIMB5SwExt_77_3															-3.70	0.23
0.3	KIMB5SwExt_78_1	90.7	36.0	126.7	28.4	5.49	1377	4.115	IaAB	do (frag)	high	colorless	1140		165.8	1.90	0.21
0.3	KIMB5SwExt_78_2	158.1	47.4	205.5	23.1	7.439	1377.7	2.31	IaAB				1121.1	18.5	163.1	-3.60	0.22
0.3	KIMB5SwExt_78_3															1.75	0.22
0.3	KIMB5SwExt_79	0	0	0.0					Type II	oc	high	colorless					
0.3	KIMB5SwExt_80_1	12.5	15.6	28.1	55.5	9.035	1376.7	8.442	IaAB	oc (frag)	low	brown	1208.1		175.8	-3.30	0.22
0.3	KIMB5SwExt_80_2	25.9	23.4	49.3	47.5	5.769	1376.7	8.711	IaAB				1184.5	23.5	172.3	-3.27	0.21
0.3	KIMB5SwExt_81	686.8	139.6	826.4	16.9	1.065	1367.5	65.572	IaAB	do (frag)	high	colorless	1079.8		157.1		
0.3	KIMB5SwExt_82_1	0	0	0.0					Type II	ir	some	colorless				-4.00	0.21
0.3	KIMB5SwExt_82_2															-3.88	0.22
0.3	KIMB5SwExt_83_1	1207.2	37.8	1245.0	3.0	13.598			IaA	do (frag)	high	yellow	1030		149.9		

0.3	KIMB5SwExt_83_2	1107.6	108.9	1216.5	9.0	15.039			IaA	do (frag)	high	yellow	1055.1	24.9	153.5		
0.3	KIMB5SwExt_84_1	830.4	660.2	1490.6	44.3	46.783	1376	122.623	IaAB	do	high	colorless	1097.5		159.7	-4.14	0.22
0.3	KIMB5SwExt_84_2															-3.8	0.2
0.3	KIMB5SwExt_85_1	1060.7	209.5	1270.2	16.5	6.6	1373.8	87.2	IaAB	oc	low	colorless	1069.5		155.6		
0.3	KIMB5SwExt_85_2	910.9	390.2	1301.1	30.0	3.664	1373.4	115.15	IaAB				1086	16.9	158.1		
0.3	KIMB5SwExt_86_1	904.9	50.4	955.3	5.3	25.982			IaA	do	high	colorless	1048.1		152.5		
0.3	KIMB5SwExt_86_2	653.2	81	734.2	11.0	19.269			IaAB				1071.3	23.3	155.9		
0.3	KIMB5SwExt_87_1	565.8	71.2	637.0	11.2		1375.8	34.52	IaAB	ir	high	colorless	1074.8		156.4	-3.93	0.22
0.3	KIMB5SwExt_87_2															-3.78	0.22
0.3	KIMB5SwExt_88_1	1196.3	306.7	1503.0	20.4	14.833	1374	2.387	IaAB	cube	some	yellow	1071.6		155.9		
0.3	KIMB5SwExt_88_2	954.7	173	1127.7	15.3	14.446	1374.6	1.639	IaAB				1070.2	1.3	155.7		
0.3	KIMB5SwExt_89_1	158.8	528.2	687.0	76.9	21.272	1365.2	416.279	IaAB	ir	some	colorless	1150.5		167.4	-5.62	0.22
0.3	KIMB5SwExt_89_2															-5.3	0.2
0.3	KIMB5SwExt_90	0	0	0					Type II	do	high	colorless					
0.3	KIMB5SwExt_91_1	38.6	129	167.6	77.0	28.838	1361.6	67.262	IaAB	do	high	brown	1186.7		172.7		
0.3	KIMB5SwExt_91_2	38.7	130.0	168.7	77.1	28.4	1361.5	64.2	IaAB				1186.7	0.0	172.7		
0.3	KIMB5SwExt_92_1	1359.7	407	1766.7	23.0	8.15	1372.3	233.534	IaAB	do (frag)	high	colorless	1071.4		155.9	-7.17	0.21
0.3	KIMB5SwExt_92_2															-7.51	0.22
0.3	KIMB5SwExt_93_1	42.4	295.1	337.5	87.4	66.526	1363.4	193.954	IaAB	oc	low	colorless	1187.6		172.8		
0.3	KIMB5SwExt_93_2	64.8	378.1	442.9	85.4	49.101	1363.1	139.447	IaAB				1175.9	11.7	171.1		
0.3	KIMB5SwExt_94_1	1084.9	0	1084.9	0.0	13.988			IaA	ir	some	colorless				-4.49	0.23
0.3	KIMB5SwExt_94_2	1009.5	0	1009.5	0.0	13.816	1373	4.153	IaA							-3.60	0.21
0.3	KIMB5SwExt_95_1	719.4	53.6	773.0	6.9	18.673	1374.9	20.155	IaA	do	high	colorless	1059.0		154.1	-3.98	0.22
0.3	KIMB5SwExt_95_2															-3.86	0.22
0.3	KIMB5SwExt_96	498.7	306.8	805.5	38.1	5.548	1378.8	90.304	IaAB	ir	low	colorless	1105.8		160.9		
0.3	KIMB5SwExt_97_1	1058.4	1115.7	2174.1	51.3	307.315	1377	187.354	IaAB	do	high	colorless	1095.2		159.4		
0.3	KIMB5SwExt_97_2	297.3	333.5	630.8	52.9	215.38	1376	105.845	IaAB				1125.9	30.7	163.8		
0.3	KIMB5SwExt_98_1	948.4	152	1100.4	13.8	20.816	1363.5	1.735	IaAB	do (frag)	high	yellow	1068.1		155.4		
0.3	KIMB5SwExt_98_2	651.2	389.5	1040.7	37.4	22.945			IaAB				1099.2	31.1	159.9		
0.3	KIMB5SwExt_99_1	111.1	104.1	215.2	48.4	7.771	1364.6	8.257	IaAB	do (frag)	high	brown	1147.8		167.0		
0.3	KIMB5SwExt_99_2	149.1	81.7	230.8	35.4	3.527	1365.7	4.054	IaAB				1132.9	14.9	164.8		

0.3	KIMB6SwExt_25	193.9	494.4	688.3	71.8	2.128	1363.3	209.523	IaAB	do (frag)	high	brown	1143.8		166.4		
0.3	KIMB6SwExt_27_1	700.9	20.7	721.6	2.9	16.934	1377	14.289	IaA	oc	low	colorless	1040.5		151.4		
0.3	KIMB6SwExt_27_2	677.1	88.4	765.5	11.5	19.005	1377.7	3.04	IaAB				1071.6	31.1	155.9		
0.3	KIMB6SwExt_28	259.8	160.1	419.9	38.1		1376.7	20.113	IaAB	agg	some	milky	1121.3		163.1		
0.3	KIMB6SwExt_29_1	0	0	0.0					Type II	do (frag)	high	milky				-4.80	0.22
0.3	KIMB6SwExt_29_2															-4.52	0.21
0.3	KIMB6SwExt_30_1									do (frag)	high	brown				-4.57	0.21
0.3	KIMB6SwExt_30_2															-5.06	0.22
0.3	KIMB6SwExt_31_1	24.5	818.1	842.6	97.1	56.709	1363.6	334.042	IaAB	ir	some	brown	1205.0		175.3	-4.66	0.22
0.3	KIMB6SwExt_31_2	82.7	479.5	562.2	85.3	61.526	1363.2	303.599					1169.6	35.4	170.2	-4.71	0.23
0.3	KIMB6SwExt_32_1	726.9	45.6	772.5	5.9		1376	42.763	IaA	do	high	brown	1055.2		153.5	-3.93	0.22
0.3	KIMB6SwExt_32_2															-3.69	0.22
0.3	KIMB6SwExt_32_3															-4.20	0.22
0.3	KIMB6SwExt_33	0	0	0.0		4.969			Type II	do (frag)	high	colorless					
0.3	KIMB6SwExt_34	878.1	89.6	967.7	9.3	12.116	1377	11.758	IaA	do (frag)	high	colorless	1060.9		154.4		
0.3	KIMB6SwExt_36_1	306.9	179.6	486.5	36.9	22.91	1363.9	116.546	IaAB	oc (frag)	low	colorless	1116.5		162.5	-3.78	0.22
0.3	KIMB6SwExt_36_2	298.6	190.2	488.8	38.9	27.147	1363.8	131.499	IaAB				1118.4	1.9	162.7	-3.31	0.22
0.3	KIMB6SwExt_37_1	1131.6	560.6	1692.2	33.1	153.781	1377.8	19.871	IaAB	ir	high	colorless	1083.7		157.7	-5.36	0.21
0.3	KIMB6SwExt_37_2															-4.19	0.21
0.3	KIMB6SwExt_37_3															-4.49	0.22
0.3	KIMB6SwExt_38_1	0	0	0.0		36.086			Type II	ir	low	colorless				-3.12	0.22
0.3	KIMB6SwExt_38_2															-3.59	0.23
0.3	KIMB6SwExt_39_1	86.2	81	167.2	48.4	13.145	1363.4	4.545	IaAB	do (frag)	high	colorless	1154.2		167.9		
0.3	KIMB6SwExt_39_2	67.7	58.1	125.8	46.2	12.113	1376.6	6.782					1159.1	4.9	168.6		
0.3	KIMB6SwExt_40	89.2	20.4	109.6	18.6	0.798	1377	28.552	IaAB	oc (frag)	some	brown	1130		164.4		
0.3	KIMB6SwExt_41	864.8	97.8	962.6	10.2	1.007	1376	76.751	IaAB	oc	low	colorless	1063.3		154.7		
0.3	KIMB6SwExt_42_1	1315.7	330.4	1646.1	20.1	171.956	1376.5	26.143	IaAB	ir	high	colorless	1069.1		155.6	-4.68	0.21
0.3	KIMB6SwExt_42_2															-4.56	0.22
0.3	KIMB6SwExt_42_3															-3.87	0.22
0.3	KIMB6SwExt_43_1	388.9	111.3	500.2	22.3	10.65	1369.7	2.55	IaAB	do (frag)	high	brown	1099.1		159.9	-5.86	0.22
0.3	KIMB6SwExt_43_2															-5.65	0.23

0.3	KIMB6SwExt_43_3															-4.95	0.22
0.3	KIMB6SwExt_44_1	1103.8	124.2	1228.0	10.1	36.287	1362.8	2.222	IaAB	do (frag)	high	yellow	1057.9		153.9		
0.3	KIMB6SwExt_44_2	1124.8	141	1265.8	11.1	35.429	1362.8	2.052	IaAB				1059.6	1.7	154.2		
0.3	KIMB6SwExt_45_1	814.1	85.4	899.5	9.5	60.634	1376.1	11.139	IaA	do (frag)	high	colorless	1063.1		154.7	-4.13	0.21
0.3	KIMB6SwExt_45_2	604.5	187.2	791.7	23.6	40.909	1376.5	17.572	IaAB				1090.3	27.2	158.6	-3.67	0.22
0.3	KIMB6SwExt_45_3															-4.16	0.22
0.3	KIMB6SwExt_45_4															-3.76	0.22
0.3	KIMB6SwExt_46_1	779.7	451.9	1231.6	36.7	115.534	1379.7	2.824	IaAB	do (frag)	high	colorless	1094.6		159.3		
0.3	KIMB6SwExt_46_2	709.9	106.2	816.1	13.0	55.478	1376.7	7.983					1073	21.4	156.1		
0.3	KIMB6SwExt_47	841.7	15.7	857.4	1.8	5.234	1375.6	31.709	IaA	do (frag)	high	brown	1027		149.5		
0.3	KIMB6SwExt_48_1	943.4	63.4	1006.8	6.3	35.745	1377	25.886	IaA	do	high	colorless	1051.0		152.9	-4.04	0.23
0.3	KIMB6SwExt_48_2															-4.91	0.21
0.3	KIMB6SwExt_48_3															-4.44	0.21
0.3	KIMB6SwExt_49	893.9	52.6	946.5	5.6	23.724	1378.9	12.998	IaA	oc (frag)	high	colorless	1049.4		152.7		
0.3	KIMB6SwExt_50_1	385.8	477.5	863.3	55.3	204.171	1377.1	107.451	IaAB	do (frag)	high	colorless	1120.7		163.1	-4.77	0.21
0.3	KIMB6SwExt_50_2															-4.97	0.22
0.3	KIMB6SwExt_51_1	0	0	0.0		5.135			Type II	macle	low	colorless				-3.56	0.21
0.3	KIMB6SwExt_51_2															-4.10	0.22
0.3	KIMB6SwExt_52_1	0	0	0.0		11.223			Type II	ir	some	colorless				-2.96	0.23
0.3	KIMB6SwExt_52_2															-3.70	0.22
0.3	KIMB6SwExt_53_1	1193.2	106.6	1299.8	8.2	69.32			IaA	do (frag)	high	colorless	1051.6		153.0	-4.88	0.22
0.3	KIMB6SwExt_53_2	1105.4	173.0	1278.4	13.5	78.512	1363.3	3.085	IaAB				1064.2	12.6	154.8	-3.50	0.22
0.3	KIMB6SwExt_53_3															-4.18	0.21
0.212	KIMB3MainS_60_1	681	195.6	876.6	22.3	49.679	1377	53.125	IaAB	ir	some	colorless	1086.3		158.1	-5.08	0.22
0.212	KIMB3MainS_60_2															-5.56	0.22
0.212	KIMB3MainS_61_1									oc	some	colorless				-2.70	0.14
0.212	KIMB3MainS_61_2															-5.74	0.14
0.212	KIMB3MainS_62_1	915.9	42.7	958.6	4.5	42.755	1376.5	30.473	IaAB	do	high	colorless	1044.2		151.9	-3.61	0.14
0.212	KIMB3MainS_62_2															-2.67	0.13
0.212	KIMB3MainS_63	993.2	572.4	1565.6	36.6	169.191	1376.9	36.569	IaAB	do	high	colorless	1088.9		158.4		
0.212	KIMB3MainS_64_1	1017.8	174.5	1192.3	14.6	87.168	1376.2	60.575	IaAB	do (frag)	high	colorless	1067.8		155.4	-5.40	0.13

0.212	KIMB3MainS_64_2														-5.13	0.12
0.212	KIMB3MainS_65	702	200.6	902.6	22.2	31.168			IaAB	do (frag)	high	colorless	1085.5	157.9		
0.212	KIMB3MainS_66	1564.5	718	2282.5	31.5	262.926	1376.5	126.103	IaAB	oc	low	colorless	1075.2	156.4		
0.212	KIMB3MainS_67	619.1	141.4	760.5	18.6	6.713			IaAB	ir	some	milky	1084.3	157.8		
0.212	KIMB3MainS_68_1									oc (frag)	low	colorless			-5.65	0.14
0.212	KIMB3MainS_68_2														-5.84	0.12
0.212	KIMB3MainS_70	31.3	1234.2	1265.5	97.5	68.195	1370.1	511.695	IaB	do	high	colorless	1198.5	174.4		
0.212	KIMB3MainS_71_1									do (frag)	high	colorless			-14.29	0.14
0.212	KIMB3MainS_71_2														-4.06	0.14
0.212	KIMB3MainS_71_3														-3.68	0.14
0.212	KIMB3MainS_72_1	620	468.7	1088.7	43.1	94.359			IaAB	ir	some	colorless	1103.6	160.6	-5.71	0.13
0.212	KIMB3MainS_72_2														-5.83	0.12
0.212	KIMB3MainS_73	685.5	31.3	716.8	4.4	4.349	1376.9	121.21	IaA	do (frag)	high	colorless	1050.0	152.8		
0.212	KIMB3MainS_74_1	810.4	447.2	1257.6	35.6	178.213	1375.2	100.79	IaAB	ir			1092.9	159.0	-5.08	0.12
0.212	KIMB3MainS_74_2														-4.69	0.13
0.212	KIMB3MainS_74_3														-5.18	0.12
0.212	KIMB3MainS_75_1	595.3	600.9	1196.2	50.2	172.368			IaAB	oc (frag)	low	brown	1108.2	161.2	-4.48	0.13
0.212	KIMB3MainS_75_2														-4.04	0.12
0.212	KIMB3MainS_75_3														-5.99	0.12
0.212	KIMB3MainS_76_1									do	high	colorless			-4.95	0.13
0.212	KIMB3MainS_76_2														-6.25	0.13
0.212	KIMB3MainS_77_1	1227.3	432.4	1659.7	26.1	106.954	1375	23.059	IaAB	oc	low	colorless	1076.4546	156.6	-4.22	0.12
0.212	KIMB3MainS_77_2														-3.80	0.12
0.212	KIMB3MainS_77_3														-4.25	0.13
0.212	KIMB3MainS_78	775.9	469.8	1245.7	37.7		1367.9	63.515	IaAB	ir			1095.3066	159.4		
0.212	KIMB3MainS_79_1	33.1	184.7	217.8	84.8	46.773	1363.5	116.188	IaAB	oc	low	colorless	1193.3435	173.6	-1.05	0.12
0.212	KIMB3MainS_79_2														-4.44	0.13
0.212	KIMB3MainS_79_3														-3.96	0.13
0.212	KIMB3MainS_81_1	0	0	0.0					Type II	agg	some	colorless			-4.36	0.12
0.212	KIMB3MainS_81_2														-3.93	0.12
0.212	KIMB3MainS_82_1	979.2	375.2	1354.4	27.7	233.358	1378	27.602	IaAB	oc	some	colorless	1082.9	157.6	-2.97	0.12

0.212	KIMB3MainS_82_2															-3.14	0.13
0.212	KIMB3MainS_84	143.3	206.0	349.3	59.0	41.263	1370.5	41.334	IaAB	oc	high	colorless	1146.4		166.8		
0.212	KIMB3MainS_85	631.2	308.6	939.8	32.8	48.604			IaAB	do (frag)	high	milky	1096.9		159.6		
0.212	KIMB3MainS_86_1	263.7	327.5	591.2	55.4				IaAB	do	high	colorless	1129.9		164.4	-3.79	0.13
0.212	KIMB3MainS_86_2															-3.98	0.12
0.212	KIMB3MainS_87_1	601	266.4	867.4	30.7	188.501	1375.5	40.887	IaAB	do (frag)	high	brown	1096.5		159.5	-4.46	0.13
0.212	KIMB3MainS_87_2															-5.43	0.12
0.212	KIMB5MainS_101_1	957.4	197.3	1154.7	17.1	47.953	1363.2	2.948	IaAB	ir	high	colorless	1072.6		156.1	-5.05	0.12
0.212	KIMB5MainS_101_2	686.2	280.1	966.3	29.0	39.206	1363.6	1.3	IaAB				1092.1	19.5	158.9	-3.79	0.14
0.212	KIMB5MainS_101_3															-3.45	0.13
0.212	KIMB5MainS_102	1138	364.6	1502.6	24.3	83.527	1375.3	84.768	IaAB	do	high	colorless	1076.6		156.6		
0.212	KIMB5MainS_103	0	0.0	0.0		1.036			Type II	ir	some	colorless					
0.212	KIMB5MainS_104_1	561.8	185.4	747.2	24.8	10.761	1377.5	11.877	IaAB	ir	high	colorless	1093.1		159.0		
0.212	KIMB5MainS_104_2	636.8	160.9	797.7	20.2	11.155	1377.5	5.755	IaAB				1085.5	7.6	157.9		
0.212	KIMB5MainS_105_1	118.7	80	198.7	40.3	2.026			IaAB	oc (frag)	low	colorless	1141.7		166.1		
0.212	KIMB5MainS_105_2	199.6	63.4	263.0	24.1	1.923			IaAB				1116.6	25.0	162.5		
0.212	KIMB5MainS_106	0	0	0.0					Type II	ir	high	brown					
0.212	KIMB5MainS_107_1	725.3	197.9	923.2	21.4	54.455	1376.3	15.72	IaAB	ir	some	colorless	1083.9		157.7		
0.212	KIMB5MainS_107_2	429.9	207.2	637.1	32.5	67.242	1376.4	19.396	IaAB				1105.6	21.7	160.9		
0.212	KIMB5MainS_108_1	735.7	164.6	900.3	18.3	31.157	1373.6	70.027	IaAB	ir	some	colorless	1080.0		157.1	-5.02	0.13
0.212	KIMB5MainS_108_2															-5.50	0.12
0.212	KIMB5MainS_108_3															-5.23	0.12
0.212	KIMB5MainS_109	29.1	54.8	83.9	65.3	12.014	1360	1.458	IaAB	ir	low	colorless	1189.8		173.1		
0.212	KIMB5MainS_110_1	542.6	76.1	618.7	12.3				IaAB	ir	low	yellow	1077.9		156.8	-5.67	0.14
0.212	KIMB5MainS_110_2															-5.55	0.14
0.212	KIMB5MainS_111	834.7	290.6	1125.3	25.8	6.629	1375.1	30.661	IaAB	do (frag)	high	brown	1085.0		157.9		
0.212	KIMB5MainS_112_1	480.9	166.1	647.0	25.7	7.157	1370.8	51.515	IaAB	do	high	colorless	1097.5		159.7		
0.212	KIMB5MainS_112_2	454.2	131.5	585.7	22.5	6.286	1370.2	42.12	IaAB				1095.7	1.8	159.4		
0.212	KIMB5MainS_113_1	821.3	29.3	850.6	3.4	15.725	1377.8	5.673	IaA	do	high	colorless	1041.0		151.5	-4.08	0.15
0.212	KIMB5MainS_113_2															-4.62	0.16
0.212	KIMB5MainS_114_1	0	0	0.0					Type II		high	brown				-3.78	0.13

0.212	KIMB5MainS_114_2															-4.20	0.13
0.212	KIMB5MainS_115_1	667.9	433.5	1101.4	39.4	49.428	1368.3	3.308	IaAB	ir	some	brown	1099.8		160.0	-4.80	0.12
0.212	KIMB5MainS_115_2															-3.80	0.13
0.212	KIMB5MainS_115_3															-4.89	0.13
0.212	KIMB5MainS_116	485.4	432.4	917.8	47.1	28.911			IaAB	ir	some	colorless	1111.5		161.7		
0.212	KIMB5MainS_117	23.2	27.8	51.0	54.5	2.184			IaAB	oc (frag)	low	colorless	1191.1		173.3		
0.212	KIMB5MainS_118_1	133.7	903.1	1036.8	87.1	297.882	1367.4	535.872	IaAB	ir	low	colorless	1157.9		168.5	-1.92	0.13
0.212	KIMB5MainS_118_2	99.1	606.4	705.5	86.0	241.531	1365.4	324.038	IaAB				1165.2	7.3	169.5	-2.87	0.14
0.212	KIMB5MainS_119_1	21.7	1006.8	1028.5	97.9	39.331	1365.5	550.3	IaB	ir	low	colorless	1208.5		175.8	-4.69	0.13
0.212	KIMB5MainS_119_2	33.3	714.9	748.2	95.5	42.796	1365.4	443.239	IaB				1196.4	12.1	174.1	-4.77	0.12
0.212	KIMB5MainS_120	812.9	338.4	1151.3	29.4	50.614	1376.6	6.423	IaAB	oc (frag)	some	colorless	1088.5		158.4		
0.212	KIMB5MainS_121_1	468	25.3	493.3	5.1	55.615			IaA	ir	some	brown	1061.8		154.5	-4.25	0.13
0.212	KIMB5MainS_121_2	723.6	124.5	848.1	14.7	71.55	1377.4	2.742	IaAB				1075.4	13.7	156.5	-4.39	0.13
0.212	KIMB5MainS_121_3															-4.82	0.12
0.212	KIMB5MainS_122	179.8	146.8	326.6	44.9	2.287	1378.5	2.347	IaAB	ir	some	colorless	1134.2		165.0		
0.212	KIMB5MainS_123_1	792.1	165.4	957.5	17.3	4.842	1373.9	32.42	IaAB	do	high	brown	1077.1		156.7		
0.212	KIMB5MainS_123_2	773.8	94.2	868.0	10.9	14.665	1374.9	31.406	IaAB				1067.2	9.8	155.3		
0.212	KIMB5MainS_124_1	218.5	131.9	350.4	37.6	6.154	1372	9.268	IaAB	do	high	colorless	1125.1		163.7	-3.65	0.13
0.212	KIMB5MainS_124_2	200.7	161.9	362.6	44.6	5.098	1376	8.33	IaAB				1131.3	6.2	164.6	-4.05	0.12
0.212	KIMB5MainS_125_1	569.6	479	1048.6	45.7	10.648	1378.7	4.524	IaAB	ir	some	colorless	1107.0		161.1	-3.35	0.13
0.212	KIMB5MainS_125_2	683.3	798.5	1481.8	53.9	46.902			IaAB				1106.6	0.0	161.0	-3.30	0.14
0.212	KIMB5MainS_126_1	776.4	399.2	1175.6	34.0	23.094	1373.4	4.881	IaAB	ir	some	yellow	1092.9		159.0	-4.87	0.13
0.212	KIMB5MainS_126_2	854.7	322.6	1177.3	27.4	23.539	1374.8	3.467	IaAB				1085.8	7.1	158.0	-4.84	0.14
0.212	KIMB5MainS_126_3															-4.77	0.14
0.212	KIMB5MainS_126_4															-4.72	0.12
0.212	KIMB5MainS_127_1	774.7	267	1041.7	25.6	53.822	1378.9	12.256	IaAB	ir	some	colorless	1086.5		158.1		
0.212	KIMB5MainS_127_2	698.1	152.6	850.7	17.9	50.512	1378.7	19.151	IaAB				1080.8	5.7	157.2		
0.212	KIMB5MainS_128_1	748.2	524.4	1272.6	41.2	36.148	1372.9	147.492	IaAB	do (frag)	high	colorless	1098.2		159.8		
0.212	KIMB5MainS_128_2	636.1	280.4	916.5	30.6	55.161	1373	99.431	IaAB				1095.1	3.1	159.3		
0.212	KIMB5MainS_129_1	190.1	404	594.1	68.0	3.386	1363.2	23.502	IaAB	oc (frag)	some	brown	1143.0		166.3	-4.64	0.12
0.212	KIMB5MainS_129_2															-5.42	0.13

0.212	KIMB5MainS_130_1	621.9	329.7	951.6	34.6	2.726	1369.5	61.362	IaAB	do	high	colorless	1098.5		159.8	-3.30	0.14
0.212	KIMB5MainS_130_2	550.2	339.3	889.5	38.1	2.107	1369.2	49.051	IaAB				1103.5	5.1	160.6	-4.26	0.12
0.212	KIMB5MainS_130_3															-4.41	0.13
0.212	KIMB5MainS_132	64.4	555.2	619.6	89.6	17.227	1361.9	183.403	IaAB	ir (frag)	some	colorless	1177.3		171.3		
0.212	KIMB5MainS_133_1	68.4	229.1	297.5	77.0	69.635	1363.6	137.595	IaAB	oc	low	colorless	1171.9		170.5	-5.37	0.13
0.212	KIMB5MainS_133_2	45.8	124.3	170.1	73.1	34.33	1363.9	66.461	IaAB				1180.9	9.0	171.8	-4.29	0.12
0.212	KIMB5MainS_134	734.1	74.8	808.9	9.2	41.311	1378.8	1.058	IaA	do	high	colorless	1064.8		154.9		
0.212	KIMB5MainS_135	0	0	0.0					Type II	ir	high	colorless					
0.212	KIMB5MainS_136	711.8	68.9	780.7	8.8	27.315	1378.2	3.575	IaA	oc	high	colorless	1064.5		154.9		
0.212	KIMB5MainS_137_1	725.4	548.6	1274.0	43.1	115.119	1370	128.481	IaAB	oc (frag)	low	colorless	1099.9		160.0		
0.212	KIMB5MainS_137_2	719.9	550.6	1270.5	43.3	91.516	1372.3	208.591	IaAB				1100.3	0.0	160.1		
0.212	KIMB5MainS_138_1									ir	some	colorless				-3.71	0.13
0.212	KIMB5MainS_138_2															-3.76	0.13
0.212	KIMB5MainS_139_1	627.7	221.6	849.3	26.1	42.491	1378.2	5.175	IaAB	do	high	colorless	1091.7		158.8		
0.212	KIMB5MainS_139_2	767.9	181.9	949.8	19.2	37.759	1378.6	2.196	IaAB	do	high	colorless	1080.1	11.6	157.2		
0.212	KIMB5MainS_140_1									ir	some	colorless				-5.06	0.12
0.212	KIMB5MainS_140_2															-5.21	0.12
0.212	KIMB5MainS_141_1	935.5	37.6	973.1	3.9	4.032			IaA	do (frag)	high	colorless	1040.7		151.4	-2.82	0.14
0.212	KIMB5MainS_141_2															-2.90	0.13
0.212	KIMB5MainS_142_1	615.5	278.7	894.2	31.2	20.31	1363	3.588	IaAB	ir	high	colorless	1096.3		159.5	-4.10	0.15
0.212	KIMB5MainS_142_2															-4.51	0.13
0.212	KIMB5MainS_142_3															-4.40	0.13
0.212	KIMB5MainS_143_1	678.1	193.8	871.9	22.2	34.269	1377.14	10.054	IaAB	ir	high	brown	1086.3		158.1	-4.75	0.12
0.212	KIMB5MainS_143_2															-4.76	0.15
0.212	KIMB5MainS_144_1	801.9	602.6	1404.5	42.9	53.395	1374.4	125.64	IaAB	do	high	colorless	1097.5		159.7	-3.03	0.13
0.212	KIMB5MainS_144_2															-3.66	0.12
0.212	KIMB5MainS_145_1	476.7	12.4	489.1	2.5	8.732	1371.9	1.364	IaA	ir	some	colorless	1046.1		152.2	-4.00	0.14
0.212	KIMB5MainS_145_2	443.5	204.7	648.2	31.6	6.854			IaAB				1104.2	58.1	160.7	-4.51	0.13
0.212	KIMB5MainS_146_1									ir	some	colorless				-4.95	0.13
0.212	KIMB5MainS_146_2															-5.22	0.14
0.212	KIMB5MainS_147_1															-4.17	0.13

0.212	KIMB5MainS_147_2	24.5	272.5	297.0	91.8				IaB	oc (frag)	low	brown	1203.5		175.1	-4.12	0.13
0.212	KIMB5MainS_149_1	768.5	76	844.5	9.0	11.328	1365.95	2.905	IaA	do	high	yellow	1063.2		154.7	-5.00	0.12
0.212	KIMB5MainS_149_2	778.2	209.8	988.0	21.2	17.189			IaAB				1082.1	18.9	157.4	-3.71	0.13
0.212	KIMB5MainS_150_1	834.9	643.5	1478.4	43.5	29.09	1373.1	141.51	IaAB	do (frag)	high	colorless	1096.9		159.6		
0.212	KIMB5MainS_150_2	1578.8	405	1983.8	20.4	9.984	1374.4	118.655	IaAB				1065.4	31.5	155.0		
0.212	KIMB5MainS_151_1									agg	some	grey/milky				-5.27	0.13
0.212	KIMB5MainS_151_2															-6.78	0.14
0.212	KIMB5MainS_152	898.2	167	1065.2	15.7	62.527	1372.4	12.522	IaAB	do	high	colorless	1072.1		156.0		
0.212	KIMB5MainS_153_1	817.7	243.2	1060.9	22.9	50.637	1367.6	1.189	IaAB	ir	some	colorless	1082.7		157.5	-5.12	0.12
0.212	KIMB5MainS_153_2	955.9	523.4	1479.3	35.4	59.548			IaAB				1089.0	6.3	158.5	-5.01	0.14
0.212	KIMB5MainS_154_1	722.6	163.9	886.5	18.5	1.566	1368.9	52.469	IaAB	oc	high	colorless	1080.7		157.2	-3.23	0.13
0.212	KIMB5MainS_154_2	621.3	170.4	791.7	21.5	1.37	1368.4	42.176	IaAB				1087.5	6.9	158.2	-4.09	0.13
0.212	KIMB5MainS_155	1058.9	407.4	1466.3	27.8	72.508	1373.2	150.363	IaAB	do	high	colorless	1081.2		157.3		
0.212	KIMB5MainS_156_1	429.7	158.1	587.8	26.9	18.253	1373.3	68.169	IaAB	ir	some	colorless	1101.2		160.2	-5.44	0.12
0.212	KIMB5MainS_156_2	434.3	259.2	693.5	37.4	47.266	1373.5	59.151	IaAB				1108.6	7.4	161.3	-4.49	0.14
0.212	KIMB5MainS_156_3															-5.16	0.13
0.212	KIMB5MainS_157_1	905.1	78.7	983.8	8.0	52.946	1362.9	0.359	IaA	do (frag)	high	colorless	1057.1		153.8	-3.58	0.13
0.212	KIMB5MainS_157_2															-3.62	0.13
0.212	KIMB5MainS_158	1017	165.9	1182.9	14.0	61.161	1363.6	1.202	IaAB	ir	some	colorless	1066.8		155.2		
0.212	KIMB5MainS_159	122.4	191.7	314.1	61.0	48.688	1361.6	56.225	IaAB	do (frag)	high	colorless	1151.2		167.5		
0.212	KIMB5MainS_160_1	628.6	283.2	911.8	31.1	56.756	1378.6	11.437	IaAB	oc (frag)	some	colorless	1095.7		159.4	-6.08	0.12
0.212	KIMB5MainS_160_2	793.7	126.7	920.4	13.8	42.436	1378.9	6.784	IaAB				1071.9	23.8	156.0	-5.94	0.12
0.212	KIMB5MainS_161_1	662.1	349.3	1011.4	34.5	21.221	1372.6	106.877	IaAB	do (frag)	high	colorless	1096.9		159.6	-3.70	0.13
0.212	KIMB5MainS_161_2	745.8	543.9	1289.7	42.2	34.8	1373.3	140.739	IaAB				1098.8	1.9	159.9	-3.86	0.14
0.212	KIMB5MainS_161_3															-3.72	0.14
0.212	KIMB5MainS_162	742.1	145.3	887.4	16.4	15.812	1372.7	47.407	IaAB	do	high	colorless	1077.3		156.8		
0.212	KIMB5MainS_163_1	863.0	46.5	909.5	5.1	81.726	1375.9	11.67	IaA	do (frag)	high	colorless	1048.4		152.5	-4.21	0.12
0.212	KIMB5MainS_163_2	831.0	54.7	885.7	6.2	59.681	1375.8	12.639	IaA				1053.3	4.9	153.3	-2.64	0.14
0.212	KIMB5MainS_163_3															-2.70	0.13
0.212	KIMB5MainS_164_1									do (frag)	high	brown				-4.13	0.12
0.212	KIMB5MainS_164_2															-5.45	0.13

0.212	KIMB5MainS_165_1	668.2	423.3	1091.5	38.8	84.629	1373.1	92.905	IaAB	ir	high	colorless	1099.4		160.0		
0.212	KIMB5MainS_165_2	703.4	391.9	1095.3	35.8	38.132	1373	134.747	IaAB				1096.4	3.1	159.5		
0.212	KIMB5MainS_166_1	1250.8	1191.9	2442.7	48.8	525.091	1377.1	58.697	IaAB	ir	high	colorless	1090.3		158.6	-5.72	0.14
0.212	KIMB5MainS_166_2	723.7	556.8	1280.5	43.5	473.007	1378.2	63.497	IaAB				1100.2	10.0	160.1	-5.76	0.14
0.212	KIMB5MainS_167_1	939.1	376.2	1315.3	28.6	22.051	1374.8	58.155	IaAB	oc	some	colorless	1084.6		157.8	-4.11	0.12
0.212	KIMB5MainS_167_2															-4.08	0.14
0.212	KIMB5MainS_167_3															-4.33	0.15
0.212	KIMB5MainS_168_1	1437.7	929.3	2367.0	39.3	24.649	1367	19.006	IaAB	do (frag)	high	brown	1082.1		157.5		
0.212	KIMB5MainS_168_2	982.1	107.8	1089.9	9.9	8.793	1375.3	20.523	IaA				1059.9	22.2	154.2		
0.212	KIMB5MainS_169	276.5	122.4	398.9	30.7	41.272	1377.5	23.906	IaAB	do	high	colorless	1114.6		162.2		
0.212	KIMB5MainS_170_1	1206.7	214.1	1420.8	15.1	17.134			IaAB	ir	some	yellow	1064.7		154.9	-4.35	0.12
0.212	KIMB5MainS_170_2															-3.18	0.13
0.212	KIMB5MainS_171_1	736.5	1329.8	2066.3	64.4	13.006	1367.6	579.167	IaAB	do	high	colorless	1109.0		161.4	-1.76	0.13
0.212	KIMB5MainS_171_2	461.1	382.1	843.2	45.3	25.447	1367.5	157.806	IaAB				1111.7	2.8	161.8	-1.47	0.13
0.212	KIMB5MainS_171_3															-1.67	0.14
0.212	KIMB5MainS_172	0	0	0.0		8.313			Type II	ir	low	colorless					
0.212	KIMB5MainS_173	1409.2	506.3	1915.5	26.4	284.454	1379.2	35.639	IaAB	do	high	colorless	1073.7		156.2		
0.212	KIMB5MainS_174	987.1	186.9	1174.0	15.9	38.041			IaAB	ir	some	colorless	1070.3		155.7		
0.212	KIMB5MainS_98_1	839.9	116.7	956.6	12.2	18.186	1372.5	47.513	IaAB	oc (frag)	high	colorless	1068.0		155.4	-4.15	0.13
0.212	KIMB5MainS_98_2	622.4	128	750.4	17.1	37.076	1372.1	40.48	IaAB				1082.2	14.2	157.5	-4.21	0.13
0.212	KIMB5MainS_98_3															-4.64	0.13
0.212	KIMB5MainS_99_1	18.8	450.7	469.5	96.0	73.949	1363.7	240.846	IaB	ir	high	colorless	1211.8		176.3		
0.212	KIMB5MainS_99_2	25.1	498.1	523.2	95.2	96.299	1363.4	194.154	IaB				1203.8	8.0	175.2		
0.212	KIMB5SwExt_132_1	375.4	458.2	833.6	55.0	12.585	1376.4	14.995	IaAB	ir	low	colorless	1121.2		163.1	-4.87	0.12
0.212	KIMB5SwExt_132_2	228.4	159.2	387.6	41.1	15.35	1374.7	16.763	IaAB				1126.2	4.9	163.9	-4.88	0.13
0.212	KIMB5SwExt_132_3															-4.49	0.14
0.212	KIMB5SwExt_133_1	40.8	84.3	125.1	67.4	29.7	1360.9	17.676	IaAB	oc	some	brown	1181.8		172.0		
0.212	KIMB5SwExt_133_2	23.9	48.6	72.5	67.0	9.915			IaAB				1195.7	13.9	174.0		
0.212	KIMB5SwExt_134_1	34.6	119.4	154.0	77.5	6.269	1360.1	47.708	IaAB	ir	low	colorless	1189.8		173.1		
0.212	KIMB5SwExt_134_2	37.3	31	68.3	45.4	5.764	1360	26.164	IaAB				1173.9	15.9	170.8		
0.212	KIMB5SwExt_135_1	74.7	176.2	250.9	70.2	13.659	1376.5	7.733	IaAB	oc (frag)	some	colorless	1167.3		169.8	-16.83	0.12

0.212	KIMB5SwExt_135_2															-16.41	0.13
0.212	KIMB5SwExt_136_1	953.5	43.4	996.9	4.4	6.452	1377.6	14.225	IaA	do	some	colorless	1042.8		151.7	-4.15	0.13
0.212	KIMB5SwExt_136_2	935.9	0	935.9	0.0	8.061	1376.9	18.487	IaA							-4.44	0.13
0.212	KIMB5SwExt_137	407	248.8	655.8	37.9	31.969	1362	2.331	IaAB	do (frag)	high	colorless	1110.5		161.6		
0.212	KIMB5SwExt_138_1	157	108.3	265.3	40.8		1361.4	37.59	IaAB	oc (frag)	some	colorless	1135.1		165.2	-4.56	0.14
0.212	KIMB5SwExt_138_2															-4.58	0.15
0.212	KIMB5SwExt_139_1	9.5	235.6	245.1	96.1	52.433	1363.5	121.577	IaB	do (frag)	high	colorless	1230.7		179.1	-3.18	0.13
0.212	KIMB5SwExt_139_2	31	451.5	482.5	93.6	64.672	1363.4	131.327	IaB				1197.7	33.0	174.3	-3.26	0.13
0.212	KIMB5SwExt_139_3															-3.10	0.13
0.212	KIMB5SwExt_140_1	458.9	351.4	810.3	43.4	6.23	1376	48.162	IaAB	ir	some	brown	1110.8		161.6		
0.212	KIMB5SwExt_140_2	734.8	142.5	877.3	16.2	6.568	1377.1	72.829	IaAB				1077.4	33.5	156.8		
0.212	KIMB5SwExt_141_1	913.4	87.5	1000.9	8.7	26.316	1371.1	40.829	IaA	do	high	colorless	1058.8		154.1		
0.212	KIMB5SwExt_141_2	872.2	144.6	1016.8	14.2	12.204	1375.8	69.27	IaAB				1070.6	11.7	155.8		
0.212	KIMB5SwExt_142_1	997.3	126.9	1124.2	11.3	9.175	1377.6	11.774	IaAB	ir	some	colorless	1062.5		154.6		
0.212	KIMB5SwExt_142_2	722.9	323	1045.9	30.9	9.518	1376.9	28.949	IaAB				1092.3	29.8	158.9		
0.212	KIMB5SwExt_143_1	556.8	91.1	647.9	14.1	2.135	1368.5	29.499	IaAB	ir	some	colorless	1080.4		157.2	-4.67	0.12
0.212	KIMB5SwExt_143_2															-7.17	0.14
0.212	KIMB5SwExt_145_1	1224.5	173.1	1397.6	12.4	21.398	1375.3	73.948	IaAB	do (frag)	some	colorless	1060.0		154.2	-4.37	0.13
0.212	KIMB5SwExt_145_2															-4.39	0.12
0.212	KIMB5SwExt_147_1	1641.1	553.4	2194.5	25.2	35.179	1378.9	55.501	IaAB	oc (frag)	some	colorless	1069.2		155.6	-3.57	0.14
0.212	KIMB5SwExt_147_2	1263.5	764.8	2028.3	37.7	55.1	1378.3	78.882	IaAB				1084.1	14.9	157.7	-4.63	0.14
0.212	KIMB5SwExt_148	236.7	228.7	465.4	49.1		1376.5	42.621	IaAB	agg	low	colorless	1129.6		164.4		
0.212	KIMB5SwExt_150_1	26.5	133.2	159.7	83.4	14.559	1361.9	11.851	IaAB	do	high	brown	1198.8		174.4	-4.10	0.13
0.212	KIMB5SwExt_150_2	26.6	173.4	200.0	86.7	17.487	1362.9	11.468	IaAB				1199.8	0.9	174.6	-4.23	0.14
0.212	KIMB5SwExt_151	826.2	173.3	999.5	17.3	114.049	1377	40.956	IaAB	do (frag)	high	colorless	1076.2		156.6		
0.212	KIMB5SwExt_154_1	325.1	43.4	368.5	11.8	14.033	1373.9	26.722	IaAB	oc	some	colorless	1088.6		158.4		
0.212	KIMB5SwExt_154_2	285.7	33.2	318.9	10.4	8.381	1377	60.289	IaAB				1088.7	0.1	158.4		
0.212	KIMB5SwExt_155	242.8	60.9	303.7	20.1		1378.3	16.02	IaAB	do (frag)	high	colorless	1107.6		161.2		
0.212	KIMB5SwExt_156_1	69.1	119.2	188.3	63.3	26.669	1360.7	37.878	IaAB	do (frag)	high	colorless	1166.6		169.7		
0.212	KIMB5SwExt_156_2	76.1	153.7	229.8	66.9	34.131	1361.4	62.382	IaAB				1165.5	1.1	169.6		
0.212	KIMB5SwExt_157_1	776.9	634	1410.9	44.9	34.62	1373.3	165.063	IaAB	macle	low	colorless	1099.3		160.0	-4.22	0.12

0.212	KIMB5SwExt_157_2															-3.12	0.13
0.212	KIMB5SwExt_158_2	39.1	31.1	70.2	44.3	4.345	1376.6	2.157	IaAB	ir	some	colorless	1172.0		170.5		
0.212	KIMB5SwExt_159	25.7	548.1	573.8	95.5	2.174	1363.6	285.5	IaB	oc (frag)	low	colorless	1203.3		175.1		
0.212	KIMB5SwExt_160	82.3	99.4	181.7	54.7	15.114	1376.8	5.779	IaAB	do (frag)	some	colorless	1158.4		168.6		
0.212	KIMB5SwExt_161_1	657.2	298.6	955.8	31.2	5.057	1375.6	114.8	IaAB	do	some	colorless	1094.8		159.3		
0.212	KIMB5SwExt_161_2	674.1	94.8	768.9	12.3	5.009	1375.5	108.7	IaAB				1073.1	21.7	156.1		
0.212	KIMB5SwExt_163_1	1053.4	141.2	1194.6	11.8	6.051	1376.8	24.941	IaAB	oc	low	colorless	1062.3		154.6		
0.212	KIMB5SwExt_163_2	486.6	327.6	814.2	40.2	4.833	1377.1	25.59	IaAB				1107.7	45.4	161.2		
0.212	KIMB5SwExt_165	590.6	370	960.6	38.5		1369.5	37.607	IaAB	do (frag)	high	colorless	1102.1		160.4		
0.212	KIMB5SwExt_166_1	545.6	941.7	1487.3	63.3	37.352	1373.7	18.014	IaAB	ir	high	colorless	1115.7		162.3		
0.212	KIMB5SwExt_166_2	665.7	425.3	1091.0	39.0	52.281	1373.5	36.21	IaAB				1099.6	16.1	160.0		
0.212	KIMB5SwExt_167	677.1	74.9	752.0	10.0	5.852	1370.6	26.573	IaAB	oc	high	colorless	1068.3		155.4		
0.212	KIMB5SwExt_168_1	77	456.3	533.3	85.6	107.376	1363.3	274.1	IaAB	cuboid	high	colorless	1171.5		170.5	-5.17	0.14
0.212	KIMB5SwExt_168_2	80.5	682.8	763.3	89.5	142.063	1363.4	291.588	IaAB				1171.5	0.0	170.5	-5.01	0.14
0.212	KIMB5SwExt_168_3															-4.99	0.13
0.212	KIMB5SwExt_169_1	1541.6	1027.0	2568.6	40.0	561.075	1379.4	62.232	IaAB	do	high	colorless	1081.0		157.3	-3.14	0.12
0.212	KIMB5SwExt_169_2															-4.24	0.14
0.212	KIMB5SwExt_170_1	1145.3	93.5	1238.8	7.5	13.64			IaA	ir	some	colorless	1050.7		152.9		
0.212	KIMB5SwExt_170_2	1217.2	40.7	1257.9	3.2	15.571			IaA				1031.4	19.3	150.1		
0.212	KIMB5SwExt_171	239.8	189.9	429.7	44.2	4.128	1377.3	15.395	IaAB	ir	some	colorless	1126.8		163.9		
0.212	KIMB5SwExt_172	427.6	522.5	950.1	55.0	26.444	1378.1	8.67	IaAB	agg	some	colorless	1118.1		162.7		
0.212	KIMB5SwExt_173_1	1167.3	408.2	1575.5	25.9	144.588	1373.8	51.184	IaAB	oc	some	colorless	1077.5		156.8	-4.66	0.12
0.212	KIMB5SwExt_173_2	1027.6	164.3	1191.9	13.8	10.026	1373.7	65.689	IaAB				1066.2	11.2	155.1	-4.58	0.13
0.212	KIMB5SwExt_174_1	0.0	480.0	480.0	100.0	7.347	1361.7	110.9	IaB	ir	some	colorless				-5.88	0.13
0.212	KIMB5SwExt_174_2	55.0	487.7	542.7	89.9	6.589	1363.4	238.8	IaAB				1181.5		171.9	-5.67	0.14
0.212	KIMB5SwExt_175_1	848.6	185.5	1034.1	17.9	14.077	1377.1	35.509	IaAB	oc	some	colorless	1076.4		156.6		
0.212	KIMB5SwExt_175_2	815.6	36.5	852.1	4.3	43.97	1376.8	14.46	IaA				1045.8	30.5	152.2		
0.212	KIMB5SwExt_176_1	670.2	90.5	760.7	11.9	22.662			IaAB	do	high	colorless	1072.5		156.0	-3.07	0.14
0.212	KIMB5SwExt_176_2															-3.80	0.13
0.212	KIMB5SwExt_177	404.2	428.4	832.6	51.5	110.169	1374.4	47.1	IaAB	ir	some	brown	1117.9		162.7		
0.212	KIMB5SwExt_178_1	867.6	508.7	1376.3	37.0	95.064	1376.2	28.468	IaAB	do	high	colorless	1092.3		158.9	-3.10	0.13

0.212	KIMB5SwExt_178_2	628.2	243.6	871.8	27.9	32.054	1370.6	9.69	IaAB				1093.3	1.0	159.1	-2.28	0.12
0.212	KIMB5SwExt_179_1	1046.5	424.0	1470.5	28.8	150.646	1374.9	58.089	IaAB	oc	low	colorless	1082.3		157.5	-3.50	0.13
0.212	KIMB5SwExt_179_2	951.4	270.8	1222.2	22.2	110.493	1373.7	58.462	IaAB				1078.5	3.8	156.9	-4.67	0.12
0.212	KIMB5SwExt_180_1	779.8	141.2	921.0	15.3	42.338	1375.9	69.096	IaAB	do	high	colorless	1074.7		156.4	-4.81	0.13
0.212	KIMB5SwExt_180_2															-4.19	0.13
0.212	KIMB5SwExt_181_1	81.9	93.3	175.2	53.3	5.718	1374.7	7.762	IaAB	ir	high	colorless	1157.9		168.5	-4.65	0.15
0.212	KIMB5SwExt_181_2															-4.42	0.14
0.212	KIMB5SwExt_182_1	664.3	293.7	958.0	30.7	36.062	1377.4	8.619	IaAB	do	high	colorless	1094.1		159.2	-4.76	0.13
0.212	KIMB5SwExt_182_2															-4.59	0.12
0.212	KIMB5SwExt_183_1	803.4	113.4	916.8	12.4	57.088	1373.6	38.954	IaAB	oc	low	colorless	1069.3		155.6		
0.212	KIMB5SwExt_183_2	777.7	186.8	964.5	19.4	53.989	1373.8	37.166	IaAB				1080.0	10.8	157.1		
0.212	KIMB5SwExt_184_1	713.5	687.6	1401.1	49.1	123.87	1377.8	9.391	IaAB	ir	high	colorless	1103.4		160.5	-4.74	0.14
0.212	KIMB5SwExt_184_2	787.9	303.1	1091.0	27.8	123.639	1378.4	6.822	IaAB				1087.9	15.4	158.3	-4.47	0.14
0.212	KIMB5SwExt_185_1	55.6	417.1	472.7	88.2	36.763	1361.3	226.023	IaAB	ir	some	colorless	1181		171.8	-5.77	0.13
0.212	KIMB5SwExt_185_2															-5.75	0.14
0.212	KIMB5SwExt_186_1	550.1	209.8	759.9	27.6	23.972	1377.7	19.547	IaAB	do	high	colorless	1096.0		159.5	-3.66	0.15
0.212	KIMB5SwExt_186_2	498.8	285.1	783.9	36.4	19.859	1378.1	37.671	IaAB				1104.7	8.7	160.7	-3.70	0.13
0.212	KIMB5SwExt_186_3															-4.84	0.12
0.212	KIMB5SwExt_187	547.1	217.9	765.0	28.5	13.842	1376.7	16.43	IaAB	do (frag)	high	colorless	1096.9		159.6		
0.212	KIMB5SwExt_188_1	36.2	66.8	103.0	64.9	1.729	1376.8	41.918	IaAB	ir	high	colorless	1183.9		172.3	-26.68	0.13
0.212	KIMB5SwExt_188_2	14.6	32	46.6	68.7	2.218	1377	53.252	IaAB				1209.6	25.7	176.0	-26.59	0.12
0.212	KIMB5SwExt_188_3															-18.43	0.14
0.212	KIMB5SwExt_189_1	671.7	159.7	831.4	19.2	10.704	1377	13.952	IaAB	oc (frag)	some	colorless	1083.2		157.6		
0.212	KIMB5SwExt_189_2	751.4	172	923.4	18.6	14.43	1377.4	7.917	IaAB				1079.9	3.2	157.1		
0.212	KIMB5SwExt_190_1	607.1	214.6	821.7	26.1	11.629	1376.3	34.641	IaAB	ir	some	colorless	1092.5		159.0	-35.34	0.17
0.212	KIMB5SwExt_190_2															-35.41	0.18
0.212	KIMB5SwExt_191_1	785	104.5	889.5	11.7	15.823	1374.1	30.718	IaAB	oc	low	colorless	1068.7		155.5	-4.42	0.14
0.212	KIMB5SwExt_191_2	725.9	86.9	812.8	10.7	22.9	1374.2	25.722	IaAB				1068.3	0.4	155.4	-4.72	0.13
0.212	KIMB5SwExt_191_3															-4.43	0.15
0.212	KIMB5SwExt_192_1															-2.72	0.14
0.212	KIMB5SwExt_192_2	11.8	108.9	120.7	90.2	26.791	1362	30.652	IaB	oc	some	colorless	1222.9		177.9	-4.66	0.12

0.212	KIMB5SwExt_193_1	0	0	0.0		14.518			Type II	ir	high	colorless				-1.92	0.12
0.212	KIMB5SwExt_193_2															-1.76	0.12
0.212	KIMB6SwExt_54_1	104.6	190.8	295.4	64.6	49.886	1365.4	129.996	IaAB	macle	low	brown	1156.6		168.3	-3.86	0.12
0.212	KIMB6SwExt_54_2															-3.85	0.14
0.212	KIMB6SwExt_54_3															-4.58	0.14
0.212	KIMB6SwExt_55_1	596.5	112	708.5	15.8	1.348	1377.1	13.744	IaAB	ir	low	colorless	1081.5		157.4	-4.10	0.12
0.212	KIMB6SwExt_55_2															-4.13	0.12
0.212	KIMB6SwExt_56	553.1	111	664.1	16.7	5.567	1375.2	45.123	IaAB	oc	low	colorless	1084.4		157.8		
0.212	KIMB6SwExt_57	704.1	34.6	738.7	4.7	23.44	1376.9	30.173	IaA	oc (frag)	some	colorless	1050.9		152.9		
0.212	KIMB6SwExt_58_1	0	0	0.0					Type II	do	high	colorless				-4.08	0.12
0.212	KIMB6SwExt_58_2															-4.11	0.13
0.212	KIMB6SwExt_59_1	126.2	109.1	235.3	46.4		1377.2	43.662	IaAB	ir	some	colorless	1143.6		166.4	-5.53	0.12
0.212	KIMB6SwExt_59_2															-5.76	0.13
0.212	KIMB6SwExt_60_1	932.9	86.7	1019.6	8.5	1.56	1376.1	49.112	IaA	do (frag)	high	colorless	1057.7		153.9		
0.212	KIMB6SwExt_60_2	1014.9	88.2	1103.1	8.0	3.495	1374.3	33.319					1054.6	3.2	153.4		
0.212	KIMB6SwExt_61_1	796.7	25.5	822.2	3.1	10.081	1377	55.129	IaA	do	high	colorless	1039.4		151.2	-3.27	0.13
0.212	KIMB6SwExt_61_2															-3.58	0.14
0.212	KIMB6SwExt_61_3															-3.56	0.14
0.212	KIMB6SwExt_62	540.5	166.9	707.4	23.6	34.595	1376.9	58.044	IaAB	ir	some	colorless	1092.8		159.0		
0.212	KIMB6SwExt_64_1	905.1	277.6	1182.7	23.5	16.297	1375.3	66.356	IaAB	ir	low	colorless	1081.0		157.3	-3.40	0.13
0.212	KIMB6SwExt_64_2															-4.60	0.14
0.212	KIMB6SwExt_65_1	873.2	63	936.2	6.7	23.836			IaA	oc	some	colorless	1054.1		153.4	-4.79	0.13
0.212	KIMB6SwExt_65_2															-4.14	0.13
0.212	KIMB6SwExt_66_1	25.2	762.1	787.3	96.8	55.041	1363.6	359.871	IaAB	ir	some	colorless	1204.2		175.2	-5.67	0.14
0.212	KIMB6SwExt_66_2															-5.83	0.14
0.212	KIMB6SwExt_67_1	812.5	117	929.5	12.6	1.843	1368.7	117.968	IaAB	do (frag)	high	colorless	1069.4		155.6	-4.32	0.15
0.212	KIMB6SwExt_67_2	430.5	280.7	711.2	39.5	4.0	1368.2	110.7					1110.1	40.7	161.5	-4.34	0.12
0.212	KIMB6SwExt_69_1									ir	low	colorless				-3.60	0.13
0.212	KIMB6SwExt_69_2	275.2	156.8	432.0	36.3	4.2	1376.7	31.6	IaAB				1118.7		162.8	-3.48	0.14
0.212	KIMB6SwExt_70	503.0	44.5	547.5	8.1	7.2	1376.5	40.5	IaA	do	high	colorless	1070.4		155.7		
0.212	KIMB6SwExt_71_1	0.0	0.0	0.0		2.4			Type II	ir	some	colorless				-3.05	0.14

0.212	KIMB6SwExt_71_2															-3.29	0.12
0.212	KIMB6SwExt_72	511.7	65.2	576.9	11.3	1.906	1375.9	2.151	IaAB	ir	some	colorless	1077.3		156.8		
0.212	KIMB6SwExt_73_1	640.3	64.6	704.9	9.2	13.733	1377.9	10.117	IaA	oc (frag)	low	colorless	1067.7		155.3	-3.80	0.13
0.212	KIMB6SwExt_73_2															-4.09	0.13
0.212	KIMB6SwExt_73_3															-3.94	0.15
0.212	KIMB6SwExt_74_1									do	high	brown				-3.89	0.13
0.212	KIMB6SwExt_74_2															-4.76	0.12
0.212	KIMB6SwExt_75	707.8	88.6	796.4	11.1	13.575	1377.3	17.514	IaAB	oc (frag)	low	colorless	1069.7		155.6		
0.212	KIMB6SwExt_76_1	0	0	0.0		3.596			Type II	do (frag)	high	colorless				-16.52	0.12
0.212	KIMB6SwExt_76_2															-16.37	0.12
0.212	KIMB6SwExt_77_1	1212.3	304.2	1516.5	20.1	25.687	1378.7	117.104	IaAB	oc	some	colorless	1070.9		155.8	-5.95	0.12
0.212	KIMB6SwExt_77_2															-5.81	0.12
0.212	KIMB6SwExt_78_1	805.1	384.8	1189.9	32.3	72.83	1376.2	10.55	IaAB	ir	some	colorless	1090.9		158.7		
0.212	KIMB6SwExt_78_2	954.2	116.1	1070.3	10.8	53.587	1376.9	13.738	IaAB				1062.6	28.3	154.6		
0.212	KIMB6SwExt_79_1	36.4	1171.4	1207.8	97.0	60.387	1367.4	768.994	IaAB	do (frag)	high	colorless	1194.4		173.8	-6.38	0.14
0.212	KIMB6SwExt_79_2															-6.11	0.13
0.212	KIMB6SwExt_80_1	0	0	0.0		4.018			Type II	ir	low	colorless				-6.06	0.13
0.212	KIMB6SwExt_80_2															-6.35	0.14
0.212	KIMB6SwExt_81	877.3	506.4	1383.7	36.6		1377	26.988	IaAB	do	high	colorless	1091.8		158.9		
0.212	KIMB6SwExt_82	545	81.2	626.2	13.0	8.709	1376.3	11.937	IaAB	oc (frag)	low	colorless	1079.0		157.0		
0.212	KIMB6SwExt_83_1	0.5	83.5	84.0	99.4	2.247	1377.8	6.584	IaAB	do	high	brown	1318.5		191.8	-5.66	0.13
0.212	KIMB6SwExt_83_2															-3.65	0.12
0.212	KIMB6SwExt_84	22.3	423.6	445.9	95.0	76.568	1365.4	294.758	IaB	do	high	milky	1206.9		175.6		
0.212	KIMB6SwExt_85_1	298.2	168.4	466.6	36.1	41.354	1376.7	28.751	IaAB	do (frag)	high	colorless	1116.7		162.5	-3.81	0.13
0.212	KIMB6SwExt_85_2															-4.29	0.12
0.212	KIMB6SwExt_86_1	767.9	144.1	912.0	15.8	33.213	1375.6	39.706	IaAB	oc (frag)	low	colorless	1075.8		156.5		
0.212	KIMB6SwExt_86_2	773	129.7	902.7	14.4	16.925	1375.2	65.681	IaAB				1073.5	2.3	156.2		
0.212	KIMB6SwExt_87_1	664.7	556.2	1220.9	45.6	323.816	1377.5	71.618	IaAB	do	high	brown	1103.3		160.5	-3.02	0.13
0.212	KIMB6SwExt_87_2															-3.62	0.14
0.212	KIMB6SwExt_88_1	240.9	90.3	331.2	27.3		1376.7	256.771	IaAB	ir	some	brown	1115.1		162.2	-3.45	0.13
0.212	KIMB6SwExt_88_2															-7.00	0.12

0.212	KIMB6SwExt_89	369.1	49.5	418.6	11.8	4.78	1377	21.197	IaAB	do	high	colorless	1085.8		158.0		
0.212	KIMB6SwExt_90_1	27.2	586.2	613.4	95.6	36.356	1361.5	165.014	IaAB	do (frag)	high	colorless	1201.8		174.9	-6.91	0.13
0.212	KIMB6SwExt_90_2															-6.82	0.12
0.212	KIMB6SwExt_91_1	99.3	61.4	160.7	38.2		1375.2	15.541	IaAB	agg	some	milky	1144.8		166.6	-2.17	0.14
0.212	KIMB6SwExt_91_2															-2.76	0.13
0.212	KIMB6SwExt_92_1	1045.3	236.4	1281.7	18.4	9.325	1376.3	33.117	IaAB	oc (frag)	low	colorless	1072.3		156.0		
0.212	KIMB6SwExt_92_2	942.2	85.9	1028.1	8.4	3.858	1374.4	42.736	IaA				1057.1	15.2	153.8		
0.212	KIMB6SwExt_93	606.7	64.1	670.8	9.6	4.138	1372.6	3.348	IaA	oc (frag)	low	colorless	1069.8		155.7		
0.212	KIMB6SwExt_94	845.8	144.5	990.3	14.6	18.923	1377.1	32.15	IaAB	ir	low	colorless	1071.8		155.9		
0.212	KIMB6SwExt_95_1	1016.8	192.6	1209.4	15.9	9.623	1376.9	15.424	IaAB	do	high	brown	1069.7		155.6	-3.15	0.14
0.212	KIMB6SwExt_95_2															-3.20	0.12
0.212	KIMB6SwExt_96_2	855.1	54.2	909.3	6.0	3.588	1370.3	2.603	IaA	do (frag)	high	colorless	1051.9		153.1		
0.212	KIMB6SwExt_97	817	171.9	988.9	17.4	23.635	1377.1	3.549	IaAB	ir	low	colorless	1076.5		156.6		
0.212	KIMB6SwExt_98	558.6	104.3	662.9	15.7	9.789	1377	51.601	IaAB	do (frag)	high	brown	1082.8		157.6		

* gradient: 1°C = 0.1455 km; taken from fig 1_2 in Stachel (2014)

oc = octahedron, do = dodecahedron, agg = aggregate, ir = irregular, frag = fragment

VPDB = Vienna Pee Dee Belemnite

Appendix B

Trace elements characteristics of Victor, Newlands, Finsch and Cullinan diamonds

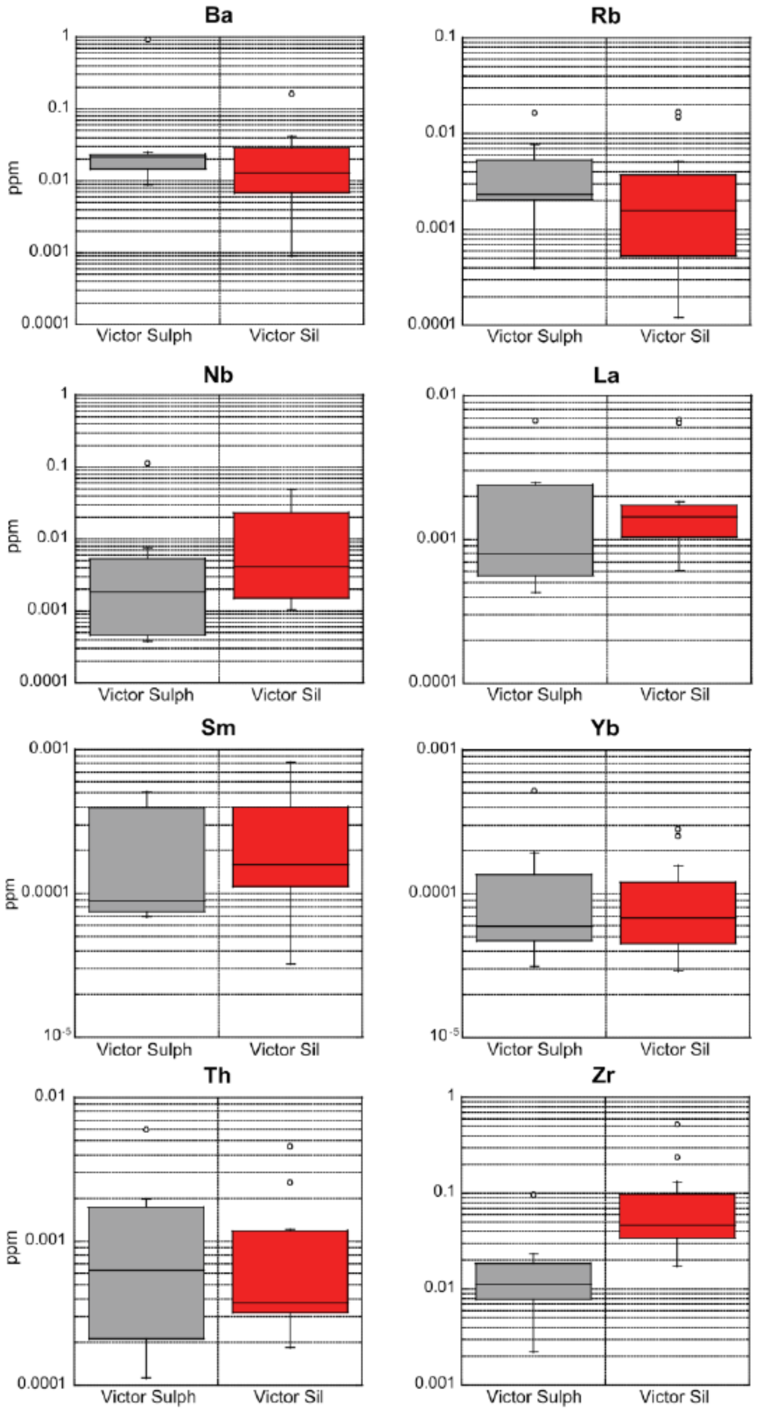

Figure B1: Box and whisker plots of selected trace element concentrations in gem quality diamonds from Victor (sulphide and silicate paragenesis). Individual data points are outliers whose value is either: greater than UQ + 1.5 * IQD or less than LQ – 1.5 * IQD.

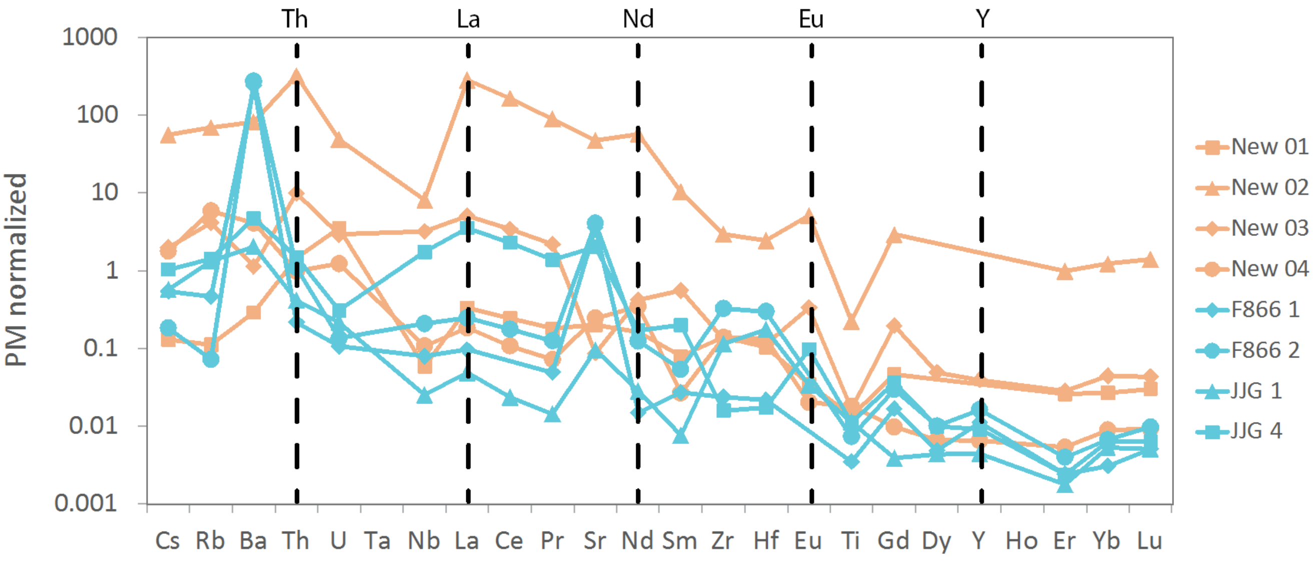

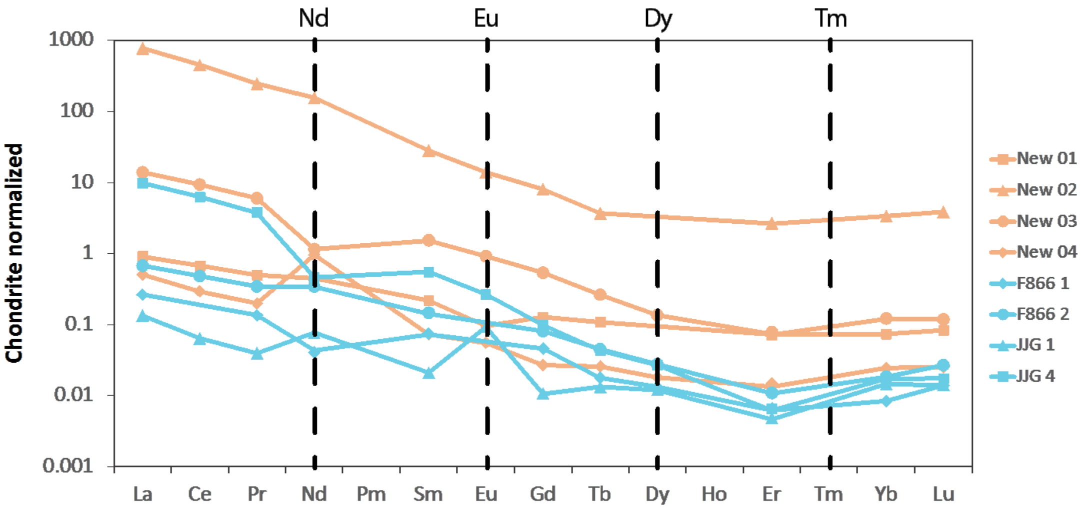

Figure B2: Primitive mantle and Chondrite normalized (McDonough and Sun, 1995) trace element concentrations of fluids in the diamonds from the Newlands and Finsch kimberlites analysed in this study.

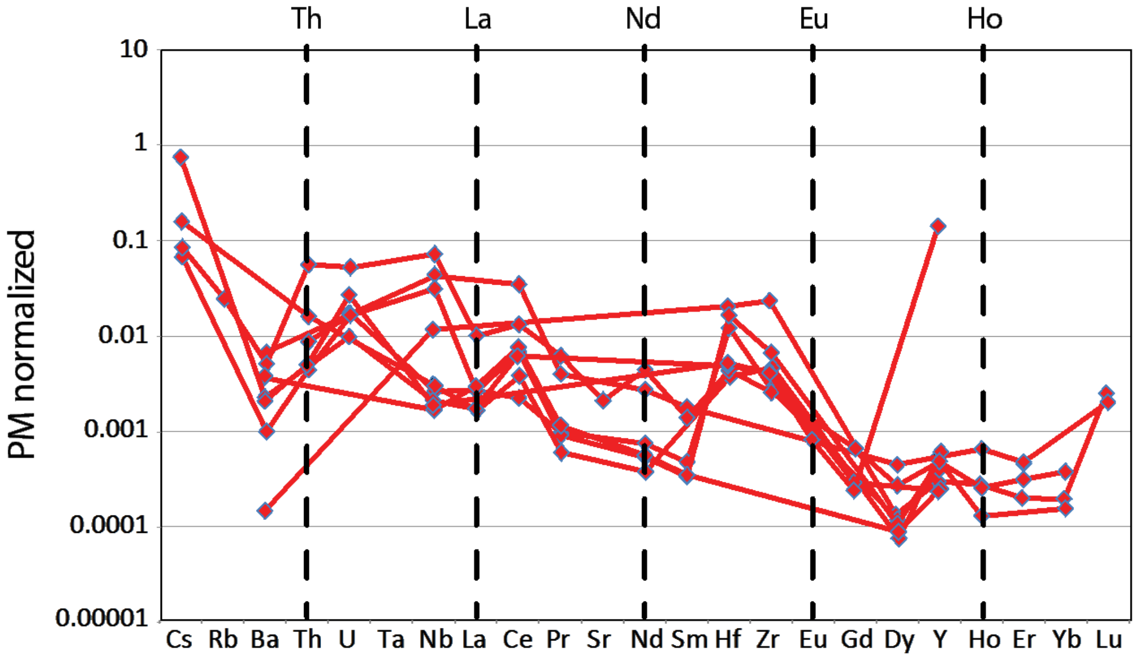

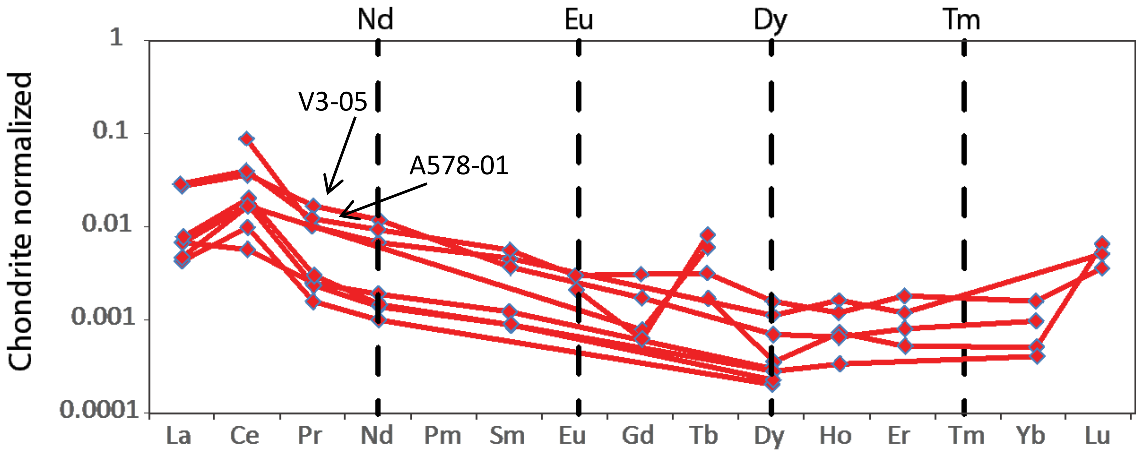

Figure B3: Primitive mantle and Chondrite normalized (McDonough and Sun, 1995) trace element concentrations of fluids in the diamonds from the Victor diamonds (silicate paragenesis) analysed in this study. Data is > LOQ.

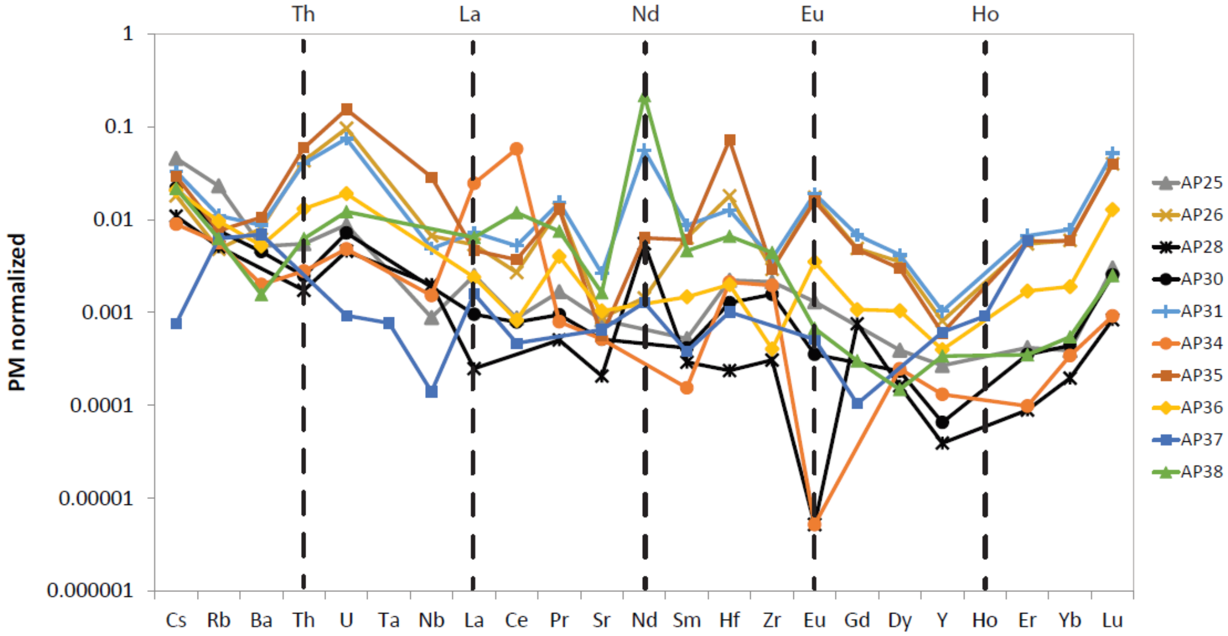

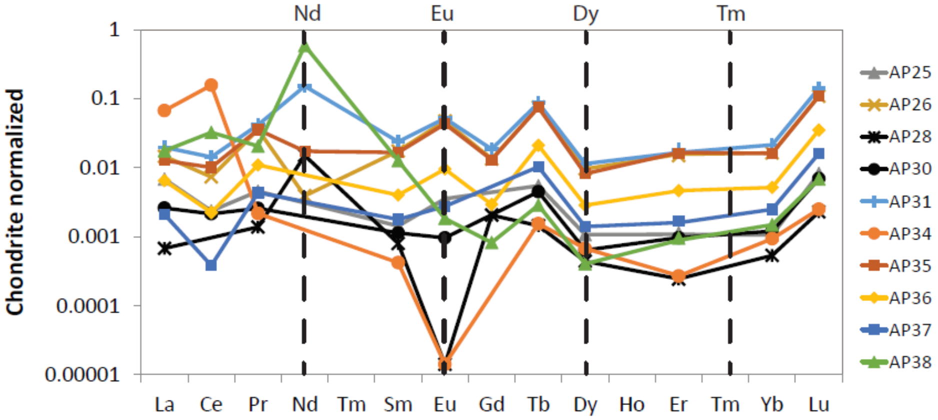

Figure B4: Primitive mantle and Chondrite normalized (McDonough and Sun, 1995) trace element concentrations of fluids in the diamonds from the Cullinan mine (Data from McNeill et al., 2009). Diamond fluid with black lines are P-type, coloured fluids are E-type.

Appendix C

LA-ICPMS Secondary Standard data, Total Procedural blank data and LA-ICPMS data of Aappaluttoq, Namahaca, Myanmar and Luc Yen rubies

Table C1: Trace element concentrations (ppm) of secondary standards NIST SRM 614 and NIST SRM 616 analysed by LA-ICPMS.

Standard	Session	Mg	Si	K	Ca	Ti	V	Cr	Mn	Fe	Ni	Cu	Zn	Ga	Rb
NIST614	**10/19/2015**	33.97	347800	30.24	86580	3.363	0.969	1.041	1.351	14.84	0.968	1.311	2.456	1.117	0.934
NIST614	**10/19/2015**	33.24	340400	29.73	86000	3.318	0.958	0.957	1.331	16.31	0.975	1.448	2.392	1.139	0.856
NIST614	**10/19/2015**	33.61	343600	29.96	87010	3.246	0.949	0.973	1.344	14.78	0.913	1.358	2.456	1.152	0.852
NIST614	**10/19/2015**	33.06	337600	29.47	85800	3.247	0.941	0.968	1.324	14.59	0.919	1.341	2.368	1.137	0.844
mean		33.47	342350	29.85	86347.5	3.2935	0.95425	0.98475	1.3375	15.13	0.94375	1.3645	2.418	1.13625	0.8715
SD		0.404	4382	0.328	551	0.0573	0.012	0.0380	0.0122	0.793	0.032	0.059	0.045	0.0144	0.0419
Average detection limit		0.0428	1.59107	0.0393	1.7264	0.0330	0.0013	0.01624	0.0016	0.1311	0.0099	0.0101	0.0066	0.0011	0.0038
GeoRem	**NIST614**	33.8	315978	30	85047	3.61	1.01	1.19	1.42	18.8	1.1	1.37	2.79	1.31	0.855
Accuracy		-0.98%	8.35%	-0.50%	1.53%	-8.77%	-5.52%	-17.25%	-5.81%	-19.52%	-14.20%	-0.40%	-13.33%	-13.26%	1.93%
NIST616	**10/19/2015**	31.99	344700	28.36	85100	2.381	0.2113	0.329	0.615	11.97	0.223	0.677	1.34	0.42	0.1736
NIST616	**10/19/2015**	31.15	329500	27.77	84100	2.29	0.2078	0.296	0.594	12.13	0.2023	0.656	1.236	0.396	0.108
NIST616	**10/19/2015**	31.59	333200	27.66	84570	2.244	0.1965	0.29	0.599	12.32	0.198	0.752	1.227	0.416	0.1078
NIST616	**10/19/2015**	31.62	336400	27.82	84540	2.153	0.2065	0.288	0.59	12.73	0.226	0.785	1.239	0.4065	0.107
mean		31.588	335950	27.9025	84577.5	2.267	0.2055	0.30075	0.5995	12.2875	0.2123	0.7175	1.2605	0.4096	0.1241
SD		0.34	6479	0.3	409.3	0.095	0.0063	0.0191	0.011	0.3279	0.0142	0.0610	0.0532	0.0107	0.0330
Average detection limit		0.04	2	0.0	1.7	0.0201	0.0009	0.0169	0.0015	0.1332	0.0098	0.0079	0.0068	0.0008	0.0035
GeoRem	**NIST616**	34.7	317731	29	84332	2.65	0.228	0.4	0.609	16	0.435	0.7	1.33	0.5	0.104
Accuracy		-8.97%	5.73%	-3.78%	0.29%	-14.45%	-9.86%	-24.81%	-1.56%	-23.20%	-51.19%	2.50%	-5.23%	-18.08%	19.33%
NIST614	**10/19/2015**	33.85	348100	30.17	87000	3.233	0.957	0.966	1.365	14.13	0.957	1.408	2.436	1.141	0.852
NIST614	**10/19/2015**	32.82	340700	29.87	87100	3.212	0.947	0.952	1.343	17.2	0.951	1.438	2.407	1.135	0.853
mean		33.335	344400	30.02	87050	3.2225	0.952	0.959	1.354	15.665	0.954	1.423	2.4215	1.138	0.8525
SD		0.7283	5232	0.212	70.7107	0.0148	0.007	0.0099	0.0156	2.1708	0.0042	0.021	0.0205	0.0042	0.0007
Average detection limit		0.0378	1.7976	0.037	2.0016	0.0226	0.0015	0.0326	0.0017	0.1361	0.0089	0.0106	0.0066	0.0012	0.00199

GeoRem	**NIST614**	33.8	315978	30	85047	3.61	1.01	1.19	1.42	18.8	1.1	1.37	2.79	1.31	0.855
Accuracy		-1.38%	8.99%	0.07%	2.36%	-10.73%	-5.74%	-19.41%	-4.65%	-16.68%	-13.27%	3.87%	-13.21%	-13.13%	-0.29%
NIST616	**10/19/2015**	31.5	334200	28.02	84200	2.257	0.1984	0.288	0.587	11.73	0.208	0.682	1.247	0.4133	0.1063
NIST616	**10/19/2015**	31.45	333300	27.62	83600	2.197	0.2067	0.304	0.602	13.32	0.2	0.646	1.209	0.4137	0.1095
mean		31.475	333750	27.82	83900	2.227	0.20255	0.296	0.5945	12.525	0.204	0.664	1.228	0.4135	0.1079
SD		0.0353	636	0.2828	424.264	0.0424	0.0059	0.0113	0.0106	1.1243	0.0057	0.0255	0.02687	0.0003	0.0023
Average detection limit		0.0326	3.1614	0.038	1.68295	0.0226	0.001	0.0152	0.0015	0.12844	0.0089	0.0087	0.00526	0.001	0.00204
GeoRem	**NIST616**	34.7	317731	29	84332	2.65	0.228	0.4	0.609	16	0.435	0.7	1.33	0.5	0.104
Accuracy		-9.29%	5.04%	-4.07%	-0.51%	-15.96%	-11.16%	-26.00%	-2.38%	-21.72%	-53.10%	-5.14%	-7.67%	-17.30%	3.75%
NIST616	**11/13/2015**	33.98	317500	28.49	81130	2.114	0.1988	0.227	0.555	11.93	0.246	0.645	1.185	0.3587	0.0955
NIST616	**11/13/2015**	32.1	316600	28.38	81300	2.038	0.1859	0.214	0.536	11.05	0.234	0.658	1.06	0.3476	0.0917
NIST616	**11/13/2015**	29.01	313300	28.17	80740	1.84	0.19	0.187	0.534	10.29	0.236	0.626	1.012	0.3492	0.0898
mean		31.7	315800	28.3	81056	1.99	0.1916	0.2093	0.5417	11.09	0.2387	0.643	1.0857	0.3518	0.0923
SD		2.5094	2211	0.163	287.112	0.141	0.0065	0.0204	0.01159	0.8207	0.0064	0.0161	0.08931	0.006	0.0029
Average detection limit		0.0093	0.533	0.012	1.2533	0.0069	0.00034	0.012	0.00123	0.093	0.0047	0.0019	0.0027	0.0008	0.0956
GeoRem	**NIST616**	34.7	317731	29	84332	2.65	0.228	0.4	0.609	16	0.435	0.7	1.33	0.5	0.104
Accuracy		-8.66%	-0.61%	-2.25%	-3.88%	-24.63%	-15.98%	-47.67%	-11.06%	-30.69%	-45.13%	-8.14%	-18.37%	-29.63%	-11.22%
NIST616	**12/23/2015**	38.7	314000	28.16	80700	2.294	0.2126	0.38	0.646	12.8	0.317	0.77	1.228	0.3898	
NIST616	**12/23/2015**	34.24	313700	27.82	80170	2.208	0.21		0.587	10.85	0.241	0.603	1.193	0.3859	
NIST616	**12/23/2015**	35.39	313400	27.67	80130	2.206	0.2073		0.593	11.46	0.248	0.622	1.192	0.3907	
mean		36.11	313700	27.88	80333	2.2	0.21	0.38	0.609	11.703	0.269	0.665	1.2043	0.3888	
SD		2.316	300	0.251	318.17	0.05	0.002		0.03247	0.9975	0.042	0.091	0.0205	0.0026	
Average detection limit		0.021	1.05	0.00736	1.13	0.00723	0.00025	0.038	0.00072	0.095	0.00606	0.00433	0.00263	0.00039	
GeoRem	**NIST616**	34.7	317731	29	84332	2.65	0.228	0.4	0.609	16	0.435	0.7	1.33	0.5	0.104
Accuracy		4.06%	-1.27%	-3.85%	-4.74%	-15.62%	-7.91%	-5.00%	-0.05%	-26.85%	-38.24%	-5.00%	-9.45%	-22.24%	

NIST614	**4/28/2016**	34.22	341300	28.15	85680	2.81	1.001	1.046	1.445	14.47	1.009	1.374	2.465	1.163	
NIST614	**4/28/2016**	33.81	336800	27.87	85330	2.58	0.994	1.034	1.417	14.1	0.992	1.354	2.441	1.142	
NIST614	**4/28/2016**	33.9	330300	28.01	84490	2.28	0.994	0.981	1.411	13.69	0.958	1.322	2.39	1.147	
NIST614	**4/28/2016**	34.32	344000	29.52	85030	2.2	1.034	1.016	1.45	14.2	1.03	1.371	2.579	1.193	
mean		34.063	338100	28.3875	85132.5	2.4675	1.00575	1.01925	1.43075	14.115	0.99725	1.35525	2.46875	1.16125	
SD		0.2458	5988.32	0.7636	504	0.28	0.01912	0.0283	0.0196	0.324	0.0304	0.0239	0.0799	0.023	
Average detection limit		0.0438	1.1325	0.00945	2.425	0.01065	0.0005	0.01975	0.001	0.16	0.00805	0.0032	0.01125	0.0015	
GeoRem	**NIST614**	33.8	315978	30	85047	3.61	1.01	1.19	1.42	18.8	1.1	1.37	2.79	1.31	0.855
Accuracy		0.78%	7.00%	-5.38%	0.10%	-31.65%	-0.42%	-14.35%	0.76%	-24.92%	-9.34%	-1.08%	-11.51%	-11.35%	
NIST616	**4/28/2016**	32.29	332800	26.29	84580	1.79	0.2095	0.291	0.645	11.79	0.222	0.686	1.242	0.4176	
NIST616	**4/28/2016**	32.58	339400	27.39	83690	1.29	0.2162	0.291	0.644	11.76	0.249	0.718	1.299	0.425	
NIST616	**4/28/2016**	32.1	338700	27.99	83600	0.91	0.2165	0.244	0.647	11.66	0.221	0.66	1.321	0.425	
NIST616	**4/28/2016**	32.28	338400	27.62	83180	0.91	0.219	0.241	0.644	11.68	0.215	0.654	1.306	0.426	
mean		32.313	337325	27.3225	83762.5	1.225	0.2153	0.26675	0.645	11.72	0.22675	0.6795	1.292	0.4234	
SD		0.1986	3045.625	0.7314	588	0.417	0.004	0.028	0.0014	0.062	0.015	0.029	0.035	0.0039	
Average detection limit		0.04	1.115	0.0094	2.45	0.0106	0.00045	0.01975	0.0011	0.155	0.00795	0.00315	0.0115	0.00159	
GeoRem	**NIST616**	34.7	317731	29	84332	2.65	0.228	0.4	0.609	16	0.435	0.7	1.33	0.5	0.104
Accuracy		-6.88%	6.17%	-5.78%	-0.68%	-53.77%	-5.57%	-33.31%	5.91%	-26.73%	-47.87%	-2.93%	-2.86%	-15.32%	
NIST614	**6/10/2016**	36.1		29.84	85420	3.392	1.081	0.975	1.495	15.81	1.092	1.311	2.378	1.184	
NIST614	**6/10/2016**	36.3		29.7	85410	3.534	1.116	0.96	1.482	16.26	1.127	1.371	2.401	1.163	
NIST614	**6/10/2016**	34.54		29.34	84790	3.495	1.055	0.77	1.449	14.74	1.112	1.339	2.424	1.15	
NIST614	**6/10/2016**	33.94		29.1	85060	3.522	1.061	0.819	1.435	15.14	1.103	1.347	2.409	1.144	
mean		35.22		29.5	85170	3.48575	1.07825	0.881	1.46525	15.4875	1.1085	1.342	2.403	1.16025	
SD		1.1607		0.3372	303	0.0646	0.0275	0.102	0.028	0.6783	0.0148	0.0247	0.0192	0.0177	
Average detection limit		0.0195		0.01225	2.275	0.0102	0.00034	0.01825	0.001	0.145	0.0074	0.00325	0.00685	0.0012	
GeoRem	**NIST614**	33.8	315978	30	85047	3.61	1.01	1.19	1.42	18.8	1.1	1.37	2.79	1.31	0.855

Accuracy		4.20%		-1.68%	0.14%	-3.44%	6.76%	-25.97%	3.19%	-17.62%	0.77%	-2.04%	-13.87%	-11.43%	
NIST616	**6/10/2016**	33.43		28.06	83770	2.42	0.2284	0.108	0.662	12.85	0.333	0.669	1.219	0.426	
NIST616	**6/10/2016**	32.22		28	83470	2.408	0.2224	0.051	0.646	12.46	0.359	0.683	1.26	0.422	
NIST616	**6/10/2016**	31.64		27.15	82690	2.37	0.2175	0.043	0.622	12.1	0.323	0.646	1.181	0.4042	
NIST616	**6/10/2016**	31.98		27.49	83470	2.397	0.2244	0.085	0.632	12.24	0.33	0.661	1.255	0.41	
mean		32.318		27.675	83350	2.39875	0.2232	0.07175	0.6405	12.41	0.33625	0.66475	1.22875	0.41555	
SD		0.7789		0.4335	462	0.0213	0.0045	0.0303	0.0174	0.3272	0.0157	0.0155	0.0367	0.0102	
Average detection limit		0.018		0.0125	2.25	0.00935	0.0004	0.01775	0.0011	0.1425	0.0069	0.00305	0.0069	0.0012	
GeoRem	**NIST616**	34.7	317731	29	84332	2.65	0.228	0.4	0.609	16	0.435	0.7	1.33	0.5	0.104
Accuracy		-6.87%		-4.57%	-1.16%	-9.48%	-2.12%	-82.06%	5.17%	-22.42%	-22.70%	-5.04%	-7.61%	-16.89%	
NIST614	**6/17/2016**	32.08	335800	29.68	86990	3.141	0.962	0.819	1.394	13.81	0.933	1.217	2.214	1.111	0.842
NIST614	**6/17/2016**	32.32	338000	29.6	86320	3.104	0.97	0.81	1.39	13.53	0.956	1.216	2.252	1.112	0.851
NIST614	**6/17/2016**	31.62	330300	28.84	85550	3.119	0.95	0.811	1.357	13.17	0.925	1.192	2.214	1.097	0.843
mean		32.007	334700	29.37	86286	3.12133	0.9607	0.8133	1.3803	13.50	0.938	1.2083	2.2267	1.1067	0.8453
SD		0.3557	3966	0.4636	720	0.01861	0.0101	0.0049	0.0203	0.3208	0.016	0.0142	0.0219	0.008	0.0049
Average detection limit		0.0183	0.4433	0.0127	1.1267	0.0073	0.0003	0.013	0.0038	0.13	0.0051	0.0026	0.0054	0.001	0.0003
GeoRem	**NIST614**	33.8	315978	30	85047	3.61	1.01	1.19	1.42	18.8	1.1	1.37	2.79	1.31	0.855
Accuracy		-5.31%	5.93%	-2.09%	1.46%	-13.54%	-4.88%	-31.65%	-2.79%	-28.17%	-14.73%	-11.80%	-20.19%	-15.52%	-1.13%
NIST616	**6/17/2016**	30.85	330600	28.19	83870	2.211	0.2105	0.136	0.634	11.51	0.233	0.614	1.173	0.4122	0.0986
NIST616	**6/17/2016**	31.13	333100	28.33	84010	2.197	0.2126	0.1507	0.631	11.38	0.243	0.611	1.179	0.4129	0.1019
NIST616	**6/17/2016**	31.12	334800	28.4	84090	2.25	0.2096	0.144	0.632	11.23	0.245	0.606	1.193	0.418	0.1026
mean		31.03	332833	28.307	83990	2.2193	0.2109	0.1436	0.6323	11.373	0.2403	0.6103	1.18167	0.414	0.1010
SD		0.159	2112	0.1069	111	0.0275	0.0015	0.00736	0.0015	0.1401	0.0064	0.0040	0.01027	0.003	0.0021
Average detection limit		0.0173	0.46667	0.013	1.1367	0.0076	0.0003	0.014	0.00413	0.13	0.0051	0.0029	0.0058	0.001	0.0003
GeoRem	**NIST616**	34.7	317731	29	84332	2.65	0.228	0.4	0.609	16	0.435	0.7	1.33	0.5	0.104

Accuracy		-10.6%	4.75%	-2.39%	-0.41%	-16.25%	-7.50%	-64.11%	3.83%	-28.92%	-44.75%	-12.81%	-11.15%	-17.13%	-2.85%
NIST614	**11/28/2016**	32.47	344800	30.57	85480	3.205	0.952	0.954	1.364	14.03	0.978	1.327	2.477	1.164	0.874
NIST614	**11/28/2016**	31.98	329900	28.8	84150	3.109	0.913	0.879	1.317	13.53	0.931	1.274	2.325	1.123	0.842
NIST614	**11/28/2016**	32.96	356000	31.1	85500	3.191	0.973	0.929	1.393	14.25	1.002	1.342	2.545	1.203	0.904
NIST614	**11/28/2016**	32.61	350000	30.3	85800	3.161	0.96	0.905	1.373	14.31	0.97	1.326	2.374	1.187	0.887
NIST614	**11/28/2016**	33.08	356000	31	85500	3.11	0.983	0.922	1.402	14.3	1.027	1.38	2.45	1.206	0.909
mean		32.62	347340	30.354	85286	3.1552	0.9562	0.9178	1.3698	14.084	0.9816	1.3298	2.4342	1.1766	0.8832
SD		0.4357	10812	0.9271	648.8297	0.0446	0.02692	0.0279	0.033	0.3298	0.036	0.038	0.086	0.034	0.0269
Average detection limit		0.042	0.908	0.0248	2	0.0156	0.0009	0.00872	0.0005	0.17	0.00564	0.00274	0.00434	0.00128	0.0005
GeoRem	**NIST614**	33.8	315978	30	85047	3.61	1.01	1.19	1.42	18.8	1.1	1.37	2.79	1.31	0.855
Accuracy		-3.49%	9.93%	1.18%	0.28%	-12.60%	-5.33%	-22.87%	-3.54%	-25.09%	-10.76%	-2.93%	-12.75%	-10.18%	3.30%
NIST616	**11/28/2016**	30.49	319100	27.05	82520	2.225	0.1979	0.2314	0.595	11.19	0.181	0.626	1.218	0.4139	0.1036
NIST616	**11/28/2016**	30.27	323000	26.88	82630	2.213	0.1951	0.2187	0.5966	11.36	0.1856	0.627	1.19	0.4222	0.1029
NIST616	**11/28/2016**	30.67	327900	27.02	82960	2.239	0.1987	0.2193	0.6016	11.42	0.1845	0.637	1.194	0.4236	0.1038
NIST616	**11/28/2016**	31.19	334400	27.77	84210	2.241	0.2064	0.2172	0.616	11.57	0.192	0.655	1.197	0.4297	0.1066
NIST616	**11/28/2016**	30.21	319400	27	81780	2.244	0.1979	0.2583	0.593	11.06	0.187	0.626	1.256	0.4116	0.101
mean		30.566	324760	27.144	82820	2.2324	0.1992	0.22898	0.60044	11.32	0.18602	0.6342	1.211	0.4202	0.10358
SD		0.3938	6454	0.36	888	0.013	0.004	0.0173	0.009	0.199	0.0040	0.0125	0.027	0.0074	0.0020
Average detection limit		0.0372	0.83	0.023	1.86	0.015	0.0009	0.0083	0.0004	0.154	0.0052	0.00254	0.00434	0.0012	0.00052
GeoRem	**NIST616**	34.7	317731	29	84332	2.65	0.228	0.4	0.609	16	0.435	0.7	1.33	0.5	0.104
Accuracy		-11.9%	2.21%	-6.40%	-1.79%	-15.76%	-12.63%	-42.76%	-1.41%	-29.25%	-57.24%	-9.40%	-8.95%	-15.96%	-0.40%
NIST614	**11/29/2016**	31.91	327000	28.86	84260	3.088	0.912	0.834	1.315	12.5	0.947	1.295	2.345	1.136	0.848
GeoRem	**NIST614**	33.8	315978	30	85047	3.61	1.01	1.19	1.42	18.8	1.1	1.37	2.79	1.31	0.855
Accuracy		-5.59%	3.49%	-3.80%	-0.93%	-14.46%	-9.70%	-29.92%	-7.39%	-33.51%	-13.91%	-5.47%	-15.95%	-13.28%	-0.82%

NIST616	**11/29/2016**	30.36	314300	26.83	81120	2.207	0.2017	0.261	0.589	10.56	0.268	0.627	1.197	0.4177	0.1035
GeoRem	**NIST616**	34.7	317731	29	84332	2.65	0.228	0.4	0.609	16	0.435	0.7	1.33	0.5	0.104
Accuracy		-12.5%	-1.08%	-7.48%	-3.81%	-16.72%	-11.54%	-34.75%	-3.28%	-34.00%	-38.39%	-10.43%	-10.00%	-16.46%	-0.48%

Standard	**Session**	**Sr**	**Y**	**Zr**	**Nb**	**Mo**	**Sn**	**Ba**	**La**	**Ce**	**Pr**	**Nd**	**Ho**	**Yb**	**Hf**	**Ta**
NIST614	**10/19/2015**	46.44	0.786	0.97	0.0088	0.014	1.453	3.265	0.676	0.753	0.7359	0.749		0.765	0.725	0.722
NIST614	**10/19/2015**	46.99	0.7992	0.833	0.012	0.014	1.507	3.285	0.683	0.746	0.728	0.756		0.769	0.726	0.7318
NIST614	**10/19/2015**	46.98	0.792	0.835	0.0089	0.018	1.449	3.248	0.6719	0.745	0.728	0.747		0.761	0.723	0.727
NIST614	**10/19/2015**	46.63	0.789	0.844	0.011	0.017	1.419	3.198	0.6673	0.727	0.718	0.737		0.761	0.722	0.727
mean		46.76	0.7916	0.8705	0.0102	0.0158	1.4570	3.2490	0.6746	0.7428	0.7275	0.7473		0.7640	0.7240	0.7270
SD		0.2712	0.0057	0.0665	0.0016	0.0021	0.0366	0.0372	0.0067	0.0111	0.0073	0.0078		0.0038	0.0018	0.0040
Average detection limit		0.0007	0.0001	0.0003	0.0001	0.0005	0.0009	0.0005	0.0001	0.0000	0.0001	0.0002		0.0001	0.0001	0.0001
GeoRem	**NIST614**	45.8	0.79	0.848	0.03	0.03	1.68	3.2	0.72	0.813	0.768	0.752	0.749	0.777	0.711	0.808
Accuracy		2.10%	0.20%	2.65%	-66.08%	-47.50%	-13.3%	1.53%	-6.31%	-8.64%	-5.28%	-0.63%		-1.67%	1.83%	-10%
NIST616	**10/19/2015**	41.84	0.0279	0.108	0.0236	0.0852	1.007	2.354	0.033	0.0339	0.0204	0.0239		0.0234	0.0207	0.029
NIST616	**10/19/2015**	41.58	0.0234	0.107	0.01902	0.0799	1.006	2.308	0.0283	0.0282	0.0148	0.0186		0.0157	0.0166	0.024
NIST616	**10/19/2015**	42.12	0.0234	0.094	0.01845	0.0775	0.974	2.325	0.027	0.0272	0.0144	0.0183		0.0159	0.0162	0.024
NIST616	**10/19/2015**	41.25	0.0212	0.0894	0.01679	0.0793	1.03	2.265	0.0257	0.026	0.0138	0.0178		0.0138	0.0141	0.0224
mean		41.7	0.0240	0.0996	0.0195	0.0805	1.0043	2.3130	0.0286	0.0288	0.0158	0.0197		0.0172	0.0169	0.0248
SD		0.3710	0.0028	0.0093	0.0029	0.0033	0.0230	0.0372	0.0031	0.0035	0.0031	0.0029		0.0042	0.0028	0.0031
Average detection limit		0.0007	0.0001	0.0002	0.0001	0.0004	0.0006	0.0004	0.0000	0.0000	0.0000	0.0001		0.0001	0.0000	0.0001
GeoRem	**NIST616**	41.72	0.0288	0.0951	0.0194	0.0879	1.18	2.31	0.0298	0.0292	0.015	0.0227	0.0169	0.0171	0.0154	0.0299
Accuracy		-0.05%	-16.8%	4.73%	0.34%	-8.45%	-14.9%	0.13%	-4.07%	-1.36%	5.62%	-13.4%		0.60%	9.74%	-17.1%
NIST614	**10/19/2015**	47.01	0.7758	0.828	0.01	0.014	1.46	3.248	0.6681	0.749	0.72	0.732		0.743	0.691	0.7211

NIST614	**10/19/2015**	46.63	0.775	0.811	0.0091	0.016	1.447	3.244	0.672	0.742	0.7216	0.735		0.753	0.702	0.7163
mean		46.82	0.7754	0.8195	0.0096	0.0150	1.4535	3.2460	0.6701	0.7455	0.7208	0.7335		0.7480	0.6965	0.7187
SD		0.2687	0.0006	0.0120	0.0006	0.0014	0.0092	0.0028	0.0028	0.0049	0.0011	0.0021		0.0071	0.0078	0.0034
Average detection limit		0.0006	0.0002	0.0003	0.0001	0.0004	0.0011	0.0006	0.0001	0.0001	0.0001	0.0001		0.0002	0.0001	0.0001
GeoRem	**NIST614**	45.8	0.79	0.848	0.03	0.03	1.68	3.2	0.72	0.813	0.768	0.752	0.749	0.777	0.711	0.808
Accuracy		2.23%	-1.85%	-3.36%	-68.17%	-50.00%	-13.5%	1.44%	-6.94%	-8.30%	-6.15%	-2.46%		-3.73%	-2.04%	-11%
NIST616	**10/19/2015**	41.38	0.022	0.105	0.01816	0.0774	0.971	2.302	0.027	0.0289	0.015	0.0174		0.0148	0.0147	0.0232
NIST616	**10/19/2015**	40.99	0.0221	0.138	0.01749	0.0773	0.98	2.272	0.0271	0.0326	0.0142	0.0189		0.0167	0.0164	0.0230
mean		41.19	0.0223	0.1215	0.0178	0.0774	0.9755	2.2870	0.0271	0.0308	0.0144	0.0182		0.0158	0.0156	0.0231
SD		0.2758	0.0003	0.0233	0.0005	0.0001	0.0064	0.0212	0.0000	0.0026	0.0003	0.0011		0.0013	0.0012	0.0001
Average detection limit		0.0006	0.0002	0.0003	0.0001	0.0003	0.0007	0.0003	0.0000	0.0000	0.0000	0.0002		0.0001	0.0001	0.0001
GeoRem	**NIST616**	41.72	0.0288	0.0951	0.0194	0.0879	1.18	2.31	0.0298	0.0292	0.015	0.0227	0.0169	0.0171	0.0154	0.0299
Accuracy		-1.28%	-22.2%	27.76%	-8.12%	-12.00%	-17.3%	-1.00%	-9.14%	5.31%	-4.07%	-20%		-7.89%	0.97%	-22.7%
NIST616	**11/13/2015**	39.78	0.024	0.148	0.01865	0.0763	0.873	2.114	0.0258	0.0314	0.0142	0.0168		0.0142	0.0132	0.0229
NIST616	**11/13/2015**	40.06	0.0239	0.0832	0.01741	0.0718	0.835	2.04	0.0251	0.0309	0.0143	0.0155		0.0131	0.0122	0.0229
NIST616	**11/13/2015**	39.62	0.0232	0.091	0.01706	0.0706	0.839	1.816	0.0248	0.0314	0.0144	0.016		0.0124	0.0108	0.022
mean		39.820	0.0237	0.1074	0.0177	0.0729	0.8490	1.9900	0.0252	0.0312	0.0143	0.0160		0.0133	0.0121	0.0226
SD		0.2227	0.0004	0.0354	0.0008	0.0030	0.0209	0.1552	0.0005	0.0003	0.0001	0.0007		0.0009	0.0012	0.0005
Average detection limit		0.0027	0.0251	0.1443	0.0181	0.0740	0.8910	2.0820	0.0267	0.0334	0.0154	0.0168		0.0141	0.0139	0.0224
GeoRem	**NIST616**	41.72	0.0288	0.0951	0.0194	0.0879	1.18	2.31	0.0298	0.0292	0.015	0.0227	0.0169	0.0171	0.0154	0.0299
Accuracy		-4.55%	-17.8%	12.93%	-8.73%	-17.06%	-28%	-13.9%	-15.4%	6.96%	-4.73%	-29.5%		-22.4%	-21.5%	-24.5%
NIST616	**12/23/2015**	39.33	0.0241	0.34	0.0224	0.0829	0.923	2.237	0.0305	0.0375	0.0188	0.0205	0.01414	0.0158	0.0178	0.0258
NIST616	**12/23/2015**	39.52	0.0231	0.134	0.0206	0.0759	0.939	2.271	0.0288	0.0283	0.0151	0.018	0.01345	0.0146	0.014	0.0254

NIST616	**12/23/2015**	39.55	0.0229	0.201	0.0201	0.0796	0.935	2.287	0.0286	0.03	0.0153	0.0192	0.014	0.0159	0.0151	0.0264
mean		39.467	0.0234	0.2250	0.0210	0.0795	0.9323	2.2650	0.0293	0.0319	0.0164	0.0192	0.0139	0.0154	0.0156	0.0259
SD		0.1193	0.0006	0.1051	0.0012	0.0035	0.0083	0.0255	0.0010	0.0049	0.0021	0.0013	0.0004	0.0007	0.0020	0.0005
Average detection limit		0.0003	0.0001	0.0001	0.0000	0.0002	0.0004	0.0002	0.0000	0.0000	0.0000	0.0001		0.0001	0.0000	0.0001
GeoRem	**NIST616**	41.72	0.0288	0.0951	0.0194	0.0879	1.18	2.31	0.0298	0.0292	0.015	0.0227	0.0169	0.0171	0.0154	0.0299
Accuracy		-5.40%	-18.9%	136%	8.42%	-9.59%	-21%	-1.95%	-1.68%	9.36%	9.29%	-15.3%	-18%	-9.75%	1.52%	-13.5%
NIST614	**4/28/2016**	46.31	0.78	0.847	0.0089	0.016	1.445	3.297	0.7265	0.799	0.786	0.756	0.762	0.771	0.701	0.782
NIST614	**4/28/2016**	45.92	0.768	0.843	0.0081	0.014	1.429	3.215	0.7188	0.783	0.776	0.74	0.756	0.764	0.684	0.771
NIST614	**4/28/2016**	45.87	0.78	0.854	0.011	0.018	1.426	3.218	0.73	0.778	0.772	0.746	0.773	0.784	0.704	0.784
NIST614	**4/28/2016**	45.73	0.769	0.8607	0.01	0.021	1.482	3.264	0.736	0.799	0.788	0.757	0.781	0.781	0.714	0.79
mean		45.96	0.7743	0.8512	0.0095	0.0173	1.4455	3.2485	0.7278	0.7898	0.7805	0.7498	0.7680	0.7750	0.7008	0.7818
SD		0.2484	0.0067	0.0078	0.0013	0.0030	0.0257	0.0393	0.0072	0.0109	0.0077	0.0082	0.0112	0.0092	0.0125	0.0079
Average detection limit		0.0004	0.0002	0.0003	0.0001	0.0002	0.0005	0.0004	0.0001	0.0001	0.0000	0.0002	0.0000	0.0001	0.0001	0.0001
GeoRem	**NIST614**	45.8	0.79	0.848	0.03	0.03	1.68	3.2	0.72	0.813	0.768	0.752	0.749	0.777	0.711	0.808
Accuracy		0.34%	-1.99%	0.37%	-68.33%	-42.50%	-14%	1.52%	1.09%	-2.86%	1.63%	-0.30%	2.54%	-0.26%	-1.44%	-3.25%
NIST616	**4/28/2016**	41.45	0.0102	0.0907	0.01851	0.0802	0.976	2.383	0.0283	0.0294	0.0158	0.0181	0.01364	0.0153	0.0147	0.0245
NIST616	**4/28/2016**	40.92	0.0112	0.0918	0.01914	0.0799	1.013	2.365	0.0293	0.0303	0.0159	0.0199	0.01409	0.0158	0.0143	0.0246
NIST616	**4/28/2016**	40.97	0.0137	0.0896	0.01916	0.0808	1.028	2.347	0.0295	0.0289	0.0156	0.0201	0.0137	0.0148	0.0145	0.0252
NIST616	**4/28/2016**	40.85	0.0084	0.0858	0.01863	0.0796	1.022	2.353	0.0287	0.0296	0.0157	0.0192	0.01387	0.0159	0.0148	0.025
mean		41.048	0.0109	0.0895	0.0189	0.0801	1.0098	2.3620	0.0290	0.0295	0.0157	0.0193	0.0138	0.0154	0.0146	0.0248
SD		0.2728	0.0022	0.0026	0.0003	0.0005	0.0233	0.0159	0.0006	0.0006	0.0001	0.0009	0.0002	0.0005	0.0002	0.0004
Average detection limit		0.0004	0.0002	0.0003	0.0001	0.0002	0.0007	0.0004	0.0001	0.0000	0.0001	0.0001	0.0000	0.0001	0.0001	0.0001
GeoRem	**NIST616**	41.72	0.0288	0.0951	0.0194	0.0879	1.18	2.31	0.0298	0.0292	0.015	0.0227	0.0169	0.0171	0.0154	0.0299

Accuracy		-1.61%	-62.2%	-5.91%	-2.78%	-8.85%	-14.4%	2.25%	-2.83%	1.16%	4.88%	-14.9%	-18.2%	-9.68%	-5.47%	-17%
NIST614	**6/10/2016**	46.98	0.7748	0.862	0.013	0.019	1.511	3.31	0.7342	0.8	0.783	0.726	0.764	0.755	0.711	0.774
NIST614	**6/10/2016**	46.98	0.772	0.823	0.015	0.022	1.643	3.241	0.717	0.792	0.776	0.725	0.755	0.73	0.683	0.768
NIST614	**6/10/2016**	45.73	0.774	0.805	0.011	0.016	1.427	3.155	0.7017	0.769	0.7523	0.714	0.74	0.701	0.659	0.744
NIST614	**6/10/2016**	45.81	0.777	0.814	0.015	0.027	1.431	3.155	0.709	0.763	0.759	0.725	0.747	0.704	0.655	0.752
mean		46.375	0.7745	0.8260	0.0135	0.0210	1.5030	3.2153	0.7155	0.7810	0.7676	0.7225	0.7515	0.7225	0.6770	0.7595
SD		0.6994	0.0021	0.0251	0.0019	0.0047	0.1010	0.0751	0.0140	0.0178	0.0143	0.0057	0.0103	0.0253	0.0258	0.0139
Average detection limit		0.0003	0.0002	0.0003	0.0001	0.0001	0.0004	0.0004	0.0001	0.0000	0.0000	0.0001	0.0000	0.0001	0.0001	0.0001
GeoRem	**NIST614**	45.8	0.79	0.848	0.03	0.03	1.68	3.2	0.72	0.813	0.768	0.752	0.749	0.777	0.711	0.808
Accuracy		1.26%	-1.97%	-2.59%	-55.00%	-30.00%	-10.5%	0.48%	-0.63%	-3.94%	-0.06%	-3.92%	0.33%	-7.01%	-4.78%	-6.00%
NIST616	**6/10/2016**	42.06	0.0124	0.0913	0.01976	0.0833	1.042	2.349	0.0295	0.0296	0.0153	0.0168	0.01333	0.0145	0.0141	0.0237
NIST616	**6/10/2016**	41.67	0.0109	0.0881	0.01863	0.0799	1.001	2.307	0.029	0.0285	0.015	0.0168	0.01333	0.0144	0.0138	0.0236
NIST616	**6/10/2016**	40.38	0.013	0.0835	0.01834	0.0744	0.939	2.204	0.0284	0.0279	0.0144	0.0173	0.01306	0.0137	0.0131	0.0235
NIST616	**6/10/2016**	40.86	0.0154	0.0837	0.01909	0.0758	0.972	2.275	0.0282	0.028	0.0151	0.0168	0.01321	0.0138	0.0132	0.0234
mean		41.24	0.0129	0.0867	0.0190	0.0784	0.9885	2.2838	0.0288	0.0285	0.0150	0.0169	0.0132	0.0141	0.0135	0.0236
SD		0.7619	0.0019	0.0038	0.0006	0.0040	0.0437	0.0612	0.0006	0.0008	0.0004	0.0002	0.0001	0.0004	0.0005	0.0001
Average detection limit		0.0003	0.0002	0.0003	0.0001	0.0001	0.0004	0.0004	0.0001	0.0000	0.0000	0.0001	0.0000	0.0001	0.0001	0.0001
GeoRem	**NIST616**	41.72	0.0288	0.0951	0.0194	0.0879	1.18	2.31	0.0298	0.0292	0.015	0.0227	0.0169	0.0171	0.0154	0.0299
Accuracy		-1.14%	-55.1%	-8.89%	-2.29%	-10.86%	-16.2%	-1.14%	-3.46%	-2.35%	-0.25%	-25.4%	-21.7%	-17.6%	-12%	-21.2%
NIST614	**6/17/2016**	46.38	0.748	0.82	0.014	0.018	1.473	3.112	0.703	0.783	0.772	0.694	0.72	0.725	0.682	0.755
NIST614	**6/17/2016**	46.35	0.74	0.814	0.013	0.02	1.461	3.171	0.712	0.792	0.779	0.69	0.723	0.736	0.69	0.765
NIST614	**6/17/2016**	46.32	0.775	0.855	0.011	0.016	1.438	3.183	0.7144	0.78	0.778	0.689	0.75	0.756	0.712	0.775
mean		46.35	0.7543	0.8297	0.0127	0.0180	1.4573	3.1553	0.7098	0.7850	0.7763	0.6910	0.7310	0.7390	0.6947	0.7650

SD		0.0300	0.0183	0.0221	0.0015	0.0020	0.0178	0.0380	0.0060	0.0062	0.0038	0.0026	0.0165	0.0157	0.0155	0.0100
Average detection limit		0.0002	0.0001	0.0002	0.0001	0.0003	0.0002	0.0003	0.0000	0.0000	0.0000	0.0001	0.0000	0.0000	0.0000	0.0000
GeoRem	**NIST614**	45.8	0.79	0.848	0.03	0.03	1.68	3.2	0.72	0.813	0.768	0.752	0.749	0.777	0.711	0.808
Accuracy		1.20%	-4.51%	-2.16%	-57.78%	-40.00%	-13.3%	-1.40%	-1.42%	-3.44%	1.09%	-8.11%	-2.40%	-4.89%	-2.30%	-5.32%
NIST616	**6/17/2016**	40.97	0.0152	0.0891	0.01863	0.0781	1.053	2.293	0.029	0.0299	0.0158	0.0168	0.01341	0.0151	0.0143	0.025
NIST616	**6/17/2016**	41.13	0.0145	0.0894	0.01802	0.0814	1.025	2.345	0.0281	0.0262	0.0158	0.0172	0.01345	0.0147	0.0144	0.0249
NIST616	**6/17/2016**	41	0.0146	0.0907	0.01853	0.0778	1.028	2.342	0.0290	0.0299	0.0156	0.0178	0.01362	0.0153	0.0147	0.0246
mean		41.033	0.0148	0.0897	0.0184	0.0791	1.0353	2.3267	0.0287	0.0287	0.0158	0.0173	0.0135	0.0150	0.0144	0.0248
SD		0.0850	0.0004	0.0009	0.0003	0.0020	0.0154	0.0292	0.0005	0.0021	0.0001	0.0005	0.0001	0.0003	0.0002	0.0002
Average detection limit		0.0002	0.0001	0.0002	0.0001	0.0003	0.0003	0.0003	0.0000	0.0000	0.0000	0.0001	0.0000	0.0001	0.0001	0.0000
GeoRem	**NIST616**	41.72	0.0288	0.0951	0.0194	0.0879	1.18	2.31	0.0298	0.0292	0.015	0.0227	0.0169	0.0171	0.0154	0.0299
Accuracy		-1.65%	-48.7%	-5.64%	-5.19%	-10.01%	-12.3%	0.72%	-3.70%	-1.83%	5.02%	-24%	-20.2%	-12%	-6.26%	-17%
NIST614	**11/28/2016**	45.97	0.7816	0.8471	0.7911	0.811	1.55	3.216	0.7163	0.799	0.7735	0.7552	0.7501	0.7714	0.7305	0.7904
NIST614	**11/28/2016**	45.3	0.7812	0.857	0.7829	0.774	1.497	3.134	0.7082	0.7711	0.7618	0.7404	0.75	0.7715	0.7256	0.7858
NIST614	**11/28/2016**	46.28	0.7877	0.855	0.795	0.844	1.598	3.258	0.7143	0.812	0.782	0.7465	0.7574	0.7752	0.7348	0.7897
NIST614	**11/28/2016**	46.33	0.7817	0.8576	0.79	0.826	1.55	3.254	0.7146	0.806	0.78	0.742	0.7587	0.7786	0.743	0.7893
NIST614	**11/28/2016**	46.23	0.7876	0.86	0.794	0.849	1.592	3.276	0.7225	0.813	0.784	0.747	0.7609	0.7805	0.7427	0.7942
mean		46.02	0.7840	0.8553	0.7906	0.8208	1.5574	3.2276	0.7152	0.8002	0.7763	0.7462	0.7554	0.7754	0.7353	0.7899
SD		0.427	0.0034	0.0049	0.0048	0.0302	0.0406	0.0567	0.0051	0.0172	0.0090	0.0058	0.0051	0.0041	0.0076	0.0030
Average detection limit		0.000	0.0001	0.0002	0.0001	0.0003	0.0002	0.0004	0.0000	0.0000	0.0000	0.0001	0.0000	0.0001	0.0001	0.0000
GeoRem	**NIST614**	45.8	0.79	0.848	0.03	0.03	1.68	3.2	0.72	0.813	0.768	0.752	0.749	0.777	0.711	0.808
Accuracy		0.48%	-0.76%	0.87%	2535%	2636%	-7.30%	0.86%	-0.67%	-1.57%	1.08%	-0.77%	0.86%	-0.20%	3.42%	-2.24%

NIST616	**11/28/2016**	40.68	0.0241	0.0904	0.01841	0.0813	1.032	2.316	0.0292	0.0299	0.0157	0.0194	0.01381	0.0158	0.0152	0.0256
NIST616	**11/28/2016**	40.67	0.0243	0.091	0.01846	0.0783	1.037	2.328	0.0291	0.0297	0.0157	0.0192	0.01366	0.0154	0.0156	0.0264
NIST616	**11/28/2016**	40.72	0.0235	0.0907	0.01901	0.0812	1.035	2.328	0.0292	0.0303	0.016	0.0178	0.01363	0.0152	0.0151	0.0257
NIST616	**11/28/2016**	41.45	0.0231	0.0915	0.01831	0.0825	1.055	2.386	0.0293	0.0321	0.0163	0.0186	0.01356	0.0154	0.0152	0.0252
NIST616	**11/28/2016**	40.21	0.0246	0.0926	0.01861	0.0779	1.022	2.293	0.0293	0.0298	0.0156	0.0188	0.01404	0.0155	0.0156	0.0263
mean		40.75	0.0239	0.0912	0.0186	0.0802	1.0362	2.3302	0.0292	0.0304	0.0158	0.0187	0.0137	0.0155	0.0153	0.0258
SD		0.4455	0.0006	0.0009	0.0003	0.0020	0.0120	0.0343	0.0001	0.0010	0.0003	0.0006	0.0002	0.0002	0.0003	0.0005
Average detection limit		0.0003	0.0001	0.0002	0.0001	0.0002	0.0002	0.0003	0.0000	0.0000	0.0000	0.0001	0.0000	0.0001	0.0001	0.0000
GeoRem	**NIST616**	41.72	0.0288	0.0951	0.0194	0.0879	1.18	2.31	0.0298	0.0292	0.015	0.0227	0.0169	0.0171	0.0154	0.0299
Accuracy		-2.33%	-17%	-4.06%	-4.33%	-8.71%	-12.2%	0.87%	-1.91%	3.96%	5.20%	-17.4%	-18.70%	-9.64%	-0.53%	-13.6%
NIST614	**11/29/2016**	45.31	0.7754	0.849	0.0069	0.012	1.475	3.15	0.7096	0.779	0.7659	0.7313	0.7467	0.7634	0.7307	0.7814
GeoRem	**NIST614**	45.8	0.79	0.848	0.03	0.03	1.68	3.2	0.72	0.813	0.768	0.752	0.749	0.777	0.711	0.808
Accuracy		-1.07%	-1.85%	0.12%	-77.00%	-60.00%	-12.2%	-1.56%	-1.44%	-4.18%	-0.27%	-2.75%	-0.31%	-1.75%	2.77%	-3.29%
NIST616	**11/29/2016**	39.71	0.0237	0.0921	0.01854	0.0782	1.018	2.25	0.0292	0.0326	0.0167	0.0189	0.01408	0.0161	0.0153	0.026
GeoRem	**NIST616**	41.72	0.0288	0.0951	0.0194	0.0879	1.18	2.31	0.0298	0.0292	0.015	0.0227	0.0169	0.0171	0.0154	0.0299
Accuracy		-4.82%	-17.7%	-3.15%	-4.43%	-11.04%	-13.7%	-2.60%	-2.11%	11.64%	11.27%	-16.8%	-16.69%	-5.96%	-0.97%	-13.1%

Standard	**Session**	**W**	**Pb**	**Th**	**U**
NIST614	**10/19/2015**	0.735	2.264	0.754	0.778
NIST614	**10/19/2015**	0.733	2.182	0.741	0.788
NIST614	**10/19/2015**	0.749	2.253	0.746	0.778
NIST614	**10/19/2015**	0.728	2.203	0.7369	0.755
mean		0.7363	2.2255	0.7445	0.7748
SD		0.0090	0.0393	0.0074	0.0140
Average detection limit		0.0000	0.0001	0.0000	0.0000
GeoRem	**NIST614**	0.806	2.32	0.748	0.823
Accuracy		-8.65%	-4.07%	-0.47%	-5.86%
NIST616	**10/19/2015**	0.0416	1.766	0.0306	0.0729
NIST616	**10/19/2015**	0.0401	1.66	0.026	0.0664
NIST616	**10/19/2015**	0.0376	1.732	0.0251	0.0642
NIST616	**10/19/2015**	0.0374	1.71	0.0234	0.0638
mean		0.0392	1.7170	0.0263	0.0668
SD		0.0020	0.0444	0.0031	0.0042
Average detection limit		0.0000	0.0001	0.0000	0.0000
GeoRem	**NIST616**	0.043	1.85	0.0252	0.0721
Accuracy		-8.90%	-7.19%	4.27%	-7.32%
NIST614	**10/19/2015**	0.774	2.32	0.72	0.791
NIST614	**10/19/2015**	0.749	2.267	0.731	0.779
mean		0.7615	2.2935	0.7255	0.7850
SD		0.0177	0.0375	0.0078	0.0085
Average detection limit		0.0000	0.0001	0.0001	0.0000
GeoRem	**NIST614**	0.806	2.32	0.748	0.823
Accuracy		-5.52%	-1.14%	-3.01%	-4.62%
NIST616	**10/19/2015**	0.0386	1.739	0.02299	0.0647
NIST616	**10/19/2015**	0.0405	1.696	0.0248	0.0647
mean		0.0396	1.7175	0.0239	0.0647
SD		0.0013	0.0304	0.0013	0.0000
Average detection limit		0.0000	0.0001	0.0000	0.0004
GeoRem	**NIST616**	0.043	1.85	0.0252	0.0721
Accuracy		-8.02%	-7.16%	-5.18%	-10.26%
NIST616	**11/13/2015**	0.0367	1.595	0.02181	0.0618

NIST616	**11/13/2015**	0.035	1.572	0.02112	0.0611
NIST616	**11/13/2015**	0.034	1.52	0.02065	0.0573
mean		0.0352	1.5623	0.0212	0.0601
SD		0.0014	0.0384	0.0006	0.0024
Average detection limit		0.0353	1.6193	0.0222	0.0628
GeoRem	**NIST616**	0.043	1.85	0.0252	0.0721
Accuracy		-18.06%	-15.55%	-15.90%	-16.69%
NIST616	**12/23/2015**	0.0435	1.637	0.0247	0.0703
NIST616	**12/23/2015**	0.0405	1.713	0.02395	0.0663
NIST616	**12/23/2015**	0.0386	1.752	0.0245	0.0664
mean		0.0409	1.7007	0.0244	0.0677
SD		0.0025	0.0585	0.0004	0.0023
Average detection limit		0.0001	0.0001	0.0000	0.0000
GeoRem	**NIST616**	0.043	1.85	0.0252	0.0721
Accuracy		-4.96%	-8.07%	-3.24%	-6.15%
NIST614	**4/28/2016**	0.791	2.459	0.771	0.863
NIST614	**4/28/2016**	0.777	2.361	0.761	0.835
NIST614	**4/28/2016**	0.767	2.327	0.778	0.83
NIST614	**4/28/2016**	0.802	2.488	0.78	0.869
mean		0.7843	2.4088	0.7725	0.8493
SD		0.0154	0.0770	0.0086	0.0196
Average detection limit		0.0007	0.0001	0.0000	0.0000
GeoRem	**NIST614**	0.806	2.32	0.748	0.823
Accuracy		-2.70%	3.83%	3.28%	3.19%
NIST616	**4/28/2016**	0.0397	1.865	0.02398	0.0698
NIST616	**4/28/2016**	0.0374	1.9	0.02479	0.0725
NIST616	**4/28/2016**	0.0417	1.913	0.02491	0.0738
NIST616	**4/28/2016**	0.0405	1.897	0.02488	0.0715
mean		0.0398	1.8938	0.0246	0.0719
SD		0.0018	0.0204	0.0004	0.0017
Average detection limit		0.0001	0.0001	0.0000	0.0000
GeoRem	**NIST616**	0.043	1.85	0.0252	0.0721
Accuracy		-7.38%	2.36%	-2.22%	-0.28%
NIST614	**6/10/2016**	0.784	2.432	0.78	0.855

NIST614	**6/10/2016**	0.771	2.263	0.77	0.864
NIST614	**6/10/2016**	0.738	2.268	0.7469	0.816
NIST614	**6/10/2016**	0.732	2.243	0.759	0.814
mean		0.7563	2.3015	0.7640	0.8373
SD		0.0252	0.0877	0.0143	0.0260
Average detection limit		0.0001	0.0001	0.0000	0.0000
GeoRem	**NIST614**	0.806	2.32	0.748	0.823
Accuracy		-6.17%	-0.80%	2.14%	1.73%
NIST616	**6/10/2016**	0.04	1.834	0.02481	0.0709
NIST616	**6/10/2016**	0.039	1.791	0.02459	0.0685
NIST616	**6/10/2016**	0.0378	1.718	0.02318	0.0644
NIST616	**6/10/2016**	0.0374	1.74	0.02347	0.0658
mean		0.0386	1.7708	0.0240	0.0674
SD		0.0012	0.0521	0.0008	0.0029
Average detection limit		0.0001	0.0001	0.0000	0.0000
GeoRem	**NIST616**	0.043	1.85	0.0252	0.0721
Accuracy		-10.35%	-4.28%	-4.71%	-6.52%
NIST614	**6/17/2016**	0.756	2.36	0.731	0.826
NIST614	**6/17/2016**	0.784	2.409	0.743	0.854
NIST614	**6/17/2016**	0.781	2.377	0.756	0.833
mean		0.7737	2.3820	0.7433	0.8377
SD		0.0154	0.0249	0.0125	0.0146
Average detection limit		0.0001	0.0001	0.0000	0.0000
GeoRem	**NIST614**	0.806	2.32	0.748	0.823
Accuracy		-4.01%	2.67%	-0.62%	1.78%
NIST616	**6/17/2016**	0.0399	1.921	0.02465	0.0719
NIST616	**6/17/2016**	0.0416	1.91	0.0245	0.0732
NIST616	**6/17/2016**	0.0429	1.937	0.02409	0.0738
mean		0.0415	1.9227	0.0244	0.0730
SD		0.0015	0.0136	0.0003	0.0010
Average detection limit		0.0001	0.0001	0.0000	0.0000
GeoRem	**NIST616**	0.043	1.85	0.0252	0.0721
Accuracy		-3.57%	3.93%	-3.12%	1.20%
NIST614	**11/28/2016**	0.818	2.503	0.7722	0.868

NIST614	**11/28/2016**	0.7822	2.392	0.7683	0.826
NIST614	**11/28/2016**	0.848	2.608	0.7739	0.882
NIST614	**11/28/2016**	0.821	2.496	0.7729	0.876
NIST614	**11/28/2016**	0.845	2.543	0.7744	0.899
mean		0.8228	2.5084	0.7723	0.8702
SD		0.0265	0.0788	0.0024	0.0272
Average detection limit		0.0001	0.0001	0.0000	0.0000
GeoRem	**NIST614**	0.806	2.32	0.748	0.823
Accuracy		2.09%	8.12%	3.25%	5.74%
NIST616	**11/28/2016**	0.0411	1.89	0.02539	0.0716
NIST616	**11/28/2016**	0.0405	1.905	0.02561	0.0714
NIST616	**11/28/2016**	0.0413	1.893	0.02492	0.0705
NIST616	**11/28/2016**	0.0426	1.946	0.02496	0.0744
NIST616	**11/28/2016**	0.0411	1.869	0.02585	0.0707
mean		0.0413	1.9006	0.0253	0.0717
SD		0.0008	0.0285	0.0004	0.0016
Average detection limit		0.0001	0.0001	0.0000	0.0000
GeoRem	**NIST616**	0.043	1.85	0.0252	0.0721
Accuracy		-3.91%	2.74%	0.58%	-0.53%
NIST614	**11/29/2016**	0.783	2.398	0.76	0.822
GeoRem	**NIST614**	0.806	2.32	0.748	0.823
Accuracy		-2.85%	3.36%	1.60%	-0.12%
NIST616	**11/29/2016**	0.0414	1.858	0.02539	0.0711
GeoRem	**NIST616**	0.043	1.85	0.0252	0.0721
Accuracy		-3.72%	0.43%	0.75%	-1.39%

Table C2: Total Procedural Blank concentrations (pg) and calculated Limits of Quantification (LOQ).

	Samples																		
	B_16_01	**B_16_02**	**B_16_03P**	**B_16_04P**	**B_17_01**	**B_17_02**	**B_17_03**	**B_17_04P**	**B_17_06P**	**B_18_01P**	**B_18_02P**	**B_18_04**	**B_19_1**	**B_19_2**	**B_19_3P**	**B_20-01P**	**B_20-02P**	**B_20-03P**	**B_20-04**
Rb		2.1	0	0.49	1.60	0	0	0.43	0.9	0	0.28	0	0.8	0.59	0.39	0	0	0	0
Sr		28	10.6	19.7	27.6		7.57	13.5	29.58	14.8	31	9.5		15	28		22	2.7	12.3
Y	1.1	1.5	0.26	0.71		0.34	0.34		0.9	0.4		0.38	0.45	0.48	0.69	1.29	0.67	0.17	0.28
Nb					0.78	0.2	0.23					1.32	0.39	0.16					2.1
Mo					24.2	68.5	29.3					51.9	34.6	49					46.9
Cs		0.09	0	0	0.11		0	0	0.15	0.015	0.009	0	0.04	0.036	0.02	0.03	0.022	0.002	0.012
Ba				30	22.8	25.8	10.6	21.9	24.4	17.9	25		23.6		17.1	14.4	9.93	3.9	5.7
La			0.53	0.8		0.24	0.28		0.94	0.81		0.81	0.4	0.85	1.78	0.87	0.59	0.19	0.12
Ce	8.8	6.08	1.03	4.85		2.1	5.46	8.75	2.4	3.5	9.1	4.1	1.3	1.06	6.4	2.1	3	1.31	0.6
Pr	0.4		0.05	0.19		0.02	0.06		0.26	0.15		0.1	0.09	0.13	0.31	0.45	0.21	0.07	0.046
Nd	1.34	1.32	0.15	0.72		0.28	0.39		1.039	0.56		0.30	0.35	0.61	0.94	1.66	0.74	0.21	0.18
Sm	0.28		0.0554	0.23		0.14	0.113		0.24	0.102		0.028	0.1	0.15	0.16	0.23	0.18	0.05	0.08
Eu	0.059		0.005	0.054		0	0.025		0.034	0.013		0.01	0.024	0.021	0.042	0.039	0.031	0.005	0.01
Gd	0.228		0.062	0.159		0.027	0.129		0.125	0.089		0.07	0.07	0.450	0.0912	0.33	0.161	0.045	0.09
Tb	0.031		0	0.0226		0.011	0.008		0.0209	0.017		0.008	0.017	0.020	0.025	0.039	0.018	0.007	0.009
Dy	0.152	0.429	0.041	0.197		0.09	0.13		0.14	0.071		0.04	0.1	0.16	0.14	0.16	0.13	0.03	0.054
Ho	0.04		0	0.0193		0.011	0.016		0.0276	0.0137		0.014	0.025	0.031	0.0263	0.047	0.032	0.008	0.014
Er	0.192		0.05	0.065		0.02	0.043		0.139	0.02		0.082	0.078	0.1	0.13	0.11	0.07	0.026	0.036
Yb	0.149		0.022	0.025		0.01	0.004		0.118	0.05		0.066	0.18	0.212	0.191	0.05	0.061	0.026	0.028
Lu	0.032		0.05	0.031	0.084	0	0	0.07	0.025	0.0006	0.09	0.011	0.068	0.063	0.07	0.016	0.004	0.002	0.003
Hf	1.39	3.9		1.2	2.99	1.62	0.56	3.56		0.41	3.1	1.9	1.15	3.27	0.25	0.067	0.007	0	0
Ta																			

Pb					3.98		3.3					6.5	4.97						2.77
Th	0.40	0.40	0.119	0.17	0.39	1.19	0.06		0.47	0.158	0.77	0.2	0.35	0.78	0.678	0.28	0.35	0.04	0.17
U	0.34		0.19	0.25	0.18	0.18	0.09	0.16	0.22	0.11		0.14	0.24	0.14	0.18	0.31	0.08	0.2	0.108
Cr		0			86.36		3790					0	1318	195					3727
Mn					45	164	81.2					60							
Fe	7317	9059	4535	6391	2951	42400	42910	16675	8349	48691	14618	0							
Co					1.04	2.98	0.67					1.67	4.77	4.9					
Ni													186	41.89					
Cu		101			56	42.8	61.8					68.3	32.8	50					
Zn	1275	1046	332	378			487		794	603		920	245	346	426	921	518	605	311
Zr	54.8	161.8		55.8		63	19	149		143		62	45	58	8.67	4.17	1.50	0.59	0.64
Nb			1.16	0.85				5.22	1.67	1.59					0.77		3.69		
Mo			62	62				114	123	108.4	61				28		104		
Pb			2.6	4.47				3.9		4.09					10.8		8.25	2.7	
Cr			14585	5784				9824	0	0	0				1422		12399		
Mn			0.54	4.09				69.2	20.35	28.69	38.7				9.4	173	64	183	
Co			0.54	4.1				69.	20.4	28.7	38.8				9.4		63.9		
Ni															363		2893		
Cu			43	0				254	171	151	213				83.4		252		

	Samples																			
	B_20-05	**B_20-06**	**B_20-07**	**B_20-08**	**B_20-09**	**B_20-10**	**B_22_01P**	**B_22-02P**	**B_22_04**	**B_22_05**	**B_22_06**	**B_26_01**	**B_26_02**	**B_31_01**	**B_31_02**	**B_31_03P**	**B_31_04P**	**mean**	**2 SD**	**LOQ (7*σ)**
Rb	0.48	0.00	0.00	0.34		0.17	0.22	0.16	0.00	0.00	0.00	0.29		0.51	0.07			0.98	4.94	3.42
Sr	26.77	2.04	21.60	16.53	31.34	6.79	4.70	3.71	0.86	3.63	2.11	6.06	10.33	10.55	14.25	5.09	5.93	18.41	31.93	67
Y	0.49	0.40	0.30	0.17	0.32	0.00	0.49	0.33	0.01	0.00	0.00	0.18	0.29	0.08	0.08	0.17	0.17	0.69	2.05	2.5
Nb	0.36	0.05	0.28	0.07	0.08	0.15			0.06	0.00	0.04	0.06	0.07	0.01	0.01			0.63	2.23	3.6
Mo	15.97	18.30	22.47	19.37	6.43	5.44			5.82	8.66	4.59	50.74	11.34	2.52	10.73			35.28	79.49	133

Cs	0.02	0.00	0.01	0.03		0.01	0.00	0.00	0.00	0.00	0.00	0.05	0.15	0.00	0.00	0.00	0.02	0.10	0.50	0.28
Ba	7.71	2.58	13.49	2.71			4.71	12.87	0.98	2.01	1.29	5.44	12.26	4.04	3.44	0.00	0.23	17.77	35.08	63.7
La	1.07	0.07	0.32	0.25	0.57		0.41		0.21	0.43	0.06	0.00	0.00	0.00	0.00	0.00	0.08	0.83	1.84	2.9
Ce		0.55	1.19	0.74	1.64		1.30	6.36	2.11		1.54	0.63	0.99	0.18	0.25	0.32	0.56	3.89	9.08	18.7
Pr	0.22	0.04	0.08	0.08	0.11		0.27	0.15	0.08	0.09	0.02	0.08	0.14	0.02	0.02	0.03	0.06	0.21	0.48	0.78
Nd	0.35	0.25	0.34	0.33	0.46	0.19	0.94	0.41	0.19	0.17	0.03	0.29	0.45	0.13	0.11	0.09	0.23	0.72	1.83	2.8
Sm	0.16	0.09	0.09	0.09	0.13	0.04	0.12	0.03	0.04	0.03	0.01	0.08	0.11	0.02	0.02	0.02	0.05	0.18	0.50	0.49
Eu	0.02	0.01	0.03	0.01	0.02	0.01	0.02	0.01	0.01	0.01	0.00	0.04	0.06	0.00	0.00	0.01	0.01	0.05	0.18	0.11
Gd	0.10	0.05	0.08	0.06	0.08	0.07	0.17	0.12	0.04	0.02	0.00	0.10	0.14	0.02	0.01	0.02	0.04	0.18	0.47	0.64
Tb	0.02	0.02	0.01	0.01	0.01	0.01	0.00	0.00	0.00	0.00	0.00	0.04	0.05	0.00	0.00	0.01	0.01	0.03	0.10	0.08
Dy	0.12	0.07	0.08	0.07	0.05	0.02	0.06	0.05	0.03	0.02	0.01	0.06	0.09	0.03	0.02	0.03	0.04	0.15	0.46	0.54
Ho	0.03	0.02	0.02	0.01	0.01	0.01	0.01	0.01	0.01	0.01	0.00	0.03	0.04	0.00	0.00	0.00	0.01	0.04	0.12	0.08
Er	0.09	0.06	0.05	0.06	0.03	0.02	0.03	0.02	0.01	0.01	0.01	0.02	0.05	0.01	0.01	0.02	0.03	0.10	0.26	0.3
Yb	0.05	0.05	0.05	0.02	0.03	0.00	0.01	0.03	0.01	0.00	0.00	0.03	0.05	0.01	0.01	0.02	0.01	0.09	0.28	0.4
Lu	0.00	0.01	0.00	0.00	0.00	0.00	0.01	0.00	0.00	0.00	0.00	0.04	0.03	0.00	0.00	0.00	0.00	0.03	0.10	0.2
Hf	0.17	0.03	0.41	0.10	0.18	0.33	0.05	0.09	0.02	0.00	0.06	0.00	0.23	0.39	0.36	0.37	0.34	1.26	4.12	8.3
Ta																		74.63	471	
Pb	2.02	0.55		1.20	4.99	0.69			0.00	6.40	0.00	4.00	4.02	0.74	0.48			4.69	8.55	15
Th	0.08	0.03	0.14	0.12	0.14	0.07	0.12	0.10	0.05	0.07	0.04	0.55	0.06	0.01	0.03	0.03	0.08	0.44	2.34	1.87
U	0.09	0.31	0.07	0.03	0.19	0.22	0.14	0.07	0.05	0.30	0.03	0.11	0.08	0.02	0.02	0.02	0.04	0.18	0.34	0.63
Cr	875	95.29	126.4	9.04	27.56	40.49			36.06	13.65	61.09	157	31.54	29.60	11.94			1087	4206	7860
Mn									16.82	13.80	53.86	132	17.94	14.74	8.89			95.11	216	347
Fe									150	94.46	301	844.8	319	115.5	105	1285	11682	16861	51439	104013
Co	7.75	1.63	2.13	0.55	0.50	1.57			0.82	0.22	0.97	0.95	0.80	0.40	0.22			7.52	30	13.5
Ni	464.3	7.41	46.52	5.44	7.22	876			16.42	13.79	25.84	66.39	51.00	36.11	6.75			257.74	1132	1619
Cu	40.69	6.44	30.88	17.89	16.03	14.66			0.20	82.45	3.69	16.40		15.55	8.83			62.23	151	195

Zn	1078	225	404.8	240	349.4	131.1	353.6	345.8	6.43	0.00	13.16	242	453	291	289	368.5	407	674	1410	2165
Zr	8.69	2.55	19.60	5.91	8.66	17.01	1.12	3.23	0.00	0.00	0.81	0.00	11.9	0.31	2.02	1.37	0.00	56.38	185	313
Nb							5.87	4.69								0.03	0.36	4.30	8.47	14
Mo							101	44.74								5.48	8.58	94.23	151	279
Pb							9.48	8.75								2.76	5.07	9.59	17.5	20
Cr								12387								160	1485	4200	14841	28908
Mn							21.90	26.87								0.65	3.03	642	4692	
Co							21.90	26.87								0.65	3.03	45.99	116	157
Ni							1056	3165								19.28	70.16	3172	7027	8966
Cu						234	305								131	32.15	222	377	667	

P = TPB with parafilm

kursic elements = TPBs for samples fixed in place with parafilm

Table C3: Median concentrations (ppm) of rubies analysed by LA-ICPMS. Where < 3 spots are analysed mean values and standard deviations are reported instead of median and MAD.

Provenance	**Namahaca, Mozambique**																	
Sample	**MOZ1_2**	**dark pink**		**MOZ1_4**	**red**		**MOZ1_5**	**red**		**MOZ1_7**	**red**		**MOZ2_1**	**dark pink**		**MOZ2_3**	**dark pink**	
N	8			8			5			8			8			6		
Element	**median/ mean**	**MAD/ SD**	**n**	**median/ mean**	**MAD/ SD**	**n**	**median/ mean**	**MAD/ SD**	**n**	**median/ mean**	**MAD/ SD**	**n**	**median/ mean**	**MAD/ SD**	**n**	**median/ mean**	**MAD/ SD**	**n**
Mg	21	0.56	8	47	1.5	8	33	1.27	5	49	9.1	8	49	6.8	8	27	5.1	6
Si	114	14	6	103	11	6	81	10	2	129	26	6	101	14	6	114	3.6	4
K	1.03	0.55	5	1.50	0.79	4	0.65	0.1	3	1.11	0.48	6	1.27	0.99	3	0.55	0.12	4
Ca(43)	644	272	8	811	248	8	786	363	5	765	267	8	999	83	8	821	179	6
Ti	44	17	8	72	11	8	45	1.14	5	77	16	8	53	10	8	34	11	6
V	3.3	0.06	8	6.9	0.36	8	5.3	0.40	5	7.8	0.18	8	3.6	0.26	8	2.9	0.10	6
Cr	1705	191	8	6551	295	8	7010	1410	5	8663	260	8	1909	276	8	1676	83	6

Mn	0.02	0	1			0	0.02	0	1	0.03	0.003	2			0			0
Fe	1051	64	8	895	35	8	1073	224	5	895	40	8	1061	43	8	1014	42	6
Ni	0.53	0.16	8	1.32	0.10	8	0.96	0.07	5	1.44	0.26	8	1.08	0.18	8	0.70	0.13	6
Cu	0.10	0.001	3	0.12	0.04	2	0.06	0	1	0.19	0.056	3	0.25	0.02	2			0
Zn	0.58	0.22	8	0.54	0.08	8	0.47	0.014	5	0.61	0.098	8	0.47	0.03	7	0.42	0.10	6
Ga	24	1.73	8	30	1.48	8	24	0.15	5	32	0.9	8	27	0.81	8	26	0.51	6
Rb			0			0			0	0.0096	0.00075	2			0			0
Sr	0.007	0.001	3			0	0.0063	0	1	0.0079	0.0019	3	0.0079	0	1	0.02	0.0014	2
Y			0			0	0.01	0	1			0			0			0
Zr	0.010	0.005	6	0.017	0.008	8	0.017	0.0074	5	0.0158	0.00115	8	0.0127	0.0046	3	0.0053	0	1
Nb	0.002	0.00017	7	0.0088	0.00045	8	0.0107	0.0042	5	0.01124	0.00205	8	0.0031	0.0007	7	0.0026	0.00014	5
Mo	0.004	0	1			0			0			0			0			0
Sn	0.016	0.0093	4	0.012	0	1	0.0075	0.0005	3	0.0100	0.0014	4	0.0151	0	1			0
Ba	0.0052	0.00095	4	0.0025	0	1	0.013	0	1	0.013	0.0001	3	0.0242	0.0098	2			0
La	0.0019	0	2	0.00056	0	1	0.0041	0	1	0.00097	0.00013	4	0.0024	0.0013	3	0.0018	0	1
Ce	0.0014	0.00058	4	0.0014	0.0005	5	0.002	0	1	0.0034	0.0002	3	0.0042	0.00085	6	0.0021	0.00082	4
Pr	0.00036	0.00028	4	0.0009	0.00033	4	0.0010	0.00014	2	0.0007	0.00009	3	0.00088	0.00009	3	0.00051	0	1
Nd	0.0013	0	1	0.0019	0	1	0.0057	0	1	0.0017	0.0001	2	0.0019	0.00016	2	0.00065	0	1
Ho	0.00022	0.00005	2	0.00015	0.00003	3	0.00038	0	1	0.0004	0.00014	3	0.00026	0	1			0
Yb	0.001	0	1			0			0			0			0	0.00047	0	1
Hf	0.00035	0.00003	2	0.00046	0	1			0	0.00084	5E-06	2			0	0.0022	0	1
Ta	0.00076	0	1			0			0	0.0014	0	1			0			0
W	0.0017	0.00055	2	0.00270	0	1			0	0.0024	0.001	2	0.00091	0.00013	3			0
Pb	0.0094	0.0023	8	0.0091	0.004	5	0.004	0.0013	5	0.0053	0.0021	8	0.0078	0.0034	6	0.0049	0.0009	5
Th	0.00032	0.00005	4	0.00028	0.00005	2	0.0015	0.00099	4	0.00079	0.00029	3	0.0010	0	1	0.00032	0.00014	2
U	0.00059	0.00033	5	0.00035	0.00015	3	0.00084	0.00067	2	0.00094	0.00046	4	0.00022	0	1	0.00063	0.00029	2
Fe/Mg	49			19			33			18			22			38		
Ga/Mg	1.15			0.64			0.72			0.65			0.55			0.97		
Cr/Fe	1.62			7.3			6.5			9.7			1.80			1.65		

Provenance	Namahaca, Mozambique																	
Sample	**moz2_2**	**dark pink**		**moz2_4**	**light pink**		**moz2_5**	**red**		**moz2_6**	**dark pink**		**moz2_7**	**red**		**moz2_8**	**red**	
N	2			2			2			2			2			2		
Element	**median/ mean**	**MAD/ SD**	**n**	**median/ mean**	**MAD/ SD**	**n**	**median/ mean**	**MAD/ SD**	**n**	**median/ mean**	**MAD/ SD**	**n**	**median/ mean**	**MAD/ SD**	**n**	**median/ mean**	**MAD/ SD**	**n**
Mg	39	7.3	2	25	3.3	2	19	0.82	2	30	9.3	2	51	1.7	2	37	5.0	2
Si	660	54	2	595	34	2	491	43	2	487	3	2	438	31	2	488	98	2
K			0			0			0			0			0			0
Ca(43)	474	5	2	417	70	2	319	24	2	653	101	2	635	115	2	617	34	2
Ti	37	0.4	2	38	4.0	2	28	2.7	2	27	3.4	2	62	3.35	2	49	9.9	2
V	5.1	0.34	2	4.4	0.11	2	5.9	0.78	2	3.0	0.10	2	6.6	0.19	2	6.6	0.50	2
Cr	4721	544	2	1912	15	2	6764	775	2	1872	39	2	2513	0.5	2	8280	910	2
Mn			0			0			0	0.15	0	1			0			0
Fe	724	36	2	815	8.5	2	735	5.6	2	1034	27	2	1268	3	2	876	95	2
Ni	1.72	0.23	2	0.60	0.064	2	0.76	0.17	2	0.72	0.18	2	2.3	0.94	2	1.28	0.18	2
Cu	0.23	0	1			1			0			0			0			0
Zn	2.5	0.85	2	1.64	1.16	2	0.79	0.10	2	1.33	0.52	2	0.74	0.04	2	1.28	0.12	2
Ga	20	0.75	2	18	0.27	2	20	0.2	2	22	0.18	2	24	0.19	2	25	0.28	2
Rb			0			0			0			0			0			0
Sr			0	0.020	0	1			0	0.037	0	1			0	0.028	0	1
Y			0	0.0062	0	1			0			0	0.0016	0	1			0
Zr	9.8	0	1			1			0	0.97	0.63	2	0.32	0	1	0.38	0	1
Nb	0.030	0.021	2	0.017	0	1	0.012	0.0006	2	0.009	0	1	0.014	0.00015	2	0.017	0.0047	2
Mo			0			0			0			0			0			0
Sn	0.027	0	1			0			0			0			0			0
Ba			0			0			0			0			0	0.115	0	1
La	0.002	0	1	0.0023	0	1	0.00081	0.00007	2	0.0033	0	1	0.00062	0	1	0.0098	0	1
Ce	0.010	0.0017	2			0	0.0032	0	1	0.0057	0	1	0.012	0.0035	2	0.088	0	1
Pr	0.0027	0.0009	2	0.0015	0	1			0			0			0	0.0021	0	1
Nd			0			0			0			0			0			0

Ho			0			0			0			0			0	0.0027	0	1
Yb			0			0			0			0			0			0
Hf			0			0			0			0			0	0.038	0	1
Ta	0.0095	0.0018	2	0.0036	0	1	0.0035	0	1			0			0			0
W			0			0			0			0			0			0
Pb			0			0			0			0			0			0
Th	0.0013	0	1			0			0	0.0020	0	1	0.00099	0	1			0
U	0.0041	0.0011	2	0.0020	0.00092	2			2	0.005	0	1			0	0.0048	0	1
Fe/Mg	18			32			39			35			25			24		
Ga/Mg	0.50			0.72			1.10			0.74			0.47			0.68		
Cr/Fe	6.5			2.3			9.2			1.81			1.98			9.5		

Provenance	**Namahaca, Mozambique**																	
Sample	**MOZ3-1_1**	**light pink**		**MOZ3-1_2**	**pink**		**MOZ3-1_3**	**pink**		**MOZ3-1_4**	**pink**		**MOZ3-1_5**	**pink**		**MOZ3-1_6**	**pink**	
N	6			4			5			7			5			6		
Element	**median/ mean**	**MAD/ SD**	**n**	**median/ mean**	**MAD/ SD**	**n**	**median/ mean**	**MAD/ SD**	**n**	**median/ mean**	**MAD/ SD**	**n**	**median/ mean**	**MAD/ SD**	**n**	**median/ mean**	**MAD/ SD**	**n**
Mg	63	8.4	6	53	11	4	58	7.3	5	66	29	7	59	32	5	45	9.2	6
Si	423	150	6	463	82	4	212	156	5	381	89	7	350	180	5	176	117	6
K	6.2	3.7	6	2.7	0.87	4	3.2	0.53	5	12	10	7	11	7.8	4	2.2	1.25	6
Ca(43)	653	153	6	737	37	4	936	266	5	556	73	7	551	55	5	869	119	6
Ti	52	2.6	6	55	13	4	58	6.6	5	45	4.5	7	42	5.2	5	51	3.0	6
V	4.2	0.16	6	4.5	0.23	4	4.3	0.078	5	4.0	0.32	7	4.4	0.29	5	4.1	0.24	6
Cr	1258	108	6	1592	78	4	1553	84	5	1465	50	7	1370	118	5	1260	115	6
Mn	0.19	0.077	4	0.43	0	1	0.13	0.096	2	0.16	0.11	5	0.87	0.04	3	0.27	0.058	3
Fe	1173	48	6	1158	59	4	979	42	5	863	25	7	1190	156	5	1056	105	6
Ni	1.89	0.77	4	1.06	0	2	0.85	0.14	3	0.93	0.48	5	1.5	0	1	0.82	0.18	5
Cu	0.82	0.54	3	0.31	0.14	2	0.15	0.061	3	0.25	0.042	5	0.49	0.1	3	0.32	0.14	5
Zn	1.03	0.26	6	1.12	0.11	4	0.9	0.35	5	1.18	0.47	7	1	0.28	5	0.65	0.23	6
Ga	21	1.25	6	23	2.3	4	22	1.86	5	20	1.19	7	22	1.02	5	23	1.34	6

Rb	0.11	0.05	4	0.25	0	1	0.025	0	1	0.095	0.016	3	0.21	0.10	2	0.072	0.058	2
Sr	0.13	0.069	6	0.19	0.086	4	0.17	0.12	4	0.12	0.062	7	0.17	0.029	5	0.092	0.048	5
Y	0.031	0.019	6	0.021	0.0087	4	0.0090	0.0016	5	0.013	0.0044	6	0.052	0.028	4	0.048	0.021	6
Zr	0.18	0.17	6	0.092	0.079	4	0.23	0.14	4	0.18	0.17	7	0.16	0.058	5	0.016	0.0066	6
Nb	0.0056	0.0015	6	0.0044	0.0011	4	0.0084	0.0048	5	0.009	0.0022	7	0.0066	0.0024	4	0.0049	0.0015	4
Mo	0.0088	0.0017	4			0			0	0.03	0.016	5	0.012	0	1	0.026	0.020	2
Sn	0.015	0.0019	6	0.017	0	2	0.021	0.0040	4	0.022	0.0061	6	0.017	0.0016	2	0.0077	0.0008	3
Ba	0.046	0.017	6	0.039	0.020	4	0.025	0.0162	5	0.064	0.037	7	0.085	0.042	4	0.020	0.0087	6
La	0.014	0.0072	6	0.0069	0.0022	4	0.0065	0.0031	5	0.0068	0.0035	7	0.023	0.0033	4	0.013	0.0021	6
Ce	0.011	0.0026	6	0.012	0.0073	4	0.012	0.0025	5	0.024	0.0159	7	0.0071	0.0015	5	0.0069	0.0036	5
Pr	0.006	0.0020	6	0.0069	0.0018	4	0.0051	0.0022	5	0.0059	0.0022	7	0.0086	0.0028	5	0.0056	0.0016	6
Nd	0.025	0.011	6	0.018	0.0094	3	0.008	0.0029	5	0.011	0.003	7	0.037	0.0057	4	0.020	0.0053	6
Ho	0.0036	0.00085	4	0.0020	0.0015	2	0.0014	0.00076	2	0.0020	0.0011	4	0.0029	4E-05	3	0.0016	6E-05	3
Yb	0.0081	0.0029	4	0.0066	0.0050	2	0.0030	0.0015	2	0.0041	0.0020	5	0.0063	0.0003	3	0.0031	0.0009	5
Hf	0.0062	0.0047	5	0.038	0.02	2	0.011	0.0006	3	0.0034	0.0023	5	0.0069	0.0056	2	0.03	0	1
Ta	0.0028	0.0003	5	0.0034	0.0007	2	0.0033	0.0005	3	0.0033	0.00062	6	0.0021	0.00057	2	0.0047	0.0016	2
W	0.0039	0.0013	6	0.0034	0.0003	3	0.0055	0.0018	4	0.011	0.0060	6	0.0055	0.0029	4	0.0054	0.0028	4
Pb	0.019	0.0074	6	0.016	0.0003	3	0.043	0.011	5	0.036	0.011	6	0.020	0.0032	3	0.014	0.0048	5
Th	0.0017	0.00086	6	0.0019	0.0015	4	0.0016	0.00051	4	0.003	0.0014	7	0.0027	0.00075	4	0.0038	0.0033	4
U	0.0075	0.0045	6	0.0028	0.00055	4	0.0047	0.0012	5	0.0117	0.0075	7	0.0083	0.0027	5	0.0029	0.0019	6
Fe/Mg	19			22			17			13			20			24		
Ga/Mg	0.33			0.43			0.38			0.31			0.38			0.51		
Cr/Fe	1.07			1.37			1.59			1.70			1.15			1.19		

Provenance	**Namahaca, Mozambique**																	
Sample	**MOZ3-1_7**	**dark pink**		**Moz3-2_1**	**pink**		**Moz3-2_2**	**dark pink**		**MOZ3-2_3**	**light pink**		**Moz3-2_4**	**pink**		**Moz3-2_5**	**pink**	

N	9			7			9			4			8			4		
Element	**median/ mean**	**MAD/ SD**	**n**	**median/ mean**	**MAD/ SD**	**n**	**median/ mean**	**MAD/ SD**	**n**	**median/ mean**	**MAD/ SD**	**n**	**median/ mean**	**MAD/ SD**	**n**	**median/ mean**	**MAD/ SD**	**n**
Mg	24	2.9	9	59	0.9	7	50	15	9	38	8.6	4	57	13	8	57	19	4
Si	259	118	6	389	79	4	283	58	6	216	11	2	276	62	6	129	23	3
K	2.2	0.91	8	4.7	2.8	7	4.1	2.9	9	1.42	0.33	4	3.5	2.2	8	9.4	8.8	4
Ca(43)	774	156	9	752	69	7	755	226	9	816	253	4	915	268	8	753	190	4
Ti	24	1.55	9	57	2.7	7	41	7.9	9	39	3.7	4	49	7.5	8	43	13	4
V	3.5	0.24	9	4.8	0.2	7	3.7	0.21	9	3.2	0.056	4	4.6	0.31	8	3.9	0.32	4
Cr	1710	91	9	1820	106	7	2104	138	9	1375	23	4	1707	136	8	1582	41	4
Mn	0.24	0.07	5	0.099	0.025	5	0.36	0.16	7	0.18	0	1	0.16	0.066	6	0.56	0.50	2
Fe	1021	122	9	1043	22	7	1077	189	9	1287	115	4	1048	114	8	1107	121	4
Ni	0.62	0.26	7	2.0	0.60	5	1.4	0.40	7	1.27	0.62	2	1.24	0.36	6	2.3	0	1
Cu	0.85	0.28	4	0.28	0.038	5	0.36	0.17	6	0.26	0.18	2	0.69	0.09	6	0.41	0.031	2
Zn	0.55	0.16	8	0.64	0.13	7	0.51	0.13	9	0.45	0.059	4	1.07	0.49	8	0.60	0.22	4
Ga	21	3.0	9	23	2.1	7	23	1.5	9	22	0.89	4	23	1.97	8	24	2	4
Rb	0.043	0	1	0.087	0.063	3	0.052	0.0022	3			0	0.11	0.01	2	0.087	0	1
Sr	0.19	0.11	3	0.21	0.082	7	0.047	0.027	8	0.085	0.031	4	0.18	0.089	6	0.069	0.047	3
Y	0.013	0.0014	3	0.033	0.018	7	0.0062	0.0014	3	0.060	0.044	3	0.031	0.020	7	0.23	0.20	2
Zr	0.21	0.15	6	0.037	0.028	6	0.032	0.027	9	0.036	0.023	4	0.049	0.039	8	0.040	0.016	4
Nb	0.0087	0.0045	8	0.0046	0.0012	7	0.0085	0.0033	9	0.0040	0.00038	4	0.0088	0.005	7	0.0052	0.0032	3
Mo	0.098	0.005	3	0.016	0.0046	3	0.024	0.0084	5			0	0.04	0.022	3			0
Sn	0.054	0.027	4	0.039	0.0015	3	0.027	0.0053	6			0	0.035	0.0045	4	0.026	0	1
Ba	0.054	0.034	5	0.036	0.017	6	0.039	0.022	8	0.024	0.0069	4	0.064	0.037	6	0.025	0.0091	4
La	0.0043	0.0021	7	0.014	0.0033	7	0.012	0.0039	8	0.022	0.0066	3	0.0079	0.0025	7	0.030	0.010	2
Ce	0.0070	0.0044	8	0.0094	0.0048	6	0.025	0.0049	9	0.012	0.0054	3	0.009	0.0057	7	0.0040	0.0015	4
Pr	0.013	0.0074	4	0.0053	0.0013	7	0.0051	0.0015	7	0.0078	0.0026	3	0.0047	0.0033	8	0.0097	0.0062	3
Nd	0.017	0.01	3	0.025	0.007	7	0.0067	0.00075	4	0.035	0.0158	3	0.011	0.0014	7	0.054	0.022	2
Ho	0.0026	0.0011	2	0.0018	0.00064	5	0.0016	0.00041	4	0.0017	0.00048	2	0.0031	0.0022	5	0.0050	0.0013	2
Yb	0.0089	0.0058	3	0.0041	0.002	4	0.0029	0.00085	6	0.0044	0.0021	2	0.0047	0.0018	5	0.0128	0.0067	2

Hf	0.022	0.012	4	0.0032	0.002	5	0.0070	0.0030	4			0	0.00725	0.0041	4			0
Ta	0.0069	0.0022	4	0.0063	0.003	5	0.0041	0.0014	5			0	0.0049	0.0001	4	0.0081	0	1
W	0.027	0.0173	4	0.016	0.009	3	0.0087	0.0044	8	0.0016	0.00002	3	0.0071	0.0060	6	0.0093	0.0057	2
Pb	0.039	0.033	7	0.035	0.007	5	0.022	0.016	7	0.0054	0.0022	2	0.066	0.056	6	0.019	0.006	3
Th	0.0066	0.0042	4	0.0024	0.00070	4	0.0045	0.0023	8	0.0032	0.0027	2	0.0034	0.0004	4	0.0011	0.00078	3
U	0.010	0.0089	6	0.0057	0.005	7	0.009	0.0071	7	0.00204	0.0003	4	0.0081	0.0065	7	0.0016	0.0011	3
Fe/Mg	43			18			22			34			18			19		
Ga/Mg	0.91			0.40			0.47			0.59			0.4			0.42		
Cr/Fe	1.67			1.74			1.95			1.07			1.63			1.43		

Provenance	**Namahaca, Mozambique**									**Aappaluttoq, Greenland**								
Sample	**moz3-2_6**	**light pink**		**moz3-2_7**	**pink**		**moz4_m**	**red**		**gl1_3**	**pink**		**gl1_5**	**pink**		**gl1_6**	**very light pink**	
N	4			2			4			9			2			9		
Element	**median/ mean**	**MAD/ SD**	**n**	**median/ mean**	**MAD/ SD**	**n**	**median/ mean**	**MAD/ SD**	**n**	**median / mean**	**MAD/ SD**	**n**	**median / mean**	**MAD/SD**	**n**	**median / mean**	**MAD/ SD**	**n**
Mg	37	14	4	33	3.0	2	27	0.665	4	51	9.7	9	34	1.75	2	46	8.4	9
Si	254	47	4	158	9	2	107	6.0	4	97	8.1	6	467	10	2	113	19	7
K	5.4	4.0	4	2.5	0.76	2	0.9	0	1	0.85	0.38	4	7.8	2.5	2	0.56	0.16	4
Ca(43)	738	186	4	698	48	2	613	209	4	613	220	9	489	0.5	2	683	325	9
Ti	28	1.53	4	39	2.8	2	63	24	4	96	25	9	47	2.8	2	78	15	9
V	3.3	0.20	4	3.7	0.39	2	6.7	0.019	4	4.9	0.84	9	14	0.085	2	22	1.97	9
Cr	1195	92	4	1651	119	2	5922	108	4	1405	209	9	1267	146	2	134	18	9
Mn	0.15	0.003	3			0			0	0.13	0.057	2	0.84	0.29	2	0.033	0.012	6
Fe	926	64	4	1086	20	2	1109	62	4	1435	122	9	1106	33	2	1225	34	9
Ni	1.09	0.35	3			0	0.84	0.12	4	0.41	0.17	9	0.56	0.13	2	0.30	0.071	9
Cu	0.38	0.07	3			0			0	0.27	0.16	4	0.54	0	1	0.18	0.069	5
Zn	1.40	0.46	4	0.70	0.065	2	0.87	0.26	4	0.76	0.34	8			0	0.53	0.098	9
Ga	20	1.52	4	21	0.055	2	30	1.98	4	27	1.1	9	21	0.27	2	31	1.28	9
Rb	0.070	0	1			0			0			0			0			0

Sr	0.11	0.035	4	0.20	0.041	2			0	0.012	0.004	3	0.12	0.027	2	0.011	0.0025	2
Y	0.020	0.0002	3	0.0098	0.0048	2			0			0	0.009	0.0022	2			0
Zr	0.37	0.15	4	0.074	0.056	2	0.0075	0.0002	3	0.012	0.0047	6			0	0.0043	0.0016	4
Nb	0.0083	0.0020	4	0.0039	0	1	0.0079	0.0014	4	0.0034	0.00065	7	0.0081	0	1	0.00084	0.00051	2
Mo	0.027	0.006	3			0			0			0	0.14	0.0055	2			0
Sn	0.041	0.024	2			0			0	0.0079	0.0009	3			0	0.011	0.0003	3
Ba	0.040	0.015	4	0.020	0.00005	2			0	0.012	0.0021	3	0.29	0.025	2	0.007	0.0005	2
La	0.012	0.0022	4	0.0053	0.0033	2			0	0.0029	0.0017	5	0.0089	0.00045	2	0.00052	0.00034	2
Ce	0.016	0.0055	4	0.0033	0.0006	2			0	0.0034	0.0017	7	0.027	0.0022	2	0.0012	0.00046	5
Pr	0.0069	0.0002	3	0.0024	0.00043	2			0	0.00025	0.00016	4			0	0.00048	0	1
Nd	0.017	0.0027	2	0.014	0	1			0	0.0016	0.0016	3			0	0.0011	0	1
Ho	0.0025		0			0			0	0.00008	0	1			0	0.00025	0.00009	2
Yb	0.0041	0.0006	3			0			0			0			0			0
Hf	0.014	0.0076	3	0.0042	0	1			0			0			0			0
Ta	0.0039	0.0014	3			0			0	0.0017	0	1			0			0
W	0.0039	0.0017	4			0			0	0.0024	0.00065	6			0	0.00083	0	1
Pb	0.058	0.025	3			0	0.0062	0	1	0.036	0.010	9			0	0.033	0.019	9
Th	0.0043	0.0002	3			0	0.00017	0	1	0.00098	0.00045	9	0.0019	0.00012	2	0.00043	0.00014	9
U	0.0072	0.0003	3	0.00082	0.0004	2	0.00024	0	1	0.0011	0.00081	9	0.0018	0	1	0.00041	0.00018	8
Fe/Mg	25			33			40			28			32			27		
Ga/Mg	0.53			0.64			1.09			0.53			0.60			0.66		
Cr/Fe	1.29			1.52			5.34			0.98			1.15			0.11		

Provenance										**Aappaluttoq, Greenland**								
Sample	**gl1_7**	**pink**		**gl1_8**	**dark pink**		**gl2_1**	**pink**		**gl2_2**	**dark pink**		**gl2_3**	**light pink**		**gl2_4**	**red**	
N	6			2			2			7			2			2		
Element	**median/ mean**	**MAD/ SD**	**n**	**median/ mean**	**MAD/ SD**	**n**	**median/ mean**	**MAD/ SD**	**n**	**median/ mean**	**MAD/ SD**	**n**	**median/ mean**	**MAD/ SD**	**n**	**median/ mean**	**MAD/ SD**	**n**
Mg	52	5.5	6	60	22	2	87	27	2	58	1.2	7	39	0.8	2	32	7.7	2
Si	116	6.5	4	549	55	2	779	35	2	114	23	5	609	7	2	646	19	2

K	0.97	0.46	3	3.9	1.15	2			0	1.22	0.53	5			0			0
Ca(43)	702	251	6	279	24	2	594	107	2	624	251	7	474	66	2	465	98	2
Ti	92	34	6	94	37	2	210	70	2	150	32	7	62	2.0		46	13	2
V	35	2.5	6	5.9	0.41	2	7.2	0.42	2	6.6	0.47	7	27	0.11	2	19	1.39	2
Cr	1375	74	6	2691	379	2	583	119	2	2871	592	7	633	12	2	2859	123	2
Mn	0.061	0.02	2	0.55	0.38	2	0.39	0	1			0			0			0
Fe	1302	29	6	1309	50	2	1564	43	2	1888	31	7	1128	14	2	2516	159	2
Ni	0.61	0.059	6	1.64	0.56	2	0.35	0	1	0.37	0.055	7	0.63	0.16	2	0.34	0.10	2
Cu	0.15	0	1	0.26	0.041	2	0.77	0.31	2	0.086	0.014	2	0.35	0	1			0
Zn	0.52	0.14	6	0.72	0.22	2	3.5	1.02	2	0.59	0.22	7	1.18	0.26	2	1.09	0.15	2
Ga	36	0.70	6	21	1.55	2	25	0.77	2	28	0.97	7	27	0.375	2	19	0.945	2
Rb			0		0	0			0			0			0			0
Sr	0.020	0.011	2	0.11	0.049	2	0.11	0.08	2	0.014	0.0054	4			0	0.015	0	1
Y	0.017	0	1	0.0039	0.00095	2	0.012	5E-05	2	0.007	0	1	0.0036	0.00055	2	0.0032	0.0016	2
Zr	0.0091	0.0019	5	0.25	0.02	2	24	3.0	2	0.0074	0.0024	7			0	0.28	0	1
Nb	0.0033	0.00088	6	0.02	0.011	2	0.12	0.052	2	0.0047	0.0011	7	0.017	0	1	0.020	0.012	2
Mo			0	0.052	0.006	2	0.0094	0	1			0			0			0
Sn	0.019	0	1			0			0	0.0066	0.0014	2	0.026	0	1			0
Ba	0.018	0	1	0.19	0.053	2	0.053	0	1	0.022	0.0094	4			0			0
La	0.0027	0.0011	6	0.010	0.0033	2	0.024	0.019	2	0.0027	0.0007	3	0.0018	0.0003	2	0.0018	0.00094	2
Ce	0.0050	0.0024	6	0.023	0.0041	2	0.056	0.0055	2	0.0045	0.00065	4	0.0023	0	1	0.0093	0	1
Pr	0.00077	0.00004	4	0.0018	0	1	0.0051	0.00055	2	0.00051	0.00007	3	0.0024	0	1			0
Nd	0.0027	0.00041	3	0.012	0	1	0.013	0	1			0			0			0
Ho	0.0011	0	1			0	0.0054	0	1	0.00084	0.00017	2			0			0
Yb	0.0012	0	1			0	0.009	0	1	0.00079	0	1			0			0
Hf	0.00048	0	1			0	0.202	0.038	2	0.0048	0	1	0.067	0.015	2			0
Ta			0	0.0086	0	1	0.046	0.016	2	0.0021	0	1			0			0
W	0.0065	0.0021	5	0.046	0.040	2	0.047	0	1	0.0012	0.00075	5			0	0.012	0	1

Pb	0.0096	0.0034	6			0	0.057	0	1	0.0132	0.0045	7	0.034	0	1			0
Th	0.0023	0.0016	6	0.0206	0	1	0.027	0	1	0.0026	0.00038	2			0			0
U	0.0017	0.00054	6	0.020	0.016	2	0.058	0.038	2	0.0015	0.0011	7	0.0037	0	1	0.0028	0	1
Fe/Mg	25			22			18			32			29			77		
Ga/Mg	0.68			0.36			0.29			0.48			0.69			0.59		
Cr/Fe	1.06			2.1			0.37			1.52			0.56			1.14		

Provenance	**Aappaluttoq, Greenland**																	
Sample	**gl2_5**	**very light pink**		**gl2_6**	**pink**		**gl2_7**	**pink**		**gl3_1**	**pink**		**gl3_2**	**very light pink**		**gl3_3**	**pink**	
N	8			9			2			4			7			7		
Element	**median / mean**	**MAD/ SD**	**n**	**median / mean**	**MAD/ SD**	**n**	**median / mean**	**MAD/ SD**	**n**	**median / mean**	**MAD/ SD**	**n**	**median / mean**	**MAD/ SD**	**n**	**median / mean**	**MAD/ SD**	**n**
Mg	48	12	8	42	4.9	9	51	2.7	2	81	5	4	59	1.5	7	59	2.6	7
Si	124	39	6	145	56	9	536	60	2	365	17	4	305	91	7	403	40	7
K	0.93	0.33	6	1.26	0.48	2			0	3.1	0.85	4	2.2	0.57	7	1.92	0.42	7
Ca(43)	836	191	8	700	264	9	495	125	2	785	88	4	656	42	7	549	144	7
Ti	114	44	8	76	13	9	71	14	2	94	16	4	101	34	7	152	66	7
V	6.8	0.60	8	24	1.13	9	6.4	1.48	2	5.9	0.24	4	2.8	0.34	7	4.8	0.41	7
Cr	260	115	8	1502	50	9	1717	1579	2	1718	165	4	436	26	7	861	196	7
Mn	0.081	0.041	6			0	0.11	0	1	0.31	0.17	2	0.26	0.11	4	0.73	0.17	3
Fe	655	25	8	1315	81	9	1566	249	2	1388	23	4	2315	197	7	1335	78	7
Ni	0.30	0.12	4	0.49	0.12	9	0.27	0	2	0.56	0.13	2	0.5	0.036	4	0.93	0.42	3
Cu	0.21	0.11	6	0.11	0.02	3	0.4	0	1	0.68	0.17	2	0.53	0.085	4	0.66	0.13	3
Zn	0.96	0.47	8	0.48	0.096	9	2.1	0.72	2	1.82	0.50	4	0.74	0.25	7	0.91	0.4	7
Ga	25	1.35	8	37	1.84	9	27	7.8	2	25	0.52	4	20	0.47	7	20	0.54	7
Rb			0			0			0			0	0.046	0	2			0
Sr	0.010	0.0017	5	0.0087	0	1	0.024	0	1	0.12	0.029	4	0.084	0.038	7	0.11	0.03	7
Y	0.011	0.0075	4	0.013	0.0074	3	0.0034	0	1	0.0061	0	1	0.0077	0.0022	7	0.0079	0.0011	4
Zr	0.0098	0.0059	3	0.012	0.002	4			0	0.22	0.094	4	0.8	0.66	7	1.27	1.04	7

Nb	0.0021	0.00032	4	0.0020	0.00023	9	0.048	0.001	2	0.012	0.0031	4	0.044	0.023	7	0.025	0.016	7
Mo			0			0			0	0.021	0.0045	2	0.032	0.011	3	0.027	0.001	3
Sn	0.0084	0.0015	3	0.024	0	1	0.031	0	1	0.020	0.0046	3	0.022	0.0035	5	0.022	0.0068	7
Ba	0.0081	0.00065	4			0			0	0.071	0.021	4	0.11	0.051	7	0.082	0.030	6
La	0.0023	0.0016	7	0.0028	0.0022	4	0.016	0.0025	2	0.0096	0.0054	4	0.0081	0.0025	7	0.015	0.0089	7
Ce	0.0068	0.0026	6	0.0027	0.0014	6	0.043	0.014	2	0.029	0.0087	4	0.024	0.0083	7	0.027	0.015	7
Pr	0.00081	0.00037	6	0.0025	0.00065	4	0.0031	0.00005	2	0.0046	0.0017	4	0.0076	0.0039	7	0.0049	0.0030	7
Nd	0.0029	0.0013	6	0.015	0.0045	3			0	0.0093	0.002	2	0.011	0.0037	7	0.0082	0.0028	5
Ho	0.0006	0.00014	2	0.00038	0.00021	3	0.0028	0	1	0.0019	0	1	0.0014	0.00042	2	0.0041	0.0011	2
Yb	0.0013	0.00005	3	0.00178	0	1			0	0.0048	0	1	0.0101	0.0051	4	0.0083	0.0013	3
Hf	0.00052	0.00027	2			0			0	0.0087	0.0059	3	0.026	0.022	7	0.046	0.028	6
Ta	0.0019	0.00069	4			0	0.0085	0	1	0.0078	0.0025	4	0.012	0.0045	6	0.0089	0.0024	7
W	0.0027	0.00066	5	0.0010	0	1	0.016	0.0064	2	0.019	0.011	3	0.041	0.018	7	0.020	0.016	7
Pb	0.018	0.006	8	0.022	0.0085	9	0.156	0	1	0.051	0.032	3	0.029	0.018	7	0.041	0.018	6
Th	0.0015	0.00048	6	0.0028	0.0015	4	0.012	0.004	2	0.005	0.0032	4	0.016	0.0035	7	0.014	0.002	7
U	0.0019	0.0014	7	0.00067	0.00044	6	0.011	0.0042	2	0.0092	0.0053	4	0.034	0.025	7	0.028	0.012	7
Fe/Mg	14			32			31			17			39			23		
Ga/Mg	0.52			0.88			0.54			0.31			0.34			0.34		
Cr/Fe	0.40			1.14			1.10			1.24			0.19			0.64		

Provenance	**Aappaluttoq, Greenland**						**Dattaw, Mandalay Region, Mogok**			**Mandalay Region, Mogok**								
Sample	**gl3_4**	**light pink**		**gl3_5**	**light pink**		**M-107637**	**pink**		**M-1_42103**	**pink**		**M-2_42103**	**pink**		**M-1_109274**	**red**	
N	4			4			4			4			4			4		
Element	**median / mean**	**MAD/ SD**	**n**	**median/ mean**	**MAD/ SD**	**n**	**median/ mean**	**MAD/ SD**	**n**	**median/ mean**	**MAD/ SD**	**n**	**median/ mean**	**MAD/ SD**	**n**	**median/ mean**	**MAD/ SD**	**n**
Mg	122	49	4	73	6.8	4	48	16	2	57	1.1	4	34	2.16	4	121	14	4

Si	372	98	4	310	43	4			0			0			0			0
K	6.9	1.75	3	1.62	0.67	4	0.59		1			0			0	1.73	0.05	3
Ca(43)	745	55	4	873	311	4	482	71	2	1016	444	4	886	279	4	1035	564	4
Ti	66	13	4	131	36	4	95	14	2	94	0.7	4	58	2.19	4	190	19	4
V	4.8	0.11	4	6.63	0.31	4	167	0.21	2	56	2.92	4	50	2.97	4	1145	110	4
Cr	1115	262	4	265	65	4	2088	1862	2	1137	197	4	1030	51	4	7095	610	4
Mn	1.14	0.41	2	0.68	0.015	2			0			0			0			0
Fe	1409	66	4	766	3.9	4	60	0.78	2	85	6.5	4	82	0.7	4	208	7.6	4
Ni	0.57	0	1	0.48	0.29	2			0	1.10	0.61	4	0.66	0.066	4	0.94	0.55	3
Cu	0.33	0.068	2	0.36	0.14	2	0.19	0.091	2	0.37	0.23	2	0.18		1	0.22	0.044	3
Zn	0.9	0.34	4	0.73	0.21	4	1.2	0.31	2	0.50	0.21	4	0.46	0.030	4	1.53	0.12	4
Ga	20	0.08	4	21	0.13	4	42	1.32	2	13	0.51	4	30	0.5	4	93	4.7	4
Rb			0			0			0			0			0	0.038		1
Sr	0.15	0.061	4	0.070	0.018	4			0			0			0			0
Y	0.0069	0.0005	3	0.017	0.0031	4			0			0			0			0
Zr	0.77	0.44	4	0.37	0.066	4	0.022	0.025	2			0			0	0.0089	0.00095	4
Nb	0.012	0.0037	4	0.018	0.0048	4	0.0044	0.0040	2			0			0	0.0033	0.00017	4
Mo	0.022	0.007	2	0.017	0.0094	2			0			0			0			0
Sn	0.027	0.0051	2	0.021	0.0019	2	0.012	0.0011	2	0.011	0.0011	4	0.012	0.0004	4	0.019	0.00025	4
Ba	0.071	0.048	3	0.085	0.044	4			0			0			0			0
La	0.014	0.0052	4	0.020	0.0049	4			0			0			0	0.00046		1
Ce	0.029	0.0092	4	0.065	0.013	4			0			0	0.0014		1			0
Pr	0.0061	0.0029	4	0.0091	0.0013	4			0			0			0	0.00043		1
Nd	0.018	0.013	3	0.039	0.013	4	0.0015		1			0			0	0.0016	0.00010	2
Ho	0.0040	0.0012	2			0			0			0			0	0.00042		1
Yb	0.011	0	1	0.0041	0	1			0			0			0			0
Hf	0.028	0.022	3	0.0046	0.0009	4	0.0013		1			0			0	0.0012		1
Ta	0.0081	0.0052	2	0.011	0.0046	4			0			0			0			0
W	0.026	0.012	4	0.017	0.0074	4			0			0			0			0
Pb	0.042	0.0031	2	0.026	0.0041	4	0.11	0.050	2	0.015	0.0036	4	0.015	0.0074	4	0.012	0.0017	4

Th	0.0093	0.0045	4	0.0049	0.0016	4			0			0			0			0
U	0.009	0.0022	4	0.017	0.0015	4	0.0035	0.0016	2			0			0			0
Fe/Mg	12			11			1.23			1.50			2.38			1.72		
Ga/Mg	0.16			0.29			0.87			0.23			0.87			0.77		
Cr/Fe	0.79			0.35			35			13			13			34		

Provenance	**Kachin State, Namya**									**Mandalay Region, Wet Loo**								
Sample	**M-2_109274**	**dark pink**		**M-3_109274**	**red**		**M-4_109274**	**red**		**M-1_110599**	**pink**		**M-2_110599**	**dark pink**		**M-3_110599**	**pink**	
N	4			4			4			2			2			2		
Element	**median/ mean**	**MAD/ SD**	**n**	**median/ mean**	**MAD/ SD**	**n**	**median/ mean**	**MAD/ SD**	**n**	**median/ mean**	**MAD/ SD**	**n**	**median/ mean**	**MAD/ SD**	**n**	**median/ mean**	**MAD/ SD**	**n**
Mg	50	3.0	4	79	32	4	46	6.0	4	46	3.7	2	65	17	2	80	0.71	2
Si			0			0			0			0			0			0
K			0	0.75		3			0	0.67		1	0.74		1			0
Ca(43)	637	207	4	902	309	4	764	219	4	728	178	2	1283	180	2	1119	210	2
Ti	79	5.8	4	129	51	4	78	9.8	4	77	3.9	2	105	30	2	134	0.21	2
V	178	8.9	4	653	185	4	331	21	4	254	6.7	2	343	17	2	332	13	2
Cr	1916	76	4	3080	124	4	3209	14	4	1468	23	2	2165	216	2	1466	235	2
Mn			0			0			0			0			0			0
Fe	56	1.45	4	67	4.9	4	71	4.3	4	255	17	2	196	28	2	161	4.6	2
Ni	0.86	0.26	4			0	0.28	0.062	3	0.97	0.66	2	0.47	0.086	2	0.59	0.013	2
Cu	0.33		1	0.32	0.076	2	0.21	0.053	2	0.11		1	0.16	0.032	2	0.13		1
Zn	0.42	0.046	4	0.52	0.014	4	0.30	0.038	4	0.35	0.029	2	0.48	0.058	2	0.38	0.016	2
Ga	17	0.22	4	77	4.8	4	60	2.1	4	133	2.9	2	174	15	2	149	11	2
Rb			0			0			0			0			0			0
Sr			0			0			0			0			0			0
Y			0			0			0			0	0.0104		1			0
Zr	0.0074	0.0011	4	0.0081	0.001	3	0.0052		1	0.004		1	0.012		1	0.015		1
Nb	0.0013	0.00009	3	0.0036	0.0023	2	0.0020	0.00003	4			0	0.0020		1	0.0050	0.0040	2

Mo			0			0			0			0			0			0
Sn	0.0097	0.00035	4	0.0113	0.00085	4	0.011	0.0013	4	0.026	0.0012	2	0.026	0.0033	2	0.024	0.0014	2
Ba			0			0			0			0			0			0
La			0			0			0			0	0.022		1			0
Ce			0			0			0	0.00053		1	0.032		1			0
Pr	0.00035		1			0			0			0	0.0084		1			0
Nd	0.0011		1			0			0			0	0.016	0.018	2			0
Ho			0			0			0			0			0			0
Yb			0			0			0			0			0			0
Hf	0.00090	0.00032	2	0.004		1			0			0			0			0
Ta			0	0.0013		1			0			0			0			0
W			0			0			0			0	0.0033	0.00011	2	0.0039		1
Pb	0.011	0.0006	4	0.012	0.0011	4	0.0089	0.0016	4	0.017	0.012	2	0.029	0.014	2	0.014	0.0072	2
Th			0	0.0011		1			0			0	0.0029	0.0033	2	0.0029	0.00045	2
U	0.0003	0.00011	2	0.014		1			0	0.00028		1	0.00088		1	0.00068	0.00013	2
Fe/Mg	1.11			0.85			1.53			5.5			3.0			2.0		
Ga/Mg	0.34			0.97			1.28			2.9			2.7			1.88		
Cr/Fe	34			46			45			5.8			11			9.1		

Provenance				**Mandalay Region, Sagyin**														
Sample	**M-4_110599**	**pink**		**M-1_112701**	**dark pink**		**M-2_112701**	**dark pink**		**M-3_112701**	**dark pink**		**M-4_112701**	**red**		**M-5_112701**	**pink**	
N	2			3			3			3			3			3		
Element	**median/ mean**	**MAD/ SD**	**n**	**median/ mean**	**MAD/ SD**	**n**	**median/ mean**	**MAD/ SD**	**n**	**median/ mean**	**MAD/ SD**	**n**	**median/ mean**	**MAD/ SD**	**n**	**median/ mean**	**MAD/ SD**	**n**
Mg	71	3.6	2	122	1.3	3	81	19	3	114	5.9	3	129	2.2	3	129	4.9	3
Si			0			0			0			0			0			0
K			0			0	1.02		1			0			0			0
Ca(43)	836	253	2	773	460	3	1083	247	3	828	363	3	920	350	3	788	412	3

Ti	118	2.8	2	203	7.8	3	129	22	3	186	7.8	3	207	0.5	3	206	11	3
V	312	22	2	272	6.8	3	352	12	3	187	21	3	337	4	3	206	25	3
Cr	1431	224	2	2540	169	3	2809	381	3	2740	158	3	6850	130	3	1199	51	3
Mn			0			0			0			0			0			0
Fe	222	35	2	145	4.2	3	84.7	0.4	3	70	1.8	3	111	10	3	131	7.8	3
Ni	0.26	0.0078	2	0.31		1	0.25		1	0.53	0.015	2	0.78	0.27	3	0.80	0.36	3
Cu	0.088		1	0.39		1	0.44	0.45	2	0.24	0.033	3	0.295	0.092	2	0.25		1
Zn	0.29	0.026	2	0.78	0.03	3	0.51	0.078	3	0.49	0.013	3	1.096	0.136	3	0.94	0.085	3
Ga	147	9.3	2	154	17	3	140	0.7	3	157	4	3	152	8.6	3	132	0.7	3
Rb			0			0			0			0			0			0
Sr			0			0			0			0			0			0
Y			0			0			0			0			0			0
Zr	0.0041		1	0.009		1	0.0063	0.0003	3	0.0070	0.00092	2	0.0082	0.00075	3	0.082	0.063	2
Nb			0	0.0017		1	0.002	0.00071	2	0.0022		1	0.0030	0.00035	3	0.0062	0.0061	2
Mo			0			0			0			0			0			0
Sn	0.027	0.0042	2	0.020	0.0015	3	0.012	0.0032	3	0.014	0.0005	3	0.021	0.00010	3	0.017	0.0024	3
Ba			0			0			0			0			0			0
La			0			0			0			0			0			0
Ce			0	0.00077		1			0			0	0.0011		1			0
Pr			0			0						0			0			0
Nd			0			0			0			0			0			0
Ho			0			0			0			0			0			0
Yb			0			0			0			0			0			0
Hf			0			0			0			0			0	0.0031		1
Ta			0			0			0			0			0			0
W			0			0			0			0	0.0016		1	0.0082	0.0092	2
Pb	0.0085	0.0028	2	0.011	0.0008	3	0.0092	0.0002	3	0.0081	0.0009	3	0.0098	0.0021	3	0.0087	0.0007	3
Th			0			0			0			0			0			0
U			0	0.00059	0.00032	2			0			0			0	0.0046	0.0034	2

Fe/Mg	3.1	1.19	1.05	0.61	0.86	1.01
Ga/Mg	2.1	1.26	1.73	1.38	1.18	1.02
Cr/Fe	6.4	18	33	39	62	9.2

Provenance	**Luc Yen, Vietnam**																	
Sample	**V-109310a**	**very light pink**		**V-109310b**	**very light pink**		**V-109310c**	**light pink**		**V-106502**	**light pink**		**LYV**	**very light pink**		**V-109086**	**pink**	
N	4					4	3			4			4			4		
Element	**median / mean**	**MAD/ SD**	**n**	**median/ mean**	**MAD/ SD**	**n**	**median/ mean**	**MAD/ SD**	**n**	**median/ mean**	**MAD/ SD**	**n**	**median/ mean**	**MAD/ SD**	**n**	**median/ mean**	**MAD/ SD**	**n**
Mg	17	0.33	4	52	7.1	4	56	7.1	4	25	3.3	4	123	7.1	4	37	3.8	4
Si			0			0			0			0			0			0
K	0.77		1			0	0.60		1	1.22		1			0	0.57		1
Ca(43)	816	189	4	730	301	4	811	140	4	931	152	4	926	46	4	941	106	4
Ti	50	14	4	222	53	4	124	12	4	176	114	4	383	141	4	61	4.6	4
V	61	4.0	4	100	1.30	4	97	3.8	4	28	3.1	4	55	0.4	4	53	12	4
Cr	267	25	4	276	19	4	715	196	4	501	105	4	257	40	4	1623	871	4
Mn			0			0			0	0.059	0.041	3	0.017		1	0.066	0.037	2
Fe	65	0.75	4	52	2.5	4	238	20	4	140	11	4	1316	3.3	4	140	18	4
Ni	0.49	0.23	4	0.50	0.095	4	0.54	0.21	4	0.28	0.039	3	0.38	0.055	4	0.36	0.084	4
Cu	0.11		1	0.24		1	0.093		1	0.21		1	0.16	0.0014	2	0.22	0.024	2
Zn	0.32	0.042	4	0.40	0.011	4	0.38	0.076	4	0.31	0.051	4	0.34	0.020	4	0.45	0.037	4
Ga	59	1.1	4	74	0.9	4	57	2.2	4	77	2.1	4	25	0.92	4	24	3.4	4
Rb			0			0			0			0			0			0
Sr			0			0			0	0.019		1			0	0.029	0.013	2
Y			0			0			0	0.0081		1			0	0.0053	0.00092	2
Zr			0			0			0			0			0	0.012	0.0072	2
Nb			0	0.0048		1			0			0	0.0052	0.00042	2	0.0018	0.00024	3
Mo			0			0			0			0			0			0

Sn	0.013	0.0014	4	0.12	0.057	4	0.019	0.00095	4	0.022	0.0025	3	0.28	0.089	4	0.013	0.0045	4
Ba			0			0			0			0			0			0
La			0			0			0	0.013	0.0008	3			0	0.0039	0.00009	3
Ce			0			0			0	0.019	0.0079	3	0.00109		1	0.0043	0.00014	3
Pr			0			0			0	0.0024	0.00077	3			0	0.0011	0.00027	3
Nd			0			0	0.0012		1	0.0064	0.0015	3			0	0.0066	0.001	3
Ho			0			0			0			0			0			0
Yb			0			0	0.0012		1			0			0			0
Hf			0			0			0			0			0			0
Ta			0	0.013	0.0081	4	0.0026		1	0.00148		1	0.0012		1			0
W			0	0.0023	0.00025	2			0	0.13	0.12	3	0.0021		1	0.0052	0.0016	2
Pb	0.024	0.0073	4	0.033	0.012	4	0.038	0.0082	4	0.036	0.0067	4	0.021	0.0067	4	0.019	0.0051	4
Th			0			0			0	0.039	0.022	3	0.0042	0.0016	4	0.0014	0.00014	3
U			0			0			0	0.00096	0.00003	3	0.0018	0.00021	4	0.0013	0.00021	3
Fe/Mg	3.7			1.00			4.2			5.5			11			3.7		
Ga/Mg	3.4			1.42			1.02			3.0			0.20			0.64		
Cr/Fe	4.1			5.3			3.0			3.6			0.20			12		

N = number of spots analysed

n = number of spots analysed > LOQ

Figure C1: TOF-LA-ICPMS multi-elemental imaging results. Multi-elemental intensity images and quantitative images of Ti, Cr, Fe and Ga. The black line encircles the ruby grain.

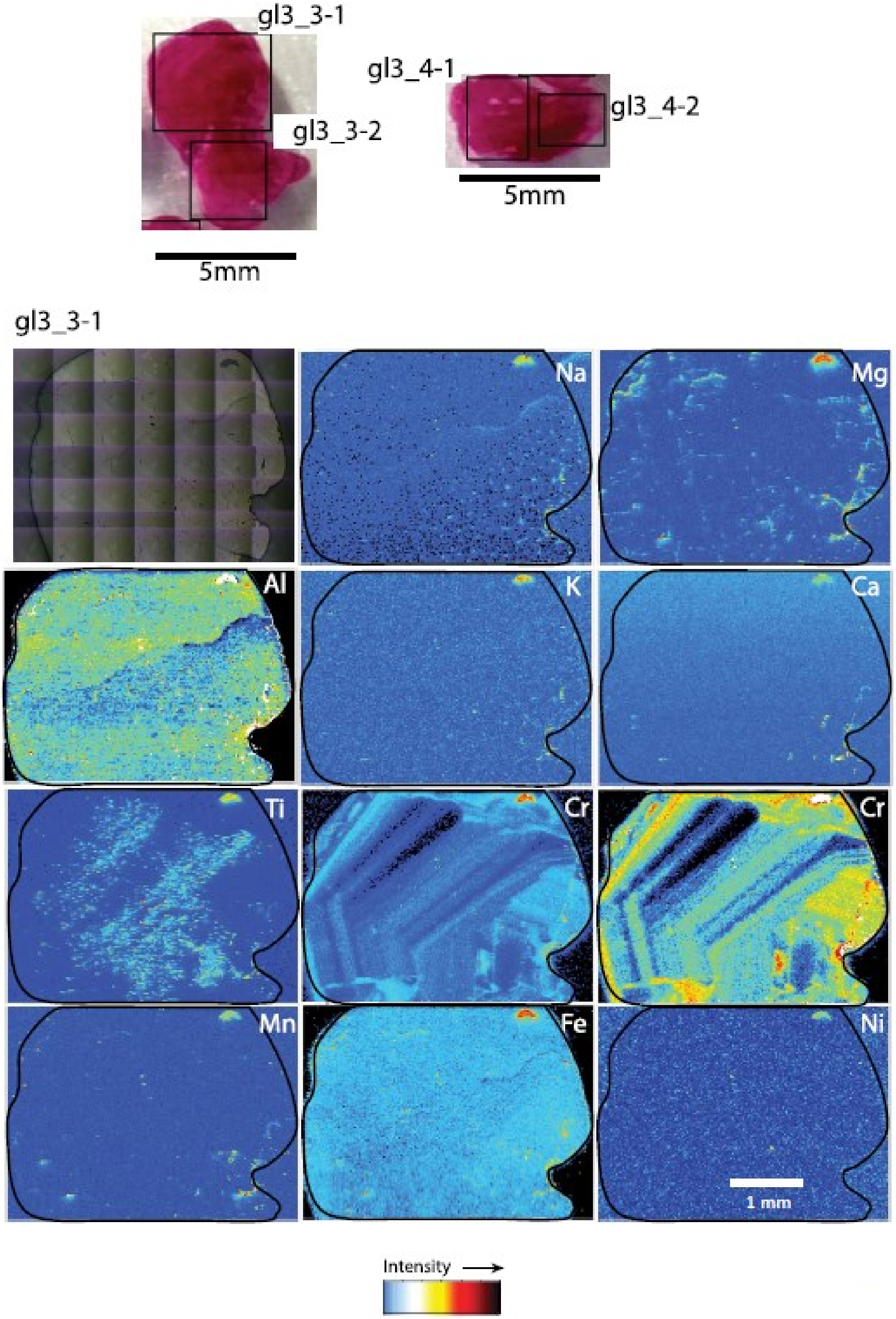

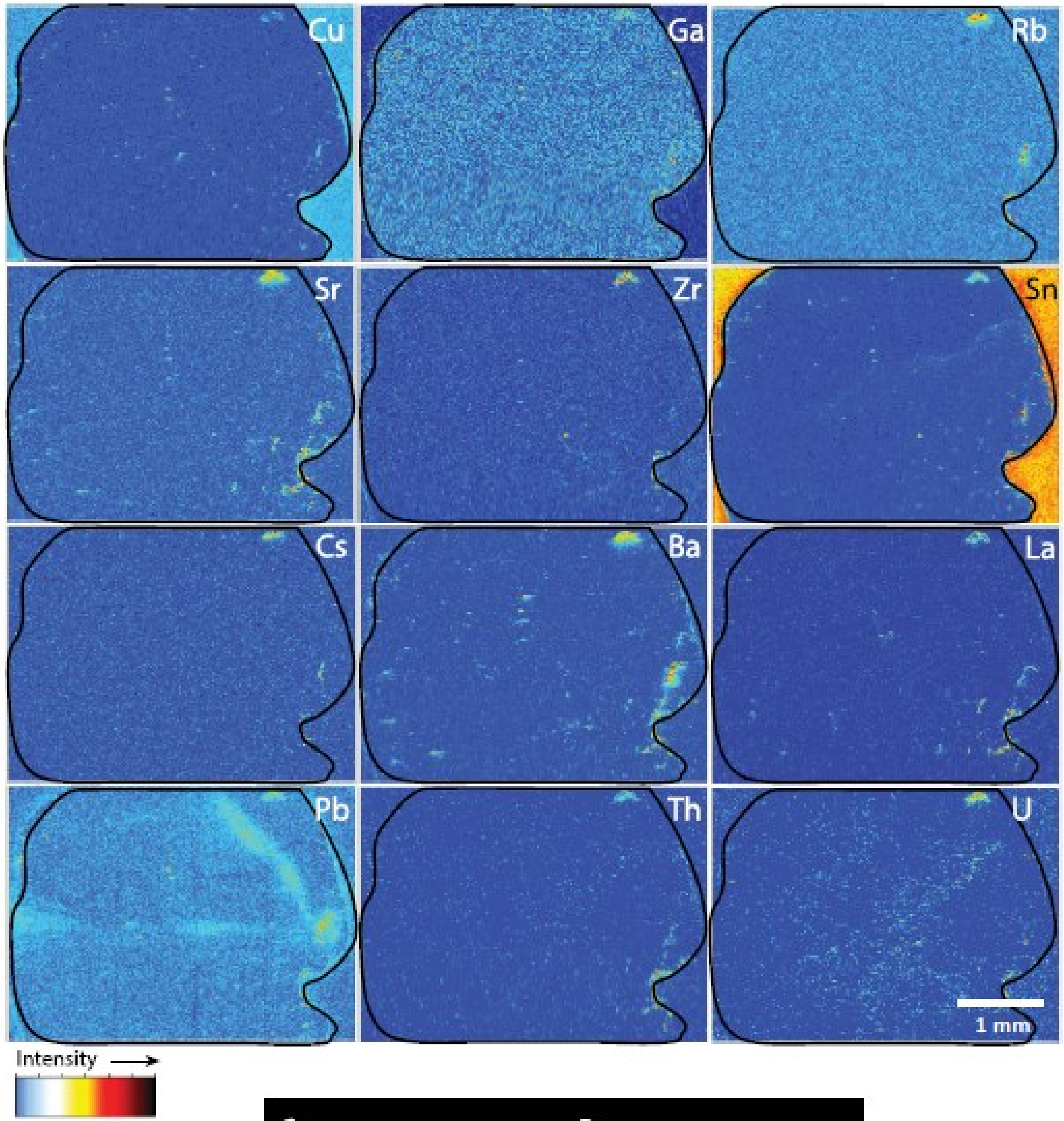
Cu
Ga
Rb
Sr
Zr
Sn
Cs
Ba
La
Pb
Th
U
1 mm
Intensity

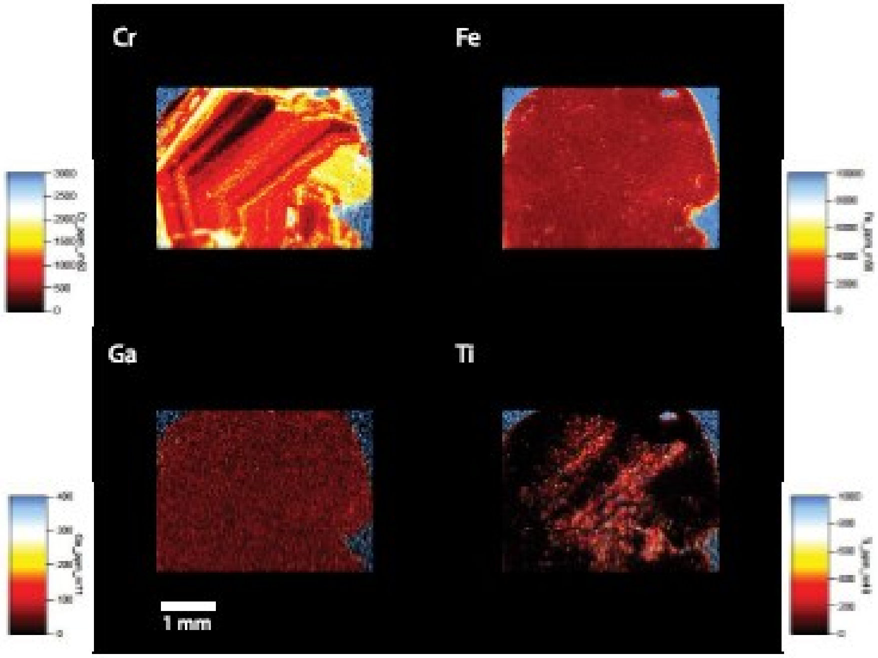
Cr
Fe
Ga
Ti
1 mm
3000
2500
2000
1500
1000
500
0
10000
8000
6000
4000
2000
0
400
300
200
100
0
1000
800
600
400
200
0

gl3_3-2

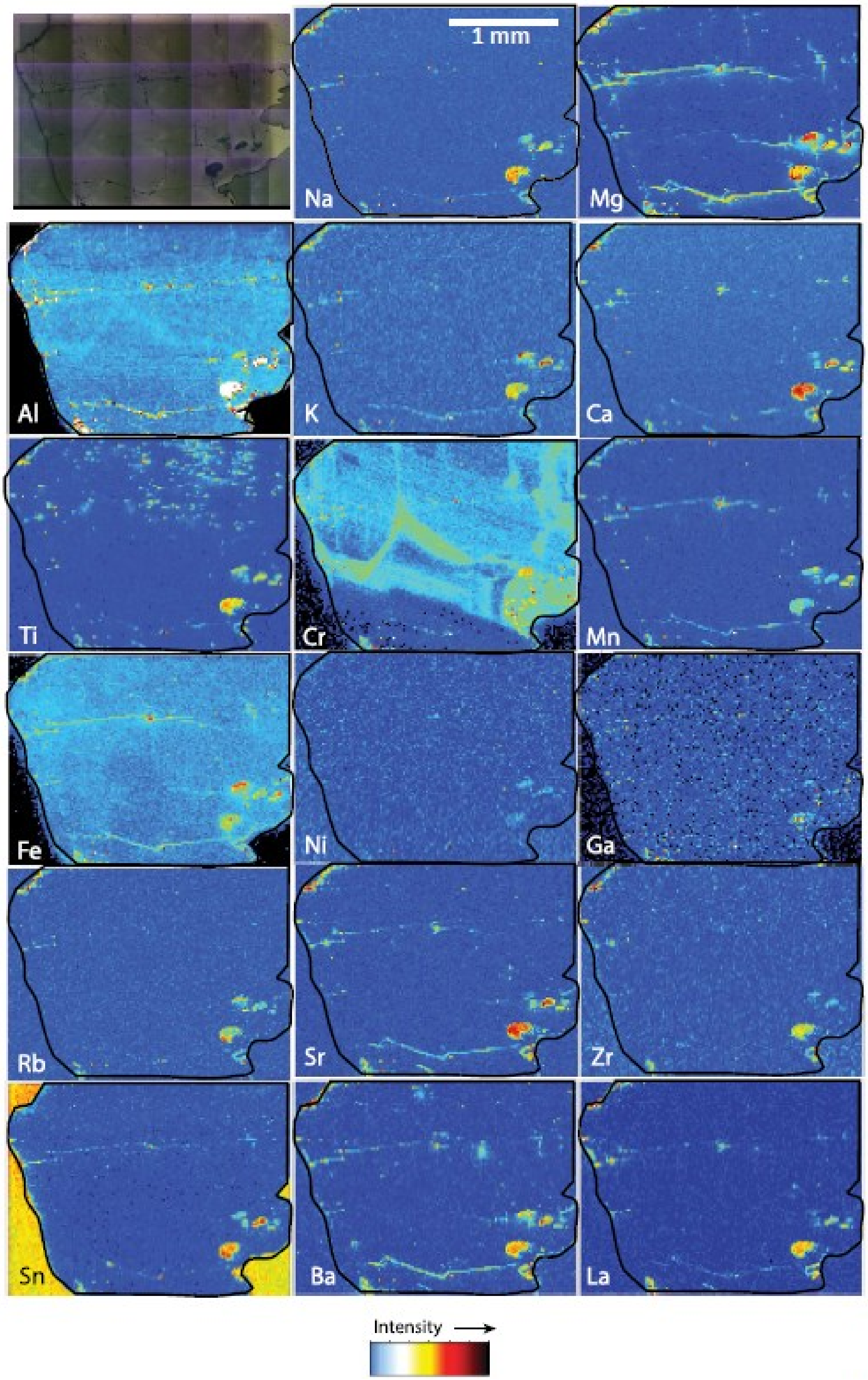

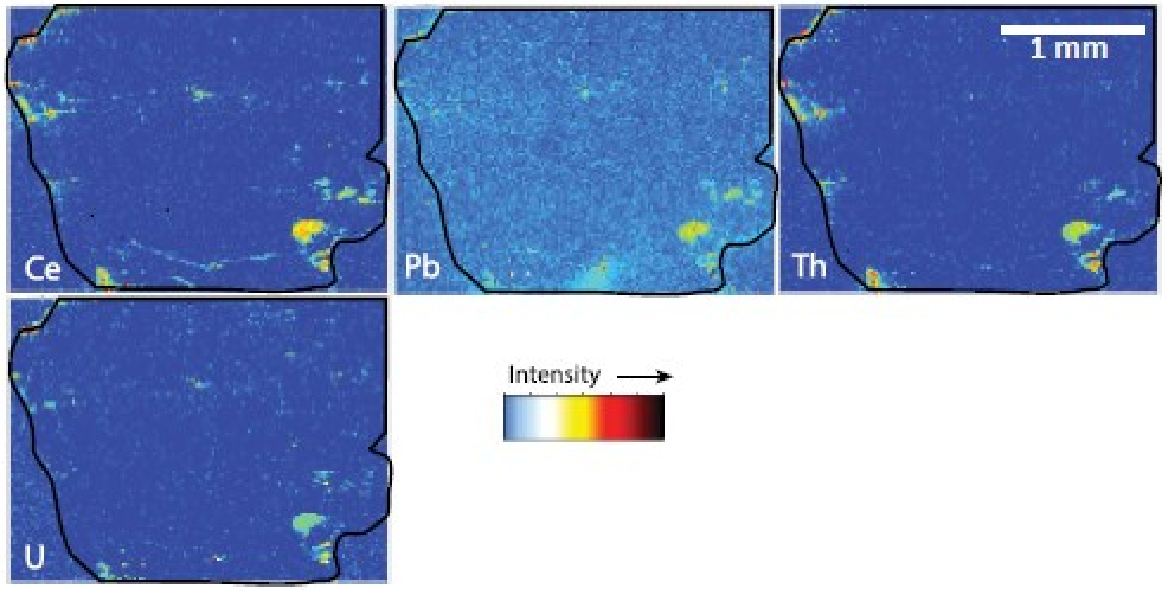
1 mm
Ce
Pb
Th
U
Intensity

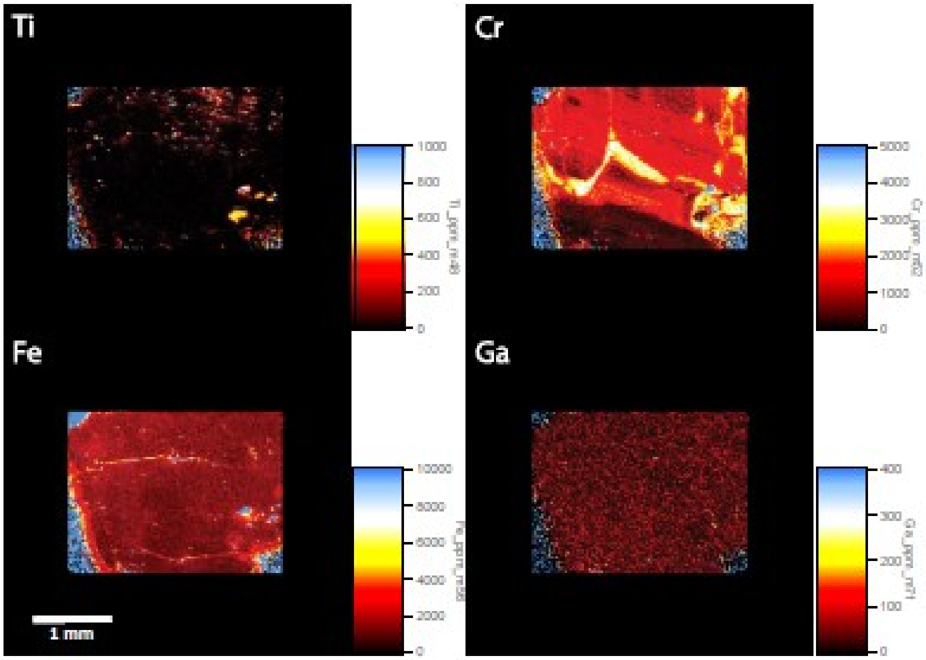
Ti
Cr
Fe
Ga
1000
800
600
400
200
0
Ti_ppm_m49
5000
4000
3000
2000
1000
0
Cr_ppm_m52
10000
8000
6000
4000
2000
0
Fe_ppm_m56
400
300
200
100
0
Ga_ppm_m71
1 mm

gl3_4-1

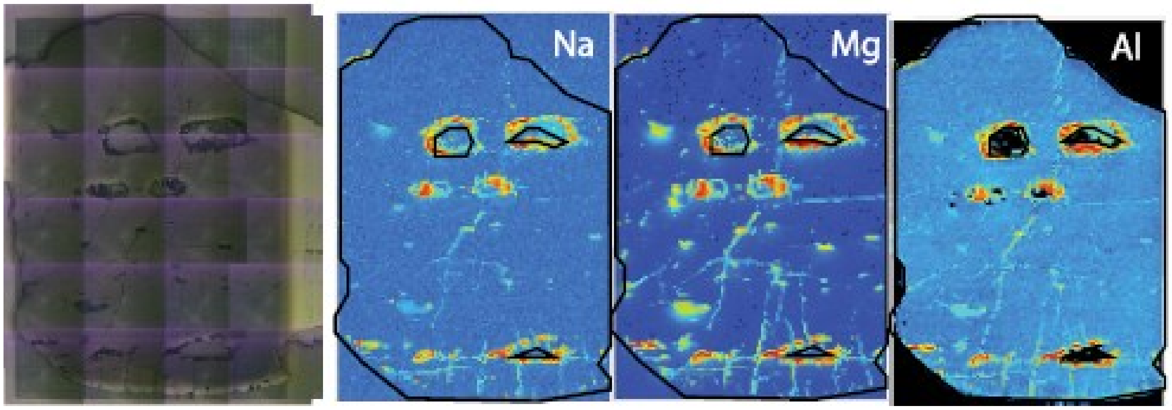
Na
Mg
Al

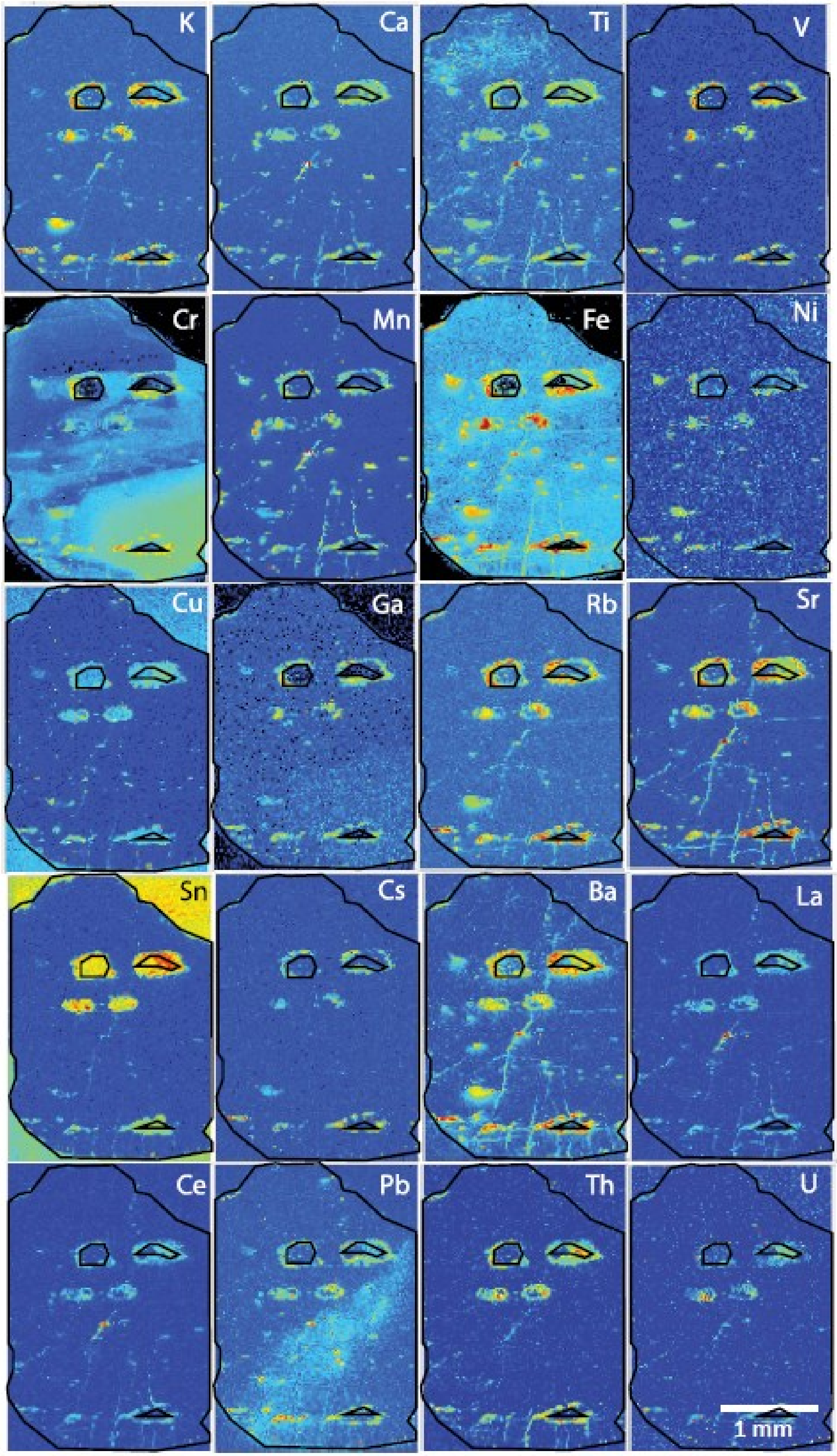
K
Ca
Ti
V
Cr
Mn
Fe
Ni
Cu
Ga
Rb
Sr
Sn
Cs
Ba
La
Ce
Pb
Th
U
1 mm

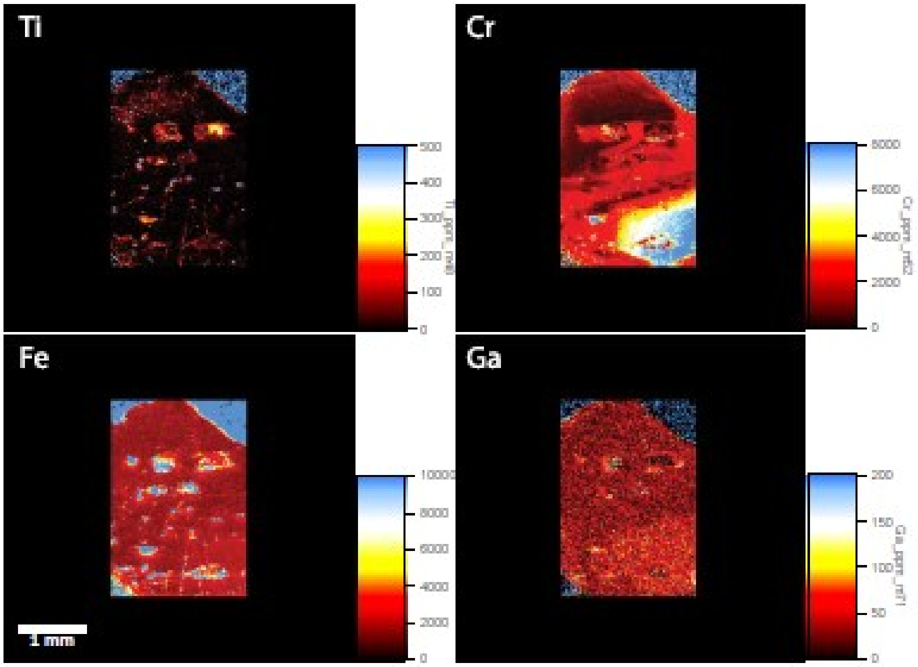
Ti
Cr
Fe
Ga
500
400
300
200
100
0
Ti_ppm_m49
8000
6000
4000
2000
0
Cr_ppm_m52
10000
8000
6000
4000
2000
0
200
150
100
50
0
Ga_ppm_m71
1 mm

gl3_4-2

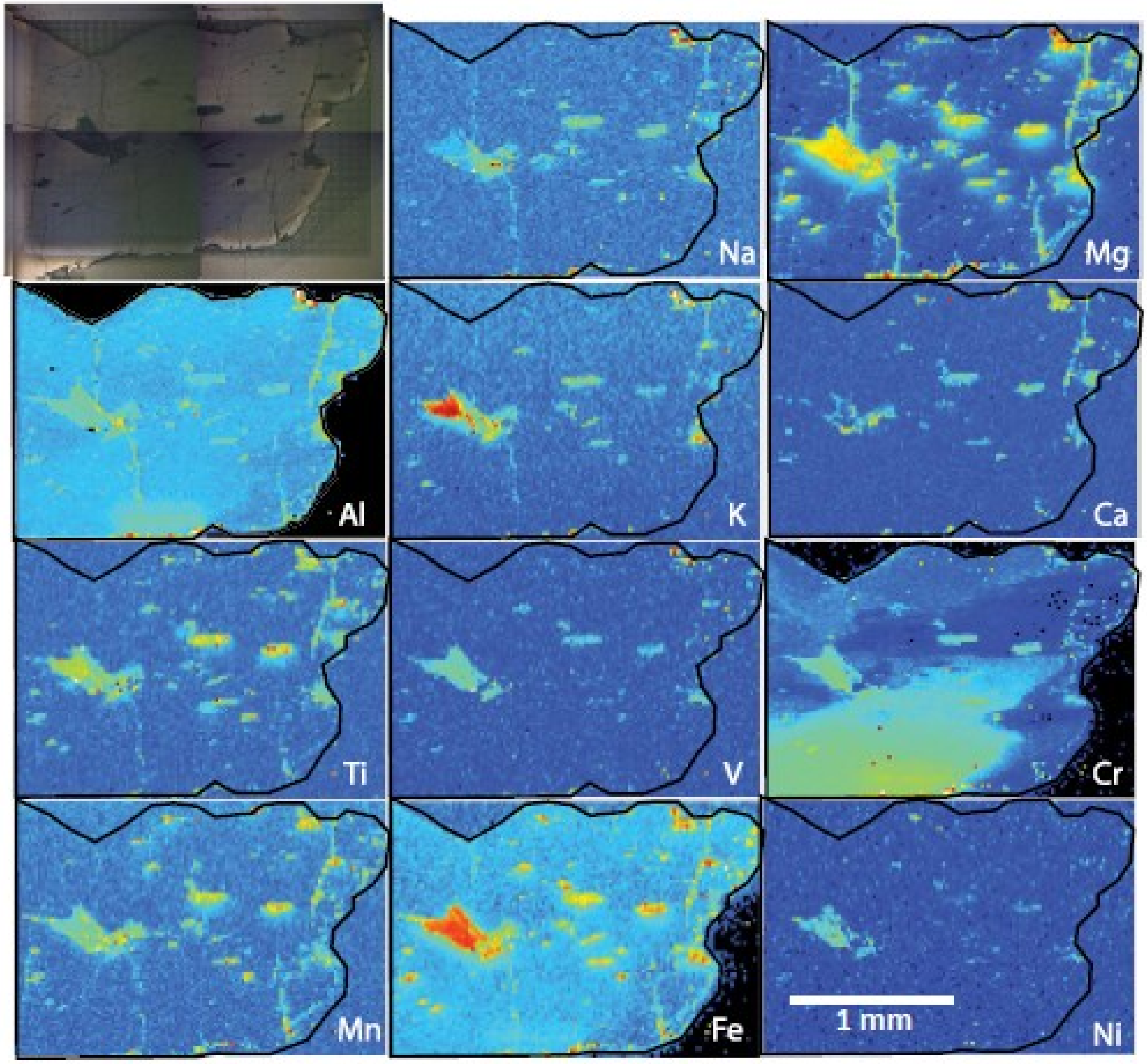
Na
Mg
Al
K
Ca
Ti
V
Cr
Mn
Fe
Ni
1 mm

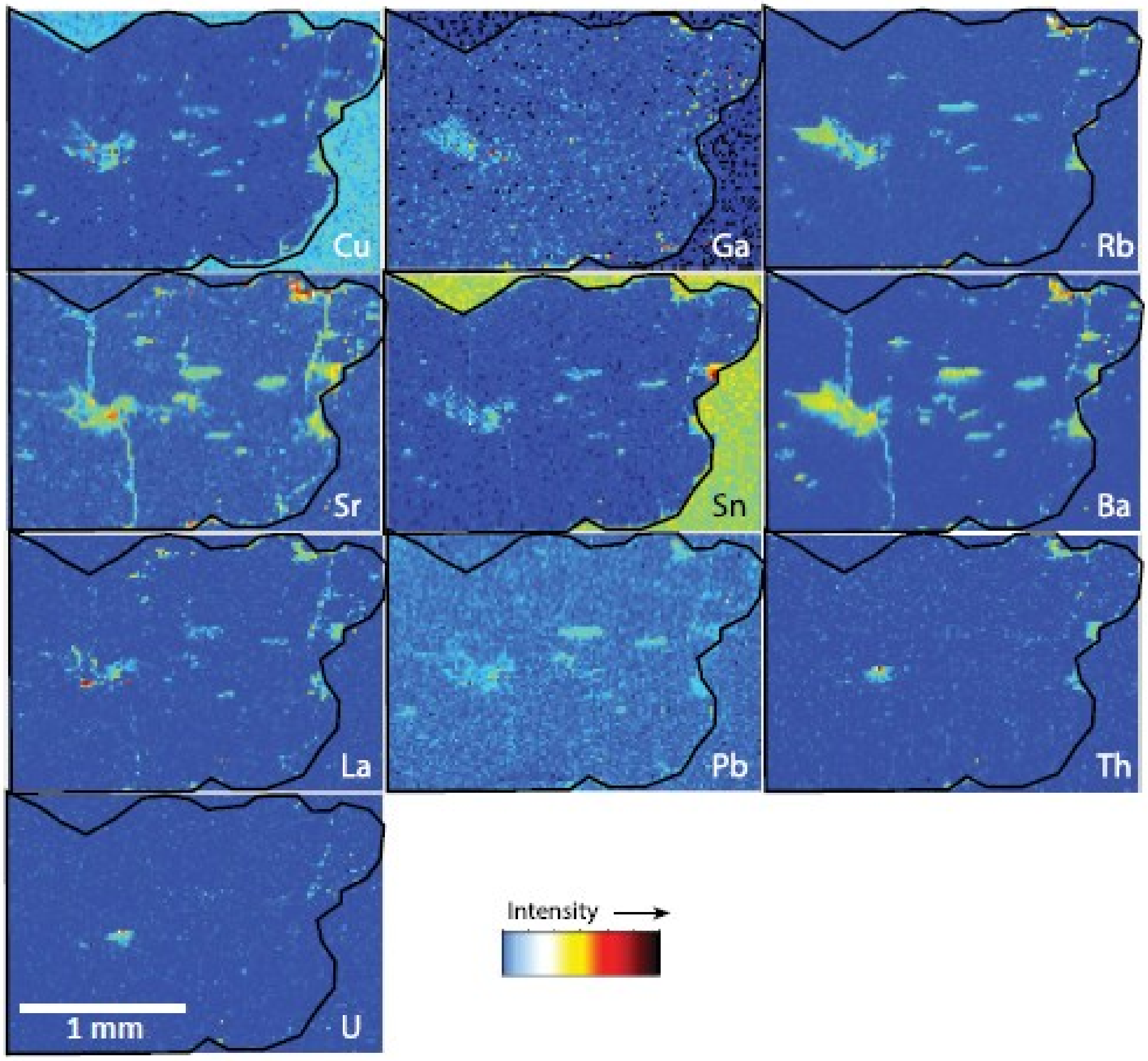
Cu
Ga
Rb
Sr
Sn
Ba
La
Pb
Th
U
1 mm
Intensity

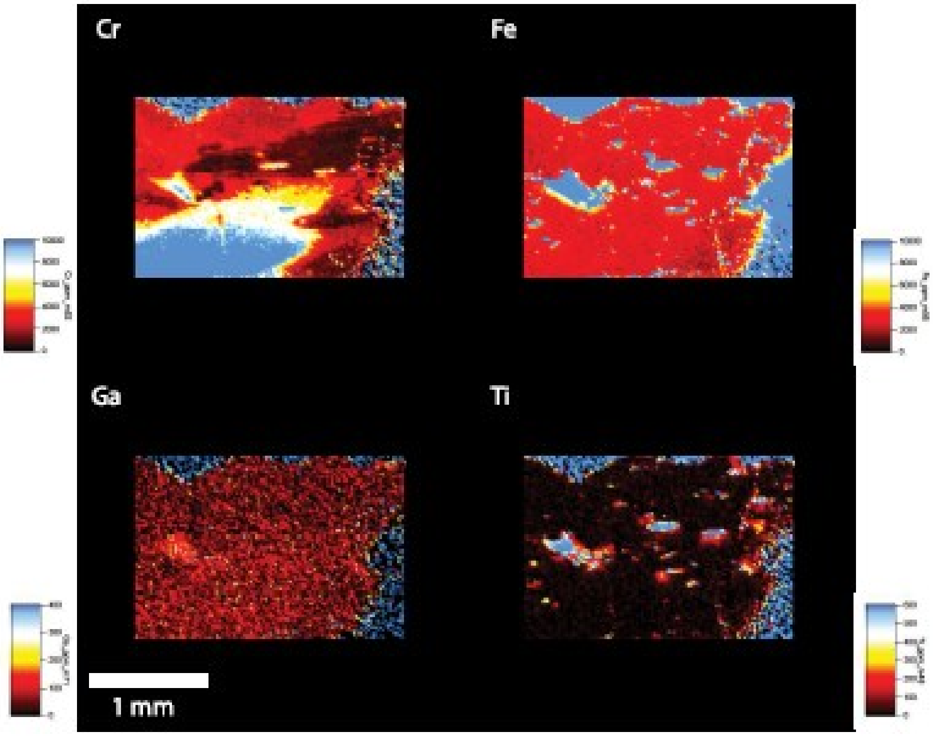
Cr
Fe
Ga
Ti
1 mm